2ND INTERNATIONAL CONFERENCE ON IRON-SULFIDE REACTIONS IN CONCRETE

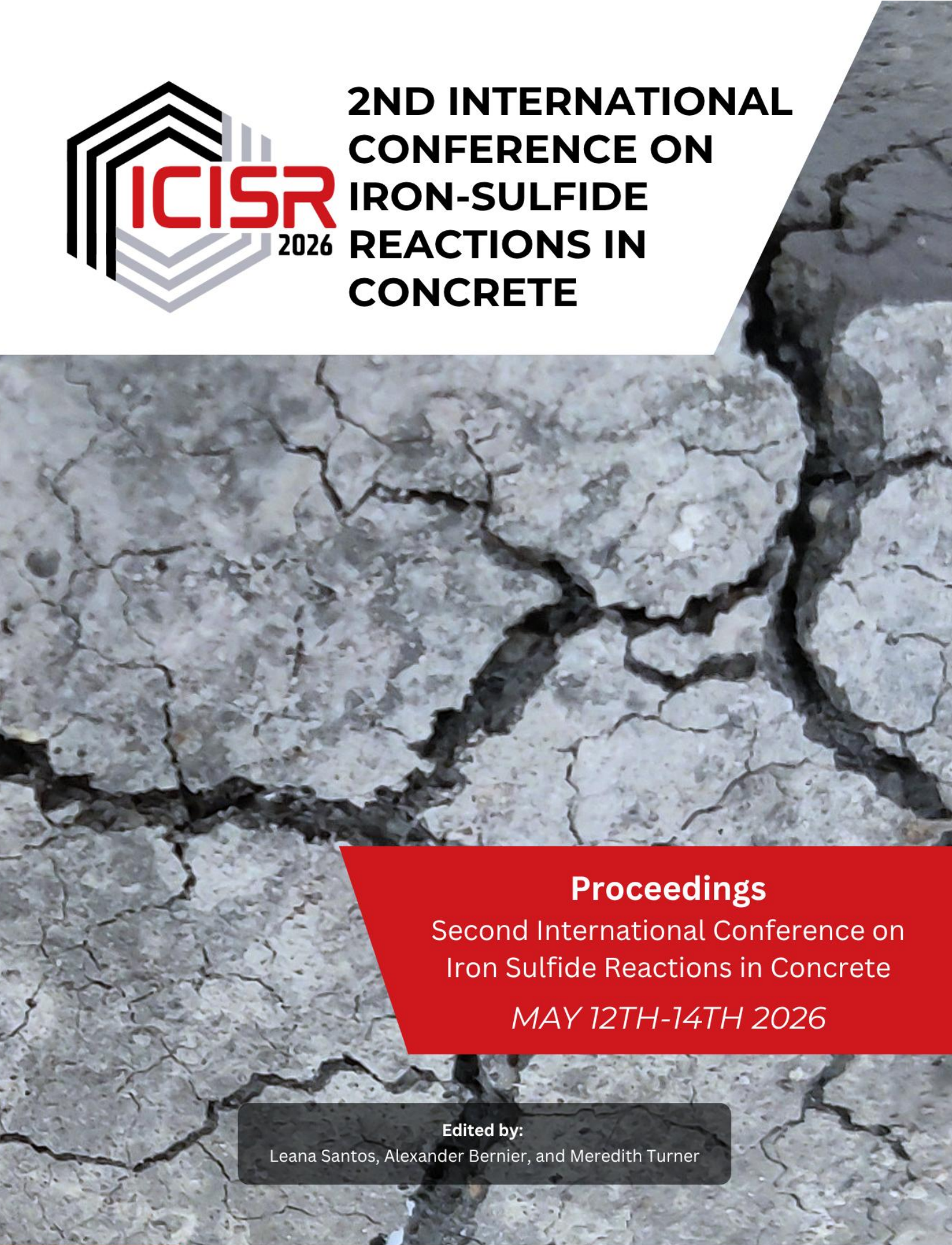

Proceedings

Second International Conference on Iron Sulfide Reactions in Concrete

MAY 12TH-14TH 2026

Edited by:
Leana Santos, Alexander Bernier, and Meredith Turner

ICISR 2026

2nd International Conference on Iron-Sulfide Reactions in Concrete

Thank you to our generous sponsors!

Gold

CCIA

Connecticut Construction Industries Association

Shaping the Future of the Construction Industry

Silver

SGI SHRIMER GEOCONSULTING INC.

NSSGA

Foundation Solutions of NE, LLC

Bronze

STERLING CONCRETE

CRMCA INC. A Division of CCIA

Massachusetts Concrete & Aggregate Products Association MaCAPA

CRIB Centre de recherche sur les infrastructures en béton Research Center on Concrete Infrastructures

Hosted by:

UCONN | COLLEGE OF ENGINEERING
SCHOOL OF CIVIL AND ENVIRONMENTAL ENGINEERING

UCONN COLLEGE OF ENGINEERING
CONNECTICUT TRANSPORTATION INSTITUTE (CTI)

2nd International Conference on Iron-Sulfide Reactions in Concrete

Organizing Team

Kay Wille, Ph.D.
Conference Chair
Professor & Director of School
School of Civil & Environmental Engineering, University of Connecticut
kay.wille@uconn.edu

James Mahoney
Organizing Co-Chair
Associate & Executive Program Director
Connecticut Transportation Institute (CTI), University of Connecticut
james.mahoney@uconn.edu

Lesley Frame, Ph.D.
Technical Program Co-Chair
Associate Professor
Materials Science & Engineering, University of Connecticut
lesley.frame@uconn.edu

Leana Santos
Technical Science & Proceedings Chair
Research Associate & Adjunct Professor
School of Civil & Environmental Engineering, University of Connecticut
leana.santos@uconn.edu

Jason Robertson
Industry Relations Lead
Director of Research & Materials
Massachusetts Department of Transportation (MASSDOT)
james.mahoney@uconn.edu

Meghan Seremet
Geology Liaison
Connecticut State Geologist
CT Department of Energy and Environmental Protection
meghan.seremet@ct.gov

Alexander Bernier
Sponsorships Lead
Program Director
Connecticut Transportation Institute (CTI), University of Connecticut
alex.bernier@uconn.edu

Ryan Soucy
Logistics & Operations Lead
Research Assistant II
Connecticut Transportation Institute (CTI), University of Connecticut
ryan.soucy@uconn.edu

Meredith Turner
Communications Lead
Instructor
Department of Communication, University of Connecticut
meredith@uconn.edu

Barbara Busch
Finance and Administration Lead
Financial Assistant II
Connecticut Transportation Institute (CTI), University of Connecticut
barbara.busch@uconn.edu

Domenico (Nico) A. Tedeschi
CTDOT Liaison
Materials Evaluation & Specifications Unit
Connecticut Department of Transportation (CT DOT)
domenico.tedeschi@ct.gov

Hosted by:

UCONN | COLLEGE OF ENGINEERING
SCHOOL OF CIVIL AND ENVIRONMENTAL ENGINEERING

UCONN
COLLEGE OF ENGINEERING
CONNECTICUT TRANSPORTATION INSTITUTE (CTI)

2nd International Conference on Iron-Sulfide Reactions in Concrete

ICISR 2026

Technical Science Committee

Leana Santos
leana.santos@uconn.edu
Chair of Technical Science Committee

Lesley Frame

Eoin McGrath

Meghan Seremet

Anthony Bentivegna

Rachel Garside

Michael Mengason

Fred Shrimer

Rodolfo Castillo Araiza

Christoph Geiss

Shintaro Miyamoto

April Snyder

Josée Duchesne

Jonathan Gourley

Aleksandra Radlińska

Bradley Staniforth

Paul Dunlop

Dipayan Jana

Hadi Rashidi

Arezki Tagnit-Hamou

Pierre-Luc Fecteau

Andreas Leemann

Jason Robertson

Stephanie Watson

Isabel Fernandes

Barbara Lothenbach

Andreia Rodrigues

Kay Wille

Benoit Fournier

James Mahoney

Nick Scaglione

Rui Zhong

Hosted by:

UCONN | COLLEGE OF ENGINEERING
SCHOOL OF CIVIL AND ENVIRONMENTAL ENGINEERING

UCONN
COLLEGE OF ENGINEERING
CONNECTICUT TRANSPORTATION INSTITUTE (CTI)

Over the past several decades, concrete deterioration associated with sulfide-bearing aggregates has been reported in several regions of the world, including Canada, the United States, Ireland, and other areas. Linked to deleterious oxidation reactions, internal sulfate attack, and related damage mechanisms, this phenomenon extends beyond the technical performance of concrete, affecting homeowners, communities, policymakers, and the construction materials industry.

Research, field assessment, testing, and policy-related work have advanced the understanding of these mechanisms and supported the development of improved methods for sampling, testing, quantification, quality control, mitigation, and repair. These efforts have also underscored the need for continued collaboration across disciplines, regions, and stakeholder groups.

The 2nd International Conference on Iron-Sulfide Reactions in Concrete — ICISR 2026 — was hosted by the University of Connecticut in Mystic, Connecticut, USA, from May 12 to 14, 2026. Building on the foundation established by the first ICISR, held at Université Laval in Quebec City, Canada, in 2024, ICISR 2026 continued this international exchange by bringing together researchers, practitioners, public agencies, industry partners, homeowners, and policy stakeholders.

The theme of ICISR 2026, “Advancing Knowledge, Standards, and Solutions for Sulfide-Bearing Aggregates,” reflected the need to connect scientific understanding with practical decision-making. The conference program addressed topics ranging from testing, standardization, deterioration mechanisms, and field performance to advanced analytical methods, mitigation strategies, policy responses, economic impacts, and homeowner support.

Hosting ICISR 2026 in Connecticut was especially meaningful because the region has experienced substantial pyrrhotite-related deterioration in residential concrete foundations. The location provided an opportunity to connect international scientific knowledge with regional experience and to strengthen the bridge between research, standards, implementation, and public service.

ICISR 2026 brought together 80 participants from 6 countries. The program featured 38 oral presentations, 6 student flash talks, and 4 homeowner association presentations. Together, these contributions reflected the multidisciplinary nature of the issue and the importance of integrating scientific research, engineering practice, public policy, and community perspectives. The homeowner association presentations added an essential dimension by highlighting the lived experiences and practical needs of affected communities.

The Proceedings of ICISR 2026 include extended abstracts prepared by conference contributors and represent a collective contribution to the growing body of scientific, technical, and practical knowledge related to iron-sulfide reactions in concrete. We hope this volume will serve as a useful reference for those working to understand, assess, manage, mitigate, and prevent damage associated with sulfide-bearing aggregates.

We are sincerely grateful to all authors, presenters, participants, homeowner representatives, sponsors, committee members, and supporting organizations. Their expertise, time, collaboration, and commitment made ICISR 2026 possible and strengthened the international community working toward durable, science-based solutions for affected and at-risk communities.

Kay Wille

James Mahoney

Table of Contents

Click the ICISR logo in the bottom right corner to return to the Table of Contents

Technical Session #1: Testing and Standardization of Iron-Sulfide–Bearing Aggregates in Concrete

Monoclinic and hexagonal pyrrhotite identification using the thermomagnetic method 5

Concrete aggregate testing for iron sulphides: oxygen consumption testing interlaboratory studies in Canada to evaluate multi-laboratory variability in view of standardization 10

Concrete aggregates testing for iron sulphides: accelerated mortar bar testing interlaboratory study in Canada to evaluate multi-laboratory variability in view of standardization 16

Pyritiferous claystone – EN12620 “compliant” aggregate and the case for thin section petrography 22

Oxygen consumption test for aggregates containing iron sulfides: sample preparation and column dimension effect 28

An Oxygen-Rich Chamber Test to Evaluate Concrete Containing Sulphide-Bearing Aggregates 34

Assessment and Refinement of Analytical Chemistry Methods to Determine Sulfide Sulfur in Concrete Aggregates toward Standardization in the U.S. 40

Technical Session #2: Mechanisms and Field Performance of Iron-Sulfide–Induced Concrete Deterioration

Differences in internal sulphate attack across the Republic of Ireland and long-term implications – how far could it go? 47

Impact of sample preparation on the quantification of sulfide-bearing aggregates using XRD 53

Screening for Pyrrhotite and its Reaction Products in Concrete using Raman and Near Infrared Spectroscopy 59

Pyrrhotite-Induced Concrete Degradation - An Exploratory Data Analysis Integrating Laboratory and Field Investigations in the Trois-Rivières Region 65

Technical Session #3: Factors and Accelerated Testing Methods for Iron-Sulfide–Induced Concrete Deterioration

Influences of Aggregate, Concrete Quality and Exposure Condition on Pyrrhotite Oxidation and ISA-Related Damage in the County Donegal, Ireland – Case Studies from Damaged to Undamaged Homes and Crumbled Blocks to Strip Concrete Foundations 73

Accelerated Assessment of Sulfide-Bearing Aggregates Using the Vacuum-Bleach Injection Technique (VBIT) 80

Accelerated concrete core test for pyrrhotite bearing concrete 86

Ozone as an oxidant for accelerated testing of pyrrhotite-induced concrete degradation 92

Deleterious internal sulfate attack on concrete caused by an aggregate with low iron sulfide content 98

Quantifying iron sulfide superstructures in concrete aggregates in the recovered solids after density-based separation 104

Technical Session #4: From Research to Remediation: Policy, Practice, and Impacts of Iron-Sulfide Reactions in Concrete

From mica to pyrrhotite: charting the impacts of scientific research on Irish standards and the government grant scheme to remediate defective concrete homes in Ireland 111

Student Talks: Experimental Studies on Sulfide-Bearing Aggregates and Concrete

Effect of iron sulfide aggregate sizes and amount on electrochemically accelerated concrete deterioration 119

Phase Transformations during Electrochemically Accelerated Testing and Deterioration of Concrete with Pyrrhotite-bearing Aggregates 125

Evaluating sampling strategy for electrochemical accelerated testing of sulfide-bearing concrete 131

Technical Session #5: Case Studies and Advanced Insights into Iron-Sulfide Concrete Damage

From CT to MA: Case Studies of Crumbled Foundations from Pyrrhotite Oxidation and Internal Sulfate Attack in the Eastern US 139

Pyrrhotite-Induced Concrete Degradation - A Machine Learning Approach for Risk Assessment in the Trois-Rivières Region 145

Case study: low permeability concrete containing sulfide-bearing aggregates 150

Crack Networks and Chemistry in Pyrrhotite-Affected Concrete Extracted from a Massachusetts Site .. 157

Internal Sulfate Attack and Premature Deterioration of Structural Concrete: Lessons from China 164

Understanding the role of type of sulphide in concrete degradation: Insights from concrete electrochemical testing scheme of diverse aggregate sources. 169

Technical Session #6: Advanced Analytical Methods for Identification and Quantification of Iron-Sulfide Minerals

Rapid Quantitative Assessment of Sulphide Species and Equivalent Total Sulphur Content of Aggregate in Concrete Samples using OI AZtecFeature Analysis and UNITY BEX Mapping 177

Petrographic Methods to Identify and Quantify Iron-Sulfide Minerals in Aggregate 184

Improving sulfur analysis: a novel approach to distinguish pyrrhotite in rock aggregates 191

Interlaboratory Study on Sulfur Quantification using the Pyrrhotite in Concrete NIST Reference Material 197

Technical Session #7: Reaction Kinetics and Evaluation of Iron- Sulfide Oxidation and Secondary Product Formation

Crack Formation Modeling in Concrete Affected by Iron-Sulfide Reactions 204

Mineralogical investigation of pristine aggregate, laboratory mortar bar and concrete field sample 209

Performance of mortar mini-bar tests under different exposure conditions for evaluating iron sulfide-bearing aggregates 216

Petrographic Characterization of Aggregates Involved in Iron-Sulfide Reactions in Residential Concrete Foundations in Northern Massachusetts and the use of Point-Count Analysis to Determine the Amount of Iron Sulfide Minerals in Concrete Aggregates 222

Linking the exposure conditions of defective blocks with expansion in an Irish home by monitoring and microstructural analysis 228

Tests for Evaluating Sulphide-Bearing Aggregates based on Coarse Aggregate-Paste and Concrete Mixture 234

Student Talks: Experimental Studies on Sulfide-Bearing Aggregates and Concrete

Phase Evolution of Iron Oxyhydroxides in Pyrrhotite-Containing Concrete under Electrochemical Accelerated Testing 242

Performance Evaluation of Sulfide-Bearing Aggregates in Mortar Bars under Accelerated Oxidation Conditions 248

Effect of Specimen Geometry on the Accelerated Deterioration of Iron Sulfide-Bearing Concrete 255

Technical Session # 8: From Quarry to Foundation: Field Mapping, Case Studies, and Mitigation of Pyrrhotite Damage

Investigation of Pyrrhotite in Quarries and Sulfidic-Heave in British Columbia, Canada 262

Potential of Commercially Available Sealants to Mitigate Further Oxidation of Pyrrhotite in Existing Foundations 270

Influence of Matrix Composition and Surface Treatments on Iron Sulfide–Induced Concrete Deterioration 276

ICISR 2026

2nd International Conference on Iron-Sulfide Reactions in Concrete

Technical Session # 1:

Testing and Standardization of Iron-Sulfide–Bearing Aggregates in Concrete

UCONN | COLLEGE OF ENGINEERING
SCHOOL OF CIVIL AND ENVIRONMENTAL ENGINEERING

UCONN
COLLEGE OF ENGINEERING
CONNECTICUT TRANSPORTATION INSTITUTE (CTI)

Monoclinic and hexagonal pyrrhotite identification using the thermomagnetic method

Christoph E. Geiss [(1)], Jonathan R. Gourley [(2)]

(1) *Trinity College, Hartford, CT, USA, christoph.geiss@trincoll.edu*

(2) *Trinity College, Hartford, CT, USA, jonathan.gourley@trincoll.edu*

Abstract

The thermomagnetic method, which measures the magnetic susceptibility of a sample between room-temperature and 700°C, has been used to identify and semi-quantify the concentration of pyrrhotite in concrete and aggregate samples. It is an effective and rapid technique for homeowners and aggregate suppliers. The authors have used this method in combination with measurements of total sulphur to estimate concentrations of pyrrhotite in concrete and aggregate samples since 2017. We present data taken from over 1000 samples on how the thermomagnetic method is useful for the identification of both the monoclinic and hexagonal phases of pyrrhotite. Pyrrhotite has a specific Curie temperature of 320°C at which point the magnetism due to pyrrhotite is lost. The presence of monoclinic pyrrhotite can be quantified from the loss in magnetic susceptibility between 320°C and 340°C. Hexagonal pyrrhotite is non-magnetic, but prior to reaching the Curie temperature, reorganization of iron atoms in the mineral's crystal lattice can lead to the (partial) conversion of hexagonal pyrrhotite into the monoclinic pyrrhotite phase. An abrupt increase in magnetic susceptibility near 220°C can be used to detect the presence of hexagonal pyrrhotite in concrete or aggregate. We investigate the relationship between the relative abundance of hexagonal and monoclinic pyrrhotite phases and concrete stability to determine if one or the other phase is more important with respect to concrete deterioration. This may be especially critical at lower pyrrhotite concentrations where concrete may not yet display cracking but does contain pyrrhotite levels that statistically favour deterioration. The stability of monoclinic versus hexagonal pyrrhotite is debated in the literature. However, these data suggest an important relationship may exist which may aid in the understanding to why some concrete deteriorates faster than others.

Keywords: *pyrrhotite, identification, hexagonal, monoclinic, thermomagnetic*

1. INTRODUCTION

Thermomagnetic analyses have been used successfully to detect and quantify pyrrhotite in natural and man-made samples [e.g., 1,2-4]. In a thermomagnetic experiment, the sample is heated (in an argon atmosphere to minimize oxidation reactions) from room temperature to approximately 700°C and its magnetic susceptibility (χ) is measured during the heating process. All magnetic substances become non-magnetic above a mineral-specific temperature, the Curie Temperature (T_C), and their magnetic susceptibility drops to zero.

Pyrrhotite is a solid solution ($Fe_{1-x}S$) between FeS (Troilite) and Fe_7S_8 (monoclinic pyrrhotite). While most of its mineral phases are non-magnetic, the iron-depleted monoclinic phase (Fe_7S_8) is ferrimagnetic with a Curie temperature T_C = 325°C [e.g., 5,6]. In addition, hexagonal pyrrhotite phases undergo transformations into ferrimagnetic phases at elevated temperatures and can also be detected through thermomagnetic analyses [7,8].

Figure 1 shows examples of thermomagnetic curves. Fig. 1a represents a pyrrhotite-free sample. Magnetic susceptibility (χ) remains relatively constant between room temperature and 580°C, the Curie-temperature of magnetite (mt) [9]. Fig. 1b represents a sample containing both pyrrhotite (po) and magnetite (mt). X remains relatively constant between room-temperature and 220°C where hexagonal pyrrhotite undergoes a phase transition and becomes partially magnetic [7]. The transition is marked by a sharp increase in χ. X increases further until it reaches a maximum just below 325°C, the Curie-temperature (T_C) of pyrrhotite [5], where χ drops sharply. The remaining changes in χ are due to the

conversion of iron-bearing minerals to magnetite and the demagnetization of magnetite at 580°C, the Curie-temperature of magnetite.

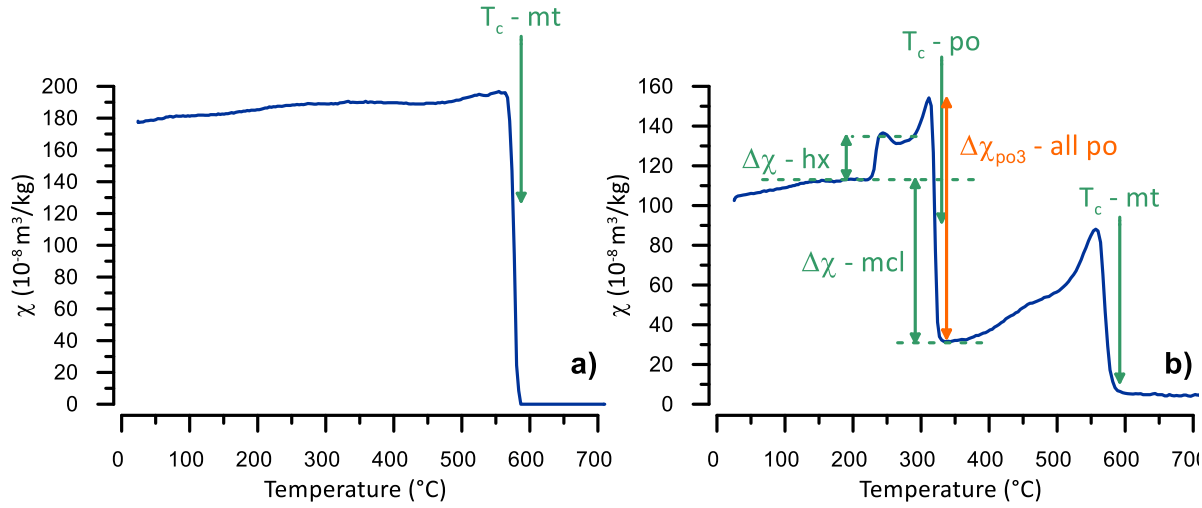

Figure. 1: Examples of thermomagnetic curves. a) sample containing magnetite b) sample containing both pyrrhotite and magnetite. For further information see text.

Figure 1b also suggests a method to discriminate between hexagonal and monoclinic pyrrhotite phases. Hexagonal phases are initially non-magnetic and do not contribute to the susceptibility signal of the sample. Upon heating they do convert, however, into ferrimagnetic phases, and the increase in χ near 220°C reflects the conversion of hexagonal into monoclinic pyrrhotite (Δχ – hx). The further increase in χ is either due to further conversion into ferrimagnetic pyrrhotite phases or the thermal unblocking of ferrimagnetic pyrrhotite as it approaches the final Curie-temperature at T_C = 325°C [5,9]. The loss in magnetic susceptibility between the pre-conversion value at ~220°C and its final Curie-temperature at T_C = 325°C is a conservative estimate for the presence of preexisting monoclinic pyrrhotite (Δχ – mcl). A more detailed analysis of thermomagnetic curves can therefore yield estimates of both hexagonal and monoclinic pyrrhotite phases.

In this study we extend our analysis of existing thermomagnetic data from over 1000 home concrete foundations to shed light on two questions: 1) Does our data suggest safe levels of pyrrhotite in concrete? and 2) Does the ratio between hexagonal (hx) and monoclinic (mcl) pyrrhotite affect concrete stability?

2. RESULTS

2.1 Pyrrhotite abundance and likelihood of concrete deterioration

Figure 2 shows the results of our analyses for over 1000 crushed core samples from Connecticut and Massachusetts following the method outlined in Geiss and Gourley [1]. Sulphur concentration has been measured using an Elementar vario Max cube elemental analyser. The amount of pyrrhotite has been estimated from the drop in magnetic susceptibility between 310°C and 325°C, which is indicated in orange in Figure 1b. The status of the investigated structure is also shown: Red circles indicate homes that display map cracking due to the presence of pyrrhotite. Yellow diamonds indicate houses that contain pyrrhotite in their structures but do not show any indication of map cracking. Green squares show homes with only trace levels of pyrrhotite that display no pyrrhotite deterioration. These observations were recorded during sample collection.

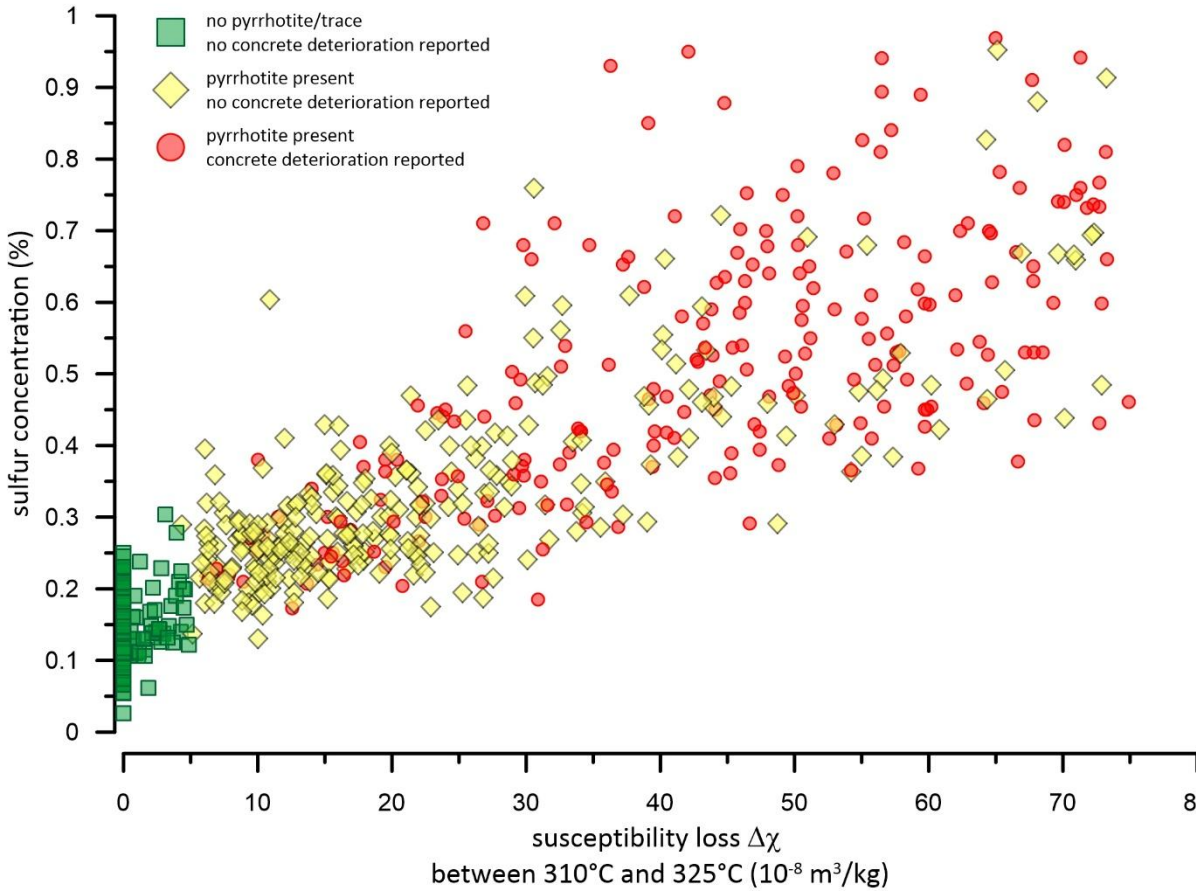

Figure 2: Total sulphur concentration (in % S) as a function of pyrrhotite abundance as determined by thermomagnetic analyses for over 1000 homes in Connecticut and Massachusetts. The status of the investigated structure is also indicated.

Figure 3 takes the same dataset and calculates the percentage of houses that show signs of concrete deterioration due to pyrrhotite (map cracking). Pyrrhotite concentrations have been estimated from the sulphur content after subtracting the average S-concentration for pyrrhotite-free samples (~0.15%). As seen in Figure 3, the amount of pyrrhotite strongly controls the likelihood of concrete deterioration but there is no clear cutoff that would indicate a “safe level” of pyrrhotite abundance in concrete.

2.2 Hexagonal vs Monoclinic Pyrrhotite

We estimated the abundance of hexagonal (hx) and monoclinic (mcl) pyrrhotite from thermomagnetic curves as outlined in the introduction (see Figure 1b). Hx/mcl ratios were calculated for 630 structures (the analysis omitted structures that were free of pyrrhotite, hence the lower number of structures analyzed). The status of the analysed structures was classified either as “shows deterioration” = 1 (same as red spheres in Figure 2) or “shows no deterioration” = 0 (all remaining pyrrhotite containing samples in Figure 2). Data were then sorted in order of increasing hx/mcl ratios and a 15 pt. running average of structure status estimated the likelihood of concrete deterioration. Figure 4a shows that samples that contain higher proportions of monoclinic pyrrhotite correlated with an increased concrete deterioration, suggesting that monoclinic pyrrhotite is less stable than hexagonal pyrrhotite.

Both Figures 2 and 3 show a strong control of pyrrhotite abundance on concrete deterioration (independent of pyrrhotite phase) we multiplied hx/mcl ratios by the total loss of susceptibility between 310°C and 325°C (χ_{po3}) and repeated our analysis. The results are shown in Figure 4b. Here, the likelihood of concrete deterioration increases rapidly for low values of hx/mcl*po3, dips slightly and reaches a plateau for the highest values of hx/mcl*po3.

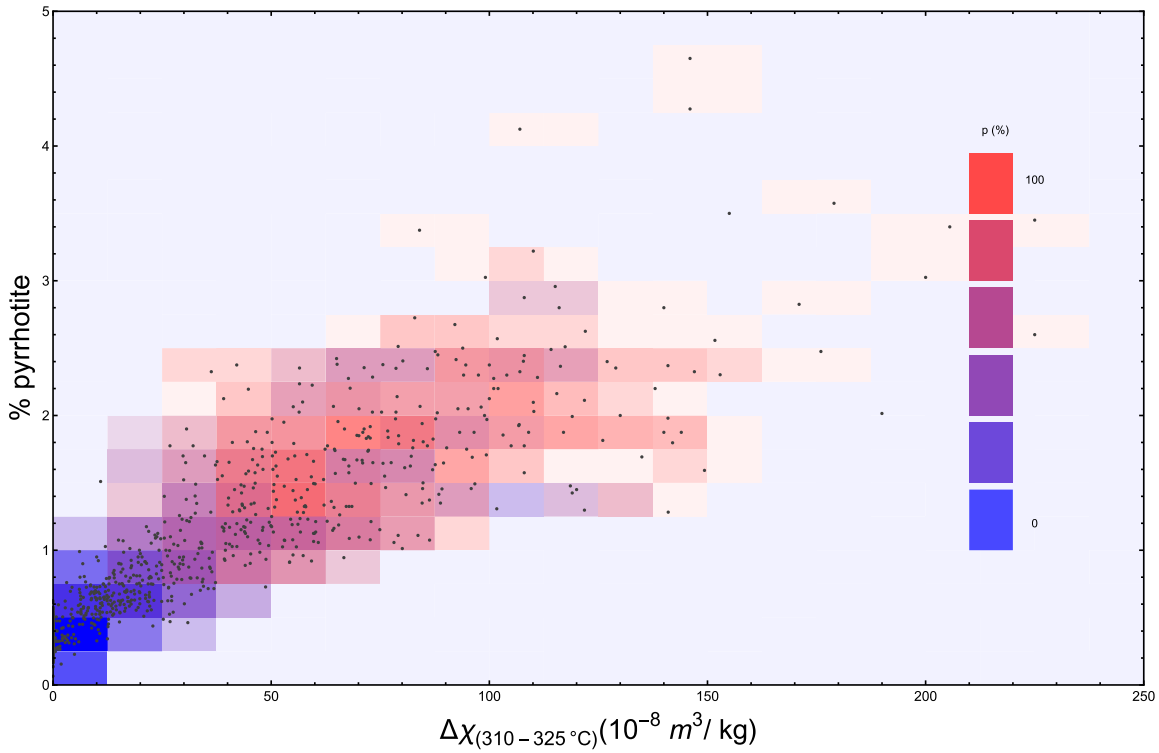

Figure 3: Likelihood of concrete deterioration. Total % pyrrhotite estimated from sulphur concentrations, change in susceptibility as shown in Figure 1b. Hue indicates likelihood of failure (red = 100%, blue = 0%), lightness of hue indicates number of structures that were used to calculate failure rate.

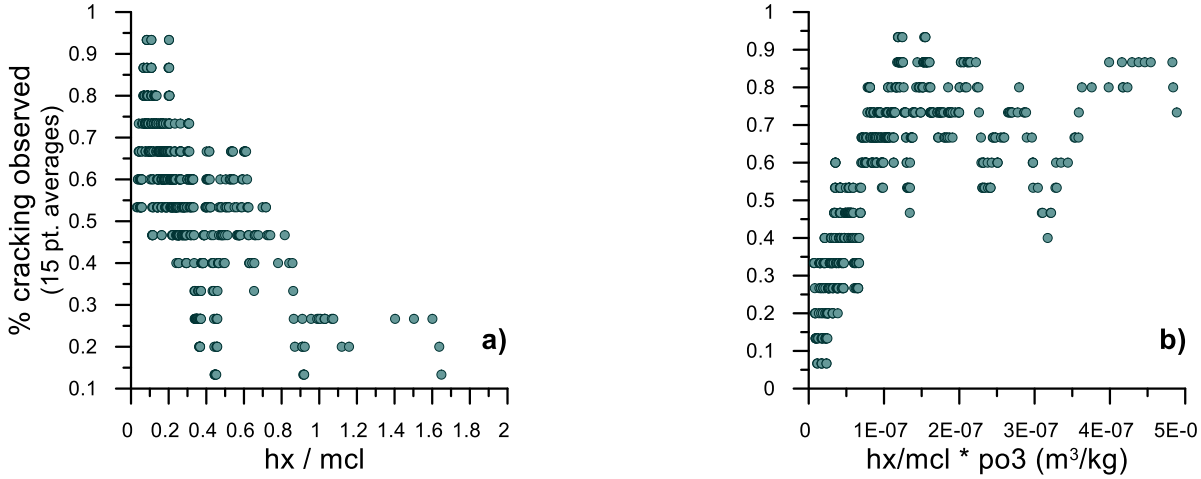

Figure 4: Likelihood of concrete deterioration as a function of a) hx/mcl and b) hx/mcl*po3. For more information see text.

3. CONCLUSIONS

Our extended analysis of over 1000 thermomagnetic curves from structures in Connecticut and Massachusetts shows a direct correlation between pyrrhotite abundance and observed concrete deterioration, independent of the pyrrhotite mineral phase. Correlative analysis suggests samples containing a higher abundance and proportion of monoclinic pyrrhotite (low hx/mcl ratios) correlate with a high risk of concrete deterioration. This suggests that the monoclinic pyrrhotite phase maybe less

stable than hexagonal phases. Our findings agree with recent studies [e.g., 10,11,12] but are in contradiction to studies by Morimoto and co-workers [13] who, based on petrological studies of natural iron sulfide ores found monoclinic Fe_7S_8 to be stable at low temperatures while hexagonal intermediate phases were only metastable.

4. REFERENCES

1. Geiss, C. E., & Gourley, J. R. (2019). A thermomagnetic technique to quantify the risk of internal sulfur attack due to pyrrhotite. *Cement and Concrete Research, 115*(C), 1-7.
2. Kontny, A., De Wall, H., Sharp, T. G., & Posfai, M. (2000). Mineralogy and magnetic behavior of pyrrhotite from a 260C section at the KTB drilling site, Germany. *American Mineralogist, 85*(10), 1416-1427.
3. van Velzen, A. J., Dekkers, M. J., & Zijderveld, J. D. A. (1993). Magnetic iron-nickel sulphides in the Pliocene and Pleistocene marine marls from the Vrica section (Calabria, Italy). *Earth and Planetary Science Letters, 115*, 43-55.
4. Vaughan, D. J., Schwarz, E. J., & Owens, D. R. (1971). Pyrrhotites from the Strathcona Mine, Sudbury, Canada: A thermomagnetic and mineralogical study. *Economic Geology, 66*, 1131 - 1144.
5. Dekkers, M. J. (1989). Magnetic properties of natural pyrrhotite. II. High- and low-temperature behaviour of J_{rs} and TRM as a function of grain size. *Physics of the Earth and Planetary Interiors, 57*, 266-283.
6. Soffel, H. C. (1971). The singledomain-multidomain transition in natural intermediate titanomagnetites. *Zeitschrift fuer Geophysik, 37*, 451-470.
7. Schwarz, E. J. (1975). Magnetic properties of pyrrhotite and their use in applied geology and geophysics. Canada: Geological Survey of Canada : Ottawa, ON, Canada.
8. Schwarz, E. J., & Vaughan, D. J. (1972). Magnetic Phase Relations of Pyrrhotite. *Journal of Geomagnetism and Geoelectricity, 24*(4), 441-458, doi:10.5636/jgg.24.441.
9. Dunlop, D. J., & Özdemir, Ö. (1997). *Rock Magnetism, Fundamentals and Frontiers* (1. ed., Cambridge Studies in Magnetism). Cambridge, New York: Cambridge University Press.
10. Belzile, N., Chen, Y.-W., Cai, M.-F., & Li, Y. (2004). A review on pyrrhotite oxidation. *Journal of Geochemical Exploration, 84*(2), 65-76, doi:https://doi.org/10.1016/j.gexplo.2004.03.003.
11. Multani, R. S., & Waters, K. E. (2018). A review of the physicochemical properties and flotation of pyrrhotite superstructures (4C – Fe7S8/ 5C – Fe9S10) in Ni-Cu sulphide mineral processing. *The Canadian Journal of Chemical Engineering, 96*(5), 1185-1206, doi:https://doi.org/10.1002/cjce.23099.
12. Rezvani, A., Raji, F., Liu, Q., & Peng, Y. (2024). Identification and quantification of pyrrhotite superstructures in base metal sulfide ore samples: A critical review. *Minerals Engineering, 218*, 108975, doi:https://doi.org/10.1016/j.mineng.2024.108975.
13. Morimoto, N., Gyobu, A., Mukaiyama, H., & Izawa, E. (1975). Crystallography and stability of pyrrhotites. *Economic Geology and the Bulletin of the Society of Economic Geologists, 70*(4), 824-833, doi:http://dx.doi.org/10.2113/gsecongeo.70.4.824.

Concrete aggregate testing for iron sulphides: oxygen consumption testing interlaboratory studies in Canada to evaluate multi-laboratory variability in view of standardization

Pierre-Luc Fecteau [(1)], Benoit Fournier [(1)], Josée Duchesne [(1)]

(1) *Department of Geology and Geological Engineering, Université Laval, CRIB, Quebec City, Canada, pierre-luc.fecteau@ggl.ulaval.ca*

Abstract

For more than a decade in Canada, researchers have been working on accelerated tests capable of predicting the potential reactivity of sulphide-bearing aggregates before their use in concrete. The oxygen consumption test (OCT) is the second step of a quality control protocol that was included in the annex P of the CSA A23.1-A23.2 standard in the 2019 edition. This test is measuring the oxygen consumed by ground aggregate materials when mixed with a certain amount of water in a sealed reaction cell, over a 180 min testing period. As part of interlaboratory studies on the above test procedure, the following four aggregates were selected: reactive Maskimo 0.9% total sulphur (MSK 0.9%), marginally reactive Maskimo 0.2% total sulphur (MSK 0.2%), HP non-reactive limestone and a harder non-reactive aggregate (PKA). A first interlaboratory study with 14 laboratories issued highly variable results. After adjustments to the procedure, the instruction documents and the test equipment, a second trial was launched with 14 participating labs.

Test results from the interlaboratory trials show that certain grinding equipments are unsuitable for materials preparation in view of oxygen consumption testing. Cr-alloy steel disc pulverisers were found to be most suitable as they activate iron sulphides without contamination in the test. A MSK 0.9% sample provided to participants in a ready-to-test (already ground) condition showed consistent results and relatively low variability (CV of ~17%). The above results highlight the critical importance of sample preparation in the OCT test procedure. Although adjustments are still needed, the experience gained and the results obtained by the participating laboratories are promising towards standardization of the procedure.

***Keywords**: Aggregate preparation, interlaboratory studies, interlaboratory variability, iron sulphides, oxygen consumption test (OCT).*

1. INTRODUCTION AND BACKGROUND INFORMATION

Iron sulphides are accessory minerals in a large variety of rock types, pyrrhotite and pyrite being the most common. A number of significant cases of concrete deterioration due to the oxidation in sulphide-bearing aggregates (SBA) have been reported over the last few decades in Canada [1], USA [2], Ireland [3], and others.

Since 2010, extensive research has been performed in Canada to develop new tests capable of predicting the potential reactivity of SBA used in concrete structures. As the main outcome of that research, an evaluation protocol for concrete aggregates containing iron sulphide minerals [4] was proposed in 2016. The above protocol was introduced as the Annex P of CSA A23.1-A23.2-19 standards; it includes the following three steps [5]: 1) total sulphur content determination (S_T%) and petrographic examination for the identification of pyrrhotite, 2) oxygen consumption test (OCT), and 3) accelerated mortar bar test for sulphide-bearing aggregates (AMBT). A research chair (U. Laval, Toronto Metropolitan University [TMU] and National Research Council of Canada [NRC]) has been established in late 2018. As part of the research chair's main objectives, studies to establish the multi-laboratory variability (precision and bias) of the Annex P protocol's tests were organized. Background and historical information regarding the various steps towards standardization of the protocol's tests is synthesized in [6]. This paper focuses on the interlaboratory studies (i.e. two trials) conducted on the OCT, for which the principle and experimental parameters were analysed in [7].

2. MATERIALS, METHODS AND REQUIRED ADAPTATIONS TO THE METHODS

2.1 OCT first interlaboratory trial

2.1.1 Multi-laboratory testing logistics

Back in 2022, a group of eighteen Canadian and international laboratories (including research chair's members) volunteered to participate in the first trial of the OCT interlaboratory study. Detailed instructions and procedures, including aggregate processing details [5, 8-9], equipment (cell and datalogger) and software user manual documents, along with a video describing the testing procedure, were provided to participants. Two questions and answers sessions were held to allow the participants to clarify any potential issues regarding the procedure and reporting requirements prior to launching the study.

2.1.2 Former test procedure

In the original OCT, a 10-cm compacted layer of ground aggregate material is exposed to oxygen (O_2) in a hermetic cell (Figure 2.1, right cell). The O_2 consumption in the 10-cm headspace, due to sulphides oxidation, is monitored over a 3h period at 23 ± 2°C after a 30 min (sensor) equilibrium period (Figure 2.1) [9].The first interlaboratory trial on OCT was launched in early 2023; it involved the testing of the following four aggregates, i.e. the reactive Maskimo gabbro at 0.9% (MSK 0.9%) and 0.2% (MSK 0.2%) total sulphur (S_T) contents, a non-reactive high purity limestone (HP) and finally, a non-reactive hard anorthosite aggregate (PKA). The amount of materials for testing in the cell was typically between 2100 and 2300 g. It consisted of 50% material passing the 160 µm sieve and retained on the 80 µm sieve, and 50% material passing the 80 µm sieve.

2.1.3 Trial 1 outcomes

Out of the 14 labs that finally issued results (of 16 that accepted to conduct the study), unexpected issues were reported by some participants that resulted in high variability in their test results. Throughout 2023, comments received and troubleshooting R&D resulted in the design/development of a smaller cell that would require much lower amounts of aggregate material to grind and test in the OCT. A second trial of interlaboratory study on the OCT was then organized.

2.2 OCT second interlaboratory trial

2.2.1 Multi-laboratory testing logistics

The second trial of the OCT interlaboratory study was launched at the beginning of 2025. Fourteen participants accepted to conduct the study and were provided with improved instructions/procedures and newly designed cells (Figure 2.1, left hand side) [10,11]. The participants were asked to test the same aggregates (MSK 0.2, 0.9, PKA and HP). Based on the results of the first OCT trial, which identified sample preparation as one of the main sources of interlaboratory variability, a "ready-to-test" specimen (prepared by U. Laval) of MSK 0.9 was provided to 12 (out of 14) participants. Two questions and answers sessions were again held with different participants before officially launching the study in March 2025.

2.2.2 Proposed test procedure

The second trial involved testing a 7-cm compacted layer of ground aggregate material (~ 700g) in the new (small) cell. The O_2 consumption in the 8-cm headspace is again monitored over the same 3.5-hr equilibrium/testing time period. Another change in the procedure was the requirement for the participants to use "suitable" crushing and grinding apparatus. Ceramic-coated crushing/grinding equipment was indeed found to prevent reactive aggregate preparations, notably pyrrhotite (e.g. MSK 0.9), to react fully to a known reference level (O_2 consumed) in the OCT [12]. Alternatively, the use of Cr-Alloy steel discs in pulverisers was strongly recommended as it was found to provide efficient pulverizing capacity without being the source of contamination or other detrimental effects on the specimen's reactivity [10,12]. Also, the use of ring/puck mill equipment powdering equipment increased the risk of generating excessive amounts of very fine material (< 80 µm), which has shown unsuitable in the test by preventing O_2 diffusion within the ground material. In order to validate the suitability of the grinding procedure used,

the different laboratories were asked to perform a sieve analysis (< 160 µm) of the test preparations after completion of OCT.

Parameters	Original	Small
Height (mm)	200 ± 2	149 ± 2
Internal diameter (mm)	142 ± 2	95 ± 2
Wall thickness (mm)	10	10
Headspace (mm)	10	8
Materials needed (g)	2100-2300	≈ 700
Particle size	80-160µm (50%) < 80µm (50%)	<160µm (100%)
Thick. ground material (mm)	10	7
Saturation	40%	40%
Other pieces	Acrylic cap and base	
Oxygen sensor	Galvanic; Apogee SO-100/200 series	
Data logger	OM-CP-IFC200, from probe manufacturer (or HOBO)	

Figure 2.1: OCT cells used in the different trials of OCT interlaboratory studies; on the right-hand side, the original (larger) cell (OCT trial 1) and on the left-hand side, the new (smaller) cell (OCT trial 2). Testing parameters used for Trial 1 (with original cell) and Trial 2 (new (small) cell).

3. RESULTS

The results reported by the participants in the OCT interlaboratory second trial are illustrated in Figure 3.1, while detailed statistics can be found in Table 3.1 for all aggregate tested. The following general comments can be drawn from the results illustrated in Figure 3.1:

- For marginally-reactive MSK 0.2, OCT values > 17% were reported by three participants (3,6,16), while all others reported results ranging from 4.2 to 30.3%;
- For highly-reactive MSK 0.9, OCT values > 30% were reported by five participants (3,6,8,10,11) and values ranging from 10.5 to 69.3 by all others;
- For non-reactive PKA, OCT values > 5% were reported by three participants (3,6,16), while all others reported values < 2%; finally,
- For non-reactive HP, one participant (16) reported an OCT value > 4%, while all others reported values < 2%,

Table 3.1: Results of the second OCT interlaboratory trial: mean OCT, standard deviation, coefficient of variation, n= number of results. Statistics are presented without and with (in brackets) outliers removed. Results of sieve analysis of material preparations are also given with basic statistics (all participants).

Aggregate tested	**Labs (n)**	**Outliers (Lab #)**	**O_2 consumed**			**Materials sieve analysis**		
			Mean (%)	Standard deviation	Coefficient of variation (%)	**below 80 µm (Mean, %)**	Standard deviation	Coefficient of variation (%)
PKA	14 [11]	3,6,16	5.3 [2.2]	6.2 [1.4]	116.4 [63.8]	54.2	11.2	20.6
HP	9 [8]	16	1.3 [1.0]	1.3 [0.8]	99.2 [79.2]	58.0	18.0	31.0
MSK 0.2	14 [11]	3,6,16	17.0 [9.4]	20.5 [3.6]	120.2 [37.9]	55.9	10.0	17.9
MSK 0.9	13 [11]	3,6	29.5 [23.6]	18.1 [9.8]	61.3 [41.6]	55.5	10.3	18.6
MSK 0.9 U. Laval	10	--	20.6	3.5	17.0	54.2	7.7	14.2

A B

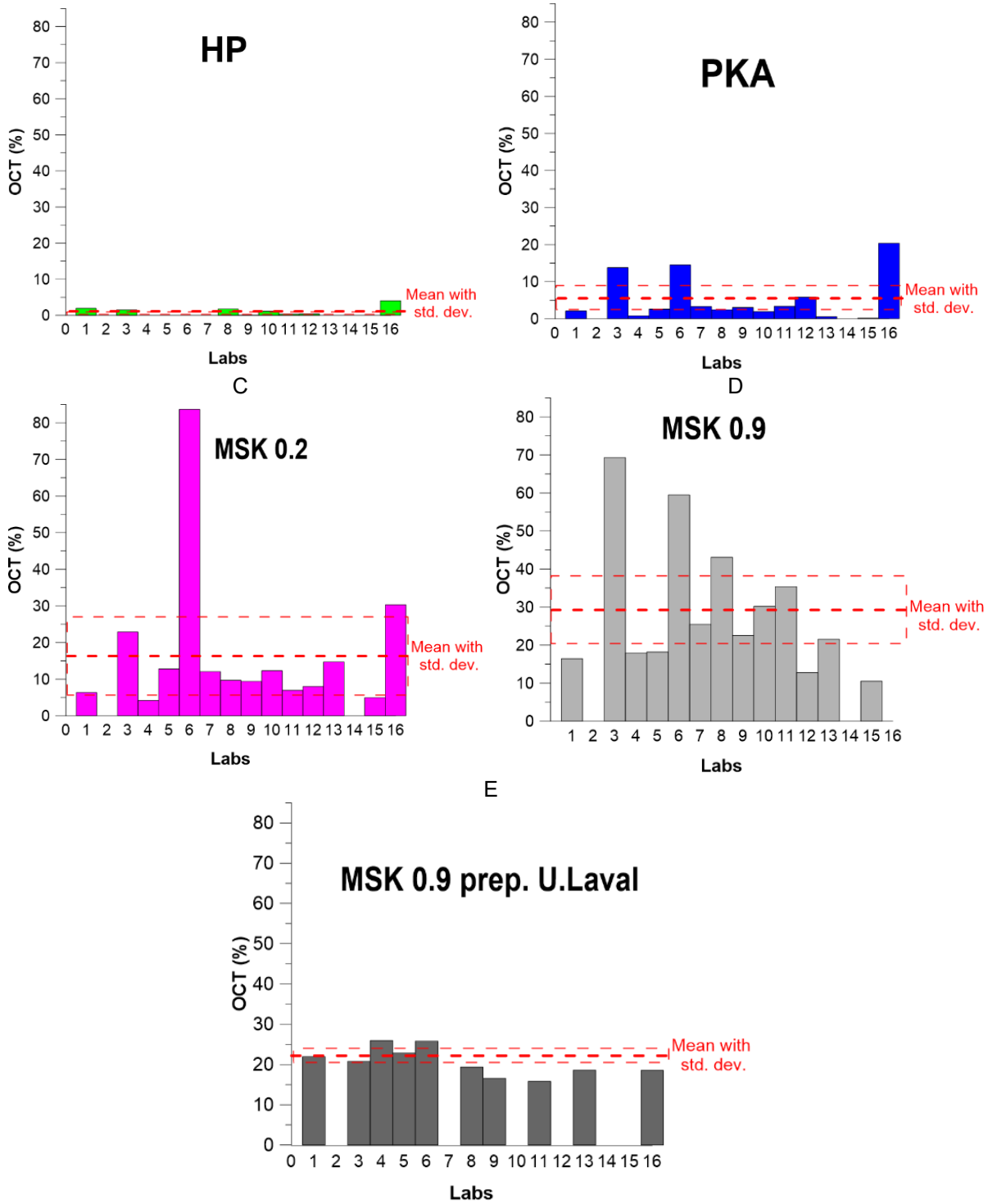

Figure 3.1: Bar charts illustrating the results (means and standard deviations] of OCT interlaboratory study (second trial]. A: OCT results for non-reactive HP, B: OCT results for non-reactive PKA, C: OCT results for marginally-reactive MSK 0.2%, D: OCT results for highly-reactive MSK 0.9%, E: OCT results for MSK 0.9% prepared by U. Laval.

The coefficient of variation (CV] ranged from 61.3 to 120.2% for the different specimens prepared and tested by the participating labs (Table 3.1]. The highest value of 120.2% was obtained for the marginally reactive MSK 0.2, which was highly influenced by the (very high] result reported by Lab 6 (Figure 3.1C]. High CV values were also obtained for non-reactive PKA and HP, which was somewhat expected considering the low OCT values obtained. Interestingly, highly reactive MSK 0.9 CV values are the lowest of the samples prepared and tested by the participants.

Data illustrated in Figure 3.1 shows that Labs 3, 6 and 16 invariably reported higher results and thus largely affected the test statistics. Table 3.1 thus also includes statistics with outliers removed (tested contaminated samples or used of unsuitable material processing equipment]. The corrected CV ranged from 37.9 to 79.2% for the different specimens prepared and tested by the participating labs. Once again, high CVs were obtained for HP and PKA because of low OCT values. Significant reductions in CV were obtained for reactive MSK 0.9 and MSK 0.2 following outliers removal, which ended up around 40%.

Table 3.1 and Figure 3.1E show OCT results for the “ready-to-test” MSK 0.9% sample prepared by U. Laval using Cr-alloy steel discs and provided to 12 participants. Results show much lower CV (17.0%] and a mean of 20.6%, falling within the historical range values for MSK 0.9%.

The proportion of < 80 µm particles measured by sieve analysis of the ground material preparations after OCT shows a tight range of mean (%] values considering the various types of materials prepared by the participants, i.e. 54.2 to 58.0% passing 80 µm sieve, which were comparable to that found with the “ready-to-test” material (54.2%]. The highest CV (20.6 and 31.0%] were obtained with the non-reactive PKA and HP, respectively. The CVs calculated for the MSK materials prepared by the participants (17.9 and 18.6%] were found to be somewhat comparable to that obtained for the “ready-to-use” material (14.2%].

4. DISCUSSION

Results obtained in the second OCT interlaboratory trial after adjustments of the test procedures and the use of a smaller cell are globally encouraging, but still pointing some issues. Looking at Table 3.1 and based on recent conversations with participants from Lab 3, 6 and 16, it was found that they all used “unsuitable” material processing equipment, i.e. magnesium steel disk pulveriser and standard Los Angeles apparatus with Cr-alloy steel balls, respectively, which resulted in either contamination or prevention of reaction of the OCT preparations (thus invalid results] [13]. Removing these three outliers brings tighter values (better means] and lower CVs in each of the four samples tested (Table 3.2], which are more reasonable for a “first time trial” of the test method from the participating laboratories. However, CVs are still considered high and improvements to the test method instructions, including stricter requirements for allowable crushing/grinding equipment are to be specified (main suspected source of variability]. Based on these results, it could be appropriate to prepare and test a non-reactive (hard] aggregate material along with unknown specimens to monitor wear of material processing equipment and thus potential risks of contamination.

The modified instructions suggesting a step-by-step materials preparation approach to limit production of excessive amounts of fines, demonstrated success as the variability in the proportions of < 80 µm particles in the test specimens of the second trial were quite limited between labs (54.2 to 58.0%].

The low-variability in the data (≈ 17% CV] obtained from the “ready-to-test” material preparations provided to participants (Figure 3.1E and Table 3.1] confirmed that the instructions and Q&A sessions allowed the participants to properly conduct an OCT test with the provided equipment.

5. CONCLUSIONS

In view of the two recent interlaboratory studies on OCT, the following conclusions can be drawn:

1] The results of the OCT interlaboratory studies reported in this paper confirmed that material processing operations have a critical impact on the variability of the test results. On one hand, some “steel-based” grinding and pulverizing equipments can indeed induced contamination of the test specimens with resulting high OCT values. On the other hand, although ceramic grinding media prevent sample contamination, they were also found to prevent oxidation reaction of pyrrhotite in the OCT, thus resulting in very low OCT values. Furthermore, planetary ball or ring/puck mill equipment is prohibited for OCT materials processing operations as they tend to produce high amounts of < 50 µm particles, which contribute at blocking oxygen diffusion and oxidation reactions, with resulting low OCT values.

2] Cr-alloy steel discs (in disc-pulverisers] induced no contamination while allowing to better discriminate reactive from non-reactive samples in the interlaboratory studies; they are thus considered the only suitable option to obtain valid OCT results at this time.

3] Significantly lower interlaboratory variability (CV of ~17%] and mean OCT value in line with historical data were obtained when participants tested a reference “ready-to-test” reactive sample prepared in one laboratory. This confirmed the suitability of the test procedure and the capacity of the participants to properly conduct an OCT test following the standard test procedure and instructions provided.

4] Because of the issues related to materials processing operations, it is believed that the establishment of reference non-reactive and reactive aggregates would improve the quality control of SBA using the OCT procedure.

6. REFERENCES

[1] Rodrigues, A., Duchesne, J., Fournier, B., Durand, B., Rivard, P., & Shehata, M. (2012] Mineralogical and chemical assessment of concrete damaged by the oxidation of sulphide-bearing aggregates: Importance of thaumasite formation on reaction mechanisms. *Cem Concr Res 42:* 1336-1347. https://doi.org/10.1016/j.cemconres.2012.06.008

[2] Jana, D. (2020]. Pyrrhotite Epidemic in Eastern Connecticut: Diagnosis and Prevention, *ACI Mater J* V 117, No. 1, January 2020. DOI: 10.14359/51740756

[3] Leemann, A., Lothenbach, B., Münch, B., Campbell, T. and Dunlop, P. (2023]. The “mica crisis” in Donegal, Ireland–A case of internal sulfate attack? *Cem Concr Res*, *168*, p.107149. https://doi.org/10.1016/j.cemconres.2023.107149

[4] Rodrigues, A., Duchesne, J., Fournier, B., Durand, B., Shehata, M. And Rivard, P. (2016]. Evaluation protocol for concrete aggregates containing iron sulphide minerals. ACI Mater J 113: 349-359. DOI: 10.14359/51688828

[5] CSA Annex P (2019]. Impact of sulphides in aggregate on concrete behaviour and global approach to determine potential deleterious reactivity of sulphide-bearing aggregates. Concrete materials and methods of concrete construction/Test methods and standard practices for concrete (A23.1 & A23.2]. Canadian Standards Association, Mississauga (Ontario, Canada], 876p.

[6] Fournier, B., Rodrigues, A., Fecteau, P.-L., Duchesne, J. (2024]. Research and standardization activities in Canada for the Quality Control of Sulphide-Bearing Aggregates. 1st International Conference on Iron-Sulphide Reactions in Concrete Proceedings, Université Laval Campus, Quebec City, Canada, May 14th-17th, p. 71-75.

[7] Rodrigues, A., Duchesne, J., Fournier, B. (2016]. Quantitative assessment of the oxidation potential of sulfide-bearing aggregates in concrete using an oxygen consumption test. *Cem Concr Compos 67: 93-100. http://dx.doi.org/10.1016/j.cemconcomp.2016.01.003*

[8] Fecteau, P.L., Fournier, B., Duchesne, J., Rodrigues, A. (2023]. Pyrrhotite Project – Interlaboratory Study, Document 1 : General Instructions of Phase 1. 9 pages.

[9] Fecteau, P.L., Fournier, B., Duchesne, J., Rodrigues, A. (2023]. Pyrrhotite Project – Interlaboratory Study, Document 3 : Detection of the Oxidation Potential of Sulphide-Bearing Aggregates by an Oxygen Consumption Test (OCT]. 12 pages.

[10] Rabieh, A., Eksteen, J.J., Albijanic, B. (2017]. The effect of grinding chemistry on cyanide leaching of gold in the presence of pyrrhotite. Hydromet, 173: 115-124. https://doi.org/10.1016/j.hydromet.2017.08.013

[11] Fecteau, P.L., Fournier, B., Duchesne, J., Rodrigues, A. (2025]. Pyrrhotite Project – Interlaboratory Study, Document 1 : General Instructions of the interlaboratory study on the Oxygen Consumption Test (OCT] (2nd trial]. 5 pages.

[12] Rodrigues, A., Duchesne, J., Fournier, B. (2025]. Oxygen Consumption test for Sulphide-Bearing Aggregates effect of Sample Preparation. For submission to Cement and Concrete Research Journal, 16 p.

[13] Leja, J., Rao, S. Ramachandra. (2004]. Surface Chemistry of Froth Flotation : Volume 2: Reagents and Mechanisms. Second Edition. Kluwer Academic / Plenum Publishers, New York, pp 505-508.

Concrete aggregates testing for iron sulphides: accelerated mortar bar testing interlaboratory study in Canada to evaluate multi-laboratory variability in view of standardization

Pierre-Luc Fecteau [(1)], Benoit Fournier [(1)], Josée Duchesne [(1)]

(1) *Department of Geology and Geological Engineering, Université Laval, CRIB, Quebec City, Canada, pierre-luc.fecteau@ggl.ulaval.ca*

Abstract

The accelerated mortar bar test (Po AMBT) is the third step of Annex P protocol present in CSA A23.1, 2019 and 2024 editions. This test is divided into two phases to promote oxidation of iron sulphides first, then internal sulphate attack, ISA. As part of an interlaboratory study on Po AMBT, the participating laboratories were asked to prepare sets of mortars with GU/GUL (general use and general use limestone cement) preselected cements and aggregates: i.e. reactive Maskimo (MSK) with 0.9% mass of total sulphur, marginally reactive MSK with 0.2% mass of total sulphur, and non-reactive PKA (Peribonka). The 15 participating laboratories issued a large range of results. Variability remains significant even when removing one outlier laboratory; MSK 0.2% aggregate with coefficient of variation of ~20% (end of Phase II) being the lowest of all samples. Large variations observed in the results reported on MSK 0.9 GU and GUL combinations may be linked to local discrepancies in the applied test procedure or intrinsic variability of the test; many labs had their very first experience with the test. In summary, all found variability hypotheses need to be validated in view of standardization. It is believed that the establishment of non-reactive and reactive reference aggregates is essential to ensure proper quality control in performance testing of iron-sulphide bearing aggregates for use in concrete.

***Keywords**: interlaboratory study, iron sulphides, interlaboratory variability, Po Accelerated Mortar Bar Test (Po AMBT), sulphide-bearing aggregates (SBA).*

1. INTRODUCTION

Field cases of concrete deterioration due to the oxidation of sulphide-bearing aggregates (SBA) and subsequent internal sulphate attack have been reported in many countries including Canada [1], USA [2] and Ireland [3], while the mechanisms involved have been well documented [3-6]. As part of a Canadian initiative since 2010, extensive research has been performed to develop new tests capable of predicting the potential reactivity of SBA for use in concrete. An evaluation protocol for such aggregates was proposed in 2016 as the key outcome of that research [7]. The protocol, which was included as the Annex P of CSA A23.1-A23.2, 2019 and 2024 editions, includes three steps [8-9]: total sulphur content determination and petrographic examination (S_T), oxygen consumption test (OCT), and accelerated mortar bar test for SBA (Po AMBT). Background and historical information regarding standardization steps towards incorporation of the protocol's tests can be found in [10]. A research chair (U. Laval, Toronto Metropolitan University [TMU] and National Research Council of Canada [NRC]) has been established in late 2018, with one of the main objectives consisting in determining the multi-laboratory variability (precision and bias) of the Annex P protocol's tests. This paper focuses on the interlaboratory study organized on the Po AMBT.

2. MATERIALS AND METHODS

2.1 Aggregates and cements used in the study

The study involved the testing of three preselected aggregates, i.e. the highly-reactive gabbroic Maskimo 0.9% mass of total sulphur content (S_T) (MSK 0.9), the marginally reactive MSK at 0.2% S_T (MSK 0.2), and finally, the non-reactive Peribonka (PKA) anorthosite aggregate. About 300 kg of each aggregate, 5-20 mm in particle size, were thoroughly mixed and sampled to ensure production of

representative subsamples to be provided to each participant. The chemical composition and physical properties of the GU and GUL cements (general use and general use limestone cement) used in this study are presented in Table 2.1.

Table 2.1: Chemical and physical properties of the cement used in this study.

Cements	Chemical properties. Values in mass %								Blaine	< 45µm	Limestone filler content
	SiO_2	CaO	Al_2O_3	Fe_2O_3	MgO	SO_3	Na_2Oeq	LOI	m^2/kg	Mass %	Mass %
GU	19.3	61.7	4.9	3.6	2.6	4.1	0.87	1.7	382	4.7	2.3
GUL	19.0	60.1	5.0	2.2	2.3	4.3	0.94	5.6	474	6.0	13.1

2.2 Interlaboratory testing logistics

Eighteen participants confirmed their interest to participate in the study. Each participant received a 20-kg bag of each of the selected aggregates and 2-kg packages of the cements listed before. Detailed testing procedures, along with all necessary equipment and a video illustrating the various steps of the Po AMBT, were provided to participants before hosting questions and answers sessions. Each participant was provided with the aggregate materials (5-14 or 5-20 mm particle size), and all other required equipment and reagents (bleach, salt, storage containers, studs for mortar bar measurements, etc.) to isolate the testing method variability from other sources. Only one laboratory did not use the designated bleach due to availability issues. Ovens, low-temperature rooms, moulds and measuring devices were deemed available by the participants.

Each participant was requested to cast one set of three mortar bars per aggregate under study (total of four tests), using either type GU (MSK 0.9 only) or GUL (all aggregates) cements. Detailed instructions regarding aggregate processing operations, mortar proportioning and manufacturing, specimen's preparation and testing were provided to the participants [11-13]. A summary of the above instructions / test procedure is presented below.

2.3 Accelerated mortar bar test (Po AMBT) procedure

2.3.1 Aggregate and mortar bar preparation

Once the aggregate samples are dried to constant mass, a representative subsample of about 5 kg obtained by splitting is processed in successive steps to the specific grading and quantities using suitable crushing/grinding equipment (120 g of 5-2.5 mm, 300 g of 2.5-1.25 mm, 300 g of 1.25mm-630 µm, 300 g of 630-315 µm and 180 g of 315-160 µm = 1200 g). The separated fractions are then washed and dried to constant mass and, unless used immediately, stored into clean airtight bags.

For mortar manufacturing, 1200 g of aggregate are mixed with 440 g of cement and 286 g of tap water to reach a 0.65 water/cement (w/c) ratio. Mortar mixtures and specimens (bars, 25 x 25 x 285 mm in size) are manufactured in accordance with the procedure described in CSA A23.2-25A (equivalent to ASTM C 1260). Titanium coated measuring studs were provided to the participants to avoid corrosion during oxidizing cycles in bleach. The mortar specimens remain in the moulds, stored in a moist cabinet at 23 ± 2 °C, for 48 ± 2 h. They are then demoulded and placed in the moist curing room (>95% R.H.), protected from dripping water, for another 24 ± 2 h (fragile due to high w/c ratio).

2.3.2 Testing of the mortar specimens and interlaboratory logistics

The initial mass and length of each bar are first recorded after 72 ± 2 h. The bars are then totally immersed in 6 vol. % bleach solution in a LocknLock container (provided) for 3 h (± 15 min). The bars are then removed from the solution, towel wiped and rapidly measured for their "zero" mass and length. The bars are then left to dry at room temperature (23 ± 2 °C) under in-service fume hood for 3 h (± 15 min). After the zero reading, the bars are placed in the Phase I testing regime setup (Figure 2.1A). Twice a week, over the 13-weeks of Phase I (e.g., "Day 1" and "Day 4" each week), the containers are removed from the storage condition. The bars are then removed from the container, left to cool for 30 minutes in air at 23 ± 2 °C and then immersed in the bleach solution for 3 h at 23 ± 2 °C. Mass and length changes are recorded once a week and the bleach solution is replaced every two weeks. Between the 3 h immersion periods, the bars are maintained under their Phase I testing conditions. After completion of Phase I, the bars are transferred in the Phase II testing regime setup (Figure 2.1B) for a final 13-week

period (Phase II) (Figure 2.1B). The bars are subjected to the same 2 x 3 h of bleach soaking/drying (at 23 ± 2 °C) and same mass/length measurements frequency. At the end of the 26 weeks testing period, final expansion and mass changes (in %) are determined. More details on the test procedure can be found in [7-9,13] or in the interlaboratory study instruction packages [11,12].

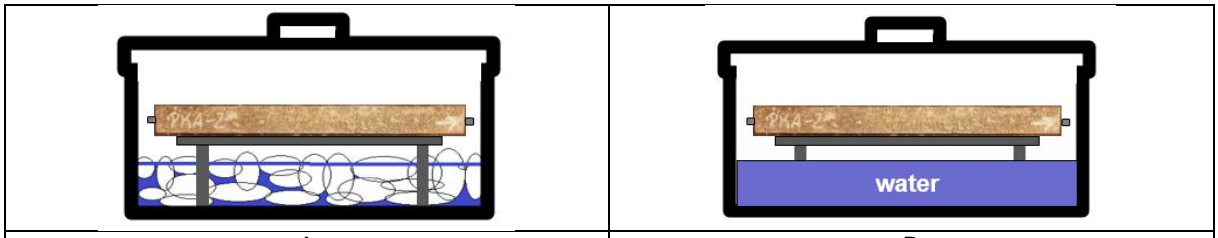

A B

Figure 2.1: Po AMBT phases I and II testing regime schematics. A: Phase I testing regime - mortar bars are supported by ABS pipe sections and plastic grid over supersaturated NaCl solution to maintain 75% R.H. at 80°C. B: Phase II testing regime – mortar bars are supported by the same setup over tap water to maintain 100% R.H. at 4° C.

3. RESULTS

The results of the Po AMBT interlaboratory study are presented in Figure 3.1 and in Table 3.1 for all aggregate samples tested. Figures 3.1A to D illustrate the expansion results obtained in both phases. Lab 10 is considered as an outlier as it used a different bleach.

Figure 3.1A shows PKA GUL results with low expansion values reported by all participants. CV values remain high, as expected considering the low expansions obtained; removing outlier Lab 10 had a limited impact. Figure 3.1B shows similar expansion trends from all laboratories for MSK 0.2 GUL, with an average Phase I expansion of 0.137%. The removal of outlier Lab 10 has a noticeable impact on the statistical parameters, that however still remained relatively high (CV of 20.6 vs 30.6%, Table 3.1). The expansion increases on average by 29% between Phase I and Phase II but the variability remained unchanged (CV of 19.9%, data from Lab 10 excluded). Figure 3.1C shows, once again, similar Phase I expansion trends for all participants, with a fairly wide variability in Phase I final expansions of MSK 0.9 GU mortar bars (avg. of 0.138, CV= 34.7%). The removal of outlier Lab 10 had a noticeable impact on the statistical parameters (CV of 27.7 vs 34.7, Table 3.1). Considering the high reactivity of MSK 0.9, a larger difference between Phase I and Phase II expansions can be observed, with an average expansion increase of 55% between those two phases (data from Lab 10 excluded); the variability between laboratories remained fairly high (CV of 31.4, outlier lab 10 removed). Finally, Figure 3.1D shows that the use of the GUL cement results in even significantly higher average expansions at the end of the test (Phase I + Phase II), i.e. average 0.296% for type GUL versus 0.227% for type GU (outlier removed); however, much higher variability is also obtained between the laboratories with GUL cement with CV reaching 43.3 vs 38.7% for Phase I + Phase II expansions, with / without outlier #10, respectively (Table 3.1).

Table 3.1 : Mean Po AMBT expansions and statistics by the participating laboratories.

Aggregate / Cement		PKA + GUL		MSK 0.2 + GUL		MSK 0.9 + GU		MSK 0.9 + GUL	
		Ph. I mean % exp.	Ph. I+II mean % exp.	Ph. I mean % exp.	Ph. I+II mean % exp.	Ph. I mean % exp.	Ph. I+II mean % exp.	Ph. I mean % exp.	Ph. I+II mean % exp.
All labs included	Mean (%)	0.010	0.024	0.137	0.178	0.138	0.217	0.148	0.282
	SD (%)	0.012	0.013	0.042	0.048	0.048	0.078	0.058	0.123
	CV (%)	120	55.7	30.6	27.1	34.7	36.2	38.9	43.4
All labs without outlier Lab 10	Mean (%)	0.011	0.025	0.145	0.187	0.146	0.227	0.156	0.296
	SD (%)	0.010	0.010	0.030	0.040	0.040	0.070	0.050	0.110
	CV (%)	107.1	52.7	20.6	19.9	27.7	31.4	33.1	38.7

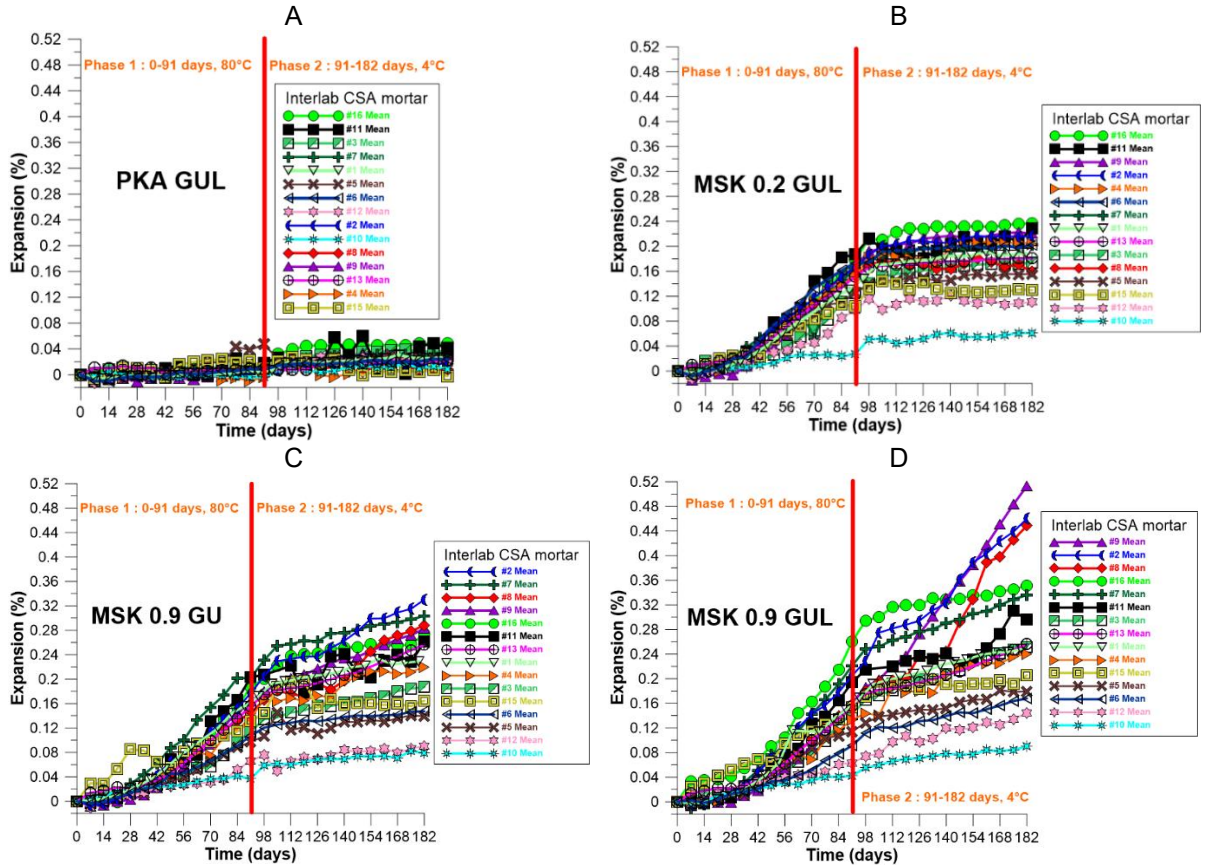

Figure 3.1: Expansion graphs of the results of the Po AMBT interlaboratory study. A: PKA with GUL cement, B: MSK 0.2% with GUL cement, C: MSK 0.9% with GU cement, D: MSK 0.9% with GUL cement.

4. DISCUSSION

4.1 Expansive behaviours of the mixtures / aggregate tested

All laboratories confirmed the non-reactive character of the PKA aggregate (avg. final exp. of 0.025% [Table 3.1]). Phase I average expansions ranged from 0.145 to 0.156% for the MSK (0.2 & 0.9) aggregates (outlier Lab 10 removed). Rodrigues et al. [14] suggested that expansions in Phase I of the Po AMBT result from oxidation reactions and initiation of ISA. Alkali-silica reactive aggregates can also expand significantly during Phase I of the test; however, MSK aggregates are not susceptible to ASR so this deleterious mechanism has not contributed to Phase I expansions [15]. On the other hand, some silicate aggregates, even non alkali-reactive or with low sulphide contents, were found to induce excessive expansion in Phase I of the AMBT Po. The exact reason for such a behaviour is still under investigation [16,17]. It is important to note that Phase I testing did not reliably differentiate marginally-reactive (MSK 0.2) from highly-reactive (MSK 0.9) aggregates. On the other hand, a noticeable difference in average expansions was obtained between those two aggregates during Phase II testing (Table 3.1), which was actually best highlighted by the use of the GUL cement (GU =0.227% and 0.296% for GUL). The storage conditions during Phase II (4° C, 100% RH) were designed to promote ISA, notably thaumasite formation [15]. They were thus expected to boost the expansive behaviour of the highly-reactive MSK 0.9 aggregate. However, and as will be discussed below, 180-day interlaboratory expansions for the MSK 0.9 GUL were found to be much more variable. Regarding the difference between the MSK 0.9 GU and MSK 09 GUL mixtures, previous work has shown that factors such as the alkali content (Na_2O_{eq}), the Blaine fineness and possibly the limestone contents of the cement have a stronger effect on the expansion obtained in the Po AMBT [18,19]. The alkali content of the cement indeed affects the pH of the pore solution, thus enhancing the oxidation reaction [19]. The alkali content of the GU and GUL cements are respectively 0.87 and 0.94%, their limestone filler content 2.3 vs 13.1%, while their Blaine fineness are 382 and 474 m^2/kg, respectively.

4.2 Multi-laboratory variability of the mixtures tested

Despite its non-reactive character, final expansions ranging from -0.002 to 0.048% were reported by the different participants for the PKA GUL specimens (Table 3.1). Most participants reported somewhat similar increasing expansive trends during Phase I of the test for each mixture incorporating MSK aggregates (Fig. 3.1B to C); however, significant spread in the 90-day expansions was observed, which actually increased from the MSK 0.2 GUL to MSK 0.9 GU and MSK 0.9 GUL mixtures, i.e. CV of 20.6, 27.7 and 33.1, respectively (Table 3.1). Figures 3.1B to D also show somewhat similar global expansive trends (i.e. shape of curves) for many laboratories during Phase II; however, the spread in the reported data increased significantly for the MSK mixtures, i.e. CV of 19.9 to 38.7, being the highest with the MSK 0.9% GUL mixture notably because of the very high expansions obtained by lab 2, 8 and 9 during Phase II compared to all other labs. The reasons for such large variability towards the end of the two phases of the test, especially with the MSK aggregates and the GUL cement, still need to be clarified (Fig. 3.1D). Factors such as intrinsic variability of the test, small or more major deviations from the test procedure described in the instructions by staff at some local laboratories and aggregate preparation process (material and type) could potentially explain the variability in the test results obtained. It is important to mention that this was the first experience with the Po AMBT for most participants. Although most of them have been involved in testing mortar bars for determining potential alkali-reactivity of concrete aggregates (e.g. CSA A23.2-25A or ASTM C 1260 procedures), testing conditions in the Po AMBT are very different. Visits of the participating labs were done to add supplementary information to that provided by lab staff at each location, hoping to help explaining the variability observed at some laboratories. However, the observations and supplementary information gathered did not allow to clearly identify some parameters of the Po AMBT that would explain the variabilities. Supplementary adjustments to the methods may then be required to optimize test conditions and procedure and reduce variability in view of potential standardization in CSA A23.1-A23.2. Finally, the establishment of a non-reactive and reactive reference aggregates seems necessary to ensure proper quality control of SBA prior to their use in concrete.

5. CONCLUSIONS

In view of the recently concluded interlaboratory study on Po AMBT, the following preliminary conclusions can be drawn:

1. All participants confirmed the non-reactive character of the PKA aggregate.
2. Phase I testing did not allow to differentiate marginally-reactive MSK 0.2 and highly-reactive MSK 0.9 aggregates. Higher average expansions were however obtained with the MSK 0.9 aggregate during Phase II testing, emphasized by the use of the GUL cement.
3. Significant spread in the 90-day and 180-day expansions was observed for the mixtures made with the MSK aggregates, the highest being MSK 0.9 GUL mixture. Visits at the participant's laboratories were conducted to try clarifying the reasons for such large variability, without clear outcomes.
4. The high variations obtained in this study were at least partly associated to the limited experience of the participants with this new Po AMBT procedure.
5. It is thus recommended that another interlaboratory study be conducted whenever sources of the observed variability are determined.
6. The establishment of non-reactive and reactive reference aggregates would largely help laboratories to ensure proper quality control of SBA prior to their use in concrete.

6. REFERENCES

[1] Rodrigues, A., Duchesne, J., Fournier, B., Durand, B., Rivard, P., Shehata, M. (2012). Mineralogical and chemical assessment of concrete damaged by the oxidation of sulphide-bearing aggregates: Importance of thaumasite formation on reaction mechanisms. *Cem Concr Res 42*: 1336-1347. https://doi.org/10.1016/j.cemconres.2012.06.008

[2] Jana, D. (2020), Pyrrhotite Epidemic in Eastern Connecticut: Diagnosis and Prevention. *ACI Mater J 117 (1)*, DOI: 10.14359/51740756

[3] Leemann, A., Lothenbach, B., Münch, B., Campbell, T., Dunlop, P. (2023). The "mica crisis" in Donegal, Ireland–A case of internal sulfate attack?. *Cem Concr Res, 168*: 107149. https://doi.org/10.1016/j.cemconres.2023.107149

[4] Mikhlin, Y. L., Kuklinski, A.V., Pavlenko, N.I., Varnek, V.A., Asanov, I.P., Okotrub, A.V., Selyutin, G.E. Solovyev, L.A. (2002). Spectroscopic and XRD studies of the air degradation of acid-reacted pyrrhotites, *Geochim. Cosmochim. Acta, 66:* 4057-4067.

[5] N. Belzile, Y.W. Chen, M.F.Cai, Li, Y. (2004). A review on pyrrhotite oxidation, *J. Geochem. Explor. 84* : 65-76. https://doi.org/10.1016/j.gexplo.2004.03.003

[6] Rodrigues, A., Duchesne, J., Fournier, B. (2024). Evaluation of the secondary products formed during the AMBT for Sulphide-Bearing Aggregates. 1st International Conference on Iron-Sulphide Reactions in Concrete Proceedings, Université Laval, Quebec City, Canada, May 14th-17th, 92-96.

[7] Rodrigues, A., Duchesne, J., Fournier, B., Durand, B., Shehata, M., Rivard, P. (2016). Evaluation protocol for concrete aggregates containing iron sulphide minerals. *ACI Mater J 113*: 349-359. DOI: 10.14359/51688828

[8] CSA Annex P (2019). Impact of sulphides in aggregate on concrete behaviour and global approach to determine potential deleterious reactivity of sulphide-bearing aggregates. Concrete materials and methods of concrete construction/Test methods and standard practices for concrete (A23.1 & A23.2). Canadian Standards Association, Mississauga (Ontario, Canada), 876p.

[9] CSA Annex P (2024). Impact of sulphides in aggregate on concrete behaviour and global approach to determine potential deleterious reactivity of sulphide-bearing aggregates. Concrete materials and methods of concrete construction/Test methods and standard practices for concrete (A23.1 & A23.2). Canadian Standards Association, Mississauga (Ontario, Canada), 932p.

[10] Fournier, B., Rodrigues, A., Fecteau, P.-L., Duchesne, J. (2024). Research and standardization activities in Canada for the Quality Control of Sulphide-Bearing Aggregates. 1st International Conference on Iron-Sulphide Reactions in Concrete Proceedings, Université Laval, Quebec City, Canada, May 14th-17th, 71-75.

[11] Fecteau, P.L., Fournier, B., Duchesne, J., Rodrigues, A. (2024). Pyrrhotite Project – Interlaboratory Study phase II, Document 1 : Detection of Potential Reactivity of Sulphide-Bearing Aggregates by Accelerated Expansion of Mortar Bars (AMBT-pyrrhotite), Context and General Instructions. 4 pages.

[12] Fecteau, P.L., Fournier, B., Duchesne, J., Rodrigues, A. (2024). Pyrrhotite Project – Interlaboratory Study phase II, Document 2 : Detection of Potential Reactivity of Sulphide-Bearing Aggregates by Accelerated Expansion of Mortar Bars (AMBT-pyrrhotite), Detailed Instructions. 14 pages.

[13] CSA Attachment P3 (2019). Test method for detection of potential reactivity of sulphide-bearing aggregates by accelerated expansion of mortar bars. Concrete materials and methods of concrete construction (A23.1). Canadian Standards Association, Mississauga (Ontario, Canada), 329-340.

[14] Rodrigues, A., Duchesne, J., Fournier, B. (2015). A new accelerated mortar bar test to assess the potential deleterious effect of sulphide-bearing aggregate in concrete. *Cem and Concr Res, 73*: 96-110. https://doi.org/10.1016/j.cemconres.2015.02.012

[15] Rodrigues, A., Duchesne, J., Fournier, B., Castillo, R., Fecteau, P-L. (2025) in prep. Reassessment of the Testing Protocol for Iron-Sulphide Aggregates using an Extended Dataset of 36 samples. For submission to Cement and Concrete Research Journal.

[16] El-Mosallamy, M., Shehata, M.H. (2020). Sulphide oxidation mortar tests for evaluation of the oxidation potential of sulphide-bearing aggregate. *Con Build Mat 264:* 120627. https://doi.org/10.1016/j.conbuildmat.2020.120627

[17] Camargo, M. H. T., Duchesne, J., Fournier, B. (2024). The role of chloride in the expansion of the mortar bar during the evaluation protocol for sulfide-bearing aggregates (Annex P – CSA A23.1-2019). Proceedings of the 1st International Conference on Iron-Sulfide Reactions in Concrete, Université Laval, Quebec City, Canada, , May 14th – May 17th,107-111.

[18] Ourgaud, G., Fournier, B., Duchesne, J., Rodrigues, A. (2024). Impact of Cementitious Composition on the Expansion Generated by the Accelerated Mortar Bar Test. 1st International Conference on Iron-Sulphide Reactions in Concrete Proceedings, Université Laval, Quebec City, Canada, May 14th-17th, 149-153.

[19] Nkinamubanzi, P.-C.., Naboka, O., Henriques, K., Das, U., Makar, J.M. (2024). Influence of the Bleach and Cement Chemistries on the Mortar Bar Expansion for Pyrrhotite Reactions in Concrete. 1st International Conference on Iron-Sulphide Reactions in Concrete Proceedings, Université Laval, Quebec City, Canada, May 14th-17th, 102-106.

Pyritiferous claystone – EN12620 "compliant" aggregate and the case for thin section petrography

Garside R [(1)], Brough C [(1)], Staniforth B [(1)], Fletcher J [(1)], Strongman J [(1)], Garner C [(1)]

(1) Petrolab Ltd, Redruth, UK, rachel@petrolab.co.uk

Abstract

Most of the focus on deleterious concrete blocks in the Republic of Ireland has been on two aggregate types which are responsible for the majority of degradation: pyrrhotite-bearing metasediments such as phyllite and schist within Co. Donegal, and framboidal pyrite in calcareous "mudrock" – calcareous mudstone, calcareous siltstone and argillaceous limestone from across the Carboniferous and Silurian lithologies of the Republic of Ireland. Both of these aggregates have significantly elevated chemical sulphur contents and the deleterious rock types can generally be identified at a macroscopic level without the need for detailed thin section analysis. This means that they should be easily classified as unsuitable for use in concrete by an experienced geologist, preventing further use of this material in concrete products and allowing for quicker screening of deleterious blockwork from damaged houses.

During work for the Defective Concrete Block Scheme for Ireland's Housing Agency, and in previous investigations, petrographic analysis has identified a more problematic aggregate in several houses across multiple counties (particularly but not exclusively Co. Carlow, Clare and Wexford) which cannot easily be identified without optical petrography and yet has still been associated with severe ISA. This aggregate is a light grey limestone with lenses of dark grey claystone containing extremely high levels of ultrafine cubic pyrite. During crushing and concrete manufacture, these claystone layers preferentially disintegrate, creating a fine pyrite rich dust and fragments of very fine pyritiferous claystone, both of which are highly susceptible to oxidation despite their relatively low proportions within the aggregate. In most cases neither can be observed without the optical microscope and since the associated limestone does not have the appearance of calcareous "mudrock", there is a high risk that this aggregate would be considered acceptable without detailed thin section analysis, which is not considered mandatory under current guidance for concrete aggregates in the ROI (S.R. 16 and EN12620). Furthermore, whilst total sulphur (S_T) values are often elevated beyond background levels they are not always elevated to such an extent that the aggregate or already manufactured concrete block is obviously deleterious. Indeed, for concrete block made from this aggregate type, petrographic analysis and SEM/EDX of multiple samples are required to make a positive identification. Updated standards for aggregates for mortar in Ireland (S.R. 18 and EN13139) now mandate thin section petrographic examination of aggregates. It is recommended that a similar rule is brought in for all aggregates for concrete to prevent future use of this or similar material in blockwork.

***Keywords**: aggregates, IS465, petrography, pyrite, pyritiferous claystone*

1. INTRODUCTION

In recent years there has been extensive documentation on degradation due to pyrite and pyrrhotite in concrete blockwork from the Republic of Ireland [1-2], including papers issued in the previous version of this conference [e.g. 3]. The extent of the research has meant that pyrrhotite has finally been acknowledged as a crucial factor in the deterioration of many deleterious blocks within Donegal, and its presence is now being taken into account during testing for remediation, as well as a greater emphasis in the updated version of I.S. 465 [4] which was released for public consultation last year. On the reactive pyrite side, more counties have been acknowledged as containing a significant number of houses with deleterious quantities of framboidal pyrite in calcareous "mudrocks" and therefore eligible for remediation. In particular these now include Clare, Limerick and Sligo (in addition to Mayo and Donegal), with additional research being conducted on multiple other counties.

Table 3.1: Aggregate three-letter code nomenclature used in the text below.

Aggregate Code	Aggregate Type
BCS	**B**lack **C**alcareous crinoidal **S**iltstone & limestone
BLS	**B**lack **L**ime**S**tone & calcareous mudstone
GLS	**G**rey **L**ime**S**tone
HFS	Mafic and pelitic **H**orn**F**el**S**, metadolerite, metapelite
LPC	Grey **L**imestone & **P**yritiferous **C**laystone
PHY	**PHY**llite & micaceous quartzite

From examining thousands of concrete core samples for deleterious aggregate, the two main “problem” aggregates are reliably recognisable in hand specimen, without the need for high magnification examination (Figure 1.1). For Donegal it is a medium grade phyllite (PHY), with crenulation cleavage and common visible pyrrhotite crystals. For the multiple counties with “mudrock”, it is a very dark grey to black blend of argillaceous limestone, calcareous mudstone and calcareous siltstone. Textures differ slightly between counties - Clare and Limerick (BCS) are more silty with coarse crinoid fossils, while Mayo (BLS) contains more mudstone - but macroscopically the aggregates appear very similar. Observing such deleterious aggregates in blockwork within a house showing significant cracking should be sufficient to confirm that degradation is the result of internal sulphate attack (ISA) even if it is not present in the specific blocks examined, without the need for an extensive testing programme to confirm its presence.

On the other hand, for aggregates where the sulphide contents are more variable, or where the lithologies are more complex, a more extensive testing of the blockwork is recommended to confirm the levels of pyrite or pyrrhotite and the type of aggregate they are present within. For example the HFS aggregate, although recognisable macroscopically (Figure 1.1), contains a variable blend of low to moderate grade metamorphosed pelitic rocks with metadolerite and other altered mafic components. The grade of the metapelite varies, as does its sulphide content, with some aggregates seen only containing a small amount of fine pyrite, while others contain a significant amount of fine or clustered pyrrhotite, requiring polished sections to identify and quantify the relative amount of deleterious aggregate and hence the risk of block degradation. The total sulphur levels are generally much lower than those seen in the obviously deleterious phyllites or even the higher grade schists. Still, despite this variability, most of the concrete blocks contain pyrrhotite in combination with a TS of >0.1%, which according to EN12620 aggregates for concrete standard [5], would make them ineligible for use in concrete blocks.

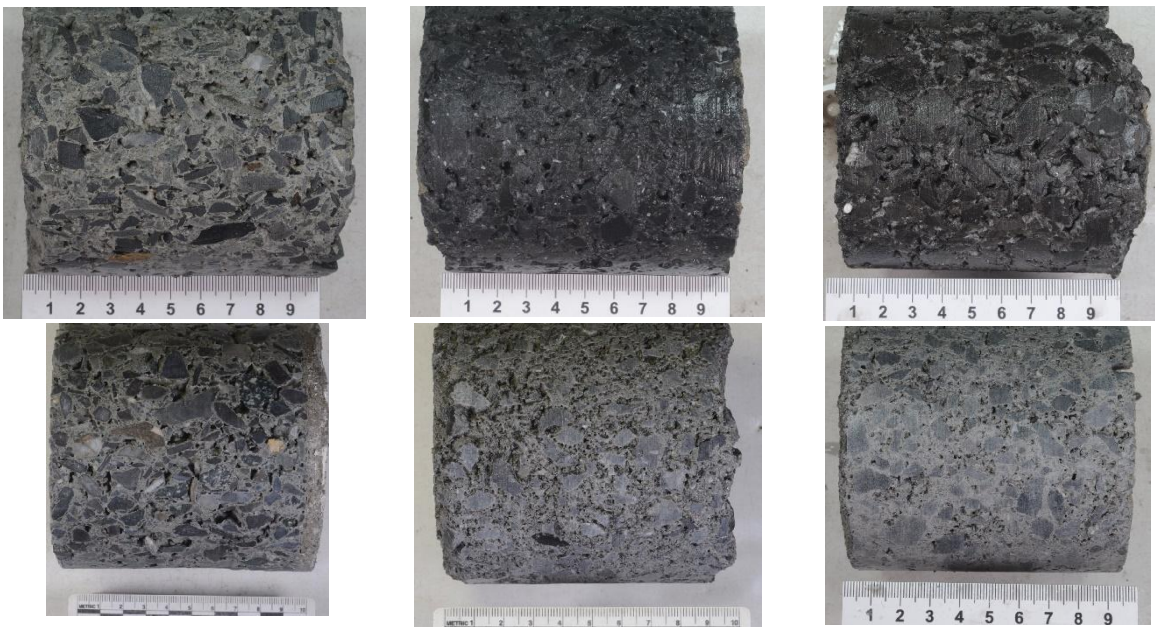

Figure 1.1: Macroscopic photos of several different types of concrete from Ireland. From left to right top row: Donegal phyllite (PHY), Clare BCS, Mayo BLS, bottom row: Donegal HFS, Clare pyritiferous claystone (LPC), Clare bioclastic limestone (GLS). Note similarity in appearance between LPC & GLS.

2. PYRITIFEROUS CLAYSTONE

But what of the blockwork where deleterious aggregate cannot be seen macroscopically? During the testing of concrete blocks from degraded homes (both under the current Defective Blocks scheme and from previous testing), an unusual type of deleterious aggregate has been encountered which does not fall into the typical category of calcareous “mudrocks”. Indeed, the first time it was experienced by Petrolab, the concrete was classified as a GLS with “negligible” risk of aggregate-related degradation i.e. a bioclastic grey limestone containing no or trace amounts of deleterious aggregates macroscopically. It was only following examination of additional thin sections that it was identified and confirmed deleterious, subsequently being named as LPC (**L**imestone & **P**yriferous **C**laystone, also referred to as “pyritiferous claystone” after the main deleterious aggregate). Since then, aggregates with the same or similar texture have been confirmed from ROI counties Clare, Carlow and Wexford, suggesting the possibilities that multiple quarries may contain this material.

Overall the LPC aggregate is dominated by non-deleterious light grey bioclastic and sparry limestone, mostly non-argillaceous, accompanied by chert and dolomite and only minor or trace amounts of typically-deleterious argillaceous limestone. However, in addition to the above, it also contains lenses of fine dark grey claystone within the limestone which contain extremely high levels of fine grained cubic pyrite, with the surrounding limestone also locally heavily mineralised. During crushing of the aggregate for concrete, it appears that the friable claystone lenses preferentially disintegrate, creating fragments of fine claystone and abundant liberated fine pyrite, present in the <1 mm fine aggregate. Due to the fine grain size this claystone is very difficult to reliably detect macroscopically at Suite A. Furthermore, these fragments are highly reactive, showing high susceptibility to oxidation, which commonly leads to abundant gypsum production and highly expansive cracking and spalling which is almost entirely the result of oxidation solely within the claystone. In one instance, oxidation within a claystone lens could be seen resulting in acid attack on the surrounding limestone, dissolving the calcite (Figure 2.1). This particular aggregate fragment was so aggressively reactive that the oxidation continued after resin impregnation of the concrete, causing localised heave of the aggregate fragment from a previously polished flat surface.

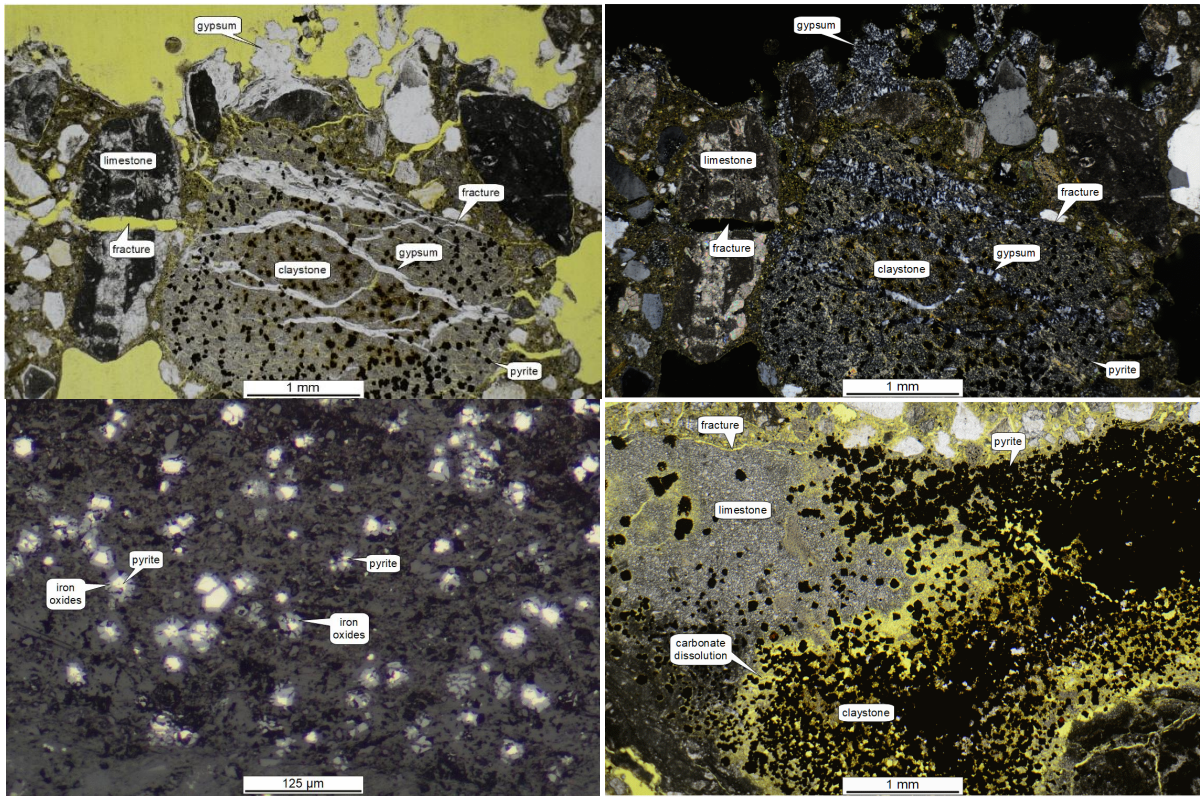

Figure 2.1: Evidence of microscopic deterioration observed associated with the pyritiferous claystone aggregate. Upper row: Expansive ISA with gypsum filled fractures radiating from claystone aggregate (plane & cross polars). Bottom row: Left – reflected light image showing abundant fine pyrite undergoing oxidation. Right – dissolution of calcite within limestone around the edge of a pyritiferous claystone lens.

Although the degradation mechanisms seen in the concrete blocks appear very similar to those seen in calcareous “mudrocks”, the claystone is unusual in several ways. Firstly, it is dominated by fine cubic pyrite, rather than the framboids which are usually associated with severe pyrite degradation in the Republic of Ireland. The ultrafine nature of much of the pyrite (<10 µm), its very high abundance within the claystone, and the poor quality nature of the claystone, which appears to show significant shrinkage cracking even when unoxidised, appear to be significant contributors to the extreme reactivity of the aggregate. In addition, the concentration of most reactive material into the aggregate fines increases the amount of material exposed to oxidising conditions.

Secondly, the reactive aggregate is generally present in low proportions, with the dominant visible aggregate being a “clean” grey limestone, and consequently with a somewhat lower TS value than typical calcareous “mudrocks”. While the hardcore aggregate standards suggest there should be a cutoff of 10% calcareous “mudrock” for the aggregate to be considered unsuitable for use in fill [6], and the RICS Mundic Guidance allows up to 30% deleterious aggregate in block before a house is considered unmortgageable within the South West of England (Cornwall and West Devon) [7], in several blocks showing evidence of expansion, the abundance of claystone lies between 5 and 8% of the aggregate. When combined with other potentially deleterious components such as pyritiferous limestone and argillaceous limestone, the abundance reaches 10-25%, but never the typical 50-90% seen with calcareous mudrock block (Figure 2.2). The concentration of the claystone into <1 mm fines also means it is extremely difficult to spot macroscopically, being generally suspected rather than confirmed prior to thin section manufacture. Only one core was encountered where the claystone was confidently confirmed macroscopically, and that was an outlier with 19.5% claystone aggregate.

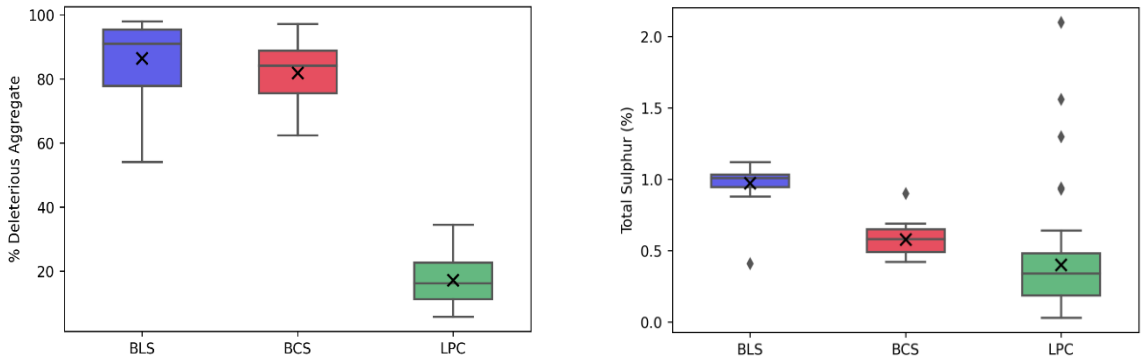

Figure 2.2: Comparative charts showing the difference in deleterious aggregate proportions (left) and total sulphur content – EN 1744, Clause 11.2 HTC (right) between the two main deleterious “mudrock” aggregates and the claystone. Due to the small sample size for LPC (n=23), similar numbers of tested samples were selected for BLS and BCS (n=21). TS values have a 0.1% “correction” subtracted as an assumption of the cement contribution as per I.S. 465.

Thirdly, the abundance of claystone across concrete blocks is highly variable, presumably related to the aggregate variation across the quarry. As such, examination of blocks containing this material is very complex. Due to that initial experience having made thin sections without encountering deleterious aggregate, and having had to make more sections in order to confirm its presence, when claystone is suspected (usually a damaged house where the only aggregate present appears to be a “clean” grey limestone), multiple cores from the house are sent off for TS quantification, from which those with the highest values are sent for full thin section and SEM examination, since those are most likely to contain claystone aggregate. In every case where claystone has been suspected, further testing using this procedure has confirmed its presence, but with thin sections showing a wide variety of abundances even within the same house.

The presence of this aggregate and its apparent extreme reactivity have also had the consequence that it is very difficult to give a negligible rating to what appears to be a “clean” limestone aggregate in other houses, in case there is “invisible” claystone material present in the fines. In these cases the procedure currently being followed by Petrolab is to verify the TS of at least one sample (though usually more) to ensure it is definitely at very low levels typical of “true” negligible concrete (~0.1%).

3. EN12620 AGGREGATES FOR CONCRETE

The presence of problematic claystone aggregate and the difficulty observing it macroscopically mean that general properties of reactive pyrite aggregates may not always apply when examining blockwork or new aggregates for concrete and/or mortar. Currently Ireland has several documents which cover such testing. For aggregates for concrete, it is EN12620 and the guidance document S.R. 16 [8], while for aggregates for mortar, it is EN13139 [9] and S.R. 18 [10]. Since there is no European or Irish standard for detailed aggregate examination, originally both standards only mandated simplified petrographic examination 932-3 [11], which can be carried out without any mandatory thin section or polished section examination, solely macroscopically with hand lens or low powered microscopes. Without thin section examination this can easily lead to aggregate or sulphide misidentification and the possibility of missing such deleterious aggregate constituents as the fine pyritiferous claystone.

S.R. 18, the Irish Guidance for aggregates for mortar, was updated in 2021. In this document the guidance for petrographic examination mandates thin section petrography of aggregates to ensure they do not contain significant amounts of deleterious lithologies (as determined by the petrographer). S.R. 16, the aggregates for concrete standard, is currently up for review, with the public consultation stage closing in November 2025. Although some elaboration has been made in the new draft on the various degradation risks associated with various lithologies (previously there was a simple list saying aggregates should not contain significant amounts of various deleterious materials including mica, shale, sulphides etc.), the examination required is still that of the simplified 932-3, with thin section and SEM examination mentioned as a possibility rather than a mandatory requirement. This is despite the widely know aggregate concrete block issues which have been documented since the SR16 document was last updated. It is not difficult to see how aggregates which do not appear to be “typically deleterious”, with only slightly elevated TS values, might be considered acceptable, with problematic components not observed without more detailed examination.

As a consequence of the issues encountered with the pyritiferous claystone and with other aggregate lithologies where the principal components of the aggregate cannot be determined without reflected light or SEM observations, it is recommended that the petrographic examination component of SR16 be changed to more closely reflect SR18, including a more detailed thin section (or SEM) analysis of the aggregate.

4. CONCLUSIONS & RECOMMENDATIONS

It is clearly possible to screen out deleterious aggregates macroscopically, and indeed it is recommended to do so in the case of concrete block from degraded buildings where the lithology is confirmed deleterious and known to be associated with high levels of reactive sulphides, with additional confirmation being made by TS testing if necessary. However, if the aggregate is ambiguous or appears no risk (particularly in examples such as this pyritiferous claystone), there is certainly a need for more detailed examination, especially of fines, to ensure reactive sulphides are not present combined with problematic aggregate. As such, to avoid deleterious aggregate ending up in concrete, reflected thin section petrography or SEM analysis should be undertaken, particularly in cases where the aggregate would otherwise be considered acceptable.

The current draft revision to SR16 does not follow the procedure of thin section petrography established in SR18 despite these acknowledged problems in concrete aggregate within the Republic of Ireland. Petrolab has suggested this is revised to mandate detailed thin section petrography through a submission to the public comment portal, as well as lowering the TS threshold to 0.2% where fine grained or framboidal pyrite is present, in a similar way to the lower pyrrhotite threshold [12]. If adopted, in combination, these suggested changes should act to identify and screen out less obvious deleterious aggregates and prevent (or at least reduce) future cases of aggregate-related concrete degradation in the Republic of Ireland.

5. REFERENCES

[1] Brough, C, Staniforth, B, Garner, C, Garside, R, Colville, R, Strongman, J & Fletcher, J. (2023) High risk concrete blocks from County Donegal: The geology of defective aggregate and the wider implications. Construction and Building Materials, 408, 133404

[2] Leeman A, Lothenbach B, Münch B, Campbell T, Dunlop P (2023) The “mica crisis” in Donegal, Ireland – A case of internal sulfate attack? Cem Concr Res 168 (107149). https://doi.org/10.1016/j.cemconres.2023.107149

[3] Jana, D. (2024) Cracking and crumbling of concrete blocks in County Donegal, Ireland: A holistic approach from cash studies on deleterious effects of open microstructure of blocks, phyllite aggregate, pyrrhotite oxidation, paste carbonation, lime leaching, and internal sulfate attacks. ICISR 2024, Québec City

[4] I.S. 465:2018+A1:2020 Assessment, testing and categorisation of damaged buildings incorporating concrete blocks containing certain deleterious materials. National Standards Authority of Ireland, Dublin

[5] I.S. EN 12620:2002+A1:2008 Aggregates for concrete. National Standards Authority of Ireland, Dublin

[6] S.R. 21:2014+A1:2016 Guidance on the use of I.S. EN 13242:2002 +A1 :2016 – Aggregates for unbound and hydraulically bound materials for use in civil engineering work and road construction. National Standards Authority of Ireland, Dublin

[7] RICS Professional Guidance, UK (2016) The Mundic problem: RICS Guidance note, UK. 3rd Edition. Royal Institute of Chartered Surveyors, London

[8] S.R. 16:2016 Guidance on the use of I.S. EN 12620:2002 +A1:2008 – Aggregates for concrete. National Standards Authority of Ireland, Dublin

[9] I.S. EN 13139:2002 Aggregates for mortar. National Standards Authority of Ireland, Dublin

[10] S.R. 18:2021 Guidance on the use of I.S. EN 13139:2002 – Aggregates for mortar. National Standards Authority of Ireland, Dublin

[11] I.S. EN 932:2022 Tests for general properties of aggregates – Part 3: Procedure and terminology for simplified petrographic description. National Standards Authority of Ireland, Dublin

[12] Brough, C, Garside, R., Staniforth, B, Garner, C, Fletcher, J & Strongman, J (2024) Framboidal pyrite in concrete block: Reassessing EN 12620 in light of the degradation observed across the Republic of Ireland. ICISR 2024, Québec City

Oxygen consumption test for aggregates containing iron sulfides: sample preparation and column dimension effect

Andreia Rodrigues [(1)], Josée Duchesne [(2)], Benoit Fournier [(3)]

(1) Research Center on Concrete Infrastructure (CRIB), Université Laval, Canada, andreia.rodrigues.1@ulaval.ca

(2) Research Center on Concrete Infrastructure (CRIB), Université Laval, CanadaJosee.Duchesne@ggl.ulaval.ca

(3) Research Center on Concrete Infrastructure (CRIB), Université Laval, Canadabenoit.fournier@ggl.ulaval.ca

Abstract

Concrete deterioration due to sulfide-bearing aggregates has been documented in several countries. As part of an evaluation protocol developed at Université Laval in 2016 and later incorporated into CSA A23.1 Appendix P, the oxygen consumption test measures the oxygen consumed at the top of a sealed column filled with compacted, finely ground aggregate.

In the 2010's, only nine (control and sulfide-bearing) aggregates were tested, but the results were promising. However, when the oxygen consumption test was conducted in different laboratories using various materials processing equipment (crushers and pulverisers), it was observed that the grinding media significantly impacted oxygen consumption values. The main goal of the subsequent test, which used fourteen different aggregates, was to assess the impact of sample preparation on test outcomes. The study also investigated how the use of a smaller volume of materials in a smaller test column influence the reliability and performance of the oxygen consumption test used to evaluate sulfide-bearing aggregates for concrete.

Of the various grinding media tested, only the disk mill with chrome alloy steel plates produced reliable results that clearly distinguished between reactive and non-reactive aggregates. The small column configuration allowed the reduction of the material needed in about 1/3, which contributes at reducing material's preparation time of the test samples.

Keywords: oxidation, optimization, oxygen consumption test, sample preparation, sulfide-bearing aggregates.

1. INTRODUCTION

Over the past two decades, cases of concrete deterioration caused by sulfide-bearing aggregates (SBA) have been reported in Canada [1], the U.S.A. [2], Ireland [3], and other countries. This damage is caused by the oxidation of sulfide minerals (mainly pyrrhotite), followed by internal sulfate attack and thaumasite formation [1-2, 4].

In 2016, a protocol was developed to address the lack of tests to predict the harmful potential of SBA [5]. Adopted by CSA A23.1 (Appendix P) in 2019 [6], it includes three phases, the second of which involves an oxygen consumption test (OCT) [7].

This test is based on a method for mine tailings [8]. The aggregates are ground and mixed with a certain amount of water before being placed in a sealed column where oxygen consumption is measured.

This is a promising quantitative method for assessing oxidation potential of SBA. However, interlaboratory trials have shown that the aggregate processing operations, notably the type of crusher or pulveriser used, can significantly affect oxygen diffusion and sulfide oxidation. In some cases, it can also contaminate the sample, leading to variable results.

2. OBJECTIVES AND SCOPE OF THE WORK

As mentioned before, the OCT is a reliable method for evaluating the oxidation potential of SBA. However, variations in materials processing equipment and operations have shown to significantly affect test results.

This study aimed at investigating the source of unexpectedly high and low oxygen consumption values observed in certain SBA and control (i.e. with only traces of sulfides) aggregates, as well as the influence of the column size on the OCT results. For the latter, comparative testing was conducted in the original Plexiglas column (BC), 141.7 mm x 200 mm in size [7], as well as in a column of similar design but 95 mm x 150 mm in size (SC).

3. MATERIALS AND METHODS

4. Sulfide-bearing control aggregates

More than 50 oxygen consumption tests were performed using 14 different aggregates, various grinding mills/ pulverisers: rod mill, disk mill, ball mill, and planetary ball mill, and two sizes of columns. All experiments were conducted in a temperature-controlled environment maintained at 22 °C to eliminate temperature-related variability. Each test lasted three and a half hours, including 30 minutes for probe stabilization followed by three hours of data collection [7].

Table 3.1.1 shows the characteristics of the 14 quarried aggregates tested. Aggregates MSK (0.9, 0.2, Rich, and 2011), GGP, WS, C, AA and AC contain iron sulfides while HP, DLS, PKA, Ottawa sand and AA aggregates have only traces of iron sulfides or no sulfides at all.

Table 3.1.1: Summary of aggregate characteristics.

Aggregate	Rock type	Sulfide minerals	TS (%)	P (g/cm3)
MSK 0.9	Gabbro	Po, Py, Cpy, Pn	0.86	2.86
MSK 0.2	Gabbro	Po, Py	0.19	2.88
MSK Rich	Gabbro	Po, Py, Cpy, Pn	1.86	2.96
MSK 2011	Norite-gabbro	Po, Py, Cpy, Pn	0.73 -1.28*	2.89
GGP	Granitic gneiss	Po, Py, Cpy	0.24-0.33*	2.93
WS	Mica schist	Po,Py,Cpy	0.05-0.07*	2.72
DLS	Dolostone	Py (traces)	0.09	2.78
C	Hornfels	Po, Cpy	0.78	2.80
AA	Phyllite	Cpy, Py	0.07	2.64
AB	Quartzite	None	0.03	2.59
AC	Phyllite	Po, Py	0.81	2.82
HP	Limestone	Py (traces)	0.00	2.71
PKA	Anorthosite	Cpy(traces)	0.03	2.74
Ottawa sand	Quartzite	None	0.00	2.65

Note: Po: pyrrhotite, Py: pyrite, Cpy: chalcopyrite, Pn: pentlandite; TS: total sulfur content; P: density.
*: Several sub-samples were analyzed for these aggregates

5. Aggregates preparation

Representative subsamples were obtained from the original (quarried aggregates, 5 to 20 mm particle size) materials by quartering. Depending on the size of the column used for testing (see section 3.3), subsamples of 5 kg or 2.5 kg, respectively, were thus obtained by quartering and ground to the size required for the OCT, i.e. about 2200 g for BC and 700 g for SC.

All subsamples were initially reduced in particle size using jaw and roller crushers until the material passed through a No. 8 sieve (2.38 mm). Following that initial crushing stage, various types of mills or pulverisers were used to achieve the desired particle size: <160 µm (Section 3.4).

6. Milling equipment and operations

Four types of mills/pulverisers were used in this study: rod mill, disk mill, ball mill, and planetary ball mill.

The rod mill consists of a steel-coated barrel in which steel rods are used to grind the (aggregate) material. Each grinding cycle was fixed at 10 minutes.

The disk mill used was a Bico pulveriser equipped with two plates one stationary and the other one revolving. Three types of plates were tested to evaluate their influence on the oxygen consumption measurements: special wear-resistant iron alloy (SWRIAP), alumina ceramic (ACP), and chrome-alloy steel plates (CASP). The special wear-resistant iron alloy plates were selected for their wear resistance, given that their composition is designed to resist abrasion over extended use. The alumina ceramic plates are known to offer a high level of contamination control, corrosion resistance, and withstand use in high temperatures. The chrome-alloy steel plates can be used with harder materials and offer a long service life. Regardless of the plate type, the grinding was performed by progressively reducing the spacing between the plates.

The ball mill consists of a ceramic jar filled with small ceramic balls of 20 mm in size. The sample is placed inside the jar, which is then placed for 10-minute cycles between two rotating arms at 34 rpm, thus allowing the sample to tumble and generate fine particles.

For all the mills/pulverisers, the material was (dry) sieved for a period of 10 minutes after each cycle, using a Ro-Tap shaker; any fraction retained on 160 µm was then returned to the mill/pulveriser for an additional cycle. This process was repeated until the entire sample passed through the 160 µm sieve.

7. Columns configuration and sample/test preparation

The required amounts of materials were first mixed with a calculated amount of water to achieve a 40% saturation degree and then thoroughly mixed. The above material was then consolidated in two equal layers (by weight) into the column using a steel pestle. The total thickness of ground aggregate material and the headspace above in the column are respectively 10 and 10 cm (BC), and 7 and 7 cm (SC).

The columns were then sealed using a thin layer of high-vacuum grease to prevent leakage and the ingress of external oxygen between the column and the Plexiglas cap. A galvanic-cell oxygen sensor (Apogee SO-210) was inserted through the Plexiglas cap and connected to a data logger (OM-CP-Quadvolt 160 MV-A2).

8. RESULTS AND DISCUSSION

9. Effects of the type of columns and configuration (BC vs SC)

The initial version of the OCT, as mentioned in Appendix P of the CSA A23.1 standard, quickly assesses the oxidation potential of SBA, but requires large quantities of ground material (≥ 5 kg for two replicates using the BC column). The smaller column (SC) contributed at reducing the material requirements to one-third.

Six aggregates were tested: three non-reactive (NR) (HP, PKA, and Dolostone) and three reactive (R) (GGP, SW, and MSK) aggregates, which had been tested previously with BC. The results showed higher oxygen consumption for the reactive aggregates in SC, and somewhat similar values for the non-reactive aggregates, thus improving the difference between the two groups (Table 4.1.1).

Table 4.1.1: OCT results: comparison between big column (BC) and small column (SC).

Sample		BC [7]			SC			TS (%)
		Test 1 (%)	Test 2 (%)	**Avg.**	Test 1 (%)	Test 2 (%)	**Avg.**	
R*	MSK 2011	21.7	21.4	**21.6**	27.7	30.5	**29.1**	1.1-0.9
	GGP	5.4	6.0	**5.7**	11.5	11.5	**11.5**	0.33
	SW	8.2	8.2	**8.2**	15.4	15.9	**15.7**	0.07
NR**	HP	1.7	0.2	**1.0**	2.2	2.1	**2.2**	0.02

	DLS	3.0	0.2	**1.6**	3.1	3.0	**3.1**	0.14
	PKA	2.6	2.8	**2.7**	2.3	2.3	**2.3**	0.04

*Reactive aggregates, ** Non-reactive aggregates.

10. Types of mills

Table 4.2.1 presents the results of oxygen consumption testing conducted with the SC but following sample preparation using different types of milling equipment.

Table 4.2.1: Oxygen consumption test results for different types of mills (using the SC).

Aggregate Identification		TS (%)	Rod mill	Ball mill (ceramic)	Disk pulveriser (different plates)		
					SWRIAP	ACP	CASP
R	MSK 0.2*	0.18	23.7				
	MSK 0.9	0.9	29.4-40.9	8.5-9.4	98.5	6.6-9.7	18.7-23.5
	AC	0.81				2.8	30.2-31.4
	GGP	0.24-0.33					11.5
	MSK 2011	0.73 -1.28					27.7-30.5
	MSK riche	1.18				14.1	
NR	Ottawa sand	0.00			91.6		
	HP	0.00				0.3	2.1-2.2
	PKA	0.03	15.3	4.3	74.4	2.3	2.3-2.3
	AB	0.03				2.2	4.0-5.5
	WS	0.05-0.07					15.4-15.9
	AA	0.07				1.6	2.7-3.1

*This aggregate is likely to be only marginally reactive.

4.2.1 Rod mill

The rod mill was used in 2016 for the OCT and produced consistent results [7]. However, in 2022, unexpectedly high oxygen consumption values were recorded for the NR PKA aggregate, as well as for the MSK 0.9 and MSK 0.2 aggregates (Table 4.2.1). Further investigations revealed that the internal steel coating of the rod mill barrel had worn down, exposing the base metal. The presence of metallic iron likely contributed to the elevated oxygen consumption values by artificially increasing the oxidation potential of the sample.

4.2.2 Ceramic ball mill

A ceramic ball mill was used with the objective of preventing contamination and potentially excessively OCT values. For MSK 0.9, OCT results were unexpectedly low, ranging from 8.5 to 9.4% considering that OCT values around 20-25% are expected for that particular aggregate (Table 4.2.1). In this case, there are two possibilities for the low values: the particle size distribution and the use of the ceramic grinding media. In the case of the particle size distribution, despite the milling process being slow (34 rpm, 10 min) and the material being sieved repeatedly over a 160 µm sieve between each 10 min cycle, the process produced excessive amounts of fine particles, about 60% of which were below 75 µm in size. Since oxygen consumption depends on diffusion, the presence of a large amount of fine particles hinders diffusion and lowers consumption values. In the case of the ceramic grinding media, as is known, the use of ceramic, contrary to steel, does not have a rest potential, which does not promote the galvanic interactions and the pyrrhotite “activation” [9].

4.2.3 Disk mill

The use of SWRIAP originally selected for their wear resistance actually contaminated all tested samples, resulting in very high OCT values, regardless of their original sulfide content (Table 4.2.1).

Following the observation of low oxygen consumption values with the ceramic ball mill, additional tests were conducted using a disk mill with ceramic plates (ACP) to pursue the objective of avoiding metallic contamination of the test samples. Surprisingly, the aggregates MSK 0.9 and AC, which are rich in sulfur and pyrrhotite, showed low oxygen consumption (Table 4.2.1), making it difficult to distinguish between R and NR aggregates. Despite containing pyrrhotite and pyrite, AC's OCT value (2.8%) was similar to that of non-sulfide bearing aggregates PKA (2.3%) and AB (2.2%).

Finally, chrome alloy steel plates (CASP) were tested in the disk mill configuration. As shown in Table 4.2.3.1, using the CASP for materials processing resulted in high oxygen consumption (OC) values for aggregates with high TS content and low values for those with low TS content. These results confirm that the CASP allow for an effective discrimination between R and NR aggregates and that they are therefore suitable for use in oxygen consumption testing.

4.3 Overall assessment of OCT results

The results presented in Table 4.2.1 highlight substantial differences in the test results when using different milling equipment for aggregate preparation. Such discrepancies had also been reported by Rabieh et al. [10].

SBA showed significantly (but not excessively) higher oxygen consumption when ground using the disk mill equipped with CASP, whereas aggregates with little or no iron sulfides did not show such an increase. This suggests that CASP does not introduce any contamination and offers superior discrimination between R and NR aggregates. On the other hand, the use of ball mill and disk mill equipped with ACP systematically resulted in low OCT values. According to [9], the use of steel disks contributes at activating the oxidation of pyrrhotite through galvanic reactions, which is not occurring in the case of milling equipment made of ceramic disks, thus resulting in low consumption values.

This study highlights the importance of properly selecting the type of equipment and monitoring its condition especially in the case of oxygen consumption testing. Attention should indeed be paid to the wear state of steel components in rod mills, since contamination from metallic iron can have a significant impact on oxygen consumption measurements. This also highlights the importance of using reference aggregate materials, ideally a non-reactive and a sulfide-bearing aggregate, to help noticing unexpected or faulty results.

11. CONCLUSIONS

The main goals of this study were to assess the effect of sample preparation and of OCT equipment (column) configuration on the reliability and performance of the OCT for evaluating oxidation potential of SBA. The following conclusions can be drawn:

- Of the various grinding media tested, only the disk mill equipped with chrome-alloy steel plates produced reliable results that clearly distinguished between R and NR aggregates. These plates do not introduce contamination of the test specimens.
- Although the rod mill has produced consistent results in previous studies, its performance depends on the condition of the steel-coated barrel. If used, careful inspection is necessary to prevent contamination from barrel wear.
- To verify the absence of contamination during grinding, it is recommended that a control aggregate with no iron sulfides and of high hardness is included to more clearly reveal potential contamination from the grinding media.
- The small column (SC) configuration proved suitable for oxygen consumption testing. Compared to the large column (BC) setup, it lowered the time required for materials processing and offered better discrimination between R and NR aggregates.

Interlaboratory test results in which samples were pulverized in one laboratory and tested by different laboratories demonstrated good reproducibility, which suggests that the OCT method can provide

reliable results. However, in view of potential standardization, more specific instructions on sample processing operations, especially regarding the type of pulverizing methods/mills to use (or not to use!), should be included. Also, the establishment of non-reactive and reactive reference aggregates would help ensure proper quality control in performance testing, including the OCT, of iron-sulphide bearing aggregates for use in concrete.

12. REFERENCES

[1] Rodrigues, A, Duchesne, J, Fournier, B, Durand, B, Rivard, P and Shehata, M (2012). Mineralogical and chemical assessment of concrete damaged by the oxidation of sulfide-bearing aggregates: Importance of thaumasite formation on reaction mechanisms, Cem and Conc Res, 42 (10): 1336-1347. https://doi.org/10.1016/j.cemconres.2012.06.008

[2] Jana, D (2020). Pyrrhotite Epidemic in Eastern Connecticut: Diagnosis and Prevention. ACI Mat J., V.117, No1 https://doi.org/10.14359/51718059

[3] Leemann, A, Lothenbach, B, Munch, B, Campbell, T and Dunlop, P (2023). The “mica crisis” in Donegal, Ireland – a case of internal sulfate attack? Cem and Conc Res,168, https://doi.org/10.1016/j.cemconres.2023.10149.

[4] Leemann, A, Munch, B, Lothenbach, B, Winnefeld, F and Dunlop, P (2024). Defective homes in Donegal, Ireland: effect of exposure conditions and concrete quality on pyrrhotite oxidation and internal sulfate attack. Cem and Conc Res, 186. https://doi.org/10.1016/j.cemconres.2024.107684.

[5] Rodrigues, A, Duchesne, J, Fournier, B, Durand, B, Shehata, M and Rivard, P (2016). Evaluation protocol for concrete aggregates containing iron sulfide minerals. ACI Mat J, 113 (3): 349-359. doi: 10.14359/5168882

[6] CSA A23.1:19/CSA A23.2:19 – Annex P – National Standard of Canada - Concrete materials and methods of concrete construction/Test methods and standard practices for concrete, CSA Group, 933 p.

[7] Rodrigues, A, Duchesne, J and Fournier, B (2016). Quantitative assessment of the oxidation potential of sulfide-bearing aggregate in concrete using an oxygen consumption test. Cem and Conc Comp, vol. 67, 93-100, http://dx.doi.org/10.1016/j.cemconcomp.2016.01.003.

[8] Elberling, B, Nicholson, RV, Reardon, EJ and Tibble, P (1994). Evaluation of sulphide oxidation rates: a laboratory study comparing oxygen fluxes and rates of oxidation product release. Can Geotech J, vol. 31, number 3, pp 375-383, https://doi.org/10.1139/t94-045

[9] Rao, SR (2004). Surface Chemistry of Froth Flotation. Volume 2: Reagents and Mechanisms, 2nd edn., Kluwer Academic/Plenum Publishers, New York, 744 pp.

[10] Rabieh, A, Eksteen, JJ and Albijanic B (2017). The effect of grinding chemistry on cyanide leaching of gold in the presence of pyrrhotite. Hydrometallurgy, vol. 173, pp 115-124, https://doi.org/10.1016/j.hydromet.2017.08.013

An Oxygen-Rich Chamber Test to Evaluate Concrete Containing Sulphide-Bearing Aggregates

Peter O. Anifowose n (1), Medhat H. Shehata (1)

(1) Department of Civil Engineering, Toronto Metropolitan University, Toronto, Canada,

n Corresponding author: panifowose@torontomu.ca

Abstract

Deterioration of concrete due to oxidizable sulphide-bearing aggregates (SBA) remains a critical durability concern. This paper presents an optimization effort on a test developed at Toronto Metropolitan University that uses high-purity oxygen in a sealed, thermally controlled chamber to evaluate potential damage to concrete containing oxidizable SBA. In the original test, specimens (40x40x285 mm) containing a concrete mixture with coarse aggregate sizes between 5 and 14 mm were examined. Aggregates with different sulphur contents, as well as control specimens *without sulphide, were investigated, with total sulphur (T.S.) ranging from 0.15% to 5.6%. The* specimens *were subjected to a two-phase conditioning protocol, an oxidation, and a sulphate attack phase. The oxidation phase involved partial drying of the* specimens *at 40 °C for 24 hours, followed by a 3-hour vacuum, then injection of oxygen and a limited amount of water into the sealed chamber containing the* specimens*. The* specimens *were stored at 40 °C for 25 days. After storage conditions,* specimens *were soaked in a lime-saturated solution for 24 h before length-change measurements. Phase II consisted of storage at 5 °C and 100% RH to enhance thaumasite and ettringite formation. To optimize the test, different cement types and alkali boosting were attempted. Also, the duration of each phase was extended from 12 to 24 weeks. Under the optimized conditions, one sulphide-bearing aggregate showed 0.130% expansion during oxidation (24 weeks) compared to 0.038% under the preliminary test, a 224% increase. The oxygen-rich chamber method provides a reproducible accelerated mechanism-promoting approach to evaluate aggregates. Ongoing research aims to refine the method to detect aggregates with lower sulphur content.*

Keywords*: aggregate oxidation, concrete durability, oxygen-rich test, sulphate attack, sulphide-bearing aggregates.*

1. INTRODUCTION

Oxidation of iron sulphide-bearing aggregates (SBA) leading to deterioration in concrete structures remains a critical durability challenge affecting structures worldwide. Cases documented globally across multiple continents, including extensive damage in Canada, particularly in Quebec, where numerous residential and commercial buildings experienced premature deterioration attributed to pyrrhotitic aggregates [1,2]. The damage mechanism initiates when the sulphide minerals, primarily pyrrhotite ($Fe_{(1-x)}S$), undergo oxidation upon exposure to oxygen and moisture, generating ferric oxide, sulphuric acid, and sulphate ions. Initial damage manifests as rust staining, and then the release of sulphate ions reacts with aluminate phases in hydrated cement paste to form expansive products such as ettringite, gypsum, and at lower temperatures, favours thaumasite formation, leading to cracks, spalling, and structural compromise [3]. This severe consequence leads to the urgent need for a reliable test method for identifying potentially reactive aggregates prior to their incorporation in concrete.

One such aggregate test method is the accelerated mortar bar test (AMBT), developed by Rodrigues et al. [4] which provides a protocol for evaluating sulphide-bearing aggregate (SBA). The test employs mortar bars with sodium hypochlorite (bleach) soaking and thermal cycling. The AMBT requires the aggregates to be crushed to achieve particle sizes not larger than 4.75 mm, presenting little resemblance to the coarse aggregates. The crushing alters surface area-to-volume ratios and creates highly reactive surfaces compared to coarse aggregate particles. However, these factors could be seen as a practical and effective mode of accelerating the reaction under laboratory conditions. In addition,

the strong oxidizing environment and elevated temperature could potentially promote expansion in non-carbonate aggregates [5].

There exists a clear need for test methodologies that, while inherently accelerated, more reliably promote the deterioration mechanisms observed in the field and remain practical in duration for aggregate prequalification. An ideal test would incorporate coarse aggregates and limit the use of aggressive chemical agents. This research addresses these needs through the development and optimization of a concrete-based accelerated screening method that employs conditioning protocols designed to promote natural sulphide oxidation and internal sulphate attack. The oxygen-rich chamber test employs high-purity oxygen in sealed containers with regulated temperature and humidity.

2. MATERIALS AND METHODS

2.1 Materials

In the preliminary test, specimens were cast with general use (GU) cement, and the test was later optimized using white GU cement due to its high C_3A content. The baseline alkali content (Na_2O_{eq}) of white cement is 0.31%, but for this research, it was increased to 1.00%. The chemical composition of the cement types under consideration is provided in Table *2-1* below.

Table 2-1: Chemical and phase composition of cement used.

Cement	Fe_2O_3 (%)	Al_2O_3 (%)	SiO_2 (%)	CaO (%)	SO_3 (%)	MgO (%)	Total alkali (%)	C_3S	C_2S	C_3A	C_4AF	Blaine (m^2/g)
GU	2.30	5.30	20.20	61.90	4.20	2.30	1.00	48	22	10	7	411
WGU	0.00	5.10	20.99	66.24	3.21	0.95	0.31	67	9	11	0	529

Table *2-2* shows the aggregates considered for this research and summarizes the chemical composition and properties of these aggregates. One of the aggregates, MSK-H (with a 0.9% total sulphur), is a gabbro-type aggregate known for contributing to a series of foundation issues in the Trois-Rivières region [2]. Also, control and Ore aggregates were combined in selected proportions to generate mixes exhibiting a range of sulphur contents. None of the tested aggregates is alkali-reactive, and their expansions due to alkali-silica reaction (ASR) are listed in the table.

Table 2-2: Chemical composition of coarse aggregate

Aggregate	SSD Density (kg/m^3)	Rock type	ASR expansion (%)*	T.S. (%)	SiO_2 (%)	CO_2 (%)	Fe_2O_3 (%)	Al_2O_3 (%)	TiO_2 (%)	CaO (%)	MgO (%)	$Na_2O + K_2O$ (%)
ORE	3221.1	Mine waste	0.11	14	33.10	0.13	39.40	8.53	0.73	4.20	3.05	2.39
MSK-H	2881.0	Gabbro	0.05[1]	0.93	50.60	0.71	8.10	19.40	0.53	8.84	6.85	3.79
MSK-L	2881.0	Gabbro	0.05[1]	0.21	50.60	0.71	8.10	19.40	0.53	8.84	6.85	3.79
C1	Not Measured	Dolostone	-	0.151	2.25	43.22	0.79	0.32	0.03	29.85	20.00	0.06
C2	Not Measured	Basalt	0.08[2]	0.027	49.09	1.30	14.24	13.91	2.12	8.12	4.70	4.42

*: Expansion due to Alkali Silica Reaction as per CSA A23.2-25A test method. [6]
[1]: Araiza et al. [7] [2]: El-Mosallamy and Shehata [8]

2.2 Experimental procedure

Microprism specimens considered in this research were of 40 mm by 40 mm by 285 mm dimensions. The coarse aggregate sizes range from 4.75 to 13 mm. Two studs were installed at the end of each specimen to keep track of the length change. From the field experience and existing literature, oxygen

and moisture are the key ingredients that promote oxidation of SBA in concrete [9]. These conditions were simulated in the laboratory. Figure 2-1 below shows a diagrammatic representation of the processes involved

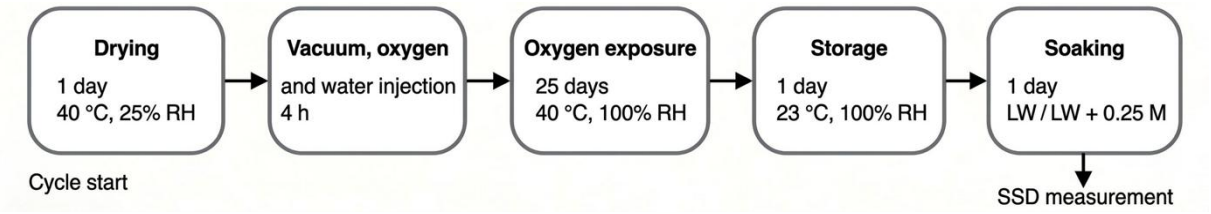

(a) Phase I (4 weeks)

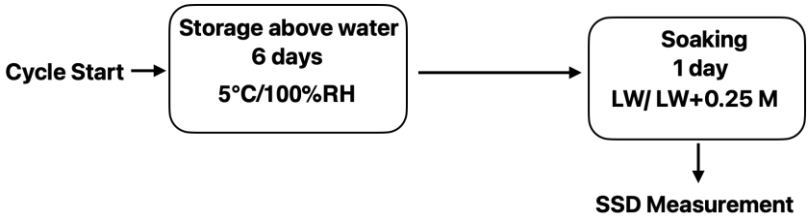

(b) Phase II (1 week)

Figure 2-1: Oxygen-rich test cycles: (a) 28 days per cycle for oxidation phase; (b) sulphate attack phase (7 days per cycle).

The specimens were subjected to a two-phase conditioning protocol. Phase I (oxidation phase) consisted of 28 days for each cycle. Each cycle began with partial drying at 40 °C/25% RH for 24 hours to achieve a 55 -70% degree of saturation. The 25% RH is the natural humidity measured in the drying room. The 55 -70% degree of saturation is assumed to be the minimum level of moisture to support oxidation. The degree of saturation is measured as the moisture content of the sample divided by the moisture content at saturation. After this, the specimens were arranged in a chamber, sealed, and subjected to a vacuum for 4 hours, followed by the injection of oxygen and a measured amount of water to rest at the bottom of the chambers without touching the samples. The chamber is then stored at 40 °C for 25 days. After 25 days of exposure, the specimens were soaked in the soaking solution for 24 hours before saturated surface dry (SSD) length-change measurements. These steps make the duration of one cycle 28 days. In the storage condition, the water remained at the bottom of the container, without touching the specimens; this was assumed to raise the degree of saturation from about 55% to 85%, thereby promoting oxidation. Phase II (sulphate attack) consisted of storage at 5 °C and 100% RH for thaumasite and ettringite formation. To optimize the test conditions, different cement types and alkali boosting were evaluated. In addition, the duration of both oxidation and sulphate attack phases was extended from 12 to 24 weeks. Different types of soaking solutions were also evaluated to assess their influence on reaction kinetics.

3. RESULTS

3.1 Initial experimental parameters

The preliminary study carried out with the developed oxygen-rich chamber test shows that only SBA with high total sulphur (T.S.) greater than 7% were detected by the test [10]. This implies that after the oxidation phase (12 weeks) and sulphate attack phase (12 weeks), only the C1+50% Ore showed high expansion of 0.16%. Other aggregate specimens, such as MSK-H, MSK-L, control, and even C1+40% Ore (5.6% T.S.), all showed low expansion. These results masked the documented reactivity of MSK-H, effectively classifying it as a non-reactive aggregate, warranting optimization, as will be presented later.

3.2 Optimization involving extended phase I.

From the earlier study [10], it was observed that the efficiency of the oxygen-rich test relies strongly on the oxidation phase. The available humidity during that stage appears sufficient to sustain subsequent sulphate attack. This necessitated extending both phases to observe how SBA with lower total sulphur (T.S. < 7%) would respond. The study was optimized by extending the length of each phase from 12 to 24 weeks. This provided additional time for sulphide oxidation and associated sulphate attack to develop.

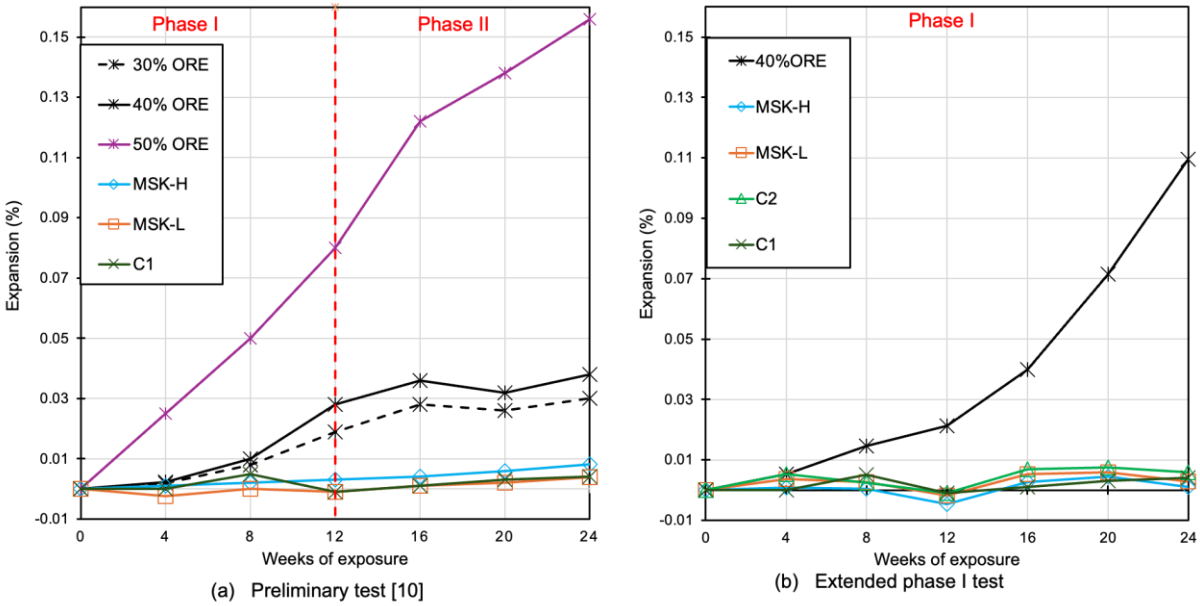

Figure 3-1: Expansion behaviour of SBA under oxygen-rich chamber exposure soaked in saturated limewater: (a) GU cement in phase I & II, each lasting 12 weeks; (b) White GU cement with 1.0% Na_2O_{eq} in phase I only lasting 24 weeks.

The results obtained from the optimization shown in Figure *3-1* above, which reflects the influence of extended phase I on the specimens. This can be seen in the C1+40% Ore specimens (5.6% T.S.). Comparatively, at the end of 12 weeks, the 40% Ore specimens (black line in Figure *3-1*a and b) exhibited close range expansion; a 0.024% expansion in the preliminary test and 0.021% during the optimized test. However, at the end of the 24 weeks, there was a significant difference in the same 40% Ore specimens exposed to the extended phase I condition. At this stage, a total expansion of 0.110% was recorded at the end of 24 weeks compared to the 0.040% expansion in the preliminary test, within the same time. This represents a 175% relative increase in expansion, highlighting the significant role of prolonged oxidation in driving sulphide reactivity. Even though an improved expansion was observed within the Ore specimens, the concrete specimen with the MSK-H aggregate, which caused issues in Quebec, did not produce significant expansion; therefore, further optimization of the test method was needed.

3.3 Optimization via higher alkalinity of the limewater soaking solution

In addition to the optimization through the extended duration of exposure, the alkalinity of the limewater soaking solution was increased with the addition of 0.25 M of sodium hydroxide. Increasing the alkalinity of the saturated limewater solution (LWS) can potentially accelerate the oxidation of sulphide minerals in SBA aggregates and promote earlier formation of sulphate [11].

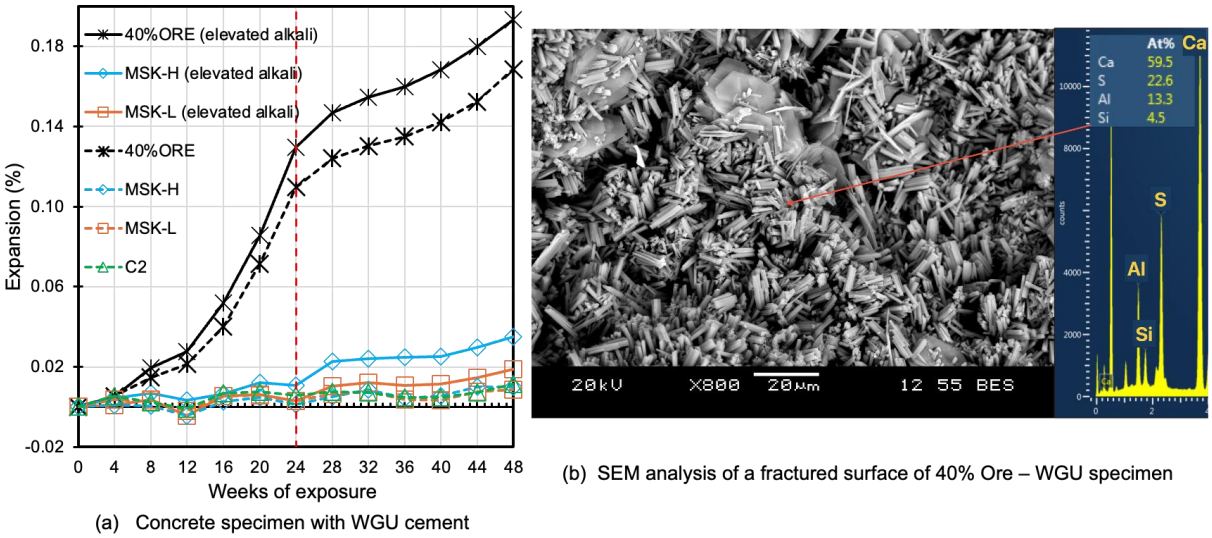

(a) Concrete specimen with WGU cement

(b) SEM analysis of a fractured surface of 40% Ore – WGU specimen

Figure 3-2: Expansion behaviour of concrete specimens containing SBA prepared with WGU (1.0% Na_2O_{eq}). **Dashed lines**: saturated limewater soaking conditions. **Solid lines**: saturated limewater with 0.25M NaOH soaking solution. The red dashed line indicates the phase I/II transition at 24 weeks: (b) SEM image of a fractured concrete surface showing ettringite-like needles in the paste adjacent to Ore aggregates, with corresponding EDS spectrum.

Figure 3-2(a) shows the influence of soaking solution composition on expansion under optimized conditioning. Specimens soaked in saturated limewater containing 0.25 M NaOH exhibited higher expansions than those soaked in saturated LWS alone, particularly for Ore and MSK-H aggregates. Increasing the alkalinity increases sodium and hydroxide ion concentrations, which can enhance sulphide oxidation and sulphate formation. The expansion curves show a clear two-stage response aligned with the exposure phases. In Phase I (40 °C, oxygen-rich chamber), C1+40% Ore specimens (T.S. 5.6%) in LWS produced a 0.1096% expansion, while the same specimens in LWS + 0.25 M condition yielded a 0.1296% expansion. In Phase II (5 °C and 100% RH), more expansion of 0.0584% and 0.0634%, giving 0.168% and 0.193% total expansion, respectively. MSK-H (T.S. 0.9%) showed moderate increases but was still more than double the former condition value, 0.0144% total in LWS and 0.0356% in LWS + 0.25 M NaOH. SEM analysis obtained from a fractured 40% Ore specimen confirms the presence of expansive ettringite-like products in the paste adjacent to sulphide-bearing Ore particles, which is consistent with the expansions measured in the optimized oxygen-rich chamber test.

The results confirm that the Phase I condition favors both sulphide oxidation and ettringite formation, which is reported to be stable at 40 °C [12]. Phase II expansion reflects continued ettringite development and potential thaumasite formation under colder, saturated conditions. The higher expansions in the Ore aggregate compared to MSK-H underscore the influence of total sulphur content and pyrrhotite abundance on oxidation and subsequent expansive phase development. The higher expansions observed with LWS + 0.25 M solution indicate that increased alkalinity promotes reaction kinetics and improves the sensitivity of the test method, supporting further refinement of the oxygen-rich chamber procedure for evaluating sulphide-bearing aggregates. Alkali silica reaction (ASR) mortar bar tests on mortars with 100% Ore aggregate yielded expansions of 0.11% at 80 °C and only 0.0045% at 40 °C, indicating that the expansion observed at 40 °C in the oxygen-rich chamber is unlikely to be governed by ASR but rather by oxidation of sulphide phases and the resulting sulphate attack. Consequently, the oxygen-rich chamber test, as configured in this study, should not be applied for assessing ASR-susceptible aggregates, since its response to ASR mechanisms has not been evaluated. More refinement is currently underway at Toronto Metropolitan University, where some promising results have been obtained for MSK-H after more refining.

4. CONCLUSION

The following conclusion can be drawn from the research carried out to develop a concrete test method for the evaluation of SBA.

1. The oxygen-rich chamber test method reflects field conditions in terms of aggregate size and reaction mechanisms. However, more optimization is needed, specifically for SBA aggregates with lower total sulphur.
2. An extended duration for the phase I condition proves to be paramount in the optimization of the test method. This is because the conditioning favors the influx of both moisture and oxygen necessary for oxidation. In addition, the temperature and humidity level also favour the formation of ettringite.
3. The alkalinity of the soaking solution influences expansion behavior, with specimens soaked in LWS + 0.25 M NaOH exhibiting higher expansion compared to limewater alone, demonstrating that elevated alkalinity enhances oxidation and may influence the stability of ettringite.

REFERENCES

[1] Chinchón JS, Ayora C, Aguado A, et al. Influence of weathering of iron sulfides contained in aggregates on concrete durability. Cem Concr Res 1995;25:1264–72.

[2] Rodrigues A, Duchesne J, Fournier B, et al. Mineralogical and chemical assessment of concrete damaged by the oxidation of sulfide-bearing aggregates: Importance of thaumasite formation on reaction mechanisms. Cem Concr Res 2012;42:1336–47.

[3] Casanova I, Agulló L, Aguado A. Aggregate expansivity due to sulfide oxidation—I. Reaction system and rate model. Cem Concr Res 1996;26:993–8.

[4] Rodrigues A, Duchesne J, Fournier B. A new accelerated mortar bar test to assess the potential deleterious effect of sulfide-bearing aggregate in concrete. Cem Concr Res 2015;73:96–110.

[5] El-Mosallamy M, Shehata MH. Sulphide oxidation mortar tests for evaluation of the oxidation potential of sulphide-bearing aggregate. Constr Build Mater 2020;264:120627.

[6] Canadian Standards Association. Detection of alkali–silica reactive aggregate by accelerated expansion of mortar bars (CSA A23.2-25A-25). Toronto, ON: 2025.

[7] Castillo Araiza R, Rodrigues A, Fournier B, et al. A new accelerated testing scheme to evaluate the potential oxidation reaction of sulfide-bearing aggregates in concrete specimens. Cem Concr Res 2024;180:107507. https://doi.org/https://doi.org/10.1016/j.cemconres.2024.107507.

[8] El-Mosallamy M, Shehata MH. Tests for oxidizable sulfides in aggregates: applicability and limitations. ACI Mater J 2020;117:229–40.

[9] Steger HF. Oxidation of sulfide minerals: VII. Effect of temperature and relative humidity on the oxidation of pyrrhotite. Chem Geol 1982;35:281–95.

[10] Shadkam HR, Shehata MH. Use of oxygen-rich environment to test concrete containing sulphide-bearing aggregate and evaluate the effect of mitigative measures. Constr Build Mater 2025;477:141244.

[11] Li Z, Gorski CA, Thompson A, et al. Dissolution kinetics of iron sulfide minerals in alkaline solutions. Cem Concr Res 2025;193:107850.

[12] Nguyen H, Carvelli V, Kunther W, et al. Phase evolution and mechanical performance of an ettringite-based binder during hydrothermal aging. Cem Concr Res 2021;143:106403. https://doi.org/https://doi.org/10.1016/j.cemconres.2021.106403.

Assessment and Refinement of Analytical Chemistry Methods to Determine Sulfide Sulfur in Concrete Aggregates toward Standardization in the U.S.

April Snyder [(1)], Michael Baker [(2)]

(1) ECS Mid-Atlantic, LLC, Pittsburgh, PA, USA, asnyder1@ecslimited.com

(2) RJ Lee Group, Inc., Monroeville, PA, USA, mbaker@rjleegroup.com

Abstract

The oxidation reaction of the iron-sulfide mineral pyrrhotite within certain concrete aggregate in the northeastern United States has resulted in deterioration of residential concrete foundations. These foundation structures experienced expansion, extensive cracking, and loss of structural integrity, with the homeowners experiencing significant financial loss. While pyrrhotite has the potential to produce concrete deterioration in some situations, the amount of pyrrhotite needed to cause damage is not fully understood. Researchers around the world are working to develop techniques for identifying and quantifying potentially deleterious iron sulfides in concrete aggregates. Due the complexities of detection and quantification, a standardized technique has not yet been established, although limits have been put in place in Connecticut and Massachusetts for sulfur content in aggregate for the concrete industry.

This paper presents the results of research evaluating high-temperature combustion and microwave digestion and detection by ICPAES for total sulfur, and acid digestion and ICPAES for speciation. The aim of the study was to evaluate parameters of existing ASTM standards, the method presented in Annex P of CSA A23.2, and a new method for digestion to determine the most reliable parameters for detection of sulfur to inform a new standard development at ASTM. A rigorous comparison of the effect of the various sample preparation, sample size and analytical methods on the variability of results when applied to a variety of different concrete aggregates with different sulfur species was performed.

***Keywords**: LECO, pyrrhotite, sulfur, sulfide-sulfur, ICP-AES*

1. INTRODUCTION

Iron sulfide minerals are susceptible to oxidation in the presence of oxygen and moisture. When present in concrete aggregates, the oxidation reaction has potential to cause deleterious reactions in concrete structures from the expansive reactions and secondary products manifesting to internal sulfate attack in the most severe cases [1]. Extensive deterioration of residential concrete foundations due to internal sulfate attack resulting from the presence of pyrrhotite in concrete aggregate identified in Trois-Rivières, Quebec, and Connecticut and Massachusetts, USA [1,2,3] has initiated testing and evaluation protocols of aggregate sources to identify and quantify potentially deleterious iron-sulfide content. Canada has developed an informative appendix (Annex P) to their concrete standard CSA A23.1/A23.2-19, with an assessment protocol including measurement of total sulfur content (S_T) in the aggregate and subsequent performance tests based on the results [4]. Connecticut legislation restricts use of sulfide-bearing aggregate for use in concrete based on S_T and presence of pyrrhotite [5], and similar measures are in process in Massachusetts.

Various existing analytical methods are available to determine S_T, but at present there is no consensus test method for detection and quantification of sulfur in concrete aggregate in North America. A test method presented in Annex P is under evaluation, and there are existing ASTM test methods for detection of sulfur in coal and ores as summarized in Table 1.1. Of note, European regulations exist for S_T in concrete aggregate and are specified in EN 12620, which has a limit of 1% by weight for aggregates (excluding slag) without pyrrhotite and 0.1% if pyrrhotite is present. Testing for S_T is outlined in EN 1744-1 [6] with the reference method of gravimetric analysis after acid digestion with $BaSO_4$ precipitate and alternatively, high temperature combustion. Our experience and others have found that the gravimetric

method consistently underestimates the S_T content [7], and the test method is generally onerous with opportunity for high variation.

The standard deviation, sample size and crushing regime differs between methods, and can influence the variability of results. Additionally, different sulfur forms, and especially sulfides, decompose at high temperatures and result in loss of S_T in vapor. Because of this, X-ray Fluorescence (XRF) using fused bead preparation was not included in the CSA Annex P method. The first round-robin investigation for CSA Annex P total sulfur test method found unreliable results even with pressed pellet XRF analyses [8]. Pyrrhotite is more reactive and less stable than pyrite, presenting additional challenges for reliable and consistent detection. Of greatest challenge is that the limit for total sulfur of 0.1% by weight when pyrrhotite is present and the standard deviation of the test procedures can be at or greater than the acceptable limit depending on the method (Table 1.1)

The objective of this study was to refine test parameters to reduce variability for applicability for a range of aggregate types containing a range of iron-sulfide mineral types with the goal of identifying the most promising methods for proposed standardization. A key component was to identify analytical methods that could be reliably performed by a wide range of commercial analytical chemistry laboratories.

Test methods for total sulfur do not distinguish between sulfate and sulfides. Sulfide content is the primary objective of this study, as aggregate used for concrete generally would not be expected to contain sulfate compounds, although this is of interest in the industry when testing concrete for iron-sulfide content.

The key components of this study included:

1. Validate a method for the use of Inductively Coupled Plasma-Atomic Emission Spectroscopy (ICP-AES) following EPA Method 6010C, after microwave digestion.
2. Refine parameters for high temperature combustion (HTC) method with regard to fineness of the sample for analysis, and general calibration procedures.
    a. Based on existing ASTM test methods for sulfur, we focused solely on combustion with infrared detection.

Table 1.1: Compilation of components of existing test methods for determining total sulfur content [9].

Standard test procedure	Method for total sulfur analysis	Sample to pass	Sample size, g	Reproducibility limit (R)
ASTM D4239	Combustion method with infrared detection	250 µm (No. 60)	0.1 to 0.2	Varies dependent on the sulfur content from 0.05914 to 0.58563. For total sulfur contents from 0.38775 to 5.6125
ASTM E1915	Combustion method with infrared detection	150 µm* (No. 100)	0.2†	Varies dependent on the sulfur content from 0.0133 to 0.648. For total sulfur contents from 0.004 to 4.70
CSA A23.1-19/ A23.2-19, Annex P	Combustion method with infrared detection or acid detection	160 µm	According to manufacturer —up to 5 g	Under development. Preliminary values vary dependent on the sulfur content from 0.08 to 0.28 for total sulfur contents 0.10 to 1.2
ASTM E1621	XRF	Varies‡	Varies 0.3 to 1.0	Function of sample preparation, calibration scheme, and sample homogeneity

*May be necessary to grind samples to pass 75 µm (No. 200) to improve precision of samples containing low contents of sulfur
†Section 10.5.1.1: Different instruments may require different sample masses for certain content ranges
‡Sample prep for powder XRF requires sample to pass 75 µm, with 50 µm ideal
Note: 1 g = 0.035 oz

2. MATERIALS AND METHODOLOGY

The following approach was followed for our evaluation.

1. Perform preliminary investigation of laboratory created standards and standard aggregate with known sulfur values
    a. Validate the ICP-AES with microwave digestion
    b. Validate HTC method with appropriate standard reference material for calibration
2. Perform validated ICP-AES and HTC procedures on a variety of aggregate samples crushed to pass the following sieve sizes: No 60 (250 µm), No. 100 (150 µm) and No. 200 (75 µm)
    a. Determine the within laboratory standard deviation of the test methods performed on different sieve sizes

   b. Determine whether the variability of results were affected by the iron-sulfide mineral type present in the aggregate as identified by petrography
3. Test the powdered aggregate samples at the different sizes for sulfide sulfur following method outline in CSA Annex P using a 5-gram sample, and using a 2-gram sample for comparison of results variability.

2.1 Preliminary Investigation and Refinement of Parameters

Following is an outline of the preliminary investigation to validate the ICP-AES method with microwave digestion and the HTC method with appropriate standard for calibration.

- Standards created with known sulfur values ranging from 0.015 – 0.292
  - Quartz Sand
  - $CaSO_4 \cdot 2H_2O$ Calcium Sulfate Dihydrate
  - FeS Fe(II)Sulfide
  - Mix of equal parts sulfate and sulfide materials by weight
  - Crushed to pass #60 (250 µm), #100 (150 µm), #200 (75 µm) sieves
- Analyses performed on 3 or more sub-samples of each Standard
  - High Temperature Combustion – LECO using Infrared Spectroscopy
  - Microwave Digestion with ICP Detection
- Analyses Performed on 3 or more sub-samples of Aggregate containing iron sulfide known amounts of sulfur
  - Pyrite-containing siliceous aggregate
  - Pyrite and Pyrrhotite containing siliceous aggregate
  - Slag

Note: XRF pressed pellet was performed in this initial stage with negative results so it was not continued for the subsequent phase of testing and therefore not included in this discussion.

2.1.1 Analytical Method Refinement for Total Sulfur (S_T) Content Determination

2.1.1.1 High-Temperature Combustion

The method used for the sample analysis generally followed ASTM D4239. A state-of-the-art TruSpec LECO CHN coupled with a Sulfur module (Model Number 630-100-700, Part Number 4318) was used for the analysis of the samples using the Sulfur-in-Flyash 3 module. Weighted samples were introduced in the high-temperature combustion furnace. The combustion converts sulfur to SO_2. The combustion gases are swept from the furnace, through scrubbing reagents, and onto the detection systems as they are being released. Total sulfur is measured as SO_2 in the optimized independent SO_2 IR detector. SO_2 absorbs IR energy at a precise wavelength within the IR spectrum. All other IR energy is prevented from reaching the IR detector by a narrow band-pass filter. The furnace temperature was at a minimum of 1350°C to 1400, the analysis stabilize comparator was set to 2, the manual load baseline delay time was 3 seconds, the baseline time was 1 second, the auto detect data missed time was 5 seconds, the minimum analysis time was 140 seconds, the comparator level was 10%, the endline time was 1 second, the conversion factor was set to 1 and the significant digits for the reporting of the results was 3.

The instrument was calibrated prior to the sample analysis using a 6-point calibration. Different concentrations of two certified reference materials were used, QAR CRM Coal 1- 1.45% Sulfur (Part Number 502-831, Lot Number 16335) and QAR CRM Coal 3- 0.383% Sulfur (Part Number 502-833, Lot Number 14255), for the instrument calibration. Before and after the analysis of the samples, blank samples and calibration verification was performed using QAR CRM Coal - 1.45% Sulfur certified reference material (Part Number 502-831, Lot Number 16335). For the calibration verification to be accepted the value of the measured sulfur should be within 10% of the theoretical value. The instrument's detection limit was also calculated using QAR CRM Coal- 0.383% Sulfur certified reference material (Part Number 502-833, Lot Number 14255). A blank sample and a calibration verification was also performed every nine samples analyzed. Analyses were performed using 0.5 g, 1 g and 2 g of each sample.

Initial evaluation of the CRM Coal with 1.45% Sulfur consistently gave results outside of the expected for the standards created due to the low sulfur level of the aggregate samples which outlined the importance of using standard reference materials that are most closely aligned with the expected sulfur content of the samples you are analyzing as outlined in ASTM 4239 and ASTM E1915. The lower sulfur

content standard was selected and used for testing. The instrument's detection limit ranged from 0.029-0.049 wt% sulfur.

2.1.1.2 Inductively Coupled Plasma Atomic Emission Spectroscopy (ICP-AES)

The ground samples were prepared for ICP-AES using microwave digestion for complete dissolution and better analyte recovery of volatiles. Homogenized, ground samples of concrete were weighed 0.1000 +/- 0.01 g and placed into CEM brand EasyPrep Vessels. To each vessel was added 1 mL 30% hydrogen peroxide. This was followed by 4 mL concentrated nitric acid and 4 mL concentrated hydrochloric acid. The vessels were sealed and placed into the microwave. A CEM Mars5 or Mars6 microwave was used. The digestion program was as follows:

1. 1600 watts at 100% power ramped 20 mins to 150°C held 5 mins
2. 1600 watts ramped 15 mins to 200°C held 10 mins

After cooling the vessels were open and the samples taken to a final volume of 50 mL with double deionized water. The solution was analyzed for sulfur using following EPA-6010C ICP-AES. The detection limit for ICP-AES is considerably smaller than HTC, as little as 0.00456 wt.%.

2.1.2 Results Discussion

Results presented in Figures 2.1.2.1 and 2.1.2.2 and Table 2.1.2.1 show that the microwave digestion test method had comparable and even better results with the HTC method. HTC method showed more consistent results with a sample size of 0.5 g, therefore that was used for the next phase of testing.

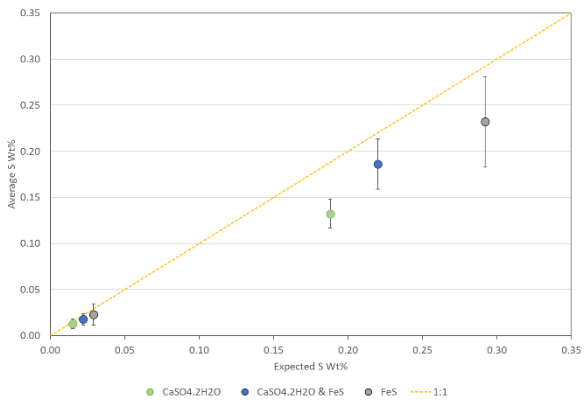

Figure 2.1.2.1: HTC Results of Standards

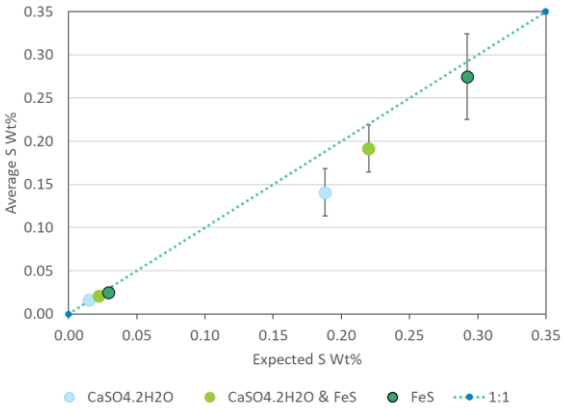

Figure 2.1.2.2: ICP-AES Results of Standards

Table 2.1.2.1: Average % and St.Dev of Rock Samples Analyzed 3-6 replicates

Aggregate	HTC Mean – St. Dev	ICP-AES Mean – St. Dev.
Pyrite bearing siliceous rock	0.522 - 0.021	0.434 - 0.027
Pyrite and pyrrhotite bearing siliceous rock	0.700 – 0.092	0.661 - 0.055
Slag crushed at 60 mesh	0.978 - 0.114	Not analyzed

2.2 Analyses of Aggregate Samples for Within Laboratory Precision

2.2.1 Aggregate Materials

The National Sand Stone and Gravel Association (NSSGA) provided sixteen (16) aggregate samples of unknown origin for the study from participating producers. The majority of aggregate supplied were a #8 sieve gradation size, with the exception of CA-WF10J which was a coarse aggregate with a top size of 1.25", and P21ZFO which was a #9 sieve gradation sized stone. Samples were collected following D75/D75M *Standard Practice for Sampling Aggregates* and reduced for testing generally following ASTM C702 *Standard Practice for Reducing Samples of Aggregate to Testing Size*. Any unwashed samples received were washed following ASTM C117 and dried at or below 110°C.

Table 2.2.1 lists the aggregate samples included in the study. Detailed petrographic analyses to identify the rock types was not performed, but the hand specimens were generally categorized, indicating that fifteen of the aggregate samples were siliceous and one was calcareous. A representative portion of each aggregate sample was mounted in epoxy, cross sectioned and finely polished for reflected light microscopy to identify the sulfide minerals present to evaluate the effect of mineral type on the results of the total sulfur tests.

Table 2.1.1: Aggregate Analyzed and Iron-Sulfide Minerals Detected

Aggregate ID	Rock Type	Sulfide Minerals
P-GGJ2A	Mafic	Cp
P-21ZF0	Intermediate	ND
P-CC2OR	Calcareous	Py
P-WMEEM	Felsic	ND
CA-WF10J	Mafic	Py, Po, Cp, Pn
P-7UR7U	Mafic	Py, Cp
P-BBPKZ	Sedimentary	Py, Po, Cp
P-084PX	Mafic	Py, Cp, Pn
P-08VSX	Mafic	Py, Cp, Pn
P-3JNLC	Felsic	Py
P-AARVS	Mafic	Po, Cp
P-69YOS	Felsic	Py
P-GY1CF	Felsic	Other
P-3RWAS	Intermediate Gneiss	Po, Py
P-Z91UM	Intermediate/Mafic Gneiss	Py, Po
P-VIT7W	Mixed siliceous	Py

Py=pyrite, Po=pyrrhotite, Cp=chalcopyrite, Pn=Pentlandite, ND-none detected

2.2.2 Preparation of Samples for Chemistry Tests

Aggregate was passed through a chipmunk jaw crusher, which allowed smaller material to be pulverized in a motorized disc mill. The spacing factor on the disc mill was set to approximately 1 mm when pulverizing to achieve material passing 60 mesh. A smaller, yet arbitrary spacing was used thereafter to achieve material passing 100 mesh, and 200 mesh. While pulverizing aggregate using the disc mill, a sieve shaker outfitted with the proper sieve size was used to pass material through efficiently. A sub-sample was taken from each size range for testing.

2.2.3 Analytical Method for Sulfide Sulfur (S^{2-}) Determination

The total sulfide sulfur was measured by difference following the procedure outlined in CSA Annex P, using a 2 g and a 5 g sub-sample of aggregate and testing the filtrate for sulfate sulfur by the alternate method of ICP-AES (also following EPA-6010C).

3. RESULTS AND DISCUSSION

Results of our investigation indicated that both HTC and the ICP-AES analysis following microwave digestion had good within-laboratory precision as indicated in Tables 3.1 and 3.2 based on three replica analyses each. The samples crushed to pass #200 had the lowest variation. Proper calibration of HTC with standard reference materials with low sulfur contents close to what would be expected for concrete aggregate, less than 0.5% wt. is necessary. Aggregate containing pyrrhotite had higher variability than those without.

Sulfate sulfur content of the aggregate samples tested were very small, generally less than 0.01% by wt. The sample size of 2 g versus 5 g had no effect on results.

Table 3.1: Analytical Results Compilation

	P-GGJ2A	P-21ZF0	P-CC2OR	P-WMEEM	CA-WF10J	P-7UR7U	P-BBPKZ	P-084PX	P-08VSX	P-3JNLC	P-AARVS	P-69YOS	P-GY1CF	P-3RWAS	P-Z91UM	P-VIT7W
#60 LECO	ND	ND	0.12	ND	0.54	0.05	0.26	0.11	0.07	0.05	0.14	0.15	0.10	0.43	0.25	0.14
St. Dev.	*n/a*	*n/a*	*0.01*	*n/a*	*0.023*	*0.003*	*0.015*	*0.017*	*0.005*	*0.004*	*0.006*	*0.006*	*0.007*	*0.006*	*0.000*	*0.000*
#60 ICP	0.014	0.016	0.136	0.010	0.596	0.062	0.224	0.114	0.092	0.054	0.177	0.144	0.103	0.447	0.250	0.141
St. Dev.	*0.0015*	*0.0022*	*0.0249*	*0.0043*	*0.0530*	*0.0134*	*0.0070*	*0.0262*	*0.0105*	*0.0221*	*0.0285*	*0.0179*	*0.0107*	*0.0721*	*0.0467*	*0.0030*
#100 LECO	ND	ND	0.12	ND	0.53	0.07	0.33	0.14	0.13	0.06	0.18	0.15	0.10	0.43	0.25	0.14
St. Dev.	*n/a*	*n/a*	*0.000*	*n/a*	*0.026*	*0.004*	*0.006*	*0.006*	*0.010*	*0.003*	*0.006*	*0.000*	*0.002*	*0.006*	*0.006*	*0.006*
#100 ICP	0.017	0.019	0.138	0.017	0.547	0.068	0.321	0.142	0.126	0.072	0.236	0.144	0.092	0.439	0.272	0.142
St. Dev.	*0.0007*	*0.0021*	*0.0104*	*0.0009*	*0.0545*	*0.0150*	*0.0569*	*0.0211*	*0.0142*	*0.0053*	*0.0131*	*0.0162*	*0.0122*	*0.0953*	*0.0227*	*0.0084*
#200 LECO	<0.013	<0.013	0.13	<0.013	0.58	0.08	0.37	0.17	0.23	0.06	0.32	0.15	0.10	0.45	0.25	0.14
St. Dev.	*n/a*	*n/a*	*0.006*	*n/a*	*0.006*	*0.001*	*0.010*	*0.006*	*0.006*	*0.001*	*0.006*	*0.006*	*0.001*	*0.006*	*0.000*	*0.000*
#200 ICP	0.026	0.027	0.146	0.015	0.599	0.083	0.391	0.190	0.247	0.063	0.338	0.144	0.098	0.481	0.260	0.140
St. Dev.	*0.0009*	*0.0014*	*0.0062*	*0.0025*	*0.0021*	*0.0058*	*0.0258*	*0.0046*	*0.0031*	*0.0032*	*0.0131*	*0.0361*	*0.0128*	*0.0395*	*0.0221*	*0.0085*

Table 3.2: Within Laboratory Precision

Sieve Size & Test Method	Average St. Dev.
#60 HTC	0.008
#100 HTC	0.006
#200 HTC	0.004
#60 ICP-AES	0.0215
#100 ICP-AES	0.0218
#200 ICP-AES	0.0117

4. ACKNOWLEDGEMENT

The research was primarily funded by the ACI Foundation (ACIF) Program under its Concrete Research Council (CRC), with initial funding from the National Ready Mix Concrete Association (NRMCA) Foundation and materials donated and shipped by members of National Sand Stone and Gravel Association (NSSGA).

5. REFERENCES

[1] Rodrigues, A., Duchesne, J., Fournier, B., Durand, B., Rivard P., and Shehata M. (2012) Mineralogical and chemical assessment of concrete damaged by the oxidation of sulfide-bearing aggregates: Importance of thaumasite formation on reaction mechanisms. Cement and Concrete Research 42 (10) pp 1336–1347

[2] Zhong R., Wille K., (2018) Deterioration of residential concrete foundations: The role of pyrrhotite- bearing aggregate. Cement & Concrete Composites 94 pp. 53-61. Doi:10.1016/j.cemconcomp.2018.08.012

[3] Scaglione N., Piercey P. (2024) Petrographic Characterization of Concrete Aggregates Involved in IronSulfide Reactions in Residential Concrete Foundations in Connecticut and Massachusetts. Proceedings of the 1st International Conference on Iron Sulfide Reactions in Concrete, Quebec City, Canada, pp 49-52

[4] CSA A23.1/A23.2 (2019), Annex P (informative) – Impact of sulphides in aggregate on concrete behavior and gloval approach to determine potential deleterious reactivity of sulphide-bearing aggregates. Canadian Standards Association, Mississauga, Ontario, Canada. 288-341

[5] State of Connecticut Substitute House Bill No. 6646 Public Act No. 21-120 (2021) An Act Concerning Crumbling Concrete Foundations. https://www.cga.ct.gov/2021/act/Pa/pdf/2021PA-00120-R00HB-06646-PA.PDF

[6] EN 1744-1:2009+A1:2012 Tests for chemical properties of aggregates – Part 1: Chemical analysis. Section 11. Determination of total sulfur content. 35-37

[7] Oberhardt N.A., Lindgard J., Aasly K., (2024) Comparative evaluation of CEN standard test methods for the determination of the total sulfur content in concrete aggregates. Proceedings of the 1st International Conference on Iron Sulfide Reactions in Concrete, Quebec City, Canada, pp 81-85

[8] Logan L., Rogers C., Fournier B., CSA Research Group (2019). Multi-laboratory study of proposed new test for determination of sulphide sulphur content of concrete aggregates. Csagroup.org

[9] Bentivegna A., Snyder A., Stacey S., (2023) Pyrrhotite in concrete aggregates. Concrete International, Vol. 45 Issue 8, pp 37-44. DOI: 10.14359/51739100

ICISR 2026

2nd International Conference on Iron-Sulfide Reactions in Concrete

Technical Session # 2:

Mechanisms and Field Performance of Iron-Sulfide–Induced Concrete Deterioration

UCONN | COLLEGE OF ENGINEERING
SCHOOL OF CIVIL AND ENVIRONMENTAL ENGINEERING

UCONN
COLLEGE OF ENGINEERING
CONNECTICUT TRANSPORTATION INSTITUTE (CTI)

Differences in internal sulphate attack across the Republic of Ireland and long-term implications – how far could it go?

Brough C(1), Staniforth B(1), Garside R(1), Colville, R(1), Fletcher J(1), Strongman J(1), Garner C(1)

(1) Petrolab Ltd, Redruth, UK, chris@petrolab.co.uk

Abstract

Internal sulphate attack in concrete blocks has damaged thousands of properties across the Republic of Ireland. Two main aggregate types are implicated: pyrrhotite-bearing metasediments in Donegal and framboidal pyrite in calcareous mudrock across other counties. The development of internal sulphate attack and the rate of deterioration differ between aggregate types, affecting how the problem develops nationally and how many properties may ultimately be impacted. In Donegal, pyrrhotite occurs within weak phyllite aggregate, which cracks readily as oxidation and expansion occur. The binder is also weak due to elevated microporosity, accelerating deterioration. In Mayo, rapid deterioration has been linked to non-compliant, high total sulphur levels, very fine-grained framboidal pyrite, and rare framboidal pyrrhotite, all of which increase reactivity. More recently, Clare and Limerick have emerged as a slower-developing hotspot. Although broadly similar to Mayo blocks, they typically have lower total sulphur levels, often within EN 12620 limits, coarser framboidal pyrite, and no framboidal pyrrhotite. These three factors mean that, despite the properties being built at a similar time to the Mayo properties, the emergence of Clare and Limerick as a hotspot occurred later.

In order to produce a reasonable prediction for the total number of impacted properties a further analysis was undertaken of estates spread across Donegal, Mayo & Clare, looking at the number of properties currently tested from each estate, against the total size of the estate, and working on the assumption that each estate would have been built from the same concrete block, from one supplier. In each of the estates analysed, only high-risk concrete has so far been identified. Within Donegal and Mayo, where the concrete blocks are faster-deteriorating, this analysis suggests numbers will still rise significantly, with a four- to six-fold increase currently predicted. However, within Clare and Limerick, the same estate-based analysis suggests that the problem is only just emerging and that the full scale of the issue may expand by a relatively much larger margin. The conclusion of the estates analysis gives a current estimate of approximately 20,000 properties across the four main hotspots. This analysis excludes social housing, businesses, business-residential duplexes, poor quality hardcore and other counties due to a lack of data, meaning that numbers could still rise significantly further above this prediction.

***Keywords**: aggregates, internal sulphate attack, petrography, pyrite, pyrrhotite*

1. INTRODUCTION

The impact of internal sulphate attack on the deterioration observed within concrete blocks across the Republic of Ireland is now well established, with either the use of pyrrhotite-bearing metasediments in Donegal ([1],[2]), or of framboidal pyrite-bearing calcareous mudrock in other impacted counties (e.g. [3]). The I.S. 465 analysis of these blocks for the Housing Agency as part of the Enhanced Grant Scheme ([4],[5]) has so far focussed on Donegal as the worst impacted county, but is now increasingly observing properties from the other impacted counties along with further incidences of properties impacted by the use of calcareous mudrock in hardfill [6], the latter representing further inappropriate use of pyrite-bearing mudrock construction material and covered by the I.S.398 standard [7]. The growth of tested properties and combining the datasets for I.S.465 testing and I.S.398 testing shows that the Republic of Ireland now has hotspots of some poor-quality aggregate used inappropriately within two separate building products. There are also emerging short-term and long-term implications that are beginning to clarify with the emerging dataset and this paper explores these.

1.1 Maps

Updated Ireland wide maps (Figure 3.1 & 3.2) are presented that cover the current extent of impacted properties across Ireland, looking at the combined dataset of I.S. 465 and I.S.398 analysed properties. Further discussion on the association with the geology of the counties and the use of inappropriate aggregate are also raised.

1.2 Aggregate deterioration rate

Internal sulphate attack is the dominant deterioration mechanism across affected Irish counties, but evidence suggests slight differences in both deterioration rate and petrographic expression between aggregate types. These differences appear linked to aggregate mineralogy and binder characteristics, with contrasts observed between Donegal's pyrrhotite-bearing phyllite blocks, Mayo's framboidal pyrite blocks, and the slower-deteriorating Clare and Limerick blockwork. Such variation has important implications for predicting the mid- to long-term impact on Ireland's housing stock, including the eventual number of affected properties.

2. MATERIALS AND METHODS

For the analysis of samples in accordance with I.S. 465 or I.S. 398 three main tools of investigation were used. These were petrography, chemical testing and database records. Analysis proceeded after sample receipt, starting with hand specimen observations (Suite A for I.S. 465 or Test Suite 0 for I.S. 398) and typically progressing onto thin section evaluation (Suite B for I.S. 465 or Test Suite 1 for I.S. 398). The three techniques are briefly described below.

2.1 Hand specimen and optical petrography

The analysis at hand specimen stage varies a little between I.S. 465 and I.S. 398. For I.S. 465 the first stage of analysis is the Suite A and the submitted samples are examined as received using a low-power stereoscopic microscope with fibre optic illuminator/ring lights. An aggregate type is assigned to each concrete sample and a preliminary risk categorisation given. Photographs of the received cores, including a cut surface of the main concrete type, are taken and recorded. Risk at Suite A is assigned based on the visual "soundness" of the core sample, the proportion of problematic lithologies (sulphide- or mica-bearing) and visual evidence of aggregate or cement paste deterioration. Where samples progress to Suite B, thin sections and polished blocks are prepared using standard geomaterials techniques and examined by transmitted, fluorescent and reflected light polarising microscopy. Results are then reported to the client and added to the overall database.

For the I.S. 398 testing a macroscopic investigation is undertaken on a riffle split sub-sample. A preliminary macroscopic examination (Suite 0) is undertaken in accordance with EN 932-3:2022 [8] using the +4 mm size fraction. Prior to washing, an examination of the surface coatings, particularly the presence of gypsum, is carried out. The aggregate is then gently washed to allow better lithology identification while still trying to retain any sulphate coatings. The wt% abundance of "mudrock" aggregates is determined. For samples which need progressing for further testing (Suite 1) a more detailed aggregate petrographic thin section examination is carried out on the full sized aggregate to confirm the abundance and type of mudrock as well as check for sulphide oxidation and sulphate growth.

2.2 Chemical testing

For concrete block tested according to I.S. 465 chemical analysis is undertaken on material taken adjacent to the selected thin/polished block section locations. For hardcore samples tested according to I.S. 398 a representative riffle split sub-samples is used. For both of these, analysis is carried out by a UKAS accredited laboratory in accordance with BS E.N. 1744-1, clauses 10, 11.2 and 12. [9] The analysis procedure involves high temperature combustion in an atmosphere of pure oxygen, followed by quantification by infrared detectors. Quantification limits are to the nearest 0.001% with data reported rounded to 0.01%. For I.S. 465 testing corrections are made to the reported total sulphur (TS) data to account for S that will be naturally present as part of the cement (taken to be ~0.1% as mentioned in Annex E of I.S.465) and to account for the density difference between binder and aggregate. This latter value resulted in a multiplier of 1.08 to the resultant TS value [e.g. 1].

2.3 Database records

Results from this testing were compiled into an overall database. For I.S. 465 tested properties a three-letter code was given to the sample representing the geological composition of the aggregate that has been used (e.g. PHY = phyllite). The three-letter codes can be used to look for patterns by aggregate type that are deducible across all the completed tests. These results can also be searched by county to quickly summarise data by county. Where possible a postcode mark is recorded allowing some spatial analysis of distribution. For the spatial analysis, the focus was on estates where all testing had so far only recorded the presence of high risk aggregate, to look at the proportion of that estate that had been tested. A percentage tested for each analysed estate was then calculated. The average percentage from all analysed estates was then taken as a prediction for the county as a whole, and the numbers so far analysed for each county were proportionally adjusted upwards to reflect this to produce an overall prediction for the county in question. For properties tested according to I.S. 398 the deleterious aggregate type used is consistent across all occurrences so far (i.e. calcareous mudrock) and therefore a record is kept of the postcode reference for plotting on an Ireland-wide map.

3. RESULTS & DISCUSSION

3.1 Maps

The geology of Ireland has been previously reported ([1],[2]) as a core factor in the distribution of poor-quality aggregate that has produced deleterious blockwork and/or hardfill. With respect to Donegal this is closely related to the use of pyrrhotite-bearing Dalradian metasediments (see map in [2]).

For the other impacted counties of the Republic of Ireland the deleterious aggregate is largely derived from the deeply deposited Carboniferous units [3], and from three main areas (Figure 3.1), namely the Shannon Basin around Clare and Limerick, the Dublin basin around Dublin and surrounding counties and the deeper early deposits of the Carboniferous around Mayo, Sligo and South Donegal.

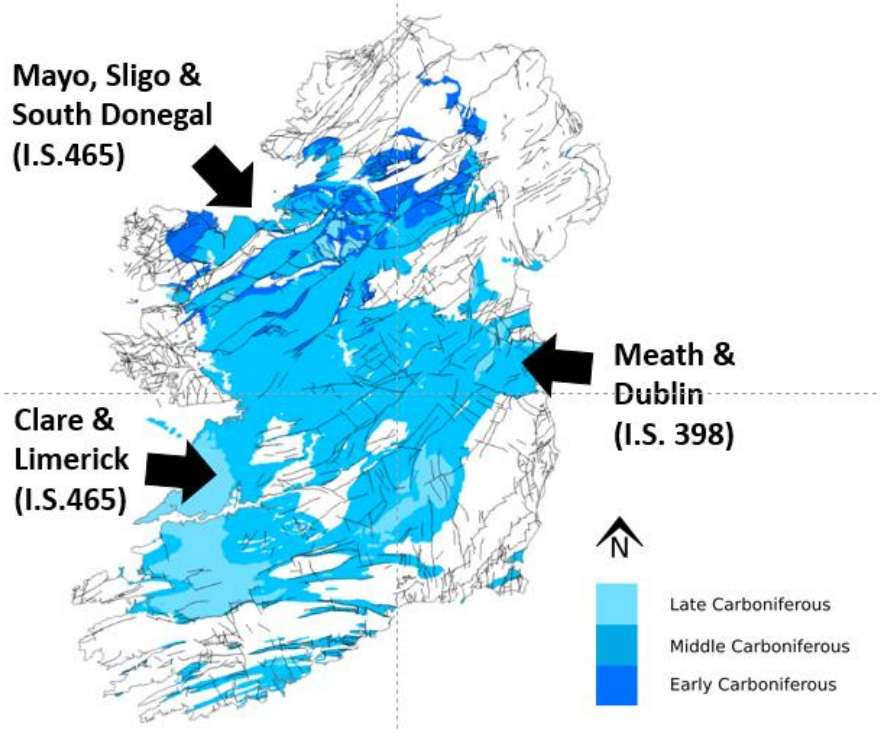

Figure 3.1: The three main areas of the Carboniferous from which poor quality calcareous mudrock aggregates have been quarried and used in construction products. The area highlighted in blue is the full extent of the Carboniferous across the island of Ireland.

Whilst there are also some isolated occurrences derived from quarrying Silurian and Ordovician units, primarily around Louth, Monaghan and Wexford, the vast majority are derived from the deep deposits of the Carboniferous. It is noted that there are also clean (i.e. low total sulphur) shallow shelf deposits across the Carboniferous that have been used to make low reactivity stable concrete block and hardcore, but the highlighted areas are where a larger proportion of the Carboniferous formed within deeper basins and therefore more likely to have developments of framboidal pyrite. The particular focus on these three areas is reflected in the 'hotspot' map (Figure 3.2), which also highlights the growth in recent impacted areas.

Overall, there are four main impacted regions across Ireland which will be partially independent of county boundaries, instead being dependent on the extent of the geological units in question and where they have been quarried, and then where that quarried material has been used and/or transported to for use.

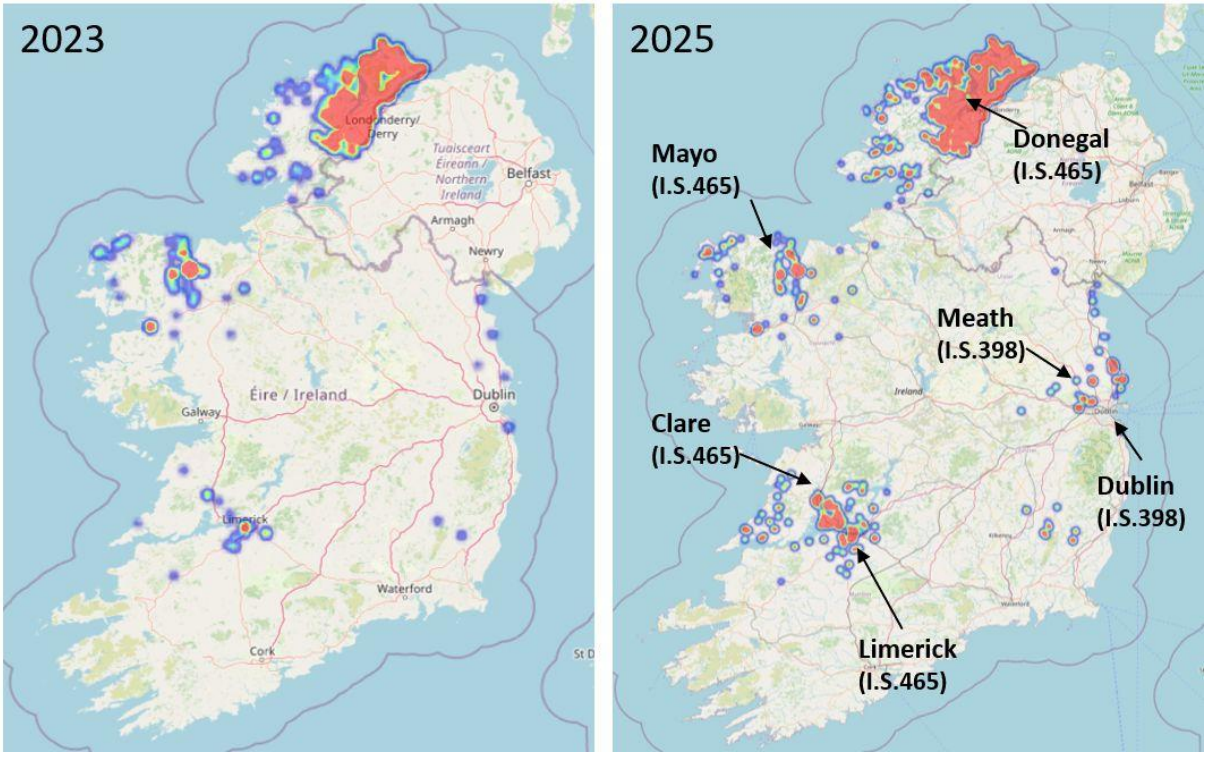

Figure 3.2: A comparison across 2 years of collecting data (2023 (see [2]) vs 2025), showing the growth of properties affected by deleterious blockwork (I.S. 465) around Clare and Limerick, as well as some other areas of Ireland. Data from recent areas of hardcore issues (I.S. 398) are also included.

3.2 Petrographic Differences

Petrographic analysis indicates that concrete blocks made with pyrrhotite-bearing metasediments are more prone to binder degradation, characterised by ettringite, thaumasite and gypsum growth. Sulphate formation within fractures is rarely well developed, with fractures often empty—reflecting expansion and softening of the binder itself, with cracking occurring as a consequence. In contrast, framboidal pyrite-bearing calcareous "mudrock" also exhibits binder degradation but more frequently develops gypsum-filled fractures. These can occur within aggregate particles, along aggregate boundaries, and, occasionally, cross-cutting the binder.

Both pyrrhotite and framboidal pyrite are highly reactive sulphides, so differences in deterioration are not due simply to oxidation rate, but to aggregate geology and binder microporosity. In pyrrhotite-bearing metasediments, oxidation causes expansion and aggregate cracking before sulphate preferentially attacks the weaker, more porous binder. This high binder microporosity, linked to abundant free mica and high water-cement ratios, likely explains the rapid deterioration seen in Donegal.

In framboidal pyrite-bearing "mudrocks", pyrite occurs within reactive carbonate-rich lithologies, so oxidation can form gypsum directly within the aggregate, causing expansive cracking and, occasionally, gypsum veins with medial lines. Binder microporosity is generally lower, which may slow deterioration.

However, the worst-affected Mayo blocks have deteriorated rapidly due to high total sulphur values, very fine framboidal pyrite, and minor framboidal pyrrhotite, which promotes early oxidation. By contrast, Clare and Limerick blocks have deteriorated more slowly, reflecting lower sulphur levels within EN 12620 limits, coarser framboidal pyrite, absence of framboidal pyrrhotite, and less argillaceous mudrock with more stable bioclastic limestone.

3.3 Estates Analysis

The postcodes from the database records were plotted up on a map of Ireland to facilitate an analysis of the extent of impact across different estates within Donegal, Mayo, Clare and Limerick. For Donegal 23 estates were counted where every property within that estate so far tested had only recorded high risk properties. On average, across those estates, 16% of the properties had completed Suite A & B testing. It is reasonable to deduce that every property within a given estate has been built with blocks from the same supplier and that therefore every property within each of those estates will eventually record a high-risk characterisation. The next assumption is that the average % tested from each estate is a fair approximation of the % tested for the county as a whole. On that basis it can be assumed that the 1900 properties so far recorded as High risk with Donegal represent only 16% of the total to be tested. This produces a rough prediction of 12,000 high risk properties within Donegal (see Table 3.1). Extending the same principals and process produces an estimated value of ~1,000 for Mayo, ~4,500 for Clare and ~2,500 for Limerick (see Table 3.1). This gives a current overall prediction of ~20,000 properties.

It is noted that for Clare and Limerick there is currently a very high degree of uncertainty. The deleterious aggregate used is the same across both counties and suggest a common block supplier. However, despite ~280 high-risk properties spread across those two counties, the concentrations within any given estates are usually very low. This is because there is a high number of impacted estates, spread over a wide geographical radius. The low incident rate is not considered to be a function of the use of variable blockwork but the fact that the deterioration rate within Clare and Limerick appears slower for framboidal-pyrite bearing calcareous mudrock compared to Mayo, due to the reasons noted in 3.2. Therefore, although the numbers of impacted houses within Clare and Limerick are currently low, the final number of impacted properties may rise to be several thousand, exceeding the occurrences within Mayo, though likely remaining below the occurrences in Donegal.

Finally, the ~20,000 prediction is likely to be an underestimate as this analysis excludes social housing, business buildings, business-residential duplex buildings. Social housing is excluded due to lack of data, and the latter business-related premises are excluded as they don't qualify for the redress scheme and haven't been tested. Data from other counties, including I.S. 398 impacted properties, are also excluded due to the current sparsity of data.

Table 3.1: Estates analysis of number of proportion of properties tested.

County	Estates Analyzed	Proportion of Each Estate Tested	Total number of High-risk properties in county so far	Estimated final number of impacted properties
Donegal	23	16%	1900	~12,000
Mayo	10	25%	240	~1,000
Clare	10	5%	200	~4,500
Limerick	5	3%	80	~2,500

4. CONCLUSIONS

The evidence from the emerging dataset of I.S. 465 and I.S. 398 analysed properties now strongly records that there are four highly impacted areas of the Republic of Ireland, where properties have been built using poor quality aggregate liable to instigate internal sulphate attack in cementitious products or structural heave in hardcore. Whilst these four areas can be considered in terms of the primarily impacted counties, the impacted areas are not bounded by county lines but are instead dependent on the extraction of key geological units (Dalradian metasediments, The Shannon Basin, The Dublin Basin

and the Mayo Limestones). It is therefore apparent that the long-term number of damaged properties will depend on the extent to which the most deleterious units within these have been quarried and used.

Whilst there are four main impacted areas there are differences between the type of deterioration observed, and the apparent speed of deterioration. The Donegal pyrrhotite-bearing metasediments tend to crack during oxidation of the pyrrhotite, with oxidation products reacting with the weak binder producing secondary sulphate formation. The combination of reactive pyrrhotite, weak binder and weak aggregate means that deterioration has been particularly rapid. The worst Mayo framboidal-pyrite bearing “mudrocks” have also deteriorated rapidly due to high total sulphur values, the particularly fine-grain size of the framboidal pyrite, and minor presence of framboidal pyrrhotite. Clare and Limerick have a similar deleterious concrete block, but this has emerged later as a hotspot as although it is also made from calcareous “mudrock”, like in Mayo, it is not as bad a product with an associated slower deterioration rate. The total sulphur values are lower; the sulphides are coarser and the there is no framboidal pyrrhotite. This hosting aggregate is also slightly more stable. Unfortunately, this in turn may have masked the number of impacted properties, compounding the problem in the long-term and meaning deleterious blockwork has been used for longer. This will particularly be the case if calcareous “mudrocks” which technically meets EN 12620 TS guidelines are still being quarried and used in concrete block.

Estates analysis predict that the numbers of impacted properties will still rise significantly across all impacted counties. For the two counties first recognised as impacted by this crisis (Mayo & Donegal) it is expected that numbers will at least quadruple, if not increase 6-fold from the numbers recorded as of March 2026. For Clare and Limerick, the number of estates recorded with an impacted property now exceeds that from Mayo, but with an incident rate per estate that remains very low. If each impacted estate begins to record numbers equivalent to estates within Mayo and Donegal then numbers will rise to exceed Mayo. For the four main counties so far impacted by poor quality concrete block the overall prediction is for ~20,000 impacted properties. Furthermore, this number likely represents an underestimate, or base case, as it excludes data from social housing, businesses and business-residential duplex buildings. For Ireland as a whole this number will also need to be adjusted upwards to account for houses impacted by poor-quality hardcore and deleterious concrete block in other counties.

5. REFERENCES

[1] Leeman A, Lothenbach B, Münch B, Campbell T, Dunlop P (2023) The “mica crisis” in Donegal, Ireland – A case of internal sulfate attack? Cement and Concrete Research, 168, (107149). https://doi.org/10.1016/j.cemconres.2023.107149

[2] Brough, C, Staniforth, B, Garner, C, Garside, R, Colville, R, Strongman, J & Fletcher, J. (2023) High risk concrete blocks from County Donegal: The geology of defective aggregate and the wider implications. Construction and Building Materials, 408, 133404

[3] Brough, C, Garside, R., Staniforth, B, Garner, C, Fletcher, J & Strongman, J (2024) Framboidal pyrite in concrete block: Reassessing EN 12620 in light of the degradation observed across the Republic of Ireland.

[4] Enhanced Grant Scheme for the Remediation of Dwellings Damaged by the Use of Defective Concrete Blocks in their Construction (2023) file:///C:/Users/Chris/Downloads/262452_c72c696d-7e65-450f-aced-aa843dcacc74.pdf

[5] I.S. 465:2018+A1:2020 Assessment, testing and categorisation of damaged buildings incorporating concrete blocks containing certain deleterious materials. National Standards Authority of Ireland, Dublin

[6] Matheson, G.D., and Quigley, P. (2016) "Evaluating pyrite-induced swelling in Dublin mudrocks." Quarterly Journal of Engineering Geology and Hydrogeology 49(1): pp 47-66.

[7] Irish Standard I.S. 398-1:2017. Reactive Pyrite in Sub-Floor Hardcore Material, Part 1: Testing and Categorisation Protocol. National Standards Authority of Ireland.

[8] EN 932-3:2022: Tests for general properties of aggregates. Procedure and terminology for simplified petrographic description.

[9] EN 1744-1:2009+A1:2012: Tests for chemical properties of aggregates. Chemical analysis

Impact of sample preparation on the quantification of sulfide-bearing aggregates using XRD

Camargo, M. H. T. (1), Duchesne, J. (1), Fournier, B. (1), Titon, B. G. (1), Rodrigues, A. (1)

(1) *Department of Geology and Geological Engineering, Université Laval; Research on Concrete Infrastructure (CRIB), Québec City, Canada, mhtac@ulaval.ca*

Abstract

Over the past two decades, premature deterioration of concrete structures has been linked to reactive iron sulfides in aggregates, particularly pyrrhotite, which can cause internal sulfate attack (ISA). The total sulfur content (TS%) is commonly used to evaluate concrete aggregates, but this method fails to distinguish pyrrhotite from more stable sulfur-bearing phases. X-ray diffraction (XRD) offers mineral-specific identification, but its accuracy depends strongly on sample preparation.

This study investigated the influence of sample preparation on sulfide quantification by XRD Rietveld refinement. Dry and wet (ethanol) grinding methods were compared at different durations (2, 5, and 10 min) using a McCrone micronizing mill. Three aggregate types were analyzed: a sulfide-rich MSK aggregate, a sulfide-free PKA aggregate, and controlled PKA mixtures containing 1, 3, or 5 wt% pyrite and pyrrhotite.

Results show that pyrrhotite is highly sensitive to preparation conditions. Wet grinding with ethanol increased measured pyrrhotite and pentlandite contents, while pyrite remained relatively stable. Grinding in water caused a decrease in pyrrhotite due to oxidation. Wet grinding with ethanol for 10 min yielded the most accurate sulfide estimates. Although XRD underestimated sulfide content in complex samples by 2-3 wt%, prolonged wet grinding reduced this bias. Overall, wet grinding with ethanol for 10 min is the most reliable method tested for sulfide quantification in concrete aggregates by XRD.

Keywords: *aggregate, concrete durability, pyrrhotite, sample preparation, XRD.*

1. INTRODUCTION

The durability of concrete infrastructure is critically dependent on the stability of its constituent materials. A major threat to this durability in regions like Eastern North America is the Internal Sulfate Attack (ISA), initiated by the oxidation of sulfide minerals within concrete aggregates [1]. This oxidation produces expansive secondary minerals, leading to cracking, spalling, and a significant loss of structural integrity [2-3].

Among sulfide minerals, pyrrhotite (Pyh) ($Fe_{1-x}S$), with x varying from 0 (FeS) to 0.125 (Fe_7S_8) [2], is notably the most reactive in concrete environments. Its oxidation susceptibility is far greater than that of pyrite (Py) (FeS_2), which is the most common sulfide mineral [4-5]. However, cases of deleterious cracking in housing concrete blocks manufactured with laminated calcareous mudrocks incorporating framboidal pyrite have been reported in Ireland [6].

Accurate quantification of Pyh in aggregates is essential for risk assessment. The European standard EN 12620 uses total sulfur content (TS%) as a proxy for reactivity, setting a limit of 1.0 wt.% TS%, which is reduced to 0.1 wt.% if Pyh is detected. However, this method has serious limitations as it cannot distinguish between different types of sulfides, such as Pyh and Py. This could result in safe aggregates being rejected unnecessarily, while reactive ones could be approved.

The XRD with Rietveld refinement provides a solution by enabling the identification and quantification of specific minerals. However, accurate quantification can be challenging due to detection limits (1-5 wt%) and peak overlaps [7]. A critical factor that is often overlooked is sample preparation. The grinding process required to produce a fine powder can induce oxidation, which can alter metastable sulfides such as Pyh before analysis [8].

Despite its importance, there has been a lack of systematic studies on how sample preparation affects the XRD quantification of sulfides in aggregates. This study aims to address this gap by evaluating the

impact of sample preparation on the quantification of sulfide minerals, with a focus on Pyh. The following parameters are investigated using a multi-technique approach involving XRD, EPMA, and Total S:

- The influence of grinding method and duration on the quantification of Pyh, Py, chalcopyrite (Ccp) ($CuFeS_2$), and pentlandite (Pn) ($(Fe,Ni)_9S_8$) according to the Rietveld method (XRD).
- The correlation between XRD-EPMA-derived sulfur ($S_{XRD\text{-}EPMA}$) and total sulfur content (TS%).

Therefore, this work seeks to establish reliable guidelines for the mineralogical assessment of aggregates and contribute to more accurate predictions of concrete durability.

2. MATERIALS AND METHODS

2.1 Sample Description

The three natural aggregates and three synthetic mixtures used in this study were fully characterized in terms of their mineralogy and sulfur content.

- **PKA:** A non-reactive anorthosite, used as a clean matrix (0.04 - 0.06 wt% S) for the controlled addition of 1%, 3%, and 5% by weight of the sulfides Py-91% (pyrite) and Pyh-92% (pyrrhotite).
- **MSK-rich:** A sulfide-enriched gabbro (3.47 - 5.08 wt% S), sourced from the problematic aggregate source used in foundations in Trois-Rivières (QC, Canada). It contains Pyh, Py, Ccp, and Pn.
- **MDS:** A fine-grained volcano-sedimentary rock, mainly composed of quartz (SiO_2) and muscovite ($KAl_2(AlSi_3O_{10})(OH)_2$) with a TS% between 1.38 - 1.62 wt% S containing Pyh and Py.
- **Pyh:** A concentrate, consisting of 92% of Pyh, along with 3% CPy and traces of siderite ($FeCO_3$) and fluorite (CaF_2). It has a high TS% content of 39.7 - 41.0 wt%.
- **Py:** A concentrate, containing 91% of Py and 4% CPy, with traces of diopside ($CaMgSi_2O_6$) and quartz. Its TS% content ranges between 49.6 - 53.3 wt%.
- **Fluorite:** A powder sample predominantly composed of fluorite (96.8 wt%), used to mimic the matrix of the MDS aggregate in the experiments, mixed with 1 wt% Py and 1 wt% Pyh.

The preparation protocol was specifically designed to test the impact of grinding on the sulfide quantification (Figure 2.1).

- **Initial Preparation:** Samples were crushed and ground using a hammer and a planetary ball mill to obtain a powder fraction with a particle size < 53 µm.
- **Fine Grinding:** Sub-samples of 2 - 3 ml were subjected to fine grinding in an XRD mill machine (McCrone), varying two main parameters:
  - **Method:** Dry grinding vs wet grinding with ethanol (to minimize oxidation). An additional experiment with water was conducted on MSK-rich.
  - **Time:** different time intervals of 2, 5, and 10 minutes, to produce particles < 10 µm.
- **XRD Analysis:** All powders were analyzed by XRD immediately after preparation to prevent further atmospheric oxidation.

The EPMA analyses were conducted on thin sections (30 µm thickness) of the sulfide-bearing samples to determine the precise sulfur content within the sulfide minerals. This data was then used as a reference to assess the accuracy of the $S_{XRD\text{-}EPMA}$ vs the TS% (section 3.2).

2.2 Analytical Techniques

A multi-technique approach was used to correlate data and obtain a comprehensive overview. The XRD analyses were performed on a PANalytical Empyrean diffractometer (Co-Kα, 40 kV/45 mA, angle 5-80° 2θ, step-size 0.008° 2θ. The results were processed using the software HighScore Plus, using the reference patterns from the Crystallography Open Database (COD).

The EPMA was used to perform a detailed chemical analysis of the Fe, S, and O content of the sulfide phases using carbon-coated thin sections. These S values were further used to estimate the $S_{XRD\text{-}EPMA}$. The analysis used a CAMECA SX-100 microprobe equipped with five wavelength-dispersive spectrometers (WDS) with diffracting crystals LLIF, LIF, TAP, and LPET. Metallic and mineral samples from P&H Developments, ASTIMEX, and ASTIMEX Scientific Ltd. were used as standards. The operating conditions were set at an accelerating voltage of 15 kV, a beam current of 20 nA, and a counting time of 60 s, under high vacuum conditions ($<10^{-5}$ Torr). The beam diameter was focused on 1 - 5 µm.

The TS% was determined by infrared absorption using an Eltra CS 800 carbon/sulfur analyzer. This procedure consists of sample combustion in an induction furnace and measurement of combustion gas absorption in the infrared region. For the analysis, 0.3 to 1 g of powdered sample (< 75 µm) is required.

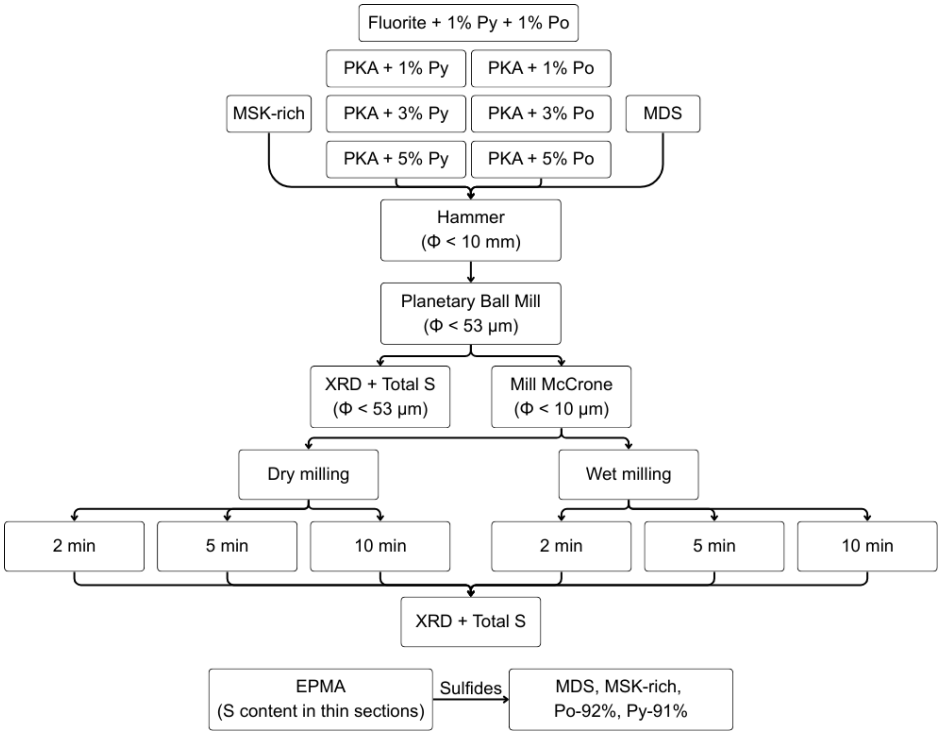

Figure 2.1. Flowchart of sample preparation and analysis of MSK-rich, MDS, PKA, and Fluorite. PKA and Fluorite were mixed with different contents of Pyh and Py. Percentages are in weight %.

3. RESULTS AND DISCUSSION

3.1 Sulfide quantification by XRD

In the MSK-rich aggregate, a clear distinction was observed between preparation methods (Figure 3.1). Wet milling (ethanol) yielded higher concentrations of Pyh (2.3 - 3.0 wt%) and Pn (0.8 - 1.3 wt%) compared to dry milling (Pyh: 1.3 - 2.0 wt%; Pn: 0.1 - 0.3 wt%). In contrast, the Py content was more affected by the milling time, exhibiting similar behavior for both dry and wet milling. After milling with water, the Pyh and Pn concentrations decreased, while the Py content exhibited a relative increase.

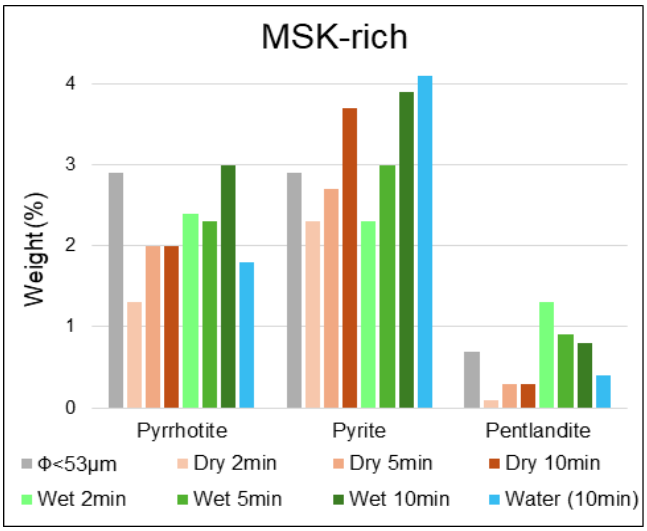

Figure 3.1. Variation in sulfide content in MSK-rich aggregate according to the sample preparation method. Results determined by Rietveld refinement (XRD).

Conversely, the MDS aggregate showed remarkable stability. The concentrations of both Pyh (0.3 wt%) and Py (1.1 - 1.3 wt%) remained virtually unchanged across all grinding methods and durations (Figure 3.2). Similar behavior is observed in experiments using synthetic mixtures of Fluorite with sulfides (Py and Pyh) (Figure 3.2). The general pattern indicated that wet milling with ethanol for longer periods provides more accurate results for sulfide content (Figure 3.3). Variability was more pronounced with shorter grinding times and under dry milling conditions.

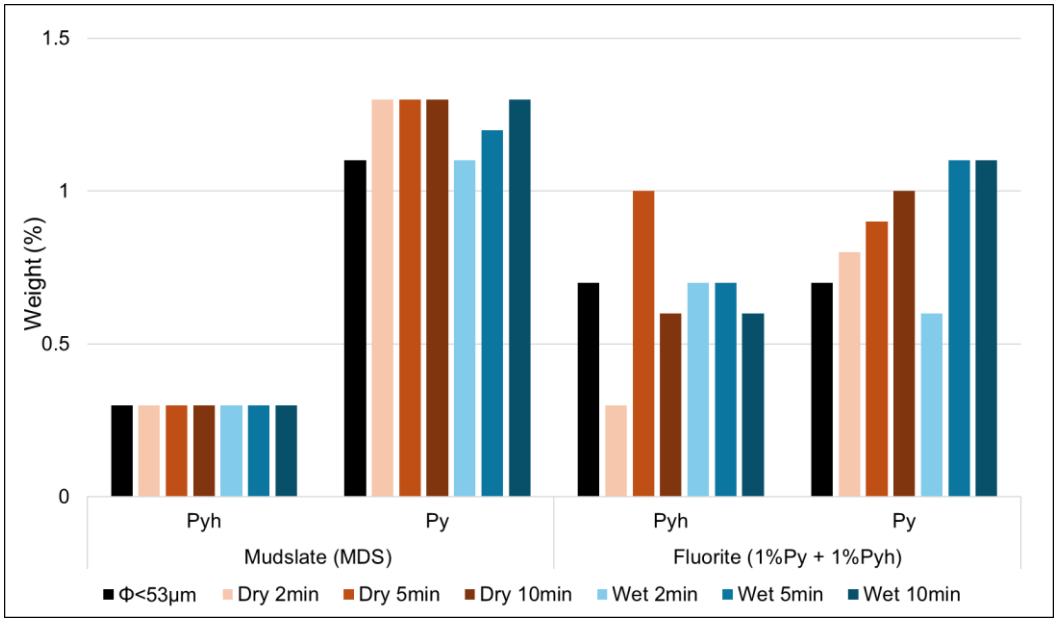

Figure 3.2. Sulfide variation in MDS (natural aggregate) and Fl+1% Py+1% Pyh (synthetic mixtures).

These results suggest two primary controlling factors. Firstly, the choice of milling solvent is critical [8]. The suppression of Pyh and Pn during dry milling and, more drastically, when using water, strongly suggests the occurrence of oxidation during sample preparation (Figure 3.1). The metastable nature of Pyh [5] makes it particularly vulnerable, and its oxidation likely leads to an underestimation of its true content. Secondly, the results seem to be influenced by grinding duration and rock microtexture [2]. Prolonged wet grinding with ethanol produces more accurate and reproducible sulfide quantification, especially for Pyh (Figure 3.3). The difference between the coarse-grained MSK-rich and fine-grained MDS aggregates suggests that microtexture plays a key role in sulfides quantification by XRD. In MSK-rich, sulfide grains may be more exposed to damage, whereas the fine-grained matrix of the MDS aggregate could potentially shield the sulfides, which explains its lower sensitivity to the preparation method.

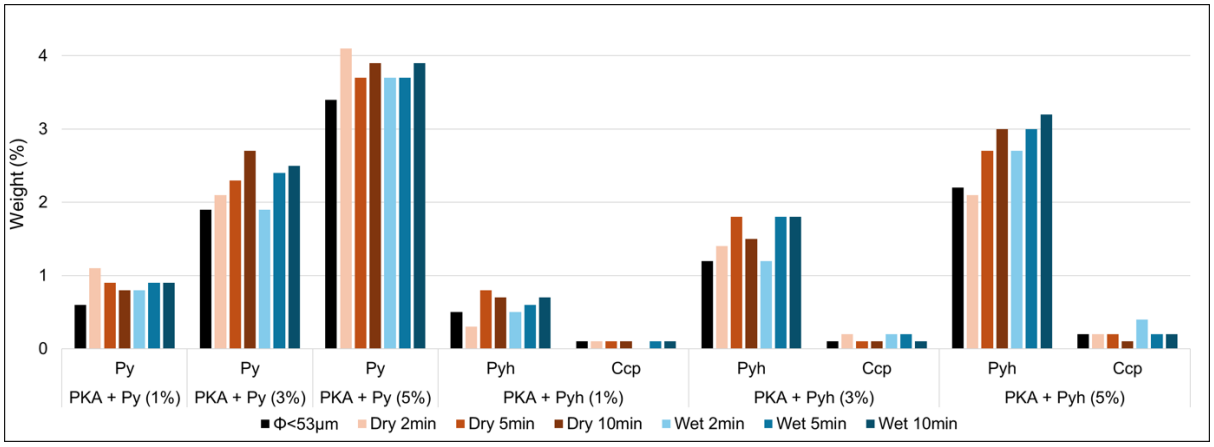

Figure 3.3. Sulfide variation according to sample preparation for all sulfide mixtures with PKA.

3.2 Sulfur quantification: $S_{XRD\text{-}EPMA}$ vs TS%

A mineralogy-derived sulfur content ($S_{XRD\text{-}EPMA}$) was estimated for the samples based on their mineralogical (XRD) and chemical (EPMA) compositions. XRD was first used to determine the modal proportions of each sulfide mineral present in the aggregate. EPMA was then employed to measure the

sulfur content of each sulfide phase. The $S_{XRD\text{-}EPMA}$ value was calculated by summing up the individual sulfur contributions of each mineral:

$$S_{XRD\text{-}EPMA} = \text{Mineral \% from XRD} \times \text{Sulfur \% in sulfide from EPMA}$$

This calculated value ($S_{XRD\text{-}EPMA}$) was finally compared to the TS%, as shown in Figure 3.4.

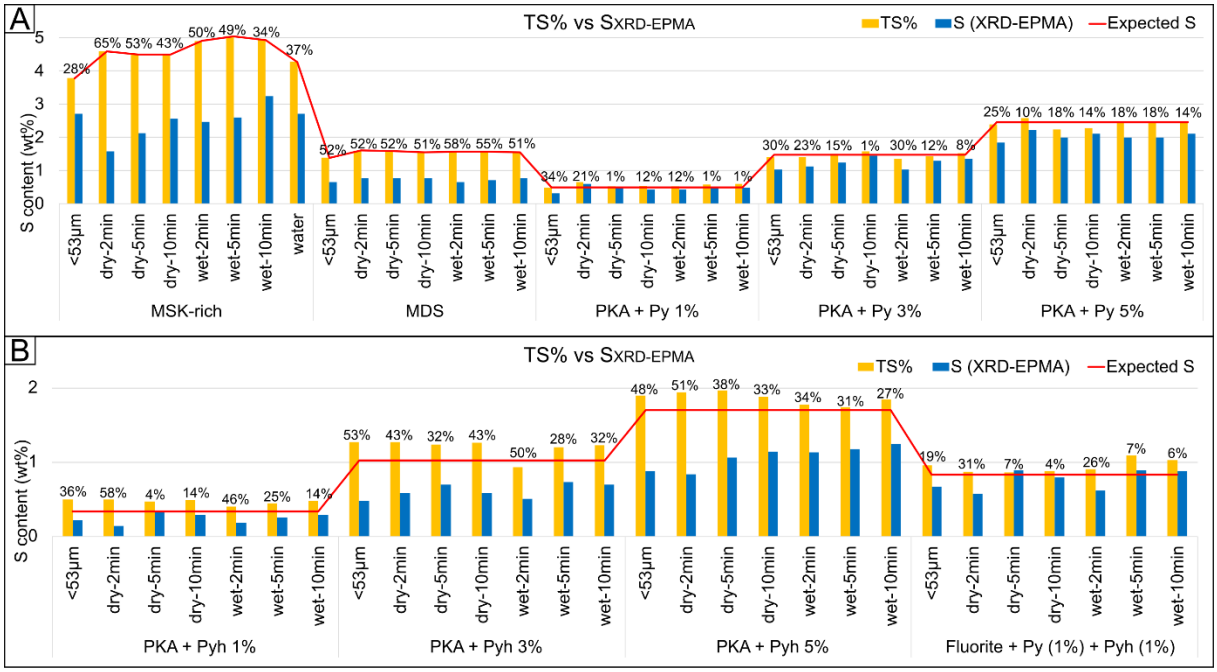

Figure 3.4. Variation between the measured sulfur from TS% vs mineralogy-derived sulfur ($S_{XRD\text{-}EPMA}$). Percentage values above the bars indicate the relative error between the two techniques.

The analysis revealed distinct patterns across the different samples. For the MSK-rich aggregate, the most accurate result was obtained from the wet-10min sample, which showed an error of 1.32 wt%. Overall, wet-milled samples consistently yielded lower sulfide quantification errors (1.69 to 2.43 wt%) than their dry-milled counterparts (1.93 to 3.00 wt%). A general trend of improved accuracy with increasing grinding time was observed, particularly for the MSK-rich and PKA+Pyh (5%) samples. The low error values observed for the water-milled sample of MSK-rich are attributed to the limited loss of TS%. However, this minimal net loss is misleading, as it results from the selective leaching of the small Pyh fraction, as shown by its diminished sulfur content (Figure 3.1). The inherent instability of Pyh in water primarily drove this process, but its low initial abundance minimized the overall impact on the TS% balance (Figure 3.4).

Previous studies on problematic sulfide-bearing aggregates, such as the MSK samples investigated here, have demonstrated that TS% between 0.7% and 1.3% can compromise concrete structures [3]. These concentrations correspond to approximately 1.8% to 3.6 wt% of Pyh. Notably, these critical thresholds align closely with the range evaluated in this study (1% to 5% wt), highlighting the practical relevance of assessing sample preparation impacts within these analytical and regulatory limits.

In contrast, the MDS aggregate showed consistently low errors (~0.8 wt%) across all preparation methods, confirming its minimal sensitivity to grinding. Experiments on synthetic PKA mixtures provided additional insights. For Py-bearing mixtures, errors were generally low (< 0.4 wt%) and decreased with increasing milling times. Conversely, Pyh-bearing mixtures showed significantly higher errors, reaching up to 1.20 wt%. Notably, in Pyh-rich samples, wet milling with ethanol improved accuracy, reducing errors by up to 0.5 wt% compared to dry milling. By contrast, PKA and Py-bearing mixtures showed higher accuracy under dry milling conditions than under wet milling.

These results highlight the complexity of sulfide quantification by XRD, which is strongly dependent on both mineralogy and sample preparation. Py proved less susceptible to preparation-induced variability and yielded higher accuracy under dry milling conditions. In contrast, Pyh quantification showed greater variability and was improved by wet milling with ethanol. This dichotomy underscores the critical influence of both the rock matrix and sample preparation on analytical outcomes. Specifically, the superior performance of wet milling for reactive samples (e.g., MSK-rich, Pyh-spiked PKA aggregates) is directly linked to the minimization of sulfide oxidation during grinding, which is particularly important for the structurally unstable Pyh. Despite these optimizations, the absolute accuracy of sulfide

quantification by XRD Rietveld refinement remained relatively low (approximately 30-75% recovery), especially for complex aggregates such as the MSK-rich sample.

Furthermore, a consistent trend was observed where XRD quantification generally underestimated total sulfide content compared to TS% analysis. This discrepancy is likely attributable to peak overlap in the diffractograms, a common issue in complex mineral assemblages [7]. Such overlaps can interfere with Rietveld refinement, leading to underestimation of individual sulfide phases and, consequently, of $S_{XRD-EPMA}$. The improved accuracy achieved with longer grinding times further suggests that achieving a homogeneous powder is essential for reliable Rietveld quantification.

4. CONCLUSIONS

The conclusions from the study of sample preparation methods for sulfide quantification by XRD are as follows:

- Wet grinding with ethanol for 10 minutes is the recommended protocol, as this method consistently yielded the most accurate quantification in Pyh-bearing samples by minimizing oxidative alteration during grinding.
- Pyh is the most susceptible to preparation-induced alteration among the sulfides, with dry grinding or the use of water leading to a significant underestimation of its content (up to 40%).
- The rock's microtexture seems to influence the sulfides grinding, as fine-grained aggregates shield sulfide minerals, providing robust quantification across different methods. In contrast, coarse-grained aggregates seem to expose sulfides to damage, increasing oxidation and error risk.
- Rietveld refinement systematically underestimates the content of sulfides and total sulfur content in complex samples compared to TS% analysis, due to peak overlap in the diffractograms.

5. REFERENCES

[1] Duchesne J, Rodrigues A, Fournier B (2021). Concrete damage due to oxidation of pyrrhotite-bearing aggregate: A review. RILEM Tech. Lett. 6: 82-92. https://doi.org/10.21809/rilemtechlett.2021.138

[2] Belzile N, Chen Y., Cai MF, Li Y (2004). A review on pyrrhotite oxidation. J.Geochem. Explor 84(2): 65-76. https://doi.org/10.1016/j.gexplo.2004.03.003

[3] Rodrigues A, Duchesne J, Fournier B (2015). A new accelerated mortar bar test to assess the potential deleterious effect of sulfide-bearing aggregate in concrete. Cem. Concr. Res. 73: 96-110. https://doi.org/10.1016/j.cemconres.2015.02.012

[4] Marcelino A P, Calixto J M, Gumieri A G, Ferreira M C, Caldeira C L, Silva M V, Costa A L (2016). Evaluation of pyrite and pyrrhotite in concretes. Rev. IBRACON Estrut. Mater. 9(03): 484-493. https://doi.org/10.1590/S1983-41952016000300009

[5] Li Z, Gorski C A, Thompson A, Shallenberger J R, Kaladharan G, Radlińska A (2025). Dissolution kinetics of iron sulfide minerals in alkaline solutions. Cem. Concr. Res. 193: 107850. https://doi.org/10.1016/j.cemconres.2025.107850

[6] Brough C, Garside R, Staniforth B, Garner C, Fletcher, Strongman J (2024). Framboidal pyrite in concrete block: Reassessing EN 12620 in light of the degradation observed across the Republic of Ireland. Proc. 1st Int. Conf. on Iron-Sulfide Reactions in Concrete, Quebec City (Canada), May 14th – May 17th 2024, 39-43.

[7] Pecharsky V K, Zavalij P Y (2003). Fundamentals of powder diffraction and structural characterization of materials. Springer US.

[8] Scrivener K, Snellings R, Lothenbach B (Eds.) (2016). A practical guide to microstructural analysis of cementitious materials. CRC Press.

Screening for Pyrrhotite and its Reaction Products in Concrete using Raman and Near Infrared Spectroscopy

Stephanie Watson[(1)], Elizabeth Hackley[(2)], Ashley Carey[(3)], Patrick Dixon[(4)], Michael Mengason[(5)]

(1) *National Institute of Standards and Technology, Gaithersburg, USA, stephanie.watson@nist.gov*
(2) National Institute of Standards and Technology, Gaithersburg, USA, elizabeth.hackley@nist.gov
(3) National Institute of Standards and Technology, Gaithersburg, USA, ashley.carey@nist.gov
(4) National Institute of Standards and Technology, Gaithersburg, USA, patrick.dixon@nist.gov
(5) National Institute of Standards and Technology, Gaithersburg, USA, michael.mengason@nist.gov

Abstract

The use of Raman and near infrared (NIR) spectroscopies was investigated to identify minerals and estimate concentrations of pyrrhotite, its reaction products, and the cementitious matrix in concrete as an additional screening tool related to pyrrhotite-induced concrete degradation. Damage to concrete structures in residential and commercial construction in the US, Canada, and Europe has been attributed to the iron sulfide mineral pyrrhotite. Iron sulfides in concrete aggregate are not desirable as their relative instability results in decomposition with associated staining, expansion, and cracking of the structure. The oxidation of pyrrhotite in concrete aggregate results in the formation of ferric oxyhydroxides and oxides with an accompanying volume increase. Sulfate is then released from pyrrhotite oxidation and initiates a secondary reaction with aluminosulfate and other phases in the hardened cement paste matrix resulting in severe cracking of the concrete. Cross sections from concrete cores obtained from pyrrhotite-affected Connecticut residential foundations were examined as-received and as-treated with concrete sealants and aged for mitigation studies. Preliminary results show that pyrrhotite oxidation products, i.e., ferric oxyhydroxides and oxides and internal sulfate attack by-products, are Raman and NIR active. These spectroscopic methods also hold promise in examining the penetration depth of select concrete sealants.

***Keywords**: concrete sealant, characterization, near infrared spectroscopy, pyrrhotite, Raman*

1. INTRODUCTION

Molecular spectroscopies, such as Raman and Near Infrared (NIR), have recently been used to obtain mineral maps and for other characterization on rocks, clay, and cement reactions [1-5]. Traditional mapping methods, like petrography and scanning electron microscopy, have relied on time-consuming sample preparation, including sectioning, epoxy impregnation, polishing, and conductive coating. Raman and NIR methods do not require as much sample preparation but have limitations due to complex composition of cementitious materials, selection rules for compounds and other secondary effects such as fluorescence interference in the spectra. In this study, the use of Raman and NIR spectroscopies were investigated to identify minerals and estimate concentrations of pyrrhotite, its reaction products, and the cementitious matrix in concrete as an additional screening tool related to pyrrhotite-induced concrete degradation.

Damage to concrete structures in residential and commercial construction in the US [Connecticut (CT) and Massachusetts (MA)], Canada, and Europe has been attributed to the iron sulfide mineral pyrrhotite [6-9]. Iron sulfides in concrete aggregate are not desirable as their relative instability results in decomposition with associated staining, expansion, and cracking of the structure. The oxidation of pyrrhotite in concrete aggregate results in the formation of ferrihydrite and other common by-products, such as geothite and/or other sulfates with an accompanying volume increase. Sulfate released from pyrrhotite oxidation leads to internal sulfate attack, a secondary reaction between the sulfates from the iron sulfide oxidation with aluminates of the hydrated Portland cement forming ettringite resulting in secondary expansion and cracking of the concrete. Raman and NIR results for the mineral concentrations, changes in composition within the concrete core, and as a function of concrete sealant/aging compared to those concentrations obtained from traditional methods used to characterize cementitious materials, such as XRF, XRD, and SEM were discussed.

2. EXPERIMENTAL

2.1 Materials

2.1.1 Concrete Specimens

Cross sections from concrete cores obtained from pyrrhotite-affected CT residential foundations were examined as- received and as-treated with concrete sealants and aged for a mitigation study.

Cores were taken from a deteriorated foundation in Stafford Springs, Connecticut that was scheduled for a full foundation replacement due to pyrrhotite oxidation [10]. Areas of the foundation walls with a range of visible damage on the interior face were chosen for coring. All cores were wet cored using a 108 mm (4.25 inch) drill bit through the entire thickness of the foundation wall, which was approximately 254 mm (10 inches). All cores were then transported to NIST for further specimen preparation and testing. For sealant mitigation studies, cores with the lowest degree of visible damage were wet sectioned into 38.1 mm (1.5 inch) pucks and allowed to dry at ambient room conditions. Specimens were sealed with various types of sealants, including silane, lithium silicate, polyurethane, and a crystalline sealant with an acrylic topcoat. Sealants were chosen to represent a wide range of mitigation treatments including coatings, membranes, penetrating sealants, and pore blocking sealants.

2.1.2 Pure Materials

Minerals, compounds and potential reaction products that could be present in the aggregate and concrete were examined in the form of pure compounds. These compounds were obtained from a variety of sources, including mineral collections, chemical manufacturers, and in-house synthesis. Cured sealant materials were also measured as pure materials.

2.2 Instrumental Methods

Raman spectra result from the scattering of monochromatic light in the visible region of the electromagnetic spectrum on a material such that the frequency of the scattered light is both higher and lower than that from the original light. The differences between the frequencies from the incident and scattered light are equal to vibrational frequencies of the material, which are characteristic of functional groups in a chemical structure. Raman spectroscopy measurements were conducted using a Raman microscope (Senterra II, Bruker, Billerica MA). Instrument conditions were chosen to obtain spectra with appropriate signal to noise ratios while reducing sample damage from the laser. Lasers at 532 nm excitation wavelength ranging from 2.5 mW to 6.25 mW and at 785 nm excitation wavelength from 10 mW to 50 mW, separately, were focused through 10x, 20x, and 50x objectives using a 50 µm x 1000 µm aperture. Up to four 3 s to 10 s exposures with 4 cm^{-1} step size were averaged together to generate each spectrum. To provide spatial resolution, line scan measurements were completed using up to 50 µm step size across the cross-sectioned concrete specimens. Up to five line scans were taken for each sample. Background subtraction was performed using OPUS software package (Bruker), and further analysis was completed with external software.

NIR spectroscopy is a common analytical technique that uses light from the electromagnetic spectrum range of 700 nm to 2500 nm to measure the chemical composition by analysing molecular overtones in a variety of materials that absorb or reflect the light. Different chemical bonds absorb energy at specific frequencies, which allows for identification and quantification of species of interest. Like Raman spectroscopy, NIR requires minimal sample preparation. NIR spectroscopy measurements were conducted using a Thermo Nicolet iS50 Fourier Transform infrared (FT-IR) spectrometer (Madison WI) with a NIR integrating sphere module and a fiber optic probe accessory, separately, that used an indium gallium arsenide (InGaAs) detector with a calcium fluoride beamsplitter. Spectra were collected using 8 cm^{-1} resolution for 128 scans at least 3 locations on the specimens.

3. PRELIMINARY RESULTS AND DISCUSSION

Raman and NIR spectroscopy were used to monitor progress of pyrrhotite oxidation and sulfate attack in concrete samples that have undergone varying amounts of natural and laboratory aging. All aging conditions start with 30 days at 50 °C and 75% relative humidity (RH). For condition 1, specimens are cooled to room temperature. For condition 2, the specimens are cooled to room temperature and undergo 15 freeze/thaw (4 °C to -18 °C) cycles as defined by ASTM C666. For condition 3, specimens are cooled to room temperature and undergo 15 wet/dry cycles, in which one cycle consists of 3-day submerge in 23 °C water followed by 4-day at 23 °C. These methods were also used to examine the use of concrete sealants and their permeation into the concrete surface. Trends, such as changes in band intensity and shifts in wavenumber that can indicate transformations of chemical structure within the concrete samples, were tracked. For both methods, actual concrete specimens were examined using optical microscopy to identify specific locations of interest, such as the presence of pyrrhotite and/or internal sulfate attack products, to improve the probability of obtaining relevant spectra using the Raman microscope and the NIR probe. Identification of minerals and other products were validated using spectra obtained from pure compounds.

4. RAMAN SPECTROSCOPY

Figure 3.1 shows Raman spectra obtained from a typical concrete sample and pure compounds for verification. In Figure 3.1A, a 532 nm laser was chosen for its stronger intensity and illustrates the challenge of fluorescence (rising background) when focused on the cement matrix. It also shows that only pyrite is Raman active for iron sulfide spectra as reported in the literature [11,12]. Changing the excitation laser to 732 nm resulted in less fluorescence and was used to examine the sulfur species resulting from internal sulfate attack. Figure 3.1B illustrates that sulfate bands from ettringite (989 cm^{-1}) can be distinguished from gypsum (1008 cm^{-1}) for a mixture with a 1:1 ratio by volume. Peak positions were similar to that reported in the literature [2,5]. However, the intensity of the sulfate peaks does not directly reflect the stochiometric difference for sulfate in ettringite compared to that in gypsum and could affect quantification. More work is needed to confirm this result.

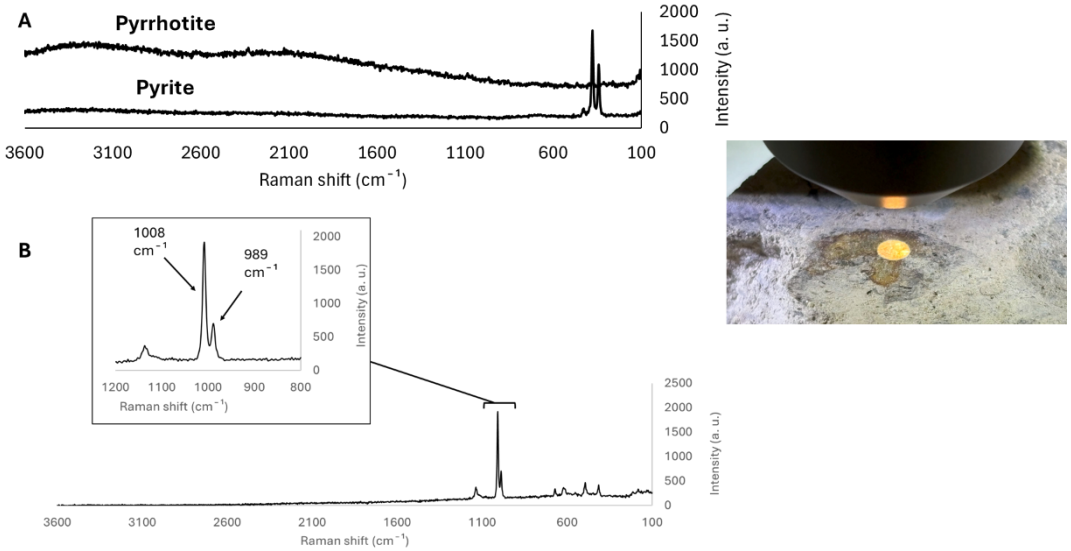

Figure 3.1: Raman spectra with 10x objective for A) concrete sample using 532 nm excitation (6.25 mW) and B) ettringite and gypsum pure compound mixture using 732 excitation (10 mW).

Raman was also useful to map the progression of ettringite formation, resulting from moisture movement through the concrete or internal sulfate attack in cement paste as shown in Figure 3.2. Moving toward the inside of the air void, evolution of the peaks indicate the presence of calcite (1086 cm^{-1}) versus ettringite (989 cm^{-1}). Peak positions of calcite and ettringite were similar to that given by Liu et.al. [5]. The Raman microscope could be used to map the chemical distribution of minerals within the concrete with the potential to provide a quantitative measurement.

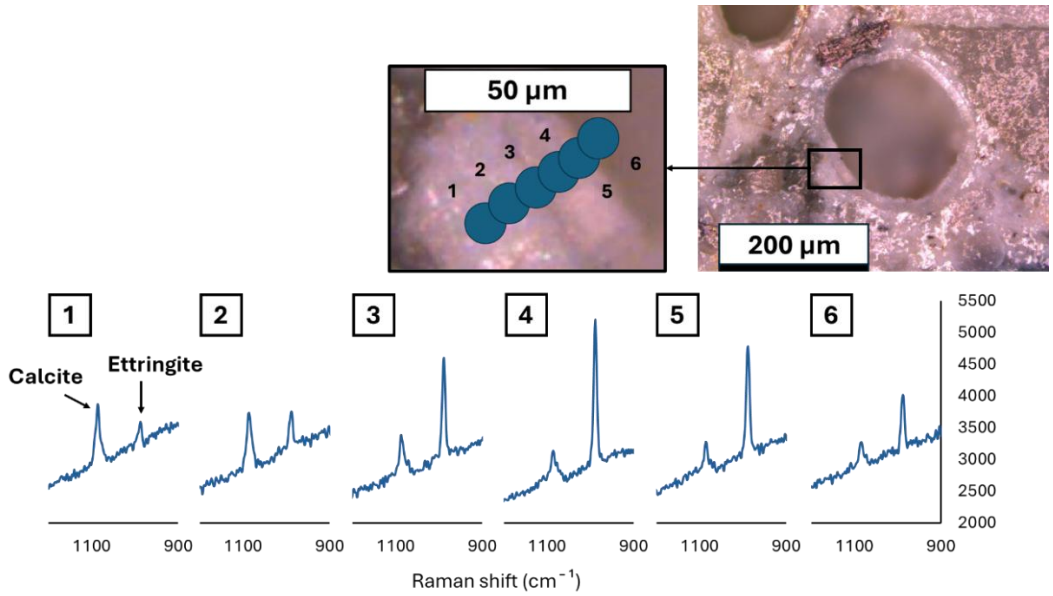

Figure 3.2: Raman spectra for concrete air void with ettringite formation using 785 nm excitation (10 mW) with 10x objective.

Concrete sealant compounds, both cementitious and polymeric, were also examined. Figure 3.3 show spectra for pure cementitious and polymeric sealant types. Preliminary results from cross sections of sealant-applied concrete show that the porous nature of the concrete dilutes the Raman signal from the sealant and the complex composition of the concrete makes it difficult to detect each specific sealant. More work is needed to optimize instrument parameters to better identify the sealant layer and subsequent sealant gradient.

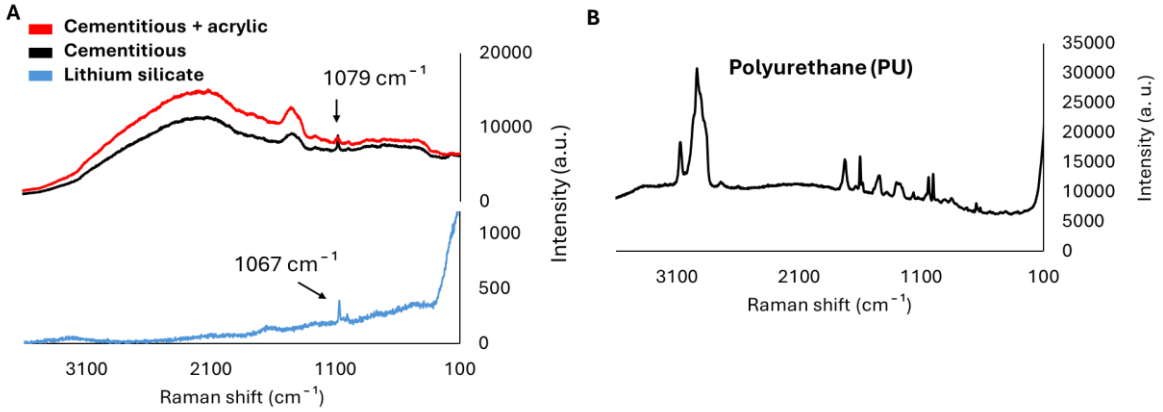

Figure 3.3: Raman spectra for concrete sealants A) cementitious types using 785 nm excitation (25mW) and B) polyurethane using 532 nm excitation (6.25 mW).

4.1 NIR Spectroscopy

Figure 3.4 shows NIR spectra for concrete samples to map internal sulfate attack products in the cement matrix. Spectra for gypsum, ettringite and hydrated cement are shown for comparison, and results are similar to those in the literature [4,5]. The spectra show how NIR produces broad peaks that make it challenging to differentiate species of interest as, in complex mixtures, minor peaks that are found in cement (7085 cm^{-1}) would be overwhelmed by gypsum or ettringite peaks. Broad peaks were also observed for iron oxyhydroxides, like lepidocrocite and goethite. Additionally, the spot size (6 mm diameter) of the NIR probe tool used in this study may restrict the isolation of specific reaction products, like ettringite or ferrihydrites.

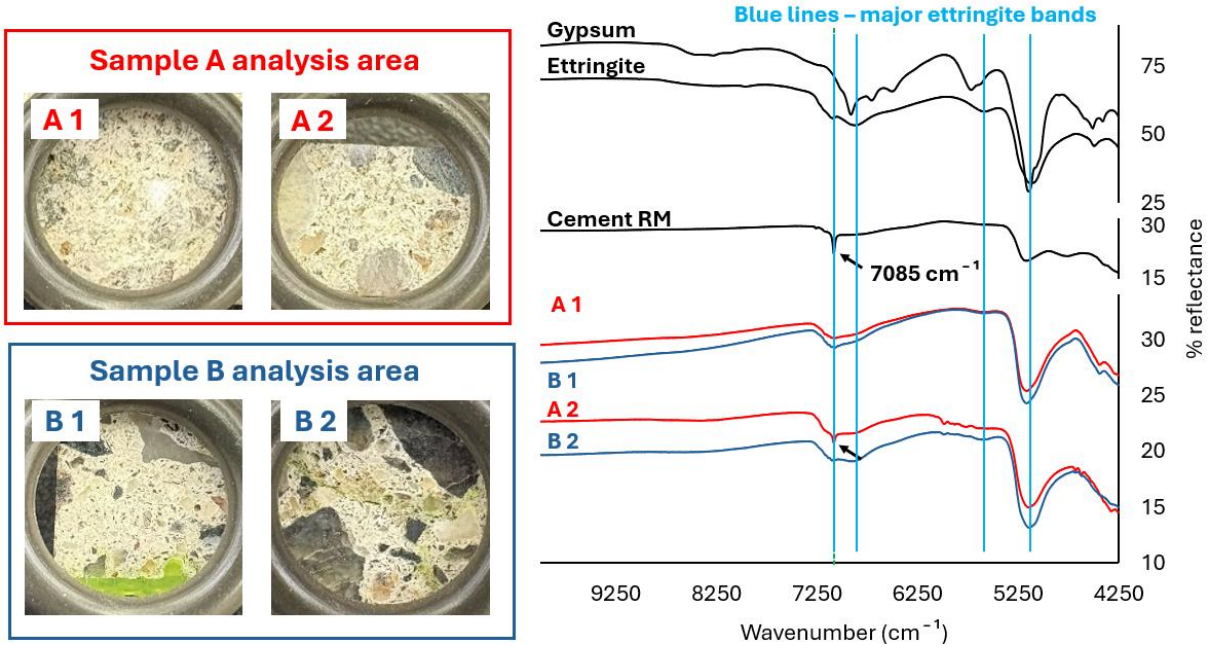

Figure 3.4: NIR spectra for gypsum, ettringite and cement compared to locations on concrete samples, sample areas (9 mm diameter) A and B.

5. CONCLUSIONS

This study showed that Raman and near infrared (NIR) spectroscopies can be used to qualitatively identify minerals such as pyrite, gypsum, calcite, ettringite and the cementitious matrix in concrete as an additional screening tool related to pyrrhotite-induced concrete degradation. Pyrrhotite is not Raman or NIR active, but its oxidation products are: FeO(OH) and Fe_2O_3 (Raman active), and FeO(OH) (NIR

active). Internal sulfate attack products can be spatially mapped by their SO_4^{2-} Raman bands and ettringite can be detected via NIR in aged concrete samples. Method optimization, including laser excitation and sample orientation, is needed to assess concrete sealants as the porous nature of the cement matrix can dilute the spectroscopic signal and the complex composition of the concrete can obscure peaks from each sealant. For both Raman and NIR, more studies to validate mineral quantification are needed.

6. DISCLAIMER

Certain commercial products or equipment are described in this paper to adequately specify the experimental procedure. In no case does such identification imply recommendation or endorsement by the National Institute of Standards and Technology, nor does it imply that it is necessarily the best available for the purpose.

7. REFERENCES

[1] Das S, Hendry MJ (2011) Application of Raman spectroscopy to identify iron minerals commonly found in mine wastes. Chem Geol 290:101-108. https://doi.org/10.1016/j.chemgeo.2011.09.001

[2] Sahu S, Exline DL, Nelson MP (2002) Identification of thaumasite in concrete by Raman chemical imaging. Cem Concr Compos 24:347-350.

[3] Garg N, Wang K, Martin SW (2013) A Raman spectroscopic study of the evolution of sulfates and hydroxides in cement-fly ash pastes. Cem Concr Res 53:91-103. https://doi.org/10.1016/j.cemconres.2013.06.009

[4] Hosseininejad S, Pedersen PK, Spencer RJ, Uwuilekhue FM (2014) Use of NIR spectroscopy in mineral identification in shale: A comparative look at NIR, XRF, and SEM. GeoConvention 2014: FOCUS, Calgary, Alberta, Canada, May 12-16, 2014, paper 90224. https://doi.org/10.1007jrs.6439

[5] Liu Y, Wang A, Freeman JJ (2009) Raman, MIR and NIR spectroscopic study of calcium sulfates: Gypsum, bassanite, and anhydrite. 40th Lunar and Planetary Science Conference, The Woodlands, Texas, paper 2128.

[6] Crumbling Foundations (July 2020) GAO Report 20-649, https://www.gao.gov/assets/gao-20-649.pdf

[7] Santos L, Chrysochoou M, Wille K (2025) Development of a risk assessment for pyrrhotite induced deterioration of concrete foundations in CT and MA. Cem Concr Res 197: 107951. https://doi.org/10.1016/j.cemconcres.2025.107951

[8] Duchesne J, Rodrigues A, Fournier B (2021) Concrete damage due to oxidation of sulfide-bearing aggregate; a review of recent advances and limitations, RILEM Tech Lett 6, 82-92

[9] Leeman A, Munch B, Lothenbach B, Winnefeld F, Dunlop P (2024) Defective homes in Donegal, Ireland: effect of exposure conditions and concrete quality on pyrrhotite oxidation and internal sulfate attack. Cem Concr Res 186: 107684.

[10] Dixon, P., Ardebili, A.H., Goodwin, D., Nikolaou, S., Harris, S., Carey, A.S., Mengason, M., and Watson, S. (2025) Field observations of a pyrrhotite-affected residential foundation and the mechanical properties of extracted concrete cores – Connecticut site 1. NIST IR 8598, National Institute of Standards and Technology, Gaithersburg, MD. https://doi.org/10.6028/NIST.IR.8598

[11] Urashima S, Narahara,K, Yui H (2022) The Raman spectra of freshly cleaved pyrrhotites: The effect of atmospheric weathering and laser-induced oxidation. J. Raman Spec 53: 2129-2136. https://doi.org/10.1007/jrs.6439

[12] Lara RH, Monroy MG, Mallet M, Dossot M, Gonzalez MA, Cruz R (2015) An experimental study of iron sulfides weathering under calcareous soil conditions. Environ Earth Sci 73: 1849-1869. https://doi.org/10.1007/sl12665-014-3540-y

Pyrrhotite-Induced Concrete Degradation - An Exploratory Data Analysis Integrating Laboratory and Field Investigations in the Trois-Rivières Region

Gilberto Cidreira Keserle [(1)], Anthony Allard [(2)]

(1) *Englobe Corp, Québec City, Canada, gilberto.cidreirakeserle@englobecorp.com*
(2) *Englobe Corp, Québec City, Canada, anthony.allard@englobecorp.com*

Abstract

This study involves an exploratory data analysis of existing buildings damaged by pyrrhotite and forms part of a larger investigation based on a comprehensive dataset comprising laboratory test results from 3 668 core samples taken from the concrete foundations of 727 structures in the Trois-Rivières area, Canada.

In June 2014, the Superior Court of Québec determined that a volumetric pyrrhotite content of 0.23% constitutes a threshold at which damage is expected to materialize. This reference value has since been used as a critical limit for assessing the risk of damage to concrete elements in the context of the pyrrhotite issue. However, it does not correspond directly to field observations.

An exploratory data analysis was made with several laboratory tests and complemented by visual inspection reports conducted by specialized experts, enabling a multi-faceted evaluation of the concrete's condition and the potential presence of pyrrhotite-related damage.

The integration of laboratory data and field observations provided a robust basis for identifying key indicators of a possible deterioration, or the lack thereof, even in elements without apparent surface defects.

***Keywords**: pyrrhotite, concrete durability, visual inspection, laboratory tests, exploratory data analysis.*

1. INTRODUCTION

The pyrrhotite problem in the Trois-Rivières region was identified at the end of the 2000s and involves concrete foundation elements built between 1996 and 2008 in approximately 8 000 buildings [1]. In 2014, the court ruled that owners whose concrete contained aggregates with a pyrrhotite content of at least 0.23 vol% were entitled to compensation, based on the premise that structures not yet exhibiting deterioration would likely develop damage over time [2]. Moreover, additional thresholds based on total sulfur content were also considered to evaluate the risk of damage [3, 4]. Nevertheless, a substantial number of buildings with pyrrhotite and total sulfur contents above these thresholds have remained undamaged more than two decades after construction.

A large case study was conducted to characterize the damage observed in affected structures and to understand the determining factors. This study is based on the analysis of 3 668 concrete samples collected from 727 distinct buildings constructed between 2003 and 2008.

2. VISUAL INSPECTION

The type of damage observed depends on the concrete element and the exposure conditions to which it is subjected. Periodic visual inspections were carried out by a team of engineers to assess the presence and extent of damage.

Figure 2.1 describes the damage patterns considered characteristic of concrete swelling caused by pyrrhotite oxidation, according to the type of concrete element analysed.

Figure 2.1: (a) Beginning of map-cracking on foundation wall; (b) Severe map-cracking on foundation wall; (c) Severe map-cracking on floor slab; (d) Blisters under vinyl covering.

For tiled floor slabs, the most common types of damage are tile detachment and cracking. No damage was observed on protected indoor concrete slabs. A more detailed investigation was conducted on fully saturated elements, excavated foundation walls, where the concrete walls are saturated except for the upper portion, as well as beneath damaged ceramic tiles and vinyl coverings.

Figure 2.2 presents the types of damage observed in each specific case. It is important to note that no damage was observed in the excavated and fully saturated concrete walls. In general, swelling damage was observed only in the upper portion, which was not fully saturated.

The floor slab beneath damaged ceramic tiles exhibited map-cracking at different levels, depending on the degree of exposure to humidity. The floor slab beneath the damaged vinyl covering (blisters) showed oxidized coarse aggregates, accompanied by deformations, cracking, and localized disintegration of the cement matrix, characterized by whitish products surrounding the aggregates.

The whitish products observed around the aggregates are likely gypsum and/or ettringite, which are probably products resulting from internal sulfate reactions (ISR) caused by the presence of pyrrhotite in the concrete.

Figure 2.2: (a) Excavated foundation wall; (b) Cracking beneath ceramic tiles (internal stairwell); (c) map-cracking beneath ceramic tiles (building entrance); (d) Deformation and localized disintegration beneath vinyl covering (blister); (e) Whitish products surrounding the aggregates beneath vinyl covering (blister)

3. LABORATORY TESTS

Several laboratory tests were carried out to evaluate the physical and chemical properties of concrete containing pyrrhotite. Table 3.1 provides a summary of the laboratory tests and their corresponding standards.

Table 3.1: Summary of laboratory tests

Laboratory test	Standard / Protocol	Quantity
Petrographic Examination	*General protocol for basic tests on concrete cores*	2 795
Total Sulphur Content by Weight	CTQ-M200 [5]	2 555
Pyrrhotite Content by Volume	*General protocol for basic tests on concrete cores*	2 555

4. STATISTICAL ANALYSIS

4.1 Comparison between damaged and undamaged concrete elements

As part of the present study, it was essential to determine whether the concrete elements showing signs of damage differed, from a statistical standpoint, from those with no apparent damage. To this end, two complementary methods were employed: the Welch t-test [6] and the Mann–Whitney U-test [7], with the significance level set at 5%. Table 4.1 presents the p-values obtained for the various features analysed.

Table 4.1: Result of statistical comparison between damaged and undamaged concrete elements

Statistical Test	Total Sulphur Content by Weight	Pyrrhotite Content by Volume
Welch t-test	$1{,}76 \times 10^{-155}$	$3{,}95 \times 10^{-141}$
Mann–Whitney U-test	$1{,}93 \times 10^{-142}$	$1{,}39 \times 10^{-138}$

4.2 Evaluation of the damage threshold

To assess the effectiveness of a damage thresholds, several statistical analyses were performed, namely the chi-square contingency test (χ^2) [8], Fisher's exact test [9], and the calculation of the odds ratio and its 95% confidence interval [10]. These analyses make it possible to compare concrete elements showing signs of damage with those exhibiting no apparent deterioration, and to evaluate whether the selected threshold adequately discriminates between the two groups.

Table 4.2: Result of statistical evaluation of the damage threshold

Statistical Test	Total Sulphur Content < 0,10 (EN 12620+A1-2008)	Total Sulphur Content < 0,15 (CSA A23.1-2024)	Pyrrhotite Content < 0,23 (Quebec Superior Court, 2014)
Chi-square test (χ^2)	n/d	0,068	$4{,}4 \times 10^{-32}$
Fisher's exact test	1	0,042	$2{,}8 \times 10^{-36}$
Odds ratio	0,9	7,2	8,6
95% confidence interval	0,0 to 44,8	0,9 to 57,4	5,7 to 13,0
False positive	100,0%	99,2%	78,5%
False negative	0,0%	0,1%	3,1%

5. EXPLORATORY DATA ANALYSIS (EDA)

An exploratory data analysis was conducted, and both theoretical and empirical probabilities were evaluated for damaged concrete elements, considering several features to better understand the behaviour of concrete affected by pyrrhotite. Figure 5.1 illustrates the distribution of damaged concrete elements as a function of total sulphur content, pyrrhotite content and damage initiation time, whereas Figure 5.2 compares the theoretical and empirical cumulative probabilities of damaged concrete elements for each feature.

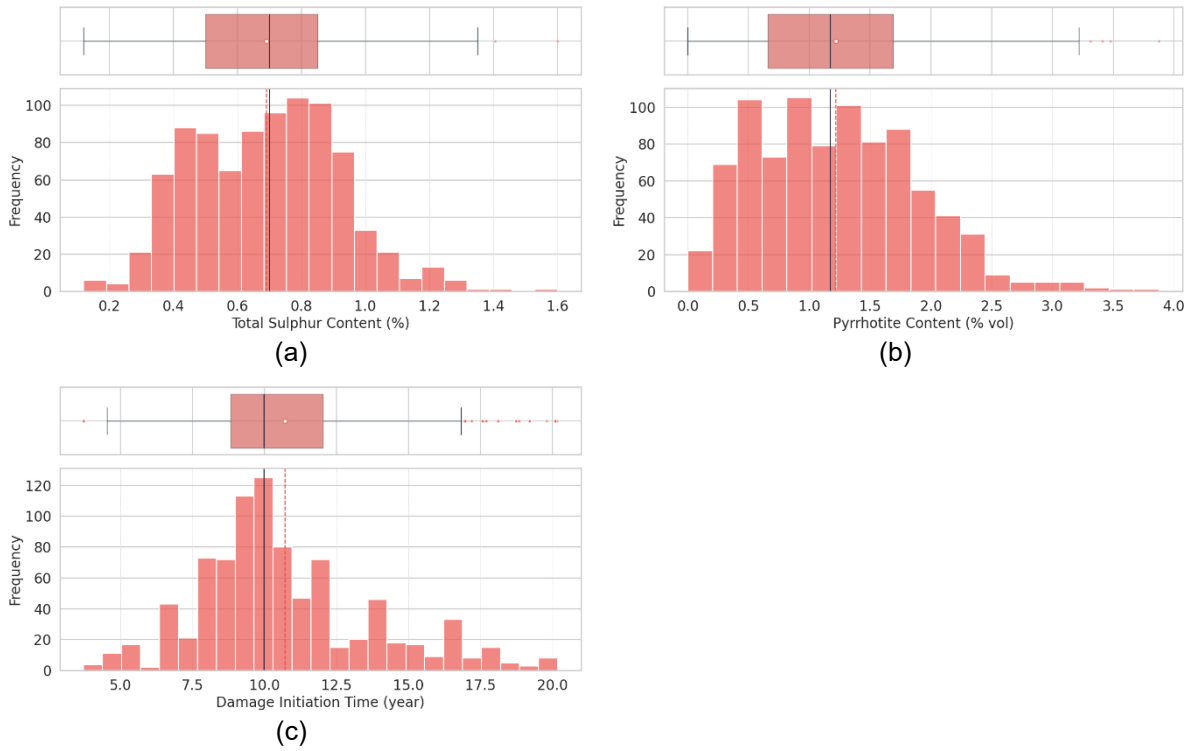

Figure 5.1: Distribution of damaged concrete in function of (a) total sulphur content, (b) pyrrhotite content and (c) damage initiation time

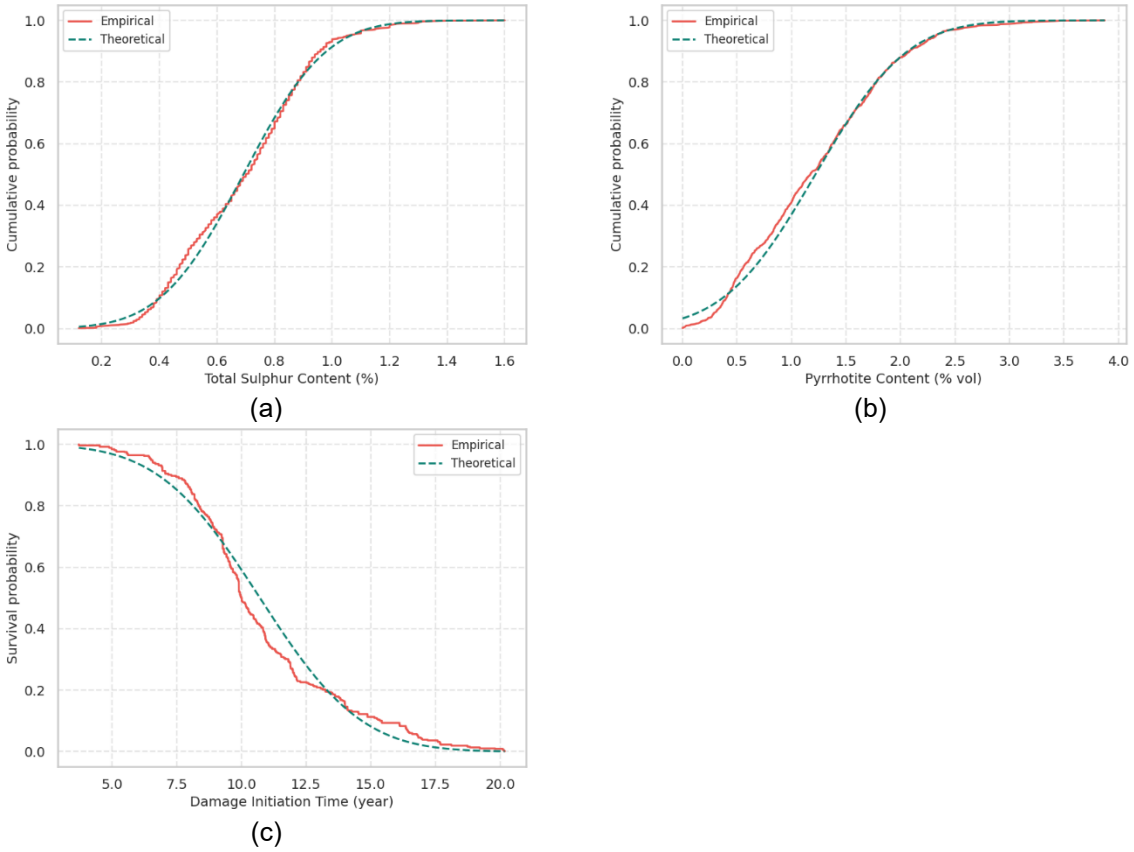

Figure 5.2: Theoretical and empirical cumulative probabilities of damaged concrete elements for (a) total sulphur content; (b) pyrrhotite content and (c) damage initiation time

6. DISCUSSION AND CONCLUSION

Visual inspections in specific cases highlighted the influence of exposure conditions on the deterioration of concrete affected by pyrrhotite. Subsurface (deeper than approximately 0.5 m) and fully saturated elements generally showed no evidence of degradation, whereas floor slabs near building entrances, where water exposure is more frequent, exhibited more pronounced damage compared to protected indoor slabs. This pattern reflects the impact of environmental conditions, since the reactions kinetics depend strongly on the availability of water and oxygen. Beneath vinyl coverings presenting blisters, deformations, cracking, and localized disintegration of the cement matrix were observed, along with whitish deposits surrounding aggregates, indicative of internal sulfate reaction sub-products.

Total sulfur and pyrrhotite contents differ significantly between damaged and undamaged concrete elements at the 95% confidence level. Nevertheless, the existing thresholds do not adequately distinguish sound concrete from deteriorated material. The high rate of false positives suggests that, while the threshold correctly identifies most damaged elements, it also incorrectly classifies many undamaged ones, reducing its effectiveness for practical decision making and targeted remediation.

Damaged concrete shows an average total sulfur content of 0.69 ± 0.23% and an average pyrrhotite content of 1.22 ± 0.66%. Analysis of the database indicates that damage typically initiates after 10.7 ± 3 years after construction. However, because inspections were not conducted annually and sometimes did not include all concrete components, this initiation period is likely overestimated, as deterioration may have started before it was formally detected during the inspection by the experts.

Based on this case study, the probability of damage in concrete with a total sulfur content below 0.15% ranges from 0.1% to 0.8%, while for pyrrhotite contents below 0.23%, the probability varies between 3.1% and 6.8%. Damage attributed to pyrrhotite was observed in elements built between 2003 and 2008, corresponding to 18 to 23 years since the issuance of the report. The probability of damage 18 years after construction is estimated at 0.9–2.2%, decreasing to nearly 0% after 23 years.

Considerable variability was noted among several parameters, including total sulfur content within the same sample, aggregate proportions within individual elements, sulfide concentrations in quarry materials, and the inherent subjectivity of petrographic assessments. For this reason, the application of a defined confidence level is essential in statistical analyses. There is, therefore, potential to refine the damage threshold using a 95% confidence level, improving its reliability for operational decision making and prioritization of interventions in structures affected by pyrrhotite.

7. REFERENCES

[1] Coalition d'aide aux victimes de la pyrrhotite - CAVP (2020) Période concernée. http://https://www.cavp.info/. Accessed 17 September 2025

[2] Cour supérieure du Québec. (2014) Jugement phare. Dossier 400-17-002016-091. Trois-Rivières

[3] CSA Group (2024) CSA A23.2 - Annex P: Impact of sulphides in aggregate on concrete behaviour and global approach to determine potential deleterious reactivity of sulphide-bearing aggregates. CSA Group, Toronto

[4] CEN (2008) EN 12620+A1- Aggregates for concrete. European Committee for Standardization, Brussels

[5] Comité technique québécois d'étude des problèmes de gonflement associés à la pyrite (2001). Appraisal procedure for existing residential buildings, Procedure CTQ-M200, Version 2.0, June 4th

[6] B. L. Welch (1947). The generalisation of `Student's' problem when several different population variances are involved. Biometrika 34(1–2), 28-35. https://doi.org/10.2307/2332510

[7] H. B. Mann, D. R. Whitney (1947). On a test of whether one of two random variables is stochastically larger than the other. Annals of Mathematical Statistics 18(1), 50-60. http://dx.doi.org/10.1214/aoms/1177730491

[8] Pearson, K. (1900). On the criterion that a given system of deviations from the probable in the case of a correlated system of variables is such that it can be reasonably supposed to have arisen from random sampling. Philosophical Magazine, 50(302), 157-175. https://doi.org/10.1007/978-1-4612-4380-9_2

[9] R. A. Fisher (1922). On the interpretation of χ^2 from contingency tables, and the calculation of P. Journal of the Royal Statistical Society 85(1), 87-94. https://doi.org/10.2307/2340521

[10] J. M. Bland, D. G. Altman (2000). Statistics notes: The odds ratio. BMJ 320(7247), 1468. https://doi.org/10.1136/bmj.320.7247.1468

ICISR 2026

2nd International Conference on Iron-Sulfide Reactions in Concrete

Technical Session # 3:

Factors and Accelerated Testing Methods for Iron-Sulfide–Induced Concrete Deterioration

UCONN | COLLEGE OF ENGINEERING
SCHOOL OF CIVIL AND ENVIRONMENTAL ENGINEERING

UCONN
COLLEGE OF ENGINEERING
CONNECTICUT TRANSPORTATION INSTITUTE (CTI)

Influences of Aggregate, Concrete Quality and Exposure Condition on Pyrrhotite Oxidation and ISA-Related Damage in the County Donegal, Ireland – Case Studies from Damaged to Undamaged Homes and Crumbled Blocks to Strip Concrete Foundations

Dipayan Jana (1)

Construction Materials Consultants, Inc. and Applied Petrographic Services, Inc.

(1) *Construction Materials Consultants, Inc.*

Abstract

Oxidation of pyrrhotite present predominantly in phyllite aggregates, and the resultant internal sulfate attacks (ISA) in paste from sulfates released from pyrrhotite oxidation are the mechanisms responsible for cracking and crumbling of concrete blocks across thousands of homes in County Donegal, Ireland. Comparing case studies of samples from (a) crumbled blocks of five damaged homes, (b) blocks from an undamaged home, and (c) strip concrete foundations of three homes all located in the County Donegal showed that the reasons for preferential distress in the blocks from outer leaf of damaged homes are directly related to the following factors: (1) abundance of reactive pyrrhotite in phyllite compared to the other aggregates (e.g., micaceous quartzite, metagreywacke, and quartzite), (2) availability of oxygen and moisture in the blocks during service for pyrrhotite oxidation, especially for easy migration through the (3) porous skeletal microstructure of low cement content blocks having 15-25% voids, (4) extensive contamination of paste with mica (muscovite-chlorite) from easily abradable phyllite (as high as 50% of the paste volume), (5) extensive alteration of paste by lime leaching leaving a Si-Al-rich gelatinous residue in the crumbled paste, and (6) formation of various products of ISA (e.g., ettringite in non-carbonated to thaumasite or gypsum in carbonated paste) especially in the outer leaf from where samples of damaged homes were received. Extensive oxidation of pyrrhotite grains not only in the mortar fractions but also in grains encashed within phyllite are seen in all distressed blocks resulting in the characteristic stripped patterns of iron oxide bands in iron sulphide matrix.

By contrast, sound conditions of blocks in the undamaged home despite having similar open microstructure as the damaged blocks are due to (a) the use of dominant denser and coarser-than-phyllite, less abradable pyrrhotite-free metagreywacke and micaceous quartzite crushed stone coarse aggregates, which have left (b) a significantly lesser (7-10%) abraded mica in paste, and (c) includes mostly non-reactive pyrite with only minor pyrrhotite found in rare phyllite gravel, which is usually unoxidized or oxidized before being added to the block.

Samples of strip foundations in two of the three homes showed crushed stone coarse aggregates of the same dominant pyrrhotite-bearing phyllite followed by mica schist or micaceous quartzite as in the distressed blocks. However, pyrrhotite oxidation is slow in the foundations with no detectable ISA in the non-carbonated interior paste. This is due to: (1) the overall denser microstructure of lower *w/c*, higher-cement-content dense, well-consolidated foundations than the open microstructure of blocks containing (2) a significantly lesser (7-10%) abraded mica in the paste and, most importantly, (3) high water saturation in foundations during service, which have restricted diffusion of oxygen needed for pyrrhotite oxidation. Typical stripped patterns of oxidized bands in pyrrhotite so common in the distressed blocks are rare in the foundations, only seen in a few poorly developed oxidized grains in the mortar fractions. Foundation of the third home has more crushed micaceous quartzite and mica schist in coarse aggregate than pyrrhotite-bearing phyllite where phyllite was added as alluvial gravel and hence showed pyrrhotite oxidation and cracking along foliation planes prior to the incorporation in concrete. As a result, although the potential for distress was higher in the two phyllite-bearing foundations (at least for oxidative expansion and cracking in aggregates than ISA in paste) than in the third but high humidity during service has restricted oxygen diffusion and, thereby, favoured those two underground foundations from development of any reported visible cracking despite 15-20 years in service.

Total sulfur contents (S_T) of blocks are 0.27 to 0.39 in the damaged home, 0.07 in the undamaged home, and 0.22 to 0.28 in the strip foundations, which are well-correlated with the abundance of pyrrhotite-bearing phyllites in aggregates. S_T values of distressed blocks and strip foundations even before conversions to aggregate S_T are all well in excess of 0.1% limit for pyrrhotite-bearing aggregates as

stated in EN 12620. Despite the absence of visible distress, high S_{TS}s from positive detection of pyrrhotite in all three foundations have prompted the homeowners to replace those foundations.

Severe distress of the outer leaf compared to the strip foundation is directly related to the concrete quality and exposure conditions of blocks versus foundations, whereas slow progress of distress in the strip foundations compared to severely cracked and crumbled residential foundations in the eastern USA indicate a rather complicated interplay of factors that are responsible for pyrrhotite oxidation and subsequent ISA. Pyrrhotite oxidation leading to paste disintegration from ISA, and lime leaching are the dominant mechanisms of distress in the blocks of damaged homes but limited pyrrhotite oxidation and perhaps limited ettringite-form of ISA in the confined spaces in non-carbonated interiors would be the early stages of distress in foundations if foundations were undersaturated for effective oxygen diffusion.

Irrespective of the exposure, use of *pyrrhotite-free* dense, coarse-grained quartzite, micaceous quartzite, or metagreywacke would have been a better aggregate choice for sound performance of blocks, as seen in the blocks of the undamaged home than *pyrrhotite-bearing metapelites* (phyllite, mica schist). This reinforces the importance of petrographic examinations of quarried stones and gravels for risk factor assessments of damaged dwellings, not for mica but for iron sulfide minerals (e.g., in a 'modified' version of I.S. 465 to include iron sulfide testing), and evaluate the potential dangers of these minerals in aggregates prior to incorporation in new concrete blocks or foundations.

Keywords: *aggregate, blocks, oxidation, pyrrhotite, sulfate.*

1. INTRODUCTION

Contrary to the hypothesis of excessive mica leading to freezing-related distress of concrete masonry blocks [1], oxidation of pyrrhotite in metapelite aggregates (phyllite, mica schist) causing decomposition of paste by internal sulfate attack (ISA) from sulfates released from pyrrhotite oxidation has been well-documented [2, 3, 4, 5] to be the primary mechanisms for cracking and crumbling of thousands of homes in County Donegal, Ireland. Furthermore, a holistic approach is being proposed [3, 5] to include influences of various factors that have aggravated the distress, e.g., (i) open microstructure of blocks to accelerate migration of moisture and oxygen for oxidation, (ii) preferential location of pyrrhotite in the easily abradable phyllite, which has facilitated easy release of sulfates to paste in moist condition, (iii) influences of aggregate types and mineralogies (relative abundances of metapelites vs metagreywacke/metaquartzite in aggregates), and (v) exposure conditions of blocks during service from moist to intermittent dry conditions influencing various modes of paste decomposition from ettringite-related ISA in non-carbonated paste to thaumasite or gypsum-related ISA in the carbonated paste to extreme decomposition by extensive lime leaching leaving crumbled Si-Al-rich residues.

The present study encompasses samples from: (a) five damaged homes (DM, SM, PD, ShM, and D) all showing extensive map cracking of renders to crumbling of the outer leaf, (b) one undamaged home (MM) without any cracking or crumbling, and (c) underground strip foundations of three homes (PD, JB, and MB) all of which have been replaced from the 'pyrrhotite fear' around the area despite no reported visible distress after 15-20 years of service. This offers an ideal opportunity for investigation of the above-mentioned influences on damage from open microstructure of distressed blocks to denser microstructure of strip foundations, which were exposed to different environmental conditions (above versus underground) during service.

1.1 Dalradian Metasediments

Damaged homes in the County Donegal, Ireland contain pyrrhotite-bearing aggregates quarried from 700-million-year-old Dalradian metasediments, e.g., (a) phyllite and mica schist, which were metamorphosed from fine-grained pelitic sedimentary rocks (mudstone, shale), or (b) quartzite, micaceous quartzite, or metagreywacke, respectively metamorphosed from coarser-grained sedimentary rocks, e.g., quartz sandstone, quartz-feldspar (arkosic) sandstone, or greywacke (having a higher micaceous matrix and a denser, darker-grey tone than arkose). Amongst these two broad classes, it is the metapelites from the finest grain phyllite to relatively coarser pelitic mica schists that are the deadliest of all with phyllite been the primary candidate for distress for hosting abundant finely disseminated pyrrhotite grains that were readily oxidized for easy penetration of moisture and oxygen first through the open porous microstructures of low-paste-content blocks and then through the weak folded foliation planes (crenulation cleavages) of phyllites.

1.2 Damaged versus Undamaged Homes

The primary difference between the five damaged home and one undamaged home is the abundance of pyrrhotite-bearing phyllite followed by mica schist in the damaged homes whereas the presence of non-pyrrhotite-bearing metagreywacke and micaceous quartzite, mainly the absence of pyrrhotite in the undamaged home.

1.3 Damaged Blocks versus Strip Concrete Foundations

Dominant pyrrhotite-bearing phyllite was found in all five damages homes and in at least two of three strip foundations. Overall denser microstructures of foundations (from the use of mixes having higher paste contents and lower water-cement ratios) than the porous skeletal microstructures of blocks (from lower interstitial paste contents and higher void contents between aggregates) and high humidity during service have slowed down the distress in the foundations mainly from slowing down pyrrhotite oxidation by restricting gas diffusion and resultant ISA-part of distress after pyrrhotite oxidation.

2. METHODS

Samples were examined by: (1) optical microscopy (reflected-light microscopy of polished thin and solid sections, and transmitted-light microscopy of polished thin sections) for iron sulfide minerals, oxidation products, aggregate mineralogy/texture, paste composition/microstructure/alteration, and secondary deposits; (2) SEM-EDS studies of polished thin/solid sections for further characterization of pyrrhotite and compositions of paste; (3) XRD studies of bulk samples for detection of iron sulfide minerals, aggregate mineralogies, and ISA products, and (4) combustion IR for total sulfur content (S_T).

3. RESULTS & DISCUSSION

3.1 Total Sulfur

Total sulfur, S_T (from pyrrhotite, pyrite and other sulfides in aggregates and cement sulfate) of the five damages homes are (in mass%) 0.342% for DM, 0.389% for SM, 0.269% for PD, 0.369% for ShM and 0.266% for DM all exceeding the limit value of <0.1% for aggregates that contain pyrrhotite stated in EN 12620 [7]. By contrast, S_T of the undamaged home is 0.066%, which is directly related to the absence of pyrrhotite. Two concrete foundations containing pyrrhotite-bearing phyllite showed S_T of 0.282% for PD and 0.268% for JB but the third foundation MB with lesser pyrrhotite (only in phyllite gravel) and more mica schist and quartzite/metagreywacke than other two foundations showed a S_T of 0.217%. Samples were tested according to I.S. 465 [6] and BS E.N. 1744-1 from high temperature combustion in an atmosphere of pure oxygen, followed by quantification by infrared detectors. When corrections were made to the bulk S_T for contributions from aggregates, the corrected values are increased by 8% for low-paste content blocks and 20% for high-paste content foundations [3], i.e., 0.287-0.420 for distressed blocks and 0.322-0.338 for foundations, which are all noticeably higher than the maximum 0.1% limit for pyrrhotite-bearing aggregates as stated in EN 12620 [7].

3.2 Petrographic Examinations

In all five damaged homes, (1) crushed phyllite followed by subordinate (2) mica schist are the dominant coarse aggregates (Fig. 1) where pyrrhotite is preferentially concentrated in phyllite whereas coarser grained non-pyrrhotite-bearing (3) micaceous quartzite and (4) metasandstone/metagreywacke are present only in minor amounts. Opposite is true for the undamaged home (MM) where pyrrhotite-free crushed metasandstone/metagreywacke is the most abundant coarse aggregate with minor micaceous quartzite and quartzite, where only one pyrrhotite-bearing phyllite gravel of an alluvial source was detected, which was probably an acidental inclusion in the dominant crushed sandstone/greywacke aggregate. Like the distressed blocks, two strip foundations (PD, JB) contained dominant crushed phylite and subordinate mica schist in coarse aggregate with the former being the common host for pyrrhotite; the third foundation (MB) has crushed mica schist and metagreywacke, and subordinate phyllite as gravel having finely disseiminated pyrrhotite in phyllite mostly pre-oxidized in alluvial source.

Phyllite in all distressed blocks contains major amounts of interlayered muscovite, chlorite and subordinate amounts of very fine-grained silty quartz and alkali feldspar all in parallel layered arrangements to form the typical foliation or sheet-like flakes and characteristic crenulation cleavages of deformed foliations. Weak zones along foliation planes and crenulation cleavages provided pathways for migration of moisture and oxygen to oxidize finely desseminated grains of pyrrhotite in phyllite. Muscovite and chlorite are nonswellable sheet silicates but their presence as easily breakable foliated

sheets in phyllite along with their inherent finer grain size than schist have contaminated the mortar fractions of blocks with abraded phyllite flakes (>10% to as high as 50%, by paste volume) to increase the water demand at a given workability and reduce the compressive strength. Mica schist is relatively coarser grained than phyllite, consisting of muscovite mica, biotite, chlorite, deformed quartz, and alkali feldspar all in parallel arrangements to define the schistose texture. Micaeous quartzite is noticeably denser and coarser than mica schist but still showing parallel alignments of mica flakes in the coarse-grained granoblastic quartz. Metasandstone and metagreywacke are coarser grained than phyllite or schist, but show typical clastic texture of sandstone or greywacke of detrital quartz and feldspar and more calcite and micaceous grains (wacke) in the matrix of the latter. Quartzite is monomineralic of all types, coarsest, of interlocking granoblastic quartz. Phyllite and mica schist are the metamorphosed derivatives (metapelites) of mudstone, shale, or micaceous stilstone, which are the common hosts for pyrrhotite, whereas micaceous quartzite, greywacke and quartzite are the coarser-grained metamorphosed derivatives of arkosic sandstone/greywacke of the Dalradian supergroup.

Abundant pyrrhotite grains in phyllite (sizes from <1 mm at long to <0.5 mm at short directions) have acted as the effective sites for expansion from oxidation during service especially at the moist and alkaline (pH >10, less to non-carbonated) conditions of blocks. Some prior oxidations (especially for gravels), however, may have occurred in geologic formation and during storage in the aggregate stockpile. Mode of occurrence of pyrrhotite varied from fine-grained isolated disseminated irregular-shaped to subhedral equant grains to mostly elongated grains aligned along the dominant foliation planes, which shows extensive reddish-brown oxidation products (e.g., goethite, ferrihydrite) causing further cracking, splitting, and disintegration of phyllite. In situ oxidation of pyrrhotite has caused further splitting and crumbling of phyllite especially since most pyrrhotite grains have crystallized along the prevailing foliation planes where the inherent phyllitic texture of foliation and deformed (crenulation) cleavage planes provided pathways for ready migration of moisture to facilitate oxidation. Additionally, spectacular radial cracks are often seen from oxidized pyrrhotite grains in phyllite as a testament of *in situ* expansion from pyrrhotite oxidation. Reddish-brown oxidized pyrrhotite products are preferentially noticed between the greenish sheened (from chlorite) foliated sheets where expansive oxidation reactions have further disintegrated the phyllite. Pyrrhotite contents in phyllite varied from 0.75 to 1.5 percent by volume. Pyrrhotite is sometimes associated with pyrite and chalcopyrite. No evidence of oxidation of pyrite or its subsequent sulfate attack (as found in the Counties Mayo, Clare and Limerick from framboidal pyrite within calcareous mudrock) was found in the present study.

After phylite and mica schist, non-pyrrhotite-bearing metagreywacke, micaceous quartzite, and metaquartzite are three less common types in the damaged homes, but they become the dominant rock types with only negligible pyrrhotite-bearing phyllite (only one gravel) in the undamaged home (MM). Quartz-feldspar-bearing arkosic quartzite and metagreywacke (both showing clastic texture but latter with higher micaceous and calcitic matrix than the former) and micaceous quartzite (with parallelism of mica in coarse-grained granoblastic quartz matrix) are the main rock types in umdamaged home.

Paste in the blocks of all damaged homes showed (i) severe carbonation, which is best depicted from its characterstically high birefringence in polarized light microscope along with (2) near-isotropic porous paste from severe lime leaching leaving only sílica-alumina rich gelatenous residues of no strength or cementitious properties. By contrast, paste in the undamaged home (MM) shows (3) ‘patchy’ carbonation to (4) non-carbonated calcium silicate hydrate (CSH) and portlandite (CH) rich areas; both carbonated and non-carbonated paste are notiecably denser than severely cabronated and leached paste in damaged homes. Abaded phyllite is abundant in all damaged blocks but more restrictred in the undamaged block for the lack of phyllite, or in the strip foundations for noticeably denser paste enclosures around coarse aggregates.

Two strip foundations (PD and JB) showed the same abundant pyrrhotite-bearing phyllite followed by subordinate mica schist (PD, JB) or micaceous quartzite (JB) as in the blocks of damaged homes except the interstitial spaces between aggregates are completely filled with noticeably denser (from use of lower *w/c*) paste from adequate consolidation with noticeably less abraded phyllite or mica in paste than in the paste of damaged blocks. For the third foundation (MB) pyrrhotite-bearing phyllite was the least abundant only in a minor gravel where most of the oxidation of pyrrhotite in phillite has occurred prior to the incorporation in concrete. The dominant rocks in foundaiton MB are mica schist, metagreywacke, micaceous quartzite, and quartzite, none with any detectable pyrrhotite to cause a threat as the other two foundations. Other than typical siliceous particles (quartz, quartzite, feldspar, chert, siltstone, and mica from abraded coarse aggregate) found in all three foundations, MB also contained a minor fraction of crushed seashell fragments in sand. Concrete in all three foundations are non air-entrained (estimated <3% air). Paste is portland cement-based in all three foundations except fly ash at <5% and 10-15% of total cementitious materials detected in PD and JB, respectively (which may have provided an aided densification of paste from pozzolanic reactions). Estimated water-cement ratios are 0.50-0.55 in PD

and MB to 0.45-0.50 in JB. Carbonation of paste is limited to the exposed surface ends (to depths of 10-20 mm) with mostly non-carbonated interiors in PD and JB (unlike pervasive leaching and carbonation of paste in the damaged blocks) but shows more pervasive carbonation in MB.

3.3 SEM-EDS Studies

SEM-EDS studies of distressed blocks from damaged homes showed (a) oxidized pyrrhotite grains in phyllite and in mortar fractions having well-developed parallel Fe-O oxidized bands in Fe-S matrix where (b) the O/Fe atomic ratios of oxidized bands are noticeably higher than the ratios found in similar oxide bands in pyrrhotite from crumbled foundations of eastern US, (c) S/Fe atomic ratios of alternate sulphide matrix in pyrrhotite are close to pyrite stoichiometry than pyrrhotite, (d) extensive microcracking in the oxidized pyrrhotite grains, often extending into the aggregate and even to the neighbouring paste, (e) thaumasite precipitation in cracks and voids in one damaged home (DM), but (e) no elevated sulfate levels (S/Ca atomic ratios are mostly within 0.0 and 0.05) in the interstitial paste fractions in four out of five damaged homes due to extreme lime leaching and alterations to form the dominant silica-alumina gel of no cementitious property sometimes with occasional islands of secondary calcite precipitates. By contrast, similar absence of sulfate enrichment in otherwise dense, non-carbonated (PD, JB) to carbonated (MB) paste in strip foundations is due to the absence of advance pyrrhotite oxidation to release sulfate in paste, which is confirmed by the absence of the typical stripped patterns of oxidized pyrrhotite grains in phyllite (except only crude Fe-O bands in some grains in the mortar fraction). Abraded phyllite contents (calculated from clustered phase maps of muscovite and chlorite from corresponding elemental maps of K and Mg) is found to be noticeably higher in the mortar fractions of distressed blocks (as high as 50%) than in the mortar fraction of undamaged home, MM (10%), or in the mortar fractions of strip foundations (< 5% in MB to 5-10% in JB and PD).

3.4 XRD

Results of XRD for pyrrhotite-bearing phyllite and mica schist in the distressed blocks and two strip foundations (PD and JB) are similar with quartz, chlorite, and muscovite as main minerals, and feldspar (albite, orthoclase) and calcite as the minor minerals. Both pyrrhotite and the oxidized form, ferrihydrite, are detected in damaged blocks but were undetected in bulk samples of undamaged blocks. Only two foundations (PD and JB) showed trace pyrrhotite in bulk concrete but no oxidized forms.

4. CONCLUSIONS

The main difference between the blocks of damaged and undamaged homes is the absence of pyrrhotite or pyrrhotite-bearing phyllite in the coarse aggregate of the latter. As a result, S_T of damaged homes are noticeably higher, i.e., in excess of the 0.1 mass% limit of pyrrhotite-bearing aggregates in EN 12620 as opposed to well within that limit in the undamaged home. Additionally, the change in rock types from crushed friable phyllite-dominant coarse aggregate in the damaged homes to crushed but non/less-friable metagreywacke/micaceus quartzite aggregate in the undamaged home has resulted in a noticeably lower abraded mica in the paste of undamaged home (<5 volume %). Severe carbonation and lime leaching of paste in damaged homes compared to less carbonated to non-carbonated, non-leached paste in undamaged home indicates more restricted access of moisture and atmospheric carbon dioxide through the uncracked painted renders of the undamaged home compared to the easy access of elements through the severely cracked to crumbled renders of the damaged homes.

Inherent higher porosity of blocks from abundant interstitial voids and low paste (cement) contents compared to lower porosity of strip foundations from lower interstitial voids, higher paste (cement) contents to well-coat the aggregates, and dense well-consolidated natures of concrete foundations as opposed to blocks have offer many benefits to the strip foundations, especially when two of the three foundations contained the exact same pyrrhotite-bearing phyllite as the dominant coarse aggregate as in the damaged blocks. First benefit is the protection of pyrrhotite from advance oxidation during service in the foundations by restricting the oxygen access through the dense foundation, especially if the foundations were water saturated during service to prevent oxygen diffusion, which was impossible in blocks of outer leaf for easy access of moisture and oxygen first through the interconnected interstitial voids to reach phyllite and then through the foliation planes of phyllite to reach pyrrhotite. As a result, well-developed stripped patterns of oxidized bands in pyrrhotite that are so common in the distressed blocks were difficult to find in the strip foundations (found mostly in the mortar fractions of foundations than within phyllite). High humidity (water saturation) during service in the underground foundations prevented diffusion of oxygen needed for pyrrhotite oxidation since oxygen diffusion in water-saturated concrete is negligible compared to dry or unsaturated concrete, often reduced by a factor of 10^4. Second, limited moisture migration through dense concrete has also restricted the possibility of leaching and

decalcification of paste in the strip foundations, which are so pervasive in the damaged blocks. Third, restricted pyrrhotite oxidation has also restricted ISA in the paste of strip foundations (only secondary ettringite crystallization in voids and relatively porous areas of paste from prolonged presence of moisture was found in one strip foundation, PD). Extensive SEM-EDS analyses of paste in all three strip foundations showed no sign of elevated S/Ca atomic ratios to indicate sulfate release from pyrrhotite oxidation, which is the primary prerequisite for ISA. Despite pervasive carbonation of paste in MB, there was no sign of thaumasite form of ISA. Higher abraded mica in the paste (from higher phyllite aggregate) of damaged blocks has facilitated moisture ingress, access of oxygen, and diffusion of sulfate ions to paste to promote ISA in the damaged blocks.

In the damaged blocks it is suggested [2,3] that (1) ettringite-form of ISA occurs in the non-carbonated paste from conversion of monocarbonate to ettringite by the released sulfate leading to expansion, (2) partial dissolution of abraded muscovite and chlorite in the alkaline environment of cement paste can provide additional monocarbonate to raise the expansion potential by additional ettringite formation, (3) carbonation of CSH and CH to calcite promotes thaumasite-form of ISA and eventually to (4) gypsum (more common in the drier inner than the moist outer leaf for faster carbonation and slower pyrrhotite oxidation in the inner leaf) leading to crumbling and loss of strength of paste from decomposition of CSH. Extensive lime leaching leading to formation of Si-Al-rich gelatinous mass in all the damaged homes in this study caused the ultimate loss in integrity of paste and large-scale crumbling of blocks.

Compared to the damaged blocks, higher quality of concrete in the strip foundations has only slowed down pyrrhotite oxidation and restricted ISA but not necessarily eliminated that potential since as long as there is pyrrhotite to be oxidized (as seen in all three foundations from the abundance in crushed phyllite in two foundations to subordinate phyllite gravel in the third) there is always potential for in situ expansion from oxidation and subsequent ISA in paste from the released sulfate. The evidence is spectacularly clear in many other foundations, e.g., from eastern US to Canada [8].

5. REFERENCES

[1] McCarthy, D., Kane, N., Lee, D, Blaney, D (2017). Report of the Expert Panel on Concrete Blocks, Department of Housing, Local Government and Heritage, 2017. https://www.gov.ie/en/publication/0218f-report-of-the-expert-panel-on-concrete-blocks.

[2] Leemann, A., Lothenbach, B., Münch, B., Campbell, T. and Dunlop, P (2023). The “mica crisis” in Donegal, Ireland–A case of internal sulfate attack? Cement and Concrete Research, 168, p.107149. https://doi.org/10.1016/j.cemconres.2023.107149.

[3] Leemann, A., Münch, B., Lothenbach, B., Winnefeld, F. and Dunlop, P (2024). Defective homes in Donegal, Ireland: effect of exposure conditions and concrete quality on pyrrhotite oxidation and internal sulfate attack. Cement and Concrete Research, 186, p.107684. https://doi.org/10.1016/j.cemconres.2024.107684.

[4] Brough C., Staniforth B., Garner C., Garside R., Colville R., Strongman J., Fletcher J (2023) High risk concrete blocks from County Donegal: The geology of defective aggregate and the wider implications. Construction and Building Materials 408:133404. https://doi.org/10.1016/j.conbuildmat.2023.133404.

[5] Jana, D. (2024) Cracking and crumbling of concrete blocks in County Donegal, Ireland: A holistic approach from case studies on deleterious effects of open microstructure of blocks, phyllite aggregate, pyrrhotite oxidation, paste carbonation, lime leaching, and internal sulfate attacks, 1st International Conference on Iron-Sulfide Reactions in Concete, Quebec City, Universite Laval Campus, Canada, May 14-17, pp. 34-38.

[6] I.S. 465:2018+A1:2020 Assessment, testing and categorisation of damaged buildings incorporating concrete blocks containing certain deleterious materials. National Standards Authority of Ireland, Dublin.

[7] EN12620, Aggregates for Concrete, European Committee for Standardization, Brussels, 2002 + A1:2008.

[8] Jana D (2023) Concrete Deterioration from the Oxidation of Pyrrhotite: A State-of-the-Art Review. In: Maher MLJ (ed) Pyrite and Pyrrhotite, Nova Science Publishers, Inc, pp. 137-221.

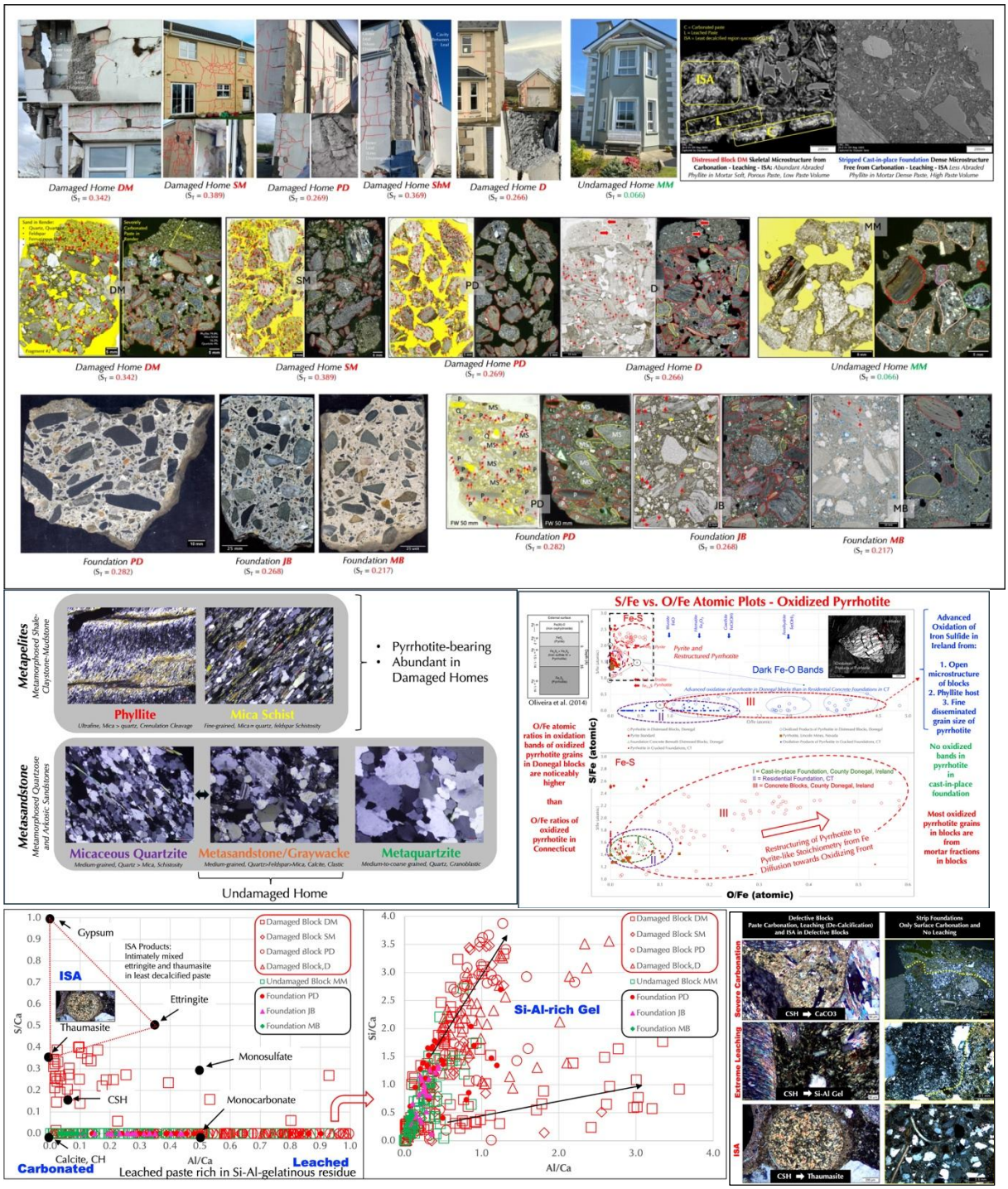

Figure 1: Row 1 left: Five damaged homes and one undamaged home and associated total sulfur (S_T). Row 1 right: BSE images of porous, leached, carbonated, ISA-affected skeletal microstructure of paste in a damaged block compared to dense microstructure of a strip foundation. Row 2: Fluorescent dye-mixed epoxy-impregnated 50 x 75 mm size thin sections of four damaged homes and one undamaged home (right most) in PPL and XPL showing dominant pyrrhotite (red arrows in PPL)-bearing phyllite (marked in red lines in XPL) in the damaged homes versus pyrrhotite-free metagreywacke (marked in beige lines in XPL) in the undamaged home. Row 3 left: Lapped cross sections of samples from three dense, well-consolidated concrete in strip foundations. Row 3 right: Scanned whole-slide thin section images in PPL and XPL of strip foundations showing the same dominant pyrrhotite-bearing phyllite as in the damaged blocks in two foundations (PD, JB) and in the third foundation (MB) having crushed mica schist/metagreywacke, and phyllite as gravel aggregate. Row 4 left: Micrographs of five dominant rock types where metapelites are the host of pyrrhotite and common in damaged homes, whereas quartzite/metagreywacke are pyrrhotite-free and found in the undamaged home. Row 4 right: SEM-EDS plots (S/Fe versus O/Fe atomic ratios) of oxidized pyrrhotite in damaged blocks versus foundations from Ireland and superposed on the data from the eastern US. Row 5 left: SEM-EDS plots (S/Ca versus Al/Ca and Si/Ca versus Al/Ca atomic ratios) of paste from damaged homes and foundations showing elevated S/Ca ratios in one damaged home from thaumasite ISA but mostly non-elevated S/Ca ratios from extensive carbonation and lime leaching in other damaged homes, and lack of sulfate contamination in the paste of three strip foundations. Row 5 right: Severe carbonation, leaching, and thaumasite formation in the paste of a damaged home (DM) compared to dense non-carbonated CSH-CH interior (in PD and JB) to carbonated paste (in MB, which also has some seashells in sand) in the strip foundations.

Accelerated Assessment of Sulfide-Bearing Aggregates Using the Vacuum-Bleach Injection Technique (VBIT)

Hamid Reza Shadkam [(1)], Medhat H. Shehata [(2)],

(1) Toronto Metropolitan University (TMU), Toronto, Canada, hshadkam@torontomu.ca

(2) Toronto Metropolitan University (TMU), Toronto, Canada, mshehata@torontomu.ca

Abstract

The oxidation of iron sulfide minerals in aggregates can result in deleterious expansion, cracking, and surface pop-outs in concrete, primarily due to internal sulfate attack and the formation of iron oxides. Laboratory evaluation of such aggregates remains challenging due to the slow rate of sulfide oxidation. This reaction is governed by the limited interaction among oxygen, sulfide minerals, and water in concrete, and therefore delays the release of sulfate ions necessary for sulfate attack.

This study presents a practical and accelerated laboratory method -referred to as the Vacuum-Bleach Injection Technique (VBIT)- developed to enhance oxidant penetration into micro-prism specimens with coarse aggregate. The procedure involves partially drying the specimens, applying a vacuum for three hours, and subsequently injecting household sodium hypochlorite (bleach) under vacuum for an additional three hours. The specimens are then stored at 40 °C and 75% relative humidity for one week. This conditioning sequence is repeated for 17 weeks. This phase is followed by 17 weeks of storage at 5 °C and 100% relative humidity to promote sulfate attack in the specimen.

For this method, micro-prism test specimens are prepared using mixes composed of cement, water, and coarse aggregate "aggregate-paste mixes". Omitting the fine aggregate increases the cement paste content and hence the sulfate vulnerable phases, around the coarse aggregate particles. The effectiveness of the VBIT protocol was evaluated against conventional bleach-soaking methods. The results indicate that VBIT-treated specimens exhibited considerable expansion for sulfide-bearing aggregates in comparison with the samples with control aggregate.

Scanning electron microscopy confirmed the formation of secondary ettringite and gypsum in the expanded specimens, consistent with internal sulfate attack driven by accelerated sulfide oxidation. The findings support the applicability of VBIT as a promising and time-efficient method for the assessment of sulfide-bearing aggregates in concrete.

Keywords: *ettringite, micro-prism specimens, sulfate attack, sulfide oxidation, vacuum-bleach injection technique (VBIT)*

1. INTRODUCTION

The deterioration of concrete containing sulfide-bearing aggregates has been studied for decades[1-7], although it has gained much attention in the last 15 years. The principal problematic minerals are pyrrhotite ($Fe_{1-x}S$) and pyrite, which oxidize according to equations 1 and 2 [5]:

$$FeS_2 + \frac{15}{4}O_2 + \frac{5}{2}H_2O \rightarrow FeOOH + 2H_2SO_4 \quad (1)$$

$$Fe_{1-x}S + \left(2 - \frac{x}{2}\right)O_2 + xH_2O \rightarrow (1-x)Fe^{2+} + SO_4^{2-} + 2xH^+ \quad (2)$$

The released sulfate reacts with portlandite to form gypsum [4], as per equation (3). Gypsum then reacts with aluminate phases of the cement matrix to form ettringite [6-7], following equation (4). Ettringite or other aluminate-based phases can subsequently reacts with C–S–H and calcium carbonate to form thaumasite [8], equation (5).

$$H_2SO_4 + Ca(OH)_2 \rightarrow CaSO_4.2H_2O \quad (3)$$

$$3(CaSO_4.2H_2O) + C_3A + 26H_2O \rightarrow C_3A.3CaSO_4.H_{32} \quad (4)$$

$$C_3S_2H_3 + C_6A\overline{S}_3H_{32} + 2C\overline{C} + 4H \rightarrow 2C_3S.\overline{CS}H_{15} + C\overline{S}H_2 + AH_3 + 4CH \quad (5)$$

Deterioration symptoms appear after short or long periods (ranging from as early as two years in severe cases [7] to more than 20 years [9]); this has driven research efforts to accelerate the reactions in the laboratory to evaluate aggregates within a practical window. Existing screening methods generally fall into two categories: (1) tests performed on aggregates outside the cement matrix, such as oxygen consumption tests (OCT) [10], the Midgley test [1], and aggregate dissolution tests[3]; and (2) tests conducted within a cementitious matrix to more realistically simulate in-situ sulfide oxidation, including mortar-bar tests[4], [11] and accelerated concrete tests using oxygen [12] or electrochemical activation [13]. The present study aims to develop a testing method focused on aggregates embedded within a cement matrix.

2. MATERIALS AND MIX DESIGN

2.1 Materials

Four aggregates with varying sulphur contents were used in this study. The chemical compositions of the aggregates are presented in Tables 2.1. One general use GU cement was used for all mixes; the chemical composition of the cement is presented in Table 2.2. The aggregate MSK H has caused significant expansion in concrete in Trois Rivière, Quebec [4]

Table 2.1: Aggregates chemical analysis

Aggregate	SSD Density	Total S%	SiO_2 %	CO_2%	Fe_2O_3%	Al_2O_3%	TiO_2%	CaO%	MgO%	Na_2O+K_2O(%)
ORE	3221.1	14.00	33.09	0.13	39.40	8.53	0.73	4.20	3.05	2.39
MSK H	2881.0	0.93	50.58	0.71	8.10	19.36	0.53	8.84	6.85	3.79
MSK L	2881.0	0.21	50.58	0.71	8.10	19.36	0.53	8.84	6.85	3.79
C1	2730	0.09	1.88	46.10	0.37	0.44	0.02	29.90	20.60	0.22

Table 2.2: Cement chemical analysis

Material	SiO_2 (%)	Al_2O_3 (%)	Fe_2O_3	CaO (%)	MgO (%)	SO_3 (%)	$Na_2O+ 0.658K_2O$	LOI at 1000°C (%)
Cement	20.20	5.30	2.30	61.90	2.30	4.20	1.00	2.20

2.2 Mix design and sample specifications

Mixes were prepared without fine aggregate and with a higher cement content, using a cement–coarse aggregate–water ratio of 1:1:0.33. These are referred to as “aggregate-paste mixes” in this paper, following the concept used in RILEM AAR-5 [14]. Such mixes are expected to exhibit higher pH due to their lower w/c ratio and increased Portland cement content [15].

Although the aggregate-paste mix has lower permeability than a conventional concrete mix, which may limit oxidant penetration, presoaking the aggregates in an oxidizing agent prior to casting helps initiate early reactions and promotes microcrack development, improving oxidizing-agent ingress during the injection. Aggregates were presoaked for ten minutes before mixing, corresponding to approximately 40% of their absorption capacity. Four sets of samples with dimensions of 40 mm x 40 mm x 285 mm, (micro-prism) were cast for VBIT, as summarized in Table 2.3. The first sample, C1 +50% Ore, contained a blend of the non-sulfide aggregate C1 and the highly oxidizable Ore at a ratio of 1:1 by mass

Table 2.3 Samples for aggregate-paste mix bleach injection conditioning

No	Aggregate for aggregate-paste mix
1	50%C1+50%ORE
2	MSK H
3	MSK L
4	C1

3. CONDITIONING (VBIT)

Soaking concrete samples in bleach (similar to the mortar-bar conditioning described in Annex P of CSA A23.1) has been explored by several researchers as a means to accelerate sulfide oxidation [12-13]. While bleach soaking produced encouraging results for mortar bars [11], it was far less effective for concrete, largely due to the greater sample thickness, which limits oxidant penetration and also lower surface area of the coarse aggregate. In such cases, deterioration was typically confined to surface pop-outs, with little measurable expansion.

The proposed Vacuum Bleach-Injection Technique aims to enhance oxidant penetration using a vacuum-soaking approach similar to that employed in ASTM C1202 for the Rapid Chloride Permeability Test (RCPT) specimen preparation [18]. A high-capacity vacuum pump and large desiccator allowed simultaneous conditioning of all samples. Prisms were cast and demoulded after one day, then stored in the curing room for six days. The conditioning cycle then began. Specimens were first oven-dried at 40 °C for 24 hours to improve bleach ingress, then placed in the desiccator and subjected to vacuum for 3 hours. Bleach was subsequently injected, and the samples remained under vacuum for an additional 3 hours. After length measurements, specimens were stored at 40 °C and 75% RH for the remainder of the week. This cycle was repeated for 17 weeks.

Following this phase, specimens entered the sulfate-attack conditioning stage, consisting of a weekly 8-hour bleach soak and storage at 5 °C and 100% RH. Figure 3.1 illustrates the overall bleach-injection conditioning protocol.

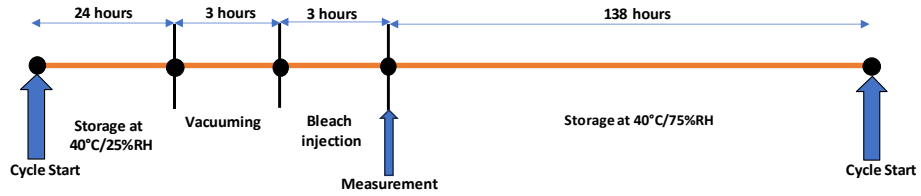

(a) Bleach injection for 17 weeks

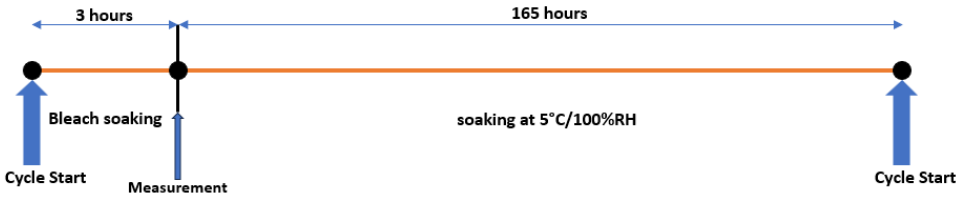

(b) Sulfate attack phase for 17 weeks

Figure 3.1: VBIT conditioning schematic details

4. RESULTS AND DISSCUSSION

4.1 Expansion Testing

The expansion results for the aggregate-paste mix samples are shown in Figure 4.1.a. The 50% ORE sample exhibited an expansion of 0.44%, compared with only 0.014% for C1. The expansion of the sample with the Ore continued to increase during the second stage, whereas C1 reached a plateau, indicating no sulfate attack. The MSK H samples also showed substantial expansion, approximately 0.38%, with continued growth in the second stage. In contrast, MSK L expansion was not continuous and levelled off during the second stage; however, despite this plateau, its final expansion remained higher than C1, reaching approximately 0.23% after 34 weeks of conditioning.

In contrast, the results for conventional bleach soaking (8 hours of bleach exposure twice per week, with storage at 40 °C/75% RH for 18 weeks followed by the same soaking regime and storage at 5 °C/100% RH for another 18 weeks) are shown in Figure 4.1.b [16] for the same aggregates. The expansion of the 50% ORE samples is significantly lower than that observed under VBIT conditioning. More importantly, the expansion behaviour of the other contaminated aggregates is indistinguishable from that of the

control aggregate (C1). The comparison indicates that just 3 hours of weekly bleach injection in aggregate-paste mixes is more effective than 16 hours of conventional bleach soaking in normal concrete. The difference is more pronounced in Figure 4.2.

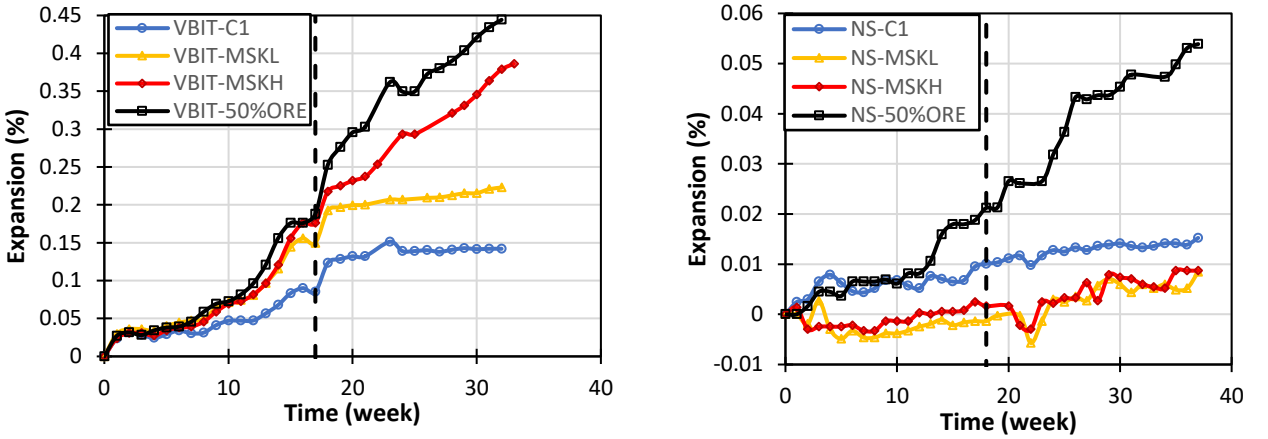

(a) **VBIT conditioning – Aggregate-paste mixes**

(b) **Bleach soaking – Normal concrete (NS) results from Moradzadeh** [16]

Figure 4.1: VBIT and Normal Bleach Soaking expansion results – Different scale of the Y-axes

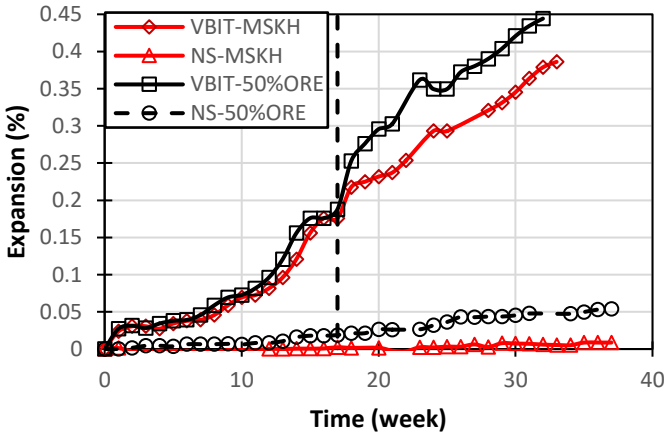

Figure 4.2: Comparison of VBIT with Normal Bleach Soaking conditionings

Figure 4.3 shows the surfaces of some of the aggregate-paste mix samples at the end of conditioning. The C1+50% ORE specimens exhibit extensive pop-outs and spalling, with surface deterioration decreasing progressively as the sulfide content decreases (MSK H, MSK L, and C1). During visual inspection, particularly while extracting material for chemical analysis, the highly contaminated samples fractured easily, and the cement paste separated readily from the aggregate.

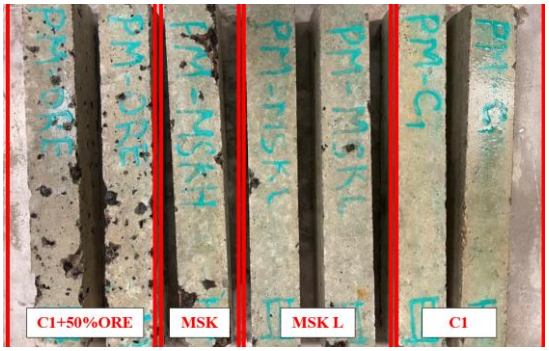

Figure 4.3: The surface of the aggregate-paste mix samples at the end of conditioning

4.2 SEM/EDS Analyses

SEM-EDS analyses were performed on the conditioned samples. Figure 4.4 shows sulfate-bearing reaction products, including an ettringite-like phase exhibiting a silica peak as well as gypsum identified within the cement paste. The S/Ca and Al/Ca ratios are consistent with ettringite, while the presence of silica suggests a mixed ettringite–thaumasite phase.

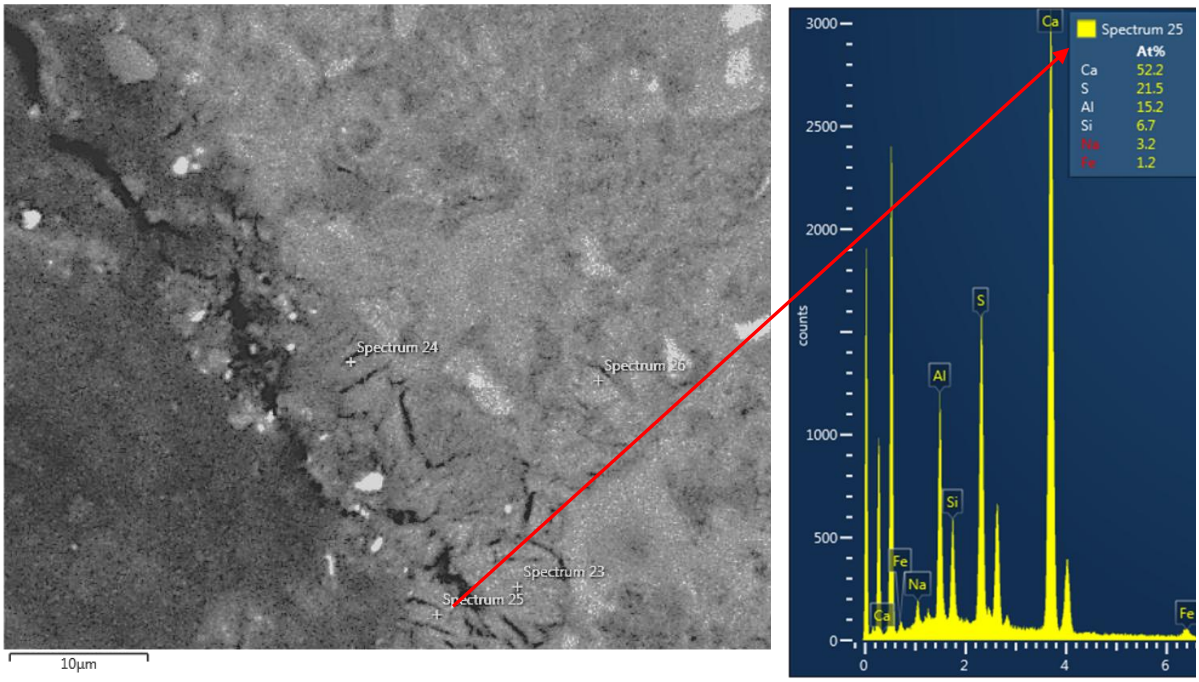

Figure 4.4: Ettringite-thaumasite products in 50%ORE sample

5. CONCLUSION

A new method for assessing aggregates within a cementitious matrix (aggregate-paste mix) was introduced, in which the oxidizing agent is injected directly into the specimens. The expansion results demonstrated that this conditioning approach provides a clear and distinguishable difference between control (non-sulfide) and contaminated aggregates. The results also show significantly higher expansions relative to simple soaking. Beyond achieving more efficient oxidant penetration compared with simple soaking, the higher expansions may also be attributed to the contribution of cement paste content, which governs the extent of sulfate-related expansion through the elevated pH and increased availability of aluminate phases in the cement matrix, promoting sulfate attack and ettringite formation .

Visual examination of the micro-prism samples also showed that higher sulfide contamination corresponds to more extensive pop-outs on the specimen surfaces. This test method is currently undergoing further evaluation.

6. REFERENCES

[1] H. G. Midgley, “The staining of concrete by pyrite,” *Mag. Concr. Res.*, vol. 10, no. 29, pp. 75–78, Aug. 1958, doi: 10.1680/macr.1958.10.29.75.

[2] B. Guirguis, M. H. Shehata, J. Duchesne, B. Fournier, B. Durand, and P. Rivard, “The application of a new oxidation mortar bar test to mixtures containing different cementing systems,” *Constr. Build. Mater.*, vol. 173, pp. 775–785, 2018.

[3] B. Guirguis and M. H. Shehata, “A new screening test to evaluate the presence of oxidizable sulfide minerals in coarse aggregates,” *Constr. Build. Mater.*, vol. 154, pp. 1096–1104, 2017.

[4] M. El-Mosallamy and M. H. Shehata, “Sulfide oxidation mortar tests for evaluation of the oxidation potential of sulfide-bearing aggregate,” *Constr. Build. Mater.*, vol. 264, p. 120627, 2020,

doi: 10.1016/j.conbuildmat.2020.120627.

[5] A. Rodrigues, J. Duchesne, B. Fournier, B. Durand, M. H. Shehata, and P. Rivard, “Evaluation protocol for concrete aggregates containing iron sulfide minerals,” *ACI Mater. J.*, vol. 113, no. 3, pp. 349–359, 2016, doi: 10.14359/51688828.

[6] J. Berard, R. Roux, and M. Durand, “Performance of Concrete Containing a Variety of Black Shale.,” *Can. J. Civ. Eng.*, vol. 2, no. 1, pp. 58–65, 1975, doi: 10.1139/l75-006.

[7] A. Rodrigues, J. Duchesne, B. Fournier, B. Durand, P. Rivard, and M. Shehata, “Mineralogical and chemical assessment of concrete damaged by the oxidation of sulfide-bearing aggregates: Importance of thaumasite formation on reaction mechanisms,” *Cem. Concr. Res.*, vol. 42, no. 10, pp. 1336–1347, Oct. 2012, doi: 10.1016/j.cemconres.2012.06.008.

[8] M. M. Rahman and M. T. Bassuoni, “Thaumasite sulfate attack on concrete: Mechanisms, influential factors and mitigation,” *Constr. Build. Mater.*, vol. 73, pp. 652–662, Dec. 2014, doi: 10.1016/j.conbuildmat.2014.09.034.

[9] D. Jana, “Pyrrhotite epidemic in eastern Connecticut: Diagnosis and prevention,” *ACI Mater. J.*, vol. 117, no. 1, pp. 1–19, Jan. 2020, doi: 10.14359/51718059.

[10] A. Rodrigues, J. Duchesne, and B. Fournier, “Quantitative assessment of the oxidation potential of sulfide-bearing aggregates in concrete using an oxygen consumption test,” *Cem. Concr. Compos.*, vol. 67, pp. 93–100, 2016, doi: 10.1016/j.cemconcomp.2016.01.003.

[11] A. Rodrigues, J. Duchesne, and B. Fournier, “A new accelerated mortar bar test to assess the potential deleterious effect of sulfide-bearing aggregate in concrete,” *Cem. Concr. Res.*, vol. 73, pp. 96–110, 2015, doi: 10.1016/j.cemconres.2015.02.012.

[12] H. R. Shadkam and M. H. Shehata, “Use of oxygen-rich environment to test concrete containing sulfide-bearing aggregate and evaluate the effect of mitigative measures,” *Constr. Build. Mater.*, vol. 477, no. January, p. 141244, 2025, doi: 10.1016/j.conbuildmat.2025.141244.

[13] R. Castillo Araiza, B. Fournier, J. Duchesne, and A. Rodrigues, “Electrochemical activation of oxidation of sulfide-bearing aggregates in concrete specimens,” *Cem. Concr. Res.*, vol. 170, no. September 2022, p. 107186, 2023, doi: 10.1016/j.cemconres.2023.107186.

[14] H. Sommer, P. J. Nixon, and I. Sims, “AAR-5: Rapid preliminary screening test for carbonate aggregates,” *Mater. Struct. Constr.*, vol. 38, no. 282, pp. 787–792, 2005, doi: 10.1617/14382.

[15] L. Divet and J. P. Davy, “Étude Des Risques D’Oxydation De La Pyrite Dans Le Milieu Basique Du Béton,” *Bull. des Lab. des Ponts Chaussees*, vol. 0, no. 204, pp. 97–107, 1996.

[16] M. Moradzadeh, “THE EFFECT OF TESTING CONDITIONS ON THE EXPANSION OF CONCRETE WITH SULFIDE-BEARING AGGREGATES,” Toronto Metropolitan University, 2022.

[17] B. Guirguis, “Test methods for evaluating the oxidization potential of sulfide –bearing aggregates and its effects on concrete durability,” Ryerson University, 2017.

[18] ASTM C1202, “Standard Test Method for Electrical Indication of Concrete’s Ability to Resist Chloride Ion Penetration,” *Am. Soc. Test. Mater.*, no. C, pp. 1–8, 2012, doi: 10.1520/C1202-12.2.

Accelerated concrete core test for pyrrhotite bearing concrete

Smith A [1], Smith K[1], Hyett A [1]

(1) *RSK Environment Limited, Hemel Hempstead, UK, asmith@rsk.co.uk*

Abstract

The presence of iron sulfides within aggregates can cause significant deterioration to concrete block utilised within residential construction. In Ireland the issue has affected thousands of domestic properties. Accordingly, the Irish Government instructed GSI (Geological Survey of Ireland) to establish a research framework, in part to classify the behaviour of the pyrrhotite bearing concrete and the relative performance of different concrete building elements common to Irish domestic construction. To address this requirement, RSK has undertaken innovative adaptions of pre-existing methodologies for assessing accelerated pyrrhotite alteration. The Accelerated Core Test (ACT) methodology consisted of a combination of the sampling/measuring regime of the mundic testing guidance from the Devon/Cornwall area of the UK and the two-stage exposure regime of the accelerated (sulfide) mortar bar test (AMBT) published in Canadian standards.

The objective of this novel approach was to investigate the relative performance of pyrrhotite bearing concrete elements from condemned properties and non-pyrrhotite bearing control properties in accelerated forced conditions, namely Phase 1 highly oxidising environments (80 °C, 75 %RH and twice weekly bleach exposures), and Phase 2 conditions designed to promote the thaumasite form of internal sulfate attack (storage above water at 4 °C and continued twice weekly bleach exposures). The ACT was applied to 43 core samples from 14 separate building elements utilising titanium DEMEC gauge studs and 6 % NaOCl domestic bleach. Due to the previously investigated, pre-existing deterioration in the tested samples, a set of anticipated failure conditions were selected and applied. Additionally, a provision for the continuation of test exposures was devised for Phase 2 of the testing to facilitate further post-test comparison.

The results of the ACT indicated that both sulfide oxidisation and ISA had been generated by the test, and that sample expansion and time to failure (TTF) were both useful metrics. The comparison of these two metrics allowed the classification of multiple sample behaviours, which were found to depend on the *in situ* exposure condition (and resultant degree of preexisting deterioration), the type of concrete element (block or mass) and the presence of significant pyrrhotite within the concrete. The ACT was tentatively found to have induced oxidation/ISA related expansion but provided a better measure of relative durability of the concrete samples to these processes.

Keywords: *Pyrrhotite, Concrete, Laboratory testing, Internal sulfate attack, Oxidisation*

1. INTRODUCTION

Since the late 2000s, significant deterioration of properties built with concrete blocks between the late 1990s to early 2010s has been observed in North West Ireland [1]. The failures were initially attributed to excessive fine, disseminated ‘free’ muscovite mica in certain regions and reactive sulfide-related deterioration caused by oxidation and/or internal sulfate attack (ISA) in other areas [1]. To investigate the issue further, the Irish Government funded a research framework in 2022. As part of this framework, RSK and other researchers have investigated the long-term performance of the affected concrete, pyrrhotite oxidation and its effect on the physical properties of deteriorated concrete blocks [1].

In deteriorated concrete blocks, the aggregates were typically crushed, all-in, mica-rich, low grade metamorphic rocks (such as phyllite) with a minor component of iron sulfides, most commonly pyrrhotite. Pyrrhotite is a non-stoichiometric iron sulfide mineral with the formula $Fe_{(1-x)}S$ (x varying from 0 to 0.125) [2]. Due to its composition and resulting crystal structure, pyrrhotite is considered more unstable in the presence of oxygen and water than the more commonly known iron sulfide mineral, pyrite (FeS_2), and tends to oxidise more readily [2]. When oxidisation occurs, the sulfides release sulfate ions into the

surrounding material, creating the potential conditions for internal sulfate attack, through a series of well-documented chemical reactions with the cement paste [3-5].

RSK was provided with samples from a control property (C1, no deterioration observed on site) comprising a meta-sandstone crushed aggregate with trace iron sulfides (predominantly pyrite with trace pyrrhotite) and three test properties (P1-P3) comprising a phyllite-quartzite crushed aggregate with a minor component of iron sulfides, predominantly pyrrhotite. The samples provided were from four different elements of each of the properties, including the inner leaf (IL), outer leaf (OL), rising wall (RW) where present and foundations (F) to investigate the effect of the environmental conditions of each building element. The in-service exposure conditions of the samples depended on the sample type, with IL and OL samples taken from concrete block (concrete masonry unit) walls installed above the dampproof membrane (DPM), whilst RW and F samples were taken respectively from concrete blocks and denser mass concrete (containing the same aggregate) below the DPM.

2. METHODOLOGY

As part of a larger suite of testing, including petrographic, chemical, expansion and physical testing, an adapted version of the Canadian sulfide AMBT detailed within Annex P of CSA A23.1:2019 [6] was selected to investigate the supplied concrete core samples. The two-stage Canadian sulfide AMBT method was developed in order to assess the potential for residual expansion due to oxidation and the possibility of thaumasite formation in aggregate [3]. To investigate the in-situ cored samples, the established sulfide oxidation testing sample geometry and measurement format of the RICS ‘the mundic problem’ Stage 3 Expansion testing was selected as an appropriate combination.

The adapted accelerated core test (ACT) method, was applied to 75 mm diameter core samples taken from the four sampled properties. Up to four sub-samples were tested from each investigated element, dependent on sample availability. Three pairs (spaced at 50 mm separation) of oxidation-resistant titanium DEMEC gauge studs were fixed at equal intervals of approximately 120° around the core, similar to those specified within RICS guidance note ‘The mundic problem, 3rd edition’ [7].

Following sample preparation, the cores were subjected to the Phase 1 test conditions as specified in CSA A23, 1:19 P3.17. Initially, the cores were immersed in 6 % sodium hypochlorite for 180 ± 15 min before being removed, weighed and measured as a zero reading. They were then left to dry for 180 ± 15 min. After drying, samples were stored at 80 °C in a closed container above a saturated sodium chloride solution in order to maintain a constant relative humidity of approximately 75 %. The beach used was Ki-Chem UK Limited t/a cleaning supplies 2U which had an advertised NaOCl content of 6 %, a determined pH of 12.3 and a NaOH 0.07 wt %.

Following the initial zero reading, the cores underwent two 3 hr±15 min immersion periods each week in 6 % sodium hypochlorite at 20± 2°C. Once weekly, the length, mass and condition of each core were taken and recorded after an immersion period. After 13 weeks of storage at 80 °C and 75 %RH the samples transitioned to Phase 2 storage conditions. Following the first weekly immersion, the samples were transferred to a cold incubator maintained at 4 ± 1 °C, and the solution in the containers was changed to water to maintain approximately 100 % humidity conditions. The twice-weekly immersions in sodium hypochlorite at 20± 2°C and once-a-week measurements were continued during this second stage of the test.

A set of additional rules was established, which included that samples were taken off test if they had disintegrated, lost structural integrity or had lost measuring stud adhesion repeatedly in Phase 1. However, in Phase 2, if this same sample deterioration occurred, requiring that measurements were stopped, the disintegrated or failed samples continued to go through the cycling in a perforated holding container to restrain the samples whilst permitting the possibility of thaumasite formation to occur and allow an equal comparison of the samples through the duration of the Phase 2 (where possible).

Post-ACT petrographic analysis of the samples was undertaken to investigate the condition of the concrete and the deterioration induced by the ACT exposure conditions (compared to baseline analyses).

3. RESULTS

As per the Canadian sulfide AMBT, the sulfide ACT results are presented as mean expansion over time, per test set. Additionally, the results of the sulfide ACT include a time to failure (TTF) metric due to the high number of failures observed during testing (see 3.3.). Additional recorded parameters included failure type, and optical microscopy observed changes in sulfide oxidisation and sulfates (type and extent) post-ACT. Chemical and physical analyses were also conducted but are not presented herein.

3.1 Expansion

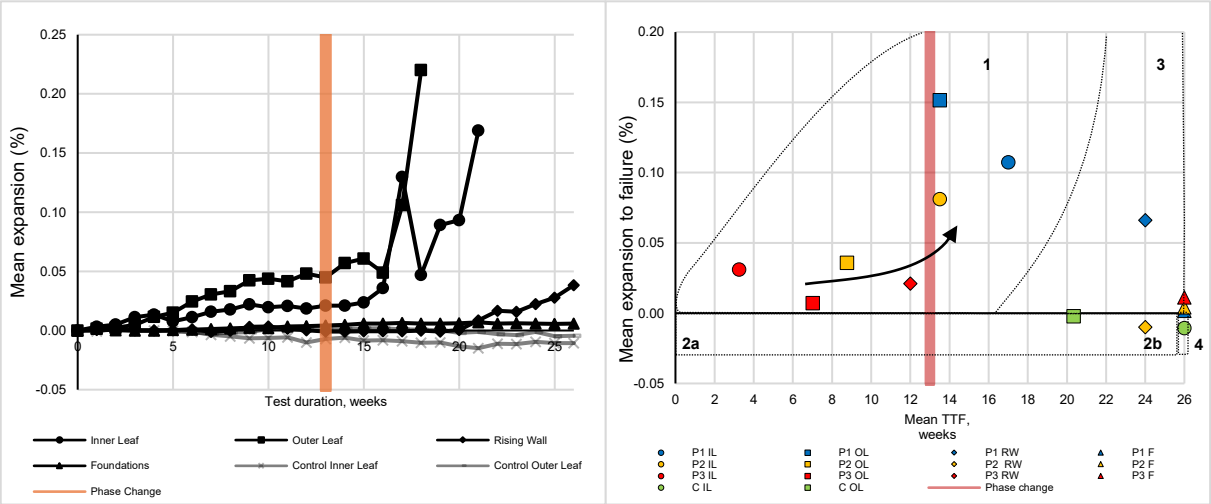

Figure 3.1 (left) Mean expansion of the test properties versus the control property, with the change of storage conditions marked at 13 weeks (red line). Figure 3.2 (right) Mean expansion at failure against time to failure exhibits approximate population areas 1 to 4, interpreted as: 1) expansive failures with greater expansion over time; 2) non-expansive failures related to initial condition or localised sample failures; 3) intact, still-expanding, typically late-stage expansive results; 4) intact samples that did not significantly expand. Note that some plots are obscured behind others. P1, P2, P3 F. A single P1 F 13-week TTF value was taken off test (non-failure for comparative reasons between phases 1 and 2) and is not included in mean TTF calculations. The arrow indicates the generalised progression of core expansion over time seen within population area 1 samples.

3.2 Mass loss

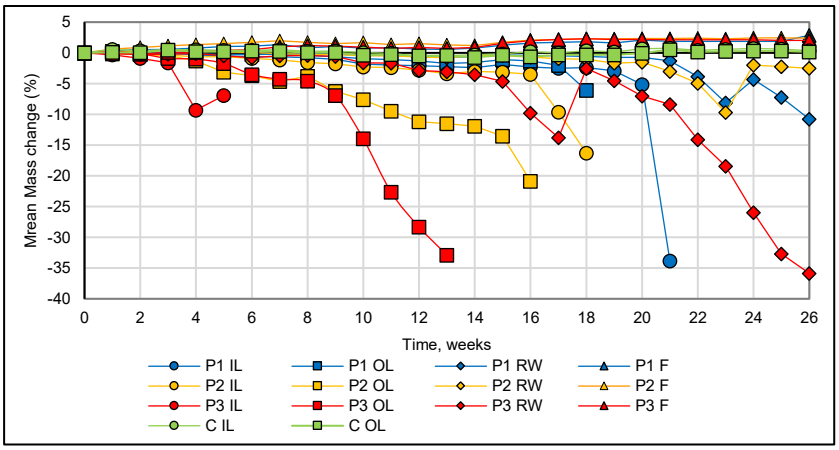

Figure 3.3 Mean mass change of each element from the three test properties and the control property over the duration of the test. Note that the mean values for each element are presented, therefore where a set of readings ends before 26 weeks this represents the failure of the last sub-sample. Where a series

increases in mass sharply, this represents a sub-sample failure that had been losing mass and the mean reverting to the remaining sub-samples.

3.3 Failure type

Figure 3.4 Photographs of the different failure morphologies a) complete failure, b) partial failure (heavily cracked, loss of stud(s)), c) Localised failure under measurement studs.

3.4 Petrographic features

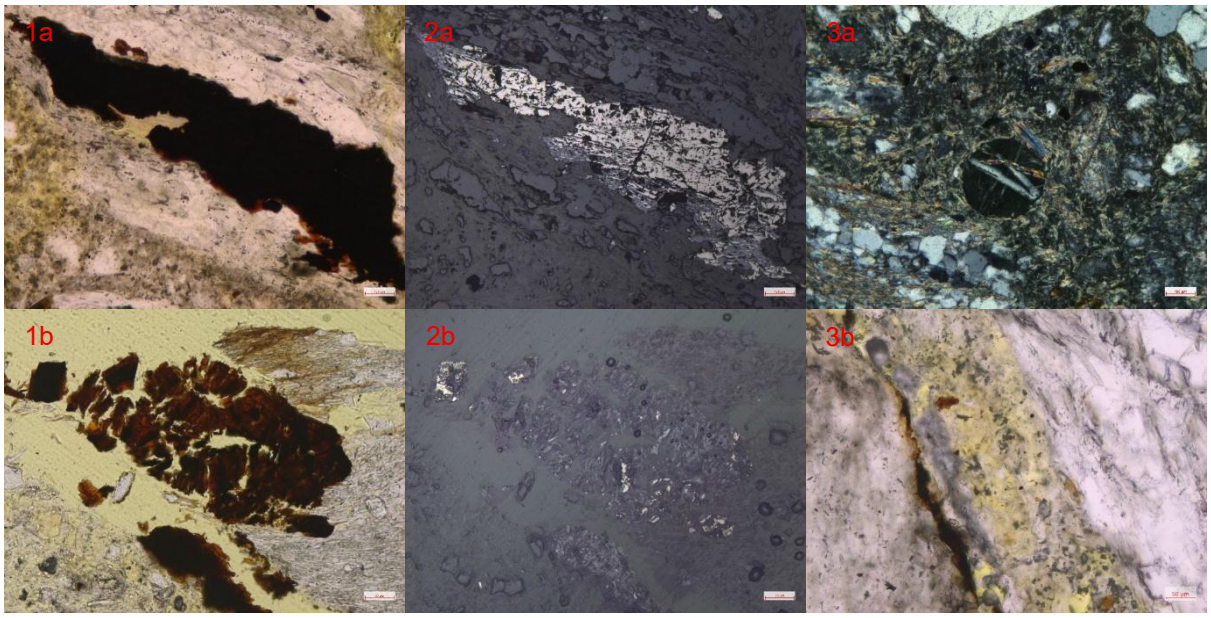

Figure 3.5 Photomicrograph examples of the test properties before (a) and after (b) the ACT showing the oxidation of the pyrrhotite in both plane polarised light (1a and 1b) and reflected light (2a and 2b), and the internal sulfate attack products (3a, gypsum XPL and 3b, ettringite PPL).

4. DISCUSSION

The results were not evaluated against the published CSA A23.1 AMBT criteria [6] because the AMBT was originally designed for mortar bars with a different grading, surface area and porosity. Given the lack of statistical representativity and interlaboratory data for the adapted ACT methodology, no preexisting universal criteria could be applied to the test. Instead, the samples of concrete blocks and mass concrete were directly compared with other samples from the test properties and the control property (where possible) for relative performance for similar sample geometry and aggregate content. However, speculative, specific performance based criteria could be derived from the metrics recorded during the test, the most useful of which currently appear to be mean expansion at failure and mean time to failure.

The general trend observed in the pyrrhotite-bearing concrete block test samples showed expansion initiated either in Phase 1 or Phase 2 of the ACT, followed by continued expansion, particularly in Phase 2, in general agreement with the expected behaviour of pyrrhotite-bearing aggregates in the AMBT [6]. It was notable that a relatively high proportion of samples failed to complete the test duration (Figure 3.1 and 3.2). When further evaluating the ACT results, test properties IL and OL sub-samples exhibited the poorest relative performance, typified by a consistent rate of expansion and mass loss during Phase 1, which correlated with the observation of further oxidation of sulfide minerals in optical microscopy. In some cases, localised sub-sample failures or rapid fragmentation failures of previously severely deteriorated (as-received) sub-samples occurred within Phase 1 (Figure 3.4). During Phase 2 of the test, rapid expansion (Figure 3.1) and mass loss (Figure 3.3) led to rapid fragmentation failure within the test property IL and OL sub-samples, indicative of possible expansive ISA.

The test property RW samples exhibited relatively steady late Phase 2 expansion after a period of innocuous behaviour (Figure 3.1). The presence of late-stage expansion suggested some degree of potential for future deterioration, but can also be tentatively correlated with the relatively better as-received condition of the RW samples compared to the test property IL and OL concrete block samples. This behaviour may imply that the as-received condition or state of deterioration may contribute to the initiation of ISA, possibly due to the different chemical conditions of the different building elements.

The control property IL and OL and all properties F samples were characterised by relatively innocuous mean expansion throughout (Figure 3.1). In the case of the F samples, this was thought to be the result of lower water:cement ratio and lower air content found in mass concrete compared to concrete block samples.

Petrographic analysis of the samples following the testing period determined that all failed concrete block samples, including the IL and OL of the test properties and sporadic RW samples, exhibited major increases in reactive sulfide oxidisation (see Figure 3.5, 1a/b and 2a/b), severely degraded cement matrix and secondary sulfates (primarily ettringite and rarely thaumasite) replacing the cement matrix (see Figure 2.5, 3b) with thaumasite, replacing cement matrix noted particularly in the OL samples. Comparatively, the control and foundation samples exhibited relatively less alteration, such as minor oxidation of sulfides, after the full 26 weeks of testing. No evidence of alkali-aggregate reactions were observed in any samples examined.

Given that induced ISA during the ACT is observed as the likely primary cause of sample failure, the behaviour and timing of the failure are relevant metrics to analyse. Notably, during the ACT the mean expansion shows that when a critical point of deterioration is reached within the test property pyrrhotite-bearing concrete block samples, severe, rapid deterioration occurs until the point of complete sample failure (Figure 3.1). In cases of severe test-generated deterioration (Figure 3.4, a and b), a comparison of time to both mean and last failure can be made. In this case, the time to failure metric likely indicates a combination of deterioration to date and the potential for further deterioration to be caused by sulfide oxidation, and subsequent ISA-related deterioration before loss of integrity. Therefore, mean TTF (see Figure 3.2) illustrates the relative resistance or susceptibility of the concrete to sulfide oxidation and any associated ISA-related failure in the forced severe conditions. The test properties' ILs and OLs exhibited the shortest overall TTF, followed by the RW samples. The F of all properties, and the IL and OL of the control property, all resisted failure (no TTF) other than localised sub-sample failures (Figure 3.4, c) for reasons previously stated.

Overall, the ACT generated an effective relative, qualitative test to destruction, indicative of both sulfide oxidation and generation of some further degree of ISA within the concrete block samples.

When considering the limitations of this study and the resulting mean values, a tentative, limited, specific performance-based criterion could be speculated. It appeared that if mean expansion to failure exceeded 0.005 % in Phase 1 of the adapted test method, deterioration, possibly coupled with significant expansion, would eventually be triggered within the concrete block samples. However, this tentative limited criterion rose to approximately 0.012 % expansion in Phase 2 of the adapted test method. When compared to the 0.10 % expansion criteria between AMBT Phase 1 and AMBT Phase 2 from CSA A23.1[6], the limits are comparably low or incomparable and perhaps indicative of the effect of both the material type and the pre-existing condition of the concrete block samples.

To better understand the viability and applicability of the test methodology for analysis or as part of a testing protocol, further work should be conducted utilising an increased number of samples to investigate the effects of wider aggregate lithology coverage and further sample type variation on test performance.

5. CONCLUSIONS

- A high proportion of the tested sample population failed to complete the full 26 weeks of the CSA P3 adapted oxidation test.
- To account for the physical sample failure (often complete fragmentation) due to induced deterioration, time-to-failure (TTF) and expansion at failure metrics were used to compare the relative performance of the ACT samples.
- The test property IL and OL samples exhibited the shortest TTFs and the greatest expansions at failure.
- Rapid expansive failure tended to follow a period of relatively steady expansion, hypothesised to be related to sulfide oxidisation and then the development of ISA.
- Control property IL and OL and all foundation samples exhibited non-expansive intact behaviour, indicative of the ability of the phyllite-bearing mass concrete and meta-sandstone bearing concrete blocks to resist deteriorative sulfide oxidisation and ISA in forced aggressive oxidisation environments designed to generate these processes.
- Test property ILs, OLs and sporadic RWs exhibited significant evidence of further sulfide oxidisation and associated ISA in post ACT analyses.
- The test was tentatively found to have induced oxidation/ISA related expansion but provided a better measure of the relative durability of the concrete samples to these processes, chiefly thought to be reflective of type, previous condition and exposure of the samples.

6. REFERENCES

[1] Dunlop P (2025) Research insights into the cause of Ireland's defective concrete crisis (abstract) https://pure.ulster.ac.uk/en/activities/research-insights-into-the-cause-of-irelands-defective-concrete-c/ Accessed 15 December 2025

[2] Duchesne J, Rodrigues A, Fournier B (2021) Concrete damage due to oxidation of sulfide-bearing aggregate: a review of recent advances and limitations. RILEM Technical Letters. 6: 82-92. https://doi.org/10.21809/rilemtechlett.2021.138

[3] Rodrigues A, Duchesne J, Fournier B, Durand B, Rivard P, Shehata M (2012) Mineralogical and chemical assessment of concrete damaged by the oxidation of sulfide-bearing aggregates: Importance of thaumasite formation on reaction mechanisms, Cem. Concr. Res, Vol 42, 10:1336-1347, ISSN 0008-8846,

[4] Zhong R, Wille K (2018) Deterioration of residential concrete foundations: the role of pyrrhotite-bearing aggregate, Cem. Concr. Compos. 94:53–61.

[5] D. Jana, (2023) Concrete Deterioration from the Oxidation of Pyrrhotite: A State-of-the-Art Review. In Maher, M.L.J, Pyrite and Pyrrhotite, ISBN 979-8-88697-329-7, Nova Science Publishers, Inc. pp139-221

[6] CSA A23.1:19/CSA A23.2:19 (2019) Concrete materials and methods of concrete construction/Test methods and standard practices for concrete, P3, pp 370-381, CSA, Canada, ISBN 978-1-4883-0744-7

[7] RICS Professional Guidance, UK (2015) The mundic problem. 3rd edition. Stage 3 testing.

Ozone as an oxidant for accelerated testing of pyrrhotite-induced concrete degradation

Michael Mengason [(1)], Patrick Dixon [(2)], Ashley Carey [(3)], Osamah Dehwah [(4,5)], Stephanie Watson [(6)]

(1) National Institute of Standards and Technology, Gaithersburg, MD, USA, Michael.Mengason@NIST.gov

(2) National Institute of Standards and Technology, Gaithersburg, MD, USA, Patrick.Dixon@NIST.gov

(3) National Institute of Standards and Technology, Gaithersburg, MD, USA, Ashley.Carey@NIST.gov

(4) PREP Associate, National Institute of Standards and Technology, Gaithersburg, USA, osamah.dehwah@NIST.gov

(5) Department of Civil and Systems Engineering, Johns Hopkins University, Maryland, USA, odehwah1@jh.edu

(6) National Institute of Standards and Technology, Gaithersburg, MD, USA, Stephanie.Watson@NIST.gov

Abstract

The iron-sulfide mineral pyrrhotite used in some home foundation construction is known to oxidize and form minerals deleterious to the concrete. Deterioration from this process can require decades to become apparent. The long timescale requires a method of accelerated aging to study the process and evaluate aggregate for use in concrete. We propose the use of ozone as an oxidant and present results of proof-of-concept experiments. Exposure of a thin mortar 'tile' to 500 ppb (ng/kg) ozone in air with 40 % humidity for 14 days tarnished some grains but did not otherwise show evidence of reaction. Exposure of a tile in a UV/Ozone cleaner with 70 % humidity and ozone concentration ranging from 40 to 50 ppm resulted in the growth of sulfate mineral encrustations on the surface and needle-like gypsum growth within the voids. Conceptually, the use of ozone avoids some complications associated with bleach submersion. Further study is needed to develop this potential method.

***Keywords**: pyrrhotite, oxidation, ozone, mortar-bar test, concrete degradation*

1. INTRODUCTION

Pyrrhotite-bearing aggregate used in concrete has led to the degradation of residential foundations in an area of the Northeastern United States [1, 2]. The crushed-rock aggregate, identified from a quarry in CT, contains pyrrhotite. The iron in pyrrhotite oxidizes (and hydrates) in the presence of water and oxygen, additionally releasing hydrogen and sulfate ions. Volumetrically larger iron-containing phases (e.g., ferrihydrite, goethite) and sulfate-containing phases (e.g., monosulfate, ettringite, thaumasite) form by deposition or reaction with the cement paste. The resulting expansion leads to fractures damaging the foundation. This degradation process spans years, presenting a challenge for laboratory study of the mechanisms involved and for the use of cast mortar bars to test for potential reactivity [3]. Methods suggested for accelerating this process include elevated temperature, humidity, oxygen content, the addition of sodium hypochlorite (bleach), and/or the use of an electrochemical cell [4]. We propose using ozone to accelerate pyrrhotite oxidation as an alternative method for exploration, and present findings from proof-of-concept experiments. The accelerated mortar bar method of Rodrigues et al. involves twice-daily submersions in NaOCl solutions [3]. One challenge with the use of bleach is the growth of Friedel salts in the cement paste. Additionally, the potential inclusion of sodium at elevated levels in the cement paste can alter the behavior in the test [5]. A counterchallenge is the loss of elements to the bleach solution, including the sulfates in question. Exposing concrete to ozone in air would not involve these complications and would reflect the fact that damage seen in CT house foundations is often above grade, where the concrete would not be water saturated [6]. Ozone (O_3) has a higher oxidation potential (2.07 V) compared with hydrogen peroxide (H_2O_2) (1.77 V) or sodium hypochlorite (NaOCl, bleach) (1.4 V). As such, ozone can be a more effective oxidizing agent. Additionally, hydroxyl radicals (2.8 V) can be generated when ozone and water are present under ultraviolet radiation. Ozone has been shown to have an accelerating effect on the oxidative leaching of

metals from sulfide ores [7, 8] and is likely applicable to the present problem. The mortar bar expansion test utilizes a geometry with a relatively low surface-to-volume ratio. To maximize the exposure of pyrrhotite to ozone, the samples used here were cast as tiles and ground flat. Rather than expansion as an indicator of reactivity, we examine the surface for evidence of mineral modification and growth. In future work, X-ray diffraction (XRD) and X-ray fluorescence (XRF) will be utilized to monitor the growth of minerals as an indicator of oxidation and reactions within the cement paste.

2. EXPERIMENTAL PROGRAM

Mortar samples, both with and without pyrrhotite, were prepared according to ASTM C305. A nominally sulfide-free diabase aggregate, pyrrhotite (Wards Scientific – Galax, Virginia, USA, passing a 4.75 mm (#4), retained on 1.18 mm (#16) sieve), and Type I/II OPC were used. The mortar solids consisted of diabase sand (ASTM C33) in a 2.25 sand-to-cement ratio with 10 % pyrrhotite replacing diabase in pyrrhotite-bearing samples. The water-to-cement ratio was 0.5. Samples were molded in a 152 mm (6”) x 152 mm (6”) cube mold filled only to an approximate 6 mm depth. Samples were cured initially in a high-humidity chamber for 24 hours, and then for 14 days in a saturated lime-water bath. Samples were trimmed to ~ 100 mm x 100 mm flat “tiles” with one surface polished to 1200 grit to aid inspection (Figure 2.1). Following curing, samples were stored in an evacuated chamber at a pressure of 8.5 x 10^{-2} MPa until use.

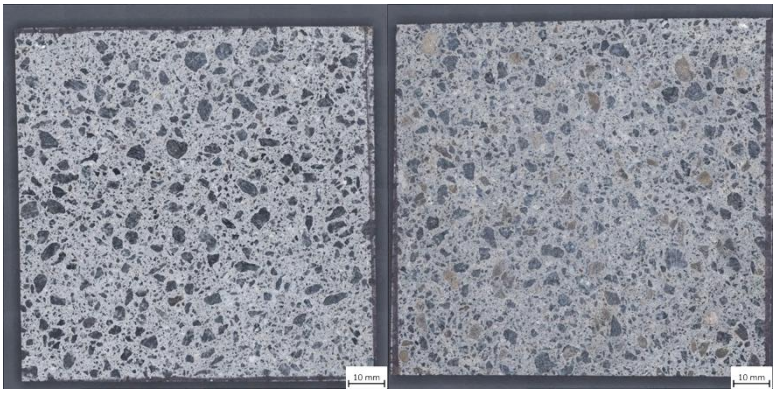

Figure 2.1: Pre-experiment mortar tiles. Left, control sample of diabase and OPC I/II cement. Right, 10 % of diabase sand replaced with natural pyrrhotite.

2.1 Controlled 500 ppb Ozone in Air

An initial experiment exposed one pyrrhotite and one control tile to ozone under a controlled atmosphere of 500 ppb (ng/kg) ozone in air (40 % humidity) for 14 days (Figure 2.1). During this time, one additional pyrrhotite-bearing tile was exposed to room conditions on a lab bench in case any effects of room air needed to be investigated.

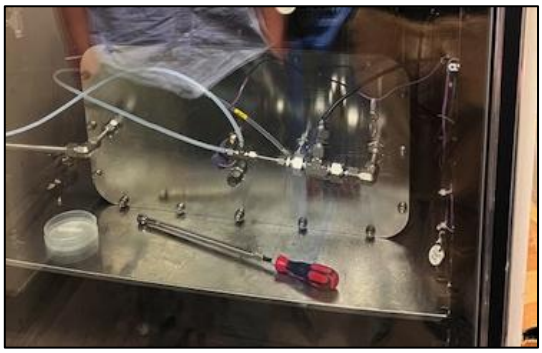

Figure 2.1: Left, 500 ppb set-up. Right, UV/ozone cleaner set-up.

2.2 UV/Ozone Exposure

To investigate a more aggressive regimen, a pyrrhotite-bearing tile was placed in a UV/Ozone cleaner (Jelight Model No. 342) suspended over water with 90-minute exposure cycles twice daily for four days, followed by three days without exposure for four weeks (Figure 2.1). The size of this device prevented the use of a pyrrhotite-free control sample. Relative humidity in the chamber was measured at 70 %. The water bath was monitored daily. In this type of device, atmospheric O_2 is exposed to UV radiation from a low-pressure mercury vapor grid lamp and converted to O_3, while H_2O in the presence of both UV and O_3 can be converted to OH^-. This type of device does not target a predetermined ozone concentration. Testing by the manufacturer gives a suggested range for our setup of 40–50 ppm ozone.

3. RESULTS

Following the completion of the two experiments, the samples were imaged, and sample the sample from the UV/Ozone experiment was studied using µXRF. A 25 mm x 25 mm square was cut from each tile for analysis by scanning electron microscopy (SEM)/energy dispersive spectrometry (EDS). The remaining material from each sample was ground and homogenized for future XRD analysis.

3.1 Visual Observations

3.1.1 500 ppb Ozone Exposure

The pyrrhotite sample exposed to 500 ppb ozone showed visual signs of oxidation, characterized by a change in the surface color (bronzing) and sheen of the pyrrhotite. There were no ‘rust stains’ or other signs of oxidation at this concentration, for this duration. No change was noted in the control sample.

3.1.2 UV/Ozone Exposure

The pyrrhotite-bearing sample exposed in the UV/Ozone cleaner showed surface evidence of reaction, including “rust” stains around pyrrhotite grains, the appearance of fine white needle-like crystals in an air void exposed at the surface, and white crust spots on the surface. Analysis of needles at three weeks by micro-Raman (Bruker Senterra II) best match spectra collected from gypsum. SEM/EDS confirmed the presence of sulfur and calcium without other cations. (Figure 3.1).

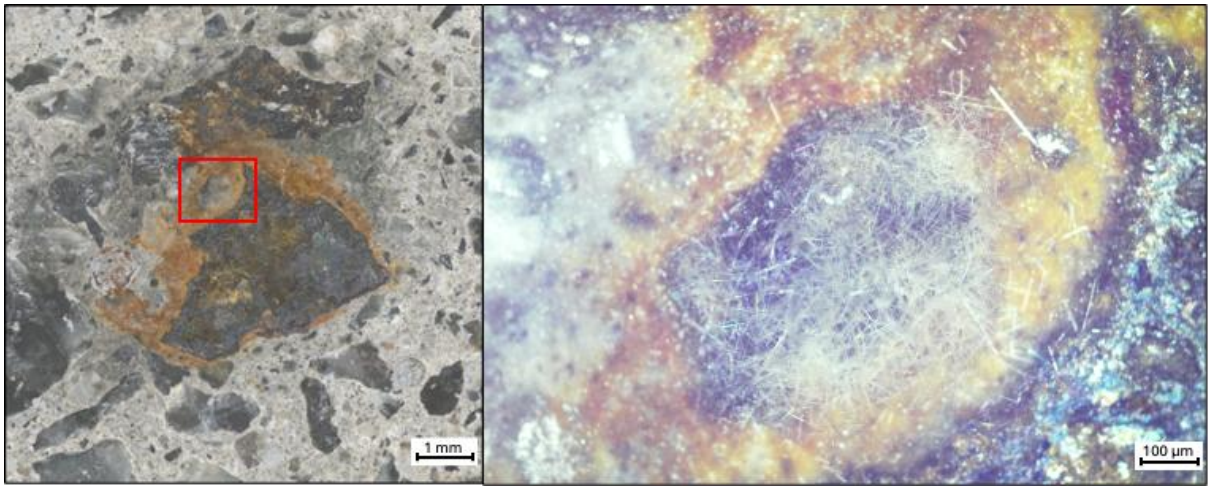

Figure 3.1: Sample P-2 (UV/ozone exposure) after three weeks. Left, staining and white mineral growth. Right, thin white needles can be seen growing into the cavity from the edges.

3.2 Analysis by µXRF

The surface of the UV/Ozone exposure sample was examined by µXRF (Bruker M4 Tornado^{plus}). µXRF is a non-invasive technique that does not require sample preparation, allowing the sample to be fully analyzed later by other methods. Mapping sulfur distribution as shown in Figure 3.2 indicated a spread of sulfur from sulfide grains across and potentially into the cement paste.

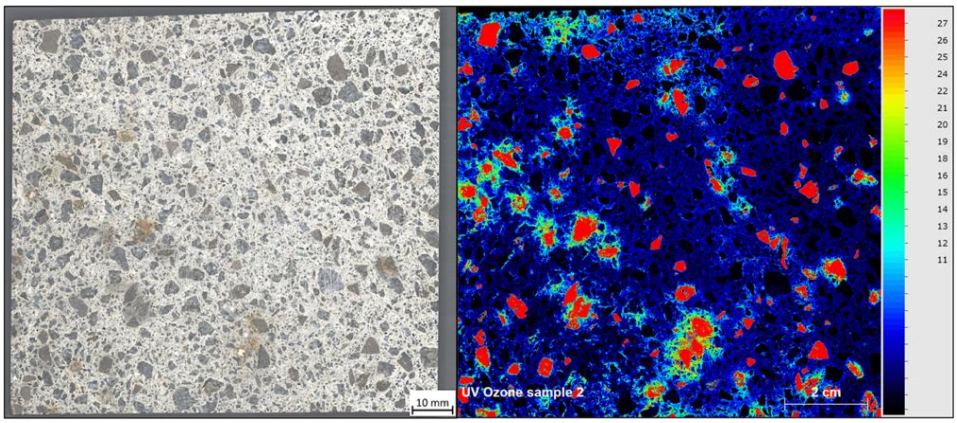

Figure 3.2: µXRF 'Heat map' of sulfur abundance (EDS) in the UV/Ozone exposure sample showing sulfides (red), non-pyrrhotite aggregate (black), cement paste (blue), and areas of elevated sulfur within or upon the surface of the sample (light-blue, green, orange).

3.3 Analysis by SEM/Energy Dispersive Spectroscopy (EDS)

Retained sections of samples P-2 (UV/Ozone) and P-3 (500 ppb) were mounted on aluminum stubs and carbon-coated for analysis by SEM/EDS on a Tescan Mira4 field emission SEM with two Bruker XFlash 70 mm EDS detectors with 12 kV accelerating voltage and 5 nA beam current. Sample P-3 from the 500 ppb exposure experiments was examined and did not show significant mineral growth. Sample P-2, from the UV/Ozone exposure, showed the growth of mineral crusts over aggregate grains. The growths, as seen in Figure 3.3 (left, center), varied in chemistry across the grain, changing broadly in bands from the center, where potassium-calcium sulfates were found, through calcium sulfates amid patches of bare iron sulfide, and out onto the surface of the cement paste. This indicates a reaction between the sulfate ions and the cations in the cement or aggregate minerals. In other areas of P-2, needle-like growths are identified on the surface. They generally contain sulfur and calcium without other cations and are likely gypsum. The needles are surrounded by patches of thin growth on the surface (Figure 3.3, right).

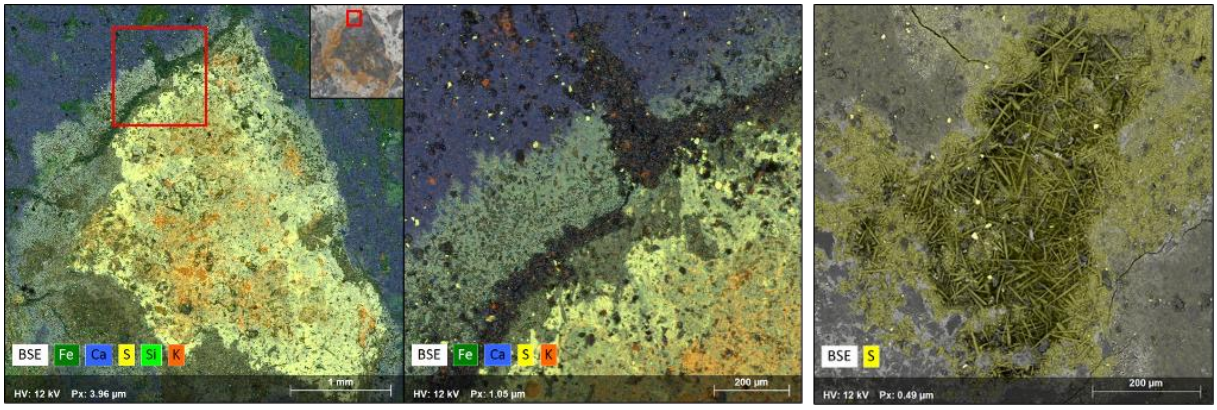

Figure 3.3: Sample surface after UV/ozone exposure. Left/Center, crust formed on an aggregate grain surface and cement paste. Inset, optical image. Others, SEM Backscatter Electron (BSE) image with EDS sulfur map overlay. Right, needle-like growth of minerals in a cavity at another spot.

4. DISCUSSION

The two methods of this study showed different levels of oxidation, as would be expected at different concentrations of ozone. The mineral crust formed is an indicator of early oxidation and reaction. Further testing by XRD and bulk XRF will help determine the extent of mineral alteration, and analysis of cross sections by EDS/SEM will help evaluate the depth of any alteration. In general, the ozone method addresses some criticisms of other acceleration methods by avoiding the addition of elements to the concrete as well as the loss of elements from it, due to the submersion bath. Furthermore, it more

accurately recreates the conditions of aqueous chemistry that occur within the concrete pore structure of foundation walls. Oxidation in this test did not proceed to the point of fracturing, and not all sulfide grains showed new mineralization indicative of oxidation and reaction. These tests show the basic feasibility of using ozone in this manner. Significant work would be required to develop this into a functional test for aggregate reactivity in concrete.

4.1 Future Work

- Reactions are limited by the diffusion of ozone through the mortar, potentially preventing the core of the sample from experiencing the full oxidizing effect. Further minimizing the thickness of sample would minimize this effect.
- Another approach to aid in ozone penetration of the sample would be to force humidified ozone/air through a sample under pressure. A flow-through system would significantly increase the cross-section of the sample exposed and continually renew the ozone that has been consumed.
- In this study, natural pyrrhotite was used, which complicates the interpretation of the results. In future studies, lab-produced pyrrhotite should be used to replace a portion of the aggregate, or a model aggregate containing pyrrhotite may be used [9].

We would like to acknowledge and thank Jana Butman of NIST for her assistance in conducting the 500 ppb experiment and discussions about ozone exposure of materials.

5. DISCLAIMER

Certain equipment, instruments, software, or materials, commercial or non-commercial, are identified in this paper in order to specify the experimental procedure adequately. Such identification does not imply recommendation or endorsement of any product or service by NIST, nor does it imply that the materials or equipment identified are necessarily the best available for the purpose.

6. REFERENCES

[1] Jana D (2022) Cracking of residential concrete foundations in eastern Connecticut, USA from oxidation of pyrrhotite. Case Studies in Construction Materials 16. https://doi.org/10.1016/j.cscm.2022.e00909

[2] Zhong R, Wille K (2018) Deterioration of residential concrete foundations: The role of pyrrhotite-bearing aggregate. Cem Concr Compos 94. https://doi.org/10.1016/j.cemconcomp.2018.08.012

[3] Rodrigues A, Duchesne J, Fournier B, et al (2016) Evaluation protocol for concrete aggregates containing iron sulfide minerals. ACI Mater J 113. https://doi.org/10.14359/51688828

[4] Ojo M, Kim D, Frame L, Wille K (2024) Electrochemical investigation of accelerated deterioration of concrete with iron-sulfide containing aggregates. Cem Concr Res 182:107570. https://doi.org/10.1016/j.cemconres.2024.107570

[5] De Weerdt K, Bagheri M, Lindgård J, et al (2025) Changes in cement paste during accelerated mortar bar testing for pyrrhotite containing aggregate. Cem Concr Res 188. https://doi.org/10.1016/j.cemconres.2024.107730

[6] Dixon P, Ardebili AH, Goodwin D, et al (2025) Field Observations of a Pyrrhotite-Affected Residential Foundation and the Mechanical Properties of Extracted Concrete Cores - Connecticut site 1. NIST IR 8598. Gaithersburg, MD https://doi.org/https://doi.org/10.6028/NIST.IR.8599

[7] Pedroza FRC, Aguilar MDJS, Treviño TP, et al (2012) Treatment of sulfide minerals by oxidative leaching with ozone. Mineral Processing and Extractive Metallurgy Review 33. https://doi.org/10.1080/08827508.2011.584093

[8] Wang J, Faraji F, Ghahreman A (2021) Evaluation of ozone as an efficient and sustainable reagent for chalcopyrite leaching: Process optimization and oxidative mechanism. Journal of Industrial and Engineering Chemistry 104:. https://doi.org/10.1016/j.jiec.2021.08.036

[9] Mengason M, Watson S (2025) Pyrrhotite Reference Material Synthesis, Technical Note (NIST TN). Gaithersburg, MD. https://doi.org/10.6028/NIST.TN.2336

Deleterious internal sulfate attack on concrete caused by an aggregate with low iron sulfide content

Andreas Leemann [1,2], Beat Münch [1], Paul Dunlop [2]

(1) *Empa, Laboratory for Concrete & Asphalt, Dübendorf, Switzerland, andreas.leemann@empa.ch*

(2) School of Geography and Environmental Sciences, Ulster University, Coleraine, Northern Ireland, UK, p.dunlop@ulster.ac.uk

Abstract

A considerably damaged Irish home in County Donegal built with concrete blocks of low total sulfur content was investigated to identify the cause of deterioration. Despite the low total sulfur content the concentration of SO_3 present in cement hydrates is in the same range as the one of homes heavily affected by internal sulfate attack. Moreover, the analysis of the cement hydrates indicate secondary ettringite formation. Residual pyrrhotite and pyrite are identified in the shells of the sea dredged sand used as aggregates in the blocks in combination with micaceous meta-quartzite and greywacke. The results indicate that ISA can be caused by an aggregate with a relatively low iron sulfide content, if oxidation has progressed close to completion.

***Keywords**: concrete blocks, cracking, ettringite formation, internal sulfate attack, microstructure*

13. INTRODUCTION

Concrete blocks are a commonly used material for building homes in Ireland. A few years after a construction boom that occurred between 2000 and 2008 (known as the 'Celtic Tiger') homes started to show signs of deterioration in the form of cracking and crumbling concrete. Thousands of homes are affected across the Irish state, with the highest concentration situated in the Northwest in County Donegal. There, the damage was originally attributed to the excessive muscovite mica content in the concrete blocks which was thought made them vulnerable to freeze-thaw damage [1]. Only recently it was confirmed that the underlying cause is the oxidation of sulfides (predominantly pyrrhotite) present in the concrete aggregates leading to internal sulfate attack (ISA) [2]. The formation of the secondary sulfate minerals ettringite and thaumasite leads to expansion, crack formation and decrease of concrete strength [2,3]. A pyrrhotite-bearing phyllite (PHY) is responsible for the majority of cases. However, there are other types of aggregates used in the concrete blocks that can lead to the deterioration of homes. An overview thereof is given in [4]. In this database concrete blocks produced with a particular aggregate, weathered micaceous quartzite (WMQ), were present in damaged homes some of them showing similar crack patterns to homes affected by ISA in spite of having a low total sulfur content.

In the present case study, a severely affected home produced with concrete blocks containing the WMQ aggregate was investigated to identify the cause of damage. Cores were taken from the inner leaf (IL), the outer leaf (OL) and the rising blocks (RB) below the damp proof course (DPC) underground. The microstructure of the concrete was investigated with optical and scanning electron microscopy with energy-dispersive X-ray spectroscopy. Additionally, X-ray diffraction and sulfur analysis were performed. The results were compared to homes damaged by ISA containing the PHY aggregate and one undamaged reference home containing a non-problematic aggregate termed river gravel (RGV).

14. MATERIALS AND METHODS

15. Materials

During January of 2024 three cores were taken below the DPC, six cores from the OL and two cores from the IL. The cores were first cut along their long axis and sprayed with the pH indicator phenolphthalein to make visible the degree of carbonation. Only the sample from the inner leaf was fully

carbonated. One sample from the OL showed mainly carbonated cement paste and the others mainly uncarbonated cement paste. The samples taken from the RB below the DPC showed no carbonation. About 500 g per sample was crushed and subsamples were ground to < 125 µm for XRD and sulfur analysis. The samples for the microstructural analysis were cut and dried in the oven at 50 °C for three days. Afterwards they were impregnated with an epoxy resin containing a fluorescent dye. After grinding and lapping thin sections with a size of ~ 48×90 mm were produced for the investigation with the optical microscope. The samples for the SEM (discs with a diameter of ~ 47 mm) were coated with a 10 nm thick carbon layer after polishing.

16. Methods

X-ray diffraction (XRD) was measured using a PANalytical X'Pert Pro MPD diffractometer in a Θ-Θ configuration with CoKα radiation, a fixed divergence slit size of 0.5°, a rotating sample stage and the X'Celerator detector. The analysis of sulfur present as sulfide and SO_3 was conducted according to EN 196-2:2013 [5] and the water soluble sulfur according to EN 1744-1 [6]. A Zeiss Axioplan polarization microscope was used for the analysis of the thin sections. The polished sections were analyzed with a SEM FEI Quanta 650 using a pressure of ~3.5 ×10^{-6} Torr. Elemental analysis was conducted by EDS with a Thermo Noran Ultra Dry 60mm^2 detector and Pathfinder X-Ray Microanalysis Software. An acceleration voltage of 12 kV and a spot size of 4.5 were used for imaging and EDS point analysis and 20 kV and 5 for the elemental maps, respectively. Concentrations are given in atom-%. The phase clustering was performed according to [7].

17. RESULTS

18. XRD

XRD data from the inner and outer leaf show muscovite, chlorite, quartz and calcite as the main components. Ettringite and portlandite are identified in the outer leaf and gypsum in the inner leaf as the only hydrates present. Because C-S-H is cryptocrystalline, it is not detected by XRD.

19. Sulfur analysis

The concrete produced with WMQ aggregates shows a low total sulfur content (Table 3.1, Figure 3.1). The concrete containing PHY aggregates displays the highest total sulfur contents and the concrete containing RGV aggregates from the undamaged reference home [3] the lowest. However, the blocks produced with WMQ and PHY aggregates do not differ in regard to the mean sulfur content present as SO_3 (present in the hydrates) and water soluble sulfur (present as gypsum).

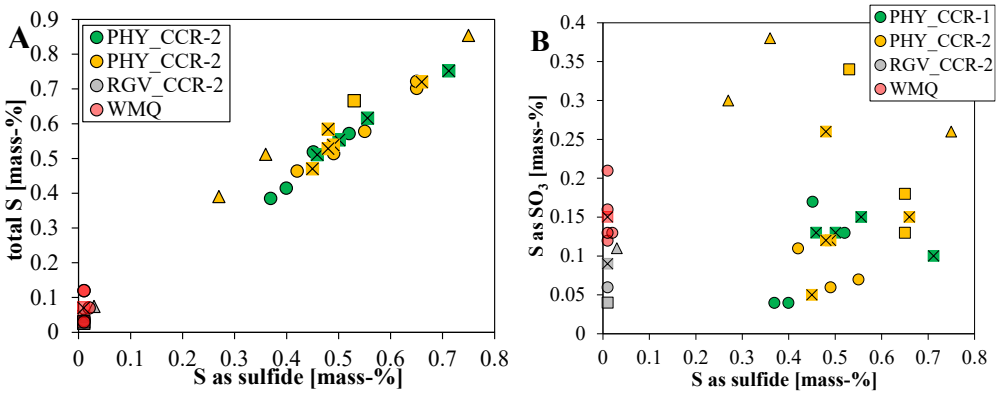

Figure 3.1: Total sulfur (S) as a function of sulfur (S) as sulfide (A) and sulfur (S) as SO_3 as a function of sulfur (S) as sulfide (B). CCR-1: data from [2], CCR-2: data from [3]. Symbols in (B): triangle = foundation concrete, square = RB, circle = OL, cross = IL.

Table 3.1: Sulfur content of concrete samples with different aggregates. Data for PHY and RGV: from [2,3].

Aggregate	WMQ (N=6)	PHY (N=22)	RGV (N=4)
Sulfur as sulfide [mass-%]	0.012 ± 0.004	0.509 ± 0.119	0.015 ± 0.010
Sulfur as SO_3 [mass-%]	0.150 ± 0.033	0.155 ± 0.096	0.075 ± 0.031
Water soluble SO_3 [mass-%]	0.073 ± 0.040	0.076 ± 0.041	0.070 ± 0.050
Total sulfur as S[1] [mass-%]	0.072 ± 0.013	0.571 ± 0.123	0.045 ± 0.021

[1] *sum of sulfur as sulfide and sulfur as SO_3*

20. Optical microscopy

The analysis of the thin sections confirmed the assessment in regard to the degree of carbonation already indicated by the phenolphthalein test (see 2.1). The rounded micaceous meta-quartzite and greywacke particles often show the presence of iron oxides/hydroxides. Some opaque minerals indicate the presence of likely oxide or sulfide phases. The content of free sheet-silicate platelets in the cement paste is relatively high. The sand mainly consists of partly rounded quartzite with a high amount of calcareous shell particles. Numerous shell particles are stained by iron oxides/hydroxides and occasionally show small opaque particles (Figure 3.2). Some air voids contain ettringite. More details on the aggregates are given in paragraph 3.4.1. The cement paste is highly porous indicating a high water-to-cement ratio.

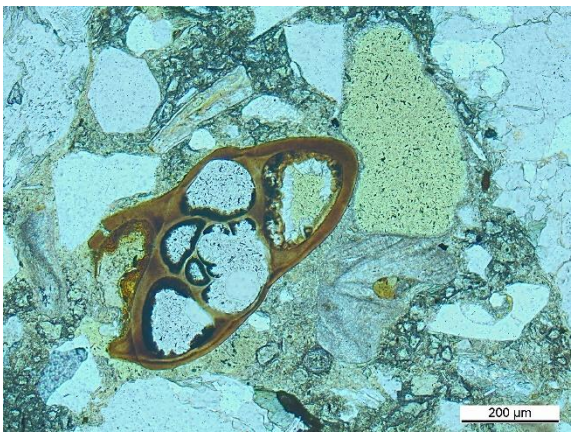

Figure 3.2: Stained shell particle with linings of opaque particles in its interior from an RB sample using polarized light.

21. SEM/EDX

22. Aggregates

The meta-quartzite contains different oxides: rutile, ilmenite and hematite. The only mineral containing sulfur in the meta-quartzite and greywacke is a phosphate. Its composition is given in Table 3.2. The sheet silicate ("mica") content in the cement paste as determined at five different locations on five different samples is 11.5 ± 4.2 volume-% (muscovite: 8.9 volume-%, chlorite: 2.6 volume-%).

Table 3.2: Composition of the sulfur-bearing phosphate additionally containing traces (not shown) of Mo, Ba, La, Ce, Pr, Nd and Tl. ~ 70 points analyzed.

Element	O	Na	Mg	Al	Si	P	S	Cl	K	Ca	Ti	Fe
[atom-%]	79.2 ±3.9	0.0 ±0.1	0.1 ±0.1	0.4 ±0.5	0.8 ±0.7	12.7 ±1.6	1.6 ±1.0	0.3 ±0.3	0.2 ±0.1	3.4 ±0.9	0.2 ±0.8	1.2 ±2.3

Iron hydroxides/oxides, pyrite and pyrrhotite can be observed in the shells (Figure 3.3 A,B). The particle size of both iron sulfides is typically < 1 µm. They only reach a larger particle size in clusters of framboidal pyrite (Fig. 3.3B). The majority of shells are stained by iron hydroxides/oxides without containing iron sulfides.

23. Cement paste

The cement hydrates in the uncarbonated zones of all samples show C-S-H, monocarbonate and portlandite as the main cement hydrates present (Figure 3.4). The amount of monocarbonate is unusually high. In addition, there is a clear shift from C-S-H towards ettringite. The Si/Ca-ratio of the C-S-H is significantly higher than usual. Chloride is present in all samples, mainly in monocarbonate, where it is absorbed in the interlayer [8] shifting the monocarbonate composition towards Friedel's salt ($Ca_2Al(OH)_6(Cl,OH).2H_2O$). There are carbonated zones in all samples of the outer leaf. Sometimes calcium is redistributed forming a layer in the transition of the leached carbonated and the unleached uncarbonated zone. Simultaneously, sulfur is absent in the carbonated zone with a relatively high content in the form of ettringite in the adjacent uncarbonated zone (Figure 3.5). In the fully carbonated inner leaf, the cement hydrates have been completely altered. Calcite and Si-Al-gel are the main phases. Small gypsum particles typically intermixed with calcite occur. There are some indications of thaumasite, but no certain identification was possible. The cement hydrates present in the RB samples are identical to the ones in the uncarbonated OL with a lower but still elevated occurrence of ettringite.

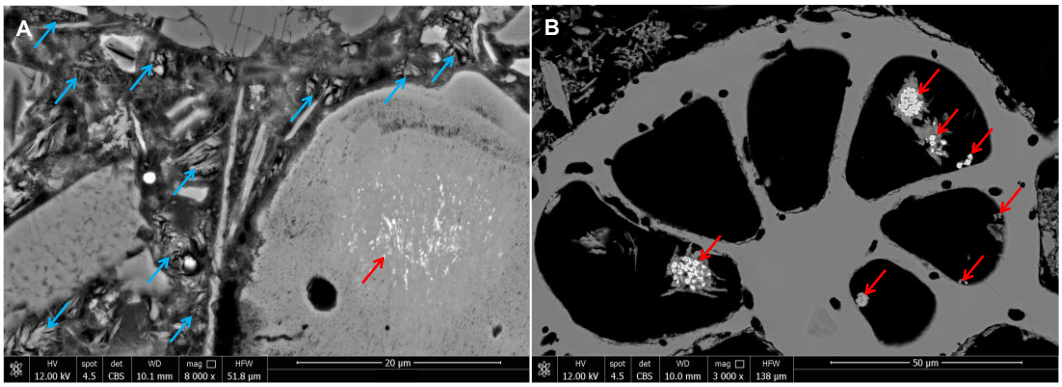

Figure 3.3: A: Partly oxidized pyrrhotite in shell particle (red arrow) and secondary ettringite (blue arrows) formed in the adjacent cement paste (HWF = 51.8 µm). Outer leaf. B: Partly oxidized framboidal pyrite clusters (red arrows) in shell particle (HWF = 138 µm). Inner leaf.

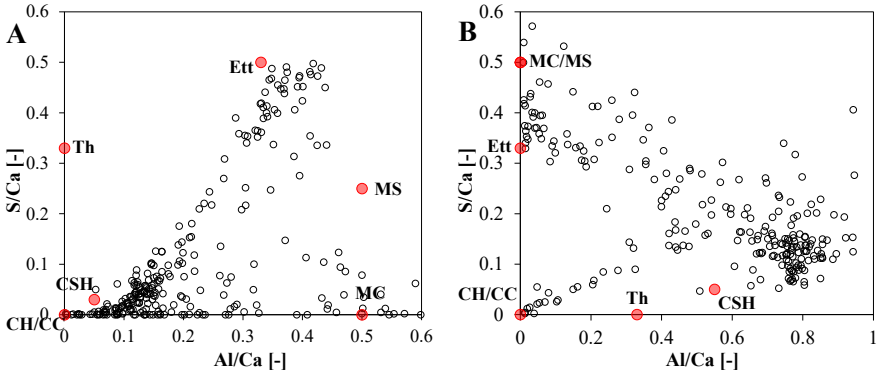

Figure 3.4: S/Ca-ratio as a function of the Al/Ca-ratio (A) and Al/Ca-ratio as a function of the Si/Ca-ratio in an outer leaf sample (B). The red dots indicate the composition of the pure phases: CC = calcite, CH = portlandite, CSH = calcium-silicate-hydrate, Th = thaumasite, MS = monosulfate, MC = monocarbonate.

24. DISCUSSION

The intensity of the XRD peaks for ettringite and gypsum in the OL and IL, respectively, are comparable to the ones obtained in the analysis of the concrete blocks of the seven damaged homes in [3,2]. As such, this result is an indication for the presence of ISA. The sulfur content present as sulfide is very low (Table 3.1), comparable to the non-damaged home in [3] (RGV aggregate). On the other hand, the content of SO_3, typically present in the cement hydrates, matches that of the heavily damaged homes in [2,3]. Consequently, the content of SO_3 seems to indicate the occurrence of ISA. Here, it has to be

considered that a concrete with a density of 2100 kg/m^3 produced with a cement content of 100 kg/m^3 will result in about 0.17 mass-% of SO_3 (assuming a SO_3 content in the cement of 3.5 mass-%). Therefore, the SO_3 content shown in Table 3.1 (WMQ, PHY) seems not to be elevated despite the very pronounced ettringite formation and the obvious iron sulfide oxidation in the blocks containing PHY aggregate [2,3]. Either EN 196-2 [5] is underestimating the SO_3 content or some of the SO_3 provided by the cement and the oxidation of iron sulfides is leached from the concrete or redistributed. The challenge to determine the representative sulfur contents in concrete affected by iron sulfide oxidation and ISA is further discussed in [9].

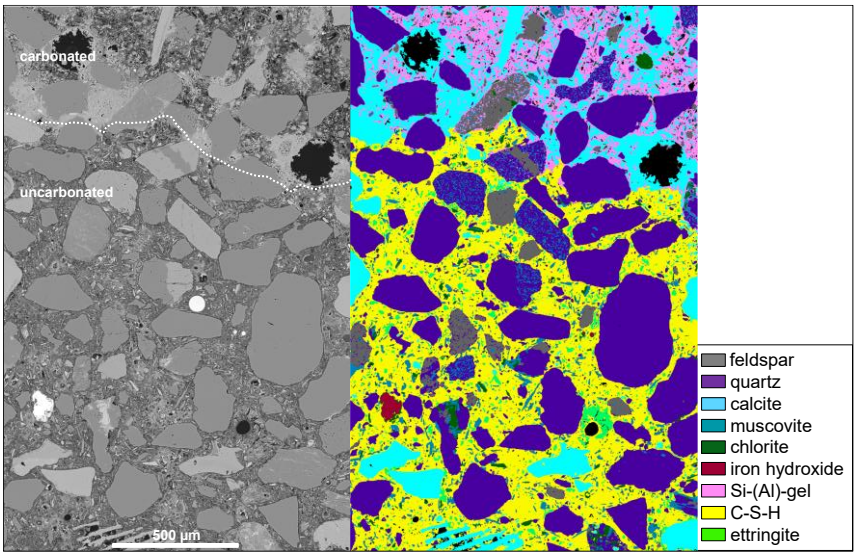

Figure 3.5: BSE-image (A) of the carbonation front (above dashed line) and phases present in the carbonated and uncarbonated cement paste (B). Outer leaf.

However, comparing the concentration of the different sulfur compounds in the concrete blocks produced with WMQ and PHY aggregates indicates that the original content of iron sulfides in the WMQ blocks was low (total sulfur), but that their oxidation has progressed close to completion (SO_3 content). This can be attributed to their very small particle size that is typically well below one micrometer. Furthermore, ISA is confirmed by EDX analysis in all investigated samples from the OL and the RB. There is a clear shift from C-S-H towards ettringite in the non-carbonated locations. However, the degree of attack is lower compared to what is typically observed in homes with blocks produced with pyrrhotite-containing PHY [2,3]. The distribution of sulfur between carbonated and uncarbonated zones in the blocks from the outer leaf clearly indicates a redistribution with the progress of carbonation. Ettringite is not stable at a pH below 10 and decomposes during the carbonation process [10]. The mobile sulfate ions released into the pore solution due to carbonation diffuse into the uncarbonated zones where they react with monocarbonate forming secondary ettringite [3]. If the sulfur level in a system is increased as in the case of ISA, the redistribution of sulfur can be expected to lead to additional strain due to the crystallization pressure of ettringite [11]. There are three potential sources of sulfur in the investigated concrete blocks. The first is the sulfur-containing phosphate in the quartzite aggregates. Although there are some signs of reaction, their total concentration is low. Therefore, a sulfur contribution sufficient enough to cause ISA seems unlikely. The second are the iron sulfides present in the shells of the sand. Their oxidation leads to the release of sulfur that reacts with monocarbonate and causes expansion by the formation of secondary ettringite. The chlorides mainly present in the monocarbonate indicate that the sand is sea dredged or at least sourced in a deposit containing some saline water. Because the conditions in such sediments are anaerobic [12], it can be assumed that no oxidation of the iron sulfides took place before the use of the sand in the concrete. However, they oxidize readily in the concrete, because of the fast oxidation kinetics in an alkaline environment [13] and the high surface area due to their extremely small size. Most of the iron sulfides have already oxidized at the time of core extraction indicated by the high number of shells stained by iron oxide/hydroxides without the presence of iron sulfides. As such, the observed damages in this case study seem to be attributable to ISA caused by the advanced oxidation of irons sulfides present in the sand. The causes of damage in other homes containing WMQ aggregates that are structurally less affected has yet to be determined. Furthermore, if the WMQ quarry was located, the possibility of other potential sulfur sources could be investigated.

25. CONCLUSIONS

The results obtained from the investigation of the OL, IL and RB of a damaged home produced with concrete containing WMQ aggregates allow the following conclusions to be drawn:

- There is the formation of secondary sulfate minerals in all investigated components strongly indicating ISA despite the low levels of total sulfur. Secondary ettringite formation is more pronounced in the OL than in the RB, while the gypsum is present in the carbonated IL.
- Small amounts of not yet oxidized pyrrhotite and framboidal pyrite are present in the shell particles of the sea dredged sand identified as an internal source of sulfur.
- The majority of the shells are stained by iron oxides/hydroxides indicating a high degree of iron sulfide oxidation.
- The typical hydrate assemblage present in ISA and the low total sulfur content indicate that even relatively small amounts of iron sulfides can trigger ISA, if the degree of iron sulfide oxidation is high.

26. REFERENCES

1. McCarthy D, Kane N, Lee F, Blaney D (2017) Report of the Expert Panel on Concrete Blocks.
2. Leemann A, Lothenbach B, Münch B, Campbell T, Dunlop P (2023) The "mica crisis" in Donegal, Ireland - a case of internal sulfate attack? Cement and Concrete Research 168:107149 (107114 pp.). doi:10.1016/j.cemconres.2023.107149
3. Leemann A, Münch B, Lothenbach B, Winnefeld F, Dunlop P (2024) Defective homes in Donegal, Ireland: effect of exposure conditions and concrete quality on pyrrhotite oxidation and internal sulfate attack. Cement and Concrete Research 186:107684 (107617 pp.). doi:10.1016/j.cemconres.2024.107684
4. Brough C, Staniforth B, Garner C, Garside R, Colville R, Strongman J, Fletcher J (2023) High risk concrete blocks from County Donegal: The geology of defective aggregate and the wider implications. Construction and Building Materials 408:133404. doi:https://doi.org/10.1016/j.conbuildmat.2023.133404
5. EN196-2 (2013) Methods of Testing Cement: Chemical analysis of cement. European Committee for Standardization, Brussels
6. EN1744-1 (2014) Tests for chemical properties of aggregates - chemical analysis. European Committee for Standardization, Brussels
7. Münch B, Martin LH, Leemann A (2015) Segmentation of elemental EDS maps by means of multiple clustering combined with phase identification. Journal of Microscopy 260 (3):411-426. doi: https://doi.org/10.1111/jmi.12309
8. Mesbah A, Cau-dit-Coumes C, Frizon F, Leroux F, Ravaux J, Renaudin G (2011) A new investigation of the Cl–CO3 substitution in AFm phases. Journal of the American Ceramic Society 94 (6):1901-1910. doi:https://doi.org/10.1111/j.1551-2916.2010.04305.x
9. Santos L, Chrysochoou M, Wille K (2025) Development of a risk assessment framework for pyrrhotite induced deterioration of concrete foundations in CT and MA. Cement and Concrete Research 197:107951. doi:https://doi.org/10.1016/j.cemconres.2025.107951
10. Shi Z, Lothenbach B, Geiker MR, Kaufmann J, Leemann A, Ferreiro S, Skibsted J (2016) Experimental studies and thermodynamic modeling of the carbonation of Portland cement, metakaolin and limestone mortars. Cement and Concrete Research 88:60-72. doi:https://doi.org/10.1016/j.cemconres.2016.06.006
11. Flatt RJ, Scherer GW (2008) Thermodynamics of crystallization stresses in DEF. Cement and Concrete Research 38 (3):325-336. doi:https://doi.org/10.1016/j.cemconres.2007.10.002
12. Morgan B, Rate AW, Burton ED (2012) Trace element reactivity in FeS-rich estuarine sediments: Influence of formation environment and acid sulfate soil drainage. Science of The Total Environment 438:463-476. doi:https://doi.org/10.1016/j.scitotenv.2012.08.088
13. Li Z, Gorski CA, Thompson A, Shallenberger JR, Kaladharan G, Radlińska A (2025) Dissolution kinetics of iron sulfide minerals in alkaline solutions. Cement and Concrete Research 193:107850. doi:https://doi.org/10.1016/j.cemconres.2025.107850

Quantifying iron sulfide superstructures in concrete aggregates in the recovered solids after density-based separation

Dip Banik [(1)], Alexander S. Brand [(2)]

(1) Virginia Tech, Blacksburg, USA, dipbanik@vt.edu

(2) Virginia Tech, Blacksburg, USA, asbrand@vt.edu

Abstract

The oxidation of iron sulfides, especially pyrrhotite and framboidal pyrite, is a degradation mechanism encountered in northeastern USA, resulting in millions of dollars of litigation in Massachusetts and Connecticut. These minerals undergo oxidation and damage concrete due to volumetric expansion and secondary sulfate attack, even if present in very low concentrations (i.e., <1 wt%). Because of very low concentration researchers report difficulties in quantifying these minerals. Moreover, pyrrhotite can be present in several different polytypes in aggregates and it is more difficult to accurately quantify the ratios between different polytypes. Because of the lack of means to directly quantify the iron sulfides, indirect qualitative or semi-quantitative assessments, e.g., thermomagnetic responses, selective leaching, oxygen consumption, accelerated mortar bar test, staining test, total sulfur content, analyzing sulfur spectra etc., are employed. This study presents a methodology for the identification and semi-quantification of iron sulfide phases, including pyrrhotite polytypes, using X-ray diffraction (XRD). XRD is one of the most widely used techniques for bulk mineralogical analysis, enabling the detection and quantification of crystalline phases. However, its effectiveness is constrained by relatively high detection limits (typically ~1–2 wt%), which can hinder the identification of trace mineral components in complex matrices. To address this limitation, density-based separation was employed to concentrate heavier mineral fractions (density > 2.95 g/cm³), including iron sulfides, from the bulk sample. XRD analysis of the density-separated fraction revealed pronounced pyrrhotite peaks and enabled clear differentiation among pyrrhotite polytypes. In one sample, 4C, 5C, and 6C pyrrhotite structures were identified, whereas the second sample contained 4C and 6C polytypes. Additionally, XRD analysis of the concentrated fraction of one sample detected pyrite and pentlandite, which were not observable in the bulk XRD scan. These results demonstrate the effectiveness of density separation combined with XRD for the characterization of minor and structurally distinct sulfide phases.

***Keywords**: density-based separation, iron sulfide quantification, X-ray diffraction, detection of pyrrhotite polytypes*

1. INTRODUCTION

Pyrrhotite and/or framboidal pyrite can be present in natural rock samples, and when these rocks are used as aggregates in concrete, these minerals undergo oxidation and damage concrete due to volumetric expansion and secondary sulfate attack [1], even if present in very low concentrations (*i.e.,* <1 wt%) [2]. Deterioration in concrete structures due to the oxidation of iron sulfides in aggregates have been observed in parts of Europe (Norway, Ireland, Spain, Wales), Canada (Quebec, Montreal), and the USA (Connecticut, Kentucky, Massachusetts) [1]. Over 35,000 homes in Connecticut and 10,000 homes in Massachusetts are reported facing widespread cracking and crumbling of foundations due to pyrrhotite oxidation in the coarse aggregates [1], resulting in millions of dollars in litigation for repair and insurance payout. Because of the difficulties in iron sulfide quantification, screening for this degradation mechanism depends on qualitative evaluations. European Standard EN 12620 and the Massachusetts and Connecticut mandates recommend a limit of 1.0 % total sulfur in any concrete aggregate and a limit of 0.1 % total sulfur when pyrrhotite has been identified in the aggregate as the primary screening method, but this method is very conservative, resulting in a greater amount of rejected aggregate than is necessary. Selective mineralogical leaching using acid [3], analyzing sulfur spectra using wave-length dispersive X-ray fluorescence (WD-XRF) [4, 5] and thermomagnetic response [6] are only available techniques that can measure pyrrhotite semi-quantitatively at low concentrations, but those methods are subject to sample-specific calibration. Except for these, currently a few qualitative evaluation

techniques [7–9], *e.g.*, accelerated mortar bar expansions in oxidizers, electrochemical activation of pyrrhotite, oxygen consumption etc. are employed to evaluate the extent of degradation. However, these evaluations are generally compared to total sulfur contents irrespective of the iron sulfide content present in the samples. Moreover, the concrete expansion and subsequent degradation observed in field and accelerated lab tests are also compared to the total sulfur content of the aggregates, which does not provide good correlation, and thus it is impossible to predict the extent of degradation from semi-quantitative tests or total sulfur content of aggregates. For better predictability of the extent of degradation, the larger focus of this study is to quantitatively measure the presence of iron sulfides with a connection to oxidation potential. The specific questions tied to this work are centered on the quantitative measurement of iron sulfides present:

- What is the concentration of iron sulfides present in the base aggregates?
- What are the polytypes of iron sulfides present in the base aggregates?
- Is it possible to leverage any readily available material characterization techniques to quantify the iron sulfides?

Among several material quantification techniques, XRD is recognized as the only rapid and accessible technique for bulk mineralogical quantification of iron sulfides present [10] and readily available in research institutes. However, benchtop XRD units are limited by low detection limits (> 1-2 wt%) to provide comprehensive trace mineral quantification and distinctions between different polytypes of iron sulfides [11].

To solve these issues and create a reliable iron sulfide quantification method, mineral separation can be applied. Several mineral separation techniques have been used for mineral separation conventionally, *e.g.*, magnetic separation, leaching, density-based separation and floatation system [12–15]. Leaching converts the sulfides to different compound, which makes quantification difficult [16], and magnetic separation is not applicable due to pyrrhotite having several non-megnatic polytypes. Floatation is a widely used technique for mineral separation and concentration, and it is a complex technique influenced by several factors, including pH, reagents, operating conditions [17]. However, even with proper controls over the parameters, the recovery is not efficient if the mineral concentration is small in the feedstock [17]. Considering these, this work will utilize the differences in density of different minerals present in rock samples for separating out the iron sulfides. Feldspars, quartz, amphiboles, micas, olivine, garnet, calcite, pyroxenes are the general rock forming minerals and the most abundant parts of rocks [18]. These minerals are lighter in comparison to the iron sulfides of interests [19, 20]. To separate out the heavier iron sulfides (density: > 3.5 g/cm^3) present in rock samples, using a dense media (liquid) of specific density of 2.9 g/cm^3 is suitable [20]. Due to buoyant force, particles having specific gravity lower than the liquid will float and denser particles will settle down and get concentrated. Recovering these concentrates will allow quantification of the iron sulfides using benchtop XRDs with higher confidence.

2. MATERIALS AND METHODS

Aggregate samples with varying quantities of iron sulfides were collected from North American quarries. The bulk samples were crushed using a jaw crusher until the particles were fine enough to pass through 90 µm. 30 g of that crushed sample was then mixed with 200 mL of Lithium Metatungstate (LMT) (density 2.95 g/cm^3) in a separatory funnel. The resultant slurry was then left to settle for 24 hours for the heavier particles to settled down. After that the supernatant is remixed and kept stranded for 24 hours. Then the settled portion was collected in a centrifuge tube. A portion of that settled slurry was transferred to another centrifuge tube, topped up with deionized (DI) water and thoroughly mixed. Then the mix was centrifuged for 10 min in 5000 rpm to separate the water and the particles. This cleaning process continued till all the settled slurry was cleaned and the supernatant was cleared. The cleaned particles were dried inside an oven with 25 mmHg vacuum and 50 °C to limit the oxidation of the samples. Both the preprocessed and the settled samples were micronized for 15 minutes inside a grinding jar with agate bead (XRD-MILL MCCRONE) in isopropanol for homogenization. The homogenized samples were then dried in similar fashion for further experiments. The floated slurry of the powders and the LMT were also collected by filtering through analytical filter papers and washed with DI water.

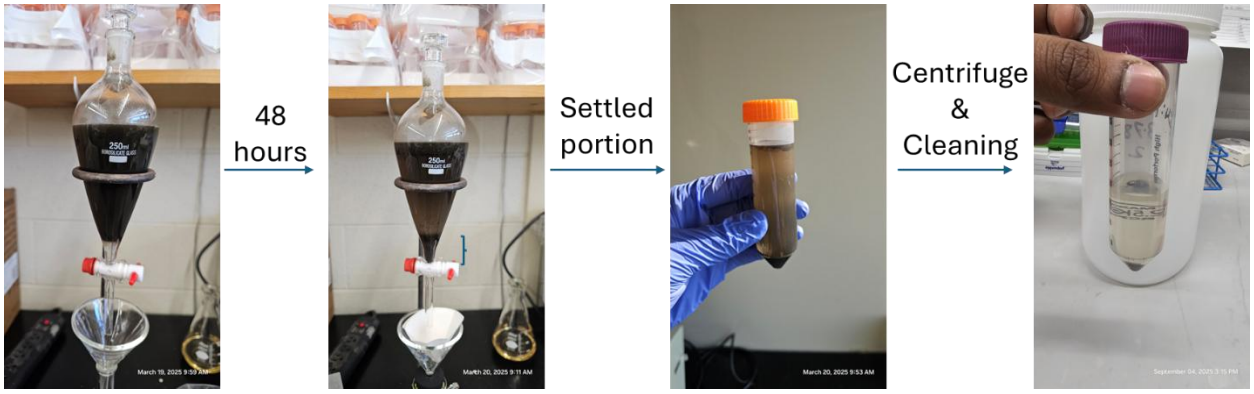

Figure 3: The flow of experiments utilized to concentrate the iron sulfides.

The XRD patterns of the pre-processed and the settled samples were collected using a Panalytical Empyrean 3 XRD equipped with Cu Kα X-ray source having a tension of 45 keV and current of 40 mA at 2θ range of 5° to 80°. Reitveld refinement of the scans were carried out using Profex to find out the relative crystalline compositions. Furthermore, total sulfur of the pre-proceesed and the floats were analyzed using an IXRF Systems' ATLAS Apex M benchtop microEDXRF (microXRF) on 30 mm pressed pellets to compare the total sulfur after the LMT processing.

3. RESULTS AND DISCUSSIONS

3.1 Results from microXRF

Table 3 presents the total sulfur measured using the microXRF of the pre-processed samples and the floats after the LMT processing. Analyzing the elemental maps collected from microXRF, Agg-1 showed the presence of different elements (rather than iron) in the sulfur locations, indicating the presence of other sulfides and/or sulfates alongside iron sulfides. Agg-2 showed only the presence of iron associated with sulfur. Comparisons between the results before and after LMT processing show changes in the total sulfur during the process. This was likely due to the heavier sulfides settling down during the separation process. However, it can be observed that Agg-1 has around 0.43% sulfur present in the floats. This could be due to the sample having presence of lighter sulfates (gypsum, anhydrites, epsomite) and some sulfides particles not settling down due to very small size. Moreover, Agg-1 sample showed presences of pyrite and pentlandite alongside pyrrhotite. Agg-2 had pyrrhotite as the major source of sulfur and almost no iron sulfides were observed in the float after LMT processing.

Table 3: Sulfur mapping and total sulfur measurements using microXRF.

Sample	Pre-processed Sample		Floats in LMT	
	Total Sulfur (%)	FeS (area%) (Including other elements)	Total Sulfur (%)	FeS (area%) (Including other elements)
Agg-1	1.29	1.90	0.43	0.18
Agg-2	0.57	1.00	0.05	0.01

3.2 XRD spectra of the samples and analysis

Figure 4 presents the XRD scans of the pre-processed and the settled samples. Pyrrhotite major peaks are observed in the 2Q range of 43.5 to 44.5 in the Cu XRD and the lattice parameters used for the refinements are presented in Table 4. These structures were successfully used by Rezvani et al. [21] to distinguish different pyrrhotite superstructures.

Table 4: The comparison between the lattice parameters of the pyrrhotite superstructures used for refinement.

Pyrrhotite Structure	Lattice Parameters			
	a (Å)	b (Å)	c (Å)	b(°)
4C	11.938	6.852	12.946	117.831
5C	6.899	28.668	6.881	120
6C	6.897	11.954	17.602	101.302

From the close-up of the spectra, it can be observed that the pre-processed samples due to having low concentrations did not show peaks reliably above the background. However, settled samples showed distinct spectra above the background. Moreover, the characteristic peaks of the different pyrrhotite superstructures can be attributed to the observed peaks.

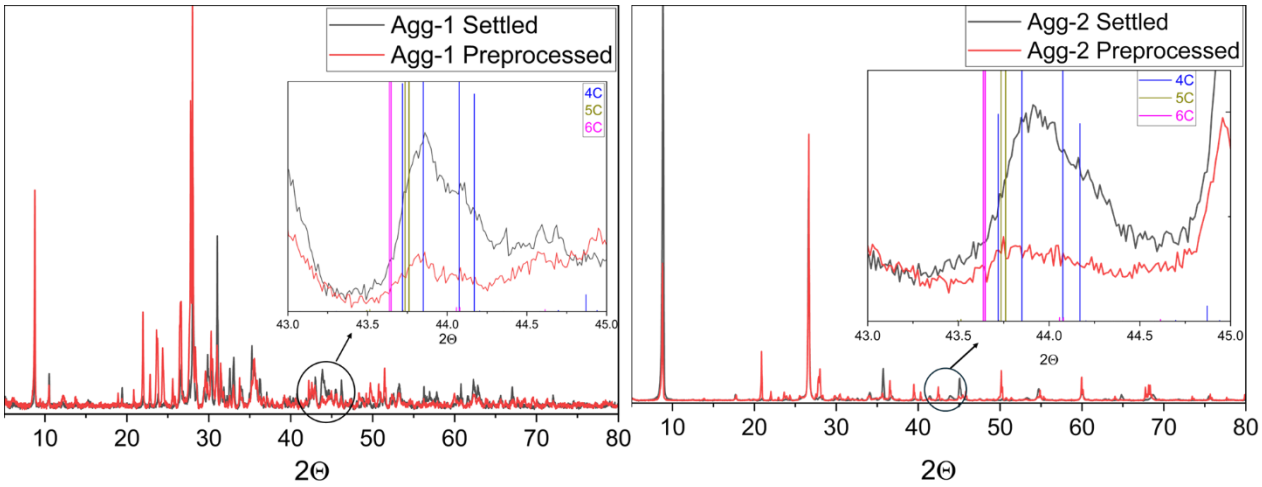

Figure 4: XRD scans of the samples before and after gravity-based separation using LMT.

Table 5 presents the relative iron sulfide concentrations obtained from the Rietveld refinement of XRD data of the settled mass. 4.66 g of the Agg-1 and 3.74 g of the Agg-2 were measured as settled mass after cleaning and drying. It can be observed that different polytypes of pyrrhotites were present in the settled mass and the concentrations were high enough for the general bulk XRD machines to pick up. Agg-1 settled showed the presence of 1.75% pyrite and 1.57% pentlandite alongside 5.9% 4C, 1.9% 5C and 1.4% 6C polytypes of pyrrhotite. Agg-2 showed the presence of 6.77% 4C and 1.50% 6C pyrrhotite without the presence of other sulfides in the samples.

Table 5: Iron sulfide concentrations in the settled mass after Rietveld Refinements.

Sample	Settled Mass (g)	Crystalline phases (%) from Rietveld Refinement				
		Pyrrhotite 4C	Pyrrhotite 5C	Pyrrhotite 6C	Pyrite	Pentlandite
Agg-1	4.66	5.90	1.90	1.40	1.75	1.57
Agg-2	3.74	6.77	-	1.50	-	-

4. CONCLUSIONS

Density based separation showed effectiveness in identification and relative quantification of the different polytypes of pyrrhotites present in the samples. Both samples showed 4C as the major pyrrhotite polytype. Moreover, the presence of other non-major sulfides can be identified following this procedure. This method utilizes relatively easy technique with available instruments for reliable

quantification of the iron sulfides present in the rock aggregates and help safeguarding structures against the iron sulfide degradation. However, from the XRF results, sulfur was found in the floating mass indicating either incomplete separation or presence of presence of lighter sulfates.

5. LIMITATIONS

This work presents analysis on just two samples with single iteration and XRDs were conducted without any standards considering the likelihood of the amorphous content being present being very low. Further comparison has to be done on the samples with other available techniques to establish the recovery efficiency.

6. REFERENCES

1. Jana D (2022) Cracking of residential concrete foundations in eastern Connecticut, USA from oxidation of pyrrhotite. Case Stud Constr Mater 16:e00909. https://doi.org/10.1016/j.cscm.2022.e00909
2. Geiss CE, Gourley JR (2019) A thermomagnetic technique to quantify the risk of internal sulfur attack due to pyrrhotite. Cem Concr Res 115:1–7. https://doi.org/10.1016/j.cemconres.2018.09.010
3. Marcelino AP, Calixto JM, Gumieri AG, et al (2016) Evaluation of pyrite and pyrrhotite in concretes. IBRACON Struct Mater J 9:. https://doi.org/10.1590/S1983-41952016000300009
4. Santos L, Wille K, Chrysochoou M (2024) Application of X-ray principles to quantify sulfur oxidation states in concrete. Spectrosc Lett 57:377–387. https://doi.org/10.1080/00387010.2024.2361709
5. Cruz-Hernandez Y, Chrysochoou M, Wille K (2020) Wavelength dispersive X-ray fluorescence method to estimate the oxidation reaction progress of sulfide minerals in concrete. Spectrochim Acta Part B At Spectrosc 172:105949. https://doi.org/10.1016/j.sab.2020.105949
6. Geiss CECE, Gourley JRJR (2019) A thermomagnetic technique to quantify the risk of internal sulfur attack due to pyrrhotite. Cem Concr Res 115:1–7. https://doi.org/10.1016/j.cemconres.2018.09.010
7. Marcelino AP, Calixto JM, Gumieri AG, et al (2020) A feasible evaluation protocol to determine the most reactive sulfide-bearing aggregate for use in concrete. Constr Build Mater 242:118031. https://doi.org/10.1016/j.conbuildmat.2020.118031
8. Rodrigues A, Duchesne J, Fournier B, et al (2016) Evaluation protocol for concrete aggregates containing iron sulfide minerals. ACI Mater J 113:349–359. https://doi.org/10.14359/51688828
9. Castillo Araiza R, Rodrigues A, Fournier B, Duchesne J (2024) A new accelerated testing scheme to evaluate the potential oxidation reaction of sulfide-bearing aggregates in concrete specimens. Cem Concr Res 180:107507. https://doi.org/10.1016/j.cemconres.2024.107507
10. Mikhlin Y., Kuklinskiy A., Pavlenko N., et al (2002) Spectroscopic and XRD studies of the air degradation of acid-reacted pyrrhotites. Geochim Cosmochim Acta 66:4057–4067. https://doi.org/10.1016/S0016-7037(02)00989-4
11. Multani RS, Waters KE (2018) A review of the physicochemical properties and flotation of pyrrhotite superstructures (4C – Fe 7 S 8 / 5C – Fe 9 S 10) in Ni-Cu sulphide mineral processing. Can J Chem Eng 96:1185–1206. https://doi.org/10.1002/cjce.23099
12. Mu Y, Peng Y, Lauten RA (2016) The depression of pyrite in selective flotation by different reagent systems – A Literature review. Miner Eng 96–97:143–156. https://doi.org/10.1016/j.mineng.2016.06.018
13. O'Connor CT, Mills PJT (1990) The effect of temperature on the pulp and froth phases in the flotation of pyrite. Miner Eng 3:615–624. https://doi.org/10.1016/0892-6875(90)90006-W
14. Oliveira CM, Machado CM, Duarte GW, Peterson M (2016) Beneficiation of pyrite from coal mining. J Clean Prod 139:821–827. https://doi.org/10.1016/j.jclepro.2016.08.124
15. Tang X, Chen Y (2022) A review of flotation and selective separation of pyrrhotite: A perspective from crystal structures. Int J Min Sci Technol 32:847–863. https://doi.org/10.1016/j.ijmst.2022.06.001
16. Mäkinen J, Pietek G, Miettinen V, et al (2022) Removal of Pyrrhotite from High-Sulphur Tailings Utilising Non-Oxidative H2SO4 Leaching. Minerals 12:1610. https://doi.org/10.3390/min12121610
17. Luo X, Feng B, Wong C, et al (2016) The critical importance of pulp concentration on the flotation of galena from a low grade lead–zinc ore. J Mater Res Technol 5:131–135. https://doi.org/10.1016/j.jmrt.2015.10.002

18. Rock-forming Minerals | Geological Society of Glasgow. https://geologyglasgow.org.uk/minerals-rocks-fossils/rock-forming-minerals/. Accessed 28 Dec 2025

19. Minerals and other Materials - Specific Gravities. https://www.engineeringtoolbox.com/minerals-specific-gravity-d_1644.html. Accessed 29 Dec 2025

20. Proske U, Wood R, Fallon S, Stevenson J (2015) Use of heavy liquid density separation to remove pyrite from sediment samples for radiocarbon dating. Quat Geochronol 25:66–71. https://doi.org/10.1016/j.quageo.2014.10.002

21. Rezvani A, Raji F, Peng Y, et al (2024) Quantifying pyrrhotite superstructures in copper-gold ore flotation through synchrotron X-ray diffraction analysis. Miner Eng 216:108894. https://doi.org/10.1016/j.mineng.2024.108894

ICISR 2026

2nd International Conference on Iron-Sulfide Reactions in Concrete

Technical Session # 4:

From Research to Remediation: Policy, Practice, and Impacts of Iron-Sulfide Reactions in Concrete

UCONN | COLLEGE OF ENGINEERING
SCHOOL OF CIVIL AND ENVIRONMENTAL ENGINEERING

UCONN
COLLEGE OF ENGINEERING
CONNECTICUT TRANSPORTATION INSTITUTE (CTI)

From mica to pyrrhotite: charting the impacts of scientific research on Irish standards and the government grant scheme to remediate defective concrete homes in Ireland

Paul Dunlop [(1)], Andreas Leemann [(1,2)], Benoit Fournier [(3)], Josée Duchesne [(3)], Pierre-Luc Fecteau [(3)], Andreia Rodrigues [(3)], Rodolfo Castillo-Araiza [(3)], Nick Scaglione [(4)], Kay Wille [(5)], James Mahoney [(5)], Marisa Chrysochoou [(6)]

(1) *School of Geography and Environmental Sciences, Ulster University, Coleraine, Northern Ireland, UK, p.dunlop@ulster.uk*
(2) Empa, Laboratory for Concrete & Asphalt, Dübendorf, Switzerland, andreas.leemann@empa.ch
(3) Department of Geology and Geological Engineering, Laval University, Québec City, Québec, Canada, benoit.fournier@ggl.ulaval.ca, Josee.Duchesne@ggl.ulaval.ca, pierre-luc.fecteau@ggl.ulaval.ca, andreia.rodrigues.1@ulaval.ca, rodolfo.castillo-araiza.1@ulaval.ca
(4) Concrete Research and Testing LLC, Columbus, Ohio, USA, nick@concretetesting.com
(5) School of Civil and Environmental Engineering, *University of Connecticut, Storrs, Connecticut, USA, kay.wille@uconn.edu, james.mahoney@uconn.edu*
(6) College of Engineering, University of Missouri, Columbia, USA, mczhd@missouri.edu

Abstract

In the Republic of Ireland, thousands of homes built with defective concrete blocks are undergoing progressive structural deterioration. What first emerged in Counties Donegal and Mayo has become a broader national crisis, with the Irish Government's grant scheme for the assessment and remediation of affected homes now extended to seven counties. Other county councils are formally seeking inclusion, while confirmed cases have also emerged in a border county of Northern Ireland. A 2017 government report attributed damage in Donegal homes to elevated muscovite mica and freeze–thaw susceptibility, while framboidal pyrite was identified as the principal cause in Mayo. This led to the development of the Irish Standard, I.S. 465, by the National Standards Authority of Ireland, with Donegal protocols focused primarily on mica testing. However, although pyrrhotite was increasingly detected in Donegal samples, it remained excluded from I.S. 465 despite microstructural and chemical analyses published in 2023 showing that pyrrhotite oxidation and internal sulfate attack, rather than mica, were responsible for the deterioration and that sulfur contents exceeded EN 12620 limits. These findings intensified campaign and political pressure, prompting a government review of the standard and the establishment of an international consortium led by Ulster University to inform its revision. This paper examines how the consortium's findings have helped reshape I.S. 465 and its remediation options.

Keywords: *defective concrete blocks, internal sulfate attack, I.S. 465, NSAI*

1. INTRODUCTION

Defective concrete blocks have caused widespread structural damage to homes across Ireland. First identified in Counties Donegal and Mayo, the crisis has since become a national issue, with cases now documented across the Republic of Ireland and recent media reports confirming that homes in Derry, Northern Ireland were built using defective concrete exported across the border [1]. Although Limerick, Clare, Wexford, Fingal and Sligo are now included in a government scheme to fix homes, Donegal remains the worst affected region, with thousands of homes experiencing cracking, disintegration and progressive structural deterioration. Early investigations, including a 2017 government-commissioned report, concluded that excessive muscovite mica in Donegal aggregates contributed to freeze–thaw susceptibility of the concrete, despite this remaining an untested hypothesis [2]. In contrast, framboidal pyrite was identified as the principal driver of deterioration in Mayo. These interpretations shaped the Irish Government's regulatory and remediation response, including the development of I.S. 465 by the NSAI to govern assessment and repair under a government-supported grant scheme, estimated at ~€3 billion. From 2020 onwards, emerging scientific evidence began to challenge the national framework. Petrolab UK, one of the main testing laboratories used by engineers working on the grant scheme, consistently reported high levels of pyrrhotite in defective Donegal concrete, prompting engineers, campaign groups and some Donegal-based politicians to call for its recognition in I.S. 465. Leemann et al. (2023) provided the first peer-reviewed evidence that pyrrhotite oxidation and internal sulfate attack (ISA), rather than mica-related freeze–thaw degradation, was the principal mechanism of damage in affected Donegal dwellings [3]. Brough et al. (2023), drawing on an extensive database of samples from defective Donegal homes, reported aggregates with a high propensity to generate ISA [4]. Collectively, these findings raised questions about the diagnostic basis and remediation strategies embedded in I.S. 465 and, by extension, the effectiveness of the grant scheme to adequately repair homes in Donegal. In response, the Irish Government initiated a formal review of I.S. 465. To inform this process, the Department of Housing, Local Government and Heritage and the Geological Survey of Ireland funded an international research consortium, led by Ulster University with partners at Empa, Concrete Research & Testing LLC, Université Laval and the University of Connecticut, to investigate pyrrhotite oxidation in three deteriorated properties and one control property in Donegal. This paper examines the evidence underpinning the transition from a mica-based to a pyrrhotite/ISA-based understanding of damage and analyses how this has influenced the revisions to I.S. 465.

2. MATERIALS AND METHODS

a. Sampling and case study design

Concrete blocks, block cores and foundation cores were extracted from four residential properties located in different parts of County Donegal, Ireland. The properties were selected by members of National Standards Authority of Ireland (NSAI) Technical Committee 63 (TC 63), which developed I.S. 465 and was later tasked with revising it. Three dwellings showed the characteristic cracking and deterioration associated with defective concrete (Mulroy View, Glendale Drive and Abbots Wood), while a fourth property (Carrowmore) served as an undamaged reference house constructed within the same timeframe. Samples were collected from all major structural elements, including strip foundations made from poured mass concrete, together with rising blocks and the inner and outer leaf walls, which were constructed using pre-cast masonry units (blocks). The sampling strategy was intended to capture variability in concrete quality, exposure conditions, and damage severity, enabling comparisons between affected and unaffected properties and supporting assessment of degradation progression within individual building components. The methodology presented here integrates complementary analytical approaches undertaken by the consortium, each contributing distinct expertise to the investigation of pyrrhotite-related degradation in defective concrete. Rather than presenting methods by institution, the paper synthesises the collective work of the consortium. The full methodological approaches of each partner are detailed in their final reports, which are now openly available for download [5].

b. Petrographic and microstructural characterisation

Petrographic examination formed the basis for identifying aggregate mineralogy, cement paste condition, and damage features within the concrete. Specimens prepared from the received samples were examined using stereo, transmitted-light and reflected-light optical microscopy in accordance with ASTM C856. Point-count analyses were conducted to quantify volumetric proportions of cement paste, air voids, aggregates, and iron sulfide minerals. Scanning electron microscopy coupled with energy-dispersive X-ray spectroscopy (SEM–EDS) was used to characterise iron sulfide morphology, oxidation features, and secondary sulfate phases within the cement paste. SEM–EDS analysis enabled identification of oxidation within pyrrhotite grains, elemental sulfur distributions, and microstructural evidence of ISA, including secondary ettringite, thaumasite and gypsum formation.

c. Sulfur analysis

Bulk chemical analyses were performed on samples extracted from the four homes. Two methods of aggregate recovery were used within the group: one using acid dissolution and the other mechanical/thermal paste removal. Total sulfur was then determined using either a LECO S832, 1450 °C in oxygen or an infrared absorption method using an Eltra CS 800 carbon/sulfur analyzer. Sulfur present as sulfide was also determined according to EN 196-2:2013 where the sample was decomposed by hydrochloric acid under reducing conditions, the sulfides were then converted to hydrogen sulfide, which was carried by a gaseous stream into an ammonium zinc sulfate solution to precipitate zinc sulfide that was quantified by iodometry. Wavelength-dispersive X-ray fluorescence (WD-XRF) was used to distinguish between sulfur contributions associated to sulfate versus sulfide, while X-ray diffraction (XRD) was used to identify primary and secondary crystalline phases formed as a result of pyrrhotite oxidation and ISA. Quantitative in-situ chemical analyses of iron sulfide minerals were conducted using electron probe microanalysis and SEM–EDS, while micro-X-ray fluorescence (μXRF) mapping was employed to quantify the distribution and proportion of pyrrhotite within concrete sections.

d. Aggregate reactivity and oxidation potential

The oxidation potential of sulfide-bearing aggregates from the damaged homes was assessed using oxygen consumption testing (OCT), in which the rate of oxygen uptake by crushed aggregates in the presence of moisture was measured under controlled conditions. Accelerated mortar bar expansion tests were conducted on samples from the damaged homes to evaluate expansion associated with sulfide oxidation and subsequent ISA. Additional electrochemical and accelerated exposure tests were used to further examine oxidation-driven deterioration mechanisms. One approach used prisms cut from the blocks that were vacuum-treated in 6% bleach that subsequently went through repeated cycles of 6% bleach submergence, drying and measuring until failure. The other used extracted aggregates to make mortar bars manufactured in accordance with CSA A23.2-25A and conducted expansion tests for ISA potential following the procedure for sulfide-bearing aggregates in Appendix P of CSA A23.1:19/A23.2:19 [6].

e. Moisture state, carbonation and thermodynamic assessment

Moisture content, water saturation, and vapor sorption behaviour of the concrete were characterised to evaluate the influence of exposure conditions on pyrrhotite oxidation. Carbonation depth was assessed using phenolphthalein indicator testing. Thermodynamic modelling was applied to simulate the chemical evolution of the cement paste during sulfide oxidation and to predict the stability of secondary phases under varying environmental conditions.

3. RESULTS

a. Aggregates, sulfur content and aggregate chemistry

The aggregates used in the damaged homes consist predominantly of phyllite and micaceous quartzite that contain mainly pyrrhotite, with lesser amounts of pyrite (Fig. 1). The phyllite in particular is a poor-quality concrete aggregate due to its low hardness, fissility and tendency to split along foliation planes.

Compressive strength tested on single cores from the inner and outer leaf ranged from 6.7 to 14.9 MPa. Chemical analyses performed independently using different approaches demonstrated consistent elevated sulfur levels in the affected dwellings compared to the reference home with values always exceeding the maximum sulfur limit of 0.1 mass-% specified in EN 12620 for concrete aggregates when pyrrhotite is present (Table 3.1).

Table 3.1: Summary of the sulfur analysis showing the minimum and maximum value measured in each home by each partner, n is the number of samples analysed.

Home	Empa - S as sulfide (mass-%)	Université Laval - Total Sulfur (% wt) from extracted aggregates	UCONN - Total Sulfur (% wt) from extracted aggregates
Carrowmore (reference home)	0.01 - 0.03 (n= 4)	Not measured	0.01 & 0.01 (n=2)
Mulroy View	0.27 - 0.55 (n= 4)	0.49 & 0.62 (n=2)	0.39 – 1.35 (n=4)
Glendale Drive	0.42 – 0.75 (n= 6)	0.44 & 0.49 (n=2)	0.44 – 0.67 (n=5)
Abbots Wood	0.49 - 0.75 (n=4)	0.60 (n=1)	0.40 - 0.79 (n=3)

Aggregate and concrete testing further showed that sulfur was predominantly associated with iron sulfide minerals, with pyrrhotite identified as the dominant sulfide phase. Oxygen consumption testing confirmed a high oxidation potential for the Donegal aggregates, indicating a strong propensity for sulfide oxidation under moist conditions.

b. Petrographic and microstructural evidence of pyrrhotite oxidation

Petrographic examination of the deteriorated concrete samples from all structural locations confirmed that aggregates were derived primarily from phyllitic and micaceous lithologies which commonly contain disseminated iron sulfide minerals. Optical microscopy and point-count analyses showed pyrrhotite to be the predominant sulfide, accounting for the majority of the iron sulfide population, with minor pyrite and trace accessory sulfides (Fig. 1A). Optical microscopy and SEM–EDS analyses consistently identified oxidation occurring within pyrrhotite grains, both within aggregate particles and where individual iron sulfide grains were liberated into the cement paste (Fig. 1B & C). These oxidised zones were commonly associated with secondary sulfate-bearing phases in the surrounding paste, providing direct microstructural evidence of ISA. SEM–EDS microanalysis identified progressive alteration of the cement paste matrix and a transition from normal hydration products toward an ISA-dominated microstructure with secondary ettringite and thaumasite in samples analysed from the three damaged properties. While secondary ettringite formation causes concrete expansion, thaumasite formation leads to a loss of cement paste strength and concrete durability.

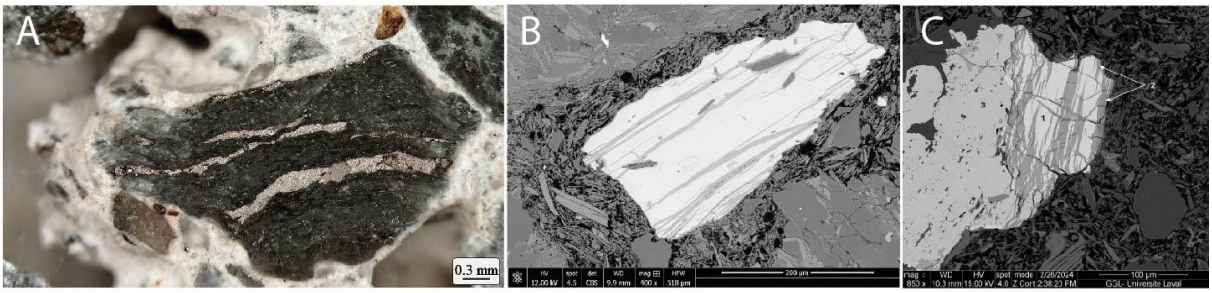

Figure 1. A shows pyrrhotite bands clearly identified in concrete aggregates (CRT). B (Empa) C (Laval) SEM images of pyrrhotite with oxidized regions.

c. Expansion and Reactivity Testing

Accelerated mortar bar expansion tests demonstrated measurable expansion associated with sulfide oxidation in aggregates sourced from Donegal. The expansion behaviour was consistent with oxidation-driven sulfate release followed by ISA. Aggregate samples exhibiting the highest sulfur contents and oxygen consumption rates produced the greatest expansion responses. Complementary electrochemical and accelerated exposure tests further confirmed the reactivity of pyrrhotite-bearing aggregates, while aggregates from the reference dwelling showed negligible expansion and low oxidation potential. These results establish a clear link between aggregate sulfur content, oxidation potential and expansive damage mechanisms.

d. Influence of exposure conditions and structural component

The extent of pyrrhotite oxidation and ISA varied systematically with exposure conditions and structural component. Microstructural analyses showed that oxidation was most advanced in outer leaf blocks, where repeated wetting and drying promoted sulfide oxidation and expansive ISA product formation. Rising blocks exhibited intermediate levels of oxidation, while strip foundations showed predominantly early-stage oxidation [7]. Phenolphthalein tests indicate a consistent building element-by-building element gradient of carbonation. Foundations are essentially uncarbonated, rising blocks show only minor carbonation, outer-leaf blocks are partially carbonated and inner-leaf blocks are nearly completely carbonated [7]. Carbonation was observed to partially limit sulfate attack in inner leaf blocks; however, microstructural evidence indicated that pyrrhotite oxidation continued within aggregates, suggesting ongoing deterioration potential over time due to gypsum formation. These findings demonstrate that both material quality and exposure conditions govern the progression of pyrrhotite-induced damage in affected dwellings.

e. Synthesis of results

Across all analytical approaches, the results consistently identified pyrrhotite oxidation and ISA as the dominant degradation mechanism in defective Donegal concrete with the formation of secondary sulfate minerals (ettringite, thaumasite and gypsum). Elevated sulfur contents above EN12620, high aggregate oxidation potential, microstructural evidence of ISA and expansion test results collectively contradict the original mica-based freeze–thaw hypothesis and provide a coherent mechanistic explanation for the observed deterioration. The high amount of mica within the aggregate was noted as being a contributing factor only because it leads to a high micro-porosity and excessive permeability of the cement paste, facilitating moisture ingress, access of oxygen and diffusion of sulfate ions which assists the advancement of ISA.

4. IMPACT ON REVISIONS TO I.S. 465

Consortium findings were communicated to NSAI TC63 during the revision process for I.S. 465 through technical briefings and provision of interim datasets, enabling the draft revision to incorporate pyrrhotite and ISA analysis and foundation assessment. As of writing, the final version of I.S. 465 is planned for release in April 2026, so the changes outlined in this section are based on the public consultation draft released in March 2025. The most significant impact of the research in the revised draft is the explicit recognition that pyrrhotite oxidation and ISA represent the primary damage mechanism in Donegal, resulting in a marked shift toward ISA-focused investigations in the proposed standard. Whereas pyrrhotite is not referenced in the 2018 edition, it appears repeatedly in the March 2025 draft alongside substantial ISA-related content and new testing protocols for ISA risk. The revised approach replaces the range of remediation options with a single remedy: full demolition where ISA risk is assessed as greater than negligible in homes classified in Groups 2–4, all of which exhibit varying degrees of damage. Group 1 homes, by contrast, are undamaged. It also extends testing to include foundations as the consortium research provided a critical rationale for their inclusion [5,7]. Foundation cores from the affected dwellings contain the same phyllite/micaceous aggregate as the blocks and include measurable iron sulfide minerals, dominated by pyrrhotite, confirmed by petrographic and SEM analyses. Point-counting quantified iron sulfide mineral contents of approximately 0.7–0.9% of concrete and 1.2–1.5%

of aggregate in the foundation cores examined and sulfur data indicate elevated sulfide sulfur relative to the reference dwelling, even where microstructural indicators of reaction progress are generally less advanced than in outer-leaf blocks. Phenolphthalein testing shows foundations are largely uncarbonated (with only a few millimetres carbonated at both ends), and the high saturation state of foundations likely limits oxygen ingress and slows pyrrhotite oxidation compared with the exposed wall elements above ground. Accordingly, foundations may show less immediate distress than outer-leaf masonry, but they cannot be treated as inherently safe; oxidation and ISA may be delayed, but the mechanism remains active and must be explicitly evaluated within the revised I.S. 465 framework. The principal changes between the 2018 edition and the March 2025 consultation draft are summarised in Table 4.1.

Table 4.1. Summary of some of the key changes to I.S. 465 relating to testing Donegal properties

Topic	Published I.S. 465: 2018	Draft I.S. 465 202X (March 2025)
Key confirmatory evidence sought	Thin-section petrography, with optional/confirmatory methods (e.g., XRD/SEM) used to support mica-focused interpretation in Donegal with no Total Sulfur (TS) tests required for Donegal homes.	Analysis focuses on identifying iron sulfides and documenting ISA-related reaction products/phases and alteration features. HTC to measure TS, currently set at 0.3%.
Classification approach that drives decisions	Mechanism-specific "risk of blockwork" style classifications notably for mica freeze-thaw degradation in Donegal.	Component-level classification combining (i) aggregate risk and (ii) active ISA risk, with element-level decisions based on the highest-risk results.
Minimum sampling burden (fieldwork impact)	Minimum 8 samples (baseline set).	Minimum 12 samples, explicitly including foundation concrete cores in the minimum set.
Remediation posture for iron sulfide / ISA-driven cases in Donegal	Sulfide deterioration was not recognised in Donegal, only mica related to freeze-thaw deterioration. 5 remediation options available ranging from full demolition to 4 options that retain portions of the original building	For iron sulfide-induced deterioration in Group 2–4 buildings where elements exceed negligible risk: demolition and rebuild is recommended as the only effective solution
Foundation testing and assessment	No testing or assessment conducted	Now included with explicit remedial decision table (retain vs consider retention vs consider removal) based on aggregate risk and active ISA risk.

5. CONCLUSION

This paper shows how robust scientific analysis, coupled with direct engagement with national standards committees, can and should reshape national standards. Although I.S. 465 remains under revision as TC 63 continues to evaluate over 640 public-consultation submissions, the 2025 draft makes the direction of travel clear for how defective concrete homes in Donegal will likely be tested and remediated. Some issues remain unresolved, including the total sulfur trigger being set at 0.3%. After deducting the 0.1% sulfur contribution expected in a typical concrete block, the remaining 0.2% is still 0.1% above the EN 12620 limit for pyrrhotite. As a result, pyrrhotite-bearing materials with a credible ISA risk could fall below the intervention threshold, potentially excluding affected homes from the scheme. The draft still implies that mica poses a frost risk to concrete, despite the evidence base not supporting this interpretation and recent research rejecting it [3,5]. However, in the draft revised I.S. 465, the evidence base has clearly shifted away from mica risk assessments, towards a multi-method diagnostic approach that focuses on the effects of pyrrhotite oxidation and ISA for Donegal. This is grounded in the robust scientific data supplied directly by the Ulster University-led research consortium and the other expert groups consulted during the revision phase [5]. Importantly, the remediation framework has evolved in line with this understanding, prioritising demolition and rebuild where ISA risk is confirmed. The draft I.S. 465 also includes foundation testing; however, the threshold for their removal is set higher than for

blocks. Given that the draft now recommends demolition for ISA-impacted homes, the safest and most coherent approach is also to replace foundations assessed as posing an ongoing risk during rebuilding.

6. REFERENCES

[1] BBC News, Northern Ireland, 7 November 2022, https://www.bbc.co.uk/news/uk-northern-ireland-63537289 (accessed 12/03/2026).
[2] McCarthy, D., Kane, N., Lee, D, Blaney, D (2017). Report of the Expert Panel on Concrete Blocks, Department of Housing, Local Government and Heritage, 2017. www.gov.ie/en/publication/0218f-report-of-the-expert-panel-on-concrete-blocks/
[3] Leemann, A., Lothenbach, B., Münch, B., Campbell, T. and Dunlop, P (2023). The “mica crisis” in Donegal, Ireland–A case of internal sulfate attack? *Cement and Concrete Research*, *168*, p.107149. https://doi.org/10.1016/j.cemconres.2023.107149
[4] Brough C., Staniforth B., Garner C., Garside R., Colville R., Strongman J., Fletcher J (2023) High risk concrete blocks from County Donegal: The geology of defective aggregate and the wider implications. Construction and Building Materials 408:133404. https://doi.org/10.1016/j.conbuildmat.2023.133404.
[5] Aggregates Research Findings, Geological Survey of Ireland, 28 March 2025. https://www.gsi.ie/en-ie/events-and-news/news/Pages/Aggregates-Research-Findings.aspx.
[6] Concrete materials and methods of concrete construction / Test methods and standard practices for concrete. CSA Group, Toronto, ON, Canada.
[7] Leemann, A., Münch, B., Lothenbach, B., Winnefeld, F. and Dunlop, P (2024). Defective homes in Donegal, Ireland: effect of exposure conditions and concrete quality on pyrrhotite oxidation and internal sulfate attack. *Cement and Concrete Research*, *186*, p.107684. https://doi.org/10.1016/j.cemconres.2024.107684.

ICISR 2026

2nd International Conference on Iron-Sulfide Reactions in Concrete

Student Talks:

Experimental Studies on Sulfide-Bearing Aggregates and Concrete

UCONN | COLLEGE OF ENGINEERING
SCHOOL OF CIVIL AND ENVIRONMENTAL ENGINEERING

UCONN
COLLEGE OF ENGINEERING
CONNECTICUT TRANSPORTATION INSTITUTE (CTI)

Effect of iron sulfide aggregate sizes and amount on electrochemically accelerated concrete deterioration

Meshach Ojo[(1)], Auishe Pauline Corraya[(2)], Aagya Dahal[(2)], Lesley Frame[(3)], Kay Wille[(4)]

(1) Ph.D. Candidate, University of Connecticut (UConn), Storrs, USA, meshach.ojo@uconn.edu

(2) Ph.D. Student, UConn, Storrs, USA, auishe_pauline.corraya@uconn.edu, aagya.dahal@uconn.edu

(3) Assoc. Professor, University of Connecticut, Storrs, USA, lesley.frame@uconn.edu

(4) Professor, University of Connecticut, Storrs, USA, kay.wille@uconn.edu

Abstract

The current study investigates how aggregate size and sulfide content influence the deterioration of concrete containing iron sulfide minerals under electrochemical accelerated testing. Cylindrical specimens were cast with iron sulfide aggregates distributed in four different size fractions, and deterioration was evaluated through resonance frequency based dynamic modulus, image-based crack length measurements, and microstructural analysis using SEM and XRD. The results clearly showed the influence of aggregate size. Specimens with 12.7 to 16 mm particles cracked earlier and lost stiffness more rapidly than those with 4.8 to 9.5 mm particles, while mixes prepared with only fine fractions remained macroscopically crack free at similar total sulfur. When coarse aggregate size was held constant, reducing sulfide content through partial replacement slowed deterioration. In this case, accumulated crack length decreased from about 2120 mm at 77 days to about 1470 mm at 112 days, and dynamic modulus loss declined from about 60 percent to about 20 percent over a comparable period. Microstructural analysis confirmed these findings by showing localized cracking around coarse inclusions and the presence of secondary expansive phases consistent with internal sulfate attack. Overall, the results demonstrate that both aggregate size and sulfide content govern deterioration: larger inclusions drive earlier cracking, while higher sulfide content accelerates the rate of damage.

***Keywords**: aggregate size; concrete deterioration; electrochemical acceleration; iron sulfide; pyrrhotite*

1. INTRODUCTION

Concrete containing aggregates with iron sulfide minerals such as pyrrhotite and pyrite has been shown to develop cracking and progressive damage in service [1]. This form of deterioration has been documented in several regions and is understood to proceed through the oxidation of iron sulfide inclusions followed by the formation of secondary sulfate phases that generate localized stress within the hardened matrix [2]. Although previous studies have described the chemical processes involved in iron sulfide oxidation, the influence of specific material characteristics that control the rate and severity of damage is still not well defined. Laboratory investigations have examined aspects of aggregate size and sulfide content [3], yet these factors have rarely been evaluated in bulk concrete under controlled conditions where their individual effects can be isolated.

Electrochemical accelerated testing (EAT) provides an effective way to address this gap because it promotes the oxidation of iron sulfide inclusions and allows deterioration to develop within a practical experimental timeframe [4]. When combined with nondestructive testing measurements and microstructural analysis, this approach enables the progression of damage to be monitored with good sensitivity and allows cracking patterns and secondary sulfate phases associated with internal sulfate related reactions to be identified.

The present study applies the EAT approach to quantify how aggregate size and sulfide content influence deterioration in concrete containing iron sulfide-bearing aggregates. The work compares coarse and fine size fractions and evaluates the effect of reducing sulfide content while keeping aggregate size constant. The findings provide new insight into how these parameters govern cracking behavior and stiffness loss in electrochemically accelerated deterioration.

2. EXPERIMENTAL PROGRAM

a. Materials and Mixes

Concrete specimens were prepared using ordinary Portland cement Type I/II conforming to ASTM C150 [5]. Two fine aggregates were used: river sand (RS) and an iron sulfide-bearing aggregate from Trois-Rivières, Quebec, Canada (CA1). The coarse aggregates consisted of the coarse fractions of CA1 and a locally sourced non-iron sulfide coarse aggregate (NP). Aggregates were separated into four size fractions to permit a structured evaluation of size effects. FR1 consisted of particles smaller than 1.18 mm, FR2 consisted of particles between 1.18 and 4.75 mm, FR3 contained particles between 4.75 and 9.5 mm, and FR4 contained particles between 12.7 and 16 mm. The measured total sulfur contents of the CA1 fractions were 1.39 ± 0.02 wt % for FR1, 1.19 ± 0.02 wt % for FR2, 1.18 ± 0.06 wt % for FR3, and 1.01 ± 0.04 wt % for FR4. In contrast, RS and NP exhibited low and relatively uniform sulfur contents of 0.04 ± 0.01 wt % and 0.06 ± 0.01 wt %, respectively. All mixtures were proportioned at a water to cement ratio of 0.60. Air content of approximately six percent was targeted using 0.9 g of air-entraining admixture per 1000 g of cement, based on trial testing, as summarized in Table 2.1.

Table 2.1: Weight-based mixture proportions

Cement	Water	Air entrainer	Fine aggregates		Coarse aggregates	
			FR 1	FR 2	FR 3	FR 4
1*	0.6	0.0009	1.02	1.02	1.02	1.02

* 386.5 kg/m^3

Cylindrical specimens measuring 76 by 152 mm were cast in accordance with ASTM C192 [6] as detailed in Table 2.2. Four concrete mixtures were prepared to isolate the influence of aggregate size and sulfide content. The labeling system follows the format P–X–CA1, where the number X indicates the aggregate fraction containing the iron sulfide-bearing CA1. For instance, P-1-CA1 contains CA1 only in FR1 and P-34-CA1 contains CA1 in both FR3 and FR4. P-34-CA1/NP follows the same coarse fraction pattern as P-34-CA1 but with CA1 partially replaced by NP to obtain a reduced sulfide content.

Table 2.2: Experimental parameters

Group	Specimen ID	Length (mm)			Aggregate size fractions (FR)				Duration (Days)	Study parameter
		1	2	3	FR 1	FR 2	FR 3	FR 4		
G1	P-1-CA1	147	147	147	CA1	RS	NP	NP	133	Aggregate size
	P-3-CA1	147	147	142	RS	RS	CA1	NP	133	
G2	P-34-CA1	137	132	145	RS	RS	CA1	CA1	77	Sulfide content
	P-34-CA1/NP	140	140		RS	RS	CA1/NP	CA1/NP	112	

After casting, specimens were cured for 13 days in a controlled curing chamber at 23 ± 2°C and 95% relative humidity, in accordance with ASTM C511 [7]. Their end faces were then ground, and the specimens were immersed in tap water for a limited duration of 24 hours, selected to ensure saturation of interconnected pores while minimizing potential leaching effects, resulting in a total curing period of 14 days. This curing duration was selected to allow sufficient hydration for specimen stability while enabling timely initiation of electrochemical accelerated testing.

b. Electrochemical accelerated testing

EAT followed the approach used in a previous investigation of iron sulfide induced deterioration [4], similar in principle to NT BUILD 492 and ASTM C1202 [8,9]. Specimens were mounted between two high-density polyethylene reservoirs containing 1.7 M sodium chloride at the cathode and 0.3 M sodium hydroxide at the anode. Perforated graphite electrodes were placed against the specimen faces to ensure uniform contact with the electrolyte solutions, and a constant 60 V direct current potential was applied across the specimen to promote ionic transport and accelerate oxidation of iron sulfide.

c. Resonance frequency and crack length measurements

Dynamic elastic modulus ($E_{dyn,c}$) was monitored using transverse resonance frequency measurements performed in accordance with ASTM C215 [10]. Three measurements were taken at 7-day interval and averaged to obtain the reported frequency.

Crack length was quantified through digital imaging following the method described in [4]. Photographs of the curved surface and end faces were captured at regular intervals, unwrapped into a continuous two-dimensional view, and analyzed using image processing software to determine total crack length.

d. Microstructural and phase analysis

Representative fragments from tested specimens were examined using scanning electron microscopy (SEM) to identify localized cracking, oxidation features, and reaction products. Imaging was performed in high vacuum mode at 10 kV and approximately 3.2 nA using secondary and backscattered electron detectors, with selected regions analyzed by EDS at 15 kV. Powdered materials prepared using a quartering procedure similar to ASTM C702 [11] were analyzed by x-ray diffraction (XRD). The XRD measurements were performed in Bragg Brentano mode from 5 to 75 degrees 2θ using a 0.015-degree step size and a scan speed of 2 degrees per minute. These observations were used to support the interpretation of cracking and stiffness loss measured during testing.

3. RESULTS AND DISCUSSIONS

a. Effect of aggregate size on damage, cracking, and stiffness

Figure 3.1 shows the visual evidence of deterioration observed in concrete mixtures containing iron sulfide aggregates under EAT. All mixtures with CA1 developed reddish brown staining and localized pop outs associated with oxidized iron sulfide-bearing particles on the end faces and specimen body.

Figure 3.1: Pictures of P-1-CA1 (left) and P-3-CA1 (middle) specimens after 133 days of EAT exposure, and the corresponding crack length increment data for P-3-CA1 (right)

The severity of this damage depended strongly on aggregate size. P-1-CA1, which contained CA1 only in FR1, exhibited discoloration and pop outs, but the extent of deterioration remained limited and no macroscopic cracking was observed at the end of testing. Under similar electrochemical conditions, P-3-CA1, which contained CA1 in FR3, exhibited visible cracking that initiated at oxidized coarse particles and propagated into the surrounding paste. The corresponding crack length data for the specimen shown in Figure 3.1 indicate a steady increase throughout the exposure period, reaching approximately 1730 mm by 133 days.

The $E_{dyn,c}$ results presented in Figure 3.2 further support the strong influence of aggregate size on deterioration. In P-1-CA1, $E_{dyn,c}$ increased during early exposure due to continued hydration and then remained relatively stable, consistent with the absence of macroscopic cracking. In contrast, mixtures with CA1 in coarse fractions exhibited clear reductions in $E_{dyn,c}$ after a short initial gain. In P-3-CA1, $E_{dyn,c}$ increased during early curing but then declined steadily, reflecting progressive stiffness loss associated with cracking.

These results demonstrate that aggregate size governs the severity of electrochemically accelerated deterioration in iron sulfide-containing concrete. Mixtures in which iron sulfide is concentrated in coarse particles exhibit faster crack initiation and more extensive damage than those in which reactive material is restricted to fine fractions with similar overall sulfur levels.

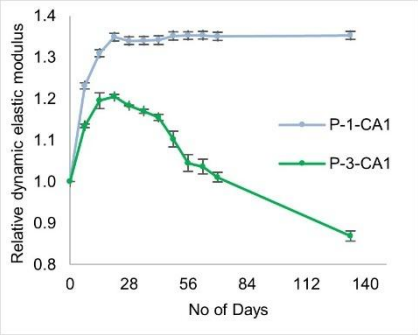

Figure 3.2: Relative $E_{dyn,c}$ plots for P-1-CA1 and P-3-CA1 specimens during EAT

b. Effect of sulfide content on damage, cracking, and stiffness

The influence of sulfide content was examined by preparing two mixtures with identical coarse aggregate sizes but different Total Sulfur (ST) levels. Although the values reported here represent total sulfur, supplementary WD XRF analysis of the CA1 aggregates confirmed that the sulfur within the aggregates was entirely in the sulfide form with no detectable sulfate. Since the sulfate contribution from cement was the same in all mixtures, variations in ST primarily reflect changes in the amount of sulfide-bearing CA1 added to the concrete. P-34-CA1, which contained CA1 in both FR3 and FR4, had an ST content of approximately 0.79 ± 0.02 wt.%. The reduced sulfide mixture, P-34-CA1/NP, in which CA1 was partially replaced with NP, had a lower ST content of approximately 0.44 ± 0.02 wt.%. For context, the mixtures in Section 3.1 (P-1-CA1 and P-3-CA1) had ST contents of 0.46 ± 0.02 and 0.48 ± 0.02 wt.%, respectively. These comparisons show that P-34-CA1 represents a distinctly higher sulfide condition, whereas P-34-CA1/NP contains sulfur levels comparable to P-1-CA1 and P-3-CA1.

Figure 3.3 presents representative images of the two mixtures as well as the corresponding crack length increments. Although both mixtures displayed surface discoloration and pop outs typical of iron sulfide oxidation, their deterioration progressed at noticeably different rates. P-34-CA1, which contained higher sulfide concentration, developed visible cracking within the first few weeks of exposure and reached a total crack length of approximately 2120 mm by 77 days. In contrast, P-34-CA1/NP exhibited a slower deterioration response. Cracking initiated later, and its rate of propagation was substantially lower, reaching about 1470 mm at 112 days.

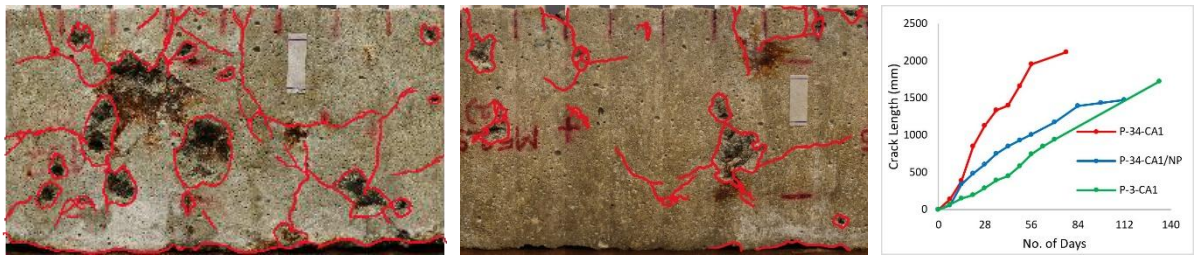

Figure 3.3: Pictures of P-34-CA1 (left) and P-34-CA1/NP (middle) specimens after 77 and 112 days of EAT exposure, respectively, and the corresponding crack length increment data (right)

A comparison to P-3-CA1 highlights that P-34-CA1 exhibited substantially greater deterioration, but this increase cannot be attributed to sulfide content alone because the mixture also introduced reactive CA1 into an additional coarse fraction. The combined change in both aggregate size distribution and sulfide level means that P-34-CA1 did not fully isolate the role of sulfide content. In contrast, P-34-CA1/NP retained the same coarse aggregate sizes as P-34-CA1 while reducing the sulfide content through partial NP replacement. This allowed the specific influence of sulfide level to be observed more clearly. P-34-CA1/NP showed a slower and less severe deterioration pattern, despite a longer exposure period.

The $E_{dyn,c}$ results shown in Figure 3.4 further support this trend. P-34-CA1 experienced a rapid decline in $E_{dyn,c}$, losing about 60 percent of its initial stiffness by day 77. This decline was larger and occurred earlier than in P-3-CA1, which exhibited a more gradual reduction in stiffness. In contrast, P-34-CA1/NP showed only a moderate decline of about 20 percent at 112 days, which is approximately one third of the loss measured in P-34-CA1 even though it remained under exposure for 35 additional days.

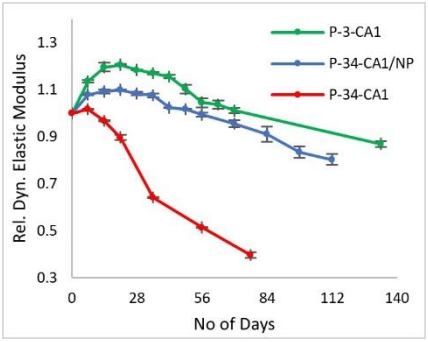

Figure 3.4: Relative $E_{dyn,c}$ plots for P-34-CA1 and P-34-CA1/NP specimens (P-3-CA1 included)

c. Microstructural and phase evidence

Microstructural and phase analysis support the trends observed in cracking and stiffness loss. Figure 3.5 (a) presents overlaid X-ray diffraction patterns for P-1-CA1, P-3-CA1, and P-34-CA1 after electrochemical exposure. P-1-CA1, which contained CA1 only in the fine fraction, showed stable hydration phases such as portlandite, ettringite, monosulfate, and Ca-rich zeolite, together with Friedel's and Kuzel's salts formed during chloride exposure [12]. This limited phase evolution aligns with the absence of visible cracking and the stable $E_{dyn,c}$ observed for this mixture.

In contrast, mixtures containing coarse CA1 exhibited clearer signatures of advanced chemical alteration. Both P-3-CA1 and P-34-CA1 showed higher calcite peak intensities and slight shifts in the Ca-rich zeolite peak, a change that has been associated with the formation of Na,Ca solid solution zeolites such as gismondine in alkaline environments [13]. In this study, the same shift was observed in mixtures that experienced greater deterioration, suggesting that the altered zeolite peak position may serve as an additional indicator of damage. Because cracking typically initiates where mineral transformation is most advanced, further XRD analyses were performed on selected popouts. These fragments contained iron sulfate phases such as ferrohexahydrite and romerite, confirming localized oxidation and sulfate-related reactions absent in P-1-CA1.

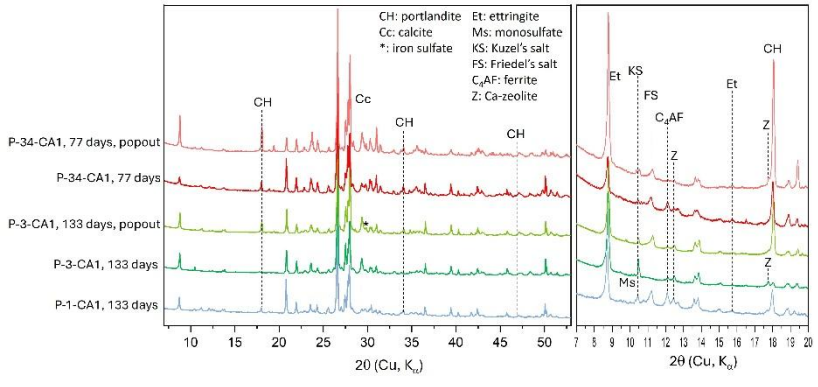

(a)

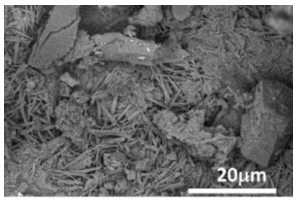

(b)

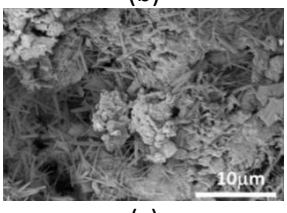

(c)

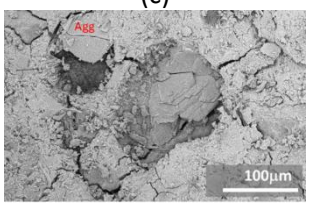

(d)

Figure 3.5: Overlaid X-ray diffraction patterns for P-1-CA1, P-3-CA1, and P-34-CA1 after EAT, showing stable hydration phases in P-1-CA1 and increased calcite and altered Ca-rich zeolite peaks in mixtures containing coarse CA1 (a); SEM images of P-3-CA1 showing the transition from ettringite primarily within pores to a disrupted matrix filled with expansion products after 133 days (b-c); P-34-CA1 showing coarse aggregates surrounded by fibrous expansion phases and microcracking

SEM observations support the XRD results. Figure 3.5 (b-d) shows images of P-3-CA1 and P-34-CA1 after EAT. For P-3-CA1, needle-like ettringite that was initially confined within pores became widespread after 133 days, with expansion products filling the matrix and disrupting the surrounding paste. For P-34-CA1, coarse aggregates were bordered by fibrous reaction products extending into the matrix and nearby pores, and microcracks were frequently observed around these regions. These microstructural features correspond directly to the higher crack lengths and greater stiffness loss measured in mixtures containing coarse CA1, in contrast to the minimal deterioration observed in mixtures with only fine CA1.

4. CONCLUSION

The experimental findings show how aggregate size and sulfide content govern the deterioration of concrete containing iron sulfide aggregates under EAT. The following conclusions can be drawn:

- **Aggregate size controlled deterioration severity:** Specimens containing CA1 only in the fine fraction (P-1-CA1) showed discoloration and pop outs but remained macroscopically crack free, while mixtures containing CA1 in a coarse fraction (P-3-CA1) developed visible cracking and experienced measurable $E_{dyn,c}$ loss under the same electrochemical conditions.
- **Sulfide content influenced deterioration when coarse aggregate size was fixed:** P-34-CA1, which contained CA1 in both coarse fractions and had a higher total sulfur level, deteriorated rapidly, reaching about 2120 mm of crack length and losing roughly 60 percent of its initial $E_{dyn,c}$ by 77 days. When the sulfide content was reduced through partial replacement with NP (P-34-CA1/NP), deterioration progressed more slowly, with crack length limited to about 1470 mm at 112 days and $E_{dyn,c}$ loss reduced to roughly 20 percent.
- **Microstructural observations supported the mechanical response:** Mixtures containing coarse CA1 exhibited localized cracking around reactive particles, fibrous expansion products extending into the surrounding paste, and secondary sulfate phases in popout fragments, whereas mixtures containing only fine CA1 showed stable hydration phases and limited alteration, consistent with their minimal deterioration during EAT.
- **Combined effects of aggregate size and sulfide level determine overall performance:** Coarse reactive inclusions promote early cracking through localized expansion, and higher sulfide content increases the rate of damage accumulation. Both parameters must therefore be considered when evaluating durability risks associated with iron sulfide-bearing aggregates.

REFERENCES

[1] R. Zhong, K. Wille, Deterioration of residential concrete foundations: The role of pyrrhotite-bearing aggregate, Cem. Concr. Compos. 94 (2018) 53–61.
[2] J. Duchesne, B. Fournier, Deterioration of concrete by the oxidation of sulphide minerals in the aggregate, J. Civ. Eng. Archit. 7 (2013) 922–931.
[3] L. Santos, M. Chrysochoou, K. Wille, Development of a risk assessment framework for pyrrhotite induced deterioration of concrete foundations in CT and MA, Cem. Concr. Res. 197 (2025) 107951.
[4] M. Ojo, D. Kim, L. Frame, K. Wille, Electrochemical investigation of accelerated deterioration of concrete with iron-sulfide containing aggregates, Cem. Concr. Res. 182 (2024).
[5] C01 Committee, ASTM C150/C150M-22, Specification for portland cement, ASTM International. (2022).
[6] C09 Committee, ASTM C192/C192M-19, Practice for making and curing concrete test specimens in the laboratory, ASTM International. 10 (2020).
[7] C01 Committee, ASTM C511-21, Specification for mixing rooms, moist cabinets, moist rooms, and water storage tanks used in the testing of hydraulic cements and concretes, ASTM International. (2021).
[8] NT BUILD 492 Concrete, mortar and cement-based repair materials: chloride migration coefficient from non-steady-state migration experiments, (1999).
[9] C09 Committee, ASTM C1202-22, Test method for electrical indication of concretes ability to resist chloride ion penetration, ASTM International. (2022).
[10] C09 Committee, ASTM C215-19, Test method for fundamental transverse, longitudinal, and torsional resonant frequencies of concrete specimens, ASTM International. (2020).
[11] C09 Committee, ASTM C702/C702M−18, Standard practice for reducing samples of aggregate to testing size, ASTM International. (2018).
[12] K. Scrivener, R. Snellings, B. Lothenbach, C. Press, A practical guide to microstructural analysis of cementitious materials, CRC press Boca Raton, FL, USA:, 2016.
[13] M.U. Okoronkwo, S.K. Mondal, B. Wang, H. Ma, A. Kumar, Formation and stability of gismondine-type zeolite in cementitious systems, J Am. Ceram. Soc. 104 (2021) 1513–1525.

Phase Transformations during Electrochemically Accelerated Testing and Deterioration of Concrete with Pyrrhotite-bearing Aggregates

Auishe Pauline Corraya [(1)], Meshach Ojo [(2)], Darcel Courtney [(3)], Shalini Devi Tulasi Ravikumar [(4)], Kay Wille [(5)], Lesley Frame [(6)]

(1) University of Connecticut, Storrs, United States, auishe_pauline.corraya@uconn.edu
(2) meshach.ojo@uconn.edu (3) darcel.courtney@uconn.edu (4) kea24004@uconn.edu
(5) kay.wille@uconn.edu (6) lesley.frame@uconn.edu

Abstract

Pyrrhotite-containing concrete foundations are crumbling worldwide. The aggregate and matrix phases are subjected to hydration, oxidation, and carbonation over the course of the concrete lifetime. Therefore, a concrete foundation's severity of deterioration might be indicated by observing the phase transformations and mineral assemblages over time. Our approach involved electrochemically accelerated testing (EAT) of concrete cylinders with pyrrhotite-bearing aggregates that were sourced from Trois-Rivières, Quebec, Canada. The test was performed at 60 V with exposure to 1.7 M NaCl and 0.3 M NaOH solution to observe the time dependent deterioration. The duration of testing was varied to include no exposure, 35 day and 77 day exposure, as well as pop-outs collected during the testing. Scanning electron microscopy (SEM) and thin section petrography for microstructural analysis and X-ray diffraction (XRD) for phase analysis were performed on the samples. Our results suggest that the calcite forming during later-stage carbonation displays a rhombohedral crystal habit rather than the classic scalenohedral form. Our analyses show that geological pyrrhotite oxidation is influenced by adjacent minerals in the aggregate, whereas EAT exposure promotes oxidation largely independent of surrounding phases. Our research will help to identify microstructural indicators of early signs deterioration for foundations testing positive for pyrrhotite. Our technical approach will contribute to the development of testing standards and analytical tools required for reliable detection, characterization, and prediction of pyrrhotite-related concrete deterioration processes.

***Keywords**: concrete deterioration, electrochemically accelerated testing, phase assemblage, pyrrhotite-containing aggregates, thin section petrograph*

1. INTRODUCTION

Deterioration of pyrrhotite-containing concrete foundations has become one of the most concerning material failures for homeowners. Signs of damage become apparent as early as 2-4 years after construction in Trois-Rivières, Quebec, Canada and within 15-30 years in northeastern Connecticut [1, 2]. With current methods, once the damage becomes visible, it is deemed irreversible, at which point the only solution available is to replace the entire foundation [1].

Electrochemically accelerated testing (EAT) is used in concrete cylinders in the laboratory to accelerate the concrete deterioration process while ensuring replication of field conditions [1, 3]. Despite multiple studies on phase evolution during degradation of pyrrhotite-containing concrete, early-stage microstructural evolution prior to onset of extensive damage remains unclear [4]. Similarly, while there exist studies on the impact of mineral assemblage on pyrrhotite oxidation in field samples, the changing role of these minerals through the deterioration process is not well understood [5].

In the current study, we evaluate changes in calcite crystal habit during the EAT exposure, and we investigate the mineral assemblage of pyrrhotite-bearing aggregates to determine oxygen pathways through the cement and adjacent minerals (e.g., biotite). Our current project explores the potential of calcite morphology as well as the extent of oxidation of pyrrhotite as early-stage microstructural indicators of damage in pyrrhotite containing concrete foundations, which could help assess future foundation failure, even for homes that currently show limited macroscopic damage.

2. MATERIALS AND METHODS

a. Concrete mix and electrochemical accelerated testing

Ordinary Portland cement (OPC) type I/II as per ASTM C150/C150M-22 with the chemical composition reported in Table 2.1 was used to cast three cylindrical concrete samples of 76 mm diameter by 152 mm length following ASTM C192/C192M-19 for the current study [6, 7].

Table 2.1: Weight percentage chemical composition of the used ordinary Portland cement

SiO_2	Al_2O_3	Fe_2O_3	CaO	MgO	SO_3	Na_2O	K_2O
18.7	5.35	4.69	61.5	2.67	3.30	0.40	0.97

Four equal fractions of different particle sizes were used for fine (river sand, RS) and coarse (iron sulfide-containing aggregates from Trois-Rivières, Quebec-CA1) aggregates (Table 2.2). The sample mixture design for P-34-CA1 sample contained fractions 1 and 2 of river sand and fractions 3 and 4 of pyrrhotite containing CA1 aggregates. The CA1 aggregate was of diorite rock type. The cement content was 386.5 kg/m^3 and the water-cement ratio was 0.6. Thereafter, sample curing was conducted for 13 days at room temperature (23 ± 2°C) and 95% relative humidity.

Table 2.2: Aggregate particle size and sample mixture details

	Fine aggregates	Fine aggregates	Coarse aggregates	Coarse aggregates
Fraction sizes	FR 1	FR 2	FR 3	FR 4
Particle sizes (mm)	<1.18	1.18 - 4.75	4.75 - 9.5	12.7 - 16
Sieve sizes	<#16	#16 - #4	#4 - 3/8”	1/2” - 5/8”
P-34-CA1 sample	RS	RS	CA1	CA1

The cured concrete cylinders were placed into a setup for electrochemical acceleration testing as described by Ojo *et al.* [1]. In this setup, cylindrical concrete samples were held between two high-density polyethylene (HDPE) reservoirs filled with 1.7 M sodium chloride (NaCl) solution and 0.3 M sodium hydroxide (NaOH) solution and maintained at 60 V DC (Model 1685B, B&K Precision, California, USA). The exposure durations for the three cylinders were 0 day, 35 day, and 77 day. Solutions were changed weekly, and the samples were monitored for cracking throughout the test period.

b. Sampling method

Fragments that popped out of the cylinder during the electrochemical test due to cracking were collected for characterization (so-called, “pop-outs”). After EAT exposure, each concrete cylinder was fractured in half longitudinally using a compression testing machine (Model # HCM-2500-H, HUMBOLDT, USA). One half was jaw crushed to prepare samples for scanning electron microscopy (SEM) and X-ray diffraction (XRD), while the other half was used for thin section analysis. The sample splitting method outlined in ASTM C702/C702M-18 [8] was used for sampling. A sample split portion of the crushed cylinder fragments were further ground to fully pass through a #60 sieve. The #60 powder was further sample split for XRD.

c. Microstructure and phase analysis

The pop-outs were mounted on standard sized aluminum SEM stubs using carbon tape and coated with up to 10 nm Au/Pd for SEM imaging (Teneo, FEI, USA). XRD powder samples were prepared by grinding the #60 powder with an agate mortar and pestle and passing through a #200 sieve to obtain a maximum particle size of 75 µm. An X-ray diffractometer equipped with a rotating Cu anode (SmartLab, Rigaku, USA) in Bragg Brentano mode was used over a 2θ range of 5º - 53º. A 0.0150º step size at 2º/min was used with the scattering screen at 2-3 mm above the sample. Thin sections were prepared

from the approximate center of the uncrushed half-cylinder samples. Sampling was done using a diamond wet tile saw (QEP, USA) and allowed to dry overnight at room temperature. Petrographic thin sections were prepared by the National Petrographic Service, Inc. (TX, USA). Samples were epoxy impregnated and ground in water to final polish. An optical microscope (Zeiss AxioImager A2, USA) was used for the petrographic analysis of the samples under reflected and transmitted light.

3. RESULTS AND DISCUSSION

a. Concrete phase characterization

Phase assemblage of the initial (day 0), intermediate (35 day), and full test period (77 day) samples were compared using XRD (Figure 3.1). The initial pattern has a small calcite peak at 29.42° (Cc) compared to the much larger peaks for the 35 day sample, while the 77 day sample shows a small calcite peak. The small calcite peak in the not accelerated sample indicates low oxidation and carbonation, which increases in the 35 day with degradation of the pyrrhotite-containing concrete sample, agreeing with the thermodynamic model by Leemann *et al* [4]. The small calcite peak in the 77 day sample may be indicative of limited carbonation. The pop-out specimens exhibit pronounced calcite peaks. Because these fragments were necessarily extracted from regions of greatest visible distress (and therefore, presumably, the highest local degrees of oxidation and subsequent carbonation), elevated signatures of carbonation are expected. This is supported by the markedly higher calcite peaks observed for the 77-day pop-out relative to its corresponding bulk specimen. Notably, the 28-day pop-out also shows strong calcite peaks, indicating that localized carbonation can develop early in highly damaged zones. Overall, the pop-out specimens capture the strongly heterogeneous and spatially localized nature of oxidation and carbonation related damage within the test samples.

Biotite (Bt), quartz (Q), and plagioclase feldspar (albite (Al), bytownite (B), oligoclase (O)) are present from the aggregates, while calcite (Cc) and portlandite (CH) represent the primary cement matrix contributions. The total sulfur of this mix was 0.79 wt%, which is typical of many field samples [1]. The relatively low Po in CA1 aggregate is not detectable with XRD of the concrete samples. There was no significant change to Cc or CH over the test period despite cracking in the 35 day and 77 day samples.

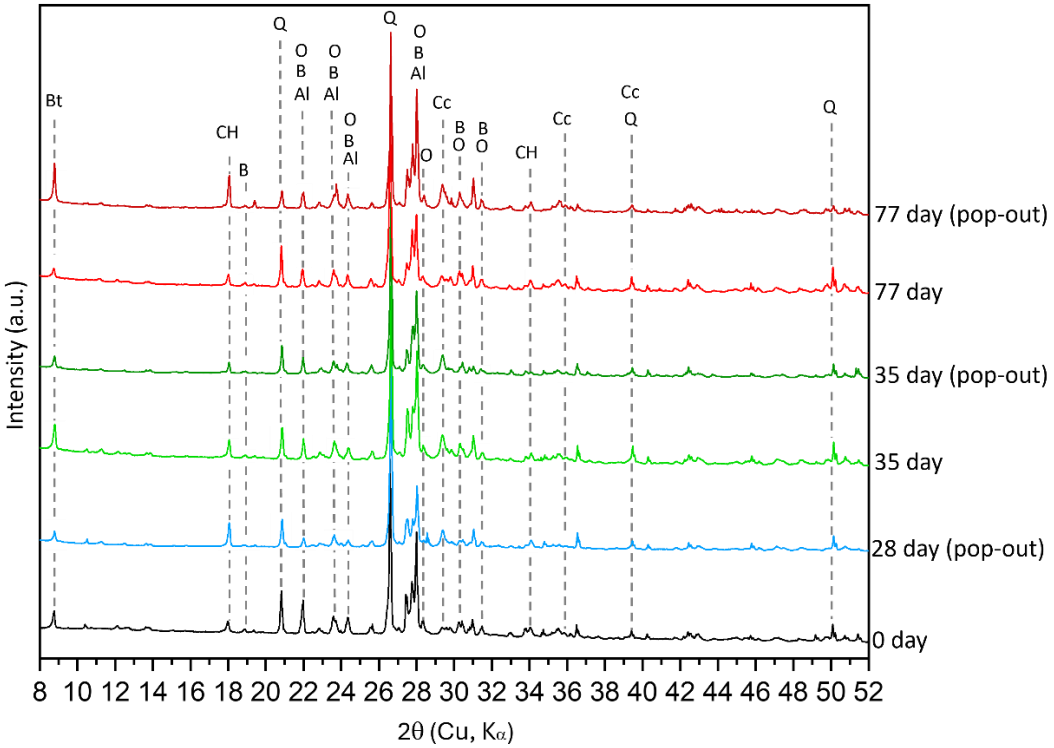

Figure 3.1: XRD pattern of P-34-CA1 samples of different oxidation and carbonation phases (Bt-biotite (9002307), CH-portlandite (9000113), Q-quartz (5000035), Al-albite (9000526), B-bytownite (9011200), O-oligoclase (9011423), Cc-calcite (45024421)).

Two different crystal habits of calcite were observed with SEM analysis (Figure 3.2) of the 28 day popout. Multiple clusters of scalenohedral calcite are seen in the BSE (backscattered electron) image (Figure 3.2a) as well as a rhombohedral calcite cluster inside the indicated region of the SE (secondary electron) image (Figure 3.2b). The presence of calcite is in agreement with the XRD patterns (Figure 3.1), but it is not possible to distinguish between rhombohedral or scalenohedral calcite crystal habits from XRD alone. The presence of calcite in the popouts aligns with Cizer *et al.* findings that scalenohedral calcite precipitates under excess Ca^{2+} and with full consumption of Ca^{2+}, dissolution of calcite results into rhombohedral calcite precipitation as carbonation proceeds [9]. The observation of rhombohedral calcite crystal habit does not unequivocally prove that calcite structure changes with later stage oxidation or through carbonation, but the different crystal habits suggest different precipitation conditions. It has been established by others that high Ca^{2+} concentration will lead to rhombohedral crystal habit [10]. The pH and ion concentration of the pore solution is likely to drive the precipitation and growth kinetics of the calcite forming during later stage oxidation and during carbonation.

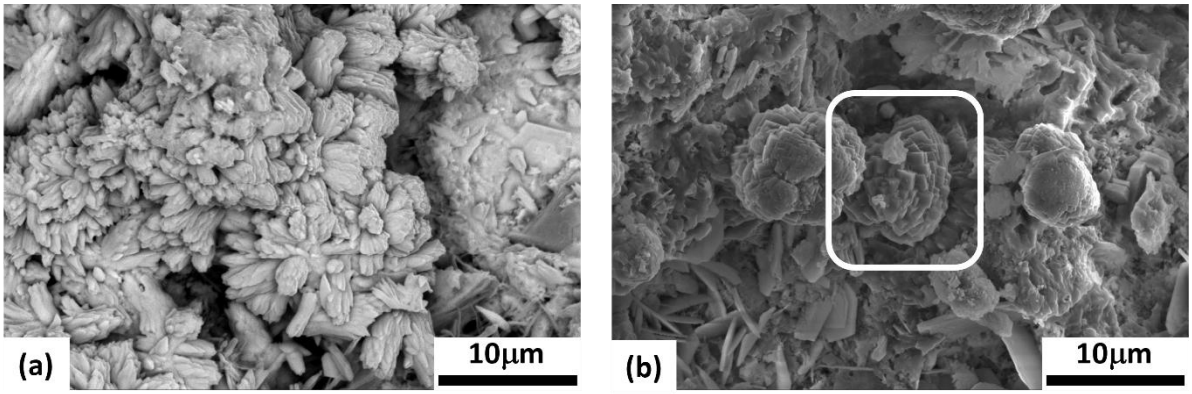

Figure 6.2: SEM of 28 day pop-out of P-34-CA1 sample showing presence of (a) scalenohedral calcite, through-the-lens BSE image, 10 kV and (b) rhombohedral calcite, ETD-SE image, 10 kV.

b. Relative position of pyrrhotite within aggregate

Because CA1 aggregate is sourced from diorite, plagioclase feldspar with little or no quartz and moderate amount of mafic minerals (such as biotite, amphibole, and pyroxene) are expected [11]. The iron sulfides present in the CA1 aggregates are mostly pyrrhotite (2.21 volume%) with less amount of pyrite (1.27 volume %) and trace amounts of chalcopyrite (0.05 volume%) as determined by point counting of aggregate petrographic thin sections. Within the concrete test sample, the iron sulfides are surrounded by plagioclase feldspar, biotite, and the cement matrix phase (Figure 3.3 and Figure 3.4). The petrographic characterization of unexposed concrete establishes a baseline of pyrrhotite position and degree of prior oxidation relative to other aggregate mineral phases and the cement matrix. Examination of EAT exposed samples allows comparative determination of the extent of oxidation in Pyrrhotite.

The petrographic images of the untested sample (0 days), displayed under reflected light, plane polarized light and cross polarized light, are shown in each row of Figure 3.3. The reflected light image (Figure 3.3a) illustrates oxidized portions of pyrrhotite that have occurred prior to EAT—most likely geologically induced oxidation. The transmitted light images (Figures 3.3b and 3.3c) demonstrate that pyrrhotite is surrounded by biotite, altered feldspar, hornblende, and cement matrix. We can only observe two-dimensional slices of the concrete volume with petrographic analysis, so the minerals adjacent to Po out-of-plane are unknown to us; meaning that ion mobility within the mineral assemblage cannot be determined from petrographic analysis alone.

In the second row of Figure 3.3, oxidation of pyrrhotite in the untested sample is also observed in regions devoid of biotite (Figures 3.3d-f). Here, the iron sulfide is surrounded by feldspar and the cement matrix with several air voids. The oxidation present in this iron sulfide was caused geologically or possibly during curing of the concrete. Geological occurrence of the oxidation is more likely due to the short period (13 days) for curing.

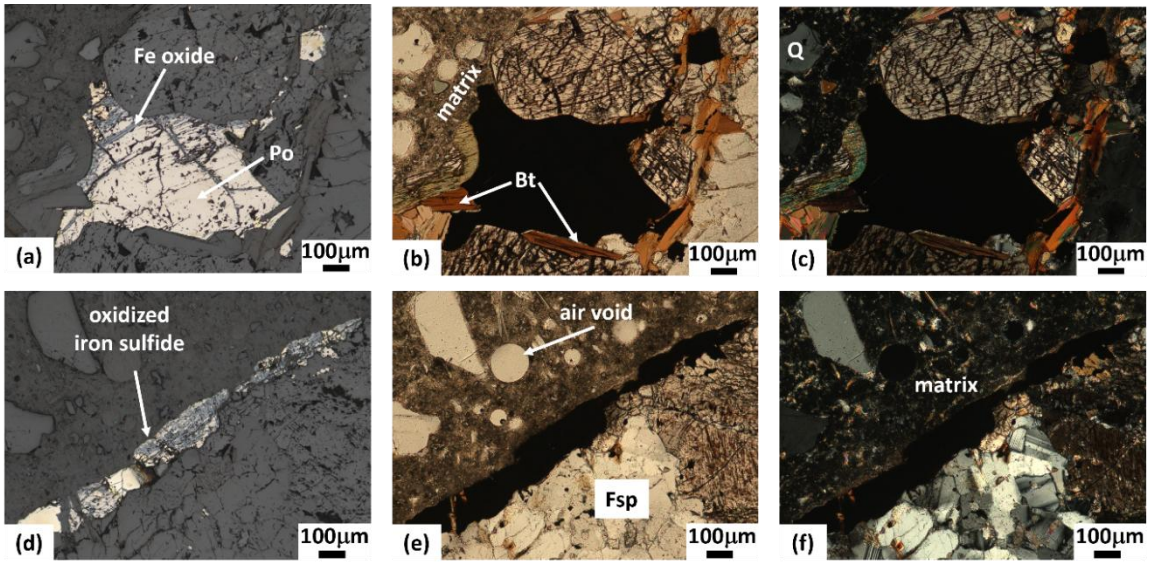

Figure 3.3: Thin section petrographic images of untested P-34-CA1 sample with particular focus on oxidized iron sulfides and its surroundings; (a) and (d) reflected light images, (b) and (e) plane polarized transmitted light images, (c) and (f) cross polarized transmitted light images.
Key: Po (Pyrrhotite), Bt (Biotite), Fsp (Feldspar), Q (Quartz)

The petrographic images of the tested (77 day) P-34-CA1 sample are displayed under reflected light, plane polarized light and cross polarized light in each row (Figure 3.4). Iron sulfides in direct contact with biotite are shown in Figure 3.4a-c, whereas iron sulfides without direct biotite in contact are shown in Figures 3.4d-f. The iron sulfides in the tested sample appear to display more extensive oxidation than the 0 day sample (Figures 3.4a and 3.4d). Oxidation is observed largely along the exterior of the iron sulfide adjacent to biotite (Figures 3.4a-c), which may have accelerated deleterious reactions and supporting the claim reported by Titon *et al.* [5]. A very damaged oxidized iron sulfide is surrounded by feldspar with reddish-brown oxidation stains, which can be explained by the application of EAT method (Figures 3.4d-f). The reddish hue surrounding the oxidized iron sulfide (Figure 3.4d) is due to the oxidized iron sulfide below the reflected light surface, while in the transmitted light image we can see the area underneath the surface too, and therefore the subtle glow is opaque in Figures 3.4e and 3.4f.

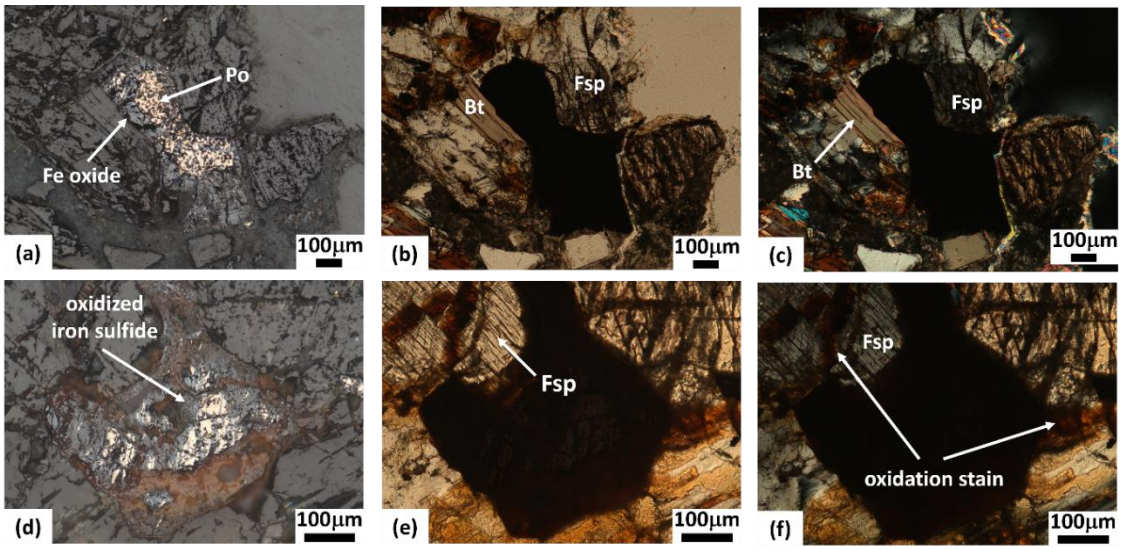

Figure 3.4: Thin section petrographic images of 77 day tested P-34-CA1 sample with particular focus on oxidized iron sulfides with and without adjacent biotite; (a) and (d) reflected light images, (b) and (e) plane polarized transmitted light images, (c) and (f) cross polarized transmitted light images.
Key: Po (Pyrrhotite), Bt (Biotite), Fsp (Feldspar)

4. CONCLUSIONS AND FUTURE WORK

The aim of our work is to identify early-stage microstructural indicators before widespread deterioration in pyrrhotite containing concrete during EAT exposure. As a result of the current study, the following conclusions can be drawn:

- Calcite is present throughout the test period (as shown with XRD data), but the calcite crystal habit is not consistent for all instances of calcite precipitation. The crystal habit may be driven by the local pore solution chemistry and rhombohedral calcite is a promising candidate as an early stage microstructural indicator for oxidation damage.
- EAT exposure results in greater pyrrhotite oxidation regardless of initial oxidation of the iron sulfide mineral and regardless of surrounding mineralogy. The increase in the extent of pyrrhotite oxidation indicates deterioration of concrete. The relative effects of surrounding minerals in oxidizing pyrrhotite need further investigation as this current study continues with a larger dataset.

5. ACKNOWLEDGMENT

The authors acknowledge National Institute of Standards and Technology, CAMMA Lab and X-Ray Lab at University of Connecticut for all their support. Thanks to Dr. T. Byrne, Dr. D. Morales, Dr. S. March, Dr. L. Zhang, Dr. L. Santos, A. Vieira Rocha, A. Dahal, and M. Tareq for their valuable insights and discussions.

6. REFERENCES

1. Ojo M, Kim D, Frame L, Wille K (2024) Electrochemical investigation of accelerated deterioration of concrete with iron-sulfide containing aggregates. Cement and Concrete Research 182:107570. https://doi.org/10.1016/j.cemconres.2024.107570

2. Zhong R, Wille K (2018) Deterioration of residential concrete foundations: The role of pyrrhotite-bearing aggregate. Cement and Concrete Composites 94:53–61. https://doi.org/10.1016/j.cemconcomp.2018.08.012

3. Araiza RC, Fournier B, Duchesne J, Rodrigues A (2023) Electrochemical activation of oxidation of sulfide-bearing aggregates in concrete specimens. Cement and Concrete Research 170:107186

4. Leemann A, Lothenbach B, Münch B, et al (2023) The “mica crisis” in Donegal, Ireland–A case of internal sulfate attack? Cement and Concrete Research 168:107149

5. Titon B, Duchesne J, Fournier B (2024) The role of biotite in the deterioration of pyrrhotite within concrete aggregates: Trois-Rivières case study. Cement and Concrete Research 183:107595. https://doi.org/10.1016/j.cemconres.2024.107595

6. ASTM Committee C01 (2022) Standard Specification for Portland Cement. ASTM International, West Conshohocken, PA

7. Fuller WB, Thompson SE (1907) The Laws of Proportioning Concrete. T Am Soc Civ Eng 59:67–143. https://doi.org/10.1061/TACEAT.0001979

8. ASTM Committee C09 (2018) Standard Practice for Reducing Samples of Aggregate to Testing Size. ASTM International, West Conshohocken, PA

9. Cizer Ö, Rodriguez-Navarro C, Ruiz-Agudo E, et al (2012) Phase and morphology evolution of calcium carbonate precipitated by carbonation of hydrated lime. J Mater Sci 47:6151–6165. https://doi.org/10.1007/s10853-012-6535-7

10. Kirov GK, Vesselinov I, Cherneva Z (1972) Conditions of Formation of Calcite Crystals of Tabular and Acute Rhombohedral Habits. Cryst Res and Technol 7:497–509. https://doi.org/10.1002/crat.19720070503

11. Press F, Siever R (2001) Understanding Earth. W.H. Freeman

Evaluating sampling strategy for electrochemical accelerated testing of sulfide-bearing concrete

Shalini Devi Tulasi Ravikumar [(1)], Meshach Ojo [(2)], Darcel Courtney [(3)], Auishe Pauline Corraya [(4)], Kay Wille [(5)], Lesley D Frame [(6)]

(1) University of Connecticut, Storrs, United States, kea24004@uconn.edu
(2)meshach.ojo@uconn.edu, (3)darcel.courtney@uconn.edu, (4)auishe_pauline.corraya@uconn.edu
(5) kay.wille@uconn.edu, (6) *lesley.frame@uconn.edu*

Abstract

Premature deterioration of concrete foundations has been attributed to the oxidation of pyrrhotite-bearing aggregates leading to significant structural and economic consequences. As deterioration progresses slowly in field conditions, accelerated laboratory methods such as Electrochemical Accelerated Testing (EAT) are used to rapidly simulate degradation under controlled conditions. The current study evaluates deterioration patterns in concrete cylinders incorporating sulfide-bearing aggregates exposed to four electrolyte configurations (NaCl/NaOH, NaOH/NaCl, NaOH/NaOH, and NaCl/NaCl) applied at anodic and cathodic ends of the test specimen during EAT. Post-exposure examination revealed spatial variation in deterioration, as indicated by pH shifts and mineralogical differences detected via X-ray Diffraction. Calcite initially present at specimen surfaces persisted following NaCl/NaOH, NaOH/NaCl, and NaOH/NaOH exposures, but exhibited substantial redistribution under NaCl/NaCl conditions, indicating distinct deterioration mechanisms driven by electrolyte exposure. Findings emphasize the need to account for localized damage when interpreting accelerated test outcomes and provide insights toward refining laboratory protocols to better mimic field deterioration mechanisms and ultimately identify deterioration mechanisms and kinetics.

Keywords: *concrete deterioration, electrochemical accelerated testing, chloride exposure, oxidation-carbonation, sulfide-bearing aggregates*.

1. INTRODUCTION

Iron sulfide-containing aggregates have been widely recognized for their detrimental impact on concrete durability. When non-stochiometric pyrrhotite ($Fe_{1-x}S$, x = 0 to 0.125) oxidizes in the presence of moisture and oxygen, it releases sulfate ions that react with cement hydration products, forming expansive phases such as gypsum, ettringite, and thaumasite. The expansive phases can exceed twice the volume of the reactants, generating internal stresses that cause swelling, cracking, and progressive structural failure [1-4]. Pyrrhotite-related deterioration is a critical concern in Eastern Connecticut and South-eastern Canada, where pyrrhotite-bearing aggregates have been used in residential construction over the past few decades. Thousands of homes have deteriorated prematurely, and complete foundation replacement, costing over $200,000 per house, is the most common remediation option [5]. The high cost and intrusive nature of foundation replacement are driving the urgent need for scientific understanding of the underlying deterioration mechanisms to support the development of reliable alternative mitigation strategies.

Direct investigation of field-damaged foundations is challenging because deterioration typically takes 10-15 years to manifest in Connecticut and 3-5 years in the Trois-Rivières regions of Canada [1]. To overcome this limitation, recent studies have used electrochemical accelerated testing (EAT) to replicate long-term damage under controlled laboratory conditions [6-8]. Exposure to voltage and NaCl and NaOH electrolyte solution (the EAT approach) successfully promotes oxidation of iron sulfide minerals, but the mechanisms driving deterioration remain uncertain. Araizo et al. [6] proposed that chloride initiates oxidation through corrosion-like electrochemical phenomenon. In contrast, a recent study by the current authors suggested that chlorides primarily function as charge carriers rather than directly reacting with iron sulfide minerals [8]. Adding to the complexity, the current authors [8] observed that the NaOH side of their electrochemical setup became highly acidic over time, unexpectedly eroding the concrete face

at the NaOH end. The acidity-induced damage raises concerns about the uniformity of deterioration during EAT and the relevance of laboratory testing to “real-world” scenarios, where such reactions are unlikely to occur. Furthermore, faster deterioration was reported in setups using NaCl on both ends (NaCl (-)/NaCl (+)) compared to the conventional NaCl (-)/NaOH (+) configuration [8], as outlined in the NT BUILD 492 1999 [9] and ASTM C1202-22 [10] standards. These observations indicate that electrolyte configuration, rather than chloride content alone, governs deterioration pathways.

The present study investigates the influence of various electrolyte combinations on deterioration patterns induced by EAT in concrete containing iron-sulfide aggregates. Beyond the standard NaCl (-)/NaOH (+) configuration, alternative setups, including NaCl (-)/NaCl (+), NaOH (-)/NaOH (+), and NaOH (-)/NaCl (+), were tested. Chemical gradients were interpreted using pH measurements, and corresponding mineralogical changes were characterized through X-ray powder diffraction (XRD). The findings clarify spatial distributions of deterioration and damage under each configuration, providing insight into reaction mechanisms and guiding future optimization of EAT as a research tool, contributing to the eventual development of cost-effective mitigation strategies.

2. MATERIALS & METHODS

a. Electrochemical Accelerated Testing

i. Concrete Mix Design

The mixture incorporated Type I/II Ordinary Portland Cement (ASTM C150), river sand (RS) as fine aggregate, and pyrrhotite-bearing coarse aggregate (CA1) sourced from Trois-Rivières, Canada. Fine aggregate (RS) was divided into two gradation fractions: FR1 (<1.18 mm) and FR2 (1.18–4.75 mm), while coarse aggregate (CA1) consisted of FR3 (4.8–9.5 mm) and FR4 (12.7–16 mm). Cylindrical specimens (76 mm × 152 mm), cast per ASTM C192/C192M–19, used a water-to-cement ratio of 0.6, and followed Fuller and Thompson’s packing model (n = 0.45) [11]. Cement accounted for 20% of total solids (386.5 kg/m³), and all aggregate fractions were incorporated at equal volume proportions. Air content was maintained between 6–8% using an air-entraining admixture (MasterBuilder Solutions Air Entrainer). Four identical specimens were prepared and subsequently exposed to different electrolyte conditions.

ii. Exposure Conditions

The experimental setup followed a previously established EAT configuration as illustrated in Figure 2.1a [8]. Four electrolyte configurations were tested: NaCl/NaOH, NaOH/NaCl, NaOH/NaOH, and NaCl/NaCl, where the notation refers to cathodic/anodic terminals, respectively. Electrolytes consisted of 1.7 M Sodium Chloride (NaCl) and 0.3 M Sodium Hydroxide (NaOH) solutions, prepared according to NT BUILD 492 (1999) [9]. The NaCl/NaOH configuration represents the standard EAT setup used in prior studies based on the Rapid Chlorine Penetration Test (RCPT) principle [12] and was tested for 19 days. In contrast, the reversed polarity NaOH/NaCl setup experienced rapid deterioration and could not remain in the test setup beyond 3 days due to severe cracking. NaOH/NaOH and NaCl/NaCl were tested for 21 days. Each assembly was powered by a regulated 60V DC supply (Model 1685B, B&K Precision, California, USA) using 18 AWG banana-to-alligator clip patch cords. The applied electric field induced electrolyte polarization, driving ionic species (e.g., Cl^-, OH^-) through the concrete toward the counter electrode, thereby accelerating deterioration via oxidation, leaching, and carbonation.

b. Compositional Analysis

Following the EAT, the concrete cylinders were split longitudinally into two halves using a hydraulic press to expose the interior matrix. From each half-cylinder, 23 sampling spots (each labeled based on alpha-numeric matrix) were selected to represent the entire cross-section. These included: electrolyte-facing ends: 1A, 1C, 1E, 7A, 7C, 7E, middle matrix region: 2C, 3C, 4B, 4C, 4D, 5C, 6C and outer edges: 2A, 2E, 3A, 3E, 4A, 4E, 5A, 5E, 6A, 6E (Fig. 2.1: b). Samples were extracted using a rotary engraver equipped with a carbide-tipped bit (Dremel engraver, 290-01, 120V), ensuring localized extraction and minimizing cross-contamination. Large aggregates were avoided during sampling to optimize collection of the cement matrix.

Powders from each location ranged from 0.7 – 1.0 g. These were split to provide 0.1 g that was dispersed in 20 mL of deionized water. pH was measured for the suspensions at 15 min intervals using a calibrated benchtop meter (Model PHH-7200, Omega). Since pH values stabilized after two intervals, 45 min readings were taken as representative to assess chemical gradients across exposure conditions. For phase analysis, remaining powders were manually ground and sieved to <75 µm (#200 mesh). Phase identification was conducted using an x-ray diffractometer equipped with rotating Cu-anode (SmartLab, Rigaku) in Bragg–Brentano configuration with a scattering screen 2 mm above the powder sample, over a 2θ range of 5 - 75° with a step size of 0.015° and a scan speed of 4°/min.

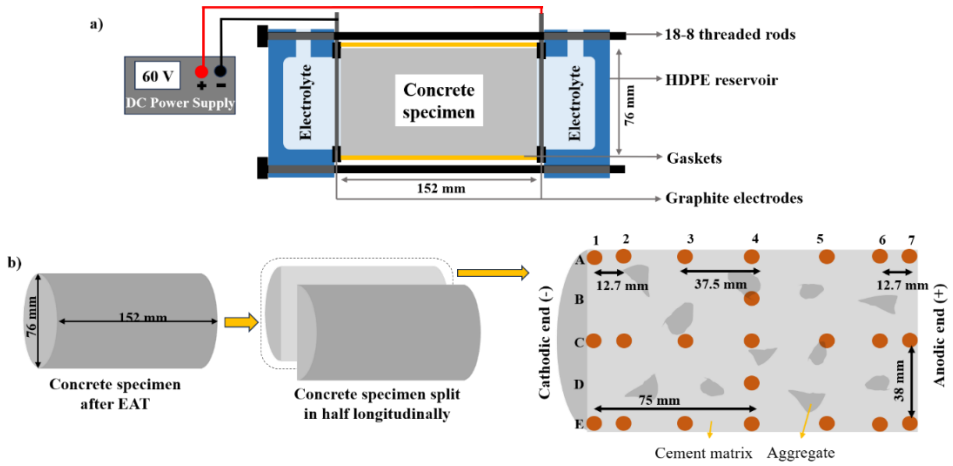

Figure 2.1: (a) Schematic representation of the EAT setup (b) Location and spacing of the spots considered for compositional analysis.

3. RESULTS AND DISCUSSION

For the four exposed samples, the pH at multiple locations across each specimen (Fig. 3.1) was measured to assess uniform electrolyte transport during testing. In the NaCl/NaOH and NaOH/NaCl (unmatched) exposure conditions, the pH is consistently lower around the electrolyte-facing ends and along the edges (Fig. 3.1: a, b), ranging between 11.0-11.5, whereas pH varies between 11.5-12 in the middle interior matrix. Although the absolute variations were minimal, their spatial concentration at the specimen perimeter suggests non-uniform ionic movement in these configurations. In contrast, specimens subjected to NaOH/NaOH and NaCl/NaCl (matched) exposure showed limited and more localized pH fluctuations (Fig. 3.1: c, d), indicating relatively uniform chemical interaction. These results imply that unmatched electrolyte exposure may influence ionic migration, leading to different chemical alteration in the concrete specimen.

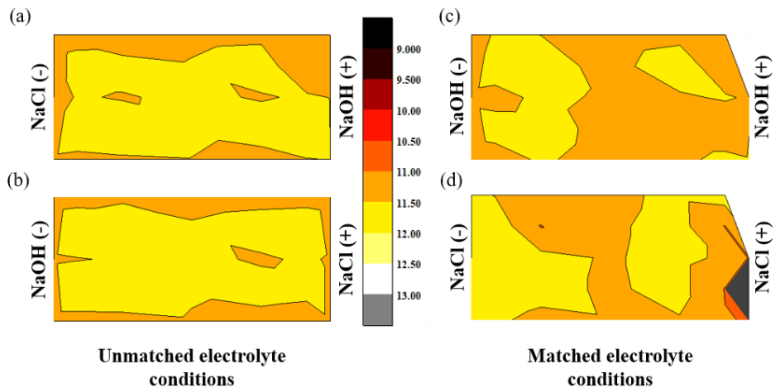

Figure 3.1: Spatial variation of pH measurements in concrete specimens after EAT under four electrolyte configurations: (a) NaCl/NaOH, (b) NaOH/NaCl, (c) NaOH/NaOH, and (d) NaCl/NaCl.

XRD analysis was employed to determine the relationship among initial condition, pH variability, and mineralogical changes. A control sample produced from the same mix as the test specimens but not exposed to EAT (NA: not accelerated) was evaluated with XRD to establish baseline conditions (Fig. 3.2). The control sample shows calcite concentrated near specimen edges with minimal presence in the interior matrix. The higher calcite at the surface than in the middle is likely due to the availability of CO_2 in the air during the curing of the concrete specimens.

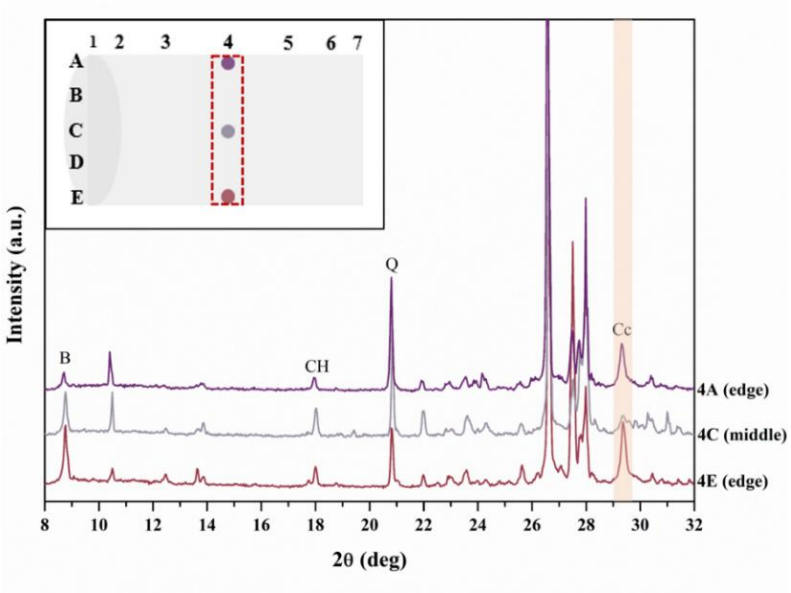

Figure 3.2. XRD pattern of non-accelerated (NA) concrete, showing calcite enrichment near surfaces and limited presence within the matrix. Phase labels: B-Biotite, CH-Portlandite, Q-Quartz, Cc-Calcite

Mineralogical changes following exposure are illustrated using representative samples from the NaCl/NaOH configuration (Fig. 3.3). Phases were identified based on PDF reference cards for Biotite (9001351), Aft (Alumina Ferric oxide trisulfate phases, particularly Ettringite-9012922 and Thaumasite-9016053), Friedel's salt (00-019-0202), Portlandite (9000113), Calcite (4502441), Albite (9009663), Quartz (1011159), and Hydrogarnet (9001426). The diffraction patterns reveal distinct mineralogical differences between the surface regions (faces and edges) and the interior matrix.

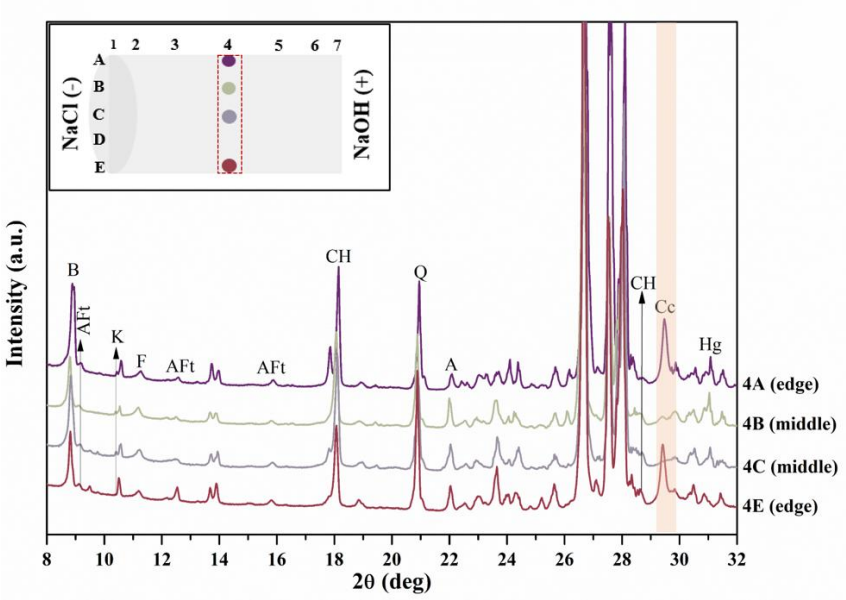

Figure 3.3: XRD profiles comparing interior and peripheral regions of specimens subjected to NaCl/NaOH exposure. Phase labels: Aft-Ettringite & Thaumasite, K-Kuzel salt, F-Friedel salt, A-Albite, and Hg-Hydrogarnet.

According to the thermodynamic model of Leemann *et al*, concrete degradation in the presence of pyrrhotite progresses through two stages: (i) oxidation, involving the consumption of pyrrhotite and magnetite, followed by (ii) carbonation, characterized by the formation of calcite, gypsum, and zeolitic phases [13]. Though phase evolution depends on initial conditions, the Leemann model provides a useful framework for assessing deterioration based on key mineralogical phases. In the NaCl/NaOH, NaOH/NaCl, and NaOH/NaOH configurations, calcite was detected in surface and edge samples (1C, 4A, 4E, 7C), with no evidence in the interior (2C, 3C, 4C, 5C, 6C, 4B), consistent with the NA condition. The EAT samples deviate from the NA condition with the appearance of hydrogarnet (Almandine) and AFt phases detected in small amounts at most sample locations. Pyrrhotite and magnetite were not identified, and this is not surprising because the sampling strategy involved selective removal of matrix material (avoiding aggregates). The relatively uniform pH (varying from 11.05 – 11.90) in the NaCl/NaOH sample is consistent with conditions for portlandite, and none of the samples exhibited pH conditions that reflect calcite production, which typically results in pH near 8 [14].

Despite identical voltage and exposure duration, matched configurations exhibit notable mineralogical changes in the cement matrix, particularly involving Friedel's salt (FS), Kuzel's salt (KS), AFt, and calcite. In the NaCl/NaCl exposure, sufficient chloride availability promotes the formation of both FS ($3CaO{\cdot}Al_2O_3{\cdot}CaCl_2{\cdot}10H_2O$) and KS ($3CaO{\cdot}Al_2O_3{\cdot}½CaSO_4{\cdot}½CaCl_2{\cdot}11H_2O$). The detection of KS under NaOH/NaOH exposure, despite having no external chloride input, suggests mobilization of bound Cl^- within the matrix. Similar KS signatures have been reported in field-deteriorated structures by other researchers [15], indicating that the NaOH/NaOH condition may potentially replicate key aspects of naturally occurring deterioration.

To further quantify how these mineralogical changes propagate spatially within the specimen, phase intensity was compared across the middle, faces, and edges of the cylinders. Figure 3.4 presents calcite XRD peak (29.4 °) intensities across the four electrolyte configurations. In unmatched electrolyte conditions, the presence of calcite is predominantly confined to the surface regions, consistent with baseline behavior observed in NA specimens. The NaOH/NaOH configuration shows reduced spatial variability but maintains a distribution similar to initial conditions. In contrast, NaCl/NaCl exposure displays nearly uniform calcite presence throughout the specimen. In addition to the calcite distribution difference, the NaCl/NaCl exposure also displayed lower amounts of AFt phases. The change in the calcite ratio and lack of AFt presence is indicative of a different deterioration mechanism at play in the NaCl/NaCl type exposure.

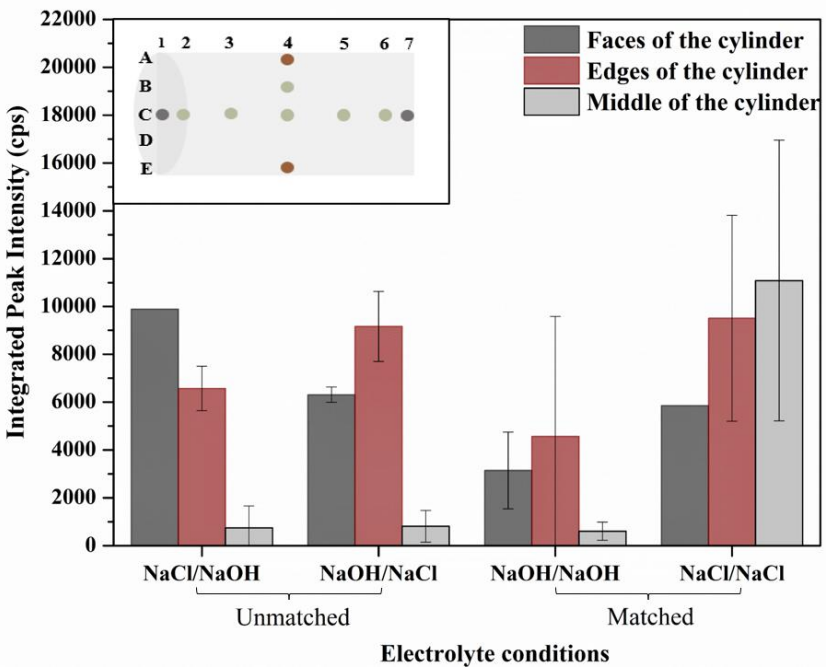

Figure 3.4: Comparison of calcite integrated peak intensities from XRD analysis across matched and unmatched electrolyte exposure configurations, highlighting variations in carbonation progression.

4. CONCLUSION & FUTURE WORK

EAT revealed different deterioration patterns in concrete under NaCl/NaOH, NaOH/NaCl, and NaOH/NaOH exposure conditions compared to the NaCl/NaCl exposure. In the first three configurations, baseline surface calcite remains largely unchanged, while NaCl/NaCl condition triggers drastic calcite distribution across the matrix. Distinct calcite evolution patterns confirm that fundamentally different mechanisms operate under matched and unmatched electrolytes. These findings highlight that EAT-induced damage cannot be assumed to progress uniformly and that electrolyte configuration plays a decisive role in the outcome of laboratory acceleration strategies. Future work will focus on identifying key deterioration phases across each exposure condition and determining which configuration most accurately replicates field-driven degradation. Establishing a linkage between deterioration mechanism and exposure condition is crucial for refining the accelerated testing methodology and enhancing the predictive accuracy of EAT for long-term structural performance.

5. REFERENCES

1. Jana D. Concrete Deterioration from the Oxidation of Pyrrhotite: A State-of-the-Art Review. Nova Science Publishers, Inc., Hauppauge, NY; 2023. p. 137-221.
2. Carey AS, Watson SS. Review of Potential Mitigation Methodologies for Existing Concrete Structures Containing Pyrrhotite-Bearing Aggregates. Journal of Building Engineering. 2025:113408. doi: https://doi.org/10.1016/j.jobe.2025.113408.
3. Duchesne J, Rodrigues A, Fournier B. Concrete damage due to oxidation of pyrrhotite-bearing aggregate: A review. RILEM Technical Letters. 2021;6:82-92. doi: https://doi.org/10.21809/rilemtechlett.2021.138
4. Rodrigues A, Duchesne J, Fournier B, Durand B, Rivard P, Shehata M. Mineralogical and chemical assessment of concrete damaged by the oxidation of sulfide-bearing aggregates: Importance of thaumasite formation on reaction mechanisms. Cement Concrete Research. 2012;42(10):1336-47. doi: https://doi.org/10.1016/j.cemconres.2012.06.008.
5. Wille K, Zhong R. Investigating the deterioration of basement walls made of concrete in CT. Department of Civil and Environmental Engineering, Advanced Cementitious …; 2016.
6. Araiza RC, Fournier B, Duchesne J, Fecteau P-L, Rodrigues A. Evaluation of detrimental effects in concrete specimens due to the oxidation of sulfide-bearing aggregates after electrochemical treatment. Construction Building Materials. 2024;411:134341. doi: https://doi.org/10.1016/j.conbuildmat.2023.134341.
7. Araiza RC, Rodrigues A, Fournier B, Duchesne J. A new accelerated testing scheme to evaluate the potential oxidation reaction of sulfide-bearing aggregates in concrete specimens. Cement Concrete Research. 2024;180:107507. doi: https://doi.org/10.1016/j.cemconres.2024.107507
8. Ojo M, Kim D, Frame L, Wille K. Electrochemical investigation of accelerated deterioration of concrete with iron-sulfide containing aggregates. Cement Concrete Research. 2024;182:107570. doi: https://doi.org/10.1016/j.cemconres.2024.107570
9. NordTest NB. Concrete, mortar and cement-based repair materials: Chloride migration coefficient from non-steady-state migration experiments. 1999.
10. Joshi R, Chatterji S, Achari G, Mackie P. Reexamination of ASTM C 1202—Standard Test Method for Electrical Indication of Concrete's Ability to Resist Chloride Ion Penetration. Journal of testing evaluation. 2000;28(1):59-61. doi: https://doi.org/10.1520/JTE12075J.
11. Gong C, Zhang J, Wang S, Lu L. Effect of aggregate gradation with fuller distribution on properties of sulphoaluminate cement concrete. Journal of Wuhan University of Technology Mater Sci Ed. 2015;30(5):1029-35. doi: https://doi.org/10.1007/s11595-015-1268-5.
12. Zhang T, Gjørv OE. An electrochemical method for accelerated testing of chloride diffusivity in concrete. Cement Concrete Research. 1994;24(8):1534-48. doi: https://doi.org/10.1016/0008-8846(94)90168-6.
13. Leemann A, Lothenbach B, Münch B, Campbell T, Dunlop P. The “mica crisis” in Donegal, Ireland–A case of internal sulfate attack? Cement Concrete Research. 2023;168:107149. doi: https://doi.org/10.1016/j.cemconres.2023.107149.
14. Fritz B, Clément A, Montes-Hernandez G, Noguera C. Calcite formation by hydrothermal carbonation of portlandite: complementary insights from experiment and simulation. CrystEngComm. 2013;15(17):3392-401. doi: https://doi.org/10.1039/C3CE26969H.
15. Luo Z, Yu H, Ma H, Tan Y, Wu C, Sun J, et al. Corrosion Products and Microstructural Evolution of Ordinary Portland Cement and High-Performance Concrete After Eight Years of Field Exposure in Qarhan Salt Lake. Materials. 2025;18(8):1769. doi: https://doi.org/10.3390/ma18081769.

Evaluating sampling strategy for electrochemical accelerated testing of sulfide-bearing concrete
Shalini Devi Tulasi Ravikumar; Meshach Ojo; Darcel Courtney; Auishe Pauline Corraya; Kay Wille; Lesley D Frame

ICISR 2026

2nd International Conference on Iron-Sulfide Reactions in Concrete

Technical Session # 5:

Case Studies and Advanced Insights into Iron-Sulfide Concrete Damage

UCONN | COLLEGE OF ENGINEERING
SCHOOL OF CIVIL AND ENVIRONMENTAL ENGINEERING

UCONN
COLLEGE OF ENGINEERING
CONNECTICUT TRANSPORTATION INSTITUTE (CTI)

From CT to MA: Case Studies of Crumbled Foundations from Pyrrhotite Oxidation and Internal Sulfate Attack in the Eastern US

Dipayan Jana [1]

(2) *Construction Materials Consultants, Inc. and Applied Petrographic Services, Inc.*

Abstract

Oxidation of pyrrhotite and the resultant internal sulfate attack (ISA) have caused widespread cracking and crumbling of thousands of residential concrete foundations across northeastern CT and central to western MA. Pyrrhotite occurred in the schist and gneiss of the Brimfield Schist formation in the Bronson Hill Anticlinorium formed during a Devonian age mountain-building event (Acadian Orogeny, approximately 416-360 million years ago) from the collision of the ancestral North American continent (Laurentia) with a microcontinent (Avalonia), resulting in the formation of the Appalachian Mountains and large-scale pyrrhotite crystallization along this mountain belt. Case studies are provided from a house of crumbled and replaced foundation in Vernon, CT and two houses in Rutland, MA built in 2002. Typical host rocks of pyrrhotite in the distressed foundations of CT are the dominant garnetiferous quartzo-feldspathic and micaceous schist and gneiss and minor micaceous quartzite supplied from the Becker's Quarry in Willington, CT. Aggregates in the examined foundations from Rutland, MA are mica schist and quartzite from a local quarry that are lithologically distinct from CT but still dominantly schistose rocks. In both cases, close association of pyrrhotite with biotite and the gneissose and schistose textures of rocks have provided pathways for access of moisture and oxygen for oxidation. Pyrrhotite-bearing crushed stone particles in both CT and MA samples are ranged from 50 to 70% of coarse aggregate. Pyrrhotite occurred as: (a) coarse subhedral to anhedral grains in the host schist/gneiss often engulfing minerals from the host rocks, indicating late intrusion from crystallization in hydrothermal vein into preexisting rocks, (b) aligned along the weak planes developed from parallel arrangements of minerals in the schist and gneiss from remobilization during the orogeny, (c) in mica-rich layers of quartzite, and (d) as finely disseminated forms, most of which are mostly present in unoxidized forms in a small fraction of nonreactive aggregates. Oxidized pyrrhotite grains showed characteristic striations from the typical banded microstructure of expansive iron oxyhydroxide strips in the iron sulfide matrix. Pyrrhotite is the dominant iron sulfide in all these rocks (ranging commonly from <10% to occasionally 20 to 50% in the individual aggregates) with minor pyrite, chalcopyrite and trace pentlandite that can be effectively distinguished from their color tones (bronze to brownish-bronze pyrrhotite to pale brass-yellow pyrite to brassy yellow often iridescent chalcopyrite to pale bronze to golden-yellow pentlandite) on the polished sections in reflected-light in a stereomicroscope or a petrographic microscope. Total sulfur contents of concretes ranged from 0.27% in the CT to 0.3-0.5% in MA samples. Extensive cracking is seen during microscopical examinations of fluorescent epoxy-impregnated polished solid and thin sections. SEM-EDS studies were performed on numerous oxidized pyrrhotite grains as well as from ettringite-infested microcracked paste fractions of concrete. XRD studies were done on some individual oxidized pyrrhotite grains to detect the reactive (magnetic, 4C) type of pyrrhotite and oxidation products. Finally, mechanisms of distress from two-stage expansions from pyrrhotite oxidation followed by ISA are discussed.

Keywords: *cracking, ISA, oxidation, pyrrhotite, sulfate.*

1. INTRODUCTION

Oxidation of pyrrhotite ($Fe_{1-x}S$, $0 < x < 0.125$) in concrete aggregates and the resultant internal sulfate attack (ISA) in paste have caused extensive cracking in thousands of residential concrete foundations across eastern Connecticut and Massachusetts. Case studies on detailed microstructural, chemical, and mineralogical evidence of pyrrhotite oxidation and the resultant internal sulfate attack from many cracked concrete foundations in CT were previously presented by Jana [1, 2, 3, 4]. At the time of this report, foundations of up to 35,000 homes built between 1983 and 2016 from 56 towns in north, east and central CT, and 10,000 homes from 51 cities and towns in 6 counties in MA (primarily at central MA and along NH and CT borders) are affected by this epidemic. Concrete for the affected homes in CT were primarily sourced from a quarry in Willington, CT operated during 1980s for 30 years that sits in a weathered

hydrothermal vein of metamorphic rocks containing significant pyrrhotite mineralization, whereas multiple quarries are reported for crumbled foundations in MA. The present study is an extension of comparative case studies of three additional distressed foundations, one from Vernon, Tolland County in Connecticut and two others from Rutland, N Worchester County in Massachusetts.

1.1 CT and MA Legislations

In order to restrict incorporation of pyrrhotite-bearing aggregates into concrete, both CT and MA legislations [5, 6] have adopted a multi-stage screening protocol based on [4] (a) total sulfur content of aggregate (S_T) to be less than 0.1% for acceptance, or (b) further examination by petrography, XRD, SEM-EDS, WDXRF for positive detection of pyrrhotite for aggregates having $0.1 \le S_T < 1.0$, and (c) long-term expansion tests of mortar bars or concrete prisms for aggregates where pyrrhotite is positively identified by petrography, or sale for a period of 1 year until further evaluation if pyrrhotite is not detected.

1.2 Mechanism of Two-Stage Expansions

In CT and MA, distress of concrete foundations are (a) primarily due to in situ expansions of unsound aggregates from oxidation of pyrrhotite in the presence of moisture and oxygen to various iron oxides/hydroxides/oxyhydroxides (ferrihydrite, goethite) causing first-stage cracking in concrete from tensile stresses, which is often followed by (b) additional expansions in paste due to attack of the released sulfate/sulfuric acid byproducts of oxidation to various cement hydrates and formation of ettringite (e.g., in CT, MA), or additional thaumasite (e.g., in Canada where pyrrhotite grains are surrounded by an iron carbonate rim, or in a concrete containing crushed limestone as a source of carbonates) in confined spaces to cause additional cracking. Compared to its close cousin, pyrite, even at a level of less than 0.5% by mass of aggregate, pyrrhotite can cause extensive cracking and crumbling of concrete.

1.3 Field Evidence of Distress

Extensive cracking of concrete foundation, popouts of exposed fractured oxidized pyrrhotite grains on the surfaces of foundation walls, and white sulfate efflorescence deposits are seen in the Vernon, CT home, which are shown in Ref 7. Ref 7 also provides a detailed optical and SEM microstructural atlas of pyrrhotite oxidation and resultant distress in these three crumbled foundations along with other laboratory data.

2. MATERIALS AND METHODS

Multiple broken concrete fragments were received from all three crumbled foundations, which were photographed, documented, and processed for various laboratory studies. Fragments were first sectioned into multiple parallel slices with a water-cooled diamond saw, followed by creating polished sections for examinations in a stereomicroscope, and subsequent trimming of other slices to 50 × 75 mm size blocks for preparation of polished fluorescent dye-mixed epoxy-impregnated thin sections for examinations in stereomicroscope and petrographic microscope *a la* ASTM C 856, and SEM-EDS *a la* ASTM C 1723. Additional pieces were pulverized to fine powders for total sulfur (ASTM D 4239), XRD and XRF studies.

3. RESULTS & DISCUSSION

3.1 Total Sulfur

S_T of the Vernon, CT foundation is 0.273%, which would have outright discarded the aggregate as per the CT legislation. S_T of the two foundations from MA are 0.302% and 0.506%, which too, as per the MA legislation, would have subjected those aggregates for further examination by petrography.

3.2 Petrographic Examinations

Concrete in the Vernon, CT foundation is dense, well-consolidated, and made using ¾-in. (19-mm) nominal size crushed schist-gneiss-quartzite coarse aggregate, $^3/_8$-in. (9.5 mm) nominal size crushed siliceous sand fine aggregate, both coarse and fine aggregates are well-graded and well-distributed, and portland cement paste having an estimated water-cement ratio (*w/c*) of 0.45. Concrete is air-entrained having an estimated air content of 5.5%. Pyrrhotite is detected in the predominant dark gray garnetiferous quartzo-feldspathic and micaceous schist and gneiss, as well as in the subordinate light brown quartz-feldspar-mica gneiss (having a higher quartz content than the dark gray gneiss) and in the

lighter micaceous quartzite in coarse aggregate [7], all of which were reportedly quarried from the Brimfield Schist formation in the Becker's Quarry in Willington, CT.

Concrete in the two crumbled foundations from Rutland, MA are equally dense, well-consolidated, and made using ¾-in. (19-mm) nominal size crushed schist and quartzite coarse aggregate, $^{3}/_{8}$-in. (9.5 mm) nominal size crushed siliceous sand fine aggregate, both coarse and fine aggregates are well-graded and well-distributed, and a paste of portland cement and fly ash (added at 15-20% by mass of total cementitious materials) having similar water-cementitious materials ratios (*w/cm*) estimated to be 0.44 to 0.48. Concrete is air-entrained having estimated air contents of 5 to 5.5%. Pyrrhotite is detected in mica schist and quartzite in coarse aggregate [7], which was reportedly derived from a local quarry that are lithologically distinct from the aggregate found in the CT foundation but still dominantly composed of schistose rocks of the Brimfield Schist formation.

Almost 60 to 70% of coarse aggregate in CT and 50 to 60% in MA are pyrrhotite-bearing [7]. In all three foundations, pyrrhotite occurred as [7]: (a) coarse subhedral to anhedral grains in the host schist/gneiss often engulfing minerals from the host rocks for late intrusion from crystallization in hydrothermal vein into preexisting rocks, (b) aligned along the weak planes developed from parallel arrangements of micaceous and quartzo-feldspathic minerals in the schist and gneiss from remobilization during the Acadian orogeny, (c) in mica-rich layers of quartzite, and (d) as finely disseminated forms, most of which are mostly present in unoxidized forms in a small fraction of nonreactive aggregates. Other sulfides detected are pyrite, chalcopyrite, and trace pentlandite, which are distinguished from their color tones, e.g., bronze to brownish-bronze pyrrhotite to pale brass-yellow pyrite to brassy yellow often iridescent chalcopyrite to pale bronze to golden-yellow pentlandite. Pyrrhotite contents varied from <10% to occasional 20-50% in individual aggregate grains.

3.3 SEM-EDS Studies

SEM-EDS studies of oxidized pyrrhotite grains and associated paste in all three foundations showed five characteristic features [7]: (a) parallel Fe-O oxidized bands in Fe-S oxidized pyrrhotite matrix, (b) pyrite-like stoichiometry of restructured oxidized pyrrhotite in Fe/S atomic ratios when SEM-EDS analyses are done from the Fe-S matrices in between the Fe-O bands, (c) extensive microcracking in the oxidized pyrrhotite grains, often extending into the aggregate and even to the neighbouring paste, (d) secondary ettringite precipitates in cracks and voids but (e) no elevated sulfate levels (S/Ca atomic ratios are mostly within 0.0 and 0.05) in the SEM-EDS data collected from the interstitial paste fractions.

3.4 XRD and XRF

For CT foundation, XRD result of bulk concrete showed [7]: (a) albite 39.4%, quartz 18.5%, microcline 4.1%, orthoclase 4.8% in the main quartzo-feldspathic minerals in schist/gneiss, (b) biotite 3.2%, and muscovite 9.6% amongst the micaceous minerals, (c) calcite 7.2% and pyrope garnet 0.5%, (d) 2.0% 4M pyrrhotite as the reactive iron sulfide, and (e) ferrihydrite 9.9% and ettringite 0.9% as the products of pyrrhotite oxidation, and resultant sulfate crystallization, respectively. Corresponding major element oxidation composition of concrete from XRF showed SiO_2 50.86%, Al_2O_3 11.03%, Fe_2O_3 6.2%, CaO 13.45%, MgO 2.33%, Na_2O 1.67%, K_2O 1.61%, TiO_2 0.52%, SO_3 1.47%, LOI 10.67%.

For two MA foundations, XRD result of bulk concrete showed [7]: (a) quartz 39% (2002), 36.8% (2024), albite 21.6% (2002), 25.5% (2024), microcline 5.4% (2002), 3.6% (2024), orthoclase 5.6% (2024 in the main quartzo-feldspathic minerals in schist/gneiss, (b) biotite 0.4% (2002), 1.9% (2024), muscovite 17.6% (2002), 13.0% (2024), (c) illite 3.0% (2002), 0.9% (2024), kaolinite 1.5% (2002), chlorite 8.0% (2024) in clay minerals, (d) calcite 2.8% (2002), 2.8% (2024), (d) pyrrhotite 0.2% (2002) and 0.2% (2024) as the reactive iron sulfide, and (e) ettringite 8.5% (2002) and 1.7% (2024) from sulfate crystallization, ferrihydrite was below the detection limit. Corresponding major element oxidation composition of concrete from XRF showed SiO_2 53.3-58.6%, Al_2O_3 12.8%, Fe_2O_3 2.8-3.9%, CaO 9.9-10.6%, MgO 1.4-1.5%, Na_2O 1-1.5%, K_2O 2.7-3.2%, TiO_2 0.48-0.52%, SO_3 0.9-1.3%, LOI 8.5-11.5%.

4. CONCLUSIONS

In all three foundations, evidence of extensive pyrrhotite oxidation was clear from: (a) striated nature of oxidized pyrrhotite and associated reddish brown oxidation products while observing polished sections under a stereomicroscope, (b) spectacular parallel bands of Fe-O in pyrrhotite while observing a polished section in a reflected-light microscope or in SEM, (c) detection of ferrihydrite in XRD analysis in the CT foundation, and, (d) extensive cracking of pyrrhotite-bearing aggregates often extending into

the paste. Evidence of subsequent ISA was more evident in the paste of crumbled Vernon, CT foundation where paste showed heavy infestation of fibrous ettringite not only as mere secondary precipitates in voids and/or cracks but more deleteriously within the porous to denser areas of paste often intimately mixed within the CSH where such formation of ettringite within the confined spaces in paste are the results of paste expansion and additional damage. SEM-EDS sulfate levels of paste in the present MA foundations (<1% S, atomic) are less than the paste sulfate in the present CT foundation, which, are still lower than sulfate levels found in other distressed foundations in CT [e.g., 1].

Contrary to extensive pyrrhotite distress of the much porous concrete blocks in the County Donegal in Ireland, where not only pyrrhotite oxidation but more profoundly ISA of sulfate-contaminated paste are found to be the primary mechanisms of crumbling of blocks, the dense concrete in the foundations of the eastern US homes along with some similar dense foundations in Ireland that the author has examined, it has appeared that perhaps the denser microstructure of concrete might have slowed down the distress by slowing the access of moisture and oxygen but as long as there is pyrrhotite and the availability of moisture and oxygen for its high reactivity, there is always the potential for distress, perhaps denser microstructure of concrete would facilitate oxidative expansion and perhaps additional distress from ettringite-related expansion in the confined spaces in paste as the more viable mechanisms than severe decomposition of paste *per se* from ISA as seen in the crumbled blocks in Ireland. In Canada, however, both the host rock of pyrrhotite (anorthositic gabbro) as well as the concrete foundation are pretty dense but still distress has reportedly occurred within 5 years of construction [3], indicating the complex nature of pyrrhotite deterioration in concrete.

To prevent future pyrrhotite-related distress, the United States Geological Survey has created a map of distribution of potentially pyrrhotite-bearing rocks [8]. Both CT and MA legislations are proposed for the much-needed steps to regulate testing of sand, gravel, and quarried stones. Along with our proposed performance-based testing protocol [4], our lab has been involved in testing of various quarries across CT and MA for pyrrhotite.

5. REFERENCES

[1] Jana, D., “Pyrrhotite Epidemic in Eastern Connecticut: Diagnosis and Prevention,” ACI Materials Journal V 117, No.1, January 2020, pp. 1-20.

[2] Jana, D., “Cracking of residential concrete foundations in eastern Connecticut, USA from oxidation of pyrrhotite,” Case Studies in Concrete Construction, Vol 16, 2022.

[3] Jana, D., “Concrete deterioration from the oxidation of pyrrhotite - A state-of-the-art review, Chapter 5, In “Pyrite and Pyrrhotite: Managing the Risks in Construction Materials and New Applications,” Michael L.J. Maher (editor), Nova Science Publishers, pp. 137-221.

[4] Jana, D., “Preventing pyrrhotite damage in concrete: Proposal for a performance-based testing protocol,” Concrete International, American Concrete Institute, 42(5), pp. 42-47.

[5] Substitute House Bill No. 6646, Connecticut Public Act No. 21-120: “An Act Concerning Crumbling Concrete Foundations,” State of Connecticut, July 6, 2021, 10 pp., www.cga.ct.gov/2021/act/Pa/ pdf/2021PA-00120-R00HB-06646-PA.PDF.

[6] Massachusetts Senate Bill No. 548, “An Act Relative to Crumbling Concrete Foundations,” The Commonwealth of Massachusetts, Feb. 18, 2021, 7 pp., https://malegislature.gov/Bills/192/S548.

[7] Jana, D., “From CT to MA: Case Studies of Crumbled Foundations from Pyrrhotite Oxidation and Internal Sulfate Attack in the Eastern US,” Data https://www.cmc-concrete.com/pyrrhotite-crumbling-foundations.

[8] Mauk, J.L.; Crafford, T.C.; Horton, J.D.; San Juan, C.A.; and Robinson, G.R. Jr., “Pyrrhotite Distribution in the Conterminous United States, 2020,” U.S. Geological Survey Fact Sheet 2020-3017, Mar. 2020, 4 pp.

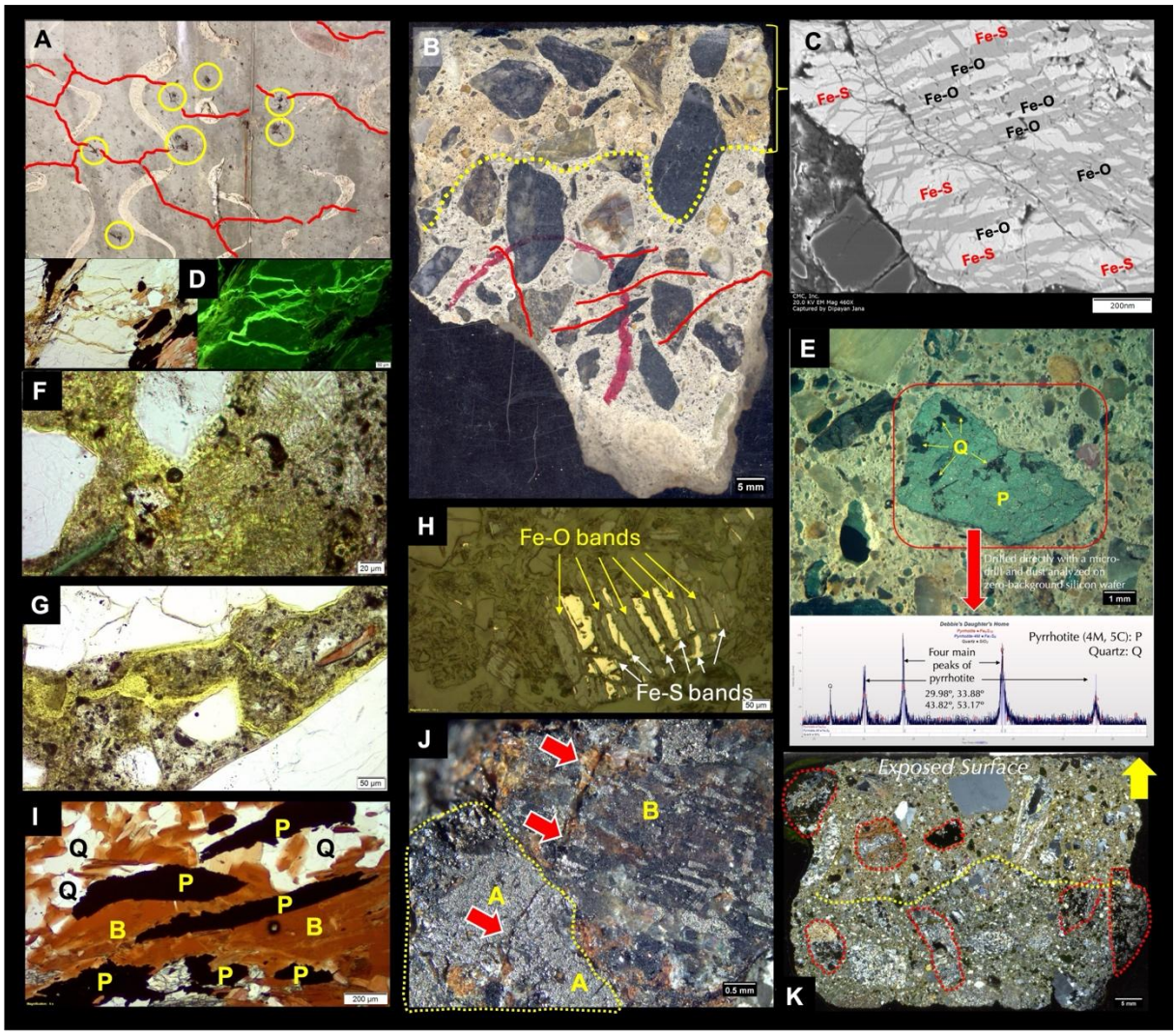

Figure 5: The Vernon, CT home. A: Extensive cracking (red lines) and popouts of oxidized pyrrhotite grains (circled) in the foundation wall. B: A polished concrete fragment showing beige discoloration at the exposed surface end of wall from atmospheric carbonation (depth of carbonation is 30-mm, which is marked by yellow dotted line as the carbonation front); visible cracks are marked with red lines. C: Backscatter electron image of a polished section of extensively cracked oxidized pyrrhotite grain showing alternate darker gray Fe-O and brighter Fe-S bands. D: Micrograph of thin section of an extensively cracked pyrrhotite-bearing coarse aggregate where cracks are highlighted by fluorescent dye in the corresponding image taken in the UV light. E: A sand-size 'chunk' of pyrrhotite with minor quartz inclusions, which has shown a spectacular four-peak diffraction pattern of 4M pyrrhotite. F: Micrograph of thin section showing extensive contamination and mixing of fibrous, acicular ettringite in cement paste, i.e., beyond the usual filling of voids and cracks by secondary ettringite, such ettringite-infested paste is the telltale evidence of ISA in paste. Ettringite-related ISA occurs only in the interior non-carbonated concrete since ettringite is unstable in the carbonated surface region of foundation, G: Cracks extending from unsound aggregates to interstitial paste, which are often filled with ettringite. H: Micrograph of polished section of oxidized pyrrhotite in the reflected-light mode of a petrographic microscope showing alternate Fe-O and Fe-S bands. I: Thin section micrograph showing close association of elongated pyrrhotite grains with biotite flakes in aggregate, where such juxtaposition pyrrhotite within biotite has fasciliated easy access of oxygen and moisture for oxidation through the biotite flakes. J: A pyrrhotite 'chunk' in a gneiss coarse aggregate showing one half of less oxidized (marked as 'A') and other half of extensively oxidized pyrrhotite, latter with parallel Fe-S bands (marked as 'B'), and a crack traversing the grain (red arrows) developed from oxidation. K: Large-area (50 × 75 mm) thin section scanned on a flatbed transparent scanner showing pyrrhotite-bearing aggregates (marked by red dotted lines) where thin section was sandwiched between two perpendicular polarizing filters to recreate cross-polarized light view of a petrographic microscope.

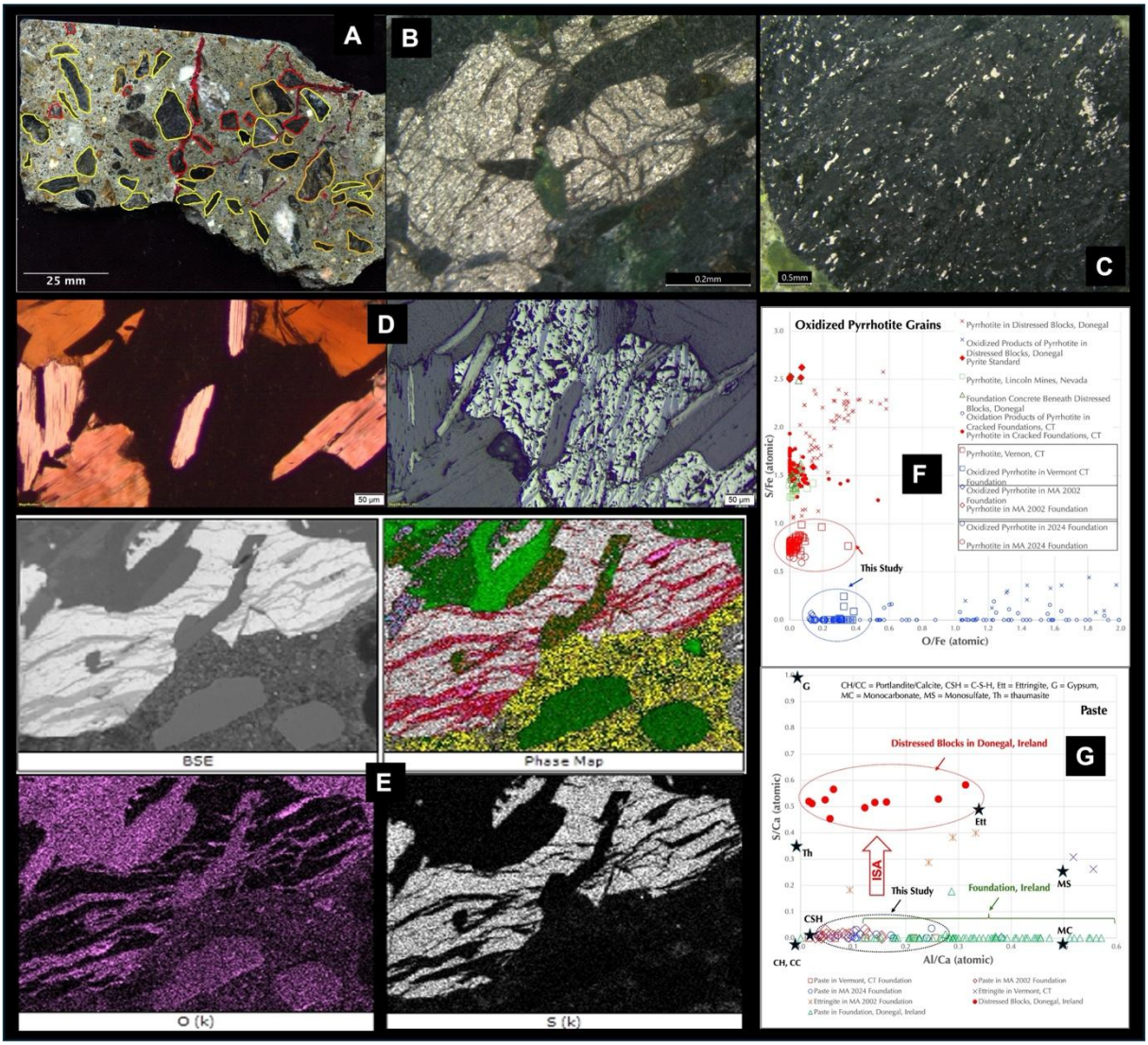

Figure 6: The Rutland, MA foundations. A: Polished cross section of a fragment where extensively and moderately pyrrhotite-bearing schist aggregates are marked by peripheral red and yellow lines, respectively, whereas non-pyrrhotite quartzite aggregates are marked in beige lines; a crack is marked in red line. B: Coarsely crystalline, subhedral to anhedral oxidized pyrrhotite grains showing characteristic striations. C: Finely disseminated forms of pyrrhotite either in random scattered grains or aligned along the weak planes of schistosity. D: Close association of pyrrhotite and biotite often one engulfed into another. E (four images): Backscatter electron image and phase map of an oxidized pyrrhotite from the elemental maps of oxygen (in pink) and sulfur (in white), omitting calcium for paste (in yellow) showing oxidized iron striations in iron sulfide matrix. F: SEM-EDS studies of iron oxide bands in oxidized pyrrhotite grains plotted in S/Fe vs. O/Fe atomic ratios from this study, other crumbled foundations from the eastern CT, and a few distressed concrete blocks and foundations from County Donegal, Ireland. G: SEM-EDS studies of paste showing the absence of elevated sulfate in the paste of dense concrete foundations from the eastern US or in some foundations in County Donegal, Ireland compared to the elevated sulfate levels (S/Ca_{atomic} 0.4-0.6) from ISA in the distressed blocks of Ireland. Absence of elevated sulfate in the dense paste of foundations, however, does not necessrily indicate the absence of ISA when all available sulfate in the pore solutions are being used up in formation of ettringite in the confined spaces in paste to cause additional expansion and damage beyond the oxidative damage.

Pyrrhotite-Induced Concrete Degradation - A Machine Learning Approach for Risk Assessment in the Trois-Rivières Region

Gilberto Cidreira Keserle [(1)], Anthony Allard [(2)]

(3) *Englobe Corp, Québec City, Canada, gilberto.cidreirakeserle@englobecorp.com*

(4) *Englobe Corp, Québec City, Canada, anthony.allard@englobecorp.com*

Abstract

This study applies a machine learning approach to the classification of pyrrhotite-induced concrete degradation and forms part of a larger investigation based on a comprehensive dataset comprising laboratory test results from 3 668 core samples taken from the concrete foundations of 727 structures in the Trois-Rivières area, Canada.

In June 2014, the Superior Court of Québec determined that a volumetric pyrrhotite content of 0.23% constitutes a threshold at which damage is expected to materialize. This reference value has since been used as a critical limit for assessing the risk of damage to concrete elements in the context of the pyrrhotite issue. However, it does not correspond directly to field observations.

Using a comprehensive dataset combining laboratory test results from core samples and field inspection reports, the model was trained to identify patterns and predict the likelihood of degradation in concrete foundations if any. The integration of multiple data sources enabled the development of a robust classification framework, providing a data-driven tool for risk assessment. Moreover, the model contributes to understanding the key factors associated with a possible deterioration, supporting both the diagnosis and the management of affected structures.

***Keywords**: pyrrhotite, concrete durability, machine learning, risk assessment.*

1. INTRODUCTION

Given the limited understanding of the mechanisms and reaction kinetics governing pyrrhotite-induced degradation in existing structures, current standards are intended mainly to exclude sulfide-bearing aggregates from concrete production, rather than to distinguish between sound and deteriorated concrete. In 2014, a court ruling determined that homeowners whose concrete contained aggregates with pyrrhotite levels of at least 0,23 vol% were eligible for compensation, based on the assumption that structures not yet exhibiting deterioration were likely to develop damage over time [1]. However, statistical analyses indicate that the thresholds currently considered for pyrrhotite and total sulfur contents [1, 2, 3] do not reliably distinguish between sound and deteriorated concrete, and their use as sole indicators of damage has proven ineffective [4]. In the present case study, more than 78% of undamaged structures exhibited pyrrhotite concentrations equal to or exceeding 0,23 vol%. To address this limitation, a data-driven classification framework was developed to enhance the accuracy of risk assessment and to advance the understanding of the key parameters governing pyrrhotite-related degradation, thereby supporting both diagnostic evaluation and long-term management of affected concrete structures.

2. INPUT DATA

To date, the mechanisms governing pyrrhotite-induced degradation remain incompletely understood. Moreover, a high coefficient of variation was observed for volumetric pyrrhotite content [4]. To minimize interdependence among chemical variables and to account for potential correlations between different iron sulfide phases, total sulfur content and petrographic examination were selected as the most relevant indicators at this stage. In addition, dry density represents a key parameter, as a higher proportion of coarse aggregate in concrete elements influences the overall density and consequently the sulfur concentration. The concrete supplier and the type of construction (residential or commercial) are also significant factors, as they influence mix design and the overall quality of the concrete.

Given that aggregate reactivity can fluctuate according to the extraction period within the quarry, the elapsed time since construction was identified as a key variable for temporal analysis. This variable more precisely captures the timeframe associated with both the construction phase and the specific conditions of quarry exploitation, thereby allowing a better assessment of time-dependent factors influencing degradation processes.

The degradation caused by iron sulfides is strongly influenced by the exposure conditions of concrete elements. Consequently, the type of concrete element constitutes a critical parameter within this domain, as it governs both the kinetics of the underlying reactions and the extent of the resulting damage [5].

3. METHODOLOGY

The methodology employed to develop the classification model aims to predict the damage state of concrete elements based on the data collected in this case study. The model is founded on a rigorous approach combining data preprocessing, dataset splitting and training, selection of appropriate algorithms, hyperparameter tuning and performance evaluation using established statistical metrics. Finally, a comprehensive model is proposed, integrating multiple algorithms to enhance predictive robustness. Figure 3.1 illustrates the overall methodological process.

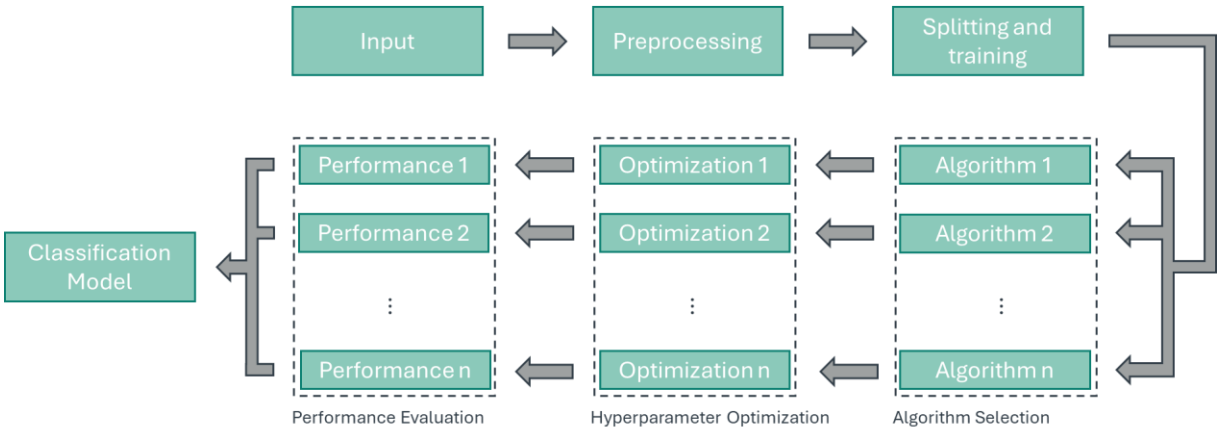

Figure 3.1: Methodological process

3.1 Data Preprocessing

Data preprocessing included importing the complete dataset and verifying its integrity. Entries without inspection records or with missing petrographic or total sulfur analyses were excluded to ensure that all retained observations contained representative values for the relevant variables.

3.2 Data Splitting and Training

The dataset was divided into training (70%) and test (30%) subsets to ensure an objective evaluation of model performance. The training set was used to learn relationships among variables, while the test set assessed generalization to unseen data. Stratified sampling preserved the class proportions of the target variable, preventing imbalance and bias. This partitioning strategy also mitigated overfitting by allowing model validation on independent data, thereby ensuring robust and generalizable results.

3.3 Algorithm Selection

Three supervised ensemble methods were evaluated: Random Forest, Gradient Boosting and HistGradient Boosting. These decision tree–based algorithms were chosen for their balance between accuracy, robustness, and interpretability. Random Forest aggregates multiple independent trees trained on random data subsets, reducing overfitting and providing stable, interpretable results. Gradient Boosting builds trees sequentially, each correcting the previous model's errors, offering higher predictive precision at the cost of greater complexity. HistGradient Boosting optimizes this approach through

histogram-based binning, enabling faster training and scalability for large datasets while maintaining high performance.

3.4 Hyperparameter Optimization

Hyperparameter tuning aimed to improve algorithm accuracy and stability. These parameters, defined before training, control the behavior of each algorithm, including tree depth, number of estimators, and learning rate. Cross validation was applied to identify the best balance between performance and generalization. Random Forest used 100 trees with unrestricted depth and the Gini criterion, providing robust and efficient baseline performance. Gradient Boosting achieved optimal results with a learning rate of 0.2, 200 trees, maximum depth of 5, and exponential loss, ensuring accuracy without overfitting. HistGradient Boosting applied L2 regularization set to 3, a learning rate of 0.05, depth of 6, and 1000 iterations, resulting in a stable and computationally efficient model suitable for large datasets.

3.5 Algorithm Performance Evaluation

Algorithm performance was evaluated with priority given to maximizing recall for the damaged class, in order to minimize false negatives where deteriorated elements might be incorrectly classified as sound. This criterion is particularly important for reliable detection of iron sulfide–related degradation and for identifying structures requiring closer monitoring.

A repeated tenfold cross-validation procedure was applied thirty times with random resampling to ensure statistical robustness. Recall values obtained from each iteration were averaged to derive an overall performance score. To compare the three models, the Shapiro–Wilk test [6] was used to verify the normality of validation results at a 0.05 significance level. When normality was confirmed, an analysis of variance followed by Tukey's HSD test [7] identified significant performance differences.

This evaluation framework provided a rigorous basis for interpreting results and verifying model reliability. It ensured high sensitivity in detecting damaged elements while maintaining strong generalization capability and robustness to data variability.

3.6 Classification Model

To enhance the robustness and reliability of predictions, an ensemble approach using a Voting Classifier was implemented. This method combines the outputs of three independent learning algorithms (Random Forest, Gradient Boosting and HistGradient Boosting) within a collective decision framework. The final class assigned to each observation corresponds to the majority vote among the individual models. It is important to note that the model does not account for potential changes in the building's use or function, which could influence exposure conditions and degradation dynamics.

This aggregation strategy improves result stability and mitigates biases specific to any single model. By integrating algorithms with complementary learning behaviors, some better capturing complex variable interactions and others more resilient to noise and data variability, the ensemble achieves a more balanced and reliable performance.

4. RESULTS

4.1 Performance

Analysis of class distribution indicated a balanced dataset, consisting of approximately 53% undamaged and 47% damaged elements. The final performance of the classification model was evaluated using standard supervised learning metrics, namely precision, recall, F1-score, and overall accuracy. These indicators respectively quantify the proportion of correct predictions for each class, the model's ability to correctly identify positive cases, the balance between precision and recall, and the overall proportion of accurate classifications.

Table 4.1 presents the metrics summarizing the classification results on the test set.

Table 4.1: Metrics for the classification model

	Precision	Recall	F1-score
Undamaged	0,93	0,97	0,95
Damaged	0,96	0,92	0,94
Accuracy	-	-	0,94

The model achieved an overall accuracy of 94%, correctly classifying the majority of test samples. The per-class results show high and well-balanced performance between the two categories, damaged and undamaged [8]. For undamaged elements, precision reached 93% and recall 97%, indicating that the model correctly identified most of the truly undamaged elements, with very few false positives. For damaged elements, precision was slightly higher (96%), while recall decreased to 92%, suggesting that a small number of truly damaged cases were missed, corresponding to a limited number of false negatives. In the context of material degradation associated with pyrrhotite, these results demonstrate that the model effectively distinguishes between damaged and sound concrete elements while maintaining excellent overall reliability. The model emphasizes stable and consistent classification of undamaged cases, making it a valuable tool for managing concrete structures that currently show no visible damage.

4.2 Parameters

A complementary approach to evaluating model performance involves assessing its overall effectiveness and then examining the relative influence of the explanatory variables in predicting pyrrhotite-related damage.

The variable importance analysis revealed that the most influential parameters, in decreasing order of relevance, are:

1. Total sulfur content,
2. Year of construction (spatial origin of the aggregate within the quarry);
3. Dry density,
4. Petrographic examination (polished concrete disks [8]);
5. Exposure condition.

These findings highlight the predominance of chemical factors, while also confirming the critical contribution of environmental parameters in the degradation process. Together, they provide valuable insights into the mechanisms governing pyrrhotite-induced deterioration and support the interpretability and reliability of the classification model.

4.3 Risk Assessment

Considering the overall performance of the model, the assessment of damage risk is based on the outcome of the final ensemble model, which integrates a majority voting system among statistically distinct algorithms.

Table 4.2 summarizes the interpretation of the damage risk for undamaged concrete elements according to the level of agreement among the classification algorithms.

Table 4.2: Damage risk of undamaged concrete elements

Risk level	Voting Result (Classification Model)
Very Low	0 out of 3 votes (0%)
Low	1 out of 3 votes (33%)
Moderate	2 out of 3 votes (67%)
High	3 out of 3 votes (100%)

5. DISCUSSION AND CONCLUSION

Currently, concrete elements containing pyrrhotite in the Trois-Rivières region have remained free of visible deterioration for 18 to 23 years, which is more than double the average overestimated initiation period observed in this case study and approximately four times longer than the values commonly reported in the literature [4,9,10].

Existing threshold for pyrrhotite and total sulfur content in aggregates [1,2,3] proved inadequate for distinguishing between sound and deteriorated concrete in Trois-Rivière region, generating a significant number of false positives [4].

The proposed conservative assessment framework addresses this limitation by providing a predictive indication of risk in elements that remain visually intact. During the evaluation of a concrete element, significant variability may arise due to differences in chemical composition, aggregate distribution, exposure conditions, and other environmental factors. In addition, multiple samples are typically collected from different locations within the same element. Consequently, the final risk level assigned to a given concrete element corresponds to the highest classification obtained among all analysed samples, thereby reflecting the potential for localized damage within the structure. This conservative criterion also provides a predictive indication of risk for concrete elements that have remained undamaged over the years, offering a useful tool for managing structures that currently show no visible signs of deterioration.

To evaluate the potential risk of damage in concrete elements that have remained sound since construction, recall was identified as the most relevant performance metric, as it reflects the proportion of genuinely undamaged elements correctly classified by the model. The model exhibited a low error rate, with false negatives estimated at approximately 3%, corresponding to cases where an element predicted as undamaged showed actual signs of deterioration.

The model suggests that pyrrhotite-related damage is governed primarily by the intrinsic properties of the concrete, particularly total sulfur content. Exposure conditions also remained influential, likely reflecting their close association with the type of concrete elements and their service environment.

5.1 References

[1] Cour supérieure du Québec. (2014) Jugement phare. Dossier 400-17-002016-091. Trois-Rivières

[2] CSA Group (2024) CSA A23.2 - Annex P: Impact of sulphides in aggregate on concrete behaviour and global approach to determine potential deleterious reactivity of sulphide-bearing aggregates. CSA Group, Toronto

[3] CEN (2008) EN 12620+A1- Aggregates for concrete. European Committee for Standardization, Brussels

[4] G. C. Keserle, A. Allard (2026) Pyrrhotite-Induced Concrete Degradation - An Exploratory Data Analysis Integrating Laboratory and Field Investigations in the Trois-Rivières Region. Proc. 2nd International Conference on Iron-Sulfide Reactions in Concrete, Connecticut (USA), Mar 2026, 6p. (Unpublish extended abstract)

[5] M. A. Bérubé, C. Tremblay, F. Gagnon, B. Ross and N. Boily (2024). Concrete damage due to pyrrhotite in the Trois-Rivières area (Québec, Canada) – Influence of type of concrete element and exposure conditions. Proc. 1st ICISR, Québec (Canada), May 2024, 5 p.

[6] P. Royston (1992). Approximating the shapiro-Wilk W-test for non-normality. Stat. Comput., 2 (3) (1992), pp. 117-119. http://dx.doi.org/10.1007/BF01891203

[7] A. Hervé, L. J. Williams (2010). Tukey's honestly significant difference (HSD) test. Encycl. Res. Des; 3:1-5. https://doi.org/10.4135/9781412961288.n478

[8] M. A. Bérubé, C. Tremblay, F. Gagnon, B. Ross and N. Boily (2024). Concrete damage due to pyrrhotite in the Trois-Rivières area (Québec, Canada) – Investigation of existing buildings. Proc. 1st ICISR, Québec (Canada), May 2024, 5 p.

[9] A. Rodrigues, J. Duchesne, B. Fournier, B. Durand, P. Rivard, M. Shehata (2012). Mineralogical and chemical assessment of concrete damaged by oxidation of sulphide-bearing aggregates, Cem. Concr. Res. 42, 1336–1347. https://doi.org/10.1016/j.cemconres.2012.06.008

[10] J. Duchesne, F. Benoit (2013). Deterioration of concrete by the oxidation of sulphide minerals in the aggregate, J. Civ. Eng. Archit. 7 (8) 922–931. 10.17265/1934-7359/2013.08.003

Case study: low permeability concrete containing sulfide-bearing aggregates

Drolet, Cédric [(1)], Francoeur, Julie [(2)], Carrier, Roxanne [(3)]

(1) *Ministère des Transports et de la Mobilité durable, Quebec, Canada, cedric.drolet@transports.gouv.qc.ca*

(2) *Ministère des Transports et de la Mobilité durable, Quebec, Canada, julie.francoeur@transports.gouv.qc.ca*

(3) *Ministère des Transports et de la Mobilité durable, Quebec, Canada, roxanne.carrier3@transports.gouv.qc.ca*

Abstract

The oxidation of iron-sulfide minerals is the initial step in the deleterious reaction of sulfide-bearing aggregates in concrete; therefore exposure to humidity and high concrete permeability are considered key factors in triggering the reaction. However, very little data is available for concrete containing supplementary cementitious materials with low water-to-binder ratio. In 2024, three different structures that had undergone construction work with a 35 MPa concrete mix containing 8% silica fume and a known sulfide-bearing aggregate were selected for this case study. A visual inspection of the concrete was made, and core samples were extracted from the structures. Petrographic examination and chemical analysis showed that the pyrrhotite content of the aggregate used in the concrete varied from 0.67 vol% to 2.65 vol%. Pyrrhotite grains showed oxidation ranging from 25 to 31% when the grains were located at the edge of the aggregate, and from 7 to 18% when the grains were located within the aggregate particles. All structures exhibited visual damage signs that could be attributed to an iron-sulfide reaction in concrete, with the extent of the damage appearing to correlate with the pyrrhotite content of the aggregate. The cracking pattern also seems to be influenced by internal reinforcement of the concrete.

Keywords: *Low permeability concrete, Oxidation, Pyrrhotite, Silica fume, Supplementary cementitious materials*

1. INTRODUCTION

In early 2000, the use of a coarse aggregate with high pyrrhotite content in concrete used for residential and commercial buildings in the Trois-Rivières area (Quebec, Canada) led to early concrete damage [1]. Extensive research has been conducted to understand the deterioration mechanisms and establish the necessary conditions to generate the reaction [2, 3, 4, 5]. It was shown that oxidation of pyrrhotite is the initial step in the reaction [2]. Therefore, exposure to humidity and high concrete permeability are considered key factors in triggering the reaction and on its kinetics. However, limited data is available for concrete containing supplementary cementitious materials with low water-to-binder ratio (w/b). The objective of the study is to evaluate the potential damage induced by sulfide-bearing aggregate when used in low permeability concrete. This paper presents a case study about three structures in which a low permeability concrete containing silica fume and sulfide-bearing aggregates was used.

2. CASE STUDY

Three different structures under the management of the Ministère des Transports et de la Mobilité durable du Québec (MTMD) that had undergone construction work between 2004 and 2007 were identified. The concrete mixes used for the construction work are known to have contained the

problematic sulfide-bearing aggregate from the Trois-Rivières area (Quebec, Canada), an anorthositic gabbro with high pyrrhotite content.

The first structure identified is an overpass constructed in 1979 for which expansion joints were replaced in 2004-2005. Thin concrete repairs were also made on curbs near to the joints (figure 2.1A). The second structure is a bridge constructed in 1957 for which the exterior sides of the deck were rebuilt in 2005 (figure 2.1B). The third structure is a retaining wall built in 2007 at the exit of a culvert (figure 2.1C). Table 2.1 presents the theoretical concrete mix designs used in each project.

Figure 2.1: Structures with concrete containing sulfide-bearing aggregates. A) Structure 1, B) structure 2 and C) structure 3.

Table 2.1: Concrete mix design

Mix design	Structure 1	Structure 2	Structure 3
Design 28 days compressive strength (MPa)	35		
Slump (mm)	80 ± 20		
Air content (%)	5 - 8		
Binder type	GUb-SF premix containing 8% silica fume		
Binder SO_3 content (%)	3.6	3.7	3.9
Total binder content (kg/m^3)	365	370	350
Concrete density (kg/m^3)	2449	2410	2420
Water-to-binder ratio	0.44	0.43	0.43
Coarse aggregate content (kg/m^3)	5-14 mm: 978	5-14 mm: 670 10-20 mm: 280	5-14 mm: 700 14-20 mm: 380
Coarse aggregate relative density	2.895	5-14 mm: 3.031 10-20 mm: 2.896	5-14 mm: 2.902 14-20 mm: 2.854

3. METHODOLOGY

In 2024, a visual inspection and core sampling campaign were carried out to evaluate the three structures. The visual inspection consisted of the observation of damages that could result from an iron-sulfide reaction in concrete, such as cracking pattern (including crack width and spacing measurements), rust stains on concrete, and pop-outs of concrete exposing aggregate particles. Three to five cores with a 100 mm diameter were extracted from each structure, depending on field accessibility constraints and extent of repairs made. Table 3.1 presents the number of core samples extracted and the laboratory test program performed on the samples.

Table 3.1: Number of core samples and laboratory tests performed

Number	Structure 1	Structure 2	Structure 3
Cores	3	5	3
Megascopic examination of cores	3	5	3
Compressive strength	-	1	2
Density, absorption and voids in hardened concrete	-	2	1
Petrographic examination under reflected light microscopy	3	3	3
Chemical analyses for total sulfur content	3	3	3

a. Laboratory testing

Compressive strength and density, absorption and voids in hardened concrete testing were carried out according to test methods CSA A23.2-14C and CSA A23.2-11C respectively [6]. For petrographic examination under reflected light microscopy, polished sections with a thickness ranging from 15 to 20 mm were prepared between 20 and 50 mm below the exposed surface of concrete. The sections were polished following a step-by-step approach, using a handheld polisher with diamond impregnated and high-gloss fiber polishing pads, ranging from 100 to 10 000 grit (150 µm to 2 µm). The polished sections were examined under reflected light microscopy for the identification of iron sulfides and determination of the extent of the oxidation of the grains, according to the protocol presented by Bérubé et al. [7]. Between 52 and 66 particles from the coarse aggregate (with a size greater than 1mm) were examined for each specimen. Chemical analyses for total sulfur content were performed at an external chemistry lab according to the CTQ-M200 protocol [8].

b. Calculations

The total sulfur content of the coarse aggregate ($S_{tot}CA$, wt%) is calculated from Equation 1. In this equation, S_{tot} is the total sulfur content measured on the concrete sample (wt%), SO_3 is the sulfur trioxide content of the binder (wt%), BC is the binder content of the mix (kg/m^3), $\rho_{concrete}$ is the density of the concrete mix (kg/m^3) and AC is the aggregate content of the mix (kg/m^3).

$$S_{tot}CA = \left(S_{tot} - SO_3 \times \frac{32.07}{80.0682} \times \frac{BC}{\rho_{concrete}}\right)\left(\frac{\rho_{concrete}}{AC}\right) \quad (1)$$

Because chemical analyses are considered less subjective than petrographic examinations, the total pyrrhotite content of the coarse aggregate (%Vol_{PO}) is calculated from $S_{tot}CA$ using Equation 2. In this equation, $\rho_{aggregate}$ is the density of the coarse aggregate, %S_{PO} is the sulfur content by weight of pyrrhotite minerals (0.3648), ρ_{PO} is the density of pyrrhotite minerals (4.6) and $SRatio_{PO}$ is the sulfur-based ratio of pyrrhotite, derived from the volumetric proportions of the different minerals determined through petrographic examination using equations 3 and 4.

$$\%Vol_{PO} = \left(\frac{S_{tot}CA \times SRatio_{PO} \times \rho_{aggregate}}{\%S_{PO} \times \rho_{PO}}\right) \quad (2)$$

$$Weight\text{-}based\ Ratio_{sulfide\ 1}(\%) = \left(\frac{Volume\text{-}based\ Ratio_{sulfide\ 1} \times \rho_{sulfide\ 1}}{\sum_{i=1}^{n} Volume\text{-}based\ Ratio_{sulfide\ i} \times \rho_{sulfide\ i}}\right) \quad (3)$$

$$Sulfur\text{-}based\ Ratio_{sulfide\ 1}(\%) = \left(\frac{\%S_{sulfide\ 1} \times Weight\text{-}based\ Ratio_{sulfide\ 1}}{\sum_{i=1}^{n} \%S_{sulfide\ i} \times Weight\text{-}based\ Ratio_{Sulfide\ i}}\right) \quad (4)$$

4. RESULTS

a. Visual inspection

i. Structure 1

For thin repairs on the curb near the replaced expansion joints, a polygonal cracking pattern was visible, with crack opening widths ranging from 0.25 to 0.5 mm (figure 4.1A). No pop-outs or rust stains were observed. However, the signs of damage may have been hidden by the concrete surface coating. On the expansion joint shoulders, a crack with a mean opening width of 0.8 mm was visible at the end of the steel plates on both sides of the joint (figure 4.1B). More recent thin repairs were also present.

ii. Structure 2

Longitudinal cracks were present on the exterior side of the bridge deck (figure 4.2A) and below the slab, near the edge of the exterior side. A light polygonal cracking pattern also seemed to be present below the slab near the deck expansion joints. However, since no access equipment was used for the visual inspection, crack widths were not evaluated. On the curb, vertical cracks with opening widths ranging from 0.1 to 0.5 mm were visible. The spacing between the cracks was variable, ranging from

0.1 m to more than 1 m. Some pop-outs with exposed aggregate particles and small rust stains were visible (figure 4.2B).

iii. Structure 3

Three vertical cracks with efflorescence products were visible at the bottom of the wall (figure 4.3A). On the top of the wall, a few longitudinal cracks with opening widths ranging from 0.1 to 0.5 mm were present (figure 4.3B). No polygonal cracking, rust stains or pop-outs were noticed.

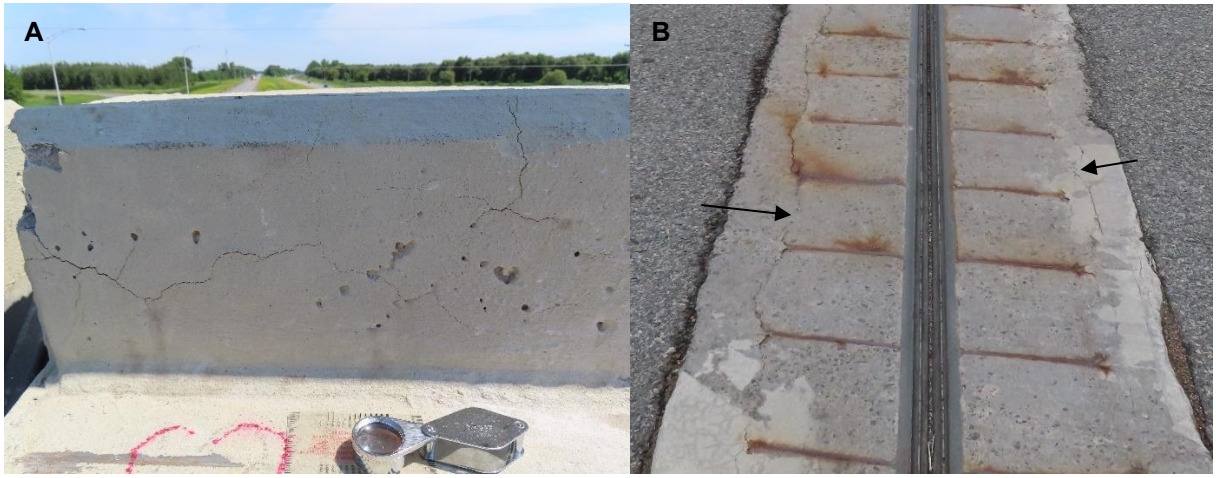

Figure 4.1: A) Polygonal cracking pattern on thin repairs on the curb. B) Large crack at the end of the steel plates of the expansion joint.

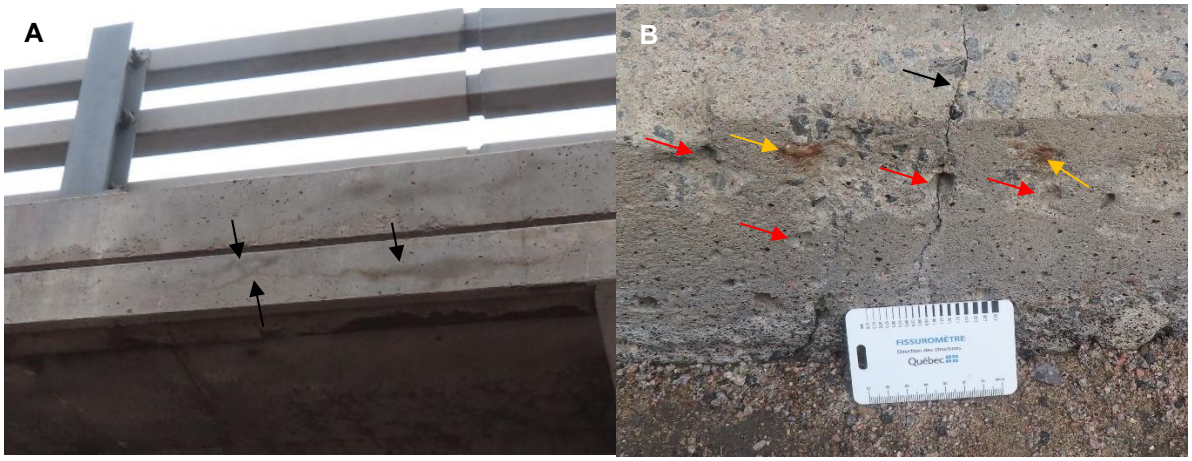

Figure 4.2: A) Longitudinal cracks on the exterior side of the deck. B) Vertical crack (black arrow), rust stains (orange arrows) and pop-outs (red arrows) on the curb.

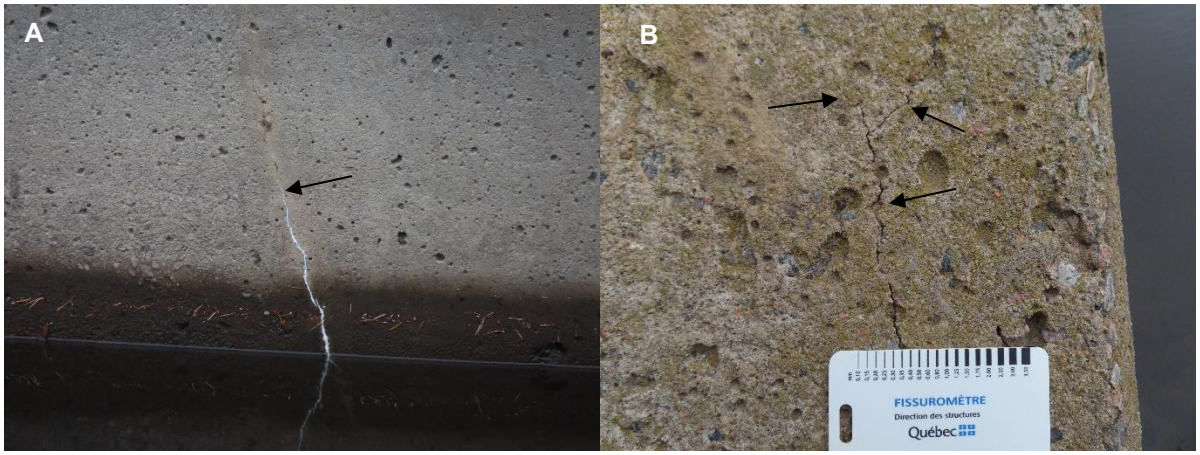

Figure 4.3: A) Vertical crack with efflorescence product. B) Longitudinal crack on the top of the wall.

b. Laboratory testing

i. Compressive strength, absorption and voids

Considering the limited number of cores extracted from structure 1, no compressive strength and absorption tests were performed for this structure.

For structures 2 and 3, the compressive strength of the concrete exceeded the minimum 35 MPa design strength, with values of 38.2 MPa and 36.0 MPa respectively.

The absorption and porosity measured on concrete from structure 2 were 6.4 wt% and 15.3 wt% respectively. For structure 3, the measured absorption was 7.2 wt%, with a porosity of 17.1 wt%.

ii. Petrographic examination and chemical analyses

For structures 1 and 2, petrographic examination confirmed the coarse aggregate used is an anorthositic gabbro. However, two different petrographic facies were observed in structure 3: a granite (about 2/3 of all coarse aggregate particles) and an anorthositic gabbro (about 1/3 of all coarse aggregate particles). From the mix design data, it is assumed that the 14-20 mm fraction used was the anorthositic gabbro, while the 5-14 mm used was the granite. All iron-sulfide minerals observed were in the anorthositic gabbro, while the granite did not contain any.

For the three cases evaluated, most of the iron-sulfide minerals identified were pyrrhotite (Po), pyrite (Py) and chalcopyrite (Cp). Traces of arsenopyrite and pentlandite were also observed. Pyrrhotite grains typically showed significant signs of oxidation, which were more prevalent when the grains were located at the edge of the aggregates (i.e., in contact with the cement paste) than within the aggregate particles (i.e., not in contact with the cement paste). Although most of the other iron-sulfide minerals observed did not show signs of oxidation, very rare traces of oxidation in pyrite grains were observed in some of the concrete samples from structures 1 and 2. Table 4.1 presents the results of the chemical analyses and petrographic examinations performed. Values are reported as the mean ± standard deviation based on the three specimens analysed.

Table 4.1: Results of chemical analyses and petrographic examination

Structure	Structure 1	Structure 2	Structure 3
Total sulfur content of the concrete (wt%)	1.08 ± 0.16	0.96 ± 0.17	0.55 ± 0.21
Estimated total sulfur content of the coarse aggregate (wt%)	2.17 ± 0.40	1.86 ± 0.42	0.73 ± 0.46[1]
Iron sulfide mineral volumetric ratio, determined by petrography (vol%)	Po: 78 ± 7 Py: 17 ± 6 Cp: 4 ± 1 Other: <1	Po: 62 ± 12 Py: 32 ± 11 Cp: 6 ± 2 Other: <1	Po: 53 ± 7 Py: 41 ± 10 Cp: 5 ±3 Other: <1
Estimated volumetric pyrrhotite content of the aggregate (vol%)	2.65 ± 0.16	1.79 ± 0.78	0.57 ± 0.42[2]
Mean maximum oxidation of pyrrhotite grains (vol%)	Within: 18 ± 6	Within: 12 ± 4	Within: 7

	Edge: 31 ± 4	Edge: 25 ± 8	Edge: 31

1. Estimated to 2.09 ± 1.31 wt% of the total content of the anorthositic gabbro.
2. Estimated to 1.61 ± 1.19 vol% of the total content of the anorthositic gabbro.

5. DISCUSSION

For all three structures investigated in this paper, visual damage signs that can be attributed to an iron-sulfide reaction in concrete were observed after less than 20 years of service. The results obtained in the present paper validate the risk assessment of damage to concrete presented by Bérubé et al [9]. Indeed, based on the exposure conditions and the pyrrhotite content of the aggregate, the calculated risk of future damage after the construction in structures 1, 2 and 3 would be 100%, 100% and 80%, respectively.

The extent of the visual damage observed on the structures appears to correlate with the pyrrhotite content of the aggregate used. The concrete from structure 3 presented the least damage and was the one with the lowest pyrrhotite content, whereas structure 1 was the one showing the most damaged concrete and contained the aggregate with the highest pyrrhotite content. It is interesting to note that for structures 1 and 2, the cracking pattern and the extent of cracking were highly influenced by the reinforcement of the concrete. The only elements showing a polygonal cracking pattern were the thin repairs in structure 1, which were mostly unreinforced. Also, for the same structure, no cracking was observed between the steel plates of the expansion joint. For structure 2, only vertical cracks were observed on the curbs despite the high pyrrhotite content of the aggregate.

The difference in absorption and porosity values measured between the concrete from structure 2 and 3 does not seem to have an influence on the extent of the oxidation of pyrrhotite grains. Even if the absorption and porosity measured on the concrete in structure 3 can be considered abnormally high for a 35 MPa concrete mix containing 8% silica fume, the oxidation of the pyrrhotite grains observed in the concrete from that structure is the same order of magnitude as the concrete of structures 1 and 2.

The results obtained in the present case study confirm that even for low permeability concrete (35 MPa mix containing silica fume), the oxidation of pyrrhotite contained in sulfide-bearing aggregate can occur and lead to early damage of the concrete.

6. CONCLUSION

Three structures under the management of the MTMD were selected for a case study of iron-sulfide reaction in low permeability concrete. The selected structures had undergone construction work between 2004 and 2007 with a 35 MPa concrete mix design containing 8% silica fume and a well-known sulfide-bearing aggregate from the Trois-Rivières area (Québec).

In 2024, a visual inspection of the structures was made, and cores were extracted for laboratory analyses.

The results obtained showed that even in the case of low permeability concrete containing silica fume, the oxidation reaction of pyrrhotite in concrete aggregate can still occur and lead to early deterioration of the concrete. The results also indicated that the extent of damage appears to correlate with the total pyrrhotite content of the aggregate. The crack pattern is also highly influenced by the internal reinforcement of concrete.

7. REFERENCES

[1] Cour Supérieure, District de Trois-Rivières, Province de Québec, Canada (2014) Jugement phare. Dossier 400-17-002016-091, june 2014, 278p.

[2] Belzile N, Chen YW, Cai MF, Li Y (2004) A review on pyrrhotite oxidation. J. Geochem. Explor., 84: 65-76.

[3] Tagnit-Hamou, A., Saric-Coric, M., Rivard, P. (2005) Internal deterioration of concrete by oxidation of pyrrhotitic aggregates. Cem. Concr. Res., 35: 99-107.

[4] Duchesne J, Fournier B (2011) Petrography of concrete deteriorated by weathering of sulphide minerals. In: Proceedings of the 33rd International conference on Cement Microscopy, San Francisco, USA, April 2011: 242-261

[5] Rodrigues A, Duchesne J, Fournier B, Rivard P, Durand B, Shehata M (2012) Mineralogical and chemical assessment of concrete damaged by the oxidation of sulphide-bearing aggregates: importance of thaumasite formation on reaction mechanisms. Cem. Concr. Res., 42: 1336-1347.

[6] CSA A23.1/A23.2 (2024) Concrete materials and methods of concrete construction/Test Methods and Standard Practices for concrete. CSA group, Toronto, Canada, June 2024, 926 p.

[7] Bérubé MA, Tremblay C, Gagnon F, Ross B (2024) Concrete damage due to pyrrhotite in the Trois-Rivières area (Québec, Canada) – Investigation of existing buildings. In: Proceedings of the 1st International conference on Iron-Sulfide Reactions in Concrete, Québec, Canada, May 2024: 180-184.

[8] CTQ M-200 (2001) Protocole d'expertise sur bâtiments résidentiels existants. Comité Technique Québécois d'étude des problèmes de gonflement associés à la pyrite. 2th ed., June 2001, 49p.

[9] Bérubé MA, Tremblay C, Gagnon F, Ross B (2024) Concrete damage due to pyrrhotite in the Trois-Rivières area (Québec, Canada) – Risk of future damage to undamaged concrete. In: Proceedings of the 1st International conference on Iron-Sulfide Reactions in Concrete, Québec, Canada, May 2024: 211-215.

Crack Networks and Chemistry in Pyrrhotite-Affected Concrete Extracted from a Massachusetts Site

Patrick G. Dixon[(1)], Michael Mengason[(2)], David G. Goodwin, Jr.[(3)], Thomas M. Russo[(4)], Ashley S. Carey[(5)], Osamah H. Dehwah[(6, 7)], Stephanie S. Watson[(8)]

(1) National Institute of Standards and Technology, Gaithersburg, MD, USA, patrick.dixon@nist.gov

(2) National Institute of Standards and Technology, Gaithersburg, MD, USA, michael.mengason@nist.gov

(3) National Institute of Standards and Technology, Gaithersburg, MD, USA, david.goodwin@nist.gov

(4) National Institute of Standards and Technology, Gaithersburg, MD, USA, thomas.russo@nist.gov

(5) National Institute of Standards and Technology, Gaithersburg, MD, USA, ashley.carey@nist.gov

(6) PREP Associate, National Institute of Standards and Technology, Gaithersburg, MD, USA, osamah.dehwah@nist.gov

(7) Department of Civil and Systems Engineering, Johns Hopkins University, Maryland, USA, odehwah1@jh.edu

(8) National Institute of Standards and Technology, Gaithersburg, MD, USA, stephanie.watson@nist.gov

Abstract

Homes in areas of Massachusetts are experiencing issues with crumbling foundations due to pyrrhotite, similar to homes in northeastern Connecticut. Concrete from the basement of a Massachusetts home, built in the mid-1990s, experiencing pyrrhotite-driven deterioration, was cored shortly before the foundation was replaced. This paper describes analysis of three cores from one wall. The cores were subjected to resonant frequency testing, revealing dynamic Young's moduli ranging from 20.0 GPa to 4.5 GPa. These cores were then impregnated with fluorescent epoxy, sliced longitudinally, and photographed. Cracks and damage were visible in all core slices. A yellow/green selection was performed on the photographs to segment the damage. To capture the full range of plausible damage areas, a wide range of brightness thresholds was used to construct a simple damage area fraction metric. In the three cores, this metric ranges from 3.5 % to 14.3 % and decreases with increasing dynamic Young's modulus. One core was preliminarily analyzed to estimate the changes in damage over the wall thickness and imaged with micro x-ray fluorescence (μXRF). μXRF on a core section revealed sulfur-rich aggregates and a localized sulfur-rich region of cement paste, suggestive of internal sulfate attack. Further imaging of cores with μXRF and data analysis will be performed to estimate the detailed chemistry of sulfur-rich regions and understand the relationship between element distribution patterns and the observed cracks and damage.

***Keywords**: cracking, dynamic elastic properties, field study, micro x-ray fluorescence, pyrrhotite*

1. INTRODUCTION

Pyrrhotite-driven deterioration of concrete foundations in afflicted areas has been associated with visible cracking patterns on the basement wall surfaces [1–5]. In Connecticut, these patterns are used in assigning a severity class to help with foundation replacement prioritization [4, 6]. These surface cracks are critical for forensic purposes, but understanding the crack network of pyrrhotite-affected concrete more holistically would provide a more complete assessment of the concrete. Indeed, several important studies have investigated cracks within the pyrrhotite-affected concrete. Jana found cracks extended through entire thickness of wall in the examinations of cores [1, 2]. Microcracking has been observed in the matrix of affected concrete in proximity to sulfate mineral deposits [3]. Additionally, microcracking has been observed within pyrrhotite-bearing aggregates [7], which pointed towards a deterioration process, accelerated by more extensive sulfate transport into the matrix through these aggregate microcracks. Titon et al. [8] have demonstrated that biotite's interlayer spaces function like roughly nanometer-sized microcracks when in proximity to pyrrhotite, enhancing the transport of the formed sulfate out of the aggregate into the cement paste.

This abstract presents a preliminary study of field samples to examine the mesoscale crack networks within a wall of a pyrrhotite-affected home in Massachusetts and the chemistry across the wall's thickness. Understanding these mesoscale crack networks will aid in assessing the structural response of pyrrhotite-affected concrete. Elemental analyses over the thickness of pyrrhotite-affected wall will provide spatial location information on the reactions. When this data is combined with the mesoscale crack network information, understanding of the relationships between the reactions and structural deterioration can be gained for the potential benefit of mitigation or even rehabilitation measures.

2. FIELDWORK

The basement of a two-story home in Massachusetts (built in the mid-1990s), experiencing deterioration consistent with pyrrhotite-driven expansion was sampled. The site featured substantial cracking in many areas along the walls. These cracks were inventoried with measurement by tape measure and crack width gauge, photographs and quick field sketches. One notable crack was a horizontal crack tapering from approximately 10 mm to 1 mm in width over a length of 3 m along one wall. This crack also intersected with a similar vertical crack running over near the full height of the wall (2 m). The slab and the wall underneath the garage showed minimal deterioration. Efflorescence was also found in areas on the walls and was sampled at multiple locations. Over 35 cores were extracted from the basement by wet coring at various locations, which were measured with tape measure, vertically from the slab and horizontally from wall corners. Locations of the wall cores were spread throughout the entirety of the basement (on 10 walls, including bump out walls in the foundation), predominantly high (approximately 1.7 m) and middle (approximately 1.1 m) positions on wall from the slab; locations were also simultaneously chosen to encompass a range of visually observed interior cracking. Cores were taken from locations, intersecting larger cracks, adjacent to larger cracks, and featuring no large observed cracks in the area, with these damage features captured in the metadata for each specimen. Six 108 mm diameter cores were removed from one wall at different positions, reflective of the described sampling. These six cores were all below the soil grade line of the wall. One core fractured during drilling or extraction from the barrel. Preliminary x-ray diffraction of the efflorescence on this wall showed thenardite as the predominant phase.

3. CORE ANALYSIS METHODS

The dynamic Young's moduli of the five intact cores of the one wall were measured with impact-driven resonant frequency testing (RFT). These tests were performed on the cores with their as-cored geometry. Namely, variable core length based on the wall thickness was possible, and both the exterior asphalt barrier and interior face of the wall were included in the samples. RFT was performed in triplicate, each measure including separate dimensional and mass measures, in addition to strikes and vibration acquisitions.

Three of the five cores, referred to as 705-F1, 707-F1, and 709-F1, at similar height along the wall and different levels of observed cracking on the interior wall surface, were then selected for sectioning. 705-

F1 was closest to a wall corner, while 707-F1 was furthest. These cores were dried at 40°C for 40 hours. Each entire core was then impregnated with ultraviolet (UV)-fluorescent epoxy. The impregnated and encased cores were cut nominally in half perpendicular to their length, resulting in two cylinders per core, one with the exterior wall surface and the other with the interior wall surface. The cylinders were then sliced longitudinally twice for a middle section of nominal thickness of 6 mm using a precision saw. Orientation of the two cylinders of one core was consistently maintained during slicing, so that exterior and interior slices are the same section of the core. Water was used in all cutting operations.

All individual sections were then photographed under UV light with a Google Pixel 7a. Images of both faces of the slices were taken with and without overhead laboratory lighting to provide different contrast levels. For each section, one image was taken with a ruler without UV light for a scale reference.

Image analysis was performed in FIJI (ImageJ) [9]. The photographs were cropped to ensure that the surrounding epoxy was not included in the analysis of the core; the area analyzed for each section ranged from approximately 101 mm to 106 mm by 122 mm to 128 mm. The segmentation of the damage in the photographs with overhead laboratory lights on was performed with Hue-Saturation-Brightness (HSB) thresholding. The full saturation range (0 to 255) was passed; the hue from 50 to 120 (0 to 255 scale) was passed, and four different thresholds were used in brightness space. The upper bound was always 255. The lower bounds for thresholding the brightness were selected based on the brightness distribution of each individual image. They were zero, the mean of the distribution minus one standard deviation of the distribution, the mean of the distribution, and the mode of the distribution. To get an initial estimate of the variation of the damage area fraction, (A_d/A_0) over the wall's thickness, approximately 20 mm (506 pixels) strips were taken from the cropped images of one face of core 709-F1, over their length, starting near the exterior and interior edges and moving towards the center of the wall. Sections less than 20 mm at the middle of the core slice were not considered.

The sections from the same core, 709-F1, were also analyzed with micro x-ray fluorescence (μXRF) with a Bruker M4 Tornado^{PLUS}. The slices were imaged under vacuum with a rhodium x-ray tube at 50 kV and 600 μA, and an x-ray spot size of 20 μm. Large area maps with step sizes of 100 μm and 35 millisecond dwell time were collected on both slices. A variety smaller-scale local maps at various locations of the wall thickness were also performed.

4. RESULTS AND DISCUSSION

The dynamic Young's moduli of the five cores spanned a large range from 20.0 GPa to 4.5 GPa. The largest absolute spread in the triplicate measures of one core was given by a standard deviation of 1.3 GPa. The largest absolute difference in the dynamic Young's moduli as measured in longitudinal and transverse modes was less than 2.0 GPa. The photographs of cores under the UV light with the overhead laboratory lights on are shown in Figure 4.1.

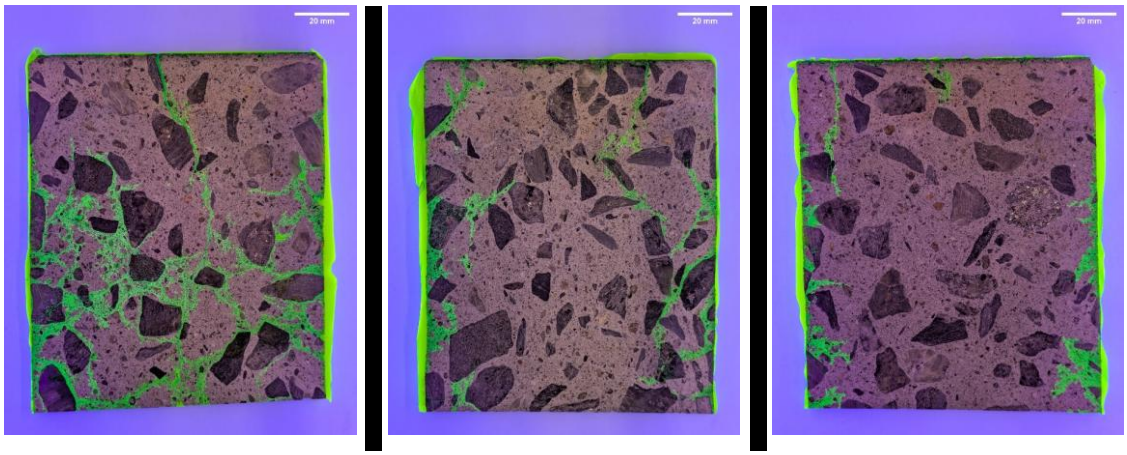

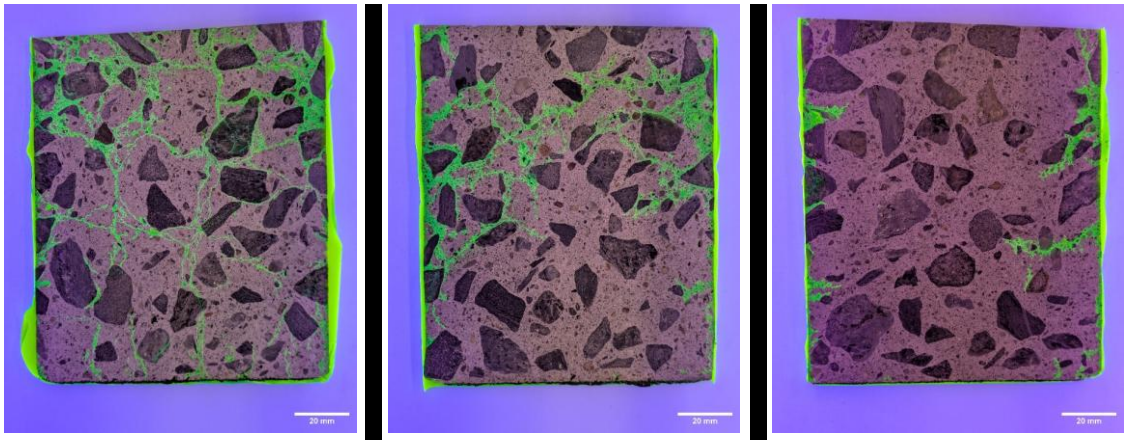

705-F1 709-F1 707-F1

Figure 4.7: Photographs of the core sections of 705-F1, 709-F1, and 707-F1 from left to right under UV light. Interior slices are above with the interior wall edge at the top, and exterior slices are below with the exterior wall edge at the bottom. The field of view for every image above is 129 mm x 158 mm

Before discussing results, this damage should be clarified. In the procedure, the epoxy only infiltrated areas that are accessible from (i.e., connected to) the core surfaces. Smaller cracks or regions of extreme permeability that do not intersect with any of the three core surfaces are not filled with the fluorescent epoxy. Thus, the damage area fraction should be considered an estimated measure of mesoscale damage, or damage with characteristic dimensions ranging in order from hundreds of micrometers to millimeter scales. While many microcracks may be excluded in this analysis, mesoscale cracks do not constitute the only feature highlighted by the epoxy. In addition to cracks, damage regions of extreme permeability and pre-existing voids that have connectivity with the core surfaces will be highlighted by the epoxy. The HSB-based damage segmentation used in the image analysis, captures all these features. Additional work could be performed to segment various features separately, but this methodology provides a simple and consistent metric. The thresholding limits of the various damage segmentation methods were purposefully broad to ensure the inclusion of plausible damage area. The brightness threshold from zero and higher gave the highest area damage fractions, while the thresholding the brightness from the mode and higher gave the lowest. In subsequent discussion about the damage area fraction, the average of the four methods is presented followed by the minimum and maximum in parentheses, unless otherwise stated.

In Figure 4.7, it is clear there is damage in all core sections, and cracks appear over the entire thickness as found by Jana [1, 2]. Cores 705-F1 and 709-F1 exhibit considerably more damage than 707-F1, which is furthest from a wall corner and has the lowest damage area fraction, 3.5 % (2.7 %, 4.0 %). 705-F1 is the closest to a wall corner and has the largest damage area fraction, 14.3 % (10.5 %, 16.7 %). The sections of 709-F1 are the only pair of the three that shows a larger than 1 % difference of the average between the interior and exterior slice, with the exterior slice damage area fraction nearly double that of the interior. In general, damage area fractions of the two faces of the same section are quite comparable, with maximum absolute differences near 1 % for all measures. In 709-F1, the analysis over the wall thickness (length of the core) on the interior section gives damage area fractions that are not drastically spatially separated. The minimum damage area fraction of the 20 mm length subsections is 4.2 % (2.8 %, 5.0 %) centered at roughly 30 mm from the wall interior, while the maximum of 9.8 % (6.9 %, 11.7 %) is centered roughly at 50 mm from the wall interior. The analysis of the exterior section on the other hand, shows considerable differences. The subsections over the 60 mm closer to the wall exterior all show substantially lower damage area fractions. The minimum damage area fraction of 1.1 % (0.6 %, 1.4 %) is centered at roughly 10 mm from the exterior edge, while the maximum of 24.8 % (17.6 %, 29.1 %) is centered at 90 mm from the exterior edge. Qualitatively, the photographs of the other two cores also suggest more damage over the middle. The lower damage, in the vicinity of the wall interior edge, may be a result of carbonation in this area.

Figure 4.8 plots the longitudinal mode dynamic Young's modulus, E_{dyn}, against the damage area fraction, (A_d/A_0). The vertical error bars are the standard deviation of the three RFT measurements,

while the horizontal bars show the minimum (mode as the lower brightness threshold) and maximum (zero as the lower brightness threshold). The trend is as expected, with the dynamic Young's modulus decreasing as the damage area fraction increases. Additionally, in Figure 4.8 the thresholding methods differ more greatly as the damage area fraction increases.

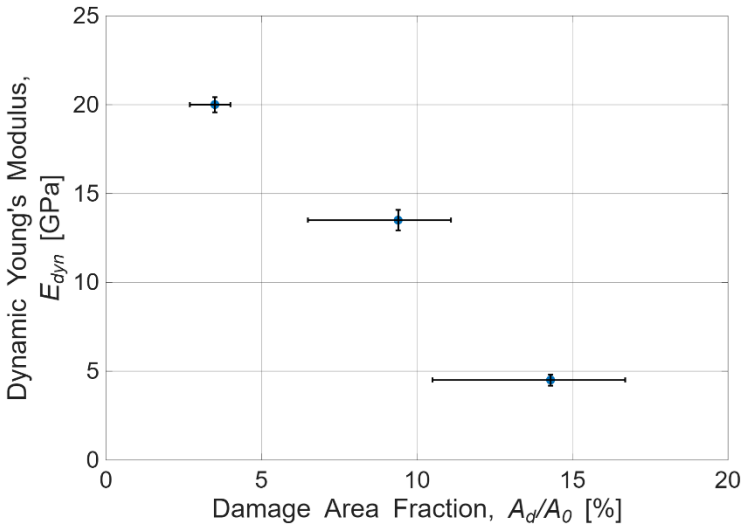

Figure 4.8: The dynamic Young's modulus (longitudinal mode) against the damage area fraction. Vertical error bars are plus/minus the standard deviation of the three, while horizontal error bars show the minimum and maximum of the damage area fraction from the four methods.

Figure 4.3 shows maps from μXRF on a subsection at middle width (middle of the core diameter) of the exterior slice of 709-F1. Figure 4.3(a) depicts the region; Figure 4.3(b) shows a μXRF chemical map and Figure 4.3(c) presents a heat map of the sulfur concentration.

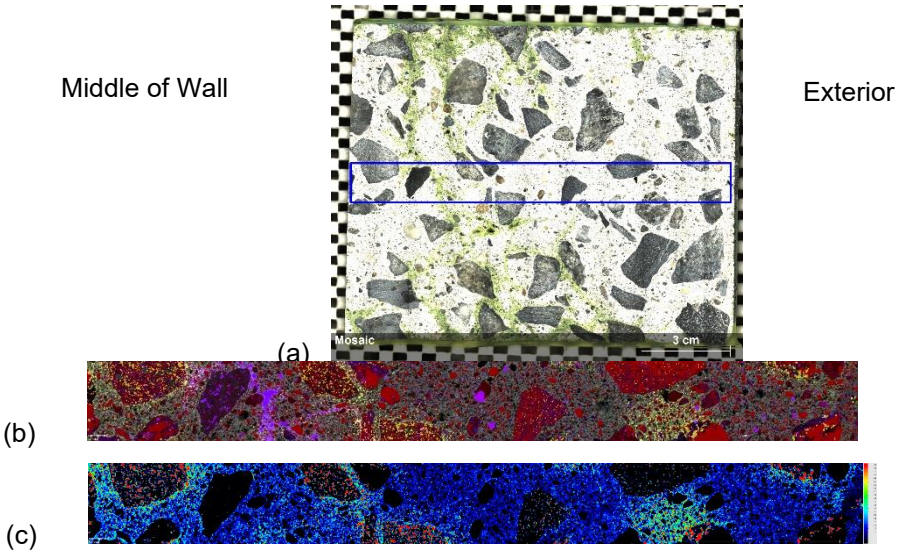

Figure 4.3: (a) The imaged subsection of the 709-F1 exterior slice; the middle of the wall is on the left and the exterior wall edge is on the right; this is consistent in subsequent images (field of view: 139 mm x 120 mm). (b) A μXRF chemical map of the subsection (Ca – green, Si – brown, S – yellow, Cl – purple; field of view: 128 mm x 13 mm). (c) The heat map of sulfur concentration from the μXRF; red is high and black is low (field of view: 128 mm x 13 mm)

Sulfur is present in both the cement paste and aggregate. Some aggregates show a very strong sulfur presence. Under first inspection, sulfur does not appear to be highly associated with the large crack, which can be located as the large purple (chlorine in the epoxy) band toward the middle (left) in Figure

4.3(b). Towards the exterior edge of the wall, there is a region of cement paste that appears to be rich in sulfate minerals. There are unlikely possibilities that this result stems from a region of cement featuring small sulfide particles or a large sulfur-bearing aggregate just below the paste, and further analysis is needed to rule these out.

5. CONCLUSIONS AND FUTURE WORK

In the three cores studied, cracks and damage are present in all and occur over their length, namely over the entire thickness of the wall. The damage area fraction ranges from 3.5 % to 14.3 % in the three cores, considering the average of four simple damage selection methods. In 709-F1, the damage area fraction tended to be greatest near the center of the wall thickness, i.e., near the middle over the core length. Further work will analyze more cores and evaluate the influence of subsection size. The dynamic Young's moduli of cores vary from 20.0 GPa to 4.5 GPa, and this property decreases with increasing damage area fraction as expected. Further work is being performed to develop the relationship between the dynamic Young's modulus and damage area fraction with the analysis of more cores. Related work is linking this nondestructive property to the conventional mechanical properties of pyrrhotite-affected concrete. μXRF is a powerful technique that permits large area examinations of the chemistry while preserving the microstructure. Sulfur is found throughout both the aggregates and cement paste. Deeper elemental analyses of the μXRF data are required to estimate the detailed chemistry.

6. DISCLAIMER

Certain equipment, instruments, software, or materials, commercial or non-commercial, are identified in this paper in order to specify the experimental procedure adequately. Such identification does not imply recommendation or endorsement of any product or service by National Institute of Standards and Technology, nor does it imply that the materials or equipment identified are necessarily the best available for the purpose.

7. ACKNOWLEDGEMENTS

Thanks to the homeowner and the contractor, Foundation Solutions of NE, LLC, for allowing NIST access to the site. Thanks also to the Federal Highway Administration for core slicing support.

References

[1] Jana D (2020) Pyrrhotite Epidemic in Eastern Connecticut: Diagnosis and Prevention. ACI Mater J 117:. https://doi.org/10.14359/51718059

[2] Jana D (2022) Cracking of residential concrete foundations in eastern Connecticut, USA from oxidation of pyrrhotite. Case Stud Constr Mater 16:e00909. https://doi.org/10.1016/j.cscm.2022.e00909

[3] Zhong R, Wille K (2018) Deterioration of residential concrete foundations: The role of pyrrhotite-bearing aggregate. Cem Concr Compos 94:53–61. https://doi.org/10.1016/j.cemconcomp.2018.08.012

[4] Connecticut Foundation Solutions Indemnity Company, Inc. (CFSIC) (2025) Connecticut Foundation Solutions Indemnity Company, Inc. ("CFSIC") Underwriting and Claims Management Program. CFSIC. https://crumblingfoundations.org/getting-started/underwriting-criteria/#prioritization. Accessed 1 December 2025

[5] Duchesne J, Fournier B, Francoeur J (2018) Study of the Deterioration of Concrete Incorporating Sulfide-Bearing Aggregates. In: ICDCS 2018. RILEM, University of Leeds, Leeds, West Yorkshire, LS2 9JT, United Kingdom, pp 273–280

[6] Santos L, Chrysochoou M, Wille K (2025) Development of a risk assessment framework for pyrrhotite induced deterioration of concrete foundations in CT and MA. Cem Concr Res 197:107951. https://doi.org/10.1016/j.cemconres.2025.107951

[7] Zhong R, Ai X, Yao Y, et al (2024) Effects of the expansion mechanisms on the pyrrhotite-induced deterioration of concrete foundations. Case Stud Constr Mater 20:e02830. https://doi.org/10.1016/j.cscm.2023.e02830

[8] Titon B, Duchesne J, Fournier B (2024) The role of biotite in the deterioration of pyrrhotite within concrete aggregates: Trois-Rivières case study. Cem Concr Res 183:107595. https://doi.org/10.1016/j.cemconres.2024.107595

[9] Schindelin J, Arganda-Carreras I, Frise E, et al (2012) Fiji: an open-source platform for biological-image analysis. Nat Methods 9:676–682. https://doi.org/10.1038/nmeth.2019

Internal Sulfate Attack and Premature Deterioration of Structural Concrete: Lessons from China

Xianbing Ai [(1)], Rui Zhong [(2)]

(1) Huazhong University of Science and Technology, Wuhan, China, xianbing_ai@hust.edu.cn

(2) Huazhong University of Science and Technology, Wuhan, China, cerzhong@hust.edu.cn

Abstract

Infrastructure construction has expanded from eastern coastal regions, which are rich in natural aggregates, to western regions with more complex geological conditions. Due to the scarcity of commonly used aggregate and high cost of long-distance transportation, the in-situ utilization of locally available aggregates has emerged as a cost-effective solution. Nevertheless, these aggregates maybe contaminated with species harmful to concrete performance. This paper presents two case studies of premature deterioration of structural concrete related to internal sulfate attack (ISA) from China. The first case involves two residential houses. Severe cracking, with widths up to 10 mm, developed in the concrete within 20 years after construction. Alunite was detected in the aggregates used for the houses. A substantial amount of ettringite was observed in the interfacial transition zone (ITZ) between the aggregates and matrix. The second case concerns a tunnel, which has to be closed for repair just one year after completion due to severe damage. The deterioration was characterized by excessive water seepage, significant pavement buckling, extensive cracking of the tunnel lining, and loss of cohesion. The ITZ was highly porous and contained abundant ettringite and thaumasite. The width of ITZ was more than five times greater than that of the control, and the microhardness of the affected concrete was also significantly lower. Excessive gypsum was identified in the aggregates used for concrete production. Water infiltrated into the interior of the concrete through the ITZ and microcracks and gypsum was then dissolved. This process accelerated ISA, ultimately resulted in premature failure of the tunnel.

Keywords: *ettringite; alunite; internal sulfate attack; residential house, tunnel*

1. INTRODUCTION

Premature deterioration of concrete structures related to iron sulfide induced internal sulphate attack (ISA) has been increasingly reported worldwide over the last two decades [1]. However, ISA-related engineering failures have not received sufficient attention and are rarely documented in China. With rapid urbanization, infrastructure construction has expanded from eastern coastal regions, which are rich in natural aggregates, to western regions with more complex geological conditions. Due to the scarcity of commonly used aggregate and high cost of long-distance transportation, non-standard locally available aggregate may be the viable cost-effective solution. Nevertheless, these aggregates maybe contaminated with species, such as iron-sulfide, which can induce ISA and harmful to concrete performance. ISA induced premature deterioration of concrete structures were sporadically reported in China [2-4]. This study review and compiled those reported cases in China.

2. CASE STUDY - RESIDENTIAL HOUSES

a. Residential house 1

Premature deterioration was reported for a seven-story, two-unit masonry–concrete residential building constructed in 1998 (Jiading District, Shanghai, China). The south side of the first floor is used as a garage, while the second floor and above comprise residential units with one staircase serving two apartments per floor. Except for the kitchen and bathroom areas, which are constructed with cast-in-place reinforced concrete slabs, the floor and roof systems are composed of 120-mm-thick precast hollow-core slabs.

Shortly after the building was put into use, cracking occurred in some ground-floor walls. In 2015, an inspection was conducted by a qualified agency, which revealed that wall cracks were mainly concentrated on the first floor, most of which were diagonal cracks (Figure 2.1a). The crack widths ranged approximately from 1 to 10 mm, and no distinct pattern was observed in the orientations of the diagonal cracks. The inspection concluded that the wall cracking resulted from differential foundation settlement. In 2016, a company was hired to strengthen the foundation. However, during the strengthening process, after excavation of the foundation, it was discovered that the foundation exhibited extensive map cracking, with local crack widths reaching 5–10 mm. At all locations where severe foundation cracking was present, the overlying walls also exhibited severe diagonal cracking (Figure 2.1b and c).

(a) Diagonal cracking of walls (b) Cracks at the base of the tie column (c) Cracking in the foundation

Figure 2.1: Deterioration characteristics of masonry residential building 1 [2]

After chiseling open the foundation concrete at several cracked locations, it was found that the concrete aggregates contained abnormal aggregates (Figure 2.2a). Portions of the abnormal aggregates were extracted, ground into fine powder, and subjected to X-ray diffraction (XRD) analysis. The results indicated that the main crystalline phases of the abnormal aggregates were alunite and quartz. Samples containing the interface between the white aggregate and the cementitious matrix were examined by scanning electron microscopy (SEM). A large number of needle-like ettringite crystals could be clearly observed at the interface between the white aggregate and the cementitious matrix (Figure 2.2b). It was concluded that the premature deterioration was primarily attributable to delayed ettringite formation resulting from alunite-bearing coarse aggregates.

(a) Abnormal aggregate (b) Ettringite in the ITZ

Figure 2.2: Abnormal aggregate from building 1 and ettringite in ITZ [2]

b. Residential house 2

This case concerns another six-story, two-unit masonry–concrete residential building located in Jiading District, Shanghai, which was also constructed in the 1990s. The building adopts a one-staircase, four-apartment-per-floor residential layout. The superstructure is similar to that of Case 1, consisting of a masonry–concrete structural system.

Shortly after the building was put into use, cracking damage occurred in some walls. In 2005, an inspection revealed that wall cracks were mainly concentrated in the central part of the building, most of which were vertical cracks, primarily distributed at the window corners from the first to the third floors. The crack widths ranged approximately from 1 to 3 mm, gradually decreasing from the lower floors upward, and almost no cracks were observed above the fourth floor. Although the measurements indicated no significant differential settlement of the building (the maximum inclination rate was less than 2‰), the inspection nevertheless concluded that the wall cracking was caused by differential foundation settlement, and foundation strengthening was recommended.

In 2006, foundation strengthening was carried out. However, within several years after the foundation strengthening, cracks in the upper-structure walls developed rapidly. By 2012, severe vertical cracks were observed at the intersections of longitudinal and transverse walls near the central part of the north façade, as well as at similar wall intersections in the central interior of the building (Figure 2.3a). The crack widths were relatively large in the lower stories, generally ranging from 3 to 8 mm, and extended upward to the fourth and fifth floors. In addition, vertical cracks were also present in most exterior longitudinal walls and at window corners, with more severe cracking at the lower floors (typically 2–8 mm in width) and relatively minor cracking at the fourth and fifth floors (Figure 2.3b).

(a) Cracks at the re-entrant corner of the exterior wall (b) Diagonal cracks in the wall (c) Fine cracks on the top surface of the foundation

Figure 2.3: Deterioration characteristics of masonry residential building 2 [2]

To clarify the cause, partial excavation of the foundation was carried out. It was found that multiple irregular fine cracks were present on the exposed foundation surface, as shown in Figure 2.3c. Grayish-white abnormal aggregates were identified within the concrete aggregates (Figure 2.4a). X-ray diffraction (XRD) results indicated that the abnormal aggregates were mainly composed of alunite. Scanning electron microscopy (SEM) analysis of the gray material surrounding the alunite revealed that these gray phases were primarily composed of ettringite.

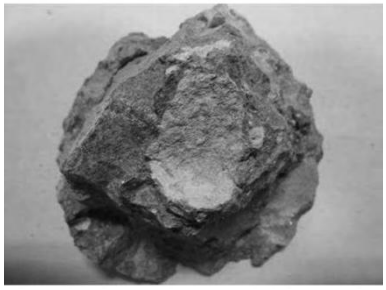

(a) Cracks at the re-entrant corner of the exterior wall

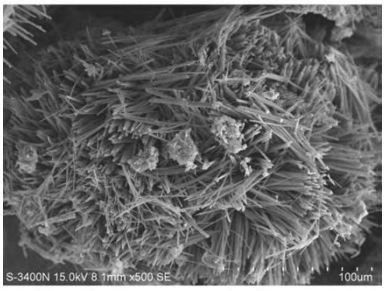

(b) Diagonal cracks in the wall

Figure 2.4: Abnormal aggregate from building 2 and ettringite in ITZ [2]

3. CASE STUDY - TUNNEL

The Shiziya Tunnel is a key control project of the Taixi section of National Highway G209, located in Badong County, Hubei Province, China. The tunnel has a total length of 453 m. Construction commenced on October 12, 2002, and full breakthrough was achieved by late May 2003, after which the tunnel entered the trial operation stage. However, severe deterioration was observed within one year after it was opened to traffic. Typical characteristics of deterioration are shown in Figure 3.1. The tunnel lining cracked and was accompanied by seepage, dripping, and formation of white deposits (Figure 3.1a). The maximum pavement heave reached 124 mm and the crack opening width has reached 20~40 mm (Figure 3.1b). Under locally humid conditions, the deterioration of the tunnel lining concrete was significantly accelerated, leading to disintegration of lining concrete (Figure 3.1c).

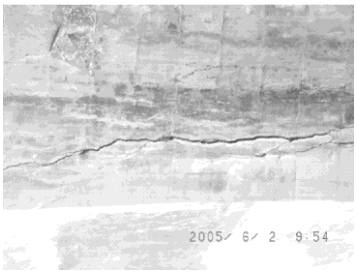

(a) Lining cracking

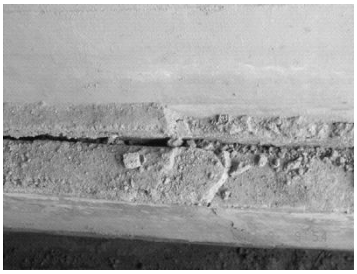

(b) Cracking and heaving of the pavement

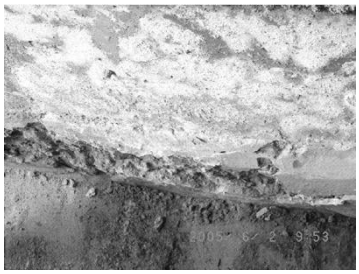

(c) Disintegration of lining concrete

Figure 3.1: Typical deterioration characteristics of Shiziya Tunnel [3]

The excavation of the Shiziya Tunnel significantly disturbed the original groundwater recharge, runoff, and drainage regime, turning the tunnel base into a groundwater discharge surface and flow-concentration corridor. The resulting groundwater accumulation played a critical role in inducing the tunnel deterioration. Subsequent inspections revealed that the aggregates used in the tunnel structure and pavement concrete are gypsum-bearing dolomite aggregate [4]. Under wet or humid conditions as in this case, ettringite and thaumasite were formed in the ITZ, leading to a severe reduction in concrete strength. Consequently, localized concrete exhibited black discoloration, cracking, and spalling.

4. RECOMMENDATIONS

Iron-sulfide-related ISA has been increasingly reported worldwide but has rarely been reported in China. However, due to the unawareness and limitations of inspection equipment, previous inspections and conclusions regarding the causes of deteriorated concrete structures may therefore warrant further examination. Premature deterioration of concrete structures induced by ISA, resulting from the use of abnormal aggregate contaminated with minerals such as alunite or gypsum, has been sporadically reported in China. There is an urgent need to establish standardized test methods to evaluate the suitability of locally available aggregates for concrete production.

5. REFERENCES

[1] Zhong R, Wille K (2018) Deterioration of Residential Concrete Foundations: the Role of Pyrrhotite-Bearing Aggregate. Cem Concr Compos 94: 53-61.

[2] Chen H, Li M, Wang X (2018) Analysis and processing of engineering accident caused by delayed ettringite reaction. Build Struct 48(11): 105-108 (in Chinese).

[3] Xiang G, Li Z, Zhang J (2008) Analysis and Treatment for Shiziya Tunnel Damage. Soil Eng and Foundation 22(1): 5-7 (in Chinese).

[4] Xing Z, Deng M, Wang A, Liu K (2014) Analysis and Treatment for Shiziya Tunnel Damage. Journal of Building Materials 17(1): 30-35 (in Chinese).

Understanding the role of type of sulphide in concrete degradation: Insights from concrete electrochemical testing scheme of diverse aggregate sources.

Castillo Araiza Rodolfo[1,2,3], Rodrigues Andrea [1,2], Fournier Benoît [1,2], Duchesne Josée [1,2]

(1) *Centre de recherche sur les infrastructures en béton, Québec, Canada,*

(2) Université Laval, Québec, Canada
(3) Corresponding author, email: rodolfo.castillo-araiza@ggl.ulaval.ca

Abstract

Over the past twenty years, the Trois-Rivières region in Canada has faced significant degradation in concrete structures incorporating sulphide-bearing aggregates. This issue prompted the development of an electrochemical testing scheme to evaluate aggregate reactivity. The 50-day experimental protocol consists of a 14-day moist-curing phase followed by a 35-day electrochemical procedure, divided into chloride ion impregnation (14 days) and impressed voltage (21 days). Within this framework, chloride ions catalyze the oxidation of sulphide minerals, specifically targeting the highly susceptible pyrrhotite (Po). Among the various parameters investigated, the modulus of elasticity (MoE) proved to be the most robust quantitative indicator of internal degradation and potential for distinguishing reactive from non-reactive aggregates. Therefore, to quantify the damage induced by reactive aggregates, a novel metric—Relative Modulus of Elasticity (RMoE)—has been proposed. The present research program seeks to further validate the efficacy of the electrochemical testing methodology by examining 19 aggregates characterized by variations in both the concentration and mineralogical nature of sulphide-bearing constituents, as well as differences in the lithological composition of the host rock materials. The findings reaffirm that Po is the principal reactive sulphide mineral, capable of initiating concrete deterioration when present above a critical concentration threshold and subjected to environmental conditions (oxygen and water). However, in certain instances, Po was observed to be finely disseminated within the aggregate matrix, thereby limiting its accessibility and delaying its activation during electrochemical testing. To date aggregates containing pyrite as the dominant sulphide mineral, have not exhibited signs of reactivity or damage within the tested concrete specimens. Future research should examine aggregates containing substantial framboidal pyrite or mixed sulphide assemblages.

Keywords: *Electrochemical testing scheme, Pyrite, Pyrrhotite, Relative MoE, sulphide-bearing aggregates.*

6. INTRODUCTION

In recent years, a significant issue affecting concrete durability has emerged worldwide. This issue is linked to the reactivity of sulphide-bearing aggregates (SBA), primarily the mineral pyrrhotite ($Fe_{1-x}S$) [Po]. The degradation process consists of two coupled chemical phenomena in an alkaline and moist concrete environment:

a) Oxidation reaction: Po oxidizes in the presence of water and oxygen. This redox reaction converts the Fe^{2+} and Fe^{3+} ions into iron hydroxides/oxides (such as rust) and, crucially, produces sulphates ions $(SO_4)^{2-}$.
b) Internal sulphate attack: The newly formed sulphate ions diffuse into the cement paste, where they react with the portlandite ($Ca(OH)_2$) and calcium aluminate phases. This reaction produces expansive (secondary) minerals, primarily ettringite and occasionally thaumasite.

The formation of these sulphate-bearing phases generates significant internal stresses, leading to micro-cracking, which eventually results in large-scale cracking and a loss of mechanical strength of the affected concrete.

Therefore, studies have been conducted to provide a better understanding of the reaction mechanisms of iron sulphides (particularly Po) that are responsible for concrete damage in the Trois-Rivières (TR) region [1]. A quality control protocol for SBA was thus developed, comprising three steps: measuring the total sulphur content (T_S), determining the oxidation potential through an oxygen consumption test, and determining the expansive potential through a mortar bar performance test [6]. Recently, this protocol was enhanced by the development of an electrochemical testing scheme for concrete specimens, which reproduces the oxidation and internal sulphate attack observed in concrete in the TR region even more reliably [4,5]. This electrochemical approach is being adopted for various applications, demonstrating its effectiveness to assess the oxidation reaction of the SBA [3].

7. SCOPE OF WORK

This research program involves 19 coarse aggregates from 18 distinct aggregate sources, characterized by variations in the concentration and mineralogical nature of sulphide minerals, and the different lithological composition of aggregate materials. All aggregates were subjected to the electrochemical testing scheme with the primary objective of further confirming its reliability for the quality control of SBA.

8. MATERIALS AND METHODS

8.1 Petrographic examination

Petrographic analysis was performed to precisely ascertain the composition (including sulphide minerals) of the 19 selected aggregates using thin section examination with a Nikon Eclipse E600 Pol transmitted and reflected light microscope.

8.2 Total sulphur content (T_S)

The presence of iron sulphide minerals in aggregates is initially screened using total sulphur determination (T_S), which is expressed as a mass percentage. A 4 kg sample of aggregate consisting of particles sized between 5 and 20 mm is subjected to progressive grinding, sieving and splitting operations. This process yields the required 1 g of pulverized sample required for subsequent chemical analysis [6].

The T_S is quantified using a carbon/sulphur chemical analyser (Eltra CS 800). These T_S values were calculated from triplicate samples to ensure reliability and provide a robust quantitative assessment of the overall sulphur concentration in the aggregates

8.3 Electrochemical testing scheme

Concrete specimens were made and tested (per aggregate source) in accordance with the testing scheme proposed by Castillo Araiza et al. [5] (Figure 3.1). The results showed that a 35-day electrochemical treatment comprising a 14-day chloride ion impregnation phase, followed by a 21-day period during which an impressed voltage is applied to the specimens, is effective in inducing damage to concrete incorporating SBA under laboratory conditions. To evaluate the reactivity of these aggregate materials, the authors suggested the determination of the relative modulus of elasticity (RMoE), which is calculated by comparing the MoE of sound concrete specimens measured after a standard 28-day moisture curing period with that of companion specimens subjected to the 35-day period of electrochemical testing scheme [4]. The efficacity of that approach has been evaluated in relation to the detection of the reactivity of a larger variety of SBA.

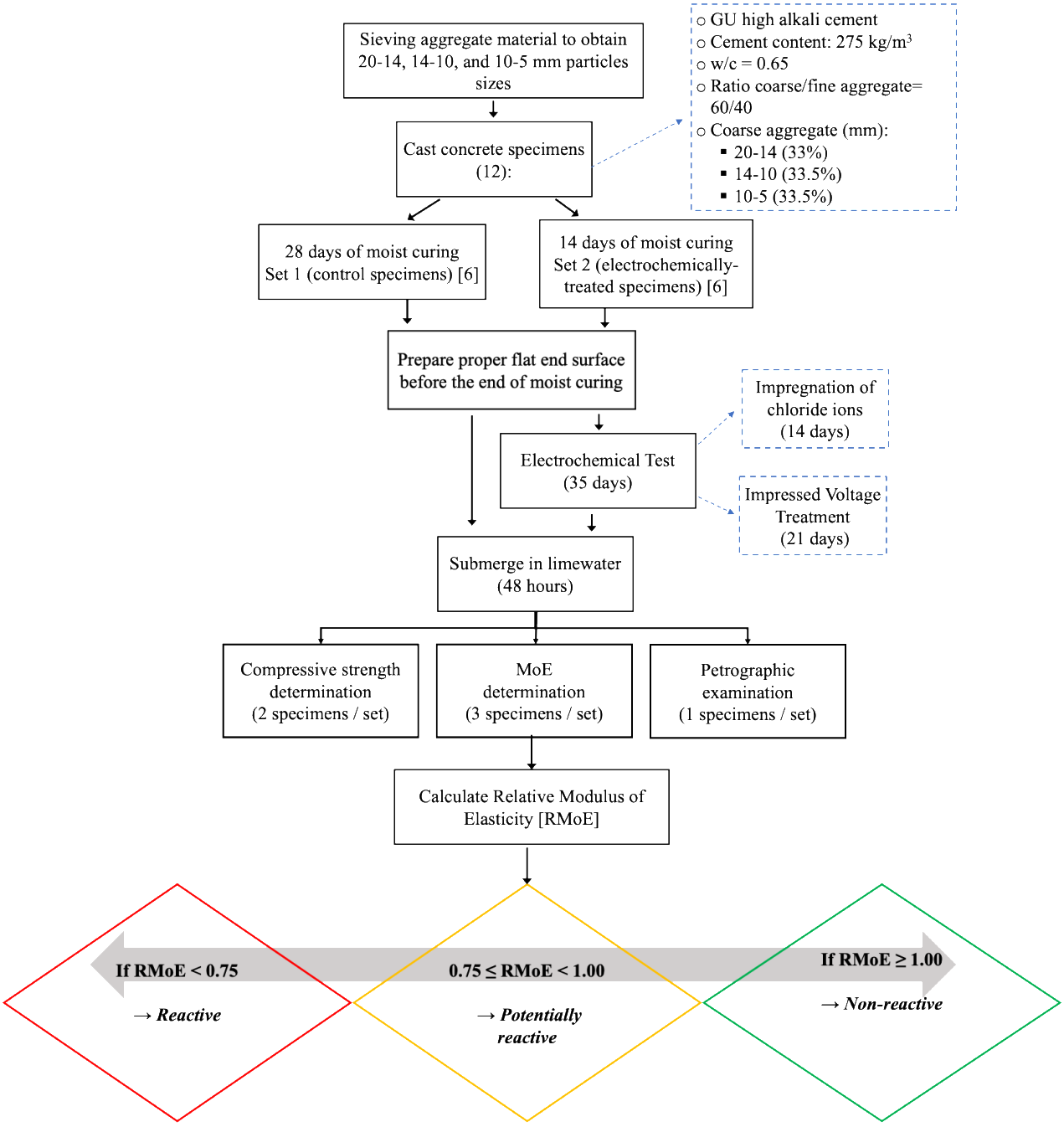

Figure 3.1: Electrochemical testing scheme proposed by Castillo Araiza et al. [5].

9. RESULTS

9.1 Aggregate characterization

The findings from the petrographic examination and chemical analysis of each aggregate are summarized in Table 4.1. Reflected light petrography confirmed the presence of iron sulphide minerals in almost all of the investigated aggregates (Figure 4.1). The sulphide mineral phases identified in the samples include pyrite (Py), pyrrhotite (Po), chalcopyrite (Cpp) and pentlandite (Pn).

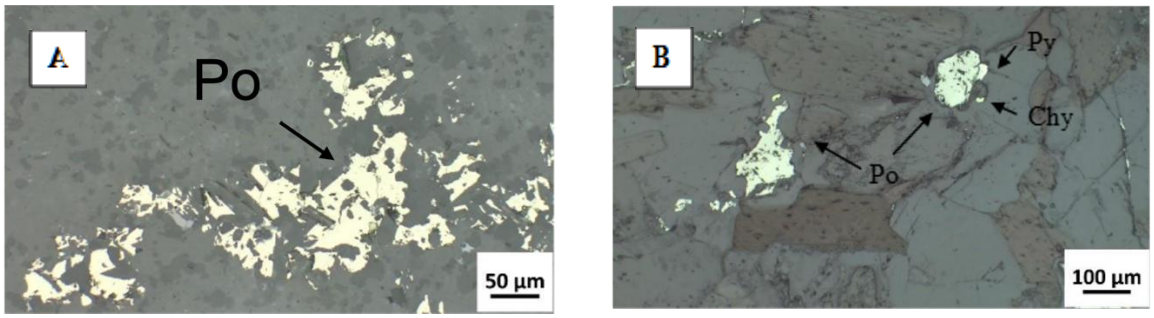

Figure 4.1: Reflected light micrographs. Po: Pyrrhotite Py: Pyrite; Chy: Chalcopyrite. [A] Epidote hornfels (C). [B] Coarse-grained garnet gneiss (M).

Table 4.1 also shows the average T_S content determined for each aggregate sample. The values are first classified in two groups, i.e. aggregates without and with Po, and then in increasing T_S contents. The aggregates without Po have Ts contents ranging from 0.02% (F) to 0.63% (J), while the Po-bearing aggregates have Ts contents ranging from 0.15 (I) to 2.85 (Pavage Boisvert).

Table 4.1: Summary of the petrographic examination and T_S content of all aggregates investigated.

Sample	Lithology	T_S (%)	Po	Py	Cpp	Pn
F	Anorthosite	0.02	no	no	yes	no
AB	Quartzite	0.03	no	no	no	no
AD	Limestone (Spratt)	0.04	no	yes	no	no
A	Basalt	0.07	no	no	no	no
AA	Phyllite	0.07	no	yes	yes	no
L	Limestone	0.26	no	yes (F)[1]	no	no
T	Trachy-Basalt	0.29	no	yes	no	no
K	Dolostone	0.36	no	yes (F) [1]	no	no
J	Dolostone	0.63	no	yes	no	no
I	Troctolite	0.15	**yes**	yes	yes	yes
R0	Gabbro	0.19	**yes**	yes	no	no
M	Gneiss	0.52	**yes**	yes	yes	no
W1	Gneiss	0.55	**yes**	yes	yes	no
C	Hornfels	0.78	**yes**	no	yes	no
AC	Phyllite, micaschist	0.81	**yes**	yes	no	no
O	Mudslate	0.87	**yes**	yes (F) [1]	yes	no
R1	Gabbro	0.90	**yes**	yes	yes	yes
V	Mont-Laurier (Mine waste)	2.06	**yes**	yes	no	no
Y	Pavage Boisvert	2.85	**yes**	no	no	yes

1: Framboidal

9.2 Electrochemical testing scheme

The results of modulus of elasticity (MoE) determination are presented in Figure 4.2. The MoE values of the control concrete specimens vary from 15.2 to 35.6 GPa due to the specific mechanical and mineralogical characteristics of the aggregate sources. Interestingly, the MoE of concrete specimens incorporating aggregates without Po and those with small amount (R0) or finely disseminated Po increased following the electrochemical treatment (by 6% to 58%). This resulted in RMoE values of 1.0 or higher (Table 4.2) suggesting limited damage in the test specimens,

On the other hand, the MoE associated with high T_S and pyrrhotite-bearing aggregates decreased significantly following the electrochemical treatment (by -28% to -68% in the worst case) (Figure 4.2). They thus displayed RMoE values ranging from 0.72 to 0.32 (Table 4.2).

Table 4.2: Results of RMoE values of concrete specimens with sulphide-bearing aggregates.

Presence of Po		Sample	Lithologie	T_S (%)	Relative MoE (RMoE)
					RMoE 35
No		F	Anorthosite	0.02	1.13
		AB	Quartzite	0.03	1.06
		AD	Limestone (Spratt)	0.04	1.13
		A	Basalt	0.07	1.09
		AA	Phyllite	0.07	1.58
		L	Limestone	0.26	1.27
		T	Trachy Basalt	0.29	1.07
		K	Dolostone	0.36	1.14
		J	Dolostone	0.63	1.01
Yes	Po>Py	I	Troctolite	0.15	0.92
	Low amount	R0	Gabbro	0.19	1.13
	Py>Po	M	Gneiss	0.52	1.08
	disseminated	C	Hornfels	0.78	1.05
		AC	Phyllite, micaschist	0.81	1.11
	High amount	W1	Gneiss	0.55	0.42
		O	Mudslate	0.87	0.36
		R1	Gabbro	0.90	0.72
		V	Mont Laurier (Mine waste)	2.06	0.45
		Y	Pavage Boisvert	2.85	0.32

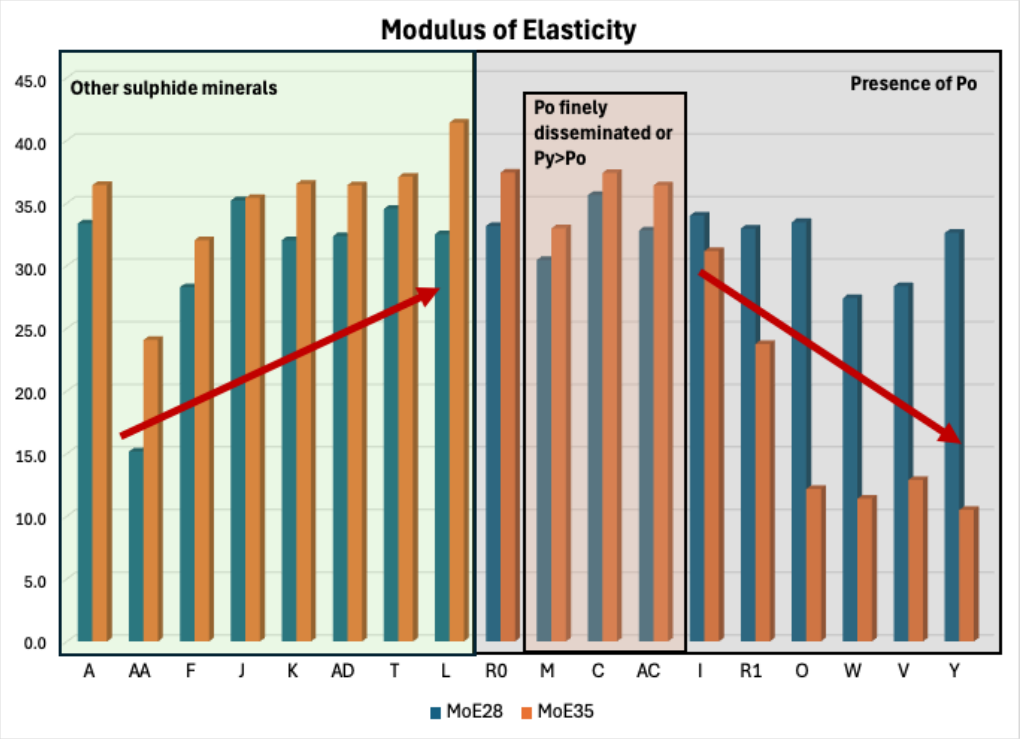

Figure 4.2: MoE values of control concrete specimens (blue bars) vs concrete specimens subjected to electrochemical testing (orange bars).

10. DISCUSSION AND PERSPECTIVES

As shown in Table 4.2, four aggregates, i.e. J, AC, C and M, resulted in RMoE values only slightly greater than 1.0 despite high S_T contents. The Dolostone J contains only pyrite (Table 4.1) and ended up to be non-reactive. Petrographic examination of aggregates C and AC revealed that Po is finely disseminated in the rock matrix; furthermore, in the case of aggregate C, the extremely hard and dense, interlocking, non-foliated texture of the hornfels rocks makes the physical/chemical attack of the encapsulated sulphide minerals exceptionally difficult. Therefore, access to chloride ions to catalyze the reaction is limited, and no significant damage was observed in the concrete specimens (Figure 4.2). Finally, in the case of aggregate M, it was difficult to determine through petrographic examination which sulphide minerals was predominant in the aggregate matrix; the results presented in Figure 4.2 suggested a higher Py content than Po but more research is necessary to determine Po/Py ratio. No field performance records regarding deleterious oxidation reaction are currently available for those last three SBA sources [C, M and AC].

The results obtained in this study suggest that a significant amount of Po in the aggregate matrix is necessary to detect visible signs of deterioration following electrochemical testing, but the pyrrhotite should also be somewhat readily accessible to the chloride ions used for accelerating damage development. For example, although Po is present in aggregate R0, its concentration is likely insufficient to cause significant damage to the specimens (i.e., RMoE of 1.13). Conversely, concrete specimens incorporating Po-bearing aggregate I showed a RMoE value of 0.92 despite a somewhat limited T_S content of 0.15%, thus suggesting that most of the sulfur content in that aggregate is associated to “accessible” Po, with only trace amounts of Py, Cpp and Pn.

By contrast, no signs of damage were observed under the same testing conditions (i.e., RMoE > 1.00) when Py was the only iron sulphide present or when it was combined with Cpy. However, it remains to be confirmed whether the electrochemical method can detect the potential reactivity of aggregates with finely disseminated framboidal pyrite, as already reported in a case of concrete damage [7].

11. CONCLUSION

The electrochemical testing scheme is sensitive to the detection of reactive pyrrhotite-bearing aggregates. In this research, 19 aggregate sources were subjected to electrochemical testing to further investigate its reliability.

No deterioration was observed in any of the aggregates without the presence of Po after they were subjected to the electrochemical testing scheme.

The test was found to reliably recognize the potential reactivity of high T_S and Po-bearing aggregates as high damage developed in the test specimens that resulted in low Relative modulus of elasticity (RMoE) values. On the other hand, aggregates with finely disseminated (C and AC) or well encapsulated Po (M), despite their T_S ranging from 0.52 to 0.81, showed limited visible damage in the test and RMoE > 1.0. It thus appears that not only the pyrrhotite content, but the textural characteristics of the host rock also impact on the performance of the SBA in the electrochemical test. Further testing is required to determine whether the methodology would be able to detect the reactivity of aggregates containing finely disseminated Po or framboidal pyrite, like those from County Donegal and County Mayo in Ireland.

12. REFERENCES

[1] Duchesne J, Rodrigues A, Fournier, B (2023) Overview of the Trois-Rivières (Québec, Canada). In: Nova Science Publishers Inc (ed) Pyrrhotite Issues. Pyrite and Pyrrhotite, 1st edn. Hauppauge, New York, pp 109-136.

[2] Castillo Araiza R, Fournier B, Duchesne J, Rodrigues A, (2023) Electrochemical activation of oxidation of sulfide-bearing aggregates in concrete specimens. Cem Concr Res 170, 107186.

[3] Ojo M, Kim D, Frame L, Wille K (2024). Electrochemical investigation of accelerated deterioration of concrete with iron-sulfide containing aggregates. Cem Concr Res 182, 107570.

[4] Castillo Araiza R, Rodrigues A, Fournier B, Duchesne J (2024) A new accelerated testing scheme to evaluate the potential oxidation reaction of sulfide-bearing aggregates in concrete specimens. Cem Conc Res 180, 107507.

[5] Castillo Araiza R, Fournier B, Duchesne J, Fecteau PL, Rodrigues A (2024) Evaluation of detrimental effects in concrete specimens due to the oxidation of sulfide-bearing aggregates after electrochemical treatment. Constr Build Mater 411, 134341.

[6] Rodrigues A, Duchesne J, Fournier B, Durand B, Shehata MH, Rivard P (2016) Evaluation Protocol for Concrete Aggregates Containing Iron Sulfide Minerals. ACI Mater J 113(3).

[7] Brough C, Garside R, Staniforth B, Garner C, Fletcher J, Strongman J (2024) Framboidal pyrite in concrete block: Reassessing EN 12620 in light of the degradation observed across the Republic of Ireland. Proceedings of International Conference on Iron Sulfides in Concrete (ICISR) pp. 39-43.

ICISR 2026

2nd International Conference on Iron-Sulfide Reactions in Concrete

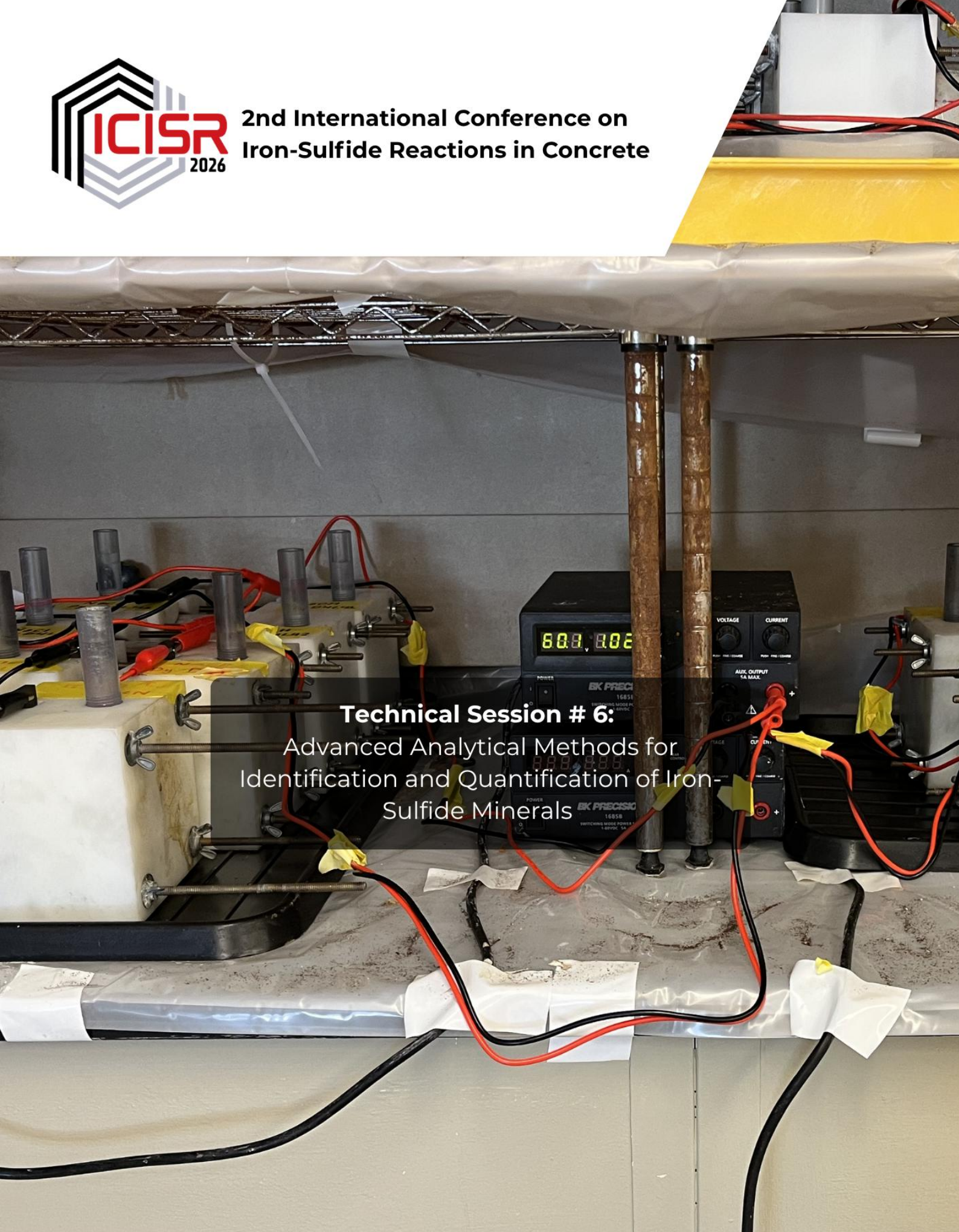

Technical Session # 6:

Advanced Analytical Methods for Identification and Quantification of Iron-Sulfide Minerals

UCONN | COLLEGE OF ENGINEERING
SCHOOL OF CIVIL AND ENVIRONMENTAL ENGINEERING

UCONN
COLLEGE OF ENGINEERING
CONNECTICUT TRANSPORTATION INSTITUTE (CTI)

Rapid Quantitative Assessment of Sulphide Species and Equivalent Total Sulphur Content of Aggregate in Concrete Samples using OI AZtecFeature Analysis and UNITY BEX Mapping

Staniforth, B.(1), Brough, C.(1), Fletcher, J.(1), Strongman, J.(1), Garside, R.(1), Garner, C.(1), Colville, R.(1)

(1) Petrolab, Redruth, UK, bradley@petrolab.co.uk

Abstract

Deterioration caused by oxidation of framboidal pyrite formed in aggregate is well documented in Cornwall & the Republic of Ireland, whilst deterioration caused by oxidation of pyrrhotite is well documented in areas such as the Republic of Ireland, North America and mainland Europe. Increasingly, there is a need to retrospectively screen concrete and concrete products for iron sulphide content which can be compared to the relevant aggregate standards, such as when assessing the risk posed to existing structures by the sulphide content of their original aggregate. Complicating factors in this include the interference of the cement hydrates, primary sulphates associated with the cement, and secondary sulphate products with chemical analysis results. A further complication is the need for quantitative speciation of sulphide phases where particularly relevant to original standard values, for example the distinction of total sulphur (ST) attributable to pyrrhotite where stringent limits are applied (e.g. 0.1 % ST EN 12620). Such retrospective analysis is required for a number of reasons; in particular it is currently being used in the Republic of Ireland, Quebec and Connecticut to facilitate access to remediation and redress schemes for iron sulphide affected properties. Presented here is a rapid technique of achieving a quantitative assessment of sulphide species and equivalent total sulphur content of aggregate in hardened concrete using the Oxford Instruments AZtecFeature package and UNITY BEX SEM/EDX analysis. It was developed to achieve the quantitative bulk modal data requested in I.S.465 Test Suite C, Appendix C under a commercial timeframe. At this time, Petrolab have completed over 300 such analyses for the Irish Housing Agency over a 9 month period. The various parameters which affect results, accuracy and precision of results, are briefly explored. Data is presented for rapid SEM analysis of 45x30 mm polished sections against ST values as determined by HTC for n = 517 bulk concrete and blockwork samples.

***Keywords**: automated mineralogy, blockwork, IS465, petrography, sulphide analysis*

1. INTRODUCTION

Behind embedded reinforcement corrosion and alkali-silica reaction, internal sulphate attack is one of the most significant deleterious processes affecting the durability of concrete structures worldwide. One mechanism of internal sulphate attack occurs following hardening of the paste where excessive concentrations of reactive iron sulphide minerals (typically framboidal pyrite – py or pyrrhotite - pyh) are incorporated into the utilised aggregate components. Under exposure to water and oxygen, iron sulphides can oxidise in the cementitious environment forming both iron oxides and sulphuric acid. The produced sulphuric acid can then react with various different cement hydrates to form expansive calcium sulphate phases such as ettringite. Both stages of reaction have the potential to be expansive. Deterioration caused by oxidation of framboidal pyrite forms in aggregate are well documented in Cornwall & the Republic of Ireland [1], whilst deterioration caused by oxidation of pyrrhotite is well documented in areas such as the Republic of Ireland [1-3], North America [4-5] and mainland Europe. Increasingly there is a need to retrospectively screen concrete and concrete products for iron sulphide content which can be compared to the relevant aggregate standards, such as when assessing the risk posed to existing structures by the sulphide content of their concrete blocks. Complicating factors in this include the interference of the cement hydrates, primary sulphur-bearing phases associated with the cement, and secondary sulphate products with chemical analysis results. A further complication is the need for quantitative speciation of sulphide phases where particularly relevant to original standard values. For example, the distinction of total sulphur (S_T) directly attributable to pyrrhotite where stringent limits are applied (e.g. 0.1 % S_T EN 12620).

Such retrospective analysis is required for a number of reasons; in particular it is being used in the Republic of Ireland, Quebec and Connecticut to facilitate access to remediation and redress schemes for iron sulphide affected properties. One method of doing this combines chemical analysis and micro-XRF analysis. However, presented here is a technique of achieving a quantitative assessment of sulphide species and equivalent total sulphur content of aggregate in hardened concrete sub-samples using the Oxford Instruments AZtecFeature package and UNITY BEX UBSE/EDX analysis. It was developed to achieve the quantitative bulk modal data requested in I.S.465 Test Suite C, Appendix C (TSC analysis hence) under a commercial timeframe, being focused on automated BSE-defined feature identification and EDX spot analysis of identified features for classification using commonly available commercial software. This was performed taking elements from well-established for automated analysis of geological materials [6] and cement hydrates [7] running on packages such as Mineralogic. At this time, Petrolab have completed over 600 such analyses for the Irish Housing Agency (HA).

2. SAMPLES

Samples undergoing TSC analysis are following pathway analysis through the Irish HA specification analysis based on I.S.465 for classification of residential dwellings. Full details including construction overview given in [2]; however, in summary, this requires sampled properties to exhibit Group 3 or 4 deterioration onsite, before examination of 12+ core samples taken from the property housing concrete blocks. As per the HA specification document, detailed examination is typically made of an inner leaf, excluding the more deteriorated outer leaf. Analysis is detailed in I.S.465, noting results contain both optical petrography and EN 1744 High Temperature Combustion (HTC) total sulphur analysis of concrete sub-samples. As part of Petrolab's investigations, identified lithologies are assigned three letter codes as outlined in [2] and are referred to throughout this paper. Samples part of the dataset below are primarily dominated by two main problematic lithologies, quarried pyh-bearing phyllite (PHY) from Co. Donegal and framboidal py-bearing calcareous mudrocks (here grouped as BLS) from Co. Mayo, Co. Clare and Co. Limerick. Additional minor lithologies are also included. TSC analysis is undertaken on sub-samples of the provided ~100 mm diameter concrete core samples. For concrete samples, 45 x 30 mm sub-samples were cut from the provided block slices, from the outer edge. These sub-samples were vacuum impregnated with fluorescent epoxy resin and thin sectioned using a Pelcon thin section machine with the accompanying offcut block polished to a 1 µm finish on a Buehler polishing system. For SEM/EDX analysis polished samples were carbon splutter coated for analysis.

3. METHOD

SEM/EDX analysis was conducted on a ZEISS EVO MA 15 scanning electron microscope (SEM) fitted with an Oxford Instruments Ultim-Max 170 mm^2 silicon drift detector and Unity BEX (backscatter and energy dispersive X-ray) detector using an acceleration voltage of 20.0 kV. Phase identification, classifications, images and energy dispersive X-ray (EDX) phase maps of the areas of interest (AOI) were acquired using Oxford Instruments AZtecFeature software 6.2. Two areas of interest were run on the analysed samples, a BSE target phase search (TPS) using spot analysis for EDX classification over a representative area and full elemental mapping (BEX) of the same area. Analyses were focused on attaining representative but rapid quantification, speciation and morphological data on sulphides using the high area detectors and BEX UNITY combined detector to attain large count values for a sufficient features to improve classification statistics, as standard automated mineralogy (AM) practice [8].

TPS phase identification utilised a BSE threshold to identify target features which are then subject to EDX feature analysis. Two separate binary particle filters (see Figure 3.1 A) were utilised. A standard erode and dilate filter set was used to remove edge effects in all pyh and cubic py samples analysed. For framboidal pyrite samples due to the small size, a dilate-separate-erode filter stack (see Figure 3.1 A) was utilised to better catch adjacent particles, before splitting along grain boundaries and eroding most of the original edge effect. TPS analysis in AZtecFeature is undertaken utilising spot analysis. Here, EDX analysis is acquired at the centre point of the longest chord as rasterised across the particle. Since the analysis is based on BSE greylevel threshold and is limited to a minimum grain size of 1.5 µm^2 area, the sulphide abundance values are considered an underestimation. This is especially the case for framboidal pyrite forms which are very fine grained and will not all have been detected during this analysis. For both types of analysis on Irish aggregate a single BSE threshold is applied as significant phase intergrowth is not common; for more complex geological settings such as those seen in Connecticut and Maskimo (Trois-Rivières, Quebec), multiple BSE thresholds may be applied to split intergrown features.

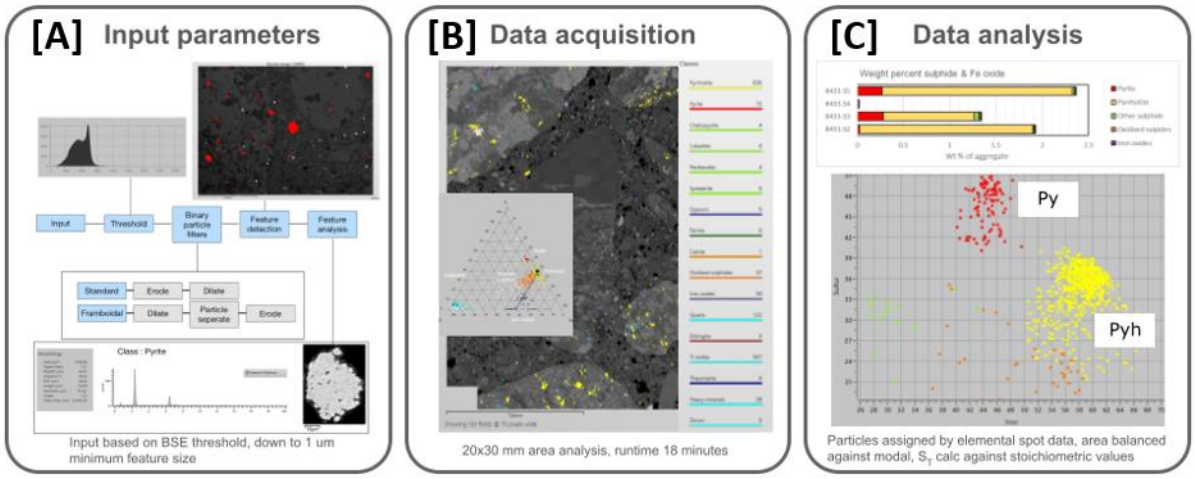

Figure 3.1: [A] Summary of TPS input parameters including binary filter stacks [B] TPS scan of Connecticut foundations highlighting pyh [C] Py & Pyh elemental splits for a PHY sample

For pyh and coarse py-bearing samples, TPS analysis is typically undertaken at x75 magnification with a pixel dwell of 4 µs/pxl with a target set to achieve 10000 counts per identified feature for classification. Analysis was targeted at a minimum of 600 mm^2 area of analysis with analysis runtime ranging between ~20-120 minutes. For framboidal or very fine pyrite-bearing samples, TPS analysis is typically undertaken at x150 magnification with a pixel dwell of 4 µs/pxl with a target set to achieve 2000 counts per identified feature for classification based on the need to classify in excess of 20000 features per analysis. Analysis was targeted at a minimum of 500 mm^2 area of analysis with runtime ranging between ~120-180 minutes, being capped with 180 minutes or 100000 features identified stop criteria. This allows for automated running of 6-8 samples for TPS and BEX analysis a night with manual analysis and sample change over undertaken during the day.

A phase classification scheme was developed using the AZtecFeature software. Delineating grains into different phase classes is achieved by matching criteria that compare the quantitative measurements of elemental composition, as determined from the EDX spectrum, with defined mineral composition. For each mineral, the elemental min./max. composition range given in normalized element weight percent

(wt%) is defined. The stoichiometric composition of the mineral phase classifications is taken from online repositories (Webmineral and RRUFF). Where fine grain components are analysed, compositional overlaps with other phases such as the cement binder, host aggregate and iron oxides formed from oxidation, are present. In this case, similar to cement hydrate analysis, additional chord filters based on ternary plots are put in place to allow for classifications (e.g. Figure 3.1 B). For example, an oxidised sulphide classification is required where additional oxygen and iron are encountered, based on the classification scheme grains trending towards an ideal iron oxide classification are assigned as oxidised, where as grains trending towards hydrate compositions are dealt with separately. Reporting of phase / mineral data is in terms of wt%. However, all data acquired is from 2D sections of 3D particles. Mass values are derived from measurement of particle / grain areas, with no correction for stereological error, and an assumed phase density. Results are then normalised against the aggregate proportion of the analysed area, as determined by petrographic point count of 500 evenly spaced points for the concrete samples allowing for phase proportion of the identified sulphide species to be calculated

Full elemental BEX mapping is utilised to target areas of relative sulphur enrichment for rapid detailed quantitative spectral analysis via EDX. Maps were typically run at a magnification of x75 with a dwell time of 6 µs/pxl before being montaged in AZtec. Montaged maps are typically smoothed for export using a 9x9 gaussian function as AZtec TruMaps. From the exported montaged elemental S map, areas of sulphur enrichment within the paste and within aggregate fractures can be rapidly targeted and analysed by AZtec live chemical imaging to provide rapid targets for confirmation via spectral point analysis.

4. RESULTS & DISCUSSION

An overview of the SEM determined S_T% equivalent values and HTC chemistry results (adjusted for 0.1% S contribution from cement) by lithology code is given in Figure 4.1, In total n=517 samples with both EN 1744 HTC sample results and TSC SEM results have been considered, with TSC analysis undertaken by Petrolab, and EN1744 HTC analysis undertaken by two accredited laboratories.

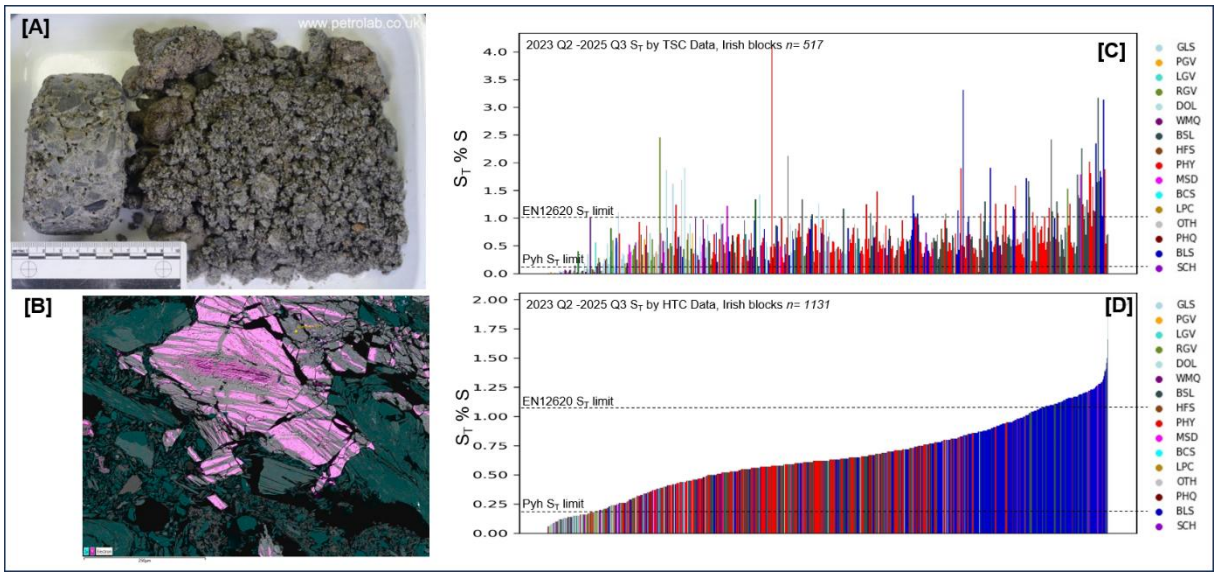

Figure 4.1: [A] Example PHY core [B] oxidised pyh in PHY aggregate [C] TSC determined S_T results coloured by lithology code and arranged by ascending HTC S% [D] HTC determined S_T results coloured by lithology code arranged by ascending HTC S%.

Figure 4.2 exploring the results for all lithologies with a focus on the PHY and BLS lithologies, including key statistical values and metrics across the dataset. As overall determined values are not known for the material in question and considering the findings of the repeatability and reproducibility study, comparison against the mean HTC value is deemed the most appropriate comparison, noting that both values are imperfect metrics in different ways. Correlation figures (*Pearson* coefficient - *r*) between the two suggests a stronger correlation of results for BLS analysis than for PHY analysis. Standard deviation values are fairly consistent between the lithologies by technique, with the SEM determined values giving a higher standard deviation result.

4.1 Quantification of different sulphide species

As part of the mineral classification scheme several criteria were used to differentiate compositionally similar sulphide species, a mean of the returned dataset is given in Figure 4.2 C. Differentiation of pyrite and pyrrhotite was achieved using an Fe range classification (e.g. Figure 3.1 C), with further proportional checks to ensure Fe always exceeds S within a pyrrhotite classification, in addition to management of py and pyh positions within the mineral list hierarchy. Within the pyh dominated PHY classification a 6C monoclinic structure close to troilite is predominant. The large variation in Fe to S elemental proportion allows for reliable distinction between the two phases with proportions being consistent with those identified in reflected light for the PHY lithology. Within the BLS lithology py classifications are dominant, however pyh is seen associated with some County Mayo BLS material where a crosscutting cpy-py-pyh bearing dolerite dyke intersects the quarry. Interestingly rare samples are identified with major very fine anhedral and framboidal pyh. Whilst initially considered to be a classification error, pyh was confirmed by detailed EDX point analysis and reflected light analysis, contextually representing alteration of original framboidal py within a high temperature de-sulphidation “skarn-style” alteration [9] halo around the dolerite dyke. As such, the TPS is considered to provide reliable rapid speciation of py and pyh in the context of the examined Irish samples. Oberhardt et al [10] note unsatisfactory splitting of py and pyh solely on Fe concentration during analysis of Maskimo material. In this case the pyh composition is much closer in Fe content to the py than in the Irish samples, and phases are also notably more intergrown, necessitating an additional backscatter electron grey-level filter at thresholding stage to fully distinguish phases.

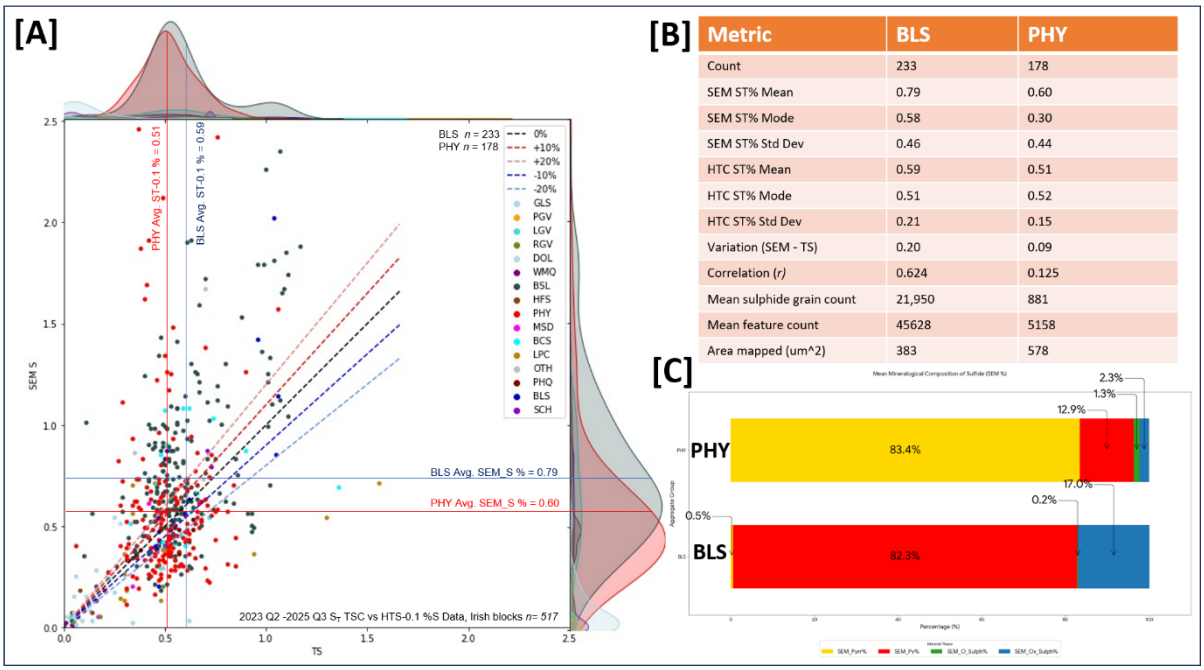

Metric	BLS	PHY
Count	233	178
SEM ST% Mean	0.79	0.60
SEM ST% Mode	0.58	0.30
SEM ST% Std Dev	0.46	0.44
HTC ST% Mean	0.59	0.51
HTC ST% Mode	0.51	0.52
HTC ST% Std Dev	0.21	0.15
Variation (SEM - TS)	0.20	0.09
Correlation (*r*)	0.624	0.125
Mean sulphide grain count	21,950	881
Mean feature count	45628	5158
Area mapped (um^2)	383	578

Figure 4.2: [A] ST TSC vs HTC-0.1%S Data, Irish blocks with modal distribution plots [B] key metrics for PHY and BLS groups [C] mean sulphide proportions for groups from mass data

4.2 SEM/EDX vs EN1744 results

As a baseline, all values recorded confirm an excess of sulphide mineralisation associated with the respective lithologies. In both cases for the two main groups, the mean S_T by SEM was in excess of the mean HTC result when a 0.1%S correction is applied. However, the other population statistics (modal and medium) remain below the mean HTC result, with mean SEM results being skewed upwards by a number of high outlying results. Correlation values for the two populations suggest that a much stronger correlation is seen between the two S_T measures for the BLS samples, with the PHY samples being much more variable. This is also seen in the variation in the two methods mean results. Results can be considered further by bringing in the two main metrics recorded for the mass data set: sulphide grain count/total feature count and area analysed. As a general observation, based on the sulphide morphology, BLS samples typically exhibit high sulphide grain counts due to the very fine framboidal py

and lower analysis area (typically due to the time restrictions applied). In comparison, PHY samples exhibited coarse sulphides present in lower quantities resulting in a larger analysis area being possible. Where the most outlying samples are considered in terms of over and under estimation against HTC, these are typically defined by much higher or lower grain density. As such, most outliers can be attributed largely to local sample bias in sulphide abundance relative to the HTC bulk samples. In terms of particle statistics, target phases (sulphides) relative to overall features and area analysed remain within standard AM parameters for reasonable uncertainty should random grain distribution be assumed. Despite the homogenisation and mixing during casting this does not appear to be fully sufficient to ensure random enough aggregate mounting and distribution for statistical purposes. That being said the full mapping of areas does provide important contextual information in the context of concrete deterioration which would be lost if a technique such as random field analysis was used in order to reduce sampling bias. This is particularly key where coarse sulphides are being analysed e.g. in the PHY. In comparison overall mapping area showed shows virtually no correlation with the sulphur results, suggesting grain density is a bigger factor than the sample areas which have been analysed in this study.

Overall, considering the limitations of 2D stereoscopic analysis against 3D powder analysis and the semi-quantitative nature of the results, the SEM determined results show reasonable correlation with the determined EN 1744 results and therefore provide satisfactory classification and determination of S_T for the samples under examination. In all cases results would provide equivalent I.S.465 risk classifications. Consideration is made that should random particle statistics criteria through fully randomised grain mounts (e.g. crushed aggregate material) be applied, statistical certainty with regards to sulphide abundance may be improved. The significant advantage of automated mineralogy data for pyh-bearing aggregate samples is that AM computes several different properties from the combination of BSE imaging and EDS analyses that can be used to analyse the properties of aggregates. It can also reliably produce different sulphide species, allowing for the determination of relative proportion of pyh and py. Automated mineralogy can be extensively tailored to achieve the best quality analysis fit for the purpose, including the possibility of combining data visualization and quantification. Furthermore, the amount of data collected is vast and, hence, eligible for use in statistical calculations and comparison of sample materials. In comparison to full EDX AM mapping applied in [10] the TPS technique is designed to run in a more commercial time frame. This comes at the expense of high level detail on mineral associations and inter-crystal variations, based on its reliance of spot analysis for classification. The technique allows for rapid semi-quantitative analysis of sulphide species, at a resolution level greater than the bulk S_T measurement, but must be operated and data interpreted by personnel with experience in the analyses and extensive mineralogical knowledge.

5. CONCLUDING REMARKS

Rapid classification and splitting of sulphide species retrospectively within concrete samples is suitably achieved using widespread commercially available software available and accessible on AZtec driven systems. Speciation is sufficient to allow for interpretations to be made with regards to the presence of highly reactive species e.g. framboidal pyrite and pyrrhotite. The S_T results attained by the TPS analysis are comparable to mean HTC results adjusted to take account of the potential contribution from cement phases. Although error and variability in results (based on the difficulty in achieving a statistically representative area) mean it does not provide a direct replacement under the parameters explored in this study, it does remain as a powerful tool for screening various sulphide bearing materials post concrete manufacture. The technique shows great potential for application on rapid screening of raw aggregate materials whereby well-established particle statistics criteria can be used to provide better statistical uncertainty and error values related to the samples representativity.

6. REFERENCES

[1] Brough, C et al. (2024). Framboidal pyrite in concrete block: Reassessing EN 12620 in light of the degradation observed across the Republic of Ireland. ICISR 2024 Quebec

[2] Brough, C., Staniforth, B., Garner, C., Garside, R., Colville, R., Strongman, J., & Fletcher, J. (2023). High risk concrete blocks from County Donegal: The geology of defective aggregate and the wider implications. Construction and Building Materials, 408, 133404.

[3] Leemann, A., Münch, B., Lothenbach, B., Winnefeld, F., & Dunlop, P. (2024). Defective homes in Donegal, Ireland: effect of exposure conditions and concrete quality on pyrrhotite oxidation and internal sulfate attack. Cement and Concrete Research, 186, 107684.

[4] Titon, B., Duchesne, J., Fournier, B., & Rodrigues, A. (2025). Concrete deterioration due to sulfide-bearing aggregates: Mineralogical and chemical characteristics of pyrrhotite in concrete aggregates from Trois-Rivières, Canada. Construction and Building Materials, 458, 139670.

[5] Jana, D. (2022). Cracking of residential concrete foundations in eastern Connecticut, USA from oxidation of pyrrhotite. Case Studies in Construction Materials, 16, e00909.

[6] Schulz, B., Sandmann, D., & Gilbricht, S. (2020). SEM-based automated mineralogy and its application in geo-and material sciences. Minerals, 10(11), 1004.

[7] Georget, F., Schmatz, J., Wellmann, E., & Matschei, T. (2024). A critical catalogue of SEM-EDS multispectral maps analysis methods and their application to hydrated cementitious materials. Journal of Microscopy, 294(2), 105-116.

[8] Brough, C., Strongman, J., Fletcher, J., Zając, M., Garside, R., Garner, C., & Rose, L. (2019). Operational mineralogy: An overview of key practices in sample analysis, sample preparation and statistics. In Proceedings of the 15th SGA biennial meeting (pp. 27-30).

[9] Coldebella, B., Laflamme, C., Malta, I. S., Guilmette, C., Barre, G., Beaudoin, G., ... & Savard, D. (2025). The chemical and isotopic characterization of the pyrite to pyrrhotite desulfidation reaction across the metamorphic gradient of a metasedimentary basin. Geochimica et Cosmochimica Acta, 392, 119-136.

[10] Oberhardt, N., Lode, S., Lindgård, J., & Aasly, K. (2025). Classification and quantification of minor iron-sulfide concentrations in concrete aggregate using automated mineralogy. Materials and Structures, 58(2), 1-27

Petrographic Methods to Identify and Quantify Iron-Sulfide Minerals in Aggregate

April Snyder [1], Michael Baker [2], Blake Restelli [3], Chesney DeTullio [4]

(1) ECS Mid-Atlantic, LLC, Pittsburgh, PA, USA, asnyder1@ecslimited.com

(2) RJ Lee Group, Inc., Monroeville, PA, USA, mbaker@rjleegroup.com

(3) ECS Mid-Atlantic, LLC, Pittsburgh, PA, USA, brestelli@ecslimited.com

(4) RJ Lee Group, Inc., Monroeville, PA, USA, cdetullio@rjleegroup.com

Abstract

Iron-sulfide minerals often co-exist as accessory minerals in a variety of rock types. The co-mingling of mineral types with similar optical and compositional characteristics creates a complex, micron-scale interspatial distribution that complicates detection and quantification. The identification and quantification of trace amounts of pyrrhotite, known to have caused deleterious reactions in residential foundations, remain challenging using existing standards and conventional petrographic techniques as in ASTM C295 Standard Guide for Petrographic Examination of Aggregate for Concrete. This limitation presents difficulties in enforcing aggregate acceptance criteria that specify maximum allowable pyrrhotite content.

This paper presents a sample preparation and analytical methodology for aggregate evaluation that combines reflected light microscopy with scanning electron microscopy and energy-dispersive x-ray spectroscopy (SEM/EDS) coupled with image analysis. The resulting data can be correlated with measured sulfide contents to calculate the amount of pyrrhotite in an aggregate sample.

***Keywords**: iron-sulfide, petrography, pyrrhotite, reflected light petrography, SEM/EDS,*

1. INTRODUCTION

Iron-sulfide minerals play a significant role in the deterioration of concrete produced with sulfide-bearing aggregates. Numerous cases in Canada and the United States have shown that even trace amounts of pyrrhotite can oxidize within hardened concrete, generating sulfate and driving expansive reactions [1,2,3]. These issues highlight the importance of reliably identifying iron-sulfide minerals in aggregates to support durability assessments and mitigate the risk of long-term deterioration.

Limits have been established to prevent use of pyrrhotite-bearing concrete aggregate with total sulfur value of 0.1% by weight [4], which translates into a pyrrhotite content as low as 0.15% by weight. Petrographic analysis using reflected light polarizing microscopy is the most popular method for identifying pyrrhotite. Conventional petrographic methods, such as those outlined in ASTM C295 [5], are effective for lithological characterization but are less suitable to detect or quantify trace components. Precise identification of such a small quantity of sulfide minerals presents a significant challenge for petrographers due to the low abundance, inherent variability of mineral distribution and the small subsample size [6].

This paper presents a practical approach for preparing and analyzing aggregate samples using reflected-light microscopy and scanning electron microscopy with energy dispersive spectroscopy (SEM/EDS). This approach enhances the accurate identification of iron-sulfide mineral types and enables estimation of their relative abundance within aggregate samples.

2. MATERIALS AND METHODS

2.1 Sample Preparation and Surface Documentation

Representative portions of coarse and fine aggregate fractions are embedded in epoxy-filled PVC molds to produce polished pucks. Coarse aggregate is placed in molds approximately 1-inch thick and 4 inches in diameter, while fine aggregate is prepared in smaller pucks approximately 5/8-inch thick and 2 inches in diameter. After curing, each puck is ground with progressively finer abrasives to expose broad cross-sectional surfaces containing numerous aggregate particles. Final polishing produces reflective surfaces suitable for metallic mineral identification under reflected light and examination by SEM/EDS.

For coarse aggregate, the polished surface is imaged using a digital microscope to produce a working reference map of the sample, and all particles larger than 3 mm are numbered. This documentation step provides a consistent reference frame for assigning sulfide mineral proportions during reflected-light analysis and provides additional insight into the number of grains containing iron-sulfide minerals.

2.2 Reflected Light and SEM/EDS Analysis

2.2.1 Reflected-light microscopy

Reflected-light microscopy is performed on the polished pucks at magnifications of up to 1000×. Pyrite, pyrrhotite, chalcopyrite, and pentlandite are distinguished based on characteristic reflectance, color, pleochroism, bireflectance, relief, and anisotropy (Figure 2.1). Pyrite typically appears yellow-white with a smooth texture and weak anisotropy; pyrrhotite displays a creamy pinkish-brown color, higher reflectance, common pitting, and pleochroism; chalcopyrite exhibits a brassy-yellow appearance with weak anisotropy; pentlandite shows a creamy white color with a pinkish to brownish tint and is isotropic [7]. The images can be entered into image software and colorized to calculate the relative percentage of each mineral type by area percent.

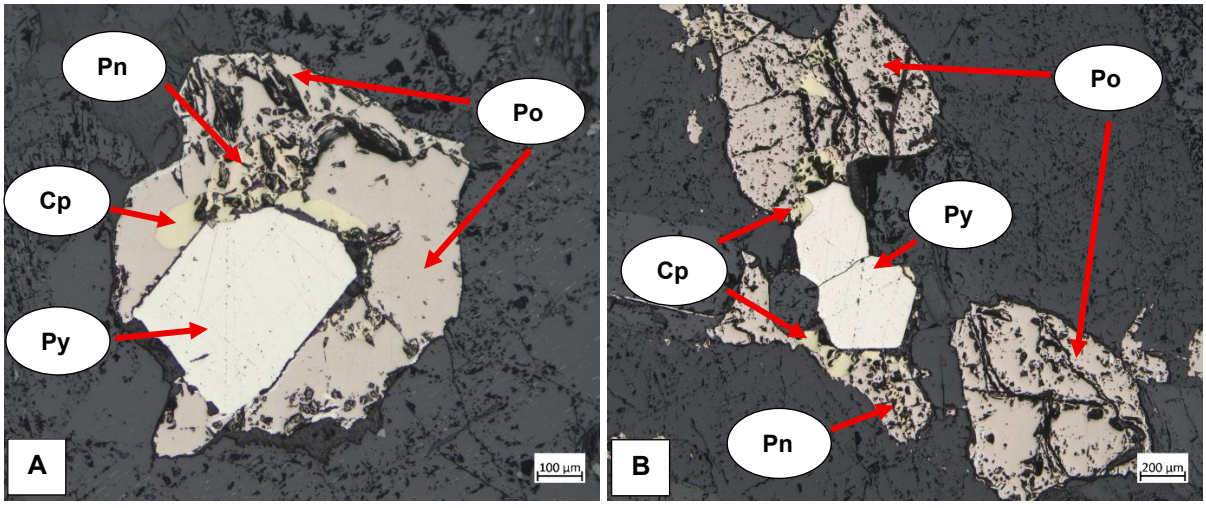

Figure 2.1: Representative reflected light images of iron-sulfide minerals. **A)** A single grain composed of four distinct iron-sulfide mineral phases: pyrrhotite enveloping pyrite, chalcopyrite, and pentlandite. **B)** Pyrrhotite exhibiting its creamy pinkish-brown hue with pitted texture, pyrite showing a smooth, bright reflective texture, and chalcopyrite displaying a brassy yellow; pentlandite is also present. Key: Py = pyrite; Po = pyrrhotite; Cp = chalcopyrite; Pn = pentlandite.

2.2.2 Scanning Electron Microscopy

SEM/EDS is used to confirm and further characterize the reflected-light observations, with backscattered electron (BSE) imaging highlighting compositional contrast and micron-scale textures not readily resolved optically. Framboidal pyrite, for example, is more clearly identified in BSE imagery by its raspberry-like morphology, which may occur as single framboids, clusters, or microcrystalline variations of both, providing insight into morphology and potential reactivity [6,8]. Representative SEM/EDS

images of framboidal pyrite are shown in Figure 2.2, depicting the type of morphology that SEM/BSE imaging can identify with greater confidence than reflected light alone.

SEM/EDS also enables qualitative evaluation of Fe–S ratios and trace elements, offering compositional distinctions among pyrrhotite, pyrite, chalcopyrite, and related sulfides (Figure 2.3). In BSE, pyrrhotite appears brighter than pyrite due to its higher average atomic number from elevated iron and lower sulfur content, and chalcopyrite appears brightest because of its copper content [9].

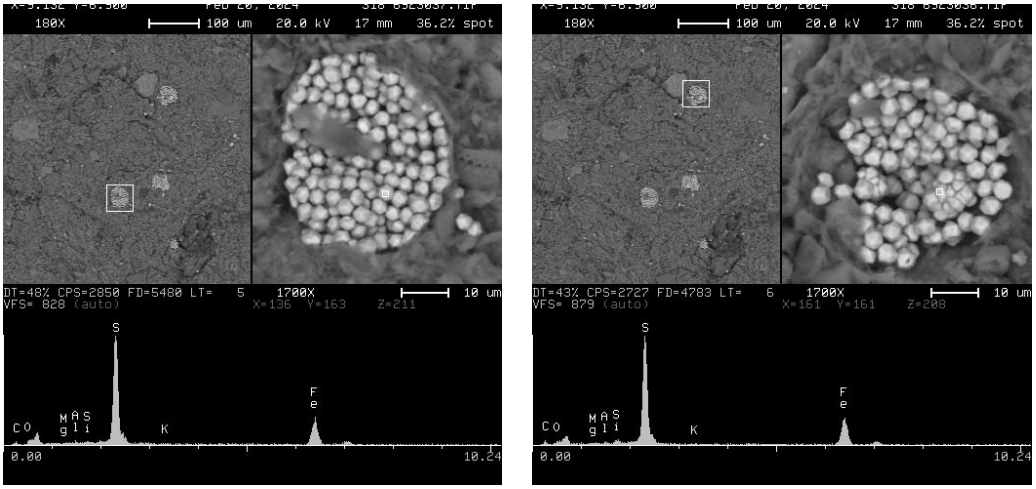

Figure 2.2: Backscattered electron (BSE) images with EDS spectra showing framboidal pyrite composed of packed, rounded microcrystals.

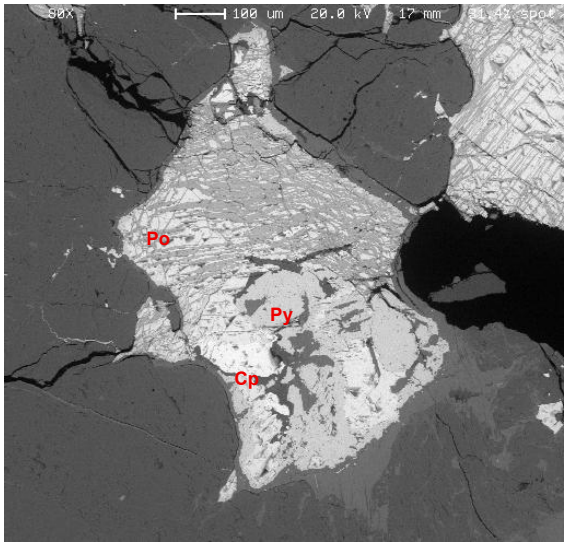

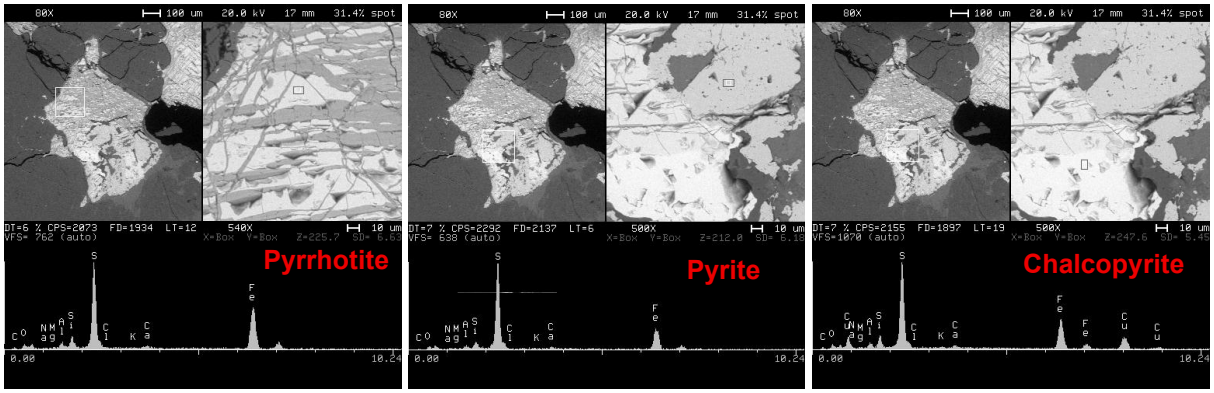

Figure 2.3: Backscattered electron (BSE) images with EDS spectra showing multiple iron sulfide mineral phases within an aggregate. Variations in BSE brightness, supported by Fe-S ratios from EDS spectra, allow these sulfides to be distinguished within the same deposit.

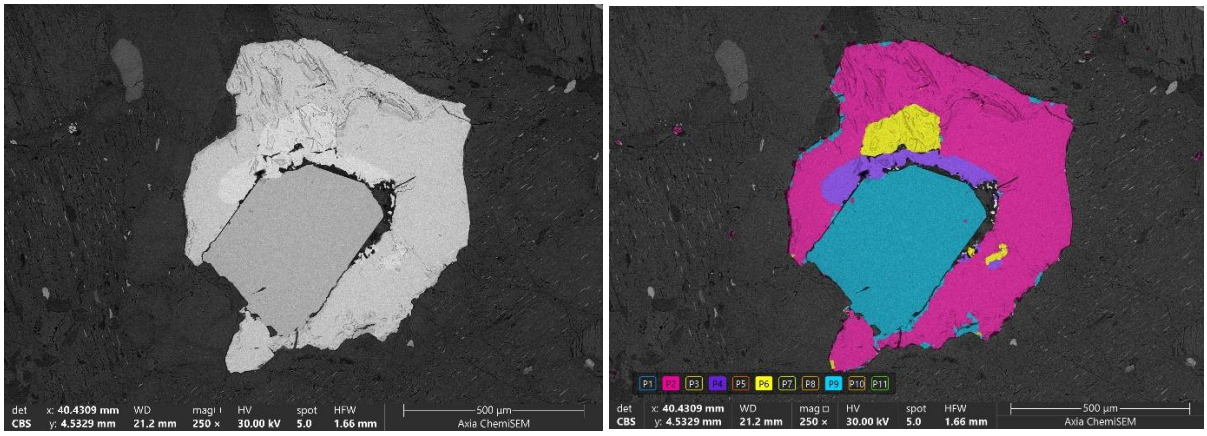

Figure 2.4: Backscattered electron (BSE) image of reflected light image field of view shown in figure 2.1A (left) and EDS x-ray phase map (right) depicting different iron-sulfide mineral phases detected through differentiation of statistically significant spectra.

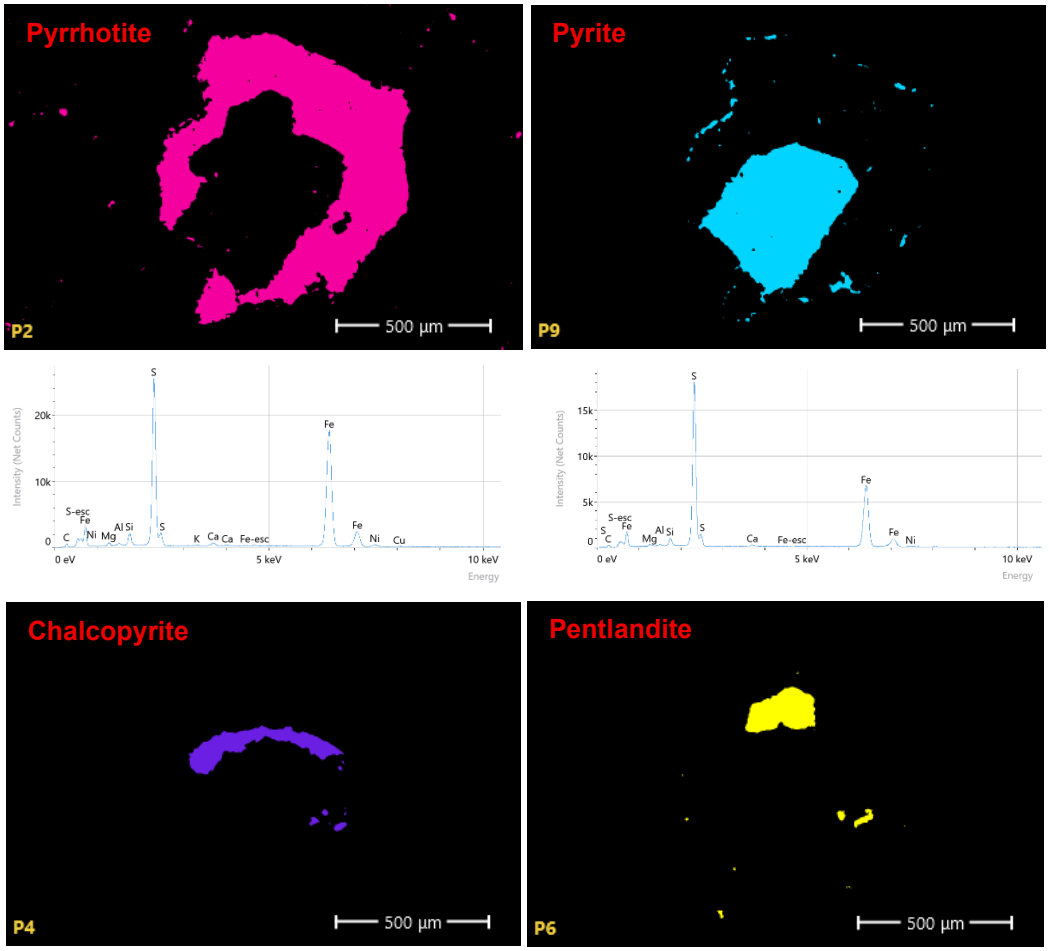

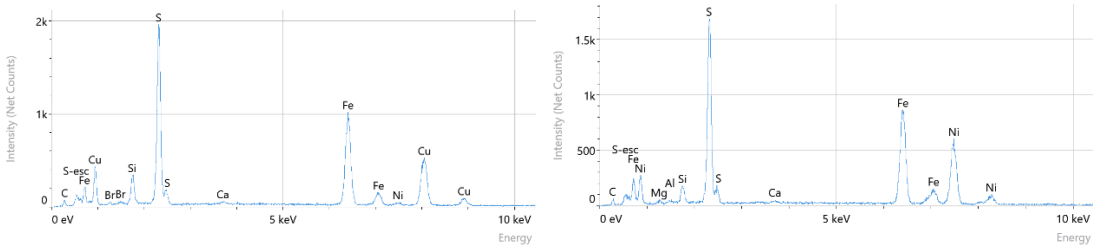

Figure 2.5: Individual phases of x-ray map separated and accompanied by associated spectra.

EDS x-ray mapping creates images showing the spatial distribution of elements in a sample collecting characteristic x-rays at each point and assigning pixel color to elemental concentrations. This tool is used to resolve iron-sulfide phases within complex mineral assemblages as shown in Figures 2.4 and 2.5. Elemental maps of iron, sulfur, and accessory elements were used to identify and color-code individual sulfide phases, improving confidence in phase identification and delineation of micron-scale intergrowths. This approach provides more reliable discrimination among pyrrhotite, pyrite, and related sulfide minerals and supports improved phase quantification in heterogeneous aggregate samples. Analytical software inherent in some EDS software packages or use of other image analyses software can then be used to measure the relative abundance of each sulfide mineral type by area percent.

2.3 Iron Sulfide Quantification and Calculation from Total Sulfur Measurements

Procedures for quantification and relative abundance of sulfide minerals differ slightly for coarse and fine aggregates. For coarse aggregate, the numbered particles from the reference image serve as the basis for evaluation. Using reflected-light microscopy supported by SEM/EDS, the relative proportions of pyrite, pyrrhotite, and chalcopyrite within each particle's sulfide mineral population are determined based on mineral identifications established in Section 2.2. The measured sulfide surface area for each mineral is summed across all evaluated coarse aggregate particles and divided by the number of particles examined to provide a relative abundance value within the coarse fraction.

Fine aggregate contains too many individual grains for efficient and effective particle-by-particle analysis. Instead, sulfide proportions are estimated across the entire polished puck surface and normalized to the total exposed area of the fine aggregate puck.

The petrographic results can then be used in conjunction with total sulfur measurements. Once dominant sulfide species are identified petrographically, their approximate proportions can be measured and the weight percent of each mineral species can be calculated using mineral stoichiometry as a theoretical basis. This interpretation must account for the fact that sulfide minerals are rarely compositionally pure and that trace phases may remain below detection thresholds, but it provides additional insight into the mineral content and distribution of sulfide species present within an aggregate [6].

Finally, the area percentages obtained through reflected-light microscopy and SEM/EDS analysis can be converted to weight percent using the Delesse principle, which states that the area fraction of a mineral observed in a random polished cross-section is equal to its volume fraction in the bulk sample [10]. Once the volume fraction is established, conversion to weight percent requires the density of the mineral of interest and the bulk particle density of the aggregate. For pyrrhotite ($Fe_{1-x}S$), this conversion is expressed as:

$$wt\%_{Po} = \frac{(\frac{A\%_{Po}}{100}) \times \rho_{Po}}{(\frac{A\%_{Po}}{100}) \times \rho_{Po} + (1 - (\frac{A\%_{Po}}{100})) \times \rho_{Matrix}} \times 100$$

Where $A\%_{Po}$ is the measured area percent of pyrrhotite, ρ_{Po} is the density of pyrrhotite (nominally 4.58 – 4.65 g/cm^3, depending on stoichiometry), and ρ_{matrix} is the bulk particle density of the aggregate, determined by typical density of the identified rock type, i.e. gabbro = 2.70 g/cm^3. The density of pyrrhotite may be further refined using quantitative EDS compositional data, as the non-stoichiometric nature of the mineral (where x ranges from 0 to approximately 0.125) directly influences its true density.

The use of the petrographic determination of area percent of individual iron-sulfide mineral species in conjunction with total sulfur results and/or with calculations based on the area percent of each mineral phase can provide a route to a semi-quantification of the weight percent of each iron-sulfide mineral species detected in an aggregate population.

3. DISCUSSION AND CONCLUSION

The workflow presented in this paper offers a more reliable basis for identifying and estimating iron-sulfide minerals in construction aggregates than traditional petrographic methods alone. Distinguishing iron-sulfide minerals from one another and from high-reflectance oxides using standard optical petrography can be challenging, particularly when they occur as small or scattered grains. Although ASTM C295 permits the use of reflected light and SEM when needed, the method is primarily oriented toward transmitted-light thin-section analysis for lithological characterization. Because these minerals are opaque in transmitted light, occur in trace amounts, and micron-sized, and are often co-associated, their reliable identification and content estimation typically require additional analytical support.

The combined use of reflected light microscopy and SEM/EDS addresses these limitations by allowing sulfide minerals to be differentiated with greater confidence and by revealing textures and compositional features. The preparation method described in this paper allows for analysis of a large grain size population cross-sectioned to reveal minerals that may not be observed on particle surfaces and produces a more representative surface that reveals the size, distribution, and associations of these minerals within the aggregate, supporting more consistent estimates. This approach improves the reliability of determining sulfide content in both coarse and fine aggregates and ensures that small or compositionally variable grains are recognized and accounted for, allowing for a more robust determination of the presence of pyrrhotite. Pairing petrographic observations with total sulfur measurements offers a theoretical means to approximate the proportions of individual sulfide species present and calculating the weight percent of each species, providing semi-quantification of the iron sulfide mineral content of the aggregate.

Overall, this workflow offers a practical alternative to conventional petrographic evaluation when the goal is to identify, differentiate, and quantify iron-sulfide minerals in aggregate materials. It builds on the strengths of traditional methods while providing the level of analytical detail necessary for reliable assessment in regions where sulfide-related durability concerns have become significant, and pyrrhotite-bearing aggregate for use in concrete is restricted.

4. REFERENCES

[1] Wille, K. and Zhong, R. 2016. “Investigating the deterioration of basement walls made of concrete in CT.” University of Connecticut, Storrs, CT. 93 p.

[2] Chinchón, J. S., Ayora, C., Aguado, A. and Guirado, F. (1995). “Influence of weathering of iron sulfides contained in aggregates on concrete durability,” Cement and Concrete Research, Vol. 25, No. 6, pp. 1264-1272.

[3] Rodrigues, A., Duchesne, J., Fournier, B. et al. 2012. “Mineralogical and chemical assessment of concrete damaged by oxidation of sulphide-bearing aggregates,” Cement and Concrete Research, ROI 42: pp. 1336-47.

[4] State of Connecticut Substitute House Bill No. 6646 Public Act No. 21-120. “An Act Concerning Crumbling Concrete Foundations.” https://www.cga.ct.gov/2021/act/Pa/pdf/2021PA-00120-R00HB-06646-PA.PDF

[5] ASTM International. (2024*). ASTM C295/C295M-19: Standard guide for petrographic examination of aggregates for concrete*. West Conshohocken, PA.

[6] Duchesne, J., Rodrigues, A., & Fournier, B. (2021). Concrete damage due to oxidation of sulfide-bearing aggregate: A review of recent advances and limitations. *RILEM Technical Letters, 6*, 82–92.

[7 Nesse, W. D. (2000). *Introduction to mineralogy*. Oxford University Press.

[8] Wilkin, R. T., Barnes, H. L., & Brantley, S. L. (1996). The size distribution of framboidal pyrite in modern sediments: An indicator of redox conditions. *Geochimica et Cosmochimica Acta, 60*(20), 3897–3912.

[9] Duchesne, J., & Fournier, B. (2013). Deterioration of concrete by the oxidation of sulphide minerals in the aggregate. *Journal of Civil Engineering and Architecture*, 7(8), 922–931.

[10] Dellese, A. (1847). "Procede mécanique pour déterminer la composition des roches". *Comptes Rendus Hebdomadaires des Sciences de l'Academie de Sciences, Paris*, 25, 544–545

Improving sulfur analysis: a novel approach to distinguish pyrrhotite in rock aggregates

Titon, B.(1), Camargo, M.H.T.(2), Duchesne, J.(3), Fournier, B.(4), Rodrigues, A.(5)

(1) Department of Geology and Geological Engineering, Université Laval; Research on Concrete Infrastructure (CRIB), Quebec City, Canada, brgut@ulaval.ca

(2) Department of Geology and Geological Engineering, Université Laval; Research on Concrete Infrastructure (CRIB), Quebec City, Canada, murilo-henrique.taques-camargo.1@ulaval.ca

(3) Department of Geology and Geological Engineering, Université Laval; Research on Concrete Infrastructure (CRIB), Quebec City, Canada, josee.duchesne@ggl.ulaval.ca

(4) Department of Geology and Geological Engineering, Université Laval; Research on Concrete Infrastructure (CRIB), Quebec City, Canada, benoit.fournier@ggl.ulaval.ca

(5) Department of Geology and Geological Engineering, Université Laval; Research on Concrete Infrastructure (CRIB), Quebec City, Canada, andreia.rodrigues.1@ulaval.ca

Abstract

Over recent years, several cases of concrete damage have been linked to sulfide-bearing aggregates causing internal sulfate attack (ISA). The Total Sulfur (TS%) test is currently the main tool for aggregate acceptance. According to EN:12620, aggregates must contain less than 1.0 wt.% total sulfur, or less than 0.1 wt.% if pyrrhotite ($Fe_{1-x}S$) is present. While pyrrhotite is not the only sulfide phase found in aggregates, it is the most susceptible to deleterious oxidizing reactions and is responsible for the sulfur release in hardened concrete. However, pyrrhotite identification by optical petrography is highly dependent on the operator qualifications/experience, and TS% analysis cannot differentiate between sulfur sources, leading to potential unnecessary rejection of otherwise stable materials.

This study proposes an improved TS% determination protocol that uses selective dissolution to quantify the sulfur amount specifically associated with pyrrhotite. Samples from known problematic sources and a sulfide-free control were analyzed. After the initial TS% determination, the first dissolution step uses HCl to target the pyrrhotite, followed by aqua regia to dissolve any remaining sulfides. The difference in sulfur content between the initial and post-HCl analyses represents the amount of sulfur exclusively related to pyrrhotite.

Preliminary results show that >90% of pyrrhotite is dissolved with minimal effect on other sulfides (<10%). For instance, in this case, samples with a TS% of less than 1.0 wt.% presented 55–62% of their sulfur content related to pyrrhotite, while those with a TS% of greater than 1.0 wt.% showed only 12–44%. The results obtained in this study highlight the ability of the method to isolate pyrrhotite-related sulfur and demonstrate that a high TS% does not necessarily indicate greater reactivity.

***Keywords**: concrete, mineralogy, pyrrhotite, selective dissolution, sulfur content.*

1. INTRODUCTION

Since coarse and fine rock aggregates constitute up to 70% of the final volume of a concrete mixture [1], their mineralogical composition and chemical stability play a decisive role in its mechanical performance, and long-term durability. Poorly selected aggregates have been widely linked to premature deterioration, particularly through internal sulfate attack (ISA) [2-4]. This phenomenon is driven by the oxidation of sulfur-bearing minerals within the aggregates, releasing sulfur compounds which, in turn, react with cement hydration products to form expansive secondary phases [5], ultimately compromising mechanical strength.

The suitability of sulfide-bearing aggregates is typically evaluated using the total sulfur (TS%) test, which quantifies overall sulfur content. However, this test cannot currently distinguish between sulfide minerals which are known to exhibit different oxidation reactivities [6,7]. Current European standards (EN 12620:2008) impose a total sulfur limit of 1.0 wt.%, which is further reduced to 0.1 wt.%

when pyrrhotite is present. However, these limits are often considered too restrictive, potentially excluding materials that would otherwise be suitable. Pyrrhotite exhibits oxidation rates up to two orders of magnitude higher than pyrite (FeS_2) [8]. This is mainly due to its variable Fe-to-S ratio and mixed valence states. Despite its significance in ISA-related deterioration cases, North American standards still lack specific criteria for addressing pyrrhotite content, and its identification largely depends on the expertise of the operator using optical microscopy techniques.

1.1 Objectives and scope of work

In view of the present limitations of concrete aggregate screening and selection procedures, the objective of this study is to propose a selective dissolution protocol to identify and quantify pyrrhotite in sulfide-bearing aggregates.

Validation of this novel technique was performed using both natural and synthetic samples across various total sulfur contents (0.15 - 1.0%), with subsequent additional tests for reproducibility purposes. By isolating the sulfur specifically related to pyrrhotite, this method distinguishes the most reactive fraction from the total sulfur content, enabling a more accurate aggregate screening and potentially reducing unnecessary rejection of acceptable materials.

2. MATERIALS AND METHODS

The selected rock aggregates originated from sources that were previously associated with ISA issues due to the presence of sulfide-bearing minerals (Table 2.1). The sampling was designed to cover a broad spectrum of TS% to comprehensively validate the proposed analytical methodology. Two sulfur-rich samples (MSK_4 and MSM_05) characterized by contrasting pyrrhotite-to-pyrite ratios, were also included to assess methodological performance at various dissolution stages using X-ray diffraction (XRD). As XRD detection becomes unreliable for mineral phases below 5% of the total composition [7, 9], samples with higher sulfide contents were required to track the occurrence and disappearance of sulfide peaks, indicating full dissolution of these phases. Alongside the reactive samples, a non-reactive control sample (PKA, anorthosite) was included to establish a comparative baseline.

Table 2.1: Characteristics of the rock samples used in the selective dissolution study.

	Rock type	Sulfide minerals	TS% $_{initial}$	TS% $_{HCl}$	TS% $_{final}$
MSK_4	Gabbronorite	Pyrrhotite (29 wt.%) Pyrite (5 wt.%)	18.3	10.3	4.9
MSM_05	Gabbronorite	Pyrrhotite (4.6 wt.%) Pyrite (21.6 wt.%) Chalcopyrite (0.8 wt.%)	15.3	13.5	0.8
Connecticut	Gneiss	Pyrrhotite (0.8 wt.%) Pyrite (0.5 wt.%)	0.9	0.4	0.05
Ireland	Phyllite	Pyrrhotite (0.9 wt.%) Pyrite (0.3 wt.%)	0.8	0.3	0.05
PKA (control)	Anorthosite	-	0.05	-	-

Prior to applying the dissolution protocol to natural samples with variable TS% and multiple sulfide phases, synthetic mixtures were prepared to test the experimental procedure and evaluate the acid concentrations used. These synthetic samples, which did not contain pyrrhotite, were made by combining different proportions of the PKA material with an ore-grade sample from the Université Laval collection. This preparation resulted in controlled materials with varying TS%, due to the presence of pyrite, but no pyrrhotite, enabling the assessment of the selectivity and effectiveness of the acid solution in targeting pyrrhotite during the dissolution process.

The proposed methodology is structured to quantify and distinguish the sulfur content of specific sulfide minerals within aggregate materials. Initially, the bulk sample's TS% was determined by combustion and infrared absorption, providing a baseline for subsequent comparisons. This preliminary

analysis establishes the overall sulfur content from all the sulfide phases present before the selective dissolution is applied.

The process then proceeds through two targeted dissolution steps, complemented by mineralogical characterization to independently verify the selectivity of the treatment. In the first step, 5g of the sample (below 150 µm) are dissolved in a specific concentration of hydrochloric acid (HCl), which is chosen for its ability to selectively dissolve pyrrhotite while leaving more stable sulfide phases, such as pyrite, chalcopyrite [$CuFeS_2$], and pentlandite [$(Fe,Ni)_9S_8$], largely unaffected [10, 11].

To confirm the efficacy of this selective leaching, XRD analysis was performed on the specimen at each stage. Before the first dissolution step, the diffractograms identified the presence of pyrrhotite, pyrite, and pentlandite. Following the HCl treatment, subsequent XRD characterization revealed the disappearance of pyrrhotite-related peaks, while the reflections for pentlandite and pyrite remained stable, confirming that only the reactive pyrrhotite fraction was removed during this initial stage. The measured sulfur content at this stage reflects only the “non-reactive” sulfides present in the system (and which were not significantly affected by the previous dissolution procedure). Consequently, the difference between the initial and post-HCl TS% values corresponds to the sulfur exclusively associated with pyrrhotite. The second dissolution step is carried out with aqua regia, a pre-defined mixture of nitric and hydrochloric acids, to dissolve the remaining sulfide minerals. After this step, the remaining solid residue is once again analyzed for TS%. In this case, the sulfur content should approach zero, confirming the complete dissolution of the sulfide phases. Together, these two sequential dissolution steps, validated by independent mineralogical data, provide a precise and reproducible approach to differentiating and quantifying the sulfur associated with reactive pyrrhotite from the non-reactive sulfide mineral components present in concrete aggregates.

3. RESULTS AND DISCUSSION

Preliminary results demonstrate that the selective dissolution methodology is effective and reproducible across aggregates with varying TS% contents. As shown in Figure 3.1, this method effectively isolates sulfur associated with pyrrhotite ($TS_{Po} = TS_{initial} - TS_{HCl}$) while leaving non-reactive sulfide phases largely unaffected (TS_{final}). The pyrrhotite-to-pyrite (Po/Py) ratios presented in Figure 3.1 were independently determined for each sample to provide a mineralogical baseline for the chemical results. For samples where high-resolution spatial data were available, these ratios were obtained via SEM-QEMSCAN. It is important to note that the bulk samples used in the dissolution protocol were ground from the same rock pucks used to prepare the thin sections, ensuring that the chemical analysis and the SEM-QEMSCAN mineral assembly are directly comparable. For the remaining samples where SEM data were not available, the Po/Py ratios were determined through quantitative XRD analysis. To verify the selective dissolution of the different sulfide species, the progressive mineralogical evolution of the specimens was monitored independently via XRD analysis of the solid residue retrieved after each step. These analyses confirmed the systematic disappearance of pyrrhotite peaks while reflections for other sulfide phases, such as pyrite and pentlandite, remained present, validating the chemical quantification results.

For samples with initial sulfur concentrations below 1.0 wt.% (Connecticut, Ireland and PKA), over 90% of pyrrhotite was removed during the first HCl dissolution step, whereas less than 10% of other sulfides were affected. Interestingly, these low-sulfur samples exhibited the highest relative proportion of pyrrhotite-derived sulfur, with values ranging from 55% to 62% of their overall total sulfur content. These results further demonstrate that aggregates with a TS% content below 1.0 wt.% can still possess reactivity potential [3, 12]. Conversely, rock aggregates with TS% exceeding 1.0 wt.% showed that only 12 - 44% of their total sulfur was actually associated with pyrrhotite, indicating that a higher bulk sulfur content does not necessarily correspond to increased susceptibility to future reactions. This distinction is critical for assessing the potential for ISA, as it emphasizes the need to consider mineralogical composition rather than relying solely on total sulfur measurements.

The XRD results corroborate the dissolution data. For instance, the MSK_4 sample, which was initially quantified as containing approximately 29% pyrrhotite and 5% pyrite, showed a total disappearance of the pyrrhotite peaks after HCl treatment (Figure 3.2). Calculations based on the sulfur content obtained from the dissolved sample yielded an estimated initial pyrrhotite content of around 18 - 22%, which is close to the value derived from XRD. Similarly, the Ireland sample (Figure 3.3) showed low pyrrhotite concentrations (around 1%), which could not be resolved visually in diffractograms due to XRD resolution limitations. Nevertheless, numerical XRD analysis and post-dissolution sulfur-based

calculations produced consistent estimates, validating the accuracy of the methodology even for low pyrrhotite-containing rock aggregates. These results demonstrate that this approach can reliably identify and quantify pyrrhotite, providing a more precise assessment of aggregate potential reactivity than the current TS% method.

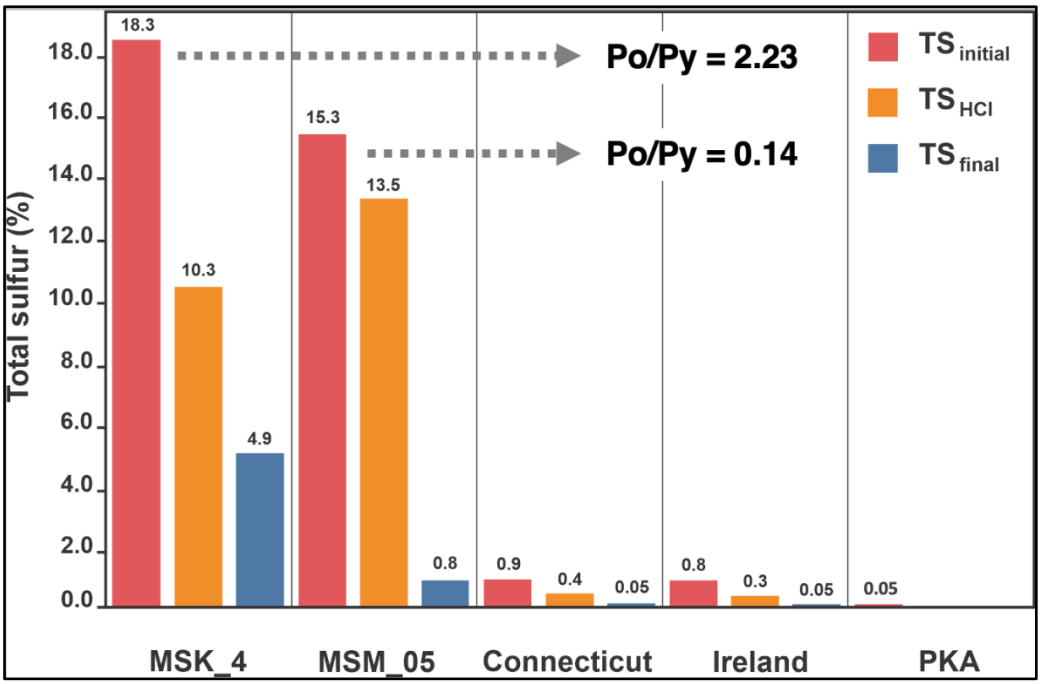

Figure 3.1: Total sulfur (TS%) results for samples with different sulfur contents subjected to the dissolution protocol. The sulfur-rich samples MSK_4 and MSM_05 were analyzed by XRD to track mineralogical evolution during the dissolution stages and their respective Po/Py original ratios were independently verified by SEM-QEMSCAN.

Despite these positive outcomes, the current methodology has some inherent limitations. Firstly, it applies to aggregates containing sulfur derived only from sulfide minerals; sulfur present in other mineral forms, such as sulfates (e.g., gypsum [$CaSO_4$•2(H_2O)]), is not considered. Additionally, prior oxidation of the aggregate may result in the presence of secondary sulfates, which could interfere with the sulfur signature of pyrrhotite. However, the samples used in this study were meticulously characterized, and previous long-term mineralogical assessments (especially for the Maskimo samples) confirmed the absence of other sulfur-bearing phases. While the current protocol focuses on differentiating pyrrhotite from other sulfides, the authors acknowledge that for aggregates where prior oxidation or primary sulfates are a concern, more complex dissolution schemes, such as those proposed by Marcelino et al. (2016, 2020), should be employed. Addressing the interference of a wider range of sulfur-bearing phases remains a goal for future refinements of this methodology.

Secondly, while the method selectively targets pyrrhotite, the presence of rare HCl-soluble sulfides, such as sphalerite ([Zn,Fe]S), could also interfere with the results, as their dissolution would be indistinguishable from that of pyrrhotite in sulfur-based measurements. To mitigate this, the methodology relies on preliminary mineralogical characterization (e.g., SEM-QEMSCAN or XRD) to identify the specific sulfide assemblage of the aggregates. In the samples studied, mineralogical monitoring before and after leaching confirmed that pyrrhotite was the only reactive phase removed, while other sulfides remained stable. While the authors acknowledge that for aggregates containing a complex mixture of HCl-soluble sulfides, this protocol would provide a combined 'reactive sulfide' value rather than a phase-specific one, the current results demonstrate its efficacy for typical pyrrhotite-bearing aggregates used in concrete.

Thirdly, rock aggregates with a high carbonate content are not suitable for this methodology as HCl reacts vigorously with carbonates, which compromises the stability and reproducibility of the dissolution test. While carbonate traces are acceptable, carbonate-rich aggregates cannot be reliably analyzed at present.

Overall, these findings confirm that the selective dissolution protocol is robust and accurate, and can isolate pyrrhotite-associated sulfur across a range of sample compositions. This approach has clear advantages over conventional TS% assessment, as it allows for a more reliable prediction of ISA potential in concrete aggregates, within the limits imposed by sample mineralogy and the inherent constraints of the technique.

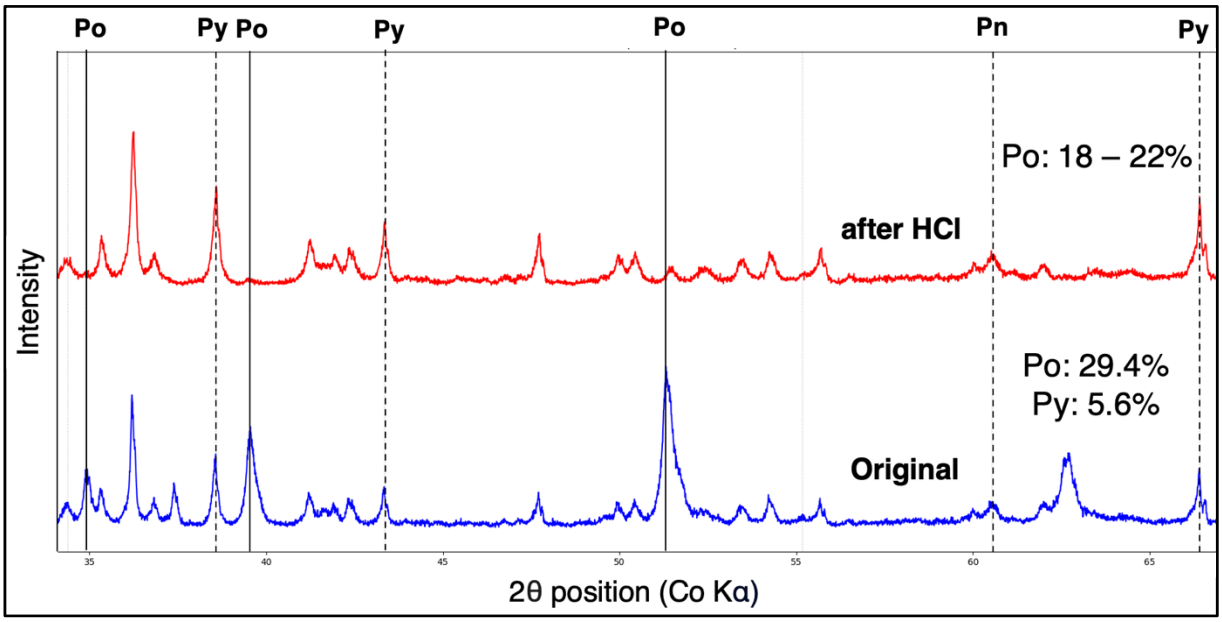

Figure 3.2: XRD diffractograms of sample MSK_4 before and after the initial HCl dissolution step. Characteristic pyrrhotite peaks disappear following the treatment, while other sulfide peaks remain. The Po content, ranging from 18% to 22%, was determined from calculations using the sulfur concentration obtained from the dissolved sample. Key: Po = pyrrhotite; Py = pyrite; Pn = pentlandite

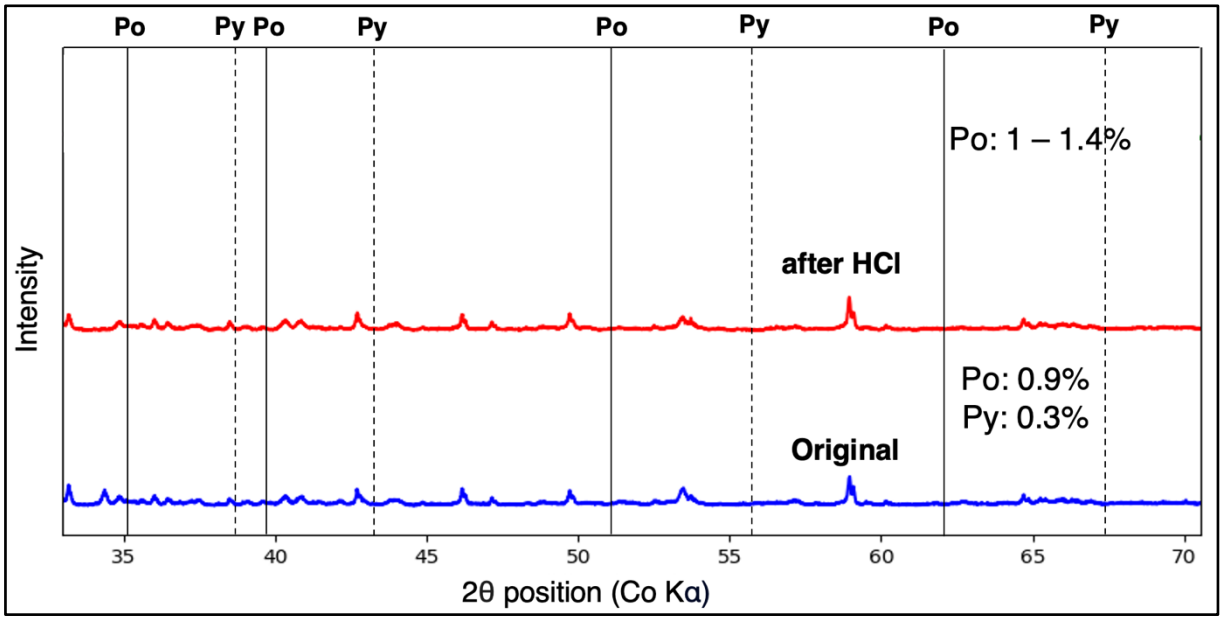

Figure 3.3: XRD diffractograms of sample from Ireland before and after the initial dissolution step. As sulfides represent only a small portion of the total mineral assemblage, their characteristic peaks are not well resolved by XRD.

4. FUTURE INVESTIGATIONS

Following the successful validation of the proposed methodology using sulfide-bearing aggregates with known ISA reactivity and varying total sulfur contents, further investigations are required to consolidate its applicability and efficacy. Future work should expand the dataset by analysing additional samples, including previously characterized materials from Ireland and Connecticut, as well as new aggregates from locations with a history of ISA-related deterioration.

A systematic expansion of the experimental dataset and an interlaboratory study will improve statistical confidence, precision, and methodological robustness. Subsequent publication of the complete dissolution protocol and final results on a larger variety of aggregate specimens in a peer-reviewed journal will allow for independent verification and critical evaluation by the scientific community. The future aim is to stimulate and support a broader adoption of this methodology, with the potential for standardization of the technique for assessing potential sulfide reactivity in concrete aggregates.

5. REFERENCES

[1] Kosmatka S H, Wilson M L, Kerkhoff B, Panarese W C, MacLeod N F, McGrath R J (2003). Design and Control of Concrete Mixtures. EB101, 7th edition, Cement Association of Canada, Ottawa, Ontario, Canada.

[2] Zhong R, Wille K (2018). Deterioration of residential concrete foundations: The role of pyrrhotite-bearing aggregate. Cem. Concr. Compos. 94: 145–157. https://doi.org/10.1016/j.cemconcomp.2018.08.012

[3] Leemann A, Lothenbach B, Münch B, Campbell T, Dunlop P (2023). The “mica crisis” in Donegal, Ireland – a case of internal sulfate attack? Cem. Concr. Res. 174: 107149. https://doi.org/10.1016/j.cemconres.2023.107149

[4] Titon B, Duchesne J, Fournier B, Rodrigues A (2025). Concrete deterioration due to sulfide-bearing aggregates: Mineralogical and chemical characteristics of pyrrhotite in concrete aggregates from Trois-Rivières, Canada. Constr. Build. Mater. 561: 139670. https://doi.org/10.1016/j.conbuildmat.2024.139670

[5] Rodrigues A, Duchesne J, Fournier B, Durand B, Rivard P, Shehata M (2012). Mineralogical and chemical assessment of concrete damaged by the oxidation of sulfide-bearing aggregates: Importance of thaumasite formation on reaction mechanisms. Cem. Concr. Res. 42(10): 1331–1343. https://doi.org/10.1016/j.cemconres.2012.06.008

[6] Rodrigues A, Duchesne J, Fournier B (2012). Microscopic analysis of the iron sulfide oxidation products used in concrete aggregates. In: Proceedings of the 34th International Conference on Cement Microscopy (ICCM), April 22–25, 2012, Bernburg, Sachsen-Anhalt, Germany.

[7] Multani R S, Waters K E (2017). A review of the physicochemical properties and flotation of pyrrhotite superstructures (4C-Fe7S8/5C-Fe9S10) in Ni–Cu sulfide mineral processing. Can. J. Chem. Eng. 95(11): 2058–2071. https://doi.org/10.1002/cjce.23099

[8] Li Z, Gorski C A, Thompson A, Shallenberger J R, Kaladharan G, Radlińska A (2025). Dissolution kinetics of iron sulfide minerals in alkaline solutions. Cem. Concr. Res. 193: 107850. https://doi.org/10.1016/j.cemconres.2025.107850

[9] Kleiv R A (2021). A flotation-based approach to the quantification of pyrrhotite in concrete aggregates. Results Eng. 12: 100243. https://doi.org/10.1016/j.rineng.2021.100243

[10] Lorenzen L (1995). Some guidelines to the design of a diagnostic leaching experiment. Miner. Eng. 8(3): 247–256. https://doi.org/10.1016/0892-6875(95)00002-4

[11] Garg S, Papangelakis V, Edwards E, Mahadevan R (2017). Application of a selective dissolution protocol to quantify the terminal dissolution extents of pyrrhotite and pentlandite from pyrrhotite tailings. Int. J. Miner. Process. 158: 37–46. https://doi.org/10.1016/j.minpro.2016.11.004

[12] Leemann A, Münch B, Lothenbach B, Winnefeld F, Dunlop P (2024). Defective homes in Donegal, Ireland: effect of exposure conditions and concrete quality on pyrrhotite oxidation and internal sulfate attack. Cem. Concr. Res. 186: 107684. https://doi.org/10.1016/j.cemconres.2024.107684

Interlaboratory Study on Sulfur Quantification using the Pyrrhotite in Concrete NIST Reference Material

Stephanie Watson[(1)], Ashley Carey[(2)], Patrick Dixon[(3)], Michael Mengason[(4)], Paul Stutzman[(5)]

(1) National Institute of Standards and Technology, Gaithersburg, USA, stephanie.watson@nist.gov

(2) National Institute of Standards and Technology, Gaithersburg, USA, ashley.carey@nist.gov

(3) National Institute of Standards and Technology, Gaithersburg, USA, patrick.dixon@nist.gov

(4) National Institute of Standards and Technology, Gaithersburg, USA, michael.mengason@nist.gov

(5) National Institute of Standards and Technology, Gaithersburg, USA, paul.stutzman@nist.gov

Abstract

To provide a means for accurate, consistent analysis of pyrrhotite in concrete, NIST produced a suite of reference samples for calibration and validation. These reference materials (RM) - 'Pyrrhotite in Concrete' - were chosen to be representative of the host rock, pyrrhotite, and cementitious matrix used by industry and consist of pyrrhotite-containing aggregate, synthesized pyrrhotite, sand, and hydrated cement. These will be combined by users in variable proportions to produce samples with a range of total sulfur concentrations. A NIST led interlaboratory study (ILS) was developed to support consistent and accurate measurements of sulfur/pyrrhotite in unknown cementitious samples by: 1) studying deviations in the sulfur (S) concentrations obtained from different test methods and errors from different labs, 2) facilitating a database of common S test methods to optimize procedures for standard test methods on aggregate and concrete materials, and 3) establishing a consensus value for the total S concentration in this NIST RM. The recommended total S concentration in the aggregate component of this NIST RM will be determined in this ILS by x-ray fluorescence spectroscopy (XRF) (instrument calibration program for pellet and glass bead), S combustion, and ASTM C114 wet chemical tests for sulfide and sulfate quantification. NIST ILS participant preliminary results, including calibration curves from a defined mix design with the NIST RM and corresponding S concentrations from NIST ILS provided unknown concrete specimens is discussed.

***Keywords**: pyrrhotite, reference material, interlaboratory study, XRF, S combustion*

1. INTRODUCTION

1.1 Background

Damage to concrete structures in residential and commercial construction in Connecticut (CT) and Massachusetts (MA) has been attributed to the iron sulfide mineral pyrrhotite (pyh) [1,2]. Iron sulfides in concrete aggregate are not desirable as their relative instability results in decomposition with associated staining, expansion, and pop-outs near concrete surfaces or cracking of the structure. In CT, 3,500 structures have been identified for replacement of damaged foundations, which is the only current solution costing approximately $250k per residence. There are no standardized test methods to assess pyh occurrence and abundance in aggregate or in concrete due to its low concentrations of the mineral in aggregate and the ability to distinguish it from the sulfur found in the cement paste.

Furthermore, enacted state regulations for sulfur content in aggregate require quantification as low as 0.1 wt. % sulfur (S) and identification of pyh in the range of (0.1 to 1.0) wt. % S [3,4]. Although there are ASTM standard test methods to quantify total S (i.e., ASTM D4239, ASTM E1915, ASTM E1621), these methods were developed on different materials: soils, ores, and coal materials, and S concentrations specifically in aggregate and concrete for each method result in a different S value, making it difficult to determine the ground truth concentration. For traditional petrographic methods, the lower pyh concentrations are also very challenging to meet and accessible for the non-geologist. An accurate S concentration is essential for the livelihood of quarry owners to avoid eliminating acceptable aggregate product and for home/building owners who need to know if their asset is at risk for damage [5].

To provide a means for accurate, consistent analysis of pyh in concrete, NIST produced a suite of reference samples for calibration and for validation. These reference materials (RM)- *pyh in concrete*- were chosen to be representative of the host rock, pyh, and the concrete matrix and consist of pyh containing aggregate, sand, hydrated cement, and pure synthesized pyh to normalize a variable pyh concentration in the aggregate. This NIST *pyh in concrete* RM must be tested on common S test methods to optimize a RM mix design and to develop standard test methods specific to aggregate and concrete applications. This study will introduce stakeholders to the NIST *pyh in concrete* RM and test methods for aggregate and concrete materials using a NIST-led interlaboratory study

1.2 Reference Materials

Techniques and methods used at NIST for characterizing measurement procedures and evaluating chemical and physical properties of materials are critically examined, and potential sources of bias and variability in these processes are addressed and documented in publicly accessible documents [6]. NIST provides six named types of materials intended to be used as measurement standards. All materials are considered 'reference materials' defined as materials, sufficiently homogeneous and stable with respect to one or more specified properties, which have been determined by NIST to be fit for their intended use. This contrasts with NIST certified reference materials (CRM) that provide higher-order calibration and validation materials to secondary standard producers and customers intending to produce metrologically traceable in-house calibrants and control materials. Although the pyh reference material (RM) is not certified, it delivers property values for established measurands that are fit for the materials' intended uses, including between-method harmonization, within-method precision assessment, and process stability assessment. It was created to contain actual concrete materials to allow for better matrix matching to ensure more accurate pyrrhotite concentration measurements in construction materials.

2. EXPERIMENTAL

2.1 Materials

The NIST *pyh in concrete* RM is made up of 4 components: aggregate containing pyh (and pyrite), hydrated Portland cement, quartz sand, and synthesized (in-house) pyh [7]. The aggregate and sand were obtained from commercial construction resources, and cement from the Cement and Concrete Reference Laboratory (ASTM International). Materials were ground separately using a ring-puck mill and sieved through a 60-micrometer screen. Each component was then homogenized and bottled, individually. NIST characterized the component's elemental/mineral composition and crystalline phases.

A mix design using mass proportions of each RM component creates specific final pyrrhotite concentration specimens for sulfur analysis. This mix design used a constant cement proportion and sand to dilute the aggregate assuming all sulfide is pyh (Table 2.1). Using the mix design, proportions of RM components are thoroughly mixed and the selected S test methods are conducted on appropriate analyte specimen masses. Calibration curves are then created from the analysis data from the mix design specimens and applied to unknown construction materials. For the ILS, corrections for the presence of pyrite will be included in the analysis of S concentrations.

Table 2.1: Example of NIST *pyh in concrete* RM Mix Design

Calculated Pyrrhotite Concentration		Reference Material Mass (g)		
Concentration (wt % S)	Concentration (wt % pyh)	Aggregate	Sand	Cement
0.025	0.067	0.720	12.456	1.8
0.074	0.202	2.160	11.016	1.8
0.123	0.337	3.600	9.576	1.8
0.172	0.471	5.040	8.136	1.8
0.221	0.606	6.480	6.696	1.8
0.270	0.740	7.920	5.256	1.8
0.319	0.875	9.360	4.536	1.8
0.368	1.010	10.800	2.376	1.8

0.417	1.144	12.240	0.936	1.8

2.2 Sulfur Test Methods

The NIST-led interlaboratory study was conducted using common total sulfur test methods: sulfur combustion, wavelength dispersive x-ray fluorescence spectroscopy (WD-XRF) with pellet and bead specimens, and wet chemical methods (ASTM C114). WD-XRF and wet chemical methods can also differentiate sulfide and sulfate species that comprise the total sulfur content. All methods utilize ground samples, and the mesh of the powder can vary for each method.

2.2.1 Sulfur Combustion

The sulfur combustion method measures total sulfur, such that *sulfide* sulfur (denoted S) will be determined with sulfate (denoted SO_3 in these test methods). There are two general combustion methods (ASTM D4239, ASTM E1915). For both methods, moisture and particulates are removed from the gas by filters and the filtered gas stream is passed through a cell in which sulfur dioxide (SO_2) is measured by an infrared (IR) absorption detector, where SO_2 absorbs IR energy at a precise wavelength within the IR spectrum. All other IR energy is prevented from reaching the detector by a wavelength filter, so that the absorption of IR energy can be attributed only to SO_2 whose concentration is proportional to the change in energy at the detector. One cell is used as both a reference and a measurement chamber, and the total S as SO_2 is detected on a continuous basis. A high temperature (>1350 °C) combustion method heats a weighed specimen in a tube furnace at a minimum combustion tube operating temperature of 1350 °C in a stream of oxygen. During combustion at temperatures above 1350 °C, all sulfur compounds in the sample are decomposed and oxidized almost exclusively to gaseous SO_2. A lower temperature (1150 °C) combustion method heats a weighed specimen and one or more accelerators (e.g., tungsten trioxide (WO_3), tin (Sn), iron chip or powder (Fe), and vanadium pentoxide (V_2O_5)) in a quartz combustion tube in a stream of oxygen by coupling with high frequency power produced by the induction furnace causing the sample to heat and decompose, and sulfur is oxidized in the oxygen stream.

2.2.2 WD-XRF

Wavelength dispersive x-ray fluorescence spectrometry (WD-XRF) was used to quantify the sulfur species associated with pyrrhotite (sulfide) and reaction products (sulfate) by examining SKα (primary) and SKβ (secondary) peaks as was done for concrete materials in ASTM E1621 and in the literature. [8-10] The NIST XRF instrument used a Ge 111-C crystal and a 150-micrometer collimator. Specimens comprised of pressed pellets for sulfur speciation and glass beads for total sulfur quantification. Instrument and in-house designed quantification programs were used to quantify the sulfur species.

2.2.3 Wet Chemical Methods

Sulfide and sulfate species are liberated and measured after decomposition of samples in hydrochloric acid (HCl) as described in ASTM C114. *Sulfide* sulfur is determined by evolution as hydrogen sulfide (H_2S) from an acid solution of the sample placed into a solution of zinc sulfate ($ZnSO_4$) or cadmium chloride ($CdCl_2$) prepared in ammonium hydroxide (NH_4OH). *Sulfide* sulfur is then titrated with a standard solution of potassium iodate (KIO_3). According to the test method, intermediate compounds, such as sulfites, thiosulfates, etc. are assumed to be absent and their presence can be a source of error. Sulfate is precipitated from an acid solution of the sample with barium chloride ($BaCl_2$). The precipitate is ignited and weighed as barium sulfate ($BaSO_4$) to calculate the SO_3 equivalent. Total sulfur is determined by the sum of the values for *sulfide* sulfur after correction of the molecular ratio to express sulfur as sulfate. There are many limitations with the wet chemical methods including solubility challenges, interference from compounds contained in aggregate and/or concrete, and errors involved in reagent preparation and the complex procedures that generate the product.

3. INTERLABORATORY STUDY

The objectives of the NIST-led interlaboratory study (ILS) that will introduce the NIST *pyh in concrete* RM and standardized S test methods to stakeholders are to 1) study deviations in the S concentrations obtained from different test methods and errors from different labs; 2) facilitate a database on common S test methods to optimize procedures for standard test methods on aggregate and concrete materials;

and 3) confirm a certified value for the total S concentration in the NIST *pyh in concrete* RM for consistent and accurate measurements of S/pyh in unknown cementitious samples.

This ILS will establish a recommended total S concentration in the aggregate component of the NIST *pyh in concrete* RM as determined by x-ray fluorescence spectroscopy (XRF) (instrument calibration program for pellet and glass bead), S combustion, and ASTM C114 wet chemical tests for sulfide and sulfate quantification. The measurable range of SO_3 as defined in ASTM C114 is 0.05 wt% to 0.20 wt%. NIST has also developed a wavelength dispersive (WD) XRF method to determine sulfide and sulfate concentrations and is working to ballot the method as a standard in ASTM C09-50-Aggregate Reactions in Concrete. Participants in the NIST ILS are ASTM members, stakeholders from the crumbling foundation community, and other interested organizations.

The NIST-led ILS is outlined in Figure 3.1. It will be conducted using common total S test methods: S combustion, XRF pellet and bead, and ASTM C114 wet chemical methods. NIST will instruct participants to generate calibration curves using a defined mix design from the NIST *pyh in concrete* RM. NIST will also provide two unknown concrete specimens to compare the participant calibration curves and corresponding S concentration results.

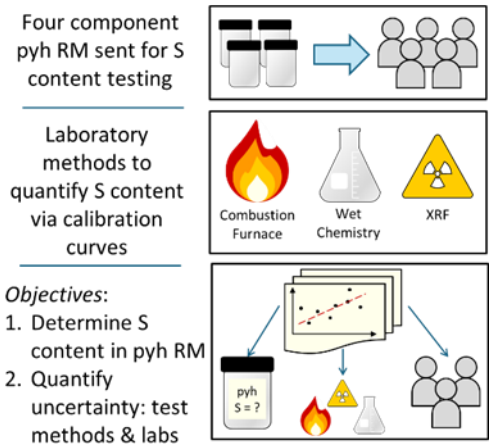

Figure 3.1: NIST-Led Interlaboratory Study Plan

An example of S combustion results from NIST using a mix design of the NIST *pyh in concrete* RM (RM 8154), is shown in Figure 3.2. Combustion analysis of RM 8154 mixtures yielded results within expected parameters of the combustion instrumentation when calculated from combustion results obtained for individual mixture components. These results demonstrated both reliable RM components and mixtures as well as consistent sample preparation and low experimental error.

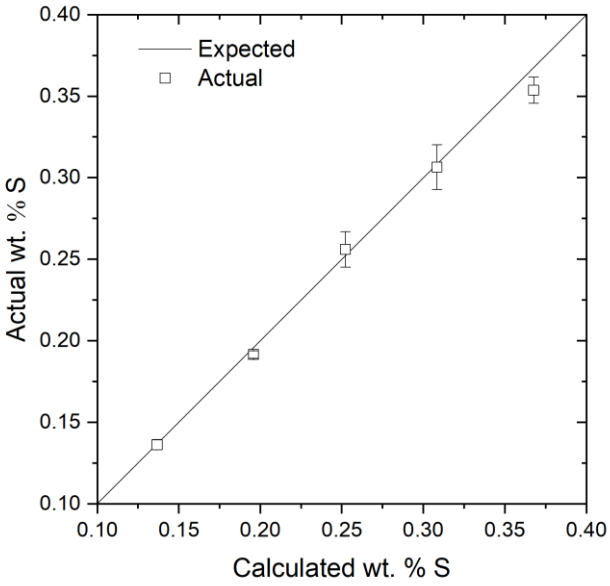

Figure 3.2. Results of component mixture combustion vs. calculated values, based on results of individual RM components. Error bars represent relative standard deviation.

4. SUMMARY

NIST has developed a set of calibration reference standards to provide a means for accurate, consistent analysis of pyrrhotite in concrete. The reference materials allow for known concentrations of pyrrhotite in a matrix of concrete (aggregate, cement, and sand) that reflects those used in concrete construction. A NIST-led interlaboratory study was conducted to 1) study deviations in the S concentrations obtained from different test methods and errors from different labs; 2) facilitate a database on common S test methods to optimize procedures for standard test methods on aggregate and concrete materials; and 3) confirm a certified value for the total S concentration in the NIST *pyh in concrete* RM for consistent and accurate measurements of S/pyh in unknown cementitious samples.

5. DISCLAIMER

Certain commercial products or equipment are described in this paper to adequately specify the experimental procedure. In no case does such identification imply recommendation or endorsement by the National Institute of Standards and Technology, nor does it imply that it is necessarily the best available for the purpose.

6. ACKNOWLEDGEMENTS

Authors acknowledge the collaboration with the Department of Civil and Environmental Engineering at the University of Connecticut (Wille group) for field concrete and aggregate materials and instrumental procedure discussions.

7. REFERENCES

[1] Crumbling Foundations (July 2020) GAO Report 20-649, https://www.gao.gov/assets/gao-20-649.pdf

[2] Warr LN (2021) IMA-CNMNC approved mineral symbols, Mineralogical Magazine 85, 291-320.[3] CT aggregate legislation report (2019) OLR 2019-R-0211, https://www.cga.ct.gov/2019/rpt/pdf/2019-R-0211.pdf

[4] Code of Massachusetts Regulation (2023) 700 CMR 19.00 Aggregate source licensing for the production of cement concrete https://www.mass.gov/regulations/700-CMR-1900-aggregate-source-licensing-for-the-production-of-cement-concrete

[5] Bentivegna AF, Snyder A, Stacey SM Pyrrhotite in Concrete Aggregates: Is legislation ahead of science? Concrete International, August 2023, p. 37-44

[6] Beauchamp C, Camara J, Carney J, Choquette S, Cole K, DeRose P, Duewer D, Epstein M, Kline M, Lippa K, Lucon E, Molloy J, Nelson M, Phinney K, Polakoski M, Possolo A, Sander L, Schiel J, Sharpless K, Toman B, Winchester M, Windover D (2021) Metrological Tools for the Reference Materials and Reference Instruments of the NIST Material Measurement Laboratory, NIST Special Publication 260-136, 1-66

[7] Mengason M, Watson S (2025) Pyrrhotite Reference Material Synthesis NIST Technical Note 2336, https://doi.org/10.6028/NIST.TN.2336

[8] Uhlig S, Möckel R, Pleßow A (2015) Quantitative analysis of sulphides and sulphates by WD-XRF: Capability and constraints, X-Ray Spectrom 45, 133–137

[9] Cruz-Hernandez Y, Chrysochoou M, Wille K (2020) Wavelength dispersive X-ray fluorescence method to estimate the oxidation reaction progress of sulfide minerals in concrete, Spectrochimica Acta Part B 172, 105949

[10] Santos L, Wille K, Chrysochoou M (2024) Application of X-ray principles to quantify sulfur oxidation states in concrete, Spectrosc Lett 57 (7) 377-397

ICISR 2026

2nd International Conference on Iron-Sulfide Reactions in Concrete

Technical Session # 7:

Reaction Kinetics and Evaluation of Iron-Sulfide Oxidation and Secondary Product Formation

UCONN | COLLEGE OF ENGINEERING
SCHOOL OF CIVIL AND ENVIRONMENTAL ENGINEERING

UCONN
COLLEGE OF ENGINEERING
CONNECTICUT TRANSPORTATION INSTITUTE (CTI)

Crack Formation Modeling in Concrete Affected by Iron-Sulfide Reactions

Osamah H.A. Dehwah [(1),(2)], Nicos S. Martys[(3)], Edward J Garboczi[(4)], Michael Mengason[(5)], Patrick G. Dixon[(6)], Stephanie S. Watson [(7)]

(1) PREP Associate, National Institute of Standards and Technology, Gaithersburg, USA, osamah.dehwah@nist.gov

(2) Department of Civil and Systems Engineering, Johns Hopkins University, Maryland, USA, odehwah1@jh.edu

(3) National Institute of Standards and Technology, Gaithersburg, USA, nicos.martys@nist.gov

(4) National Institute of Standards and Technology, Boulder, USA, edward.garboczi@nist.gov

(5) National Institute of Standards and Technology, Gaithersburg, USA, michael.mengason@nist.gov

(6) National Institute of Standards and Technology, Gaithersburg, USA, patrick.dixon@nist.gov

(7) National Institute of Standards and Technology, Gaithersburg, USA, stephanie.watson@nist.gov

Abstract

Damage in concrete containing sulfide-bearing aggregates has become a critical issue in several countries such as the USA, Canada, and Ireland. This deterioration unfolds over decades and is driven by oxidation reactions in sulfide-bearing aggregates, followed by internal sulfate attack within the cementitious matrix. About 60 % to 75 % of concrete is composed of aggregates, and the oxidation of sulfide-bearing particles causes aggregate expansion, enabling sulfate release and leading to progressive cracking. This process severely impacts the mechanical and durability properties of concrete by altering its microstructure.

Pyrrhotite-related deterioration has prompted extensive research aimed at understanding the underlying chemical and mechanical mechanisms. To investigate crack formation and propagation, a quasistatic two-dimensional finite element model (FEM) was developed to simulate crack network evolution with a pixelated approach used to identify the different phases in concrete. The model provides valuable insights into the influence of microstructural characteristics on crack network formation and the role of internal phase expansion in degrading the elastic properties of concrete. A scanning electron microscopy (SEM) image of undamaged concrete from a Connecticut (CT) house that had a damaged foundation was examined, and the crack network was simulated using the developed FEM. A sensitivity analysis was performed to assess the impact of convergence criteria on model precision and computational efficiency. The model can be used to clarify damage mechanisms caused by internal chemical reactions and localized expansion.

Keywords: *concrete degradation; crack nucleation and initiation; crack propagation; pyrrhotite*

1. INTRODUCTION

Concrete deterioration associated with the oxidation of iron sulfide minerals has been reported in several regions worldwide [1]. In Connecticut, thousands of residential foundations have been confirmed to exhibit damage attributable to pyrrhotite oxidation [2]. The observed distress typically includes whitish surface deposits, yellowish discoloration, pop-outs, and characteristic map cracking [3–5]. Pyrrhotite ($Fe_{1-x}S$) can be naturally present in aggregates. It oxidizes upon exposure to moisture and oxygen, forming iron hydroxides. During this process, sulfate ions (SO_4^{2-}) are released into the surrounding cement matrix, triggering internal sulfate attack [6, 7]. These reactions produce expansive iron corrosion products such as goethite and ferrihydrite, as well as secondary phases including gypsum, ettringite, and thaumasite. The continued accumulation of these products over time leads to progressive expansion, cracking, and deterioration of concrete foundations (see Figure 1.1).

This deterioration has motivated extensive research aimed at understanding the underlying chemical and mechanical processes driving pyrrhotite-induced damage. Studying how cracks nucleate and propagate provides important insight into the progression of damage caused by pyrrhotite oxidation. To

investigate these mechanisms, a quasistatic two-dimensional finite element model was developed to simulate crack initiation and formation in concrete containing sulfide-bearing aggregates. A pixelated approach was used to capture the distinct mechanical behavior of different concrete phases such as aggregates, mortar, voids, and pyrrhotite, while expansion was applied at pyrrhotite locations to represent internal phase expansion [8]. Furthermore, the developed model in general helps in understanding damage mechanisms associated with internal chemical reactions and/or expansion and provides a foundation for future efforts to mitigate deterioration in affected structures. It can also predict elastic properties, including Young's, bulk, and shear moduli and Poisson's ratio as a function of the degree of deterioration. This extended abstract presents the model framework and its development, along with field sampling and laboratory testing. It also summarizes the model's sensitivity analysis and the preliminary simulation results.

Figure 1.1: Deterioration of concrete foundation due to pyrrhotite

2. QUASISTATIC NUMERICAL MODEL

2.1 Model Development

The model represents concrete microstructures by discretizing a 2-D image into pixels with each pixel assigned material properties corresponding to its phase. Chemically driven expansion associated with pyrrhotite oxidation is introduced through an intrinsic strain applied to the relevant phases. When the stress (or strain) at a given pixel exceeds a predefined critical stress (or strain), it is converted into a crack pixel with zero stiffness [9]. Following each cracking event, the stress field is recalculated, and the procedure is repeated iteratively to simulate the progressive development of crack networks. Additional details are provided in [8, 10].

Concrete behaves as a quasi-brittle material; therefore, a quasistatic, linear-elastic framework is adopted to capture its crack-formation mechanics. The stress field is obtained by minimizing the elastic potential energy with the governing equations discretized using bilinear four-node quadrilateral finite elements. Previous evaluations of this formulation have demonstrated that it yields reliable elastic properties [11]. The elastic modulus and Poisson's ratio are assigned to the various concrete phases such as aggregate, mortar, and voids, while the pyrrhotite-bearing phases are assigned a predefined intrinsic strain of 0.01 to promote crack initiation at those locations under the adopted failure criterion [8]. Additionally, the number of cracks permitted per iteration, N, can be specified to control how many pixels are converted into crack pixels during each iteration.

2.2 Field Sampling and Laboratory Testing

Cores were collected from a deteriorated foundation in Stafford Springs, Connecticut, scheduled for full replacement due to pyrrhotite-related deterioration. Samples were obtained from multiple structural elements, including walls, slabs, and foundation. The specimens were tested for elastic properties via resonance frequency testing (RFT), as well as for compressive strength [12]. Moreover, selected cores were sliced into 10.8 cm by 25.4 cm sections, Figure 2.2 (a), for further evaluation, including carbonation assessment and UV epoxy impregnation to highlight internal crack networks, see Figure 2.2 (b). The sliced sections were further divided into smaller sections and carbon-coated for SEM analysis. Selected

undamaged regions i.e., areas without visible cracking were then extracted from the SEM images and used as input microstructures for the model, see Figure 3.2 (a).

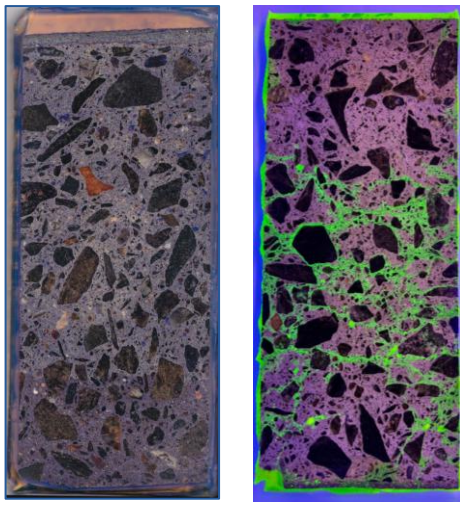

(a) (b)

Figure 2.2: Field sample preparation: (a) sliced section; (b) cracked sample

3. RESULTS AND DISCUSSIONS

3.1 Sensitivity Analysis

As with any numerical model, computational time becomes an important factor especially when the system includes very large pixel counts, as is the case here. In addition, the distribution of pyrrhotite within aggregates is heterogeneous: some aggregates contain no pyrrhotite, while others contain varying amounts. To control computational time, a sensitivity analysis was performed focusing on two key parameters: the convergence criterion and the number of cracks allowed per iteration, N [8]. A very small convergence threshold improves numerical accuracy but also leads to longer run times. Similarly, reducing N yields a more realistic representation of crack evolution in concrete, yet it also requires substantially higher number of iterations. The goal of this analysis is to identify parameter values that balance physical realism with practical computational efficiency. In these simulations, N = 400 cracks per iteration was selected, which is sufficient for expediting the study, while creating a representative crack map pattern of the damaged concrete [8].

Two main parameters were examined for the convergence criteria: (1) the elastic modulus and (2) the cracking pattern. In FEM, consistent output is essential to ensure that the numerical approach is reliable. First, the elastic modulus should stabilize as the solution approaches convergence. An initial convergence threshold of 10^{-14} was selected, as this level has been shown to produce reliable results [11]. To assess the effect of higher convergence thresholds, the elastic modulus obtained at each level was compared to the 10^{-14} reference solution. The percent error was approximately 23.3 % at 10^{-6}, but dropped sharply to 0.37 % at 10^{-8}, 0.62 % at 10^{-10}, and 1.63 % at 10^{-12}. The results show that a convergence level of 10^{-8} or lower yields accurate elastic properties, with errors below 2 %. Second, the crack formation pattern was examined. The crack networks were consistent when convergence criteria of 10^{-10} or lower was selected. Based on these observations, a convergence criterion of 10^{-10} was selected. This choice provides reliable results while requiring less computational time compared to the 10^{-14} case. Higher resolution reduces anisotropy effects; however, it significantly increases computational time. In this study, the resolution was limited to that of the SEM images, and no further refinement was performed due to computational constraints.

3.2 Microstructural Imaging and Digital Model Development

Modeling of microstructural degradation driven by sulfide diffusion from a pyrrhotite source is demonstrated in this section. After the sample was polished and carbon-coated, it was examined using SEM. Selected crack-free image was further processed and segmented into the main constituent

phases, aggregate, mortar, voids, and pyrrhotite, as shown in Figure 3.2 (b). Appropriate elastic properties and predefined expansion strains were then assigned to the relevant phases. The resulting digital microstructure image generated from the developed model is presented in Figure 3.2 (c), with image dimensions of 1,000 by 1,000 pixels, representing 3 cm by 3 cm (30 μm/pixel).

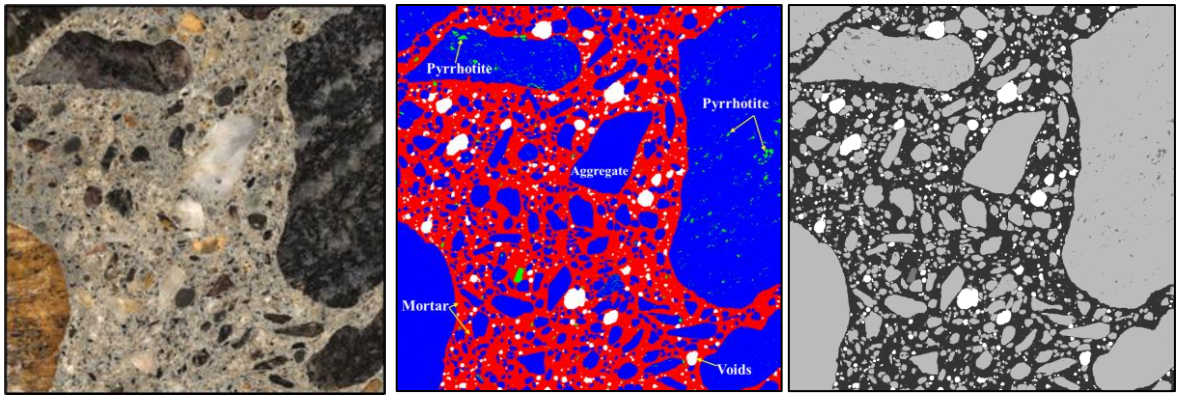

Figure 3.2: (a) Polished cross-section; (b) segmented SEM image (Blue: Aggregate, Red: Mortar, White: void, Green: Pyrrhotite); (c) digital microstructure

3.3 Crack Initiation and Propagation

Crack formation was examined. The expansive phases develop hoop tension around them, which drive cracks radially outward. Moreover, the results show that cracks initiate within the pyrrhotite-bearing phases and then extend toward other nearby pyrrhotite regions, where stresses are increased due to expansion. Cracks then propagate through the aggregates and continue into the surrounding mortar. The crack propagation after 30 and 80 iterations is shown in Figure 3.3.

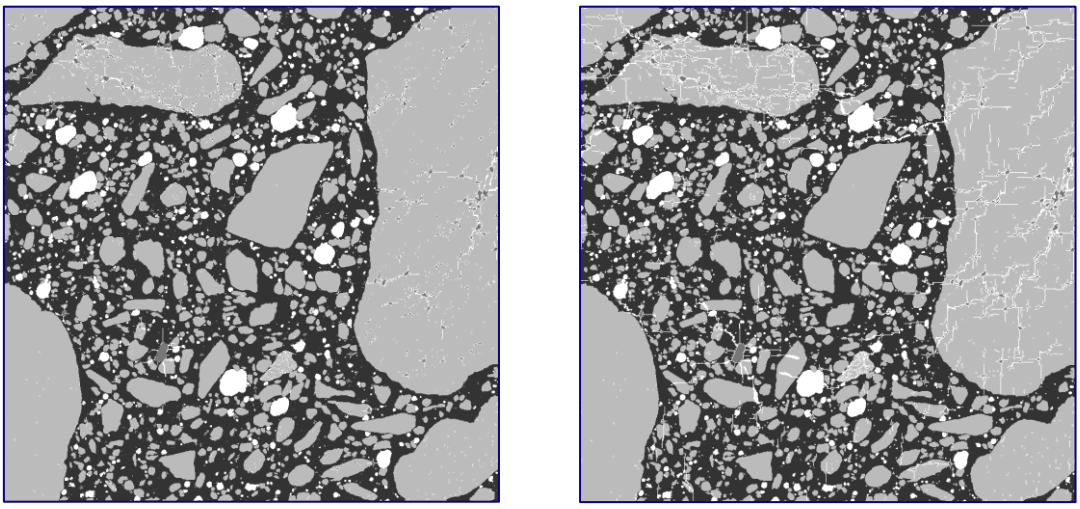

Figure 3.3: Crack formation after (a) 30 iterations and (b) 80 iterations

4. CONCLUSIONS

This work presented a finite element model designed to illustrate how cracks might develop when internal phases within cement-based materials expand due to pyrrhotite oxidation. A key advantage of the model is the ability to start from actual microstructural images, allowing the simulations to better reflect the real material. A sensitivity analysis was conducted and proper convergence criteria were selected. The model also provides estimates of how the elastic properties change as damage progresses, offering a way to evaluate the mechanical consequences of internal phase expansions in concrete materials. Future work will focus on extending the framework to capture internal sulfate attack, thereby allowing a more complete representation of sulfate driven deterioration.

5. ACKNOWLEDGMENT

This work was funded by congressionally appropriated Scientific and Technical Research and Services (STRS) to assess pyrrhotite in concrete. Osamah H.A. Dehwah was supported through Professional Research Experience Program (PREP) agreement No. 70NANB23H021 under award No. PREP0002340 between NIST and Johns Hopkins University. Also, Nicos S. Martys was supported through Domestic Guest Researcher – Research and Science (DGRRS) under Agreement No. 1333ND25FNB73008. Thanks to Dr. David Goodwin for core collection and images.

6. REFERENCES

1. Zhong R, Ai X, Yao Y, et al (2024) Effects of the expansion mechanisms on the pyrrhotite-induced deterioration of concrete foundations. Case Stud Constr Mater 20:e02830. https://doi.org/10.1016/j.cscm.2023.e02830
2. Jana D (2020) Pyrrhotite Epidemic in Eastern Connecticut : Diagnosis and Prevention. ACI Mater J 1–20. https://doi.org/10.14359/51718059
3. El-mosallamy M, Shehata MH (2020) Sulphide oxidation mortar tests for evaluation of the oxidation potential of sulphide-bearing aggregate. Constr Build Mater 264:120627. https://doi.org/10.1016/j.conbuildmat.2020.120627
4. Zhong R, Wille K (2018) Deterioration of residential concrete foundations: The role of pyrrhotite-bearing aggregate. Cem Concr Compos 94:53–61. https://doi.org/10.1016/j.cemconcomp.2018.08.012
5. Rodrigues A, Duchesne J, Fournier B, et al (2012) Mineralogical and chemical assessment of concrete damaged by the oxidation of sul fi de-bearing aggregates : Importance of thaumasite formation on reaction mechanisms. Cem Concr Res 42:1336–1347. https://doi.org/10.1016/j.cemconres.2012.06.008
6. Oliveira I, Cavalaro SHP, Aguado A (2013) New kinetic model to quantify the internal sulfate attack in concrete. Cem Concr Res 43:95–104. https://doi.org/10.1016/j.cemconres.2012.09.010
7. Guirguis B, Shehata MH, Duchesne J, et al (2018) The application of a new oxidation mortar bar test to mixtures containing different cementing systems. Constr Build Mater 173:775–785. https://doi.org/10.1016/j.conbuildmat.2018.04.026
8. Dehwah OHA, Garboczi E, Martys N, Watson S (2025) Quasistatic Crack Formation in Multiphase Materials Driven by Internal Phases Expansion Mechanisms: Application to Cement-Based-Materials. National Institute of Standards and Technology (NIST), Gaithersburg, MD. NIST Intern Rep (NIST IR-8591). https://doi.org/10.6028/NIST.IR.8591
9. Stutzman PE, Bright DS, Garboczi EJ (2001) Finite Element Stress Computations Applied to Images of Damaged Concrete: A Possible New Diagnostic Tool for Concrete Petrography. In: Twenty-Third International Conference on Cement Microscopy
10. Dehwah OHA., Garboczi EJ, Martys NS, Watson SS (2025) 2D Finite Element Based Model of Quasistatic Crack Formation Driven by Driven by Expansion of Internal Phases in Multi-phase Materials. National Institute of Standards and Technology (NIST), Gaithersburg, MD. https://doi.org/10.18434/mds2-4002
11. Garboczi EJ (1998) Finite element and finite difference programs for computing the linear electric and elastic properties of digital images of random materials. NIST Interagency/Internal Rep. - 6269 198
12. Dixon P, Hariri-Ardebili M, Goodwin D, et al (2025) Field Observations of a Pyrrhotite-Affected Residential Foundation and the Mechanical Properties of Extracted Concrete Cores – Connecticut Site 1. National Institute of Standards and Technology (NIST), Gaithersburg, MD. NIST Intern Rep (NIST IR-8599). https://doi.org/10.6028/NIST.IR.8599

Mineralogical investigation of pristine aggregate, laboratory mortar bar and concrete field sample

Nikolas Ålgård Oberhardt [(1)(2)], Tobias Danner [(3)], Jan Lindgård [(3)], Kurt Aasly [(1)], Klaartje De Weerdt [(1)]

(1) Norwegian University of Science and Technology, Trondheim, Norway, nikolas.oberhardt@vegvesen.no

(2) Norwegian Public Roads Administration, Oslo, Norway

(3) SINTEF Community, Trondheim, Norway

Abstract

In this study, we investigated the oxidation sequence of pyrrhotite and the corresponding secondary-phase formation in the aggregate and the interfacial transition zone (ITZ) of the cement paste. The oxidation sequence was studied in fresh aggregate samples, accelerated mortar bar test samples (AMBT, 285 x 25 x 25 mm) exposed to bi-weekly (3h) immersion in NaOCl bleach (RBI comparable to Lava Pro 6) for 12, 27 and 52 weeks, and one drill core from an internal sulfate attack (ISA) affected housing foundation from Trois Rivières, Canada. All samples comprised aggregates from the Maskimo quarry in St. Boniface, Quebec, Canada. Petrographic samples from pristine aggregates, the AMBT samples, and the concrete field sample were investigated using SEM-based automated mineralogy (AM) and optical microscopy (OM). Automated mineral mapping, with step sizes ranging from 1 to 20 µm, was performed using EDS on a Zeiss SEM with the *Mineralogic* Mining software. Mineral concentrations as low as 0.01 wt.% and mineral association data were acquired to approximate phase alterations in the aggregates and the cement paste. Specific attention was drawn to characterizing and quantifying secondary sulfide oxidation products in the interfacial transition zone (ITZ) of the AMBT samples. The results provide new insights into the sequential oxidation propagation of pyrrhotite from the ISA-unaffected MSK aggregate to the moderately affected laboratory samples and the severely affected ISA field samples.

***Keywords**: accelerated mortar bar samples; automated mineralogy; oxidation sequence pyrrhotite*

1. INTRODUCTION

Pyrrhotite-bearing aggregates have been linked to severe cases of internal sulfate attack (ISA), where the oxidation of $Fe_{1-x}S$ activates sulfate release and the formation of expansive secondary oxidation products in concrete. Across reported incidents from Canada, the United States, and Ireland [1,2,3], damage has been consistently associated with the progressive oxidation of pyrrhotite embedded in the concrete aggregates. Therefore, understanding the oxidation sequence of pyrrhotite—from initial grain-boundary alteration of pyrrhotite and the resulting secondary formation of iron oxides and (oxy)hydroxides— in the early-stage of pyrrhotite oxidation is critical for assessing ISA. This study investigates the oxidation sequence of pyrrhotite in Maskimo aggregate (MSK 0.9%) in the fresh rock, in accelerated mortar bar samples after 12, 27, and 52 weeks of bi-weekly (3 hours each) exposure to NaOCl, and a field concrete sample from Trois-Rivières, Canada. The mineralogical alteration of pyrrhotite at the cement paste–aggregate interface was studied using SEM-based automated mineralogy.

2. MATERIALS AND METHODS

2.1 Materials

2.1.1 Crushed concrete aggregate samples

The aggregate from the Maskimo quarry in St. Boniface, Quebec, Canada, was provided by the University of Laval. Detailed mineralogical investigations of the aggregate batch used in this study and the mortar samples analyzed by De Weerdt et al. [4] are presented by Oberhardt et al. [5]. The Maskimo quarry consists of a noritic micro gabbro, mainly composed of plagioclase feldspar (55-60 wt.%), orthopyroxene (15-20 wt.%), magnesiohornblende (6-10 wt.%), and biotite (~5 wt.%). The total sulfur content ranged between 0.85 wt.% (MSK 0.9%) and 1.8% (MSK 1.8%, not included in this study), entirely bound in sulfides. Pyrite was the main sulfide mineral present in the samples, accounting for 1.43 wt.%. Pyrrhotite was the second most abundant sulfide in the MSK samples, with an average of 0.50 wt.% distinguished by AM. The pyrrhotite minerals frequently included minor associations of pentlandite (0.15 - 0.25 wt.%) and chalcopyrite (0.05 - 0.15 wt.%), see Oberhardt et al. [5].

2.1.2 Accelerated mortar bar test (AMBT) samples

The mortar bar samples examined in this study were exposed to accelerated testing for 12, 27, and 52 weeks. A detailed description of the test campaign and AMBT results is provided in De Weerdt et al. [4]. The accelerated test procedure is described in the Canadian standard CSA A23.1:19, P3.10.4. The 25 x 25 x 285 mm mortar bars were prepared according to ASTM C490/C90M, with a cement-to-aggregate ratio of 0.37 (1760 g cement and 4800 g aggregate [0.16/5 mm]) and a water-to-cement ratio of 0.65 (1144 g mixing water). Mortar bars were soaked in NaOCl for 3 hours bi-weekly. For the first 13 weeks, the samples were stored at 80°C and 80% room humidity (RH). Thereafter, the mortar bars were stored at 5°C at 100 RH after bleach immersion. The bleach used for accelerated expansion testing was RBI (for a detailed analysis of the bleach, see [4]), which had a composition similar to that of the proposed Lava Pro 6 by Rodrigues et al.

2.1.3 Field samples Canada

The University of Laval provided one concrete field sample from a damaged concrete housing foundation wall in Trois-Rivières, QC, Canada. The concrete drill core measured 205 mm in length and 104 mm in diameter.

2.2 Methods

2.2.1 Sample preparation

Polished thin sections were cut from the center of the rectangular mortar prisms (25 x 25 x 285 mm) and oriented orthogonally to the end face. Pelcon Materials & Testing ApS, Denmark, produced the 25 x 25 mm polished thin sections of the mortar bars. The concrete field sample specimens FS 1-5 were produced as 45 x 25 mm sections. All sections were vacuum-impregnated with yellow, low-viscosity epoxy dye. For SEM-EDS analysis, the sections were carbon-coated, and copper tape was used to affix them to the sample holder.

2.2.2 Automated Mineralogy

Scanning electron microscope–based automated mineralogy (AM) was conducted on the polished thin sections using a Zeiss Sigma 300VP field-emission SEM equipped with two Bruker xflash 6|60 EDS detectors. Mineral classification, bulk mineralogy, and mineral associations were determined with Zeiss Mineralogic (Mining plugin), while Bruker Esprit handled matrix corrections and peak deconvolution, classifying EDS spectra against a master mineral list and storing pixel-based chemical data for retrospective spatial analysis. Previous work by Oberhardt et al. [5] demonstrated a high correlation between AM-EDS and WDS analyses for sulfide minerals from the same sample batch.

Analyses were performed under high vacuum at 20 kV, with a 120 µm aperture, 8.5 mm working distance, 0.008 s dwell time (400 kcps), a minimum of 2000 counts per spectrum, and 178.6×

magnification. Bulk mineralogy was assessed using field mapping at 10–20 µm step sizes, while higher-resolution scans (2 µm field scans and 1 µm line scans) were required to resolve cement hydration products and sulfide oxidation phases. Four sections were initially scanned at 10 µm; finer scans were then applied to selected areas to distinguish cryptocrystalline cement phases from secondary oxidation products. Quantitative results are reported as area % and normalized elemental wt.%, accepting up to 6 area % (2 µm scans) and 8 area % (1 µm line scans) unclassified pixels.

The pyrrhotite oxidation sequence in the laboratory mortar samples after 12, 27 and 52 weeks of treatment using NaOCl, and the naturally deteriorated concrete field sample from Trois-Rivières is shown in Fig. 1. The MSK 0.9 % aggregate contained on average 0.50 wt.% pyrrhotite and 1.08 wt.% sulfur-bearing phases, with chalcopyrite (0.07 wt.%) and pentlandite (0.10 wt.%) as accessory minerals.

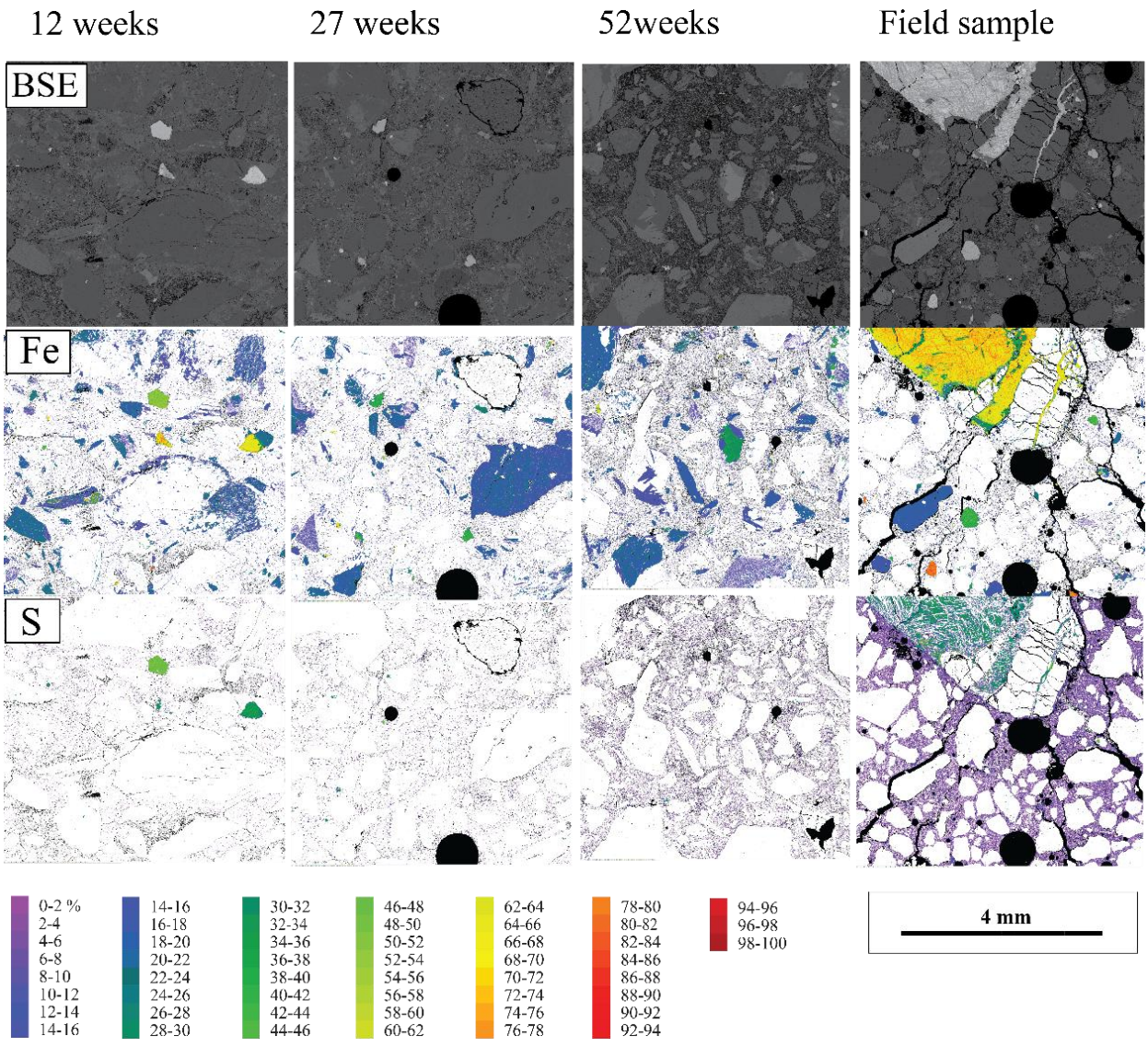

Figure 1: AM field mapping of the AMBT samples and the concrete field sample. Images were acquired with a 2 μm step size. Elemental heat mapping of Fe and S using 2% concentration intervals

3. RESULTS AND DISCUSSION

3.1 Oxidation sequence in pyrrhotite

Accelerated mortar samples 12 weeks, 27 weeks, and 52 weeks, contained less pyrrhotite (between 0.19 and 0.37 wt.%) than the original MSK 0.9% aggregate (0.50 wt.%) and the concrete field sample (1.66 wt.%). Pyrite was measured with only 0.13-0.22 wt.%. The concrete field sample contained 1.06-2.30 wt.% pyrrhotite and only 0.09-0.12 wt.% pyrite. The AM analysis of the fresh MSK aggregate was performed at a 20 µm step size, as described by Oberhardt et al. [5]. The degree of oxidation of pyrrhotite minerals was initially examined by optical microscope on the fresh aggregate, the AMBT samples, and the concrete field sample, to ensure the representativeness of the mineral grains displayed in Fig. 2. The presented pyrrhotite grains from the AMBT samples illustrated in Fig. 2 show the typical sequence of oxidation in these samples.

Selected areas were then targeted at a 2 µm step size. Fig. 2 shows the BSE image, the automated mineralogy (AM) image of the classified bulk mineralogy, and the element heat maps (EHM) for elemental sulfur and iron, along with their percentile distributions measured in 2 wt.% increments in the analyzed area.

Pyrrhotite in the pristine aggregate exhibited incipient surface oxidation along its boundaries, similar to the 12-week AMBT sample shown in Fig. 2. Secondary oxidation products consisted mainly of hematite (Fe_2O_3) and magnetite (Fe_3O_4). The element heat map for iron and sulfur reflected the distribution of < 60 wt.% Fe and around 30-40 wt.% S, as expected for unoxidized pyrrhotite.

The pyrrhotite in the 12-week mortar sample showed that oxidation progressively affects the mineral's interior by etch pitting (BSE and AM images). The sulfur concentration in the mineral's interior appears to remain constant, as shown by the EHM image, whereas it decreases along the mineral boundaries. The AM image of the 12-week sample shows the growth of an oxidation rim surrounding the pyrrhotite periphery. The Fe-oxides consisted mainly of hematite (0.22 wt.%) and magnetite (0.30 wt.%). The oxidation progression is indicated in the EHM by an increase in Fe concentration, due to the leaching of SO_4^{2-} from the pyrrhotite grain into the cement paste.

3.2 Oxidation reaction in bulk mineralogy

The consecutive micro-images of the AMBT sections from 12 to 52 weeks of 2 x 3h per week exposure to NaOCl and the concrete field sample are shown in Fig. 2. The backscattering images are illustrated alongside the elemental heat maps for Fe and S.

In mortar and concrete, pyrrhotite progressively altered to Fe-oxides and Fe-(oxy)hydroxide. First signs of Ca ingress from the cement paste were observed by the formation of the composite phase Fe–O–S–Ca, crystallizing along cracks adjacent to the oxidized pyrrhotite grains (see Fig. 2). The composite contained an average of 10 wt.% S while the sulfur concentration of gypsum was measured around 40 wt.% in the samples. The Fe-O-S-Ca could be described as a precursor for the formation of gypsum.

Sulfide-bound sulfur becomes increasingly mobile during oxidation of pyrrhotite, migrating into the cement paste, while Fe remained largely immobile (Fig. 2). Gypsum formed primarily near pyrrhotite, but in larger proximity to the Fe-O-S-Ca composite phase. The formation of gypsum can indicate a local pH reduction and alkali depletion.

These oxidation pathways differ from those in pristine aggregate without cement paste, where Fe-oxides dominate. AMBT samples showed limited expansion and low ettringite contents (see Figure 3 in the Appendix), suggesting that expansion was mainly governed by volume increase of Fe-oxide (e.g. hematite) and Fe-(oxy)hydroxide (e.g. FeOOH and ferrihydrite). Field concrete showed extensivecracking and debonding at the ITZ, consistent with advanced oxidation of abundant pyrrhotite and the formation of ferrihydrite, gypsum, and ettringite.

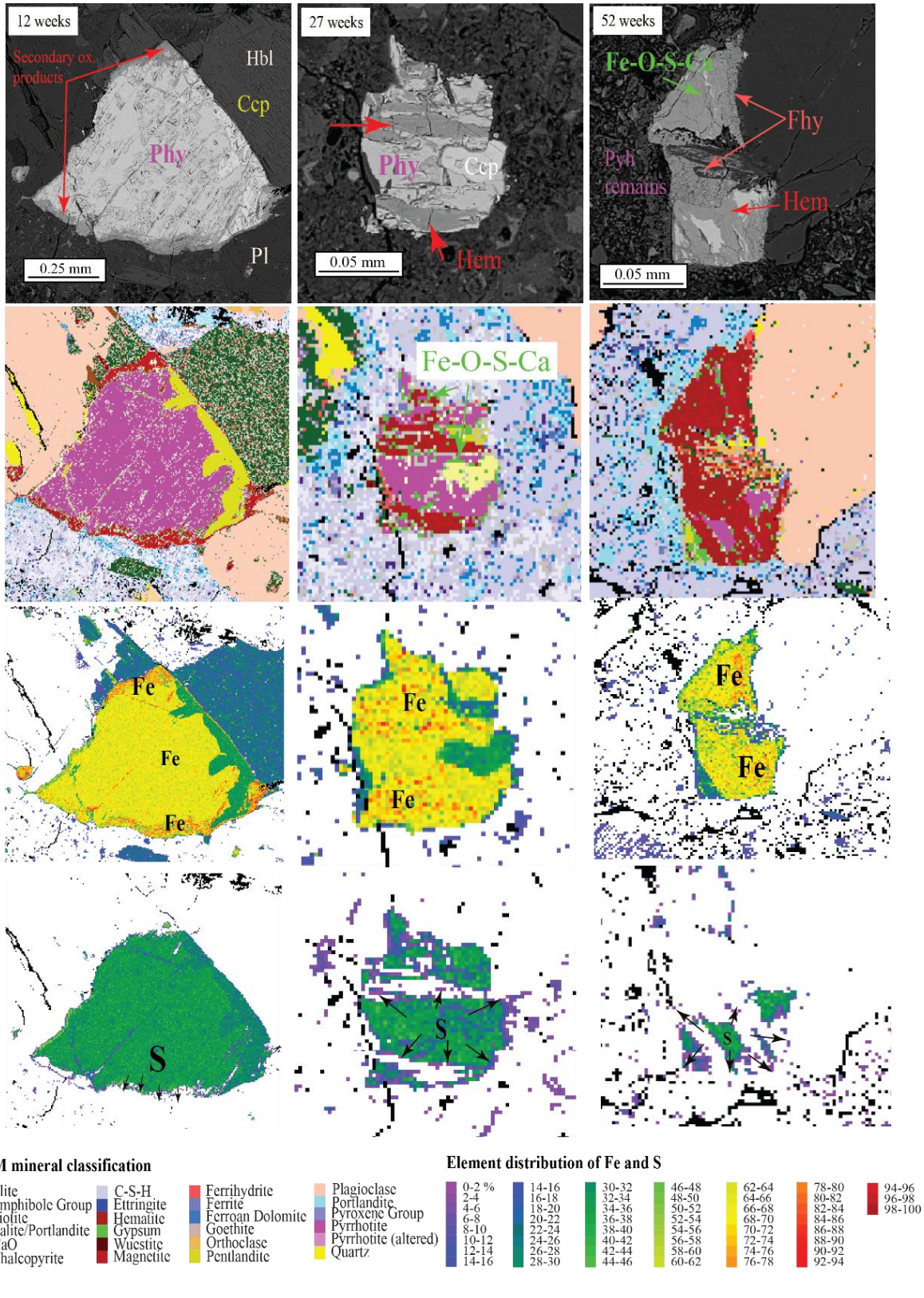

Figure 2: Oxidation progression of pyrrhotite studied in the accelerated mortar bar samples from 12 to 52 weeks. The AM mapping of the AMBT samples was obtained using a 2 µm step size. Phy remains = Pyrrhotite residues after oxidation and alteration to iron oxides and (oxi) hydroxides; Fhy = Ferrihydrite; Ccp = Chalcopyrite; Hbl= Hornblende; Pl = Plagioclase; Hem = Hematite; Fe-O-S-Ca = Composite phase.

4. CONCLUSION

Pyrrhotite oxidation followed a consistent sequence from fresh aggregate to mortar and field concrete: early rim oxidation (magnetite, minor oxidized pyrrhotite) progressed to complete replacement by Fe-oxide, Fe-(oxy)hydroxide, Fe–O–S–Ca, gypsum, and ettringite. This sequence reflects the release of sulfate into the paste and the subsequent formation of secondary sulfate phases under locally reduced pH conditions.

Sulfur maps confirmed increasing sulfate migration with exposure time, with significant accumulation in the cement paste only after prolonged AMBT exposure and in field concrete. AM effectively identified these subtle phase transformations, linking hematite → ferrihydrite and Fe–O–S–Ca → gypsum transitions to oxidation degree.

Lower-than-expected sulfur and pyrrhotite contents in the AMBT samples are likely to explain the reduced expansions relative to previously published results. Routine sulfur quantification of test batches is therefore recommended.

Overall, the study shows that pyrrhotite oxidation in Maskimo aggregate progresses in a predictable mineralogical sequence that governs internal sulfate attack. Automated mineralogy, despite some limitations in distinguishing cryptocrystalline hydration phases, provides a robust diagnostic framework for assessing aggregate reactivity and predicting ISA-related deterioration in pyrrhotite-bearing concrete.

5. REFERENCES

[1] J. Duchesne, Benoît Fournier (2013) "Deterioration of Concrete by the Oxidation of Sulphide Minerals in the Aggregate", Journal of Civil Engineering and Architecture 7 URL: http://www.davidpublisher.org/index.php/Home/Article/index?id=8090.html. doi:10.17265/1934-7359/2013.08.003.

[2] R. Zhong, K. Wille (2018) "Deterioration of residential concrete foundations The role of pyrrhotite-bearing aggregate", Cement and Concrete Composites 94 53–61. URL: https://linkinghub.elsevier. com/retrieve/pii/S0958946517310788. doi:10.1016/j.cemconcomp.2018. 08.012.

[3] A. Leemann, B. Münch, P. Dunlop (2022) Internal sulfate attack on concrete1209 – a case study from homes in Inishowen, in: 4th International Con-1210 conference on the Chemistry of Construction Materials 2022, Northwest1211 Donegal, Ireland, p. 1.1212

[4] De Weerdt K et al. (2025) "Changes in cement paste during accelerated mortar bar testing for pyrrhotite containing aggregate." *Cement and Concrete Research,* 188, p. 107730. ISSN: 0008-8846. DOI: 10.1016/j.cemconres. 2024.107730. url: https://www.sciencedirect.com/science/article/ pii/S0008884624003119.

[5] Oberhardt N, Lode S, Lindgård J, and Aasly K. (2025) "Classification and quantification of minor iron-sulfide concentrations in concrete aggregate using automated mineralogy." *Materials and Structures,* 58.2, p. 71. ISSN: 1871-6873. DOI: 10.1617/s11527-025-02591-3. url: https://doi.org/10.1617/ s11527-025-02591-3.

6. APPENDIX

6.1 Secondary mineral concentration

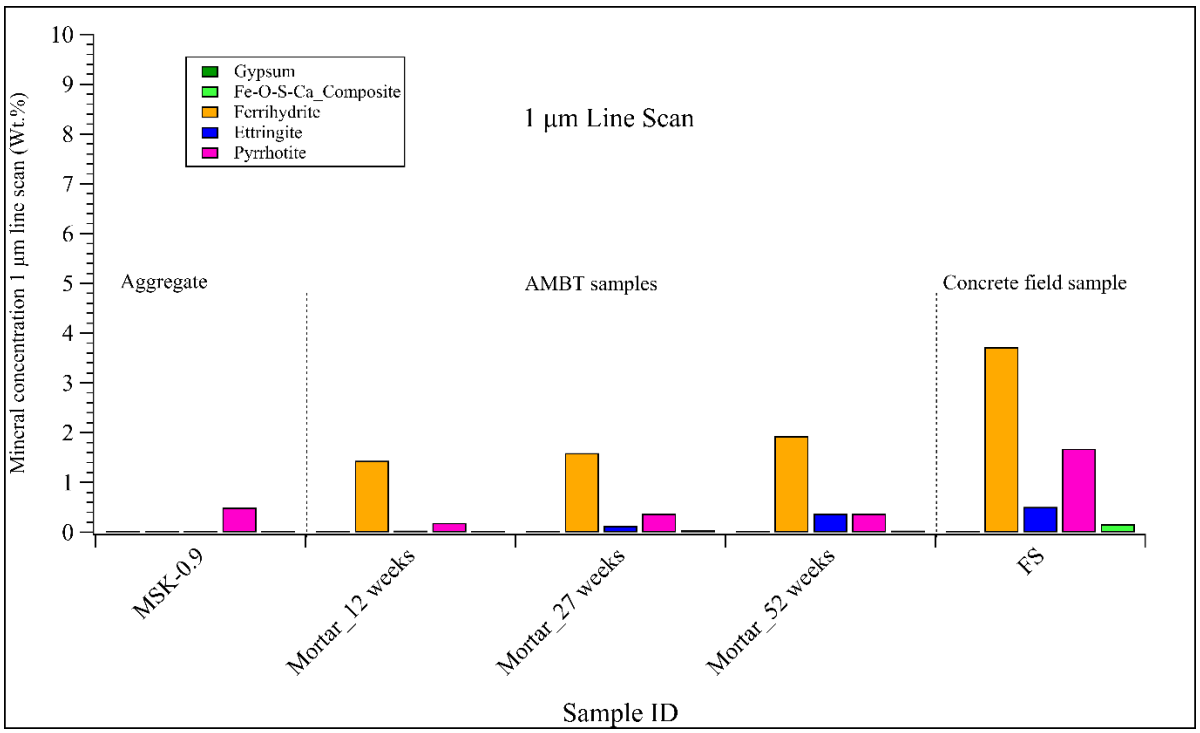

Figure 3: Concentration of pyrrhotite and secondary oxidation minerals present in the fresh aggregate (MSK-0.9), the mortar bar samples, and the concrete field sample (FS), measured by automated mineralogy using 1 µm line scanning mode.

Performance of mortar mini-bar tests under different exposure conditions for evaluating iron sulfide-bearing aggregates

Farhad Kooban [1,†], Zhanzhao Li [1,2,†], Kai Gong [2], Aleksandra Radlińska [1]

(1) The Pennsylvania State University, University Park, PA, USA, fqk5115@psu.edu, azr172@psu.edu

(2) Rice University, Houston, TX, USA, zl188@rice.edu, kg51@rice.edu

(†) These authors contributed equally to this work.

Abstract

The deleterious reactions of iron sulfide-bearing aggregates have been observed in concrete structures worldwide, leading to significant durability concerns. With the growing demand for construction aggregates, there is an urgent need for efficient, reliable, performance-based test methods to assess their reactivity potential. This study presents a systematic comparison of mortar mini-bar test performance under three exposure conditions for evaluating iron sulfide-bearing aggregates: (i) cyclic immersion in bleach solution, (ii) cyclic immersion in limewater solution, and (iii) constant exposure to atmospheric oxygen. Portland cement mortar mini-bars incorporating high-purity pyrrhotite were used to accelerate reaction kinetics, and the effects of pyrrhotite dosage and particle size were also examined. Experimental results revealed that significant expansion occurred only under bleach exposure, developing after approximately 150 days during storage at 4°C and 100% relative humidity and reaching a length change of 0.54% at 300 days. Limewater exposure produced minimal expansion (not exceeding 0.10%), and oxygen exposure resulted in drying shrinkage with no measurable expansion. Despite the absence of expansion under oxygen exposure, thermodynamic modeling predicted substantial expansion potential, with up to 17.9% solid volume increase primarily associated with ettringite formation. This contrast between the experimental observations and modeling results indicates that thermodynamic driving force alone is insufficient to produce measurable expansion within the experimental timeframe. Instead, reaction rates and expansion development can be strongly influenced by kinetic and transport limitations, including oxygen diffusion, moisture availability, pyrrhotite dissolution, and sulfate transport. These findings provide important insights into the future development of accelerated test protocols for iron sulfide-bearing aggregates.

Keywords: *iron sulfide reactions; mortar bar test; exposure conditions; length changes; thermodynamic modeling*

1. INTRODUCTION

Tens of thousands of concrete structures have recently been affected by extensive deterioration due to the oxidation of iron sulfide minerals, particularly pyrrhotite, in aggregates. Several localized cases in Canada [1], the United States [2], and Ireland [3] have attracted widespread attention within the concrete community. These incidents demonstrate that even trace amounts of pyrrhotite can initiate severe cracking and expansion through oxidation reactions and subsequent internal sulfate attack, ultimately leading to the progressive disintegration of concrete structures. Such deterioration has raised serious safety concerns and caused substantial economic losses for stakeholders and governments.

However, there is still no consensus on standardized test procedures for evaluating the oxidation potential of iron-sulfide-bearing aggregates in concrete. Rodrigues *et al*. [4] proposed an accelerated mortar bar test in 2015, which was later incorporated into the annex of CSA A23.1 [5]. The test consists of a two-stage exposure protocol: an initial 90-day period at 80°C and 80% relative humidity (RH), followed by a second 90-day period at 4°C and 100% RH. During each stage, specimens undergo two 3-h immersion cycles per week in a 6% sodium hypochlorite (bleach) solution. While this method provides a relatively rapid, performance-based screening, its applicability remains under debate due to the highly aggressive exposure conditions, which may not represent realistic field environments.

Recent studies have therefore explored less aggressive exposure conditions, such as limewater [6] and oxygen [7, 8]. However, a systematic comparison among these different exposure regimens is still lacking. To address this gap, this study investigates mortar performance under three exposure conditions, *i.e.*, bleach, limewater, and oxygen, using a mortar mini-bar test complemented by thermodynamic modeling. Natural pyrrhotite mineral was used as the aggregate, and the effects of both pyrrhotite content and particle size were explored.

2. MATERIALS AND METHODS

To accelerate reaction kinetics, a non-standardized mold was used to cast mortar mini-bars with dimensions of 12.7 × 12.7 × 139.7 mm. The specimens were prepared with ASTM Type I Portland cement and high-purity natural pyrrhotite (83.1% purity) [9], with a water-to-cement ratio fixed at 0.65. Three experimental sets were designed to investigate the effect of pyrrhotite content and particle size:

- Set 1: 10 g of pyrrhotite (0.15–0.30 mm; No. 50–100) per 100 g of cement.
- Set 2: 10 g of pyrrhotite (0.30–0.60 mm; No. 30–50) per 100 g of cement.
- Set 3: 50 g of pyrrhotite (0.15–0.30 mm; No. 50–100) per 100 g of cement.

For each set, corresponding control specimens were prepared by replacing pyrrhotite with non-reactive aggregate, using natural sand from Northumberland, PA or quartz sand. All cast specimens were sealed and cured for 1–2 days at 100% RH and 23°C. Following initial curing and demolding, the specimens were subjected to three distinct exposure regimes:

- Condition I (Bleach): Two-phase cyclic immersion in a 6% bleach solution (90 days at 80°C and 80% RH, then at least 80 days at 4°C and 100% RH) [4], followed by extended storage at 4°C and 100% RH with no further immersion.
- Condition II (Limewater): Two-phase cyclic immersion in limewater following the same protocol as Condition I, with subsequent storage at 4°C and 100% RH.
- Condition III (Oxygen): Constant exposure to normal atmospheric oxygen at 23°C and 70% RH).

For cyclic immersion, wetting was performed twice per week for 3 h at 23°C, following [4]. The specimens were measured longitudinally and labeled using the format S#-X-Y, where S# denotes the set number, X the exposure condition (BL = bleach, LW = limewater, O2 = normal atmosphere oxygen), and Y the specimen type (C = control sample, P = pyrrhotite-bearing sample).

Phase assemblage evolution under different exposure conditions was evaluated using thermodynamic modeling with the geochemical software GEMS [10]. The Portland cement composition was adopted from [11], with the degree of hydration assumed to be 0.9 prior to exposure. The pyrrhotite content was set at 10 g per 100 g of cement, and the bleach composition was adopted from [12]. All other parameters were kept consistent with the experimental conditions.

3. RESULTS AND DISCUSSION

Under two-phase cyclic immersion in bleach (Condition I, Figure 3.1a), pyrrhotite-bearing and control specimens exhibited similar behavior during the first ~150 days across all three experimental sets, with no significant length change observed. However, after this period, especially following the onset of extended storage at 4°C and 100% RH, pyrrhotite-bearing specimens exhibited pronounced expansion relative to their corresponding controls. Among the pyrrhotite-bearing specimens, all three sets exhibited broadly comparable expansion during the common cyclic immersion period, reaching approximately 0.10–0.13% by about 170 days. After this point, the exposure histories differed: cyclic immersion continued for Set 1 up to ~300 days, whereas Sets 2 and 3 entered extended storage without further immersion after ~170 days. This difference in exposure duration may have constrained the ultimate expansion observed in the pyrrhotite-bearing specimens of Sets 2 and 3. However, the Set 1 results suggest that clear acceleration of expansion under bleach exposure began only after approximately 180 days of cyclic immersion, indicating that such immersion duration may not be sufficient to fully activate or capture the expansion potential of pyrrhotite-bearing mortar. Set 1 subsequently showed a higher rate of expansion, reaching approximately 0.52% at 330 days and about 0.85% by 450 days. In comparison, Sets 2 and 3 reached approximately 0.25% and 0.30% expansion at 330 days, respectively. Therefore, the larger ultimate expansion of Set 1 cannot be attributed solely to the finer pyrrhotite particle

size or lower aggregate content; it mostly reflects the longer duration of cyclic bleach exposure. Compared with Set 2, Set 3 contained a substantially higher pyrrhotite dosage, 50 g per 100 g of cement versus 10 g per 100 g of cement, as well as finer particles with a higher specific surface area and faster oxidation kinetics. These factors likely increased its reaction potential and contributed to its slightly greater expansion.

In all cases, control specimens exhibited only minor length changes throughout the entire experimental timeframe. The continued expansion of pyrrhotite-bearing specimens during the extended storage period suggests that reaction processes continued to evolve even after immersion ceased.

Upon limewater exposure (Condition II, Figure 3.1b), all pyrrhotite-bearing specimens exhibited substantially smaller length changes ($\leq 0.10\%$) than those observed in bleach, and no abrupt expansion was detected, indicating limited expansive reaction. Upon exposure, pyrrhotite-bearing specimens showed slight recovery toward zero strain or minor expansion, whereas control specimens remained in net shrinkage. Notably, all pyrrhotite-bearing specimens in Set 2 fractured during Phase I, preventing further length change measurements for this set under limewater exposure. Visual inspection of fractured and sectioned specimens showed that solution penetration was largely confined to the near-surface zone (approximately 1–2 mm), implying that the 3-h soaking was insufficient to supply the moisture and transport pathways needed to sustain reaction throughout the specimens. These results suggest that, under the current cyclic immersion protocol, limewater exposure may be too mild or too transport-limited to serve as an effective accelerated test condition for evaluating the expansion potential of pyrrhotite-bearing mortar.

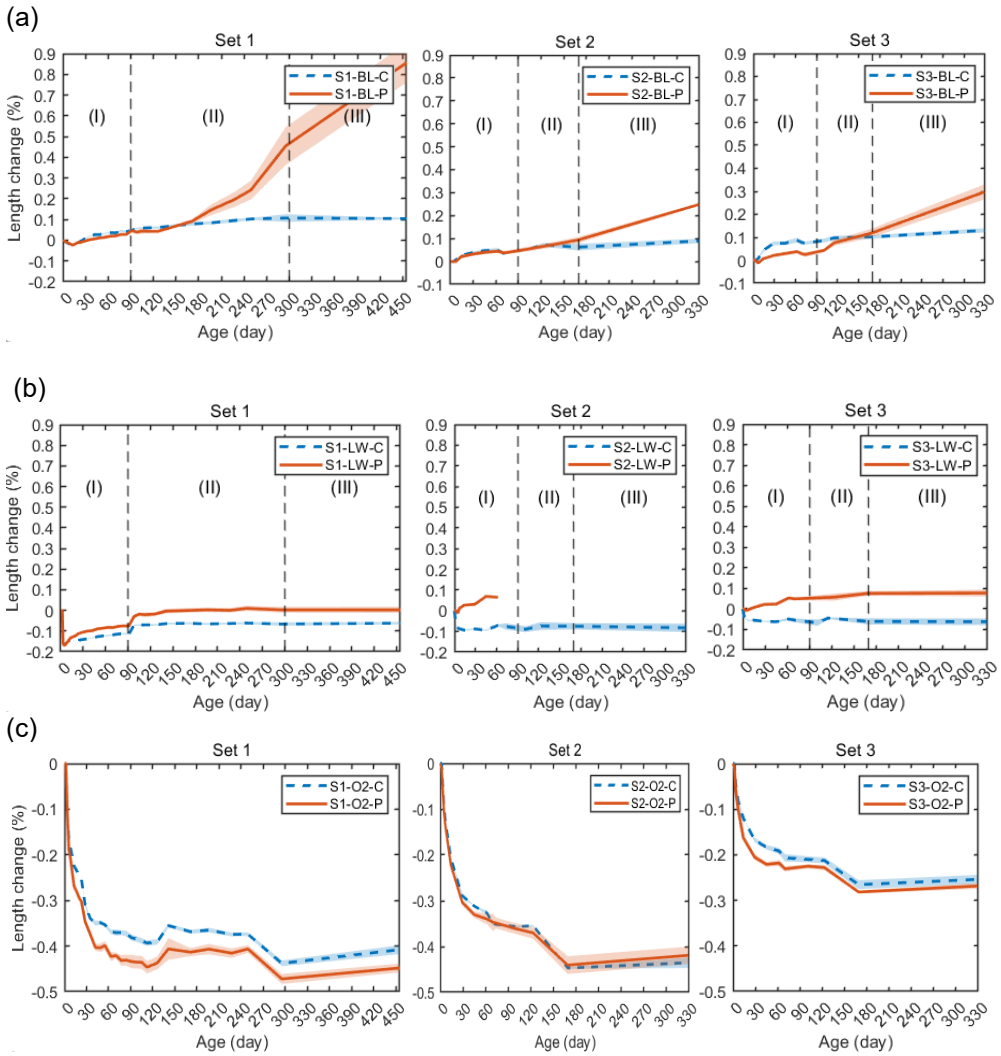

Figure 3.1: Measured length change over time for (a) Condition I: cyclic immersion in bleach solution, (b) Condition II: cyclic immersion in limewater solution, and (c) Condition III: (constant exposure to atmospheric oxygen. Phases I and II involve storage at 80°C/80% RH and 4°C/100% RH, respectively,

with cyclic immersion applied in both phases. Phase III corresponds to extended storage at 4°C/100% RH with no further immersion. Vertical dashed lines indicate transitions between Phases I, II, and III. Shaded regions represent the standard deviation derived from at least three specimens.

When exposed to atmospheric oxygen (Condition III, Figure 3.1c), all specimens across Sets 1–3 exhibited rapid early drying shrinkage followed by gradual stabilization, with no evident expansion throughout the test duration. For each set, pyrrhotite-bearing specimens consistently showed slightly greater shrinkage than the corresponding control specimens. This behavior can be attributed to differences in aggregate properties: the control mixtures contained harder sand, whereas pyrrhotite particles are softer and provide less internal restraint against matrix contraction during drying. The comparatively lower shrinkage of Set 3 is likely related to its higher aggregate content and reduced paste volume, which limited drying-induced matrix contraction.

To better understand the influence of different exposure conditions, thermodynamic calculations were performed to evaluate bulk phase assemblage evolution (Figure 3.2). Inherent material heterogeneity (e.g., local reactions and porosity), as well as transport and reaction kinetics, were not considered. Prior to exposure, the predicted hydration products at different temperatures included C–S–H, portlandite, ettringite, monosulfate (at 80°C) or monocarbonate (at 4°C and 23°C), hydrogarnet, calcite, and hydrotalcite. Upon exposure of the hydrated cement containing pyrrhotite to bleach at 80°C, ettringite was predicted to form at the expense of monosulfate and portlandite (Figure 3.2a). With continued exposure and progressive pyrrhotite oxidation, gypsum and additional hydrogarnet formation were also predicted. The maximum solid volume increase (5.9%) occurred at a bleach addition of 275 mL per 100 g of cement. When exposed to bleach at 4°C, the formation of ettringite, thaumasite, Friedel's salt, and goethite was predicted (Figure 3.2b). The volume increases due to ettringite and thaumasite were particularly noticeable, resulting in a maximum solid volume increase of 18.5% (at 575 mL bleach per 100 g cement). The substantially higher volume change potential predicted at 4°C compared to 80°C is consistent with the experimentally observed expansion behavior shown in Figure 3.1. When hydrated cement was exposed to atmospheric oxygen at 23°C, the predicted phase changes were dominated by the formation of ettringite, with minor contributions from goethite and brucite (Figure 3.2c). The maximum solid volume increase was 17.9%, occurring at ~9 g oxygen per 100 g cement, and was primarily driven by ettringite formation.

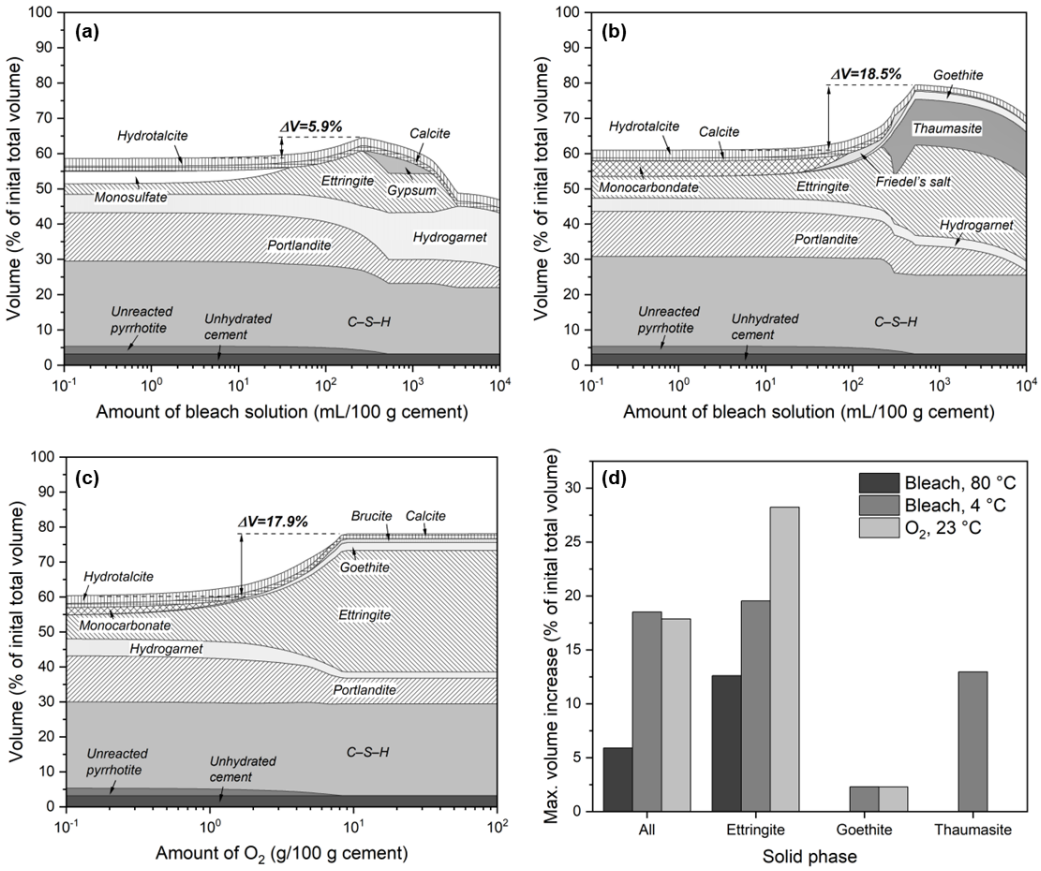

Figure 3.2: Predicted phase assemblages upon exposure to (a) bleach at 80°C, (b) bleach at 4°C, and (c) atmospheric oxygen at 23°C. A comparison of the phase assemblages is summarized in panel (d).

Figure 3.2d compares the total predicted solid volume changes and the contributions from individual expansive phases across different exposure conditions. Bleach exposure at 4°C and oxygen exposure at 23°C exhibited the highest potential for overall solid volume increase. Notably, the predicted potential for ettringite formation was the highest under oxygen exposure at 23°C. Nevertheless, predicted expansion under oxygen exposure was not observed during the experimental timeframe of this study, nor in previous investigations [8, 13]. This discrepancy indicates that, despite a strong thermodynamic driving force, kinetic processes (such as oxygen diffusion, moisture availability, dissolution of reactive phases, and the transport of dissolved sulfate into the cement matrix) play a crucial role in governing the overall reaction and the expansion behavior.

4. CONCLUSIONS

This study compares the expansion behavior of pyrrhotite-bearing mortar under bleach, limewater, and atmospheric oxygen exposure using a mortar mini-bar test (length change monitored up to 450 days) and thermodynamic modeling. Bleach exposure led to the largest expansion, reaching about 0.85% in Set 1 after ~150 days during storage at 4°C and 100% RH. A key finding is that faster acceleration of expansion began after approximately 180 days of cyclic immersion. This indicates that such immersion duration may not be sufficient to fully activate or capture the expansion potential of pyrrhotite-bearing mortar. Also, the larger ultimate expansion of Set 1 cannot be attributed solely to its pyrrhotite particle size or aggregate content; it is due to the longer duration of cyclic bleach exposure compared with Sets 2 and 3. Similarly, the limited solution penetration observed under limewater exposure, approximately 1–2 mm from the specimen surface, suggests that the current 3-h soaking protocol may be too mild or too transport-limited to sustain reaction throughout the specimens. Another finding is that limewater exposure led to minimal expansion less than 0.10%, while no expansion was observed under atmospheric oxygen exposure despite thermodynamic predictions of high expansion potential. The discrepancy between modeled volume increases and experimentally observed behavior under oxygen exposure highlights the critical role of kinetic and transport limitations, including oxygen ingress,

moisture availability, dissolution of reactive pyrrhotite, and sulfate migration through the cementitious matrix, in controlling the rate of pyrrhotite oxidation and the associated expansion. Overall, these results show that future accelerated testing protocols should account not only for the potential formation of expansive phases, but also for the exposure conditions required to overcome these kinetic and transport barriers.

5. ACKNOWLEDGMENTS

This work was supported by the National Institute of Standards and Technology (NIST) under Award #70NANB24H056. Any opinions, findings and conclusions or recommendations expressed in this material are those of the authors and do not necessarily reflect the views of the NIST.

6. REFERENCES

1. Rodrigues A, Duchesne J, Fournier B, et al (2012) Mineralogical and chemical assessment of concrete damaged by the oxidation of sulfide-bearing aggregates: Importance of thaumasite formation on reaction mechanisms. Cement and Concrete Research 42:1336–1347. https://doi.org/10.1016/j.cemconres.2012.06.008
2. Zhong R, Wille K (2018) Deterioration of residential concrete foundations: The role of pyrrhotite-bearing aggregate. Cement and Concrete Composites 94:53–61. https://doi.org/10.1016/j.cemconcomp.2018.08.012
3. Leemann A, Lothenbach B, Münch B, et al (2023) The “Mica Crisis” in Donegal, Ireland – a case of internal sulfate attack? Cement and Concrete Research 168:107149. https://doi.org/10.1016/j.cemconres.2023.107149
4. Rodrigues A, Duchesne J, Fournier B (2015) A new accelerated mortar bar test to assess the potential deleterious effect of sulfide-bearing aggregate in concrete. Cement and Concrete Research 73:96–110. https://doi.org/10.1016/j.cemconres.2015.02.012
5. Canadian Standards Association (2019) CSA A23.1/A23.2 Concrete materials and methods of concrete construction/Test methods and standard practices for concrete
6. El-Mosallamy M, Shehata MH (2020) Sulphide oxidation mortar tests for evaluation of the oxidation potential of sulphide-bearing aggregate. Construction and Building Materials 264:120627. https://doi.org/10.1016/j.conbuildmat.2020.120627
7. Shadkam HR, Shehata MH (2025) Use of oxygen-rich environment to test concrete containing sulphide-bearing aggregate and evaluate the effect of mitigative measures. Construction and Building Materials 477:141244. https://doi.org/10.1016/j.conbuildmat.2025.141244
8. Li Z, Kaladharan G, Bentivegna A, Radlińska A (2023) On the performance-based approaches to evaluate the oxidation potential of iron sulfide-bearing aggregates in concrete. Cement 12:100059. https://doi.org/10.1016/j.cement.2023.100059
9. Li Z, Gorski CA, Thompson A, et al (2025) Dissolution kinetics of iron sulfide minerals in alkaline solutions. Cement and Concrete Research 193:107850. https://doi.org/10.1016/j.cemconres.2025.107850
10. Kulik DA, Wagner T, Dmytrieva S V., et al (2013) GEM-Selektor geochemical modeling package: Revised algorithm and GEMS3K numerical kernel for coupled simulation codes. Computational Geosciences 17:1–24. https://doi.org/10.1007/s10596-012-9310-6
11. Lothenbach B, Le Saout G, Gallucci E, Scrivener K (2008) Influence of limestone on the hydration of Portland cements. Cement and Concrete Research 38:848–860. https://doi.org/10.1016/j.cemconres.2008.01.002
12. De Weerdt K, Bagheri M, Lindgård J, et al (2025) Changes in cement paste during accelerated mortar bar testing for pyrrhotite containing aggregate. Cement and Concrete Research 188:. https://doi.org/10.1016/j.cemconres.2024.107730
13. Akter S, Wille K (2024) Expansion of mortar bars containing reactive iron-sulfide bearing aggregates. In: Fournier B, Duchesne J, Araiza R, et al (eds) Proceedings of 1st International Conference on Iron-Sulfide Reactions in Concrete. Université Laval, Quebec City, Canada, pp 97–101

Petrographic Characterization of Aggregates Involved in Iron-Sulfide Reactions in Residential Concrete Foundations in Northern Massachusetts and the use of Point-Count Analysis to Determine the Amount of Iron Sulfide Minerals in Concrete Aggregates

Nick Scaglione [(1)], Patricia Piercey [(2)]

(1) Concrete Research & Testing, LLC

(2) Concrete Research & Testing, LLC

Abstract

The state of Massachusetts has multiple sources of pyrrhotite-bearing coarse aggregates that have caused severe cracking distress of residential foundations. Distressed foundations in south-central and central Massachusetts have been linked to the Becker quarry in Willington, Connecticut, and to a quarry in Rutland, Massachusetts, respectively. Recently, two additional sources of pyrrhotite-bearing aggregates in northern Massachusetts have been identified that are responsible for severely distressed foundations. The aggregates from northern Massachusetts are crushed gravels with lithologies distinct from each other and from other known sources of pyrrhotite-bearing aggregates. This paper details the petrographic characterization of these newly discovered coarse aggregates. The paper also discusses a methodology for determining the pyrrhotite content of iron-sulfide bearing aggregates in concrete using point count analysis performed on polished concrete sections under the stereomicroscope.

***Keywords**: cracking, Massachusetts, petrography, point-count-analysis, pyrrhotite*

1. INTRODUCTION

Residential concrete foundations in Connecticut and Massachusetts exhibit severe cracking distress related to pyrrhotite ($Fe_{1-x}S$) in the coarse aggregate. The pyrrhotite is a component of metamorphic rocks of the Merrimack Terrane in southern New England, specifically sulfidic schists, gneisses, and quartzites.

The pyrrhotite-bearing aggregate in Connecticut and south-central Massachusetts was derived from the Becker Quarry in Willington, Connecticut. The underlying bedrock at the Becker Quarry is the Brimfield Schist [1]. The first known report of distress in Connecticut was in 1995. To date, roughly 2600 Connecticut foundations have tested positive for reactive aggregate. The pyrrhotite-bearing aggregate in central Massachusetts has been linked to a quarry in Rutland, Massachusetts. The underlying bedrock at this quarry is primarily the Paxton Formation [2]. The Paxton Formation structurally and conformably underlies the Brimfield Schist. The first reported claims of pyrrhotite-related foundation cracking in this area of Massachusetts was in 2020. The authors previously published a detailed petrographic characterization of the Connecticut and central Massachusetts aggregates [3].

In Northern Massachusetts, residential foundations in the towns of Dracut, Winchendon, and Ashburnham have been confirmed by Concrete Research & Testing (CRT) to contain reactive pyrrhotite-bearing coarse aggregates that have caused severe cracking distress within the concrete. Two distinct aggregate sources have been identified, which are both crushed gravels. Other Northern Massachusetts towns reported to have foundations with reactive aggregate include towns as far west as Orange and as far east as Boxford. The distress in the Northern Massachusetts foundations was first reported in Dracut in 2024, and in the Winchendon/Ashburnham area in 2025. To date, there have only been about 300 Massachusetts foundations that have tested positive for reactive aggregate.

1.1 Massachusetts Quarry Testing

In October of 2023, the Massachusetts government signed into law “An Act Relative to Requiring the Highway Division of the Massachusetts Department of Transportation to Establish a Department and Licensure Process to Oversee Quarries Producing Concrete Aggregate.” The law required MassDOT to

develop regulations to establish a license program for concrete aggregate manufacturers. In September of 2025, MassDOT adopted *Regulation 700 CMR 19.00: Aggregate Source Licensing for the Production of Cement Concrete*. The regulation requires all Massachusetts quarries that supply aggregates used in concrete to be tested for sulfur content. If the sulfur content exceeds 0.1 percent, a petrographic examination of the aggregate is required to determine the presence of pyrrhotite or framboidal pyrite. If either is detected, the aggregate is prohibited from use in concrete.

1.2 Background

Pyrrhotite is an Iron-Sulfide Mineral (ISM) that is a relatively common accessory mineral in igneous and metamorphic rocks. When present in concrete and exposed to moisture, iron in the pyrrhotite is highly susceptible to expansive oxidation, resulting in cracking and the liberation of sulfur from the pyrrhotite. The liberated sulfur can then react with the cement paste to cause internal sulfate attack, which is also highly expansive. These distress mechanisms, termed Iron-Sulfide Reactions (ISR), are discussed in detail by others [4-7].

CRT first received concrete samples from distressed residential foundations in Connecticut in 2008. To date, CRT has examined samples from 340 structures in southern New England with about 75 percent of the projects containing iron-sulfide bearing reactive coarse aggregate. Of the 340 projects, 30 were from Massachusetts, and only 9 of these contained reactive, pyrrhotite-bearing aggregate that was not from the Becker Quarry in Connecticut. The reactive aggregate from central Massachusetts was identified by CRT in 2022.

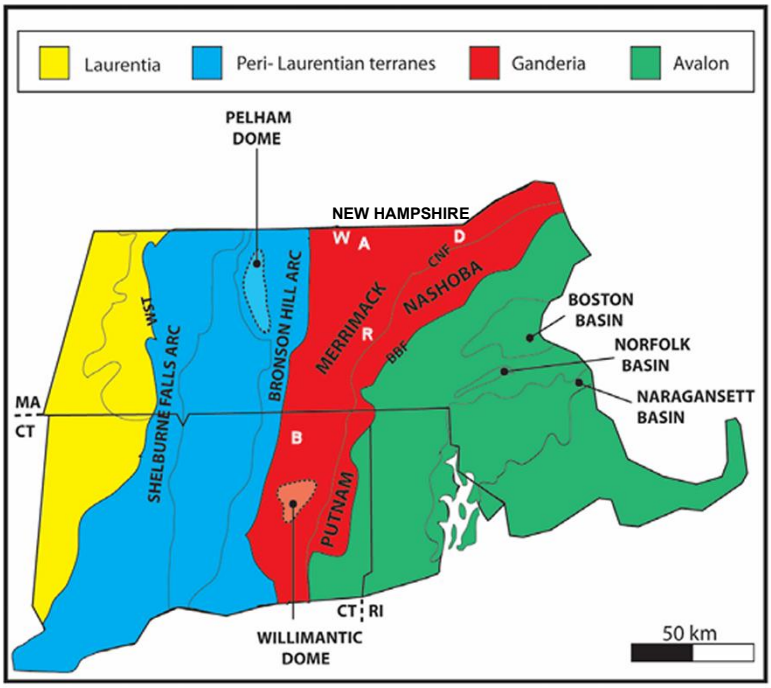

Figure 1: Simplified tectonic map of Southern New England [8]. Major structural features are marked: BBF=Bloody Bluff Fault; CNF=Clinton-Newbury fault zone, WST=Whitcomb Summit thrust zone. Referenced locations in the paper are marked: B=Becker Quarry, R=Rutland, W=Winchendon, A=Ashburnham, D=Dracut. All of the reactive aggregates are located in the Merrimack Terrane.

Concrete foundations exhibiting ISR typically exhibit pattern cracking, although the cracking at interior walls often shows a distinct horizontal orientation. The cracking distress is typically most severe at the exterior, above-grade corners of the foundation. The expansion of the concrete may result in bowing of the foundation walls. The distressed foundations often exhibit white, powdery efflorescence consisting of sodium sulfate on the interior surface of the walls.

The affected foundations typically began showing cracking distress about 10 years after placement. However, the distress often went unnoticed until about 15 to 18 years after construction, when the cracking distress became more severe and the rate of distress accelerated significantly. In some cases, cracks having widths of up 0.5 in. occurred after about 20 years.

Not all the pyrrhotite-bearing aggregate is reactive, and the overall reactivity of individual particles is controlled by the mineralogy and texture of the rock. That is, rock particles with a tight, impermeable texture are not reactive, while highly foliated and micaceous rocks are more permeable and susceptible

to moisture intrusion and oxidation of the ISMs. The non-reactive, aggregate particles typically contain trace to minor amounts of pyrrhotite, present as small, individual grains dispersed within the rock.

2. PETROGRAPHY

The examined samples are cores taken from the foundation walls or large irregular concrete chunks taken from demolished foundatons.

Petrographic examinations were performed on lapped/polished sections and thin sections prepared from the samples in accordance with ASTM C856: “Standard Practice for Petrographic Examination of Hardened Concrete” [9]. The amounts of reactive and non-reactive pyrrhotite-bearing coarse aggregate particles were counted in the prepared sections. The results are based on one chunk sample from the Ashburnham foundation, two chunk samples from the Winchendon foundation, and four cores representing four condominium foundations in Dracut, although the aggregate counts were performed on multiple surfaces prepared from each sample.

Point count analyses were performed on polished sections of concrete using the procedures outlined in ASTM C457 “Standard Test Method for the Microscopical Determination of Parameters of the Air-Void System in Hardened Concrete” [10]. The point count analyses were performed to measure the amount of ISMs in the coarse and fine aggregates.

2.1 Ashburnham / Winchendon (A/W) Aggregates

The Ashburnham and Winchendon coarse aggregates are very similar and judged to be from the same source. The coarse aggregate is a ¾ in. maximum size natural/crushed gravel. The gravel is dominated by gneiss and schist with small amounts of granite and quartzite and minor amounts of feldspar and pyrite particles.

The ISMs in the A/W samples are dominated by pyrrhotite with small amounts of pyrite [FeS_2] and chalcopyrite [$CuFeS_2$] and trace amounts of pentlandite [$(Fe, Ni)_9S_8$]. The ISMs are present in gneiss, schist, and quartzite rock types. About 60 percent of the coarse aggregate particles contain ISMs, with 52 percent of these judged to be reactive and 8 pecent judged to be non-reactive. Rare coarse aggregate particles are comprised almost entirely of pyrite.

The reactive rock consists of schist, gneiss, and quartzite and contains small to moderate amounts of ISMs. The schist often exhibits folding and typically contains biotite and quartz, commonly contains graphite and muscovite, and occasionally contains sillimanite. The gneiss primarily contains quartz, feldspar, and biotite with graphite and sillimanite, occasionally contains muscovite, and rarely contains augite or garnet. The quartzite is dominated by quartz and feldspar and is typically micaceous. The amount of pyrrhotite within individual reactive particles typically ranges from roughly 5 to 50 percent with rare particles containing 85 to 95 percent pyrrhotite. The pyrrhotite in the schist exhibits significant oxidation, and the pyrrhotite at the exterior portions of gneiss and quartzite particles is often oxidized.

Point count analyses of the samples shows coarse aggregate ISM contents of 3.6 percent in the Ashburnham concrete (all of which is pyrrhotite), and 1.8 percent in the Winchendon concrete. The ISMs in the Winchendon concrete was comprised of 1.1 percent pyrrhotite and 0.7 percent pyrite. The pyrite content is due to the presence of two coarse aggregate particles comprised almost entirely of pyrite. The significanly higher amount of pyrrhotite within the Ashburnham concrete is due to several coarse aggregate particles containing greater than 50 percent pyrrhotite.

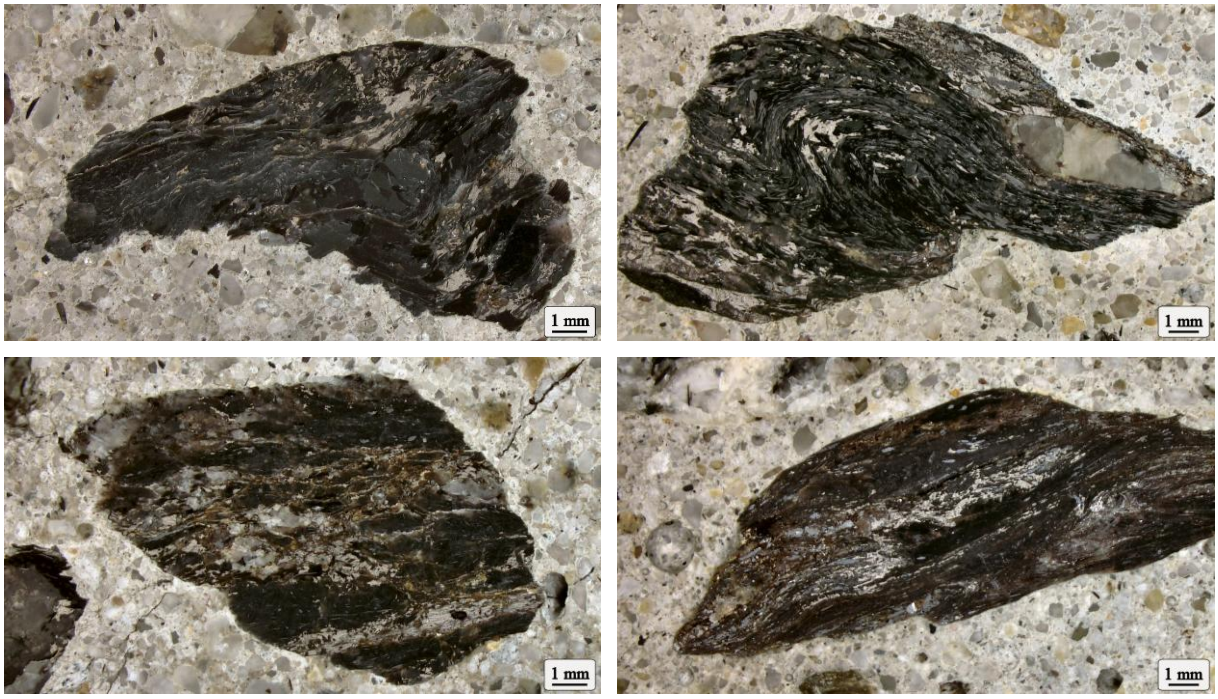

Figure 2: Examples of the reactive, pyrrhotite-bearing A/W schist coarse aggregate particles.

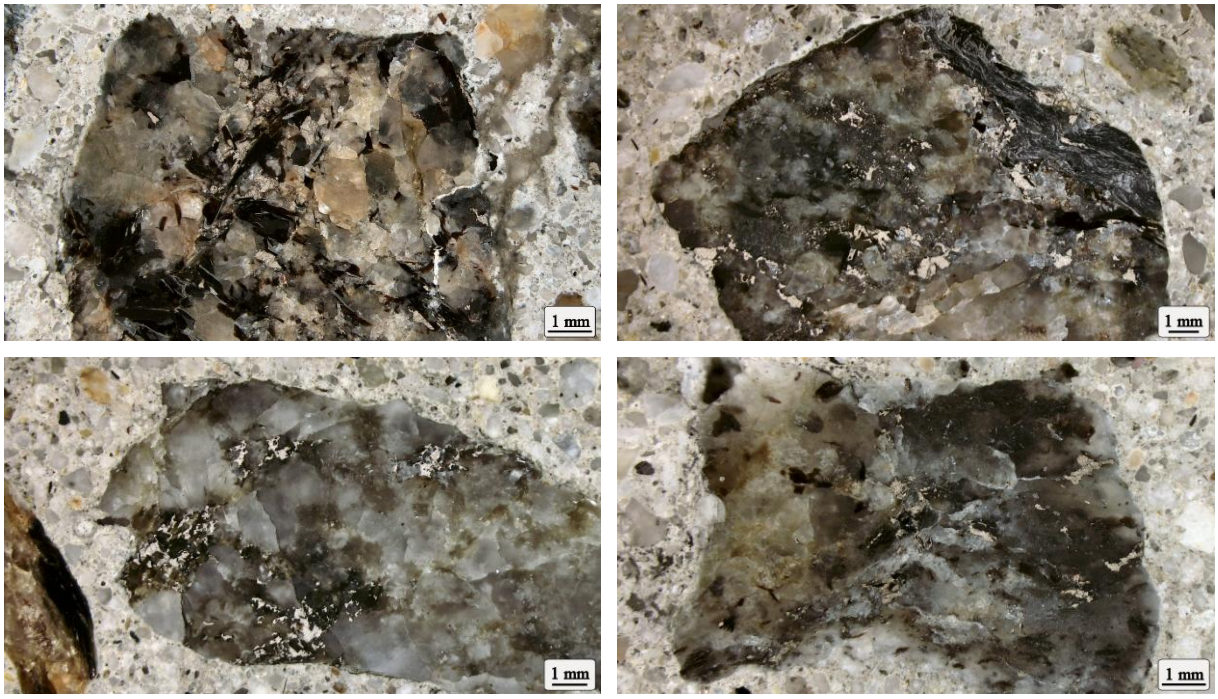

Figure 3: Representative examples of the reactive, pyrrhotite-bearing A/W coarse aggregate particles; the upper photos show gneiss particles and the lower photos show micaceous quartzite particles.

2.2 Dracut Aggregates

The coarse aggregate in the Dracut foundations is a 1-in. maximum size natural/crushed gravel. The gravel is dominated by gneiss and schist with small to moderate amounts of metabasite and weakly metamorphosed sandstone/siltstone particles, and small amounts of diabase, quartzite, phyllite, and granite particles. Most of the metabasite rock is coarse grained and dominated by plagioclase and

pyroxene altered to hornblende, chlorite, serpentine, and epidote. Some of the metabasite is pyrrhotite-bearing chlorite schist, and some of these particles are are almost entirely comprised of pyrrhotite.

The ISMs in the Dracut samples are dominated by pyrrhotite with minor to small amounts of chalcopyrite, minor amounts of pyrite, and trace amounts of pentlandite. The ISMs are present in the gneiss, schist, quartzite, diabase, and metabasite rock types. The portion of coarse aggregate containing ISMs ranges from about 20 to 40 percent in the four examined concrete cores. The majority of these particles are judged to be non-reactive.

The chlorite schist contains highly variable amounts of pyrrhotite and is judged to be reactive. The chlorite schist matrix is comprised primarily of chlorite, altered clinopyroxene and plagioclase, anthrophyllite, and quartz. The chlorite schist also commonly contains minor to small amounts of sillimanite, biotite, muscovite, calcite, and epidote. Some of the particles are almost entirely comprised of pyrrhotite and also contain olivine altered to serpentine, altered clinopyroxene, chlorite, titanite, quartz, and plagioclase. These reactive aggregate particles range from 2 to 9 percent of the coarse aggregate particles in the examined cores. The pyrrhotite in the reactive particles typically ranges between 20 to 95 percent and is commonly in excess of 50 percent. The pyrrhotite is commonly heavily oxidized.

Point count analyses of the samples shows coarse aggregate ISM contents of 0.8, 0.9, and 3.8 percent in three analyzed cores.

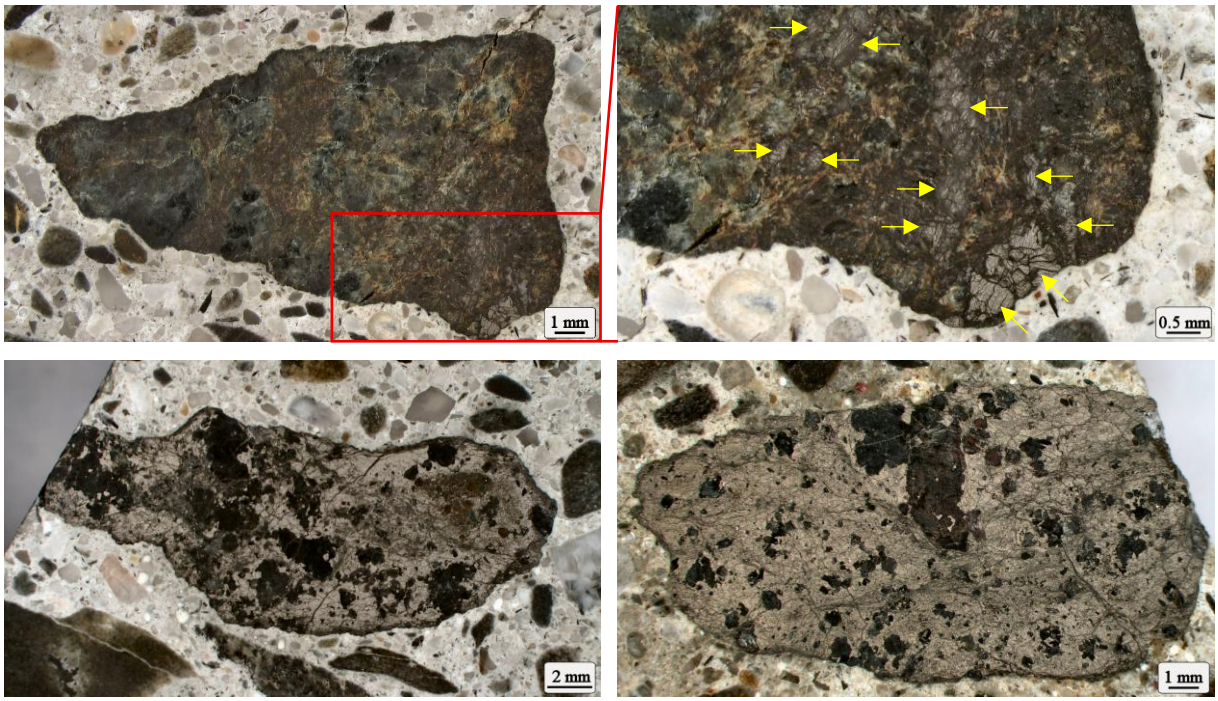

Figure 4: Representative examples of the reactive, pyrrhotite-bearing Dracut coarse aggregate particles. The upper photos show a chlorite schist particle with highly oxidized pyrrhotite (arrows), while the lower photos show particles comprised almost entirely of pyrrhotite.

2.3 Discussion

The concretes containing the two natural gravel aggregates are located in the same region of the state but are very different in both the amount of the reactive particles and the amount of pyrrhotite in the particles. For the A/W aggregate, roughly 52 percent of the particles are determined to be potentially reactive, while only about 2 to 9 percent of the Dracut aggregate particles are judged to be reactive. Although the potentially reactive aggregate particles within the A/W aggregate have relatively high pyrrhotite contents, typically up to 50 percent, most of the reactive Dracut aggregate particles have very high pyrrhotite amounts, often in the range of 50 to 95 percent.

The low amount of reactive aggregate particles in the Dracut aggregate makes proper sampling of the foundations critical. A low number of small diameter cores taken through the partial thickness of the

foundation may not intersect reactive aggregate particles. Also, prepared sections for petrographic examination should maximize the number of aggregate particles for examination by sectioning lengthwise as opposed to perpendicular to the length of the core and by preparing both sides of the section. Proper sampling of concrete containing this aggregate for sulfur testing is also critical.

3. POINT-COUNT ANALYSES

The point count analyses determined the amount of ISMs as a percentage of the coarse aggregate, the fine aggregate, the total aggregate, and the concrete. Due to the similar composition of the coarse aggregate and the coarse fractions of the fine aggregate, the particle size was used to differentiate between them. The analyses were also used to measure the relative amounts of the different ISMs in the aggregates (ie. pyrrhotite and pyrite). The cement paste contents and air contents were also determined as part of the analyses.

At least 3200 points were counted for each analysis, which represents more than twice the number of required points counted for a standard ASTM C457 analysis. The relatively high number of points provides a more accurate value for the amounts of ISMs, which can be present at relatively low percentages. The surface area of the examined specimens typically ranged from 30 to over 40 in^2, roughly 3 to 4 times the area required by ASTM C457. The large surface area allows for a high number of coarse aggregate particles to be included in the analysis.

4. CONCLUSIONS

Two additional pyrrhotite-bearing reactive coarse aggregates have been identified in Massachusetts. Including the Becker Quarry aggregate in Connecticut, used in many residential foundations in south-central Massachusetts, there are at least four lithologically distinct reactive coarse aggegates used in Massachusetts residential foundations. Due to the multiple sources of reactive aggregate, it is possible that the number of affected foundations in Massachusetts may eventually exceed the number of affected Connecticut foundations. Since the Merrimack Terrane extends into New Hampshire, it is possible that pyrrhotite-bearing reactive aggregates are also present in New Hampshire.

References

[1] USGS Brimfield Schist (includes Hamilton Reservoir Formation) https://mrdata.usgs.gov/geology/state/sgmc-unit.php?unit=CTObr1%3B0 Accessed 26 September 2023.

[2] USGS Paxton Formation https://mrdata.usgs.gov/geology/state/sgmc-unit.php?unit=CTObr1%3B0 Accessed 17 July 2023 and 26 September 2023.

[3] Scaglione N, Piercey P (2024) Petrographic characterization of concrete aggregates Involved in iron-sulfide reactions in residential concrete foundations in Connecticut and Massachusetts. ICISR Quebec, Canada

[4] Wille K, Zhong R (2016) Investigating the deterioration of basement walls made of concrete in Connecticut. Department of Civil and Environmental Engineering Advanced Cementitious Materials and Composites Laboratory, produced for the Attorney General of the State of Connecticut. 99 pp.

[5] Jana D (2020) Pyrrhotite epidemic in Eastern Connecticut: diagnosis and prevention. ACI Materials Journal 17.1: 1-20. https://doi.org/10.14359/51718059

[6] Duchesne J, Fornier B (2011) Petrography of concrete deteriorated by weathering of sulphide minerals. 33rd International Conference on Cement Microscopy 2011. 242-261.

[7] Rodrigues A, Duchesne J, Fornier B, Durand B, Rivard P. Shehata M (2012) Mineralogical and chemical assessment of concrete damaged by the oxidation of sulfide-bearing aggregates: importance of thaumasite formation on reaction mechanisms. Cement and Concrete Research 42.10: 1336-1347. https://doi.org/10.1016/j.cemconres.2012.06.008

[8] Reynolds EC (2012) New 40Ar/39Ar age constraints on the timing of metamorphism and deformation in the western Nashoba Terrane, Eastern Massachusetts. Dissertation, Boston College.

[9] ASTM C856-20 Standard guide for the petrographic examination of hardened concrete. ASTM International, West Conshohocken, PA. 2020. https://doi.org/10.1520/C0856_C0856-20

[10] ASTM C457-M23 Standard test method microscopical determination of parameters of the air-void system in hardened concrete. ASTM International, West Conshohocken, PA. 2023. https://doi.org/10.1520/C0457_C0457M-23A

Linking the exposure conditions of defective blocks with expansion in an Irish home by monitoring and microstructural analysis

Pierre-Luc Fecteau [(1)], Andreas Leemann [(2,3)], Paul Dunlop [(3)], Myra Lydon [(4)], Benoit Fournier [(1)]

(1) Department of Geology and Geological Engineering, Université Laval, Québec City, Québec, Canada, pierre-luc.fecteau@ggl.ulaval.ca, benoit.fournier@ggl.ulaval.ca

(2) EMPA, Laboratory for Concrete & Asphalt, Dübendorf, Switzerland, andreas.leemann@empa.ch

(3) School of Geography and Environmental Sciences, Ulster University, Coleraine, Northern Ireland, UK, p.dunlop@ulster.uk

(4) School of Engineering, University of Galway, Galway, Ireland, myra.lydon@universityofgalway.ie

Abstract

County Donegal is the epicentre of Ireland's crumbling-concrete-blocks crisis, with thousands of homes exhibiting severe cracking, loss of strength, and reduced structural integrity within 10–15 years of construction. The damage was initially attributed to high mica content, which was thought to increase vulnerability to freeze–thaw deterioration. However, recent research has demonstrated that internal sulphate attack (ISA) is the primary cause of the observed degradation in defective Donegal homes. This study aims to document the exposure conditions and expansive behaviour of concrete blocks in the outer and inner leaf walls, as well as the rising wall, below ground level and an internal partition wall of a home that was confirmed to be defective as part of the Irish Government grant scheme to repair homes. To characterise field conditions and expansion, manual and automatic in-situ expansion, temperature and relative humidity monitoring was performed since January 2024 at selected locations within the inner and outer leaf walls and an interior partition wall. During the same period, temperature and relative humidity (R.H.) sensors, together with fibre-optic vibrating-wire gauges (VWG), were installed in both leaf walls and at a selected location in the rising wall to enable automated monitoring of expansion with temperature and RH. The findings rule out freeze–thaw as a potential deterioration mechanism in the home, as expansion was recorded during warmer months, and outdoor temperatures remained well above 0 °C throughout the winter of 2024. Microstructural (SEM/EDS) analysis confirms ISA in the blocks of the inner, outer, and rising walls. Results also indicate the potential for further expansion at least in the rising wall. Monitoring will continue for approximately one more year to further capture the exposure conditions and ongoing expansive behaviour.

***Keywords**: concrete blocks, cracking, internal sulphate attack, monitoring, microstructure*

1. INTRODUCTION

Thousands of homes in County Donegal, the region most severely affected by Ireland's crumbling-concrete-blocks crisis, have developed extensive damage 10-15 years after construction due to defective concrete blocks used as building material. The damage was originally attributed to the excess occurrence of mica in the concrete blocks wrongly hypothesised as making them vulnerable to freeze-thaw attack [1]. However, it has recently been shown that the oxidation of pyrrhotite and subsequent internal sulphate attack (ISA) are rather the cause of cracking and integrity loss of the concrete blocks [2,3]. To date, there has been no field trials to quantify the impact of temperature and relative humidity fluctuations in the concrete blocks of the inner leaf, the outer leaf exposed to the environment and the buried rising blocks. The magnitude of expansion/swelling over time is also not documented to date, even if obvious visual deterioration is observed in the field. As many families are still living within the affected homes, it is vital to establish the rate of deterioration as most are still waiting to join a government grant scheme established to help homeowners but that has been widely criticised. Firstly, because access to it still relies on a widely discredited Irish standard, known as I.S. 465, that is used to test and offer remediation options and secondly for not going far enough with financial support.

The goal of this project was to gain information about the temperature, humidity and expansive behaviour within the concrete blocks to establish a link to the temporal progress of pyrrhotite oxidation and ISA. The case study home, which has been approved for demolition under the government grant scheme and confirmed to show the typical damage resulting from the formation of secondary sulphate minerals, was selected for investigation.

Cores to be subjected to microstructural analysis using scanning electron microscopy (SEM) with energy-dispersive X-ray spectroscopy (EDS) were also extracted from the inner leaf, the outer leaf and the rising blocks during January of 2024.

Selected locations within blocks of the inner and outer leaf of exterior walls, as well as an interior partition wall of the selected home were drilled to insert studs for (in-situ) manual expansion monitoring from January 2024. Inner/outer leaf selected blocks as well as one location within the rising wall blocks were also drilled and equipped with temperature and relative humidity (R.H.) sensors in addition to vibrating wire gauges (VWG) for automatic expansion monitoring (Fig. 1.1).

2. MATERIALS AND METHODS

2.1 Materials and methods

The selected home is located near Ramelton village, north of Letterkenny, County Donegal, Ireland. It was built in 2005 and has a floor area of 249m^2 across two floors. Internal cracking appeared in 2018-2019. Vertical cracking in the external walls first appeared in 2020, mainly at the corners of the house and below / above the windows. The sides of the house show more horizontal cracks in addition to vertical cracks.

Cores (Ø = 100 mm, L ~ 100 mm) were extracted from the inner leaf (front of home), outer leaf (front and back of home), and rising blocks (front of home) (Figure 1.1 A). Phenolphthalein testing showed that the two samples from the outer leaf were partially carbonated, samples from the inner leaf were fully carbonated and the sample from the rising blocks was not carbonated. The concrete is typical for the blocks produced in Ireland with a high share of voids, as reported in [2,3].

Sections of the cores were first cut to appropriate size (discs with a diameter of ~ 48 mm and a thickness of ~15 mm) and dried in the oven at 50 °C for three days. The samples were subsequently vacuum and pressure impregnated with an epoxy resin containing a fluorescent dye. The samples were then lapped with SiC powders (12 and 9 µm), prior to polishing with oil-based diamond suspensions of 6, 1 and 0.25 µm particle size. Samples were finally coated with a 10 nm thick carbon layer.

The microstructural analysis was performed with a SEM FEI Quanta 650. The samples were investigated at a pressure between 3.5 and 4.5×10^{-6} Torr. Elemental analyses were conducted by EDS with a Thermo Noran Ultra Dry 60mm^2 detector and Pathfinder X-Ray Microanalysis Software. An acceleration voltage of 12 kV and a spot size of 4.5 were used for imaging and EDS point analysis, while the former was increased to 20 kV for the acquisition of the elemental maps. All concentrations and ratios thereof are given in atom-%. The phase mapping was performed according to current standards [4].

Figure 1.1 shows some of the selected monitoring locations. 19mm holes were drilled to the width center of the selected outer leaf blocks (50mm, ~60 mm at angle)) upward at 45° (to reduce the risk of rain water ingress), in which a plastic sleeve was inserted for temperature, R.H. and other fibre optics sensors installation (Vaisala HMP60, Sylex, HS-01). In the inner leaf blocks, 19mm holes were drilled perpendicular (since there was no risk of rain water ingress) to the surface at the center of the widest part of the block (50mm). VWG (Geosense-2000, 150mm nominal) and studs for manual expansion monitoring were also installed and fixed with fast-set epoxy resin within the same selected block locations in the outer and inner leaf and internal partition wall. All electrical sensor measurements were logged into a datalogger and computer. The inner leaf bathroom monitoring location is directly placed over a radiator below a window. The rising wall location was drilled at 110mm in depth (center of height of the block, placed aside) perpendicular to the surface and installed with R.H. and temperature sensors in addition to the VWG fibre optic strain sensor. That location was carefully backfilled with sand and gravel once the sensors installation was completed. Zero measurements were taken once the epoxy was adequately cured at all locations. All sensors installation locations were within a selected block (between mortar joints), with the exception being the corners of the gable walls of the home. Manual

measurements of the fixed studs were done periodically using a Mayes dial gauge of 100mm nominal length.

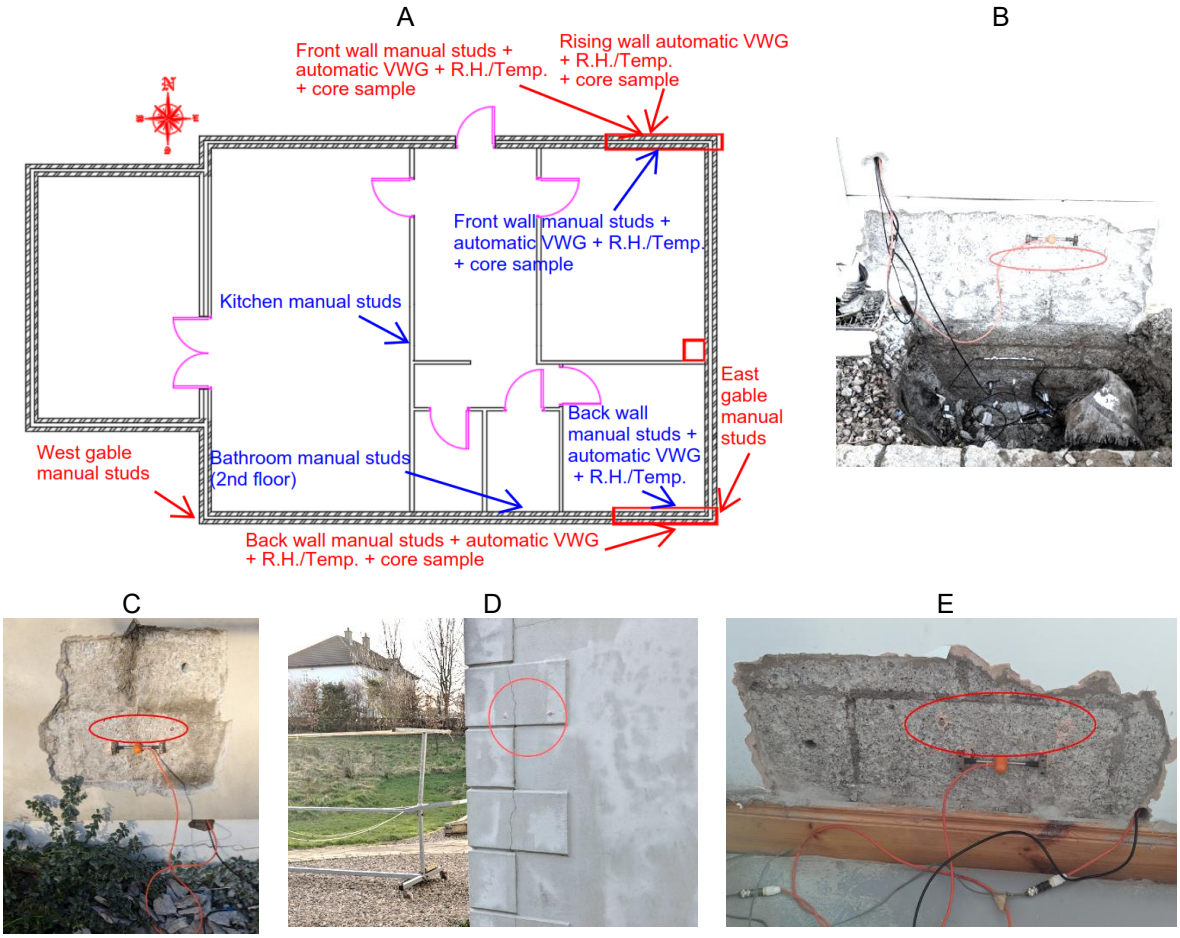

Figure 1.1: Selection of locations of monitoring and core samples within the selected concrete blocks (red circles show locations of manual expansion measurements with studs). A: Schematic of the monitoring and core sample locations, B: Exterior wall outer leaf and rising wall block below, front of house (facing north), C: Exterior wall outer leaf, back of house (facing south), D: Exterior wall outer leaf, east facing gable, E: Exterior wall inner leaf, back of house (facing south).

3. RESULTS

3.1 Microstructure

The aggregates in the four cores all consist of a phyllite with quartz, albite and a high amount of muscovite and chlorite. A micaceous quartzite containing albite, muscovite and chlorite is also present. Both types of aggregates contain pyrrhotite ($Fe_{(1-x)}S$) and pyrite (FeS_2) with higher sulphides concentrations in the phyllite. Pyrrhotite is about five times more frequent than pyrite, as assessed qualitatively by EDS point analysis of several dozen iron sulphide particles.

The microstructural analysis shows an increasing level of pyrrhotite oxidation in the form of oxidized layers (Figure 3.1) from inner leaf to rising blocks to outer leaf. The fully carbonated assemblage of cement hydrates in the inner leaf consists of calcite, decalcified calcium-silicate hydrate (C-S-H) with varying amounts of aluminium and traces of thaumasite and gypsum. The partly carbonated cement paste of both outer leaf samples consists of decalcified C-S-H, calcite and a high amount of ettringite present in still uncarbonated patches (Figure 3.1). Thaumasite was not detected. The presence of C-S-H and portlandite shows that the concrete in the rising blocks is still uncarbonated. However, the Si/Ca-ratio of the C-S-H is elevated indicating a partial reaction with muscovite [3]. The amount of ettringite is higher than in concrete without an additional source of sulphur (Figure 3.2).

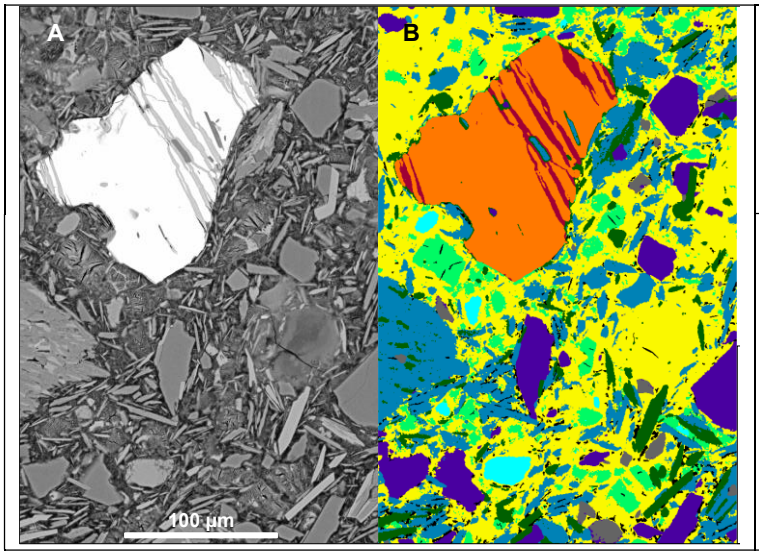

Figure 3.1: Back-scattering image (A) and phase clustering (B) showing pyrrhotite with oxidized layers and clusters of ettringite in the cement paste. Outer leaf, back of home.

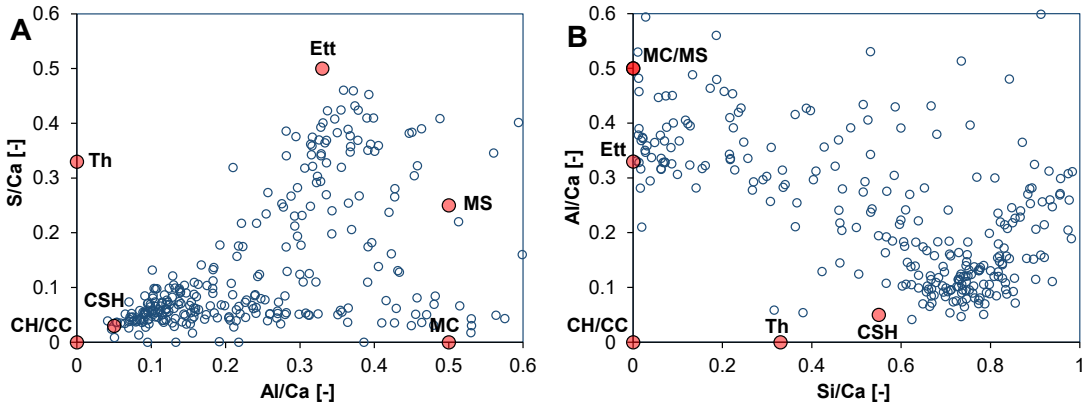

Figure 3.2: S/Ca-ratio as a function of the Al/Ca-ratio (left) and Al/Ca-ratio as a function of the Si/Ca-ratio (right). CH = portlandite, CC = calcite, CSH = calcium-silicate-hydrate, Th = thaumasite, Ett = ettringite, MS = monosulphate, MC = monocarbonate. Front of home, rising blocks.

3.2 Monitoring

Manual expansion measurements were obtained between January 2024 and November 2025 (almost two years); however, automatic measurements (VWG [expansion], R.H. and temperature [Vaisala or fibre optics] were only available during the first ~3 months of the study because of unforeseen equipment malfunction. The cracking observed in the home is confirmed by the manual and automatic [VWG] expansion measurements, specifically in the outer leaf gables, the rising wall and the inner leaf of the bathroom on the second floor (Figures 3.3 A and D). Temperatures above 0°C are measured in the outer and inner leaf blocks throughout the entire winter of 2024, in addition to outside temperatures being well above 0°C (Figures 3.3 B, C and D). R.H. measurements shown in Figure 3.3 C are well over 100%, indicating sensor malfunction (or water condensation in direct contact with the sensor). This equipment malfunction was resolved in November 2025 and will allow for further monitoring for at least another year before the home demolition/reconstruction planned for 2027.

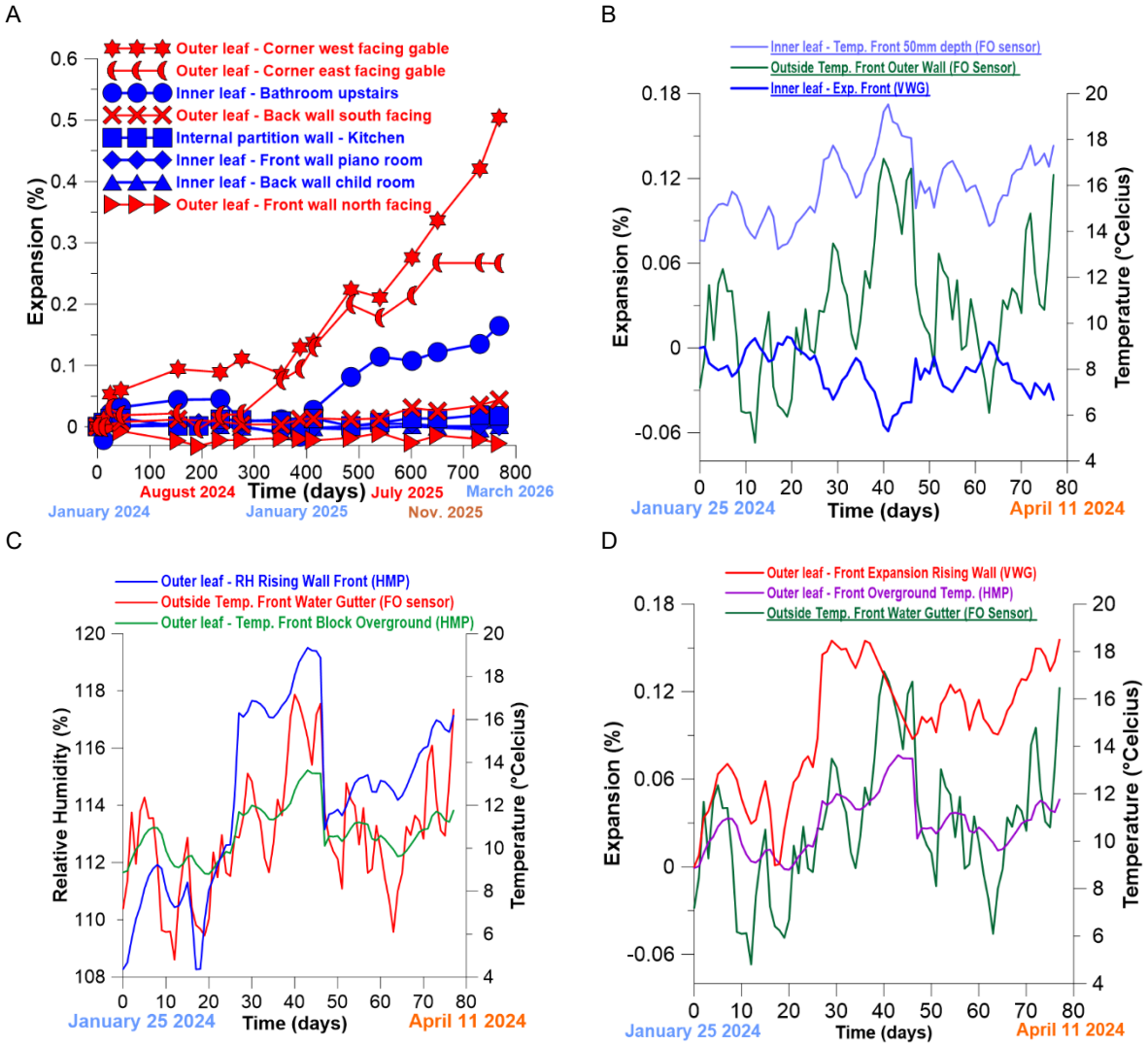

Figure 3.3: Graphs of expansion, temperature and R.H. monitoring A: Manual expansion measurements over almost two years, B: Inner leaf and outside temperature data, along with VWG (automatic) expansion measurements (first three months), C: Outer leaf and outside temperature data, along with rising wall R.H. (first three months), D: Outer leaf and outside temperature data, along with VWG rising wall expansion (first three months).

4. DISCUSSION

The simultaneous observations of external temperatures well above 0°C, which is also the case for the rising wall and outer and inner leaf blocks, together with the increasing expansion trends (Figure 3.3) and microstructural analyses of concrete block samples provide clear evidence that, i) freeze-thaw related damage is not occurring within the concrete blocks and ii) ISA is the cause of damage and expansion. Moreover, the fact that expansion is occurring during the warmer months of the monitoring period, when freeze–thaw conditions are absent, unequivocally demonstrates that the hypothesis that high mica levels are responsible for freeze–thaw damage in defective Donegal homes is untenable. Expansion values (~0.15%) measured over an approximately two-year period in the inner leaf of the bathroom (recorded just above a radiator and below a window) clearly indicate that R.H. > ~75–80% is necessary to promote ISA and pyrrhotite oxidation [5]. Furthermore, acceleration of the reaction appears to be associated with temperature–humidity cycles [3]. These findings also suggest that the other inner-leaf monitoring locations in this particular home did not reach humidity levels sufficient for ISA to develop, at least over the monitoring period, to the same extent as observed at the bathroom location. The much higher expansion in the east and west gables (Figure 3.2A) is likely explained by the accumulative effect of ISA related expansion in all blocks at the same level on the exterior wall. The significant expansion measured by the VWG sensor in the rising wall monitoring location within the first

three months also confirms that ISA is occurring in that part of the home [3]. The analyses confirms that oxidation of pyrrhotite and ISA are the reasons for the observed crack formation in the investigated home. The degree of reaction is the highest in the outer leaf followed by the rising wall blocks and the internal leaf. Although no bulk analysis of sulphur was conducted, the comparison with the microstructure of the homes investigated in [2,3] clearly suggests the sulphur content in the aggregates is well above the limit value of 0.1 mass-% [6]. Although the degree of reaction is the highest in the outer leaf, the comparison with other homes with the same aggregate type in Donegal [2,3] suggests that ISA will progress further. As pyrrhotite oxidation is strongly pH dependent [7], the partial carbonation and the simultaneous decrease of pH may slow its progress to a certain extent; however, the carbonation increases the availability of carbonates, thus improving the conditions for thaumasite formation that leads to strength loss of the concrete due to the consumption of C-S-H [8-11]. In the rising wall blocks, ISA is not affected by carbonation yet. The kinetics of ISA are likely governed by the availability of oxygen that is limited by the typically high water saturation in the rising blocks underground [3]. In any case, further reaction and expansion of the rising wall blocks has to be expected.

5. CONCLUSION

In-situ expansion, temperature and R.H. monitoring rule out freeze-thaw cycles as a source of damage in the concrete blocks of the investigated home. Microstructural analysis of cores confirms the occurrence of pyrrhotite oxidation and ISA in the blocks, while monitoring confirms ISA-related expansion in the inner (localized higher R.H. conditions) and outer leaves and in the rising walls. Moreover, the study confirms that there is potential for ISA to progress further and to develop in the rising wall exposed to an underground environment (as well as inner and outer leafs). Ongoing monitoring is planned for one more year to further document the exposure conditions.

6. REFERENCES

[1] D. McCarthy, N. Kane, F. Lee, D. Blaney, Report of the Expert Panel on Concrete Blocks, Department of Housing, Local Government and Heritage, 2017. https:// www.gov.ie/en/publication/0218f-report-of-the-expert-panel-on-concrete-blocks/

[2] Leemann, A., Lothenbach, B., Münch, B., Campbell, T. and Dunlop, P., 2023. The “mica crisis” in Donegal, Ireland–A case of internal sulfate attack?. *Cement and Concrete Research*, *168*, p.107149. https://doi.org/10.1016/j.cemconres.2023.107149

[3] Leemann, A., Münch, B., Lothenbach, B., Winnefeld, F. and Dunlop, P., 2024. Defective homes in Donegal, Ireland: effect of exposure conditions and concrete quality on pyrrhotite oxidation and internal sulfate attack. *Cement and Concrete Research*, *186*, p.107684. https://doi.org/10.1016/j.cemconres.2024.107684

[4] Münch, B., Martin, L.H. and Leemann, A., 2015. Segmentation of elemental EDS maps by means of multiple clustering combined with phase identification. *Journal of Microscopy*, *260*(3), pp.411-426. https://doi.org/10.1111/jmi.12309

[5] Steger, H.F., 1982. Oxidation of sulfide minerals: VII. Effect of temperature and relative humidity on the oxidation of pyrrhotite, Chem. Geol., 35 (3–4) (1982), pp. 281-295.

[6] EN 12620:2013, Aggregates for concrete, European Committee for Standardization, Brussels, 2013.

[7] Li, Z., Gorski, C.A., Thompson, A., Shallenberger, J.R., Kaladharan, G. and Radlińska, A., 2025. Dissolution kinetics of iron sulfide minerals in alkaline solutions. Cement and Concrete Research, 193, p.107850. https://doi.org/10.1016/j.cemconres.2025.107850

[8] Van Aardt, J.H.P. and Visser, S., 1975. Thaumasite formation: A cause of deterioration of Portland cement and related substances in the presence of sulphates. *Cement and concrete Research*, *5*(3), pp.225-232. https://doi.org/10.1016/0008-8846(75)90004-6

[9] Romer, M., Holzer, L. and Pfiffner, M., 2003. Swiss tunnel structures: concrete damage by formation of thaumasite. *Cement and Concrete Composites*, *25*(8), pp.1111-1117.

[10] Bellmann, F., 2004. On the formation of thaumasite $CaSiO_3 \cdot CaSO_4 \cdot CaCO_3 \cdot 15H_2O$: Part II. *Advances in cement research*, *16*(3), pp.89-94. https://doi.org/10.1016/S0958-9465(03)00141-0

[11] Leemann, A. and Loser, R., 2011. Analysis of concrete in a vertical ventilation shaft exposed to sulfate-containing groundwater for 45 years. *Cement and Concrete Composites*, *33*(1), pp.74-83. https://doi.org/10.1016/j.cemconcomp.2010.09.012

Tests for Evaluating Sulphide-Bearing Aggregates based on Coarse Aggregate-Paste and Concrete Mixture

Peter O. Anifowose n (1), Medhat H. Shehata (1)

(2) Department of Civil Engineering, Toronto Metropolitan University, Toronto, Canada,

n Corresponding author: panifowose@torontomu.ca

Abstract

The use of oxidizable sulphide-bearing aggregates (SBA) in concrete poses a significant durability threat because they generate internal sulphate, leading to expansive reactions and structural deterioration. This study presents accelerated conditioning methods developed at Toronto Metropolitan University (TMU) to detect the potential oxidation of sulphides in coarse aggregates (CA). Paste-mix specimens were cast using a water-to-cement-to-coarse aggregate (W:C:CA) ratio of 0.33:1:1 without fine aggregate. The CA were presoaked in a sodium hypochlorite (bleach) solution of 6% concentration for 10 minutes before casting to allow absorption of the oxidizing agent by the aggregate and then surface-dried. Paste-mix specimens were cyclically immersed in saturated limewater soaking (LWS) at room temperature for 8 hours twice weekly, then stored at 40 °C and 75% RH. After the first phase, specimens were transferred to the second phase at 5 °C and 100% RH. In this test, one SBA showed an expansion of about 0.4%, while the specimens with the control aggregate were about 0.19%. The expansion in some control specimens is likely attributed to wetting-drying effects on some aggregates that are suspected to be vulnerable to wetting/drying cycles. The second test method involves concrete specimens cast with 0.65 w/c ratio and subjected to the bleach injection method. The specimens were oven-dried at 40 °C for 24 hours, vacuumed for 3 hours, and injected with bleach under vacuum. Bleach injection revealed higher second phase expansions in SBA, one of which showed 0.16%, another with lower total sulphur showed 0.1% expansion compared to 0.04% for the control. Ongoing optimization, involving repeating the conditioning cycles and utilizing White General Use (WGU) cement with higher C_3A content and fineness, is being evaluated.

***Keywords**: aggregate oxidation, bleach injection, durability, sulphate attack, sulphide-bearing aggregates.*

1. INTRODUCTION

The deterioration of concrete specifically caused by oxidation of sulphide-bearing aggregates (SBA) is recognized as a major durability concern globally, with occurrences in Europe [1], the United States [2], and Canada [3]. Among the various iron sulphide minerals, including pyrite, marcasite (both FeS_2), and pyrrhotite ($Fe_{(1-x)}S$), it has been established that pyrrhotite exhibits the highest reactivity [4]. The mechanism involves oxidation of iron sulphide minerals, producing iron oxide, sulphuric acid, and potentially elemental sulphur under low oxygen conditions [5]. Rust staining appears as the initial damage, followed by expansion from the volume increase of oxidation products. Subsequently, the release of sulphate ions triggers internal sulphate attack through the formation of gypsum, ettringite, and thaumasite, resulting in cracks and pop-outs. Prevention methods remain limited, often necessitating costly replacement of affected structures.

Various screening methods have been proposed for evaluating SBA. The limewater soaking test proposed by Midgley and adopted in EN 1744 relies on visual inspection of surface discoloration, but Ramos et al. [6] found this approach fails to identify certain reactive materials, prompting identification of sodium hypochlorite as a reliable replacement. The ASTM C641 procedure utilizes steam exposure with qualitative staining assessment but demonstrates insufficient accuracy for identifying reactive iron sulphide minerals. Rodrigues et al. [7] developed the Oxygen Consumption Test (OCT) as a quantitative aggregate test, although El-Mosallamy and Shehata [8] noted its susceptibility to variations in aggregate preparation methods. Guirguis and Shehata [9] proposed an aggregate dissolution protocol employing household bleach solution combined with paralyzing the solution after the test. The Accelerated Mortar

Bar Test (AMBT) [10,11] applies bleach oxidation with thermal cycling (80 °C for 13 weeks, then 5 °C for 13 weeks). The AMBT methodology requires aggregate crushing and grinding to specific particle sizes, which does not replicate the coarse aggregate size.

This study introduces and evaluates the concepts for possible new tests, focusing mainly on testing coarse aggregate size using different accelerating methods.

1.1 Materials

Three types of Portland cements were used in this investigation: general use (GU), limestone general use (GUL), and white general use (WGU). The chemical composition and fineness of the cements are listed in Table 2-1. Different cementing blends were used under the different testing conditions, as will be explained in section 2.2.

Table 1-1: Chemical and phase composition of cement used.

Cement	Fe_2O_3 (%)	Al_2O_3 (%)	SiO_2 (%)	CaO (%)	SO_3 (%)	MgO (%)	Total alkali (%)	C_3S	C_2S	C_3A	C_4AF	Blaine (m^2/kg)
GU	2.30	5.30	20.2	61.90	4.20	2.30	1.00	48	22	10	7	411
GUL	2.20	4.11	19.2	60.00	4.20	2.30	0.92	50	18	10	7	506
WGU	0.00	5.10	20.9	66.24	3.21	0.95	0.31	67	9	11	0	529

Five coarse aggregate types were selected for this research. The aggregate MSKH (with a 0.9% total sulphur) is a gabbro-type aggregate known for contributing to a series of foundation issues in the Trois-Rivières region, in Canada. Table 2-2 summarizes the composition and properties of these aggregates. All tested aggregates were non-alkali-reactive based on testing or field performance.

Table 1-2: Chemical composition of coarse aggregate

Aggre-gate	SSD Density (kg/m^3)	Rock type	Total sulphur TS (%)	SiO_2 (%)	CO_2 (%)	Fe_2O_3 (%)	Al_2O_3 (%)	TiO_2 (%)	CaO (%)	MgO (%)	$Na_2O + K_2O$ (%)
ORE	3221	Mine waste	14.00	33.10	0.13	39.40	8.53	0.73	4.20	3.05	2.39
MSKH	2881	Gabbro	0.930	50.60	0.71	8.10	19.40	0.53	8.84	6.85	3.79
MSKL	2881	Gabbro	0.210	50.60	0.71	8.10	19.40	0.53	8.84	6.85	3.79
C1	Not measured	Dolostone	0.161	5.310	42.36	0.91	0.93	0.05	28.25	19.42	0.37
C2	Not measured	Basalt	0.027	49.09	1.30	14.24	13.91	2.12	8.12	4.70	4.42
C3	2730	Dolostone	0.151	2.250	43.22	0.79	0.32	0.03	29.85	20.0	0.06
C4	Not measured	Gabbro	0.151	51.27	1.13	12.54	14.87	2.25	3.00	5.39	1.35

1.2 Experimental procedure

Two types of specimens were investigated here: (a) a paste-coarse aggregate mixture that was investigated using microprism moulds of 40 mm by 40 mm by 285 mm. The term microprism was used for these specimens as their cross-section is smaller than that of the traditional concrete prisms used for volume change monitoring, including shrinkage and alkali-aggregate reaction evaluation, and (b) the concrete microprism test, which uses the same specimen size, but with a traditional concrete mix with coarse and fine aggregates. Two titanium studs were installed at the ends of each microprism specimen to keep track of the length change. The observed length variation was measured each week via a length comparator and reported as a percentage of their original length.

1.2.1 Microprism paste-aggregate mix design.

Microprism specimens were cast using a water-to-cement-to-coarse aggregate (W:C:CA) ratio of 0.33:1:1. This mix design, adapted from RILEM AAR 5 guidelines for alkali-silica reactivity testing, ensures high cement content and elevated aluminate concentration, which promotes the formation of

sulphate attack products when internal oxidation occurs. Aggregates were presoaked in 6% sodium hypochlorite (bleach) solution for 10 minutes before casting to allow absorption of the oxidizing agent by the aggregate, then surface-dried. After seven days of curing, initial readings were taken, and specimens were subjected to the limewater soaking (LWS) condition for 8 hours twice a week. After each soaking period, specimens were stored at 40 °C/75% relative humidity (RH). This stage of testing was run for 13 weeks and aimed at oxidizing the sulphide phases in the aggregate. At the end of this 13-week phase of testing or 26 cycles, the specimens were stored above water (100% RH) at 5 °C for 13 weeks, to promote sulphate attack. By the end of the 26 weeks, both the oxidation (Phase I) and the sulphate attack (Phase II) were repeated for another 26 weeks, making the test 52 weeks in total.

In addition to testing the aggregates listed in Table 2-2, blends of the control aggregate C1 and Ore were tested to represent aggregates of different sulphur contents. The two mixtures investigated were C1 + 30% and C1+ 50% Ore. The microprism paste mix specimens were cast with GU cement or WGU cement.

1.2.2 Concrete bleach injection test

In this test, microprism concrete specimens were cast using GUL cement with the inclusion of fine aggregate. A 0.65 water-to-cement ratio was considered for the mix design, and the coarse aggregates were pre-soaked in bleach solution before casting. Two control aggregates (with no sulphides), C3 and C4, were used as representatives of carbonate and silicate control aggregates, respectively. After seven days of curing, initial readings were taken while the specimens were in a saturated surface dry condition (SSD). After the curing, the test starts by drying the specimens at 40 °C / 25%RH for 24 hours to achieve about 65% degree of saturation (DoS) within the specimens. The DoS was measured as the moisture content of the sample relative to the moisture content at saturation. Following this, a vacuum of 50 mm Hg was applied to the specimens for 3 hours. Finally, the bleach was introduced to the specimens while under vacuum, which were kept soaked in bleach for an additional 3 hours. After that, the specimens were taken out of the bleach bath, measured, and placed at 40 °C/75% RH for the remainder of the week (around 5 days and 18 hours). This process was repeated for 19 weeks, constituting Stage I of the test, which aimed at oxidizing the sulphide minerals in the aggregates. At the end of the 19 weeks, the specimens were transferred to 5 °C/100% RH, Stage II, for 19 weeks, aiming at sustaining the sulphate attack. All measurements were taken after bringing the samples to SSD conditions.

2. RESULTS

2.1 Paste-mix microprism test.

The results of the mixtures with GU cement are presented in *Figure 2-1*(a). The results show that the sulphide-bearing aggregates exhibited higher expansion than controls. However, major drawbacks of the test are: (a) the control aggregate C2 showed expansion very close to that of the aggregate with high oxidizable sulphide content, such as C1 + 50% Ore, and (b) the two aggregates MSKH and MSKL showed similar expansion despite their difference in sulphide content. In an attempt to widen the gap in the expansion values between non-sulphide and sulphide-bearing aggregates, the test was repeated using WGU cement, which has a higher C_3A content. *Figure 2-1*(b) presents the results obtained with WGU specimens.

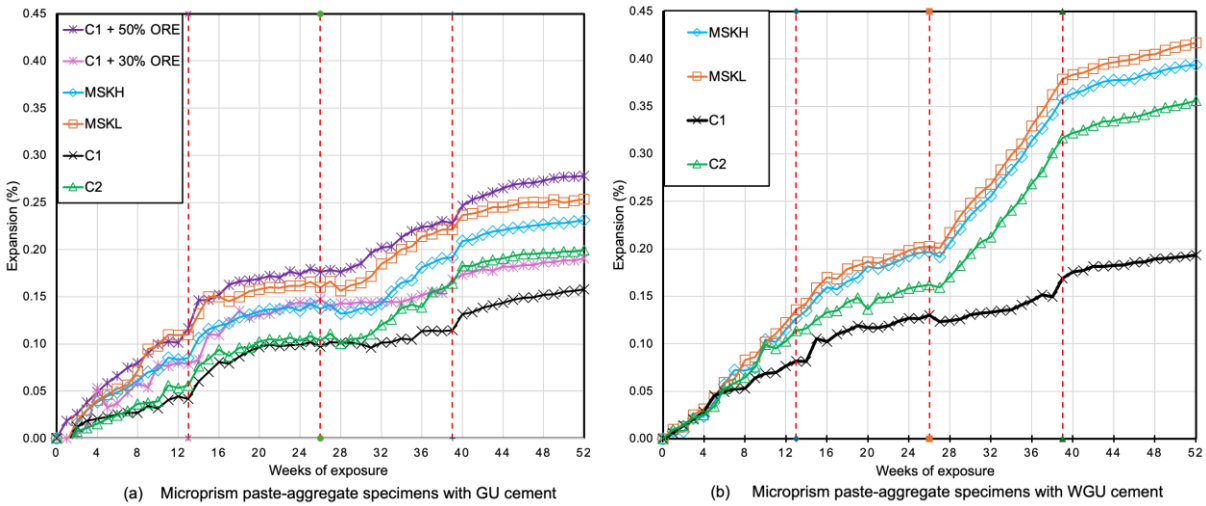

Figure 2-1: Repeated cycle of paste-aggregate testing: (a) specimens with WGU cement; (b) specimens with GU cement.

Although a higher expansion was achieved, the difference in expansion between MSKL and MSKH remains limited, and the expansion of the non-sulphide aggregate (C2) remains high. The result suggests that the wetting and drying cycles could have produced expansion unrelated to sulphide oxidation. Such expansion is manifested in non-carbonate aggregate, which could have suffered deterioration or expansion associated with excessive wetting/drying cycles. This does not mean, however, that all silicate-based aggregates would have suffered from the same effect. Nevertheless, this, in the authors' view, limits the applicability of the test.

2.2 Concrete bleach injection test

To better enhance the permeation of the oxidizing agent (bleach) through the pores of the concrete, the specimens were partially dried at 40 °C/25% RH. This enabled the specimens to achieve about 65% DoS. It was believed that the oxidizing agent would enhance the oxidation of the sulphide minerals within the aggregate. The results are presented in *Figure 2-2* below.

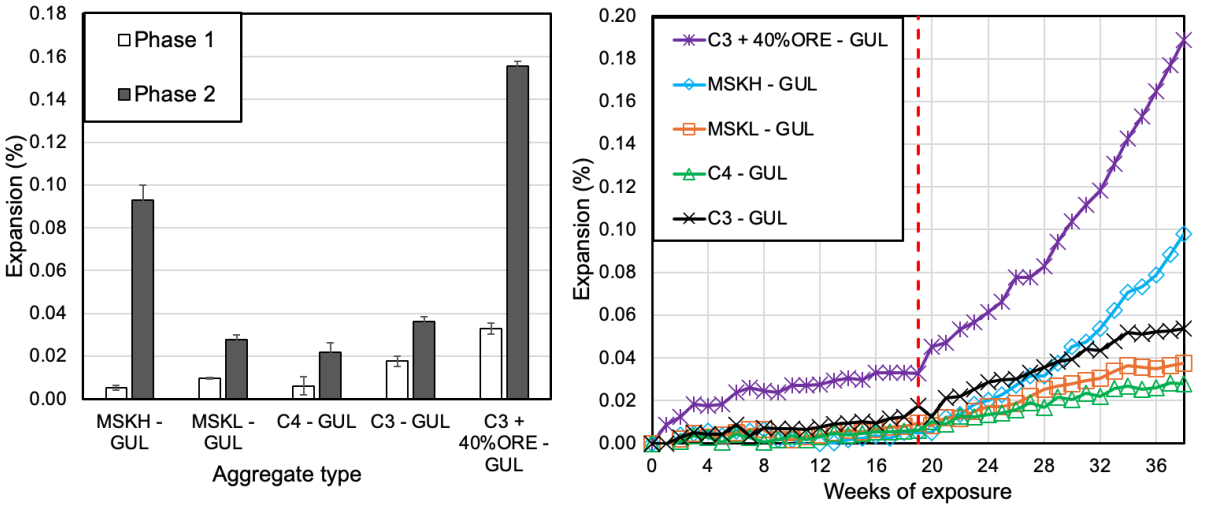

Figure 2-2: Bleach-Injection Conditioning of Concrete Micro-Prism Specimens under a Two-Phase Exposure System (19 Weeks per Phase)

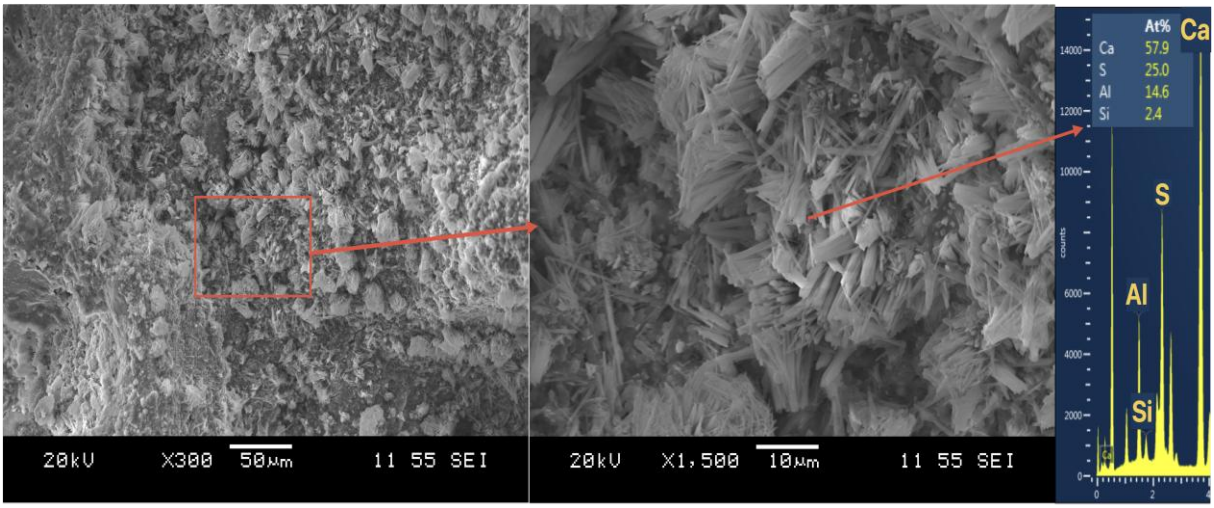

Figure 2-3: SEM-EDS of a fractured concrete surface showing ettringite-like needles in the paste adjacent to MSKH aggregates.

As shown in Figure 2-2, the bleach injection test method on concrete specimens showed a clear distinction between sulphide-bearing and non-sulphide-bearing aggregates. As observed, the oxidation phase, or Phase I (40 °C/75%RH), showed very low expansion, while the sulphate attack phase (5 °C/100%RH) showed very high expansion in the specimen with high TS. During the sulphate attack phase (19 weeks), concrete specimens with MSKH (total sulphur of 0.9%) and C1+40% Ore (total sulphur of 5.6%) showed a 0.093% and 0.155% expansion, respectively. Non-sulphide bearing aggregate specimens showed lower sulphate attack phase expansion as seen with MSKL (0.027%), C4 (0.022%), and C3 (0.033%) expansion. SEM observations obtained from a fractured MSKH-GUL specimen surface show that ettringite is present in abundance and can be readily identified, as illustrated in Figure 2-3. The SEM-EDS analysis confirms that these expansive ettringite-like products form in the paste adjacent to sulphide-bearing MSKH particles, which is consistent with the second-phase expansion measured under the bleach injection test.

It is believed that the partial drying of the concrete specimen to about 65 -70% degree of saturation enhances the ability of the oxidizing agent (bleach) to get through the pores of the concrete. This reaches the aggregate within the concrete and then activates and oxidizes the sulphide mineral phases. The bleach injection cycle enhances oxidation in the first phase of testing (19 weeks), releasing sulphate, which then causes sulphate attack during phase II when the humidity is maintained at 100%. It should be stated that our research team attempted soaking the concrete samples in bleach solution without vacuum application; however, no expansion was achieved within a reasonable time.

3. CONCLUSION

The following conclusions can be drawn from the presented research :

4. The paste-coarse aggregate test presented here appears to cause expansion due to factors other than oxidation of sulphide, particularly in aggregates that are silicate-based.
5. White cement of high fineness and C_3A caused higher expansion in the paste test; the underlying reasons were not confirmed in this study. However, the use of WGU or GU cement caused expansion in non-sulphide silicate-based aggregate under these test conditions.
6. The bleach injection method for concrete is a very promising diagnostic method for evaluating and detecting reactive sulphide-bearing minerals. The second phase expansion can be used as a criterion for discriminating sulphide-bearing from non-sulphide-bearing aggregates. However, more aggregates should be tested to confirm the applicability of the method to a wide range of aggregate compositions.

REFERENCES

[1] Chinchón JS, Ayora C, Aguado A, et al. Influence of weathering of iron sulfides contained in aggregates on concrete durability. Cem Concr Res 1995;25:1264–72.

[2] Jana D. Pyrrhotite epidemic in Eastern Connecticut: diagnosis and prevention. ACI Mater J 2020;117:61–70.

[3] Duchesne J, Fournier B. Deterioration of Concrete by the Oxidation of Sulphide Minerals in the Aggregate. Journal of Civil Engineering and Architecture 2013;7:922.

[4] Duchesne J, Rodrigues A, Fournier B. Concrete damage due to oxidation of pyrrhotite-bearing aggregate: a review. RILEM Technical Letters 2021;6:82–92.

[5] Wang X. Exploring conditions leading to self-heating of pyrrhotite-rich materials. McGill University, 2007.

[6] Ramos V, Rodrigues A, Fournier B, et al. Development of a quick screening staining test for detecting the oxidation potential of iron sulfide-bearing aggregates for use in concrete. Cem Concr Res 2016;81:49–58. https://doi.org/https://doi.org/10.1016/j.cemconres.2015.11.011.

[7] Rodrigues A, Duchesne J, Fournier B. Quantitative assessment of the oxidation potential of sulfide-bearing aggregates in concrete using an oxygen consumption test. Cem Concr Compos 2016;67:93–100.

[8] El-Mosallamy M, Shehata M. Effects of sample preparation on the results of the oxygen consumption test used to evaluate oxidation potential of sulphide-bearing aggregate. CSCE Conference, vol. 555, 2017, p. 1–10.

[9] Guirguis B, Shehata MH. A new screening test to evaluate the presence of oxidizable sulphide minerals in coarse aggregates. Constr Build Mater 2017;154:1096–104.

[10] CSA Group (Canadian Standards Association). CSA A23.1/A23.2:19 — Concrete Materials and Methods of Concrete Construction / Test Methods and Standard Practices for Concrete. Toronto: 2019.

[11] Rodrigues A, Duchesne J, Fournier B. A new accelerated mortar bar test to assess the potential deleterious effect of sulfide-bearing aggregate in concrete. Cem Concr Res 2015;73:96–110.

ICISR 2026

2nd International Conference on Iron-Sulfide Reactions in Concrete

Student Talks:
Experimental Studies on Sulfide-Bearing Aggregates and Concrete

UCONN | COLLEGE OF ENGINEERING
SCHOOL OF CIVIL AND ENVIRONMENTAL ENGINEERING

UCONN
COLLEGE OF ENGINEERING
CONNECTICUT TRANSPORTATION INSTITUTE (CTI)

Phase Evolution of Iron Oxyhydroxides in Pyrrhotite-Containing Concrete under Electrochemical Accelerated Testing

Aagya Dahal [(1)], Lesley Frame [(2)], Kay Wille [(3)]

(1) PhD Student, School of Civil and Environmental Engineering, University of Connecticut (UConn), Storrs, USA, aagya.dahal@uconn.edu

(2) Associate Professor, Department of Materials Science and Engineering, UConn, Storrs, USA, lesley.frame@uconn.edu

(3) Professor, School of Civil and Environmental Engineering, UConn, Storrs, USA, kay.wille@uconn.edu

Abstract

An electrochemical accelerated test was performed to investigate early-stage deterioration and Fe-bearing corrosion product formation in pyrrhotite-aggregate bearing concrete under OH–Cl reverse-polarity exposure. The concrete mixture contained CA1 pyrrhotite-bearing aggregates in three of the four aggregate size fractions, while the remaining fraction consisted of non-pyrrhotite aggregates. This mix was subjected to 60 V for three days between the NaOH cathodic chamber and the NaCl anodic chamber. The applied potential drove ion migration across the concrete, with OH^- flux from the cathode and Cl^- flux from the anode creating steep chemical gradients that promoted oxidation of pyrrhotite-bearing aggregate particles. Under these conditions, pyrrhotite oxidation is expected to release Fe^{2+}, which can subsequently hydrolyze and oxidize to Fe^{3+}, leading to the formation of iron oxyhydroxide type products. Visible cracking and reddish-brown corrosion staining suggest an early deterioration stage associated with the formation and accumulation of Fe-bearing oxidation products. Scanning electron microscopy, supported by qualitative energy-dispersive X-ray spectroscopy, revealed morphologies most consistent with γ-FeOOH (lepidocrocite) as the predominant corrosion product, characterized by thin, flaky, plate-like structures forming flowery rust layers. Additional morphologies consistent with α-FeOOH (goethite), ferrihydrite, and minor β-FeOOH (akaganeite) were also observed, suggesting a possible transformation pathway under accelerated conditions. Within the duration of this test and in the examined regions, the observed damage appeared to be primarily associated with Fe-bearing oxidation products. Although pyrrhotite oxidation can release sulfate, no clear microstructural evidence of gypsum or ettringite-dominated secondary sulfate attack was observed within the duration of this study. The results indicate that electrochemical acceleration appears to capture important features of early-stage deterioration dominated by iron oxidation processes

Keywords: chemical gradients, corrosion product, iron oxyhydroxide

1. INTRODUCTION

The crumbling of concrete foundations in residential buildings has emerged as a pressing problem in several parts of the world. In Northeastern Connecticut, South-central Massachusetts, and the Trois-Rivières area of Quebec (Canada), thousands of homes have been affected, and similar cases have also been documented in Spain and Ireland [1–3]. A common cause behind these failures is the presence of the iron sulfide mineral pyrrhotite ($Fe_{1-x}S$) in quarried aggregates. Once incorporated into concrete, pyrrhotite can become unstable under favorable moisture, oxygen, and chemical exposure conditions. With time, pyrrhotite can oxidize, releasing iron species and sulfate that may contribute to the formation of expansive reaction products and microstructural damage [4]. These reactions disrupt the concrete's microstructure and reduce service life.

Although the mechanisms of pyrrhotite oxidation are well documented, the rate of deterioration can vary widely depending on local conditions. In Connecticut and Massachusetts, visible cracking in foundations may take decades to develop, making field monitoring and laboratory simulation a slow process [2,5]. By contrast, in the Trois-Rivières region of Quebec, foundations built with pyrrhotite-bearing aggregates have shown serious cracking in as little as 2–4 years after construction [6]. The long latency period observed in Connecticut and Massachusetts makes it difficult to evaluate deterioration mechanisms, assess risk, and test mitigation strategies within practical timeframes. To shorten this timescale, researchers have been experimenting with accelerated test methods [7]Among the available approaches, electrochemical acceleration is promising because it can impose strong ionic gradients and accelerate oxidation-related deterioration. By applying an external potential across a specimen, ion migration is forced and aggressive chemical gradients are created, allowing selected oxidation-related deterioration processes to be accelerated within days [7–9].

The present work applies this method to examine the formation and possible evolution of Fe-bearing oxidation products in concrete containing pyrrhotite-bearing aggregates. In our setup, the specimen was positioned between a sodium hydroxide (NaOH) cathodic chamber and a sodium chloride (NaCl) anodic chamber. A voltage was applied so that hydroxide (OH^-) and chloride (Cl^-) ions migrated simultaneously into the concrete. These opposing fluxes generated highly aggressive conditions, promoting pyrrhotite oxidation and the formation of Fe-bearing corrosion products. The study focuses on documenting the morphologies of these corrosion-products, comparing them with known iron oxyhydroxide forms, and discussing their possible role in early-stage cracking and deterioration.

2. MATERIALS AND METHODS

2.1 Materials

The concrete mix in this study was prepared using Ordinary Portland Cement (OPC) Type I/II, conforming to ASTM C 150 [10]. Pyrrhotite-containing CA1 aggregate sourced from the Trois-Rivières area of Quebec, Canada, was used for two coarse aggregate size fractions: particles passing the 16 mm sieve and retained on the 12.7 mm sieve, and particles passing the 9.5 mm sieve and retained on the 4.8 mm sieve. For the fine aggregate fractions, the material passing the 4.8 mm sieve and retained on the 1.18 mm sieve consisted of river sand, whereas the fraction passing the 1.18 mm sieve consisted of the same CA1 pyrrhotite-containing aggregate. The four aggregate size fractions were proportioned equally, with each fraction representing 25% of the total aggregate fraction. The water-cement ratio was 0.6, and air entrainment was 1.50 %.

2.2 Preparation of cylindrical samples

Concrete cylinders of 76 mm by 152 mm (3" by 6") in size were cast and cured at 95% RH for 28 days in accordance with ASTM C192/C192M-19 [11]. Before testing, the samples were prepared as described in [9].

2.3 Accelerated Testing

An electrochemical accelerated testing setup based on the procedure described in [9] was used to impose ionic migration through the concrete cylinder. The concrete cylinders were subjected to an applied potential of 60 V for three days between a NaOH cathodic chamber and a NaCl anodic chamber. This configuration is referred to as the OH–Cl reverse exposure condition because the hydroxide-rich

chamber was placed on the cathodic side and the chloride-rich chamber on the anodic side, opposite to the normal Cl–OH configuration described in [9].

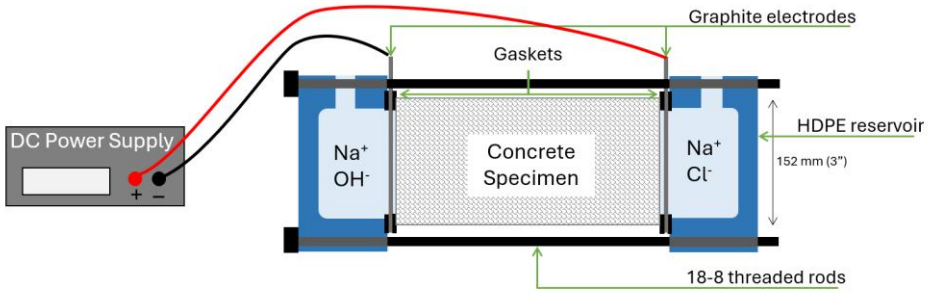

Figure 2.1. Configuration of experimental procedure (Adapted from Ojo et al. [9])

2.4 Relevant Oxidation Reactions and Expected Fe-Bearing Products

In the presence of water and oxygen, pyrrhotite can oxidize and release ferrous iron, which may further oxidize to ferric iron and precipitate as ferric hydroxide or iron oxyhydroxide phases when the local chemical conditions are favorable [12,13]. Fe^{2+} may oxidize to Fe^{3+} and precipitate as ferric hydroxide or iron oxyhydroxide phases, including ferrihydrite, goethite-like phases, and other FeOOH polymorphs depending on local pH, oxygen availability, chloride concentration, and exposure conditions.

$$Fe_{1-x}S + (2-x/2)\,O_2 + x\,H_2O \longrightarrow (1-x)\,Fe^{2+} + SO_4^{2-} + 2x\,H^+$$

$$Fe^{2+} + \tfrac{1}{4}\,O_2 \longrightarrow Fe^{3+} + \tfrac{1}{2}\,H_2O$$

$$Fe^{3+} + 3H_2O \longrightarrow Fe(OH)_3 + 3H^+$$

$$Fe(OH)_3 \longrightarrow \alpha\text{-FeOOH or } \gamma\text{-FeOOH} + H_2O$$

$$2FeOOH \longrightarrow Fe_2O_3 + H_2O$$

The following flowchart shows a color-coded phase evolution of pyrrhotite oxidation.

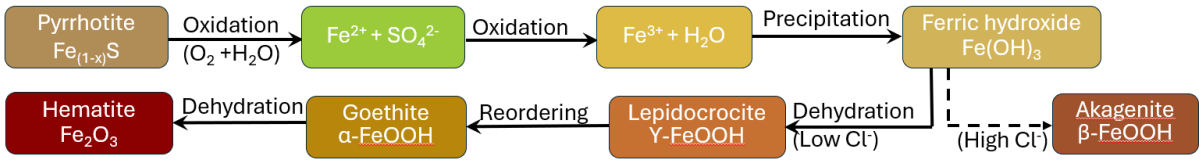

Figure 2.2. Conceptual pathway for possible Fe-bearing product formation during pyrrhotite oxidation.

2.5 Microstructural Investigation

Microstructural analysis was performed by using Scanning Electron Microscopy (Teneo, FEI, USA) supported by qualitative Energy Dispersive X-ray Spectroscopy (EDS) point scanning to assess local elemental composition. SEM specimens were collected from jaw-crushed fragments obtained from the broken half of the tested cylinder. Fragments showing orange to brown discoloration were prioritized because these regions were expected to contain Fe-bearing oxidation products. Imaging was conducted in backscattered electron mode using the T1 detector under high vacuum, with a beam current of 3.2 nA and an accelerating voltage of 15 kV. EDS point analyses were performed at selected locations corresponding to the SEM-imaged Fe-rich products.

3. RESULTS AND DISCUSSION

3.1 Formation of Iron Oxyhydroxides

The observed corrosion products were Fe-rich and displayed morphologies consistent with iron oxyhydroxide-type products, including features resembling γ-FeOOH-like lepidocrocite. These features

appeared as thin, flaky, plate-like crystals arranged in flower-like rust structures. In addition, cotton ball-like, acicular, and rod-like Fe-rich morphologies were observed; these features are morphologically consistent with ferrihydrite-like, goethite-like, and other FeOOH-type products reported in the literature. The coexistence of these different Fe-rich morphologies may indicate a possible phase-evolution pathway under the imposed electrochemical conditions; however, the sequence of formation cannot be confirmed from the present SEM/EDS observations alone. Figure 3.1 shows the SEM micrographs of Fe-rich corrosion products observed after electrochemical acceleration.

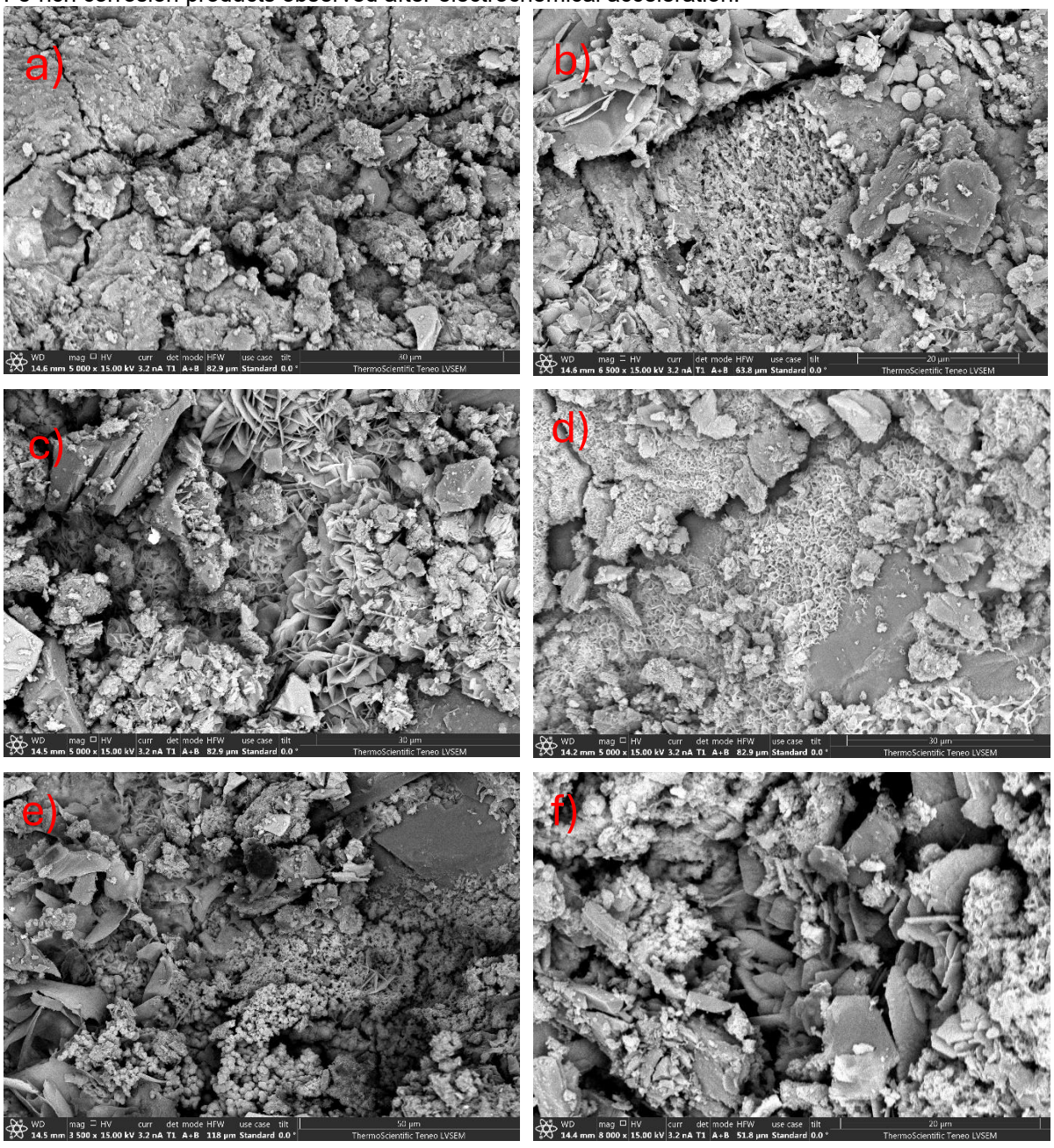

Figure 3.1. SEM micrographs showing representative Fe-rich corrosion products observed after electrochemical acceleration: (a) cotton ball-like morphology consistent with ferrihydrite-like products; (b) Fe-rich corrosion front; (c) transitional FeOOH-like morphology; (d) plate-like morphology consistent with lepidocrocite-like products; (e) acicular morphology consistent with goethite-like products; and (f) oxide-like Fe-rich product morphology.

3.2 Expansion and Cracking

The observed cracking, surface deterioration, and reddish-brown staining are consistent with early-stage damage associated with Fe-bearing oxidation-product formation. The cracking and reddish-brown staining suggest that the formation and accumulation of Fe-bearing oxidation products contributed to local internal stresses and early damage development. Because substantial cracking and deterioration developed during the exposure, the test was stopped after three days to prevent further specimen damage and loss of test integrity.

3.3 Lack of Clear Microstructural Evidence for Sulfate-Driven Secondary Products

Although pyrrhotite oxidation has the potential to release sulfate, no clear SEM-based evidence of progression to a sulfate-driven secondary deterioration stage was observed in the examined regions within the duration of this test. Within the SEM-observed regions, features clearly attributable to expansive ettringite or gypsum were not observed. The observed damage appeared to be primarily associated with Fe-bearing oxidation-product formation. This outcome suggests that, under the short-duration reverse-polarity conditions used in this study, the observed early-stage degradation was governed primarily by iron oxidation processes rather than by clearly detectable sulfate-driven product formation.

4. CONCLUSION

The results indicate that reverse-polarity electrochemical testing can accelerate early-stage deterioration in pyrrhotite-bearing concrete. The observed corrosion products were Fe-rich and included morphologies consistent with iron oxyhydroxide-type products, including lepidocrocite-like, ferrihydrite-like, and goethite-like features. The associated cracking and deterioration are consistent with early-stage damage linked to the formation and accumulation of Fe-bearing oxidation products. Within the duration of this study and in the examined SEM regions, no clear evidence of sulfate-driven secondary products was observed. These findings highlight the importance of iron oxidation processes in early deterioration and support the potential use of electrochemical methods as rapid screening tools for pyrrhotite-bearing concrete.

REFERENCES

[1] Zhong R, Wille K. Deterioration of residential concrete foundations: The role of pyrrhotite-bearing aggregate. Cem Concr Compos 2018;94:53–61. https://doi.org/https://doi.org/10.1016/j.cemconcomp.2018.08.012.

[2] Jana D. Cracking of residential concrete foundations in eastern Connecticut, USA from oxidation of pyrrhotite. Case Studies in Construction Materials 2022;16:e00909. https://doi.org/https://doi.org/10.1016/j.cscm.2022.e00909.

[3] Rodrigues A, Duchesne J, Fournier B, Durand B, Rivard P, Shehata M. Mineralogical and chemical assessment of concrete damaged by the oxidation of sulfide-bearing aggregates: Importance of thaumasite formation on reaction mechanisms. Cem Concr Res 2012;42:1336–47. https://doi.org/https://doi.org/10.1016/j.cemconres.2012.06.008.

[4] Duchesne J, Rodrigues A, Fournier B. Concrete damage due to oxidation of sulfide-bearing aggregate: A review of recent advances and limitations. RILEM Technical Letters 2021;6:82–92. https://doi.org/10.21809/rilemtechlett.2021.138.

[5] Drake O. Researchers Aim to Predict the Probability of Concrete Foundation Failure in Connecticut Homes. UConn Today 2024.

[6] Bérubé MA, Tremblay C, Gagnon F, Ross B. Concrete damage due to pyrrhotite in the Trois-Rivières area (Québec, Canada): risk of future damage to undamaged concrete. Canadian Journal of Civil Engineering 2025;52:2480–8. https://doi.org/10.1139/cjce-2024-0474.

[7] Castillo Araiza R, Rodrigues A, Fournier B, Duchesne J. A new accelerated testing scheme to evaluate the potential oxidation reaction of sulfide-bearing aggregates in concrete specimens. Cem Concr Res 2024;180:107507. https://doi.org/https://doi.org/10.1016/j.cemconres.2024.107507.

[8] Castillo Araiza R, Fournier B, Duchesne J, Fecteau P-L, Rodrigues A. Evaluation of detrimental effects in concrete specimens due to the oxidation of sulfide-bearing aggregates after electrochemical treatment. Constr Build Mater 2024;411:134341. https://doi.org/https://doi.org/10.1016/j.conbuildmat.2023.134341.

[9] Ojo M, Kim D, Frame L, Wille K. Electrochemical investigation of accelerated deterioration of concrete with iron-sulfide containing aggregates. Cem Concr Res 2024;182. https://doi.org/10.1016/j.cemconres.2024.107570.

[10] ASTM International. ASTM C150/C150M-22 Specification for Portland Cement. 2022.

[11] ASTM C192/C192M-19 Standard Practice for Making and Curing Concrete Test Specimens in the Laboratory. 2024.

[12] Belzile N, Chen YW, Cai MF, Li Y. A review on pyrrhotite oxidation. J Geochem Explor 2004;84:65–76. https://doi.org/10.1016/j.gexplo.2004.03.003.

[13] Nicholson R V, Scharer JM, Kwong ECM, Janzen MP. Inco Limited Centre Technologie Noranda Principal Investigators Research Assistants. 1998.

Performance Evaluation of Sulfide-Bearing Aggregates in Mortar Bars under Accelerated Oxidation Conditions

Sampa Akter and Kay Wille

School of Civil and Environmental Engineering, University of Connecticut, Storrs, Connecticut, USA, Email: sampa.akter@uconn.edu, kay.wille@uconn.edu,

Abstract

Oxidation of iron sulfide–bearing aggregates in concrete can lead to expansive reactions, cracking, and premature structural deterioration. Accelerated laboratory methods are required to evaluate this mechanism within practical timeframe. This study evaluates sodium hypochlorite (NaOCl)–based mortar-bar testing by examining the coupled effects of oxidant transport and solution chemistry under accelerated exposure conditions. Four sulfide-bearing aggregates with documented field deterioration histories and one non-reactive reference aggregate were investigated. The total sulfur content of the mortar mixtures ranged from 0.30 to 1.25 wt.%. Three 6% NaOCl exposure strategies were examined: short-duration immersion, long-term static submersion, and vacuum-assisted impregnation with limited immersion time. Expansion behavior was evaluated as a function of temperature, relative humidity, aggregate type, sulfur content, and particle size. The results demonstrate that oxidant availability is the primary rate-controlling factor governing sulfide oxidation in mortar bars. Elevated temperature (80°C) and controlled relative humidity (80%) significantly accelerated expansion relative to atmospheric exposure. However, prolonged static submersion in 6% NaOCl resulted in hypochlorite depletion and pH reduction, leading to chemically exhausted conditions and suppressed oxidation kinetics, particularly in sulfur-rich systems. Aggregate mineralogy and particle size were found to exert a stronger influence on deterioration severity and cracking behavior than total sulfur content alone. Overall, the findings indicate that effective accelerated testing requires balancing oxidant delivery with chemical stability. Short-duration and vacuum-assisted 6% NaOCl exposure protocols provide a more mechanistically consistent and reliable basis for performance-based screening of sulfide-bearing aggregates.

Keywords: *accelerated mortar bar test; oxidation; sulfide-bearing aggregates; sodium hypochlorite; wet–dry cycling.*

1. INTRODUCTION AND MOTIVATION

Concrete deterioration associated with the oxidation of iron sulfide–bearing aggregates has been widely documented in regions such as northeastern United States, Canada, and Ireland [1–7]. Oxidation of sulfide minerals, primarily pyrrhotite, produces ferric iron, sulfate ions, and acidity, which in turn promotes the formation of expansive reaction products that cause cracking, stiffness loss, and progressive structural distress. Unlike alkali–silica reaction, sulfide oxidation is governed by strongly coupled transport–reaction processes involving oxygen availability, moisture conditions, solution chemistry, and sulfide mineralogy, which complicates laboratory evaluation [6]. Accelerated laboratory methods have therefore relied on elevated temperature, high relative humidity, and chemical oxidants to reproduce field-relevant deterioration within practical timeframes. Rodrigues et al. [8] demonstrated that short-term immersion in sodium hypochlorite (NaOCl) can induce expansion in mortar bars containing sulfide-bearing aggregates. However, subsequent studies [9–11] have shown that test outcomes are sensitive to oxidant penetration, exposure duration, and changes in solution chemistry, particularly under prolonged or static exposure. The present study systematically investigates the influence of oxidant availability and environmental conditions on the expansion of sulfide-bearing aggregates in mortar bars. The effects of temperature, relative humidity, aggregate type, sulfur content, and particle size are examined together with different NaOCl exposure strategies. In addition to conventional short-duration NaOCl immersion, long-term static NaOCl submersion is evaluated to assess its limitations, as prolonged exposure can reduce oxidizing effectiveness and influence measured expansion. To address this drawback, vacuum-assisted NaOCl impregnation is introduced as a new approach and evaluated within the broader parametric framework to improve oxidant access while avoiding extended solution exposure.

2. MATERIALS AND EXPERIMENTAL METHODS

Four sulfide-bearing aggregates with documented field deterioration histories were investigated: two Canadian aggregates (CA1 and CA2) sourced from an anorthosite–gabbro formation and two Connecticut aggregates (CT1 and CT2) derived from granitic gneiss and schist. These materials contain varying proportions of pyrrhotite and pyrite [1–2]. A non-reactive river sand (R) with negligible sulfur content (<0.1 wt.%) was used as the reference aggregate. Total sulfur content (ST, wt.%) was quantified by combustion analysis, and the sulfur contents of all sulfide-bearing aggregates and the reference sand are summarized in Table 2.1. Mortar bars (25 × 25 × 285 mm) were cast to evaluate expansion behavior. Three replicate specimens were prepared for each aggregate condition using ASTM C150 [12] Type I/II Portland cement, with a water-to-cement ratio of 0.65 and a cement-to-aggregate ratio of 1:2.73 by mass. These mixture proportions were selected to represent the relatively high porosity characteristic of residential foundation concretes affected by sulfide oxidation in Canada and Connecticut [1, 5]. Aggregate particle sizes generally followed ASTM C1260 [13] guidelines. However, additional mixtures incorporating coarser aggregate fractions (16–4.75 mm and 9.5–4.75 mm) were prepared to investigate the influence of particle size on expansion behavior (Figure 3.2b). Mixing, casting, and curing procedures generally followed ASTM C1260 [13], with titanium gauge studs used to prevent corrosion-related measurement artifacts. Specimens were moist cured at 23 ± 2°C for 72 h prior to demolding. Initial length measurements were recorded in accordance with ASTM C490 [14], establishing the reference length for subsequent expansion monitoring

Table 2.1: Total sulfur content of reactive and non-reactive aggregates.

Aggregates source	IDs	Total sulfur content (% by wt.)
Connecticut aggregates	CT1	1.005±0.03
	CT2	0.786±0.03
Canadian aggregates	CA1	1.156 ±0.02
	CA2	1.245 ±0.008
River sand	R	0.034±0.01

Three NaOCl-based exposure protocols were evaluated to investigate oxidation-induced deterioration kinetics (Figure 2.1):

1. Short-duration cyclic immersion (Cycle #1): Specimens were immersed in 6 % NaOCl for 3 h, twice per week, followed by sealed exposure in an environmental chamber, where specimens were stored in closed containers under controlled temperature and relative humidity to minimize moisture exchange with the surroundings. This protocol served as the baseline and was adapted from Rodrigues et al. [8].
2. Long-term static submersion (Cycle #2): Specimens were continuously submerged in 6 % NaOCl for approximately one week using the same solution, followed by sealed exposure under controlled temperature and relative humidity conditions for an additional one week.
3. Vacuum-assisted exposure (Cycle #3): Specimens were vacuum-impregnated in 6 % NaOCl for 15 min, followed by 3 h immersion, conducted twice per week, and then subjected to sealed exposure under controlled temperature and relative humidity conditions.

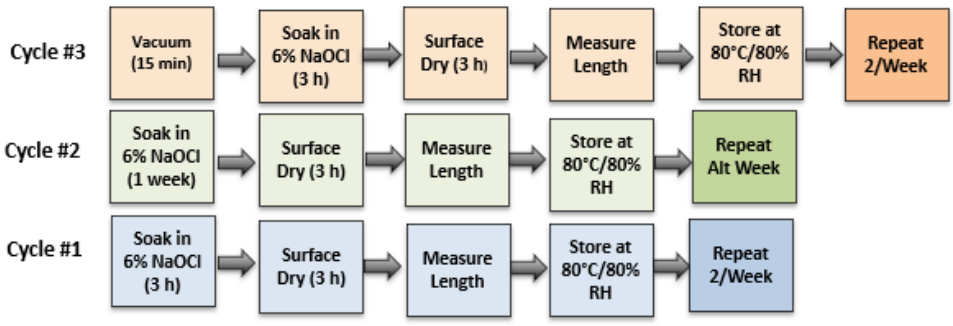

Figure 2.1. Schematic representation of accelerated oxidation–expansion testing cycles (Cycle #1: baseline after Rodrigues et al. [8]; Cycles #2–3: parametric investigations).

Each cycle represents an independent exposure condition applied to separate sets of specimens. The specimens were not subjected sequentially to multiple cycles.

Between exposure cycles, specimens were cooled to room temperature (23°C) prior to length measurements. NaOCl solutions were renewed biweekly unless otherwise noted. Temperature (23, 60, and 80°C), relative humidity (~80–95%), aggregate type, total sulfur content, and aggregate particle size were systematically varied to isolate their effects on deterioration behavior.

Temperature conditions (23, 60, and 80°C) were applied within Cycle #1 to evaluate the influence of thermal conditions on oxidation behavior.

It is noted that the present study evaluates system-level responses under different exposure conditions and does not isolate all chemical contributions to solution evolution (e.g., natural NaOCl aging versus specimen-driven reactions).

3. RESULTS AND DISCUSSION

3.1 Oxidant availability and environmental exposures

Figures 3.1a to 3.1d show the effect of oxidizing solutions (6% NaOCl), temperature, low temperature transfers, relative humidity on the expansion behavior of mortar bars containing sulfide-bearing aggregates.

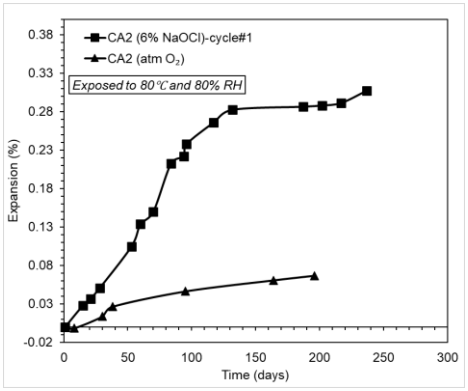

(a) Effect of 6% NaOCl

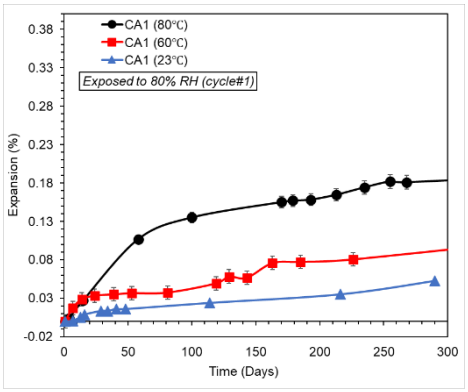

(b) Effect of temperature

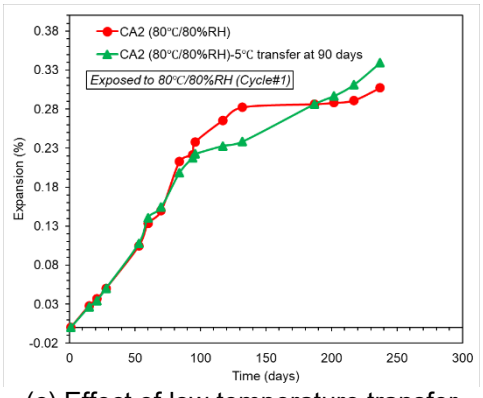

(c) Effect of low temperature transfer

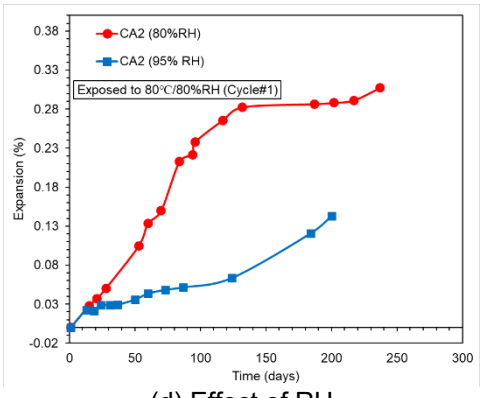

(d) Effect of RH

Figure 3.1. Effect of environmental exposures on the expansion of sulfide-bearing aggregate.

Specimens exposed exclusively to atmospheric oxygen exhibited negligible expansion, even under elevated temperature (80°C) and high relative humidity (80 % RH), indicating that thermal and moisture effects alone are insufficient to drive sulfide oxidation in mortar bars, even after 200 days of exposure. In contrast, exposure to 6 % NaOCl induced rapid and pronounced expansion, exceeding 0.10% within two months, demonstrating that oxidant availability is the dominant rate-controlling factor governing sulfide oxidation kinetics. For example, CA2 mortar bars exposed to 6 % NaOCl under Cycle #1 at 80°C and 80 % RH reached an expansion of 0.29% at 150 days, whereas companion specimens subjected to identical thermal and humidity conditions under atmospheric oxygen exhibited only 0.06% expansion

over the same period (Figure 3.1a). Temperature strongly amplified the influence of oxidant availability by increasing reaction kinetics and reducing solution viscosity, which can enhance ionic mobility and diffusion within the pore solution, as illustrated in Figure 3.1b. CA1 mortar bars exposed at 23℃ exhibited minimal expansion (0.03%), whereas exposure at 60℃ initiated moderate expansion (0.06%) after 150 days. In contrast, specimens exposed at 80℃ developed rapid expansion, reaching 0.29%, accompanied by visible cracking that initiated between 70 and 80 days. These results indicate a temperature-driven transition from transport-limited to reaction-dominated sulfide oxidation at elevated temperature. When specimens initially exposed at 80°C were transferred to a low-temperature environment (5°C) at 90 days, a temporary reduction in expansion rate was observed, consistent with reduced reaction kinetics and decreased diffusion rates at lower temperature. However, expansion resumed at later ages despite continued low-temperature exposure. These observations reflect the coupled influence of temperature on both reaction kinetics and transport processes, rather than a single controlling mechanism. Relative humidity (RH) further influenced oxidation behavior by controlling moisture continuity and gas transport within the mortar matrix as shown in Figure 3.1c.
Between 80% and 95% RH, specimens exposed at 80% RH consistently exhibited greater expansion, consistent with transport-controlled oxidation in which excessive saturation limits oxygen diffusion. As shown in Figure 3.1c, mortar bars exposed at 80% RH reached 0.29% expansion at 150 days, whereas those exposed at 95% RH exhibited only 0.09% expansion over the same duration. These results underscore the coupled roles of oxidant availability, temperature, and moisture state in governing sulfide oxidation kinetics and the resulting expansion behavior.

3.2 Role of Sulfur Content and Aggregate Size

Figure 3.2 illustrates the influence of total sulfur content on the mortar and the particle size of sulfide-bearing aggregates on the expansion behavior of mortar bars. At 80°C and 80% RH, the expansion trends across the aggregate set shown in Figure 3.2a reflect the combined influence of total sulfur content (ST) and aggregate mineralogical characteristics, rather than sulfur content alone. To reduce the effect of mineralogical variability, expansion behavior was therefore interpreted primarily through within-source comparisons. The Canadian aggregates CA1 and CA2 originate from the same anorthosite–gabbro formation and thus provide a basis for comparison using the same aggregate source to minimize mineralogical variability. Under identical exposure conditions, mortar bars cast with CA2 aggregates, which contain a higher total sulfur content (ST = 1.25 wt.%), exhibited visible cracking between 70 and 80 days, after which expansion accelerated, reaching approximately 0.31% at 230 days. In contrast, CA1 specimens, with a lower total sulfur content (ST = 1.02 wt.%), exhibited lower overall expansion, reaching approximately 0.17% at 230 days, and did not exhibit visible cracking over the same period. This within-source comparison indicates that sulfur loading contributes to the magnitude of expansion.

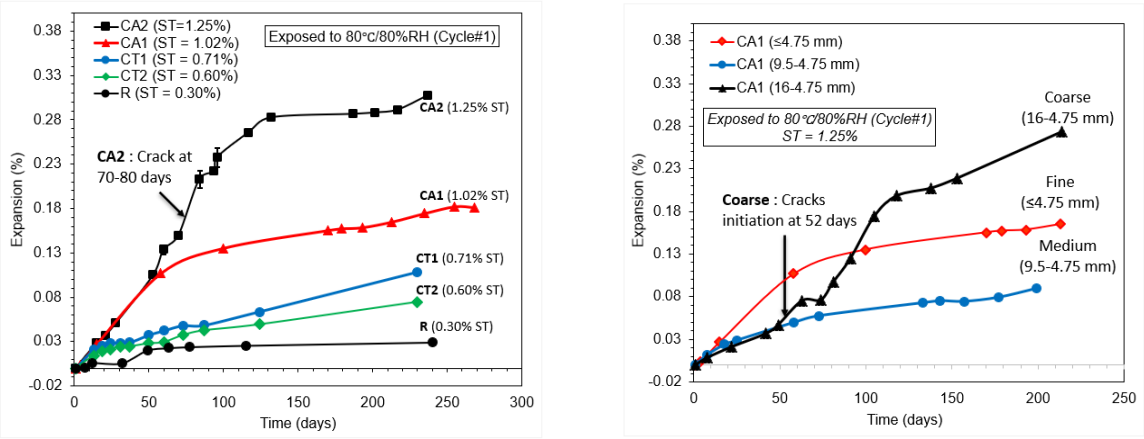

(a) Aggregate type and sulfur content (80℃) (b) Aggregate size

Figure 3.2. Effect of sulfur content and aggregates size on the expansion of sulfide-bearing aggregate.

A similar within-source comparison can be made for the Connecticut aggregates CT1 and CT2, both derived from gneiss–schist lithologies. Under the same exposure conditions, mortar bars cast with CT1 (ST = 0.71 wt.%) exhibited approximately 0.11% expansion at 230 days, whereas those cast with CT2, which has a lower sulfur content (ST = 0.60 wt.%), exhibited only about 0.08% expansion at the same

age. No visible cracking was observed in mortar bars incorporating either Connecticut aggregate through 230 days of exposure. Although the absolute expansions of the Connecticut aggregates were substantially lower than those of the Canadian aggregates, the within-source trend remains consistent with a sulfur-loading effect under a common regional mineralogical context. Mortar bars incorporating the non-reactive reference aggregate exhibited negligible expansion (<0.03%) throughout the exposure period, confirming that the observed expansion was associated with sulfide-bearing aggregates rather than oxidant or thermal and moisture effects alone. No visible cracking was observed in mortar bars incorporating either Connecticut aggregate through 230 days of exposure. Aggregate particle size exerted an additional influence on expansion behavior, particularly on the timing and severity of post-cracking deformation. As shown in Figure 3.2b, CA1 mortar bars containing coarser sulfide-bearing aggregate fractions (16–4.75 mm) did not exhibit higher expansion rates prior to cracking. Instead, pre-cracking expansion rates were slightly lower than those of specimens containing medium (9.5–4.75 mm) and fine (≤4.75 mm) aggregate fractions, consistent with reduced reactive surface area in larger particles. For example, at 50 days, CA1 mortar bars cast with 16–4.75 mm aggregates exhibited an expansion of 0.046%, whereas companion specimens cast with medium and fine aggregate fractions exhibited expansions of 0.047% and 0.095%, respectively. A pronounced divergence in expansion behavior emerged after crack initiation. Cracking initiated earlier in specimens containing coarser aggregates, occurring at approximately 52 days, after which expansion accelerated markedly, reaching 0.26% expansion at 200 days. In contrast, specimens incorporating medium and fine aggregate fractions did not exhibit visible cracking up to 200 days and showed substantially lower expansion, reaching approximately 0.09 and 0.16% at 200 days.

3.3 Effect of 6% NaOCl Exposure Cycles

As shown in Figure 3.3a, Cycle #2 highlights a key limitation associated with prolonged static submersion (1 week) in 6% NaOCl. A progressive reduction in solution pH was observed during the exposure period (Figure 3.3b), indicating that the chemical environment was not maintained under stable oxidizing conditions. The evolution of a reference 6% NaOCl solution (without specimens), also included in Figure 3.3b, exhibits only minor pH variation over time. In contrast, substantially greater pH reductions occur in specimen-containing systems, particularly for mixtures incorporating high-sulfide aggregates (CA2). This pH reduction is critical because sulfide oxidation in cementitious systems is strongly pH dependent. As reported by Divet and Davy [15], oxidation rates increase exponentially above pH ≈ 12.5 and can reach up to 50 times higher at pH ≈ 13.7. Consequently, as the NaOCl solution pH decreased below this highly alkaline regime during Cycle #2, the effective oxidizing capacity diminished, transitioning the system from a kinetically accelerated state to a chemically depleted condition. This effect is most pronounced in mixtures incorporating high-sulfide aggregates (CA2), which exhibited rapid early expansion followed by a clear reduction or plateau in expansion rate despite the continued presence of unreacted sulfide. This behavior indicates that expansion of kinetics became governed by oxidant availability rather than intrinsic material reactivity. As a result, prolonged static NaOCl exposure leads to an underestimation of deterioration severity in systems with high oxidation demand. Accordingly, the observed trends in Cycle #2 primarily reflect oxidant depletion and pH reduction rather than material-controlled reactivity.

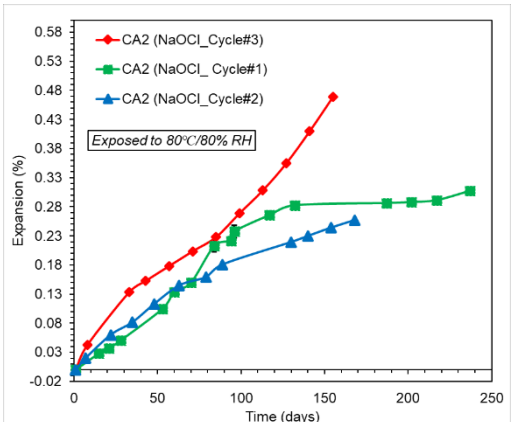

(a) Solution Cycle

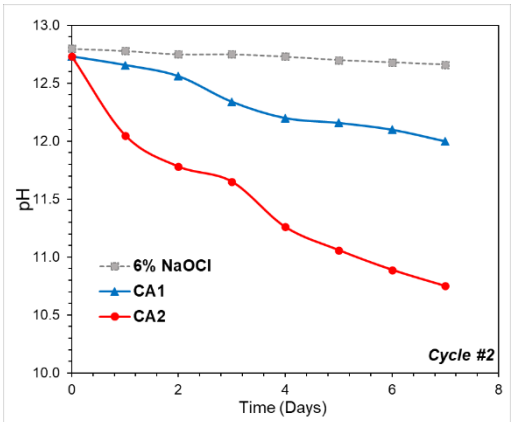

(b) pH

Figure 3.3. Effect of 6% NaOCl exposure protocols on mortar-bar expansion and corresponding changes in solution pH.

In contrast, Cycle #3 enhanced oxidant ingress and sustained early-stage expansion without inducing the chemical exhaustion observed in Cycle #2. By limiting immersion duration while improving transport, this protocol preserved solution alkalinity and oxidizing efficiency. However, Cycle #3 is best interpreted as a short-term intensification method rather than a stand-alone long-term exposure condition. Overall, these results demonstrate that chemical acceleration must be balanced against solution stability. Short-duration NaOCl exposure (Cycle #1) provides a reliable baseline for comparative evaluation, while vacuum-assisted exposure (Cycle #3) enhances sensitivity without compromising chemical control. In contrast, prolonged static submersion (Cycle #2) alters solution chemistry and obscures intrinsic material behavior, limiting its suitability for reliable reactivity assessment.

4. CONCLUSION

Accelerated sulfide oxidation in mortar bars was governed by oxidant availability in combination with temperature, relative humidity, sulfur content, and aggregate characteristics. Under atmospheric oxygen, negligible expansion occurred even at 80 °C and 80 % RH, whereas exposure to 6 % NaOCl produced more than an order-of-magnitude increase in deterioration under the same thermal and moisture conditions. Expansion was maximized at 80 % RH, reduced to 95 % RH due to limited oxygen transport, and temporarily suppressed by cooling from 80 °C to 5 °C, although damage progression resumed with time. Within-source comparisons indicated that higher sulfur content increased expansion magnitude, while aggregate particle size primarily influenced post-cracking behavior, with coarse particles (16–4.75 mm) exhibiting earlier local cracking at 52 days and accelerated post-cracking expansion. Comparison of exposure protocols showed that Cycle #2 (long-term static NaOCl submersion) led to hypochlorite depletion and pH reduction, masking intrinsic material behavior, whereas Cycle #1 (short-duration immersion) provided a stable baseline and Cycle #3 (vacuum-assisted exposure) enhanced early-stage sensitivity without chemical exhaustion. Overall, short-duration and vacuum-assisted NaOCl exposures offer the most reliable balance between acceleration and chemical stability for screening sulfide-bearing aggregates.

5. ACKNOWLEDGEMENT

This research was supported by the U.S. Department of Commerce, National Institute of Standards and Technology (NIST), under award numbers 60NANB20D135, 70NANB21H113, 70NANB23H009 and 60NANB23D187. The authors would like to thank Ryan Soucy, Research Assistant II at the Connecticut Advanced Pavement Laboratory, Harley Jeanty and Shane McLean, undergraduate students at the University of Connecticut, for their valuable assistance with aggregate processing and pulverization, which were vital to the success of this experimental program.

7. REFERENCES

[1]. Zhong R, Ai X, Yao Y, Wang J, Wille K (2024) Effects of the expansion mechanisms on the pyrrhotite-induced deterioration of concrete foundations. Case Stud Constr Mater 20: e02830. https://doi.org/10.1016/j.cscm.2023.e02830

[2]. Zhong R, Wille K (2018) Deterioration of residential concrete foundations: the role of pyrrhotite-bearing aggregate. Cem Concr Compos 94:53–61. https://doi.org/10.1016/j.cemconcomp.2018.08.012

[3]. Akter S, Wille K (2024) Expansion of mortar bars containing reactive iron-sulfide-bearing aggregates. In: Proc 1st Int Conf on Iron-Sulfide Reactions in Concrete, Québec City, Canada, 14–17 May 2024.

[4]. Rodrigues A, Duchesne J, Fournier B, Durand B, Rivard P, Shehata M (2012) Mineralogical and chemical assessment of concrete damaged by the oxidation of sulfide-bearing aggregates: importance of thaumasite formation on reaction mechanisms. Cem Concr Res 42:1336–1347. https://doi.org/10.1016/j.cemconres.2012.06.008

[5]. Duchesne J, Rodrigues A, Fournier B (2021) Concrete damage due to oxidation of pyrrhotite-bearing aggregate: a review. RILEM Tech Lett 6:82–92. https://doi.org/10.21809/rilemtechlett.2021.138

[6]. Leemann A, Lothenbach B, Münch B, Campbell T, Dunlop P (2023) The “mica crisis” in Donegal, Ireland – a case of internal sulfate attack? Cem Concr Res 168:107149. https://doi.org/10.1016/j.cemconres.2023.107149

[7]. Leemann A, Münch B, Lothenbach B, Winnefeld F, Dunlop P (2024) Defective homes in Donegal, Ireland: Effect of exposure conditions and concrete quality on pyrrhotite oxidation and internal sulfate attack. Cem Concr Res 186:107684. https://doi.org/10.1016/j.cemconres.2024.107684

[8]. Rodrigues A, Duchesne J, Fournier B (2015) A new accelerated mortar bar test to assess the potential deleterious effect of sulfide-bearing aggregate in concrete. Cem Concr Res 73:96–110. https://doi.org/10.1016/j.cemconres.2015.02.012

[9]. El-Mosallamy M, Shehata MH (2020) Tests for oxidizable sulfides in aggregates: applicability and limitations. ACI Mater J 117:229–240. https://doi.org/10.14359/51723347

[10]. Guirguis B, Shehata MH, Duchesne J, Fournier B, Durand B, Rivard P (2018) Application of a new oxidation mortar bar test to mixtures containing different cementing systems. Constr Build Mater 173:775–785. https://doi.org/10.1016/j.conbuildmat.2018.04.026

[11]. El-Mosallamy M, Shehata MH (2020) Sulphide oxidation mortar tests for evaluation of the oxidation potential of sulphide-bearing aggregate. Constr Build Mater 264:120627. https://doi.org/10.1016/j.conbuildmat.2020.120627

[12]. ASTM C150/C150M-18 (2018) Standard specification for portland cement. ASTM International, West Conshohocken, PA. https://doi.org/10.1520/C0150_C0150M-18

[13]. ASTM C1260-14 (2014) Standard test method for potential alkali reactivity of aggregates (mortar-bar method). ASTM International, West Conshohocken, PA. https://doi.org/10.1520/C1260-14

[14]. ASTM C490/C490M-21 (2021) Standard practice for use of apparatus for the determination of length change of hardened cement paste, mortar, and concrete. ASTM International, West Conshohocken, PA. https://doi.org/10.1520/C0490_C0490M-21

[15]. Divet L, Davy JP (1996) Étude des risques d'oxydation de la pyrite dans le milieu basique du béton, Bull. Lab. Ponts Chaussées 204: 97–107.

Effect of Specimen Geometry on the Accelerated Deterioration of Iron Sulfide-Bearing Concrete

A T M Masum [(1)], Kay Wille [(2)]

(1) *University of Connecticut, Storrs, CT, United States of America, a_t_m.masum@uconn.edu*

(2) *University of Connecticut, Storrs, CT, United States of America, kay.wille@uconn.edu*

Abstract

Concrete foundations containing iron sulfide-bearing aggregates have experienced severe deterioration in regions such as northeastern United States and other parts of the world. Accelerated electrochemical methods on cylindrical concrete specimen enable replication of sulfide-induced damage within laboratory timeframes. This study systematically investigates the effect of specimen geometry on the accelerated deterioration of concrete containing iron sulfide-bearing aggregates. Concrete cylinders were prepared using iron-sulfide bearing aggregates from Canada with three diameters (51, 76, and 102 mm) and three target L/D ratios (2.0, 1.0, and 0.5). Deterioration was induced using a longitudinal electrochemical acceleration method and monitored using bulk electrical resistivity, dynamic elastic modulus, and visual cracking. Oxidation initiation occurred at similar times for all specimens; however, shorter specimens and lower L/D ratios exhibited substantially faster resistivity reduction, stiffness loss, earlier cracking, and reduced time to failure. Specimen length and L/D ratio govern deterioration kinetics by controlling transport length, while diameter plays a secondary role. The results demonstrate that specimen geometry must be explicitly considered when interpreting accelerated test results from non-standard field cores.

Keywords: *Iron-sulfide, Concrete deterioration, Geometric configuration, L/D ratio, Time to failure*

6. INTRODUCTION

Concrete foundations in northeastern United States and other parts of the world have exhibited progressive cracking and structural degradation due to oxidation of iron sulfide-bearing aggregates, primarily pyrrhotite (Po) and pyrite (Py) [1-2]. Oxidation of these minerals produces volumetrically expansive iron oxides and oxyhydroxides, followed by sulfate generation and secondary expansive reactions, leading to internal stresses, cracking, stiffness degradation, and eventual structural failure [2,3]. The severity and rate of deterioration vary widely depending on aggregate mineralogy, sulfur content, moisture availability, and exposure conditions [2-4]. Because natural oxidation progresses over years and decades, accelerated electrochemical methods adapted from NT BUILD 492 and ASTM C1202 have been developed to reproduce sulfide-induced deterioration within laboratory timeframes [5-8]. These methods have been shown to capture key features observed in field-affected foundations, including stiffness loss, transport property changes, and cracking [7,8]. A critical limitation arises when applying these methods to field-extracted cores. While standard laboratory specimens typically employ length-to-diameter (L/D) ratios of approximately 2.0, field cores often vary in length and could be substantially shorter due to drilling constraints. This geometric deviation alters transport distance, effective electric field intensity, and damage localization, thereby directly influencing deterioration kinetics. Despite its practical importance, the role of specimen geometry in accelerated sulfide-induced deterioration has not been systematically quantified.

The present study addresses this knowledge gap. Concrete cylinders prepared using natural aggregates sourced from Québec, Canada (CA1) were tested using three diameters (51, 76, and 102 mm) and three target L/D ratios (2.0, 1.0, and 0.5). A validated electrochemical acceleration method was employed to induce iron sulfide oxidation [7], and deterioration progression was monitored using non-destructive indicators, including bulk electrical resistivity and dynamic elastic modulus, supplemented by qualitative visual assessment of cracking and failure progression. By isolating geometric effects while maintaining identical material composition and exposure conditions, this study clarifies the relative roles of specimen length, diameter, and L/D ratio in controlling deterioration kinetics. These findings establish a mechanistic framework for interpreting accelerated test results from laboratory specimens with non-standard geometries and strengthening the relevance of laboratory testing for evaluating iron sulfide-bearing concrete.

7. MATERIALS AND METHODS

7.1 Materials

Iron sulfide-bearing coarse aggregates (CA1) were sourced from Trois-Rivières, Québec, Canada, a region known for sulfide-induced concrete deterioration. The coarse aggregate was separated into two size fractions: CA-S (9.5-4.75 mm; US Sieve No. 3/8″-4) and CA-L (16.0-12.5 mm; Sieve No. 5/8″-1/2″). Natural river sand with negligible sulfur content was used as fine aggregate (FA) and divided into FA-L (4.75-1.18 mm; Sieve No. 4-No.16) and FA-S (< 1.18 mm; passing Sieve No.16). Type I Ordinary Portland Cement served as the binder. Total sulfur contents (ST) were 1.15 wt.% for cement, 0.02 wt.% for FA, and 0.88 wt.% for CA1. All mixtures were proportioned at a constant water-to-cement ratio of 0.60 with an air-entraining admixture. The mixture proportions are summarized in Table 1.

Table 1: Concrete mixture proportions

Cement (kg/m^3)	Water (kg/m^3)	Air-entrainer (kg/m^3)	FA-S (kg/m^3)	FA-L (kg/m^3)	CA-S (kg/m^3)	CA-L (kg/m^3)
386.5 (1*)	231.7 (0.60*)	0.348 (0.0009*)	394.4 (1.02*)	394.4 (1.02*)	394.4 (1.02*)	394.4 (1.02*)

*Value in parentheses indicates quantity relative to cement mass.

7.2 Concrete Mix Design and Sample Preparation

Concrete cylinders with nominal diameters of 51, 76, and 102 mm were cast and moist cured. Specimens were then cut to achieve target L/D ratios of approximately 2, 1, and 0.5 for each diameter, resulting in nine distinct geometry sets. Two replicate specimens were tested per set. Each specimen was designated to encode nominal diameter, length, and replicate; for example, D4L81 denotes the first replicate of a 4 in diameter cylinder cut to approximately 8 in length (L/D ≈ 2.0), with D4L82 as the second replicate. Specimen designations and exact dimensions are summarized in Table 2.

Table 2: Specimen geometry and designation

Cylinder diameter (mm)	Length (mm)	L/D ratios	Samples per set	Sample Designation	Total specimens
102 (4")	198 (7.80")	1.95	2	D4L81 & D4L82	18
	99 (3.90")	0.98		D4L41 & D4L42	
	53 (2.10")	0.52		D4L21 & D4L22	
76 (3")	147 (5.78")	1.93		D3L61 & D3L62	
	75 (2.94")	0.98		D3L31 & D3L32	
	39 (1.52")	0.51		D3L1.51 & D3L1.52	
51 (2")	96 (3.78")	1.89		D2L41 & D2L42	
	51 (2")	1		D2L21 & D2L22	
	25.4 (1")	0.50		D2L11 & D2L12	

7.3 Experimental Program

Accelerated deterioration was induced using a longitudinal electrochemical configuration in which specimens were polarized end-to-end at a constant 60 V DC. Sodium chloride (1.7 M) and sodium hydroxide (0.3 M) solutions were used at the cathode and anode, respectively, and replaced weekly. Bulk electrical resistivity was measured periodically using a direct-contact configuration following ASTM C1876 [9]. Dynamic elastic modulus was determined using the resonance frequency test method in accordance with ASTM C215 [10]. Surface cracking was documented photographically at predefined intervals, with images taken at fixed 45° increments around the cylindrical surface and at both end faces. The photographs were used to qualitatively track crack initiation and surface damage during electrochemical exposure. The overall experimental workflow, including specimen geometry variation, electrochemical acceleration, and multi-modal deterioration measurements, is summarized schematically in Figure 1.

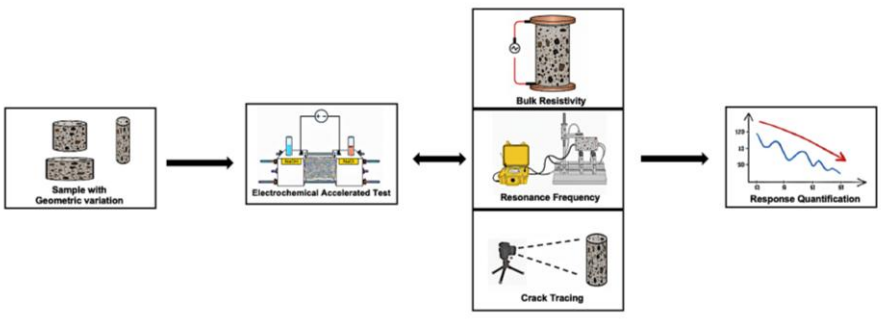

Figure 1: Experimental workflow for accelerated deterioration testing.

8. RESULTS AND DISCUSSION

8.1 Geometry-controlled bulk electrical resistivity response during iron sulfide deterioration

Figure 2 illustrates the influence of specimen geometry on the evolution of relative bulk electrical resistivity of CA1 concrete cylinders with diameters of 51 mm (2″), 76 mm (3″), and 102 mm (4″) subjected to electrochemical exposure. For all geometries, relative bulk resistivity decreases approximately linearly with time (Figure 2a), indicating progressive internal damage associated with sulfide oxidation. For 102 mm (4″) diameter specimens, the resistivity reduction rate increases from approximately 0.003 day^{-1} at L/D = 1.95 to 0.008 day^{-1} at L/D = 0.98, corresponding to an increase of about 2.7 times. A more pronounced amplification is observed for smaller-diameter specimens (51 and 76 mm), for which degradation rates increase by approximately 3.6-3.7 times as L/D decreases from ~1.9 to ~1.0.

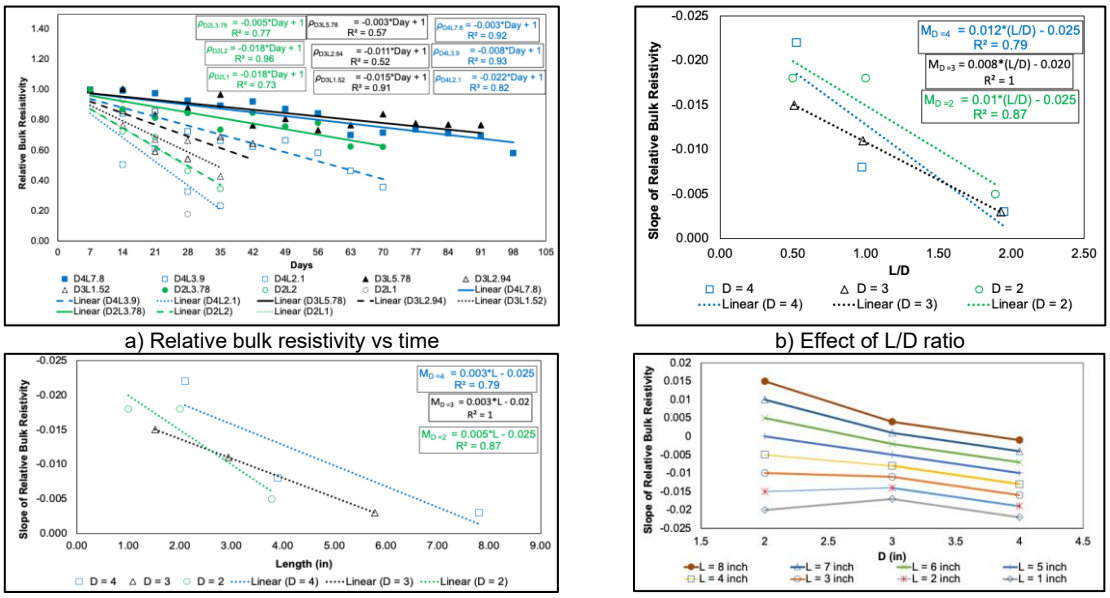

a) Relative bulk resistivity vs time

b) Effect of L/D ratio

c) Effect of specimen length

d) Effect of specimen diameter

Figure 2: Influence of sample geometry on bulk electrical resistivity evolution of CA1 concrete

When expressed as a function of L/D ratio (Figure 2b), degradation rate exhibits a strong linear relationship for all diameters, with lower L/D ratios consistently producing faster resistivity loss. Replotting the data as a function of absolute specimen length (Figure 2c) reveals an even stronger dependence, with longer specimens exhibiting systematically lower negative slopes regardless of diameter, confirming specimen length as the dominant geometric parameter. In contrast, specimen diameter exerts a secondary influence (Figure 2d), with only modest reductions in degradation rate for larger diameters at a given length. This behavior reflects the reduced ionic transport distance and increased effective electric field intensity in shorter specimens, which promote more rapid electrochemically driven ion migration under a constant applied voltage, thereby accelerating sulfide oxidation. In addition to transport length, differences in electric field intensity (E ≈ V/L) under constant voltage may also contribute to the observed geometry-dependent deterioration. The progressive reduction in bulk electrical resistivity reflects increasing pore connectivity resulting from oxidation-induced microcracking at the aggregate-paste interface and within the cement paste. Overall, these results demonstrate that bulk electrical resistivity is a sensitive, geometry-dependent indicator of sulfide-induced deterioration, governed primarily by specimen length and L/D ratio rather than diameter.

8.2 Effect of specimen geometry on dynamic elastic modulus degradation of CA1 concrete

Figure 3 presents the time-dependent evolution of the relative dynamic elastic modulus of CA1 concrete cylinders subjected to electrochemical exposure. Due to resonance testing constraints, measurements were obtained for five geometries: 102 mm (4″) diameter specimens with L/D = 1.95 and 0.98, 76 mm (3″) diameter specimens with L/D = 1.93 and 0.98, and 51 mm (2″) diameter specimens with L/D = 1.89.

For all tested geometries, the relative dynamic elastic modulus decreases with exposure time (Figure 3a), indicating progressive stiffness loss associated with iron sulfide oxidation.

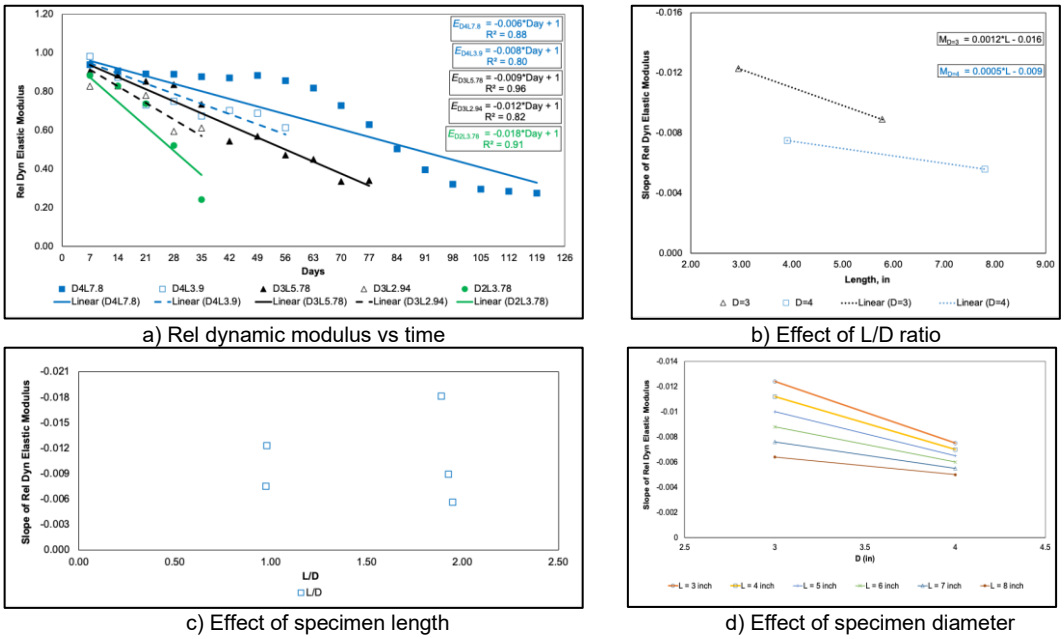

a) Rel dynamic modulus vs time
b) Effect of L/D ratio
c) Effect of specimen length
d) Effect of specimen diameter

Figure 3: Effect of specimen geometry on dynamic elastic modulus degradation of CA1 concrete

As shown in Figure 3(b), the relationship between modulus degradation rate and L/D ratio exhibits greater scatter than that observed for bulk electrical resistivity, indicating that L/D alone does not uniquely govern stiffness loss. In contrast, replotting the data as a function of absolute specimen length (Figure 3c) reveals a more consistent dependence, with shorter specimens exhibiting systematically faster modulus degradation across all diameters. The influence of specimen diameter is secondary, with only modest reductions in degradation rate for larger diameters at a given length (Figure 3d). The reduction in dynamic elastic modulus reflects the cumulative mechanical effects of iron sulfide oxidation, as expansive reaction products induce microcracking at the aggregate-paste interface and progressive crack interaction over a shorter axial distance more rapidly disrupts the load-bearing skeleton. Unlike bulk electrical resistivity, which is sensitive to transport-driven damage, dynamic modulus captures the mechanically significant cracking. Consequently, shorter specimens reach this critical damage state more rapidly, whereas longer specimens delay stiffness degradation by distributing damage over a greater length.

8.3 Geometry-controlled surface cracking and during accelerated test

a) Sample D3L62 (L/D = 1.93) b) Sample D3L32 (L/D = 0.98) c) Sample D3L1.51 (L/D =0.51)

Figure 4: Surface cracking of 76 mm diameter specimens with varying L/D after 3 weeks of electrochemical exposure.

Figure 4 presents representative surface cracking after three weeks of electrochemical exposure for 76 mm (3″) diameter concrete cylinders with varying L/D ratios, demonstrating a clear geometry dependence. The shortest specimen (L/D = 0.51) exhibits severe, early surface cracking with dense, interconnected crack networks (Figure 4c), whereas the intermediate specimen (L/D = 0.98) shows moderate cracking (Figure 4b). In contrast, the longest specimen (L/D = 1.93) displays only sparse, isolated surface cracks at the same exposure time (Figure 4a). These observations are consistent with the geometry-dependent trends observed in bulk electrical resistivity and dynamic elastic modulus. Shorter specimens accumulate damage more rapidly, promoting early crack initiation and formation of interconnected crack networks, while longer specimens delay crack development by distributing

oxidation-induced damage over a greater transport length. Overall, surface cracking provides direct visual confirmation that specimen length and L/D ratio govern the rate and severity of sulfide-induced deterioration.

8.4 Integrated geometry-controlled deterioration and failure behavior of CA1 concrete

Table 3: Summary of specimen geometry, cracking behavior, oxidation onset, and time-to-failure

Diameter (mm)	Length (mm)	L/D	Oxidation Starts (T_0), Days	Oxidation Severity at T_0	Time to First Crack (T_C), Days	Crack Severity at T_C	Time to Failure (T_F), Days
102 (4")	198 (7.80")	1.95	7	Low	14	Low	119
	99 (3.90")	0.98	7	Low	7	Low	80.5
	53 (2.10")	0.52	7	Moderate	7	High	38.5
76 (3")	147 (5.78")	1.93	7	Low	7	Low	91
	75 (2.94")	0.98	7	Moderate	7	Moderate	66.5
	39 (1.52")	0.51	7	High	7	High	49
51 (2")	96 (3.78")	1.89	7	Moderate	7	Moderate	70
	51 (2")	1	7	High	7	High	49
	25.4 (1")	0.50	7	High	7	High	45.5

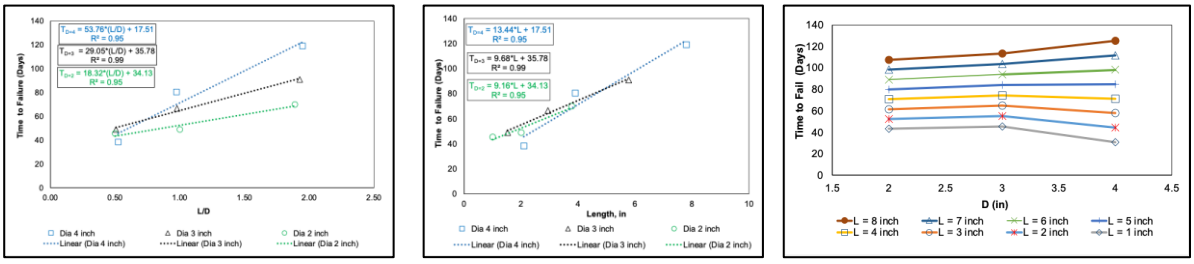

a) Effect of L/D ratio b) Effect of length c) Effect of diameter

Figure 5: Effect of specimen geometry on time to failure of CA1 concrete

The combined results in Table 3 and Figure 5 summarize the influence of specimen geometry on deterioration progression and time to failure of CA1 concrete under electrochemical exposure. Time to failure (T_F) is defined as the exposure duration at which electrochemical testing was discontinued due to severe specimen damage accompanied by negligible further change in resonance frequency. Table 3 integrates specimen geometry with key deterioration milestones, including oxidation onset (T_0), time to first cracking (T_C), crack severity, and ultimate time to failure (T_F), while Figure 5 isolates the effects of L/D ratio, specimen length, and diameter on failure kinetics. As shown in Table 3, oxidation onset (T_0), identified by visible surface discoloration, was first observed at approximately 7 days (initial inspection interval), indicating that oxidation initiation is governed primarily by material chemistry and exposure conditions rather than geometry. Visual crack initiation likewise occurred at approximately 7 days for most specimens, with the exception of the longest specimen (102 mm diameter, L/D = 1.95), for which cracking was delayed to 14 days. In contrast to initiation, oxidation severity at T_0 and subsequent crack severity exhibited a strong geometry dependence, increasing systematically as specimen length and L/D ratio decreased. These severity trends are reflected in the time-to-failure results. As summarized in Table 3 and Figure 5a, T_F decreases markedly with decreasing L/D ratio for all diameters. For 102 mm (4″) diameter specimens, T_F decreases from 119 days at L/D = 1.95 to 38.5 days at L/D = 0.52, representing an approximately three times reduction, with similar reductions observed for 76 mm (3″) and 51 mm (2″) specimens. When expressed as a function of absolute specimen length (Figure 5b), T_F increases consistently with increasing length, indicating that longer specimens require more time for oxidation-induced damage to accumulate and develop into through-cracking. In contrast, specimen diameter exerts only a minor influence on T_F for a given length (Figure 5c). Collectively, these results demonstrate that specimen length and L/D ratio dominate deterioration progression and failure kinetics, while oxidation initiation remains largely geometry independent.

9. CONCLUSION

This study systematically investigated the influence of specimen geometry on the accelerated electrochemical deterioration of concrete containing iron sulfide-bearing aggregates. By isolating geometric parameters while maintaining identical material composition and exposure conditions, the following conclusions are drawn:

i. Oxidation initiation occurred at approximately the same time for all specimens, independent of diameter, length, or L/D ratio, indicating that oxidation onset is governed primarily by material chemistry and electrochemical exposure conditions rather than geometry.
ii. Deterioration progression after initiation was strongly geometry controlled. Shorter specimens and lower L/D ratios exhibited earlier cracking, and reduced time to failure.
iii. Bulk electrical resistivity proved to be a sensitive indicator of geometry-dependent deterioration. For a given diameter, resistivity reduction rates increased by approximately 2.5-4 times as the L/D ratio decreased from ~2.0 to ~0.5, scaling inversely with specimen length.
iv. Dynamic elastic modulus captured mechanical damage. Stiffness degradation rates increased with decreasing specimen length, with shorter specimens exhibiting rates up to three times higher than the longest specimens, while specimen diameter had a secondary influence.
v. Time to failure was governed primarily by specimen geometry rather than oxidation onset. Decreasing specimen length and L/D ratio resulted in reductions of up to threefold in time to failure, reflecting earlier crack interaction and faster transition to mechanically unstable damage states.

Overall, these results demonstrate that accelerated electrochemical testing of iron sulfide-bearing concrete is highly sensitive to specimen geometry, requiring explicit consideration of specimen length and L/D ratio when interpreting results from non-standard geometries. Future work is needed to establish standardized test procedures through validation using field-extracted cores and a broader range of specimen geometries, materials, and test conditions, and by incorporating parameters such as electric field intensity, cumulative charge, and temperature effects.

ACKNOWLEDGEMENT

This work was supported by the U.S. Department of Commerce, National Institute of Standards and Technology (NIST), under awards 60NANB20D135, 70NANB21H113, 70NANB23H009, and 60NANB23D187. The authors gratefully acknowledge the undergraduate students and researchers of the Advanced Cementitious Materials & Composites Laboratory, University of Connecticut, for their technical support.

REFERENCES

[1] Jana D (2022) Cracking of residential concrete foundations in eastern Connecticut, USA from oxidation of pyrrhotite. Case Studies in Construction Materials 16, e00909. https://doi.org/10.1016/j.cscm.2022.e00909
[2] Zhong R, Wille K (2018) Deterioration of residential concrete foundations: the role of pyrrhotite-bearing aggregate. Cem Concr Compos 94, 53-61. https://doi.org/10.1016/j.cemconcomp.2018.08.012
[3] Rodrigues A, Duchesne J, Fournier B, Durand B, Rivard P, Shehata M (2012) Mineralogical and chemical assessment of concrete damaged by the oxidation of sulfide-bearing aggregates: importance of thaumasite formation on reaction mechanisms. Cem Concr Res 42, 1336-1347. https://doi.org/10.1016/j.cemconres.2012.06.008
[4] Santos L, Chrysochoou M, Wille K (2025) Development of a risk assessment framework for pyrrhotite induced deterioration of concrete foundations in CT and MA. Cem Concr Res 197, 107951. https://doi.org/10.1016/j.cemconres.2025.107951
[5] NT BUILD 492 (1999) Concrete, Mortar and Cement-Based Repair Materials: Chloride Migration Coefficient from Non-Steady-State Migration Experiment. Nordtest, Espoo, Finland.
[6] ASTM C1202-22 (2022). Test method for electrical indication of concrete's ability to resist chloride ion penetration. ASTM International, West Conshohocken, PA.
[7] Ojo M, Kim D, Frame L, Wille K (2024) Electrochemical investigation of accelerated deterioration of concrete with iron-sulfide containing aggregates. Cem Concr Res 182, 107570. https://doi.org/10.1016/j.cemconres.2024.107570
[8] Castillo Araiza R, Rodrigues A, Fournier B, Duchesne J (2024) A new accelerated testing scheme for oxidation of sulfide-bearing aggregates. Cem Concr Res 180, 107507. https://doi.org/10.1016/j.cemconres.2024.107507
[9] ASTM C1876-24 (2024) Standard test method for bulk electrical resistivity or bulk conductivity of concrete. ASTM International, West Conshohocken, PA.
[10] ASTM C215-19 (2020) Standard test method for fundamental transverse, longitudinal, and torsional resonant frequencies of concrete specimens. ASTM International, West Conshohocken, PA.

ICISR 2026

2nd International Conference on Iron-Sulfide Reactions in Concrete

Technical Session # 8:

From Quarry to Foundation: Field Mapping, Case Studies, and Mitigation of Pyrrhotite Damage

UCONN | COLLEGE OF ENGINEERING
SCHOOL OF CIVIL AND ENVIRONMENTAL ENGINEERING

UCONN
COLLEGE OF ENGINEERING
CONNECTICUT TRANSPORTATION INSTITUTE (CTI)

Investigation of Pyrrhotite in Quarries and Sulfidic-Heave in British Columbia, Canada

Fred Shrimer (1)

(1) Shrimer Geoconsulting Inc., Vancouver, Canada, fred.shrimer@shrimergeoconsulting.com

Abstract

For several years, issues suspected to be related to heave of concrete slabs-on-grade have been reported in the northwest coastal City of Prince Rupert, British Columbia. Although some investigations have been carried out to try to understand and characterize this phenomenon on a case-by-case basis, the cause has not yet been delineated adequately.

In recent years, however, more in-depth efforts have been made of a number of sites to determine and hopefully isolate the cause of the observed heaving in the various constructed works, which range from buildings to civil infrastructure. Samples taken at several local active and inactive quarries, along with samples obtained at local cut-and-fill excavation sites, were tested to provide additional characterization, as well as geological, mineralogic and geochemical data.

The investigations that were undertaken have determined that the most likely cause is the presence of pyrrhotite in the structural fill aggregates that were used to support these elements (i.e., slabs-on-grade, sidewalks, etc.). Pyrrhotite is generally present within the rock formations that are exploited as aggregate sources in several of the quarries in this region and community.

Concurrently to this, investigations were undertaken to assist the concrete industry and aggregate producers in mapping pyrrhotite in bedrock quarries in the Prince Rupert area. This was in response to concerns about the notable deleterious effects of the mineral pyrrhotite in concrete aggregates as experienced in the Trois-Rivieres region of Quebec, as well as similar pyrrhotite-related problems reported in Connecticut and Massachusetts, USA. These undertakings have identified practical issues, challenges and uncertainties.

This paper examines both of these intertwined efforts, and provides commentary on the results.

***Keywords**: heave, iron-sulfide reaction, mapping, pyrrhotite, quarry.*

1. INTRODUCTION

1.1 Pyrrhotite Mapping – Use of quarried rock as Concrete Aggregate

Over the past several years, in response to the growing awareness of the potential for pyrrhotite-bearing aggregates to cause deleterious effects in concrete, as observed in the Trois-Rivières region of Quebec, in Massachussetts and Connecticut, USA, as well as in northwestern Ireland, concerns have been raised regarding the possibility that pyrrhotite could be present in other bedrock aggregate sources in Canada. These concerns have spurred interest in determining whether the mineral exists in aggregate quarries in other regions of Canada.

In Canada, the Canadian Standards Association (CSA) provides guidance on this issue, in the form of its publication, "*Concrete materials and methods of concrete construction/Test Methods and Standard Practices for concrete"*, which provides the standards and specifications that are used in Canada.

Given that Canadian aggregate consumption is in the range of 400 million tonnes annually, with about 15% of that being used in concrete production, and that the number of quarries is estimated to be in the thousands, the scope of the potential issue is of some concern to the concrete and aggregate production industries. Thus far, significant alarm has not been raised because most concrete manufacture in the country has exhibited no ill effects attrributed to pyrrhotite degradation of concrete. The only exception is the well-documented but localized issue within the Trois-Rivières region.

However, there are nuances that colour this perspective, such as:

- The geology of the problematic aggregates in the Trois-Rivières cases is characterized by dominantly metamorphosed mafic igneous rocks;
- The geology of the quarries in the rest of Canada that have not exhibited any issues is widely variable:
  - Carbonate rocks in much of southern Ontario and parts of Quebec;
  - Metamorphic and plutonic igneous rock in many Canadian Shield quarries in Quebec, Ontario, Manitoba, northern Saskatchewan;
  - Carbonate rocks in Manitoba;
  - A wide range of geological formations in British Columbia.

In recent years, in order to assist the concrete industry in general, and aggregate producers in specific, efforts have been made to determine whether pyrrhotite occurs in bedrock quarries in British Columbia, Canada. These undertakings have produced a mixed results, and have identified numerous practical issues, challenges and uncertainties.

Geological database information in the form of mineral occurrences is available from the Geological Survey of Canada. Based on this, pyrrhotite occurrences have been mapped for all regions of Canada. Such data has been generated largely to support mineral exploration. In British Columbia, the mapped pyrrhotite occurrences are primarily located within the geologically diverse Cordillera mountain belts, which dominate the western portion of the province.

In a recent demonstration pyrrhotite-mapping project carried out in British Columbia ("BC"), the primary hurdle that was encountered was obtaining permission to conduct mapping, sampling and testing at quarry sites. Owners of the quarry sites sometimes declined to participate or allow access to their sites, in case pyrrhotite was found and might thereby pose a commercial/liability issue to the site.

In undeveloped bedrock locations, access was variable due to exposure, terrain and geological conditions. In most of the BC quarry sites, the analytical data did not detect pyrrhotite within sampled sites. However, the mapping/sampling work conducted in the Prince Rupert area of BC consistently identified pyrrhotite in several regional samples, and is the focus of this paper.

1.2 Investigation of Regional Aggregate Sites

1.2.1 Regional Geology

The bedrock geology of the Prince Rupert area is characterized by a range of metamorphic rocks thought to be of Paleozoic to early Mesozoic age. These rocks broadly represent formerly fine-grained sediments that have been subjected to metamorphism that has resulted in very fine-grained phyllites,

schists and gneisses – essentially, varying grades of metapelitic rocks. In 1982, the Geological Survey of Canada (GSC) published Memoir 394, which provided bedrock mapping of the Rupert-Skeena area.

Glaciation of the Prince Rupert area has scoured the bedrock and, over most locations, left only a thin veneer of unconsoildated material with boggy organic deposits commonly overlying bedrock, which is typically at a shallow depth. Hence, the Prince Rupert area is not blessed with granular deposits of sand and gravel that is more common throughout much of BC. In the past, what few sand and gravel deposits were found in the area were depleted long ago. Occasional dredging of the harbour provided a few opportunities for local access and use of these granular materials as aggregate.

Thereby, for decades, sand and gravel aggregates have not been available locally, and are required to be transported to the City, generally by truck from Terrace, to the east about an hour and a half. Thus, the only aggregate supplies that are local to Prince Rupert are necessarily derived from local bedrock quarries. These quarries extract bedrock that is typically characterized by the metamorphic rocks described above: metamorphosed pelitic sediments ranging from phyllite on the fine-grained end of the textural scale to gneiss, sometimes with very large crystals, with variable mineralogic composition and engineering properties.

1.2.2 Quarry Sites in the Prince Rupert Area

There are several operating and historic quarries in the Prince Rupert region, as well as a number of known 'informal' rock cut sites that have produced fill materials in connection with the rock cuts. These are outlined in Table 2.1 below.

Table 2.1: Quarry Sites in the Prince Rupert Area

Site Name	Geology	Comments
Seal Cove (City of Prince Rupert site, now closed)	Phyllite-Schist-Amphibolite	Site used to supply various aggregates for City uses
Metlakatla village quarry	Phyllite-Schist	Inactive quarry excavation
Ridley Island Landfill	Phyllite-Schist-(?)	City-owned landfill site
Adventure Quarry	Phyllite-Schist-Amphibolite	
Storey Galloway Quarry	Phyllite-Schist-Gneiss	
Storey Prudhomme Quarry	Gneiss w granite	
Rainbow South Quarry	Gneiss	
Rainbow North Quarry	Gneiss	Inactive
Tyee Quarry	Granite-Gneiss	
Fairview Terminals	Phyllite-Schist	Rock cut for construction
PR Industrial Park	Phyllite-Schist	Rock cut for construction
Ridley Island rail quarry	Phyllite-Schist	inactive

Over the past few years, samples of aggregate and of rock have been obtained from most of these sites, and subsamples submitted various tests, including thin-section petrography, XRF and XRD.

1.3 Suspected Heave Cases)

Several examples of heave have been reported in and around Prince Rupert over the past few decades. The cases have included industrial and commercial buildings as well as residential and infrastructure construction, examples are outlined in Table 2.2. below.

Table 2.2: Sites of reported heave, Prince Rupert area

Site Name	Samples tested	Comments
Lax Kxeen Elementary School	Yes	Investigations conducted
Charles Hays Secondary School	Yes	Investigation conducted
Acropolis Manor	No	Not formally investigated
Ciccone Civic Ice Arena	Yes	Investigation conducted
ICBC facility	Yes	Informal investigation conducted

Coldfish Seafood Processing Plant	Yes	Informal investigation conducted
Rainbow Chrysler Warehouse	Yes	Visual appraisal only
Port Edward School	No	Investigation conducted
C-Force Building	No	Visual assessment
Municipal infrastructure	No	Visual assessment
Various commercial buildings	No	Visual assessments
Various private residences	Yes	Visual & informal investigations

The materials used as structural fills in these cases are for the most part locally-derived crushed rock aggregate.

2. SAMPLE TESTING

Samples of (1) aggregate/rock from the quarrries and (2) the fill that supported the slabs were obtained as noted in the Table above. Testing of the samples included petrographic / thin-section examination, X-Ray fluorescence (XRF) and X-Ray Diffraction (XRD). In some instances, physical testing was also conducted to determine various physical properties such as abrasion loss, specific gravity or absorption.

2.1 Rock Petrography

Petrographic examination determined that the rock from the quarries and from the samples of fill share general characteristics. They range from phyllites to schists and gneisses, are of variable texture, and broadly similar mineral composition. Virtually all of the rocks include iron sulphides and oxides, including pyrite, ilmenite and pyrrhotite. Varieties of garnet were identified in small amounts.

These photos illustrate the typical fill aggregate samples, which were supplied by local quarries. They consist of particles of crushed grey schist and phyllite rock.

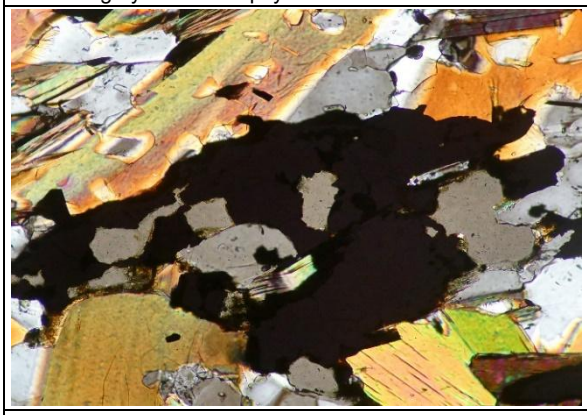

Views of a thin-section of schist from locally-sourced aggregate, viewed in cross-polarized light (left) and reflected light (right) showing opaque minerals among quartz and biotite (left). In the right image, pyrrhotite with accessory rutile and chalcopyrite are recognized. 200x magnification, field of view 0.5 mm across.

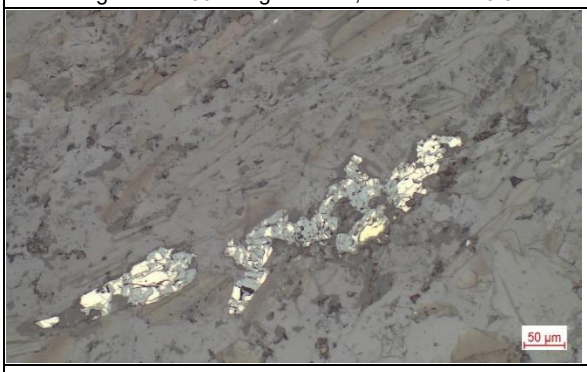

Pyrrhotite grains in schist fill particles from a school that has experienced effects of heave. The pyrrhotite is observed to have been heavily altered to iron oxides. Images are at magnifications of 50x (left) and 500x (right).

Figure 2.1: Sample images from petrographic examinations

2.2 Chemical Analyses

The primary chemical analytical techniques that were used for characterization of the fill aggregate samples from the various structures and the aggregate and rock samples obtained from the quarries were XRF and XRD-Rietveld analysis; for some samples, Acid-Base Accounting (ABA) tests were also done, as well as trace element scans.

Table 3: XRD Results for Fill Samples

Sa.	Actin	Al ma	Dol	Apat	Biot	Calc	Clino ch	Cli noz	Gyp	Ill-Mus	Hem -Ilm	K-feld	Plag	Pyr	Pyrr	Qtz	Titn
PE-1	2.0	1.3	0.8	0.6	11.8	5.5	2.2		3.1	9.6	0.2	1.6	27.5		1.4	32.4	
PE-2	1.0	1.6	0.7	0.6	11.2	4.5	1.8		0.5	10.5	0.2	3.5	26.7		1.9	35.2	
PE-3	1.8	1.2	0.7	0.5	12.8	5.7	2.3		3.1	9.6	0.3	1.4	26.9		1.4	32.3	

Sa.	Actin	Alma	Dol	Apat	Biot	Calc	Clinoch	Clinoz	Gyp	Ill-Mus	Hem-Ilm	K-feld	Plag	Pyr	Pyrr	Qtz	Titn
PE-4	3.4	2.1	0.7	0.6	10.3	5.3	2.4		0.6	7.9	0.4	1.8	27.0		1.7	35.7	
LK-1	2.4	1.7	1.1	0.6	13.6	2.9	2.5		2.6	5.1	0.3	1.0	32.1		0.6	33.7	
LK-2	4.5	2.6	0.9	0.5	12.0	4.6	2.3		1.0	4.9	0.4		30.4			35.9	
CH-1				0.4	16.7	2.4	1.5		1.6	13.3		1.3	35.9			26.8	
CH-2	3.0		0.4	0.4	15.7	1.5	2.2		1.0	7.2		2.0	41.9			24.7	

Table 4: XRD Results for Replacement Fill Samples

Sa.	Actin	Alma	Dol	Apat	Biot	Calc	Clinoch	Clinoz	Gyp	Ill-Mus	Hem-Ilm	K-feld	Plag	Pyr	Pyrr	Qtz	Titn
OM-1	1.2	1.4	0.9	0.6	11.6	7.4	3.5			9.6		1.6	30.6	1.4	1.3	29.0	
OM-2	0.5	1.1	0.9	0.7	10.4	6.3	3.8			7.6		1.8	34.9		1.8	30.2	

Table 5: XRD Results for Quarry Samples

Sa.	Actin	Alma	Dol	Apat	Biot	Calc	Clinoch	Clinoz	Gyp	Ill-Mus	Hem-Ilm	K-feld	Plag	Pyr	Pyrr	Qtz	Titn
QA-1	2.7	0.9	0.5	0.4	8.6	6.1	3.7			7.1		3.8	32.3	0.5	1.3	32.1	
QA-2	1.4	1.4	0.7	0.5	11.0	8.0	3.0			9.0		2.2	30.9	1.1	1.3	29.6	
QA-3	1.0	1.6		0.3	9.6	7.2	3.8			9.0	0.3	4.1	29.6	1.2	1.3	31.1	
QA-4	0.5	1.1		0.3	10.0	6.9	3.6			8.3	0.3	4.2	32.6	0.3	1.8	30.2	
QB-1	2.0	2.6	0.8	0.3	12.3	1.9	3.6			7.0	0.4	2.2	36.0			30.9	
QB-2	3.0	1.8	0.9	0.3	12.1	4.4	3.5			7.4	0.4	2.7	38.4		0.5	24.6	
QB-3	3.4	0.5	0.6	0.6	17.3	4.7	2.6			9.9	0.8	1.7	33.1		1.7	23.0	
QC-1	8.2			0.4	7.9	0.3	3.4	6.3				7.3	46.7			17.7	1.8
QD-1				0.5	14.7	3.3	1.9			15.7			34.6		2.0	27.3	
QD-2	0.4	0.9	1.6	0.4	15.1	7.7	2.3			8.0	0.2	0.8	42.0		1.0	19.4	
QE-1	5.7			0.4	7.7	0.3	1.2	5.3			0.4	4.3	57.6			16.2	0.9
QE-2	5.5			0.7	9.6	0.5	0.7	5.0				4.0	55.9			17.4	0.7
QF-1	6.7		0.6	0.7	18.8	0.7	2.5			4.2			41.8	0.9	2.3	18.8	1.9
QF-2	26.7				16.4	0.4	1.6	11					31.6			9.8	2.6

It was observed that the fill samples obtained from structures affected by heave all contain gypsum, whereas the aggregate and rock samples from the quarries are absent of gypsum. Pyrrhotite is the more common sulfide mineral in all of the samples, and we note that pyrite occurs in only a few samples. In thin-section, chalcopyrite was also observed, but it was not picked up in XRD analyses, likely being below the limit of reliable detection.

3. WORKING HYPOTHESIS REGARDING HEAVE

Currently, the following data and observations have been developed:

- Clear signs of heave have been observed in numerous building sites in and around Prince Rupert. In some cases, heave magnitudes have been measured up to 4" (100 mm) of vertical displacement;
- The heave is observed within a few years to up to ten years;
- Structural fill aggregates, upon removal under heaved slabs, have exhibited alteration and granular breakdown ranging from slight to significant. The material removed is often observed to be finer in texture than the material that would have been placed;
- Gypsum has been detected in all cases in the fill extracted from heave sites where *in situ* oxidation is attributed as the deterioration mechanism, in contrast;
- No gypsum has been identified in "fresh" samples of quarried aggregate or of rock from rock cut sites;
- Ferrous oxides and ferrous sulfates have been observed in many of the fill aggregate samples extracted from heaved buildings;
- Sulfide minerals are present in much of the bedrock underlying the Prince Rupert region.
- Minor (0.5-2%) proportions of sulfides are detected in the majority of the quarry sites in the Prince Rupert region, with the exception of QE as analyzed by bulk rock XRD.
- The coarser-grained metamorphic rock types (typically the pelite and igneous-derived gneisses) tend to be nominally absent of sulfides, based on preliminary characterization work

only. Identified sulfides (primarily pyrrhotite) were more typically associated with finer schist / phyllite lithologies examined. Confirmation would require additional investigation, sampling and testing.

Based on the data that is currently available, the working theory is that sulfide minerals, consisting in the main of pyrrhotite (but possibly also including pyrite), rapidly degrade due to exposure to oxygen and moisture, being hosted in rocks that are highly micaceous, and of variable strength and durability. This is similar to the phyllite-hosted pyrrhotite deterioration seen in Co. Donegal in Ireland.

The resulting alteration products are ferric oxides, ferrous sulfate and sulfuric acid. The sulfuric acid accesses Ca ions, provided by calcite (which is common in small amounts in the rocks), which then produces gypsum.

The gypsum in turn expands and, in combination with the ferrous sulfate, produces expansive forces within the mass of fill, which results in heave in cases where the fill is of sufficient thickness, and where the fill contains a sufficient proportion of reacting rock particles. Gypsum has been observed on aggregate particle surfaces and within partings in the rock particles.

Anecdotally, in many cases where heave has been observed, and the structure remediated by removal of the concrete slab, and removal of the fill supporting the slab, the same material was supplied as replacement fill. Some of these structures are now undergoing a new episode of heave.

3.1 Mapping and Sampling in Quarries

Requests for access to the quarry sites for geological review and to procure samples of aggregate and/or rock have been met with outright refusal by some operators and approval by others. Negative enterprise and liability effects were cited by those who declined permission for access, while other owners were willing to participate and support the work.

This mirrors the experience in a wider, similar mapping/sampling effort covering a much larger a portion of British Columbia, conducted about the same time (unpublished). Shrimer (2022) outlined proposed approaches for avoidance of issues related to sulfides in existing and new quarries intended for aggregate production.

4. DISCUSSION

The geological mapping/sampling work conducted in the Prince Rupert area of bedrock quarries and rock cuts is considered to be ‘preliminary’ or ‘informal’, and thus is not definitive or comprehensive. It does, however, provide some initial insights into the question, “Are there quarries in which pyrrhotite occurs in British Columbia?” As noted, some of these are past-producers (now closed), or are temporarily inoperative, but some are permitted and in current production.

In order to produce a more definitive perspective, additional mapping, sampling and testing will be necessary within these sites. The results of previous geotechnical and geological investigations have shown that regional bedrock in the Prince Rupert area is frequently characterized by fine-grained metasedimentary rocks/metapelites -- variously phyllites, slates, schists and gneisses -- and that these rocks often host pyrrhotite as well as other sulfide minerals, including pyrite and chalcopyrite.

Of these sulfides, pyrrhotite is the least stable. Much of the pyrite has been observed to be euhedral crystalline in form, and thereby is less prone to alteration/deterioration than framboidal pyrite, which is commonly found to be unstable.

The second issue, involving the investigation of the mechanics of the heave issues related to the regional aggregates, is ongoing and it is hoped that additional work will bring further clarity to this phenomenon that affects constructed works in Prince Rupert.

5. REFERENCES

[1] CSA Group (2024) CSA A23.1:24/CSA A23.2:24, Concrete Materials and methods of concrete construction/*Test methods and standard practices for concrete*. Toronto, Canada.

[2] Hutchison, W.W. (1982). Geology of the Prince Rupert-Skeena map area, British Columbia. Geological Survey of Canada, Memoir 394.
[3] Shrimer, F. (2022) Avoidance of Sulfide Problems in Aggregates. *In*: Maher, Michael (ed) Pyrite and Pyrrhotite – Managing the Risks in Construction Materials and New Applications, New York, Nova Science Publishers, Inc., pp. 349 – 367.

Potential of Commercially Available Sealants to Mitigate Further Oxidation of Pyrrhotite in Existing Foundations

Ashley S. Carey [(1)], Patrick G. Dixon [(2)], Michael J. Mengason [(3)], Stephanie S. Watson [(4)]

(1) National Institute of Standards and Technology, Gaithersburg, MD, USA, ashley.carey@nist.gov

(2) National Institute of Standards and Technology, Gaithersburg, MD, USA, patrick.dixon@nist.gov

(3) National Institute of Standards and Technology, Gaithersburg, MD, USA, michael.mengason@nist.gov

(4) National Institute of Standards and Technology, Gaithersburg, MD, USA, stephanie.watson@nist.gov

Abstract

In parts of Connecticut and Massachusetts in the northeastern United States, concrete foundations are deteriorating due to the inclusion of pyrrhotite-bearing aggregates. This deterioration can take decades to visibly manifest, thus, increasing the likelihood that hundreds of foundations built with pyrrhotite-bearing aggregates have not started to show damage. This study aims to evaluate mitigation methods (specifically, applying commercially available concrete sealants) to extend the lifespan of foundations that have yet to show visible pyrrhotite induced damage. Cores from a deteriorated foundation as well as laboratory mixed concrete not containing reactive aggregate were sealed with one of five sealant combinations covering a range of concrete sealing mechanisms. These specimens were then aged to evaluate the efficacy of the sealant-substrate. Water absorption tests (ASTM C1585) were performed to quantify each sealant's ability to mitigate moisture ingress for both field cores and laboratory cast specimens. It was found that the type of sealant as well as the condition of the concrete had a meaningful impact on the reported absorption values. These findings highlight the need for: 1) a maximum damage threshold for an existing foundation in which sealants are a viable mitigation strategy, and 2) a performance-based specification to determine acceptable sealants.

***Keywords**: mitigation; pyrrhotite; sealants*

6. INTRODUCTION

Concrete foundations in parts of Connecticut and Massachusetts have begun to deteriorate and lose their structural integrity due to the oxidation of pyrrhotite primarily in the coarse aggregate [1, 2]. Pyrrhotite ($Fe_{1-x}S$, $0 < x < 0.125$) is a naturally occurring iron-sulfide mineral that oxidizes in the presence of oxygen and moisture, leading to the precipitation of iron oxyhydroxides and the release of sulfate into the cementitious matrix, initiating internal sulfate attack [3-5]. Both the pyrrhotite oxidation and internal sulfate attack initiate the precipitation of volumetrically larger minerals such as goethite, ferrihydrite, ettringite, and thaumasite, which cause expansion and cracking, resulting in deterioration of concrete. These reactions can take decades before they visibly manifest as cracking and structural failure.

Previous studies have focused heavily on developing screening tools for quarries and accelerated aging protocols to facilitate the study of pyrrhotite-bearing aggregate [6-8]. Although these tools are useful for mitigating pyrrhotite deterioration in future structures, there are no readily available methodologies to slow pyrrhotite oxidation in existing concrete structures. A review conducted by the National Institute of Standards and Technology (NIST) detailed how a performance-based framework should be developed to allow for a wide range of potentially viable mitigation methods to be vetted [3]. This abstract presents initial findings towards the development of this framework by 1) highlighting the need for a maximum damage threshold to be considered for potential mitigation techniques, and 2) developing of a performance-based specification of assessing mitigating sealants for potential pyrrhotite mitigation efforts.

7. EXPERIMENTAL PROGRAM

7.1 Concrete Specimens

7.1.1 Field Cores

Six cores were taken from a deteriorated foundation in Stafford Springs, Connecticut that was scheduled for a full foundation replacement due to pyrrhotite oxidation [9]. Areas of the foundation walls with a low degree of visible damage on the interior face were chosen for coring. All cores were wet cored using a 108 mm (4.25 inch) drill bit through the entirety of the foundation wall, which was approximately 254 mm (10 inches). After coring, all cores were transported to NIST for further specimen preparation and testing. Upon arrival at NIST, cores were sliced into 38.1 mm (1.5 inch) pucks for laboratory testing. Once cut, specimens were sealed with various types of sealants as described in the following sections.

7.1.2 Laboratory Specimens

Laboratory mixed concrete containing no pyrrhotite was prepared as a baseline for the deteriorated concrete cores. The concrete mixture with a water to cementitious materials ratio (w/cm) of 0.50, which was intermediate to w/cm ratios found in today's residential foundations and pyrrhotite affected foundations, and followed a simple 1:2:3 concrete mixture (mass) proportion and contained one part ASTM C150 Type I/II cement, two parts ASTM C33 manufactured concrete sand of diabase mineralogy, and three parts ASTM C33 #57 crushed stone of diabase mineralogy. This mix design was chosen as a basic mixture for comparison to mixtures used in the 1980s and 1990s while also minimizing variables in the matrix. All concrete was cast into (102 by 203) mm [(4 by 8) inch] cylinder molds and cured for 28 days in a room temperature chamber at 100% relative humidity. After 28 days, specimens were sliced into 50 mm (2 inch) pucks for additional laboratory testing. Once cut, specimens were sealed with various types of sealants as described in the following sections.

7.2 Sealants and Application Methods

Five sealant combinations were used to evaluate the efficacy of sealants in slowing water intrusion into concrete of varying deterioration levels and thus slowing pyrrhotite oxidation. These sealant combinations are: no sealant (i.e., a control; N), silane (S), lithium silicate (LS), polyurethane (PU), and a crystalline sealant with an acrylic topcoat (CA) (Table 2.1). These sealants were chosen to represent a wide range of mitigation treatments including coatings and membranes, penetrating sealants, and pore blocking sealants. All sealants were applied to the pucks using a paint brush and cured at ambient conditions for the manufacturer's recommended duration in a fume hood, which minimized potential odors and solvent release into the laboratory. Although specimens were uniformly coated, sealant thickness was not specified during application. Once sealed and fully cured, pucks were stored in sealed plastic bags until undergoing an accelerated aging protocol to induce deterioration of the sealant-substrate interface.

Table 2.1. Sealants used in study

Sealant Type	Symbol	Mitigation Mechanism	Product	Dry Time (h)	Total Cure Time (h)
Silane	S	Penetrating	JE Tomes Concrete Sealer	1-2	8-12
Lithium Silicate	LS	Pore blocking	PS103 Lithium Silicate Densifier	1-3	6-12
Polyurethane	PU	Coating	ArmorPoxy (Two-Part)	4	24
Crystalline + Acrylic Topcoat	CA	Coating Coating	Krystol T1 (Crystalline) Foundation Armor AR350 (Acrylic)	6 4-6	72 24

7.3 Accelerated Aging Protocols

Four protocols were chosen to age the concrete-sealant interface to determine the performance at initial application and after aging had occurred. This study used three accelerated aging protocols and one baseline protocol. The baseline protocol, denoted as AA0, did not expose specimens to any accelerated aging protocols and were stored in sealed plastic bags, and was used as a reference for all other accelerated aging conditions. All accelerated aging protocols first exposed specimens to a 50 °C,

75 % relative humidity (RH) environment for 28 days. A relative humidity of 75 % was chosen to allow for adequate available moisture for pyrrhotite oxidation without decreasing the diffusion rate of oxygen. For specimens undergoing accelerated aging protocol 1 (AA1), aging was complete after this 28-day period of 50 °C, 75 % RH exposure. Specimens undergoing accelerated aging protocol 2 (AA2) were removed from the 50 °C, 75 % RH environment after 28 days and subjected to 15 freeze-thaw cycles where the temperature was lowered from 4 to -18 °C in 2 hours and then raised from 18 to 4 °C in five hours, which met the thermal ramping met the requirements of ASTM C666, and were then held at 4 °C for the remainder of the day, resulting in one cycle per day. Specimens undergoing accelerated aging protocol 3 (AA3), were removed from the 50 °C, 75 % RH environment after 28 days and subjected to 15 wet-dry cycles where one cycle was defined as 4 days in wet conditions (submerged in tap water) and 3 days in dry conditions (ambient temperature). All wet-dry cycling occurred in a temperature-controlled space where relative humidity was variable, ranging between 45 % RH to 80 % RH.

7.4 Testing Methods

All sealed specimens were tested following ASTM C1585, *Standard Test Method for Measurement of Rate of Absorption of Water by Hydraulic Cement Concretes,* to evaluate the ability of the aged concrete-sealant interface to mitigate the intrusion of water into the concrete [10]. Specimens were preconditioned in a 50 °C, 80 % RH environment for 5 days followed by a minimum of 15 days in a sealed container at 23 °C with no RH control. After preconditioning, specimens were sealed around the outer circumference with metal tape to stop capillary absorption around the edges of the specimen and facilitate one-dimensional water absorption. The seal of the metal tape did vary depending on the surface roughness of the specimen due to the concrete sealant. Mass change was recorded at designated intervals to quantify the rate of absorption. It should be noted that ASTM C1585 requires vacuum saturation step for field cores to ensure moisture equilibrium prior to testing. This preconditioning step was not followed as cores had already been sealed, and putting sealed specimens under vacuum opened the possibility for changes to the integrity of the sealant-concrete interface.

8. PRELIMINARY RESULTS

Water absorption tests were vetted as a potential performance-based test to be included in a mitigation assessment framework. For this assessment, various deterioration states were considered to determine to what extent a sealant's efficacy may be impacted. A comparison of final absorption (I) data calculated from ASTM C1585 absorption tests is presented in Table 3.1. When evaluating ASTM C1585 data, deteriorated field cores had statistically higher water absorption values than identically sealed laboratory concrete in 14 of 16 cases. This statistical analysis should be taken lightly as the field core replication is not robust, which could lead to changes in values, but likely not to change in overall trends.

The findings presented in Table 3.1 highlight the need to determine a maximum damage threshold for an existing foundation in which sealants are a viable mitigation strategy. Sealants clearly perform best on a concrete that is not deteriorated. The results also depend on the absorption capacity of the reference concrete, for which the w/cm ratio was different to that of the pyrrhotite affected foundation specimens, but the efficacy of the sealant is secondary to the concrete substrate on which it is applied. However, it is not clear at what point the efficacy of the sealant does not meaningfully impact the water absorption as the overall condition of the concrete is the primary driver. More research is needed to determine the level of foundation deterioration.

Table 3.1. Comparison of final water absorption (I) of sealed field core and laboratory mixed concrete

Aging Protocol	Sealant	Field Cores		Lab Specimen		Statistical Analysis	
		n	Final I (mm)	n	Final I (mm)	p-value	Significant?
AA0	N	6	4.93 +/- 0.29	9	3.75 +/- 0.10	< 0.01	Yes
AA1	N	2	4.98 +/- 0.20	9	3.91 +/- 0.18	< 0.01	Yes
AA1	S	2	4.15 +/- 0.09	9	3.13 +/- 0.92	0.17	No
AA1	LS	2	5.23 +/- 0.43	9	4.24 +/- 0.78	0.12	No
AA1	PU	2	4.99 +/- 0.59	9	1.72 +/- 0.67	< 0.01	Yes
AA1	CA	2	5.67 +/- 1.05	9	4.62 +/- 0.17	< 0.01	Yes
AA2	N	2	5.59 +/- 0.56	9	4.30 +/- 0.16	< 0.01	Yes
AA2	S	2	5.49 +/- 0.10	9	3.94 +/- 0.32	< 0.01	Yes
AA2	LS	2	5.25 +/- 0.47	9	4.09 +/- 0.17	< 0.01	Yes
AA2	PU	2	5.02 +/- 0.47	9	1.40 +/- 1.00	< 0.01	Yes
AA2	CA	2	5.72 +/- 0.85	9	4.46 +/- 0.21	<0.01	Yes
AA3	N	2	5.16 +/- 1.08	9	2.41 +/- 0.27	< 0.01	Yes
AA3	S	2	5.88 +/- 0.48	9	2.81 +/- 0.22	< 0.01	Yes
AA3	LS	2	5.26 +/- 0.49	9	2.59 +/- 0.16	< 0.01	Yes
AA3	PU	2	1.29 +/- 1.19	9	0.14 +/- 0.04	< 0.01	Yes
AA3	CA	2	5.96 +/- 0.15	9	3.21 +/- 0.20	< 0.01	Yes

Note: I = water absorption calculated from ASTM C1585

In addition to evaluating absorption data with respect to the concrete's damage state, absorption as a function of sealant type was also evaluated. Initial and secondary absorption calculated per ASTM C1585 were compared for each aging protocol. To facilitate comparisons across concrete types, all absorption values were normalized by its AA0-N final absorption value. For example, AA0-N field cores had a final absorption value of 4.93 mm while lab specimens had a final absorption of 3.75 mm. All absorption values measured for AA1, AA2, and AA3 specimens were then divided by either 4.93 mm or 3.75 mm, depending on whether it was a field core or lab specimen. Once normalized, absorption as a function of the square root of time could be plotted per ASTM C1585 (Figure 3.1). In Figure 3.1, all data is plotted as either a circle (field core) or triangle (lab concrete) where the color indicates which sealant type was used.

When evaluating the trends, it was clear that deteriorated field concrete absorbed water at a faster rate than identically cured laboratory mixed concrete, even with the different absorption capacity. This was expected as the deteriorated field concrete had a greater internal cracking network compared to laboratory mixed concrete. The standard deviation of the normalized initial absorption values for field cores was, on average, 0.131 mm/mm greater than laboratory concrete indicating that field cores were much more variable. When evaluating secondary absorption values, the findings were not as informative. Since most field cores were fully saturated by the end of the initial absorption period, the secondary absorption values were nearly constant, leading to a higher standard deviation for laboratory cast specimens. It should be noted that the purpose of this study is to determine if or when sealants can be applied to a foundation to be useful to slow pyrrhotite related deterioration.

Generally, silane (S) and polyurethane (PU) had the lowest normalized absorptions for both field and laboratory concrete and trended this way for all accelerated laboratory aging protocols evaluated. This could be a result of the aging protocol not being aggressive enough to age the concrete. However, the aging protocols in this study were intended to age the sealants to evaluate efficacy over time. ASTM C1585 appears to be capable of distinguishing between sealant performance and should be further evaluated as a potential test for a performance-based specification for sealants.

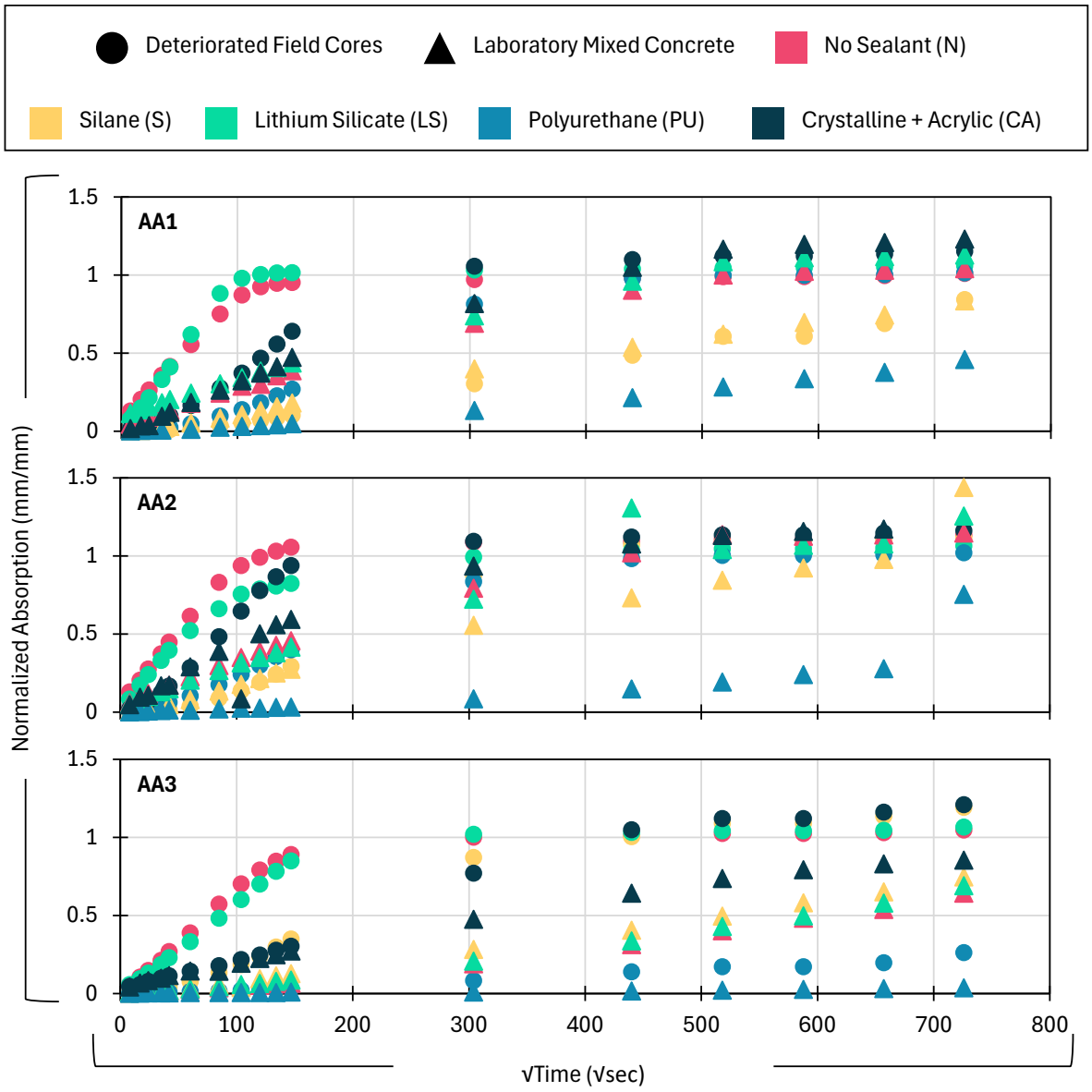

Figure 3.1. Initial and secondary absorption for different sealants. The uncertainty (relative standard deviation) for absorption value series was 5% for the field cores and was 3% for the lab cores.

9. CONCLUSIONS

This extended abstract aimed to provide initial findings related to the evaluation of potential mitigation methods for existing concrete foundations that were built with pyrrhotite bearing aggregate. Two conclusions could be drawn from this preliminary evaluation of data.

- In 14 of the 16 cases evaluated, laboratory mixed concrete had a lower absorption than identically sealed and aged field cores. A maximum damage threshold is necessary to adequately prescribe sealants or similar mitigation methods for existing foundations. This threshold should be determined by a physical evaluation of the concrete foundation (e.g., coring or non-destructive testing), rather than only relying on available information such as foundation age.

- Silane and polyurethane sealants meaningfully slowed water absorption in both field and laboratory concrete compared to other sealants evaluated. A performance-based framework to determine allowable mitigation techniques would provide for sealants/membranes of any chemical composition to be an eligible mitigation technique so

long as it meets the minimum performance requirements. Additional work is needed to fully develop this framework (e.g., which test method(s)) and the pass/fail metrics.

10. DISCLAIMERS

Certain commercial products or equipment are described in this paper to adequately specify the experimental procedure. In no case does such identification imply recommendation or endorsement by the National Institute of Standards and Technology, nor does it imply that it is necessarily the best available for the purpose.

11. ACKNOWLEDGEMENTS

This work was funded by congressionally appropriated Science and Technical Research Services (STRS) funds to assess pyrrhotite in concrete. Shawn Harris, David Goodwin, and Thomas Russo (all NIST) are thanked for their assistance with on-site coring and laboratory testing while Hariharan Iyer of NIST is thanked for help with statistical randomization of cores for testing. Foundation Solutions of New England, LLC and homeowners are also thanked for allowing NIST site access to sample deteriorated foundations prior to removal and replacement.

12. REFERENCES

[1] Jana, D. (2022) Cracking of residential concrete foundations in easter Connecticut, USA form oxidation of pyrrhotite. Case Stud. Constr. Mater. 16:e00909. https://doi.org/10.1016/j.cscm.2022.e00909

[2] Bashaw J.T. (2023) Connecticut's crumbling foundations: legal remedies and legislative responses, Conn. Law Rev. 55(4):855-925. https://digitalcommons.lib.uconn.edu/cgi/viewcontent.cgi?article=1571&context=law_review

[3] Carey, A.S. and Watson, S.S. (2025) Review of potential mitigation methodologies for existing concrete structures containing pyrrhotite-bearing aggregates. J. Build. Eng. 111:113408. https://doi.org/10.1016/j.jobe.2025.113408

[4] Jana, D. (2020) Pyrrhotite epidemic in eastern Connecticut: diagnosis and prevention. ACI Mater. J. 117(1):1-20. https://doi.org/10.14359/51718059

[5] Zhong, R., and Wille, K. (2018) Deterioration of residential concrete foundations: the role of pyrrhotite-bearing aggregate. Cement Concr. Compos. 94:53-61. https://doi.org/10.1016/j.cemconcomp.2018.08.012

[6] Rodrigues A, Duchesne J, Fournier B, Durand B, Shehata M, Rivard P (2016) Evaluation Protocol for Concrete Aggregates Containing Iron Sulfide Minerals. ACI Mat. J. 113 (3):349-359.

[7] Santos L, Chrysochoou M, Wille K, (2024) Influence of Instrument and Measurement Parameters on WD-XRF Method for Quantification of Sulfate and Sulfide in Concrete. Proc. of 1st Intern. Conf. on Iron-Sulfide Reactions in Conc. 44-48.

[8] MacDonald C, (2024) Interlaboratory Study of ISO 17025 Accredited Labs for Analysis of Total Sulphur in Aggregates Proc. of 1st Intern. Conf. on Iron-Sulfide Reactions in Conc. 66-70.

[9] Dixon, P., Ardebili, A.H., Goodwin, D., Nikolaou, S., Harris, S., Carey, A.S., Mengason, M., and Watson, S. (2025) Field observations of a pyrrhotite-affected residential foundation and the mechanical properties of extracted concrete cores – Connecticut site 1. NIST IR 8598, National Institute of Standards and Technology, Gaithersburg, MD. https://doi.org/10.6028/NIST.IR.8598

[10] ASTM International. ASTM C1585-20 – Standard Test Method for Measurement of Rate of Absorption of Water by Hydraulic-Cement Concretes, ASTM International, West Conshohocken, PA, 2020. https://doi.org/10.1520/C1585-20

Influence of Matrix Composition and Surface Treatments on Iron Sulfide–Induced Concrete Deterioration

Ana Rocha [(1)], Meshach Ojo [(2)], Richard Mulcahy [(3)], Kay Wille [(4)]

(1) Ph.D. Student, University of Connecticut (UConn), Storrs, CT USA, ana_carolina.vieira_rocha@uconn.edu

(2) Ph.D. Candidate, University of Connecticut (UConn), Storrs, CT USA, meshach.ojo@uconn.edu

(3) Massachusetts Department of Transportation, Hopkinton, MA USA, Richard.Mulcahy@dot.state.ma.us

(4) Professor, University of Connecticut (UConn), Storrs, CT USA, kay.wille@uconn.edu

Abstract

Concrete produced with pyrrhotite-bearing aggregates can experience progressive cracking and deterioration driven by pyrrhotite oxidation and associated expansive reactions, leading to severe damage in residential foundations. This study evaluates mitigation strategies using an Electrochemical Accelerated Test (EAT), in which a constant voltage accelerates ionic transport and deterioration. Three experimental groups were investigated. Group 1 evaluated cement composition by casting concrete cylinders (76 mm × 152 mm) with Type I, Oil-Well Class G, or Type IL cement while keeping the water-to-cement ratio constant. Group 2 evaluated matrix density by comparing mixtures cast at water-to-cement ratios of 0.40 and 0.60 using the same cement type. Group 3 evaluated external barriers by applying commercial surface treatments, including hydrophobic impregnation, pore-blocking agents, and a polymer coating, under vacuum prior to EAT exposure. Changes in cement composition alone did not prevent deterioration, although limestone cement reduced visible surface damage. Reducing the water-to-cement ratio delayed crack initiation from 7 to 14 days. Surface treatments influenced damage progression, with specimens treated with the film-forming coating exhibiting an 11 percent increase in relative dynamic elastic modulus and no visible surface cracking at the end of testing.

Keywords: *cement type; electrochemical accelerated test; polymer coating; pyrrhotite; water-to-cement ratio*

1. INTRODUCTION

Iron sulfide minerals such as pyrrhotite occur naturally in many rock types used as concrete aggregates. When incorporated into concrete, pyrrhotite oxidizes in the presence of oxygen and moisture, forming iron oxides and/or hydroxides and generating sulfuric acid, which leads to sulfate formation. These sulfates react with cementitious phases to form expansive products such as ettringite and, under carbonated conditions, thaumasite [1,2]. These reactions cause cracking and progressive deterioration [3], which can lead to loss of stiffness. Pyrrhotite induced deterioration has been widely reported in concrete infrastructure, with severe cases in northeastern Connecticut and Massachusetts [4].

Current mitigation efforts primarily focus on screening aggregates before construction or replacing foundations once deterioration becomes advanced. Several methods have been developed to identify sulfide bearing aggregates [5-7]. Risk based frameworks have also been proposed to support decision making for existing structures [8]. While effective for prevention and classification, these approaches do not offer mitigation strategies to use these aggregates safely or to extend the life span of affected foundations in early stages.

Lower water-to-cement ratios (w/c) produce denser cementitious matrices with reduced permeability, which limits the ingress of oxygen and moisture required for sulfide oxidation [9]. Cement composition also affects resistance to sulfate related distress, as systems with lower tricalcium aluminate (C_3A) content have been associated with improved phase stability [10]. In addition, concrete surface treatments were reported to limit moisture and oxygen transport through different mechanisms [11].

Studies focused on iron sulfide-bearing aggregates indicate that film forming coatings generally provide the greatest reduction in cracking and expansion, while other treatments show more variable performance [12].

This study evaluates the influence of cement type, water-to-cement ratio, and surface treatments on the deterioration of iron sulfide–bearing concrete using an Electrochemical Accelerated Test (EAT). The testing approach is based on electrochemical methods previously proposed to accelerate sulfide oxidation and assess deterioration in concrete specimens [13-16]. Damage progression was quantified using resonance frequency measurements and crack monitoring. The objective of this work is to assess how matrix chemistry and density affect deterioration in new construction and to determine the extent to which surface treatments can delay damage progression and extend the service life of existing foundations.

2. MATERIALS AND METHODS

2.1 Materials

Cements

Four cement types were used across different phases of the study. For the evaluation of cement composition, three cement types were used: a portland cement Type I (TI), an oil well cement Class G (OW), and a portland limestone cement Type IL (TIL). For the water to cement ratio study, a portland cement Type I/II was used exclusively to isolate the effect of water content while maintaining consistent cement chemistry. All portland cements conformed to ASTM C150 [17], the oil well cement conformed to API specifications, and the portland limestone cement conformed to ASTM C595 [18]. The reported oxide compositions of the cements are summarized in Table 2.1. The oxide composition of the Type IL cement is not reported, as the presence of limestone skews oxide-based analyses and makes them not representative of clinker chemistry [19].

Table 2.1: Percentage chemical composition of cements used in the study

Cement	SiO_2	Al_2O_3	Fe_2O_3	CaO	MgO	SO_3	Na_2O	K_2O
Type I/II	18.7	5.35	4.69	61.5	2.67	3.3	0.4	0.97
Type I	18.88	5.4	1.91	61.64	2.43	4.08	0.24	1.23
Oil-Well Class G	21.15	3.47	5.61	63.03	2.83	2.31	0.23	0.69

Aggregates

Natural river sand (RS) was used as the fine aggregate. Coarse aggregates included nonreactive aggregates sourced from Connecticut (NP) and pyrrhotite bearing aggregates sourced from Trois-Rivières, Quebec, Canada (CA1) with total sulfur content of 1.7 wt%. The nonreactive aggregates were selected based on their low total sulfur content, with measured values of 0.003 wt% for the sand and 0.009 wt% for the coarse aggregate. Coarse aggregates were divided into four size fractions: FR1 (<1.18 mm), FR2 (1.18–4.8 mm), FR3 (4.8–9.5 mm), and FR4 (12.7–16 mm). This simplified gradation allowed control over the placement of iron sulfide bearing aggregates within the concrete matrix. For the surface treatment phase of the study, concrete mixtures were prepared using nonreactive aggregates. A portion of the FR3 fraction was partially replaced with high-grade pyrrhotite-bearing material to introduce a controlled source of iron sulfide, resulting in an expected total sulfur content of approximately 0.5 percent in the concrete.

Surface Treatments

Three commercially available surface treatments were evaluated to represent different protection mechanisms used for existing concrete foundations. These included a hydrophobic impregnation (Po_HI), a pore blocking treatment based on sodium silicate (Po_PB), and a film forming acrylic polymer coating (Po_FF). Untreated specimens (Po_NT) were included as reference controls. The surface treatment groups, and specimen identifiers are summarized in Table 2.2.

Table 2.2: Experimental Parameters

Group	Specimen ID	w/c	Aggregate size fractions (FR)				Duration (days)	Study parameter
			FR1	FR2	FR3	FR4		
G1 (60V)	OW-NP	0.6	RS	RS	NP	NP	91	Reference
	TI-NP	0.6	RS	RS	NP	NP	91	Reference
	TIL-NP	0.6	RS	RS	NP	NP	91	Reference
	OW	0.6	RS	RS	CA1	CA1	42	Cement Composition
	TI	0.6	RS	RS	CA1	CA1	91	Cement Composition
	TIL	0.6	RS	RS	CA1	CA1	91	Cement Composition
G2 (60V)	w/c 0.4	0.6	RS	RS	CA1	CA1	140	w/c
	w/c 0.6	0.4	RS	RS	CA1	CA1	77	w/c
G3 (30V)	Po_NT	0.6	RS	RS	NP/Po	NP	35	Reference
	Po_HI	0.6	RS	RS	NP/Po	NP	105	Surface Treatment
	Po_PB	0.6	RS	RS	NP/Po	NP	56	Surface Treatment
	Po_FF	0.6	RS	RS	NP/Po	NP	112	Surface Treatment

2.2 Sample Preparation

Concrete mixtures were proportioned to represent typical residential foundation concrete used in Connecticut. For the cement composition study, mixtures were prepared with a water to cement ratio of 0.60 using Type I, Class G, or Type IL cement. For the water to cement ratio study, mixtures were prepared using Type I/II cement at water to cement ratios of 0.60 and 0.40. Cylindrical specimens measuring 76 mm in diameter and 152 mm in height were cast following ASTM C192 [20]. After casting, specimens were cured for 28 days under controlled conditions at approximately 23 °C and high relative humidity. All specimens were immersed in deionized water for 24 hours prior to electrochemical testing to achieve saturation.

For the surface treatment evaluation, cylindrical specimens measuring 50 mm in diameter and 100 mm in height were used. The smaller specimen diameter was selected to improve the relative penetration of surface treatments. Prior to treatment, specimens were submerged in the respective surface treatment and placed under vacuum (-0.05 MPa) for 8 minutes to promote penetration. Treated specimens were then allowed to air dry in accordance with manufacturer recommendations before accelerated exposure.

2.3 Electrochemical Accelerated Test

Deterioration was accelerated using the Electrochemical Accelerated Test, adapted from NT BUILD 4921999 and ASTM C1202-22, following modifications proposed by Rodolfo et al. (2023) and methodology by Ojo et al. (2024) [15,21,22]. In this method, saturated concrete specimens were positioned between two electrolyte reservoirs containing sodium chloride and sodium hydroxide solutions. Perforated graphite electrodes were placed against the exposed end faces of the specimens, and a constant electrical potential was applied across the specimen to promote ionic transport and accelerate oxidation of iron sulfide minerals. For the cement composition and water to cement ratio evaluations (Groups G1 and G2), a voltage of 60 V was applied to promote accelerated deterioration within a practical testing period. For the surface treatment evaluation (Group G3), a reduced voltage of 30 V was used to slow deterioration kinetics and limit premature degradation of polymer based treatments.

Damage progression was monitored using resonance frequency testing and visual crack assessment. Resonance frequency measurements were performed at selected intervals to calculate relative dynamic elastic modulus ($E_{dyn,c}$) in accordance with ASTM C215 [23]. Surface cracking and discoloration were documented through visual inspection and photographic records.

3. RESULTS AND DISCUSSION

3.1 Cement Composition (Group 1)

Figure 3.1 shows specimens cast with reactive aggregates using Oil Well Class G, Type I, and Type IL cements at the end of testing. Specimens cast with the limestone cement exhibited less visible cracking and fewer popouts, while Type I and Oil Well Class G specimens showed comparable damage. Testing of the Oil Well Class G specimens was stopped after 42 days due to increase in temperature during electrochemical exposure, which occurred after extensive surface cracking. Heating was observed during handling of the specimens, and testing was stopped as a precaution to prevent uncontrolled degradation. Specimens cast with nonreactive aggregates showed no visible cracking or oxidation after 91 days.

Figure 3.2 presents the evolution of $E_{dyn,c}$ during testing. Specimens cast with nonreactive aggregates showed an initial increase in $E_{dyn,c}$, followed by stabilization after approximately 40 days. In contrast, specimens with reactive aggregates exhibited an immediate decrease in $E_{dyn,c}$. Despite reduced surface damage, specimens cast with Type IL cement still experienced progressive loss of $E_{dyn,c}$, indicating that changes in cement chemistry alone did not prevent deterioration.

(a) TI body at 91 days (b) OW body at 42 days (c) TIL body at 91 days

Figure 3.1: Crack mapping at the end of EAT (Group 1)

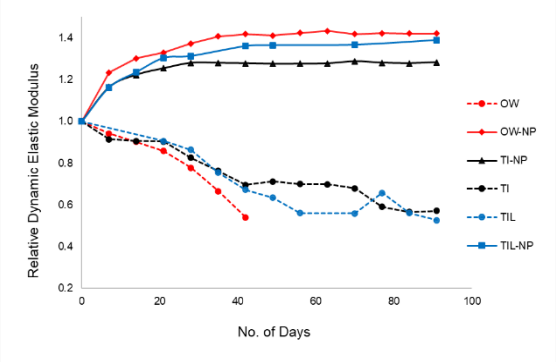

Figure 3.2: Relative $E_{dyn,c}$ over number of days (Group 1)

3.2 Water-to-cement ratio

The effect of the water-to-cement ratio was examined using concrete mixtures with w/c = 0.6 and w/c = 0.4. Specimens with w/c = 0.6 developed visible cracks within the first week of electrochemical exposure. In contrast, cracking in specimens with w/c = 0.4 was first observed after approximately 14 days. Both mixtures showed surface discoloration associated with iron oxidation. Figure 3.3 shows the measurements of $E_{dyn,c}$. The w/c = 0.6 specimens experienced rapid stiffness loss, reaching approximately 65 percent of the initial value by day 35 and about 40 percent by day 77. The w/c = 0.4 specimens retained nearly their initial stiffness at day 35 and remained above 75 percent through day 100. Stiffness decreased 50 percent at the end of testing, at 140 days, indicating delayed deterioration compared to w/c= 0.6 specimen.

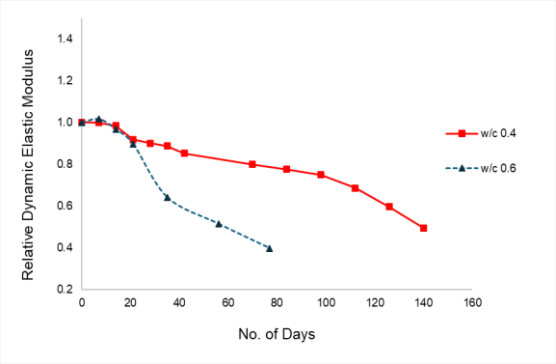

Figure 3.3: Relative $E_{dyn,c}$ over number of days (Group 2)

3.3 Surface Treatments

Surface treatment performance was evaluated by comparing three treated specimens with an untreated specimen containing pyrrhotite after exposure to the Electrochemical Accelerated Testing (EAT). Figure 3.4 shows the condition of the specimens at the end of testing. The untreated specimen (Po_NT) developed continuous cracking and popouts, leading to failure at 35 days despite the reduced test voltage. The pore blocking treatment (Po_PB) also showed continuous cracking and popouts, with failure at 56 days. The hydrophobic impregnation (Po_HI) delayed damage, with localized cracking observed after 105 days. In contrast, the acrylic film forming coating (Po_FF) showed no visible oxidation, cracking, or popouts after 112 days.

Figure 3.5 shows the relative $E_{dyn,c}$ of all specimens during the testing period. At 35 days, specimens that developed cracking showed reductions of 32 percent (Po_NT) and 45 percent (Po_PB), while Po_HI showed an increase of 2 percent. Po_NT specimen failed at 35 days, and Po_PB reached a 55 percent reduction by the end of testing. Po_HI progressively decreased to a 45 percent reduction by the end of testing. In contrast, Po_FF, which showed no visible damage, exhibited an increase of 11 percent at the end of testing.

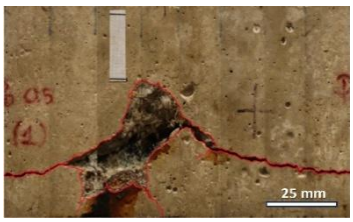

(a) Po_NT body at 35 days

(b) Po_PB body at 56 days

(c) Po_HI body at 105 days

(d) Po_FF body at 112 days

Figure 3.4: Crack mapping at the end of EAT (Group 3)

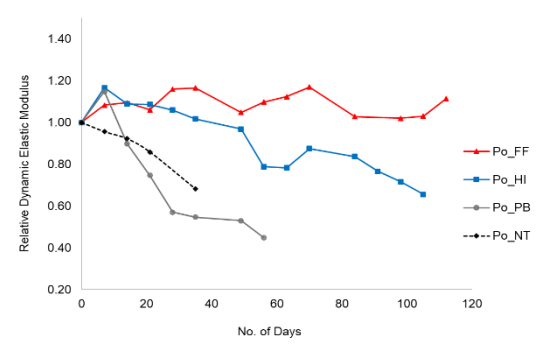

Figure 3.5: Relative $E_{dyn,c}$ over number of days (Group 3)

4. CONCLUSION

Changes in cement composition alone did not prevent deterioration, although limestone cement reduced visible surface damage. Reducing the water-to-cement ratio to 0.4 delayed crack formation. Surface treatments delayed damage progression, with film-forming coatings preventing cracking and maintaining stiffness over the test period.

ACKNOWLEDGEMENT

The research was funded by the US Department of Commerce, National Institute of Standards and Technology under award numbers: 70NANB21H113, 70NANB23H009 & 60NANB23D187, as well as by the Massachusetts Department of Transportation (MassDOT) under Project Part 1 (Award No. 015258-9240) and Project Part 2. The SEM was performed using the facilities in the Center for Advanced Microscopy and Materials Analysis (CAMMA) and XRD was performed at the X-Ray Lab, UConn. The authors thank Ryan Soucy, Melanie Ramos, Gaylene Frere, Luke Pellerin, and Wenting Liu for their assistance.

REFERENCES

[1] Zhong R, Wille K (2018) Deterioration of residential concrete foundations: The role of pyrrhotite-bearing aggregate. Cement and Concrete Composites 94:53–61.
[2] Duchesne J, Rodrigues A, Fournier B (2021) Concrete damage due to oxidation of sulfide-bearing aggregate: A review of recent advances and limitations. RILEM Technical Letters 6:82–92.
[3] Casanova I, Agulló L, Aguado A (1996) Aggregate expansivity due to sulfide oxidation: I. Reaction system and rate model. Cement and Concrete Research 26:993–998.
[4] Jana D (2022) Concrete deterioration from the oxidation of pyrrhotite: A state-of-the-art review. In: Maher MLJ (ed) Pyrite and Pyrrhotite: Managing the Risks in Construction Materials and New Applications. Nova Science Publishers, New York.
[5] Rodrigues A, Duchesne J, Fournier B (2016) Quantitative assessment of the oxidation potential of sulfide-bearing aggregates in concrete using an oxygen consumption test. Cement and Concrete Composites 67:93–100.
[6] Ramos V, Rodrigues A, Fournier B, Duchesne J (2016) Development of a quick screening staining test for detecting the oxidation potential of iron sulfide-bearing aggregates for use in concrete. Cement and Concrete Research 81:49–58.
[7] Marcelino AP, Calixto JM, Gumieri AG, Caldeira CL, Delbem ID, Ferreira MC (2020) A feasible evaluation protocol to determine the most reactive sulfide-bearing aggregate for use in concrete. Construction and Building Materials 242:118021.
[8] Santos L, Chrysochoou M, Wille K (2025) Development of a risk assessment framework for pyrrhotite-induced deterioration of concrete foundations in Connecticut and Massachusetts. Cement and Concrete Research 197:107006.
[9] Hover KC (2011) The influence of water on the performance of concrete. Construction and Building Materials 25:3003–3013.
[10] Sotiriadis K, Mróz R, Mácová P, Mazur AS, Krajnc A (2022) Long-term sulfate resistance of synthesized cement systems with variable C_3A/C_4AF ratio at low temperature or ambient conditions: Insights into the crystalline and amorphous phase assemblage. Cement and Concrete Research 160:106902.

[11] Pan X, Shi Z, Shi C, Ling T, Li N (2017) A review on concrete surface treatment: Part I—Types and mechanisms. Construction and Building Materials 132:578–590.
[12] Jeyakaran T, Pornsiri N, Saengsoy W, Tangtermsirikul S (2024) Surface treatments to control concrete deterioration caused by iron sulfide-bearing aggregates. Construction and Building Materials 416:135135.
[13] Ojo M, Kim D, Frame L, Wille K (2024) Electrochemical investigation of accelerated deterioration of concrete with iron-sulfide-containing aggregates. Cement and Concrete Research 182:107570.
[14] Castillo Araiza R, Fournier B, Duchesne J, Fecteau PL, Rodrigues A (2023) Evaluation of detrimental effects in concrete specimens due to the oxidation of sulfide-bearing aggregates after electrochemical treatment. Construction and Building Materials 411:134341.
[15] Castillo Araiza R, Fournier B, Duchesne J, Rodrigues A (2023) Electrochemical activation of oxidation of sulfide-bearing aggregates in concrete specimens. Cement and Concrete Research 170:107186.
[16] Castillo Araiza R, Rodrigues A, Fournier B, Duchesne J (2024) A new accelerated testing scheme to evaluate the potential oxidation reaction of sulfide-bearing aggregates in concrete specimens. Cement and Concrete Research 180:107507.
[17] ASTM International (2022) ASTM C150/C150M–22: Standard Specification for Portland Cement. ASTM International, West Conshohocken, PA.
[18] ASTM International (2024) ASTM C595/C595M–24: Standard Specification for Blended Hydraulic Cements. ASTM International, West Conshohocken, PA.
[19] Portland Cement Association (PCA). (2024). Why Bogue phase estimates are not applicable for blended cements (IS791). Washington, DC: Portland Cement Association.
[20] ASTM International (2025) ASTM C192/C192M–25: Standard Practice for Making and Curing Concrete Test Specimens in the Laboratory. ASTM International, West Conshohocken, PA.
[21] Nordtest (1999) NT BUILD 492: Concrete, mortar, and cement-based repair materials—Chloride migration coefficient from non-steady-state migration experiments. Nordtest, Espoo, Finland.
[22] ASTM International (2022) ASTM C1202-22: Standard test method for electrical indication of concrete's ability to resist chloride ion penetration. ASTM International, West Conshohocken, PA.
[23] ASTM International (2019) ASTM C215–19: Standard Test Method for Fundamental Transverse, Longitudinal, and Torsional Resonant Frequencies of Concrete Specimens. ASTM International, West Conshohocken,PA.